UNDERSTANDING THE MARGINAL SEAS OF NORTHEAST ASIA FOR TECTONICS AND SUBMARINE GEOHAZARDS

EDITED BY: Kwang-Hee Kim, Han-Joon Kim, Tianyao Hao and Xunhua Zhang

PUBLISHED IN: Frontiers in Earth Science

frontiers Research Topics

frontiers

ISSN 1664-8714
ISBN 978-2-88976-864-6
DOI 10.3389/978-2-88976-864-6

About Frontiers

Frontiers is more than just an open-access publisher of scholarly articles: it is a pioneering approach to the world of academia, radically improving the way scholarly research is managed. The grand vision of Frontiers is a world where all people have an equal opportunity to seek, share and generate knowledge. Frontiers provides immediate and permanent online open access to all its publications, but this alone is not enough to realize our grand goals.

Frontiers Journal Series

The Frontiers Journal Series is a multi-tier and interdisciplinary set of open-access, online journals, promising a paradigm shift from the current review, selection and dissemination processes in academic publishing. All Frontiers journals are driven by researchers for researchers; therefore, they constitute a service to the scholarly community. At the same time, the Frontiers Journal Series operates on a revolutionary invention, the tiered publishing system, initially addressing specific communities of scholars, and gradually climbing up to broader public understanding, thus serving the interests of the lay society, too.

Dedication to Quality

Each Frontiers article is a landmark of the highest quality, thanks to genuinely collaborative interactions between authors and review editors, who include some of the world's best academicians. Research must be certified by peers before entering a stream of knowledge that may eventually reach the public - and shape society; therefore, Frontiers only applies the most rigorous and unbiased reviews.
Frontiers revolutionizes research publishing by freely delivering the most outstanding research, evaluated with no bias from both the academic and social point of view. By applying the most advanced information technologies, Frontiers is catapulting scholarly publishing into a new generation.

What are Frontiers Research Topics?

Frontiers Research Topics are very popular trademarks of the Frontiers Journals Series: they are collections of at least ten articles, all centered on a particular subject. With their unique mix of varied contributions from Original Research to Review Articles, Frontiers Research Topics unify the most influential researchers, the latest key findings and historical advances in a hot research area! Find out more on how to host your own Frontiers Research Topic or contribute to one as an author by contacting the Frontiers Editorial Office: frontiersin.org/about/contact

UNDERSTANDING THE MARGINAL SEAS OF NORTHEAST ASIA FOR TECTONICS AND SUBMARINE GEOHAZARDS

Topic Editors:
Kwang-Hee Kim, Pusan National University, South Korea
Han-Joon Kim, Korea Institute of Ocean Science and Technology (KIOST), South Korea
Tianyao Hao, Institute of Geology and Geophysics, Chinese Academy of Sciences (CAS), China
Xunhua Zhang, Qingdao Institute of Marine Geology (QIMG), China

Citation: Kim, K.-H., Kim, H.-J., Hao, T., Zhang, X., eds. (2022). Understanding the Marginal Seas of Northeast Asia for Tectonics and Submarine Geohazards. Lausanne: Frontiers Media SA. doi: 10.3389/978-2-88976-864-6

Table of Contents

frontiers | Frontiers in Earth Science

TYPE Editorial
PUBLISHED 22 July 2022
DOI 10.3389/feart.2022.969451

OPEN ACCESS

EDITED AND REVIEWED BY
Alessandro Tibaldi,
University of Milano-Bicocca, Italy

*CORRESPONDENCE
Kwang-Hee Kim,
kwanghee@pusan.ac.kr

SPECIALTY SECTION
This article was submitted to Marine Geoscience,
a section of the journal
Frontiers in Earth Science

RECEIVED 15 June 2022
ACCEPTED 28 June 2022
PUBLISHED 22 July 2022

CITATION
Kim K-H, Kim H-J, Hao T and Zhang X (2022), Editorial: Understanding the marginal seas of northeast asia for tectonics and submarine geohazards. *Front. Earth Sci.* 10:969451.
doi: 10.3389/feart.2022.969451

Editorial: Understanding the marginal seas of northeast asia for tectonics and submarine geohazards

Kwang-Hee Kim[1]*, Han-Joon Kim[2], Tianyao Hao[3,4,5] and Xunhua Zhang[6]

[1]Department of Geological Sciences, Pusan National University, Busan, South Korea, [2]Marine Active Fault Research Center, Korea Institute of Ocean Science and Technology, Busan, South Korea, [3]Key Laboratory of Petroleum Resources Research, Institute of Geology and Geophysics, Chinese Academy of Sciences, Beijing, China, [4]Institutions of Earth Science, Chinese Academy of Sciences, Beijing, China, [5]University of Chinese Academy of Sciences, Beijing, China, [6]Qingdao Institute of Marine Geology, Qingdao, China

KEYWORDS

crust and upper mantle structure, submarine active fault, tectonics in Northeast Asia, submarine landslide, active and passive marine seismic methods, seismic hazards, marine sedimentary processes, Paleoenviroment

Editorial on the Research Topic
Understanding the marginal seas of northeast asia for tectonics and submarine geohazards

The past three decades have brought large steps forward in our understanding of the tectonics and submarine geohazards of the marginal seas of Northeast Asia. This improved understanding has been accompanied by a major increase in the number of geophysical experiments and data, which have shed light on this topic. Given the rise in urbanization and population growth, assessing the risk of submarine geohazards is increasingly important; therefore, this is the ideal time to present the latest observations, models, applications, data syntheses, and advances. This Research Topic comprises eleven papers covering multiple aspects of the tectonics and submarine geohazards of Northeast Asia. Many articles in this Research Topic present integrated studies linking multiple geophysical datasets and techniques to advance innovative ideas and models.

Zhang and Luan investigated variations of the crustal thickness, heat flow, fault patterns, and petrology to unravel the tectonic evolution of the Okinawa Trough. Their study shows that the northern, central, and southern sections of the Okinawa Trough are in an early back-arc extensional setting, a transition between back-arc rifting and oceanic spreading, and an early seafloor spreading setting, respectively.

Xu et al. analyzed the data from the third phase of the China Array to reveal details of the crustal thickness, V_p/V_s ratio, and polarization direction beneath the Trans-

North China Orogen (TNCO). Their results reveal lateral variations in crustal structure, which are correlated with the Bouguer anomaly. They further propose that the crustal deformation of the TNCO could be a consequence of the counterclockwise rotation of the Ordos block.

Li et al. studied the fault system in the southern Liaodong Bay sub-basin by analyzing 3-D seismic reflection data. Their results reveal the geometry of the fault system and of the stratigraphic units controlled by the fault system, as well as the complex evolutionary history of the area. They applied their results to better understand hydrocarbon accumulation in the study area.

Kim et al. confirmed a close spatial relationship between the rift bounding fault and earthquake epicenters in the South Korea Plateau (SKP) in the East Sea (Japan Sea). The faults in the SKP were reactivated in the mid-Miocene and have continued moving with a strike-slip sense. Kim et al. estimated the maximum expected magnitude and return period of earthquakes at the SKP using a statistical approach.

Liu et al. produced high-resolution P-wave velocity models of the eastern North China Craton (NCC) and the Yangtze Craton (YZC) using four active-source wide-angle onshore–offshore seismic surveys. They propose a five-stage model for the collision between the YZC and NCC based on these velocity models and regional gravity and magnetic anomalies.

Seismic and electromagnetic images by Deng et al. show low-velocity, high-conductivity anomalies associated with the volcanic plumbing system in northeast China. Their images suggest that these volcanoes are back-arc intraplate volcanos and that the genesis of their magma is closely linked to subduction of the western Pacific slab into the mantle transition zone and the water released during this process. They conclude that more extensive, higher-resolution geophysical images are required to reliably determine volcanogenic mechanisms in northeast China.

Wang et al. imaged the strong, complex lateral velocity variations and low velocities in the shallow sediment on the floor of the Yellow Sea using ocean bottom seismometers (OBS) and multicomponent Scholte-wave dispersion analysis. Uplift, active faults, and thrust nappe structures can be identified in their pseudo-2D shear-wave velocity profile of the shallow sediments.

Routine operations in seismic data processing including phase detection, phase picking, association, and determination of earthquake source parameters are time-consuming and labor-intensive. Wu et al. tackled this issue by building a deep learning-powered automatic workflow and applying it to an OBS array in the Challenger Deep. The automated workflow produced a high-resolution local earthquake catalog, which is essential for understanding the active faults in the study area. Although they applied the method to OBS data, it is also applicable to land-based seismic observations.

Yao et al. analyzed the geophysical characteristics of the southwestern margin of the South China Sea (SCS), including the thermal structure, 3D shear wave velocity, and gravity. Their results provide a framework for understanding the geological evolution and continental margin dynamics of the SCS.

Although there are clear historical records of tsunamis in Korea, the magnitude of the earthquakes recorded since the start of instrumental seismic observations is too low to produce such devastating tsunamis. Ha et al. revisited the historical tsunami record, compiled active fault maps for the area off the eastern coast of the Korean peninsula, and constructed tsunami scenarios. They then used numerical modeling to estimate runup heights in the proposed scenarios. Their results successfully hindcast the occurrence and effects of tsunamis in the local historical literature.

Lee et al. investigated the tectonostratigraphic evolution of the southwestern Ulleung Basin in the East Sea (Japan Sea) using multi-channel seismic reflection profiles and offshore wells. They divided the sedimentary succession of the Ulleung Basin into four sequences and proposed a four-stage tectonic model that includes back-arc opening, tectonic inversion, post inversion, and neotectonic stages.

Submarine landslides have attracted attention as a cause of large tsunamis. Pan et al. analyzed the potential for submarine landslides to trigger damaging tsunamis along the coast of Southern Central Vietnam (SCV). Their results show a tsunami with wave heights of 5 m may arrive at the closest coastline <30 min after a submarine landslide. This is a serious threat to communities along the coastlines of the SCS and sustained action is required to reduce the risk to life and property.

We hope the wide spectrum of geophysical data and applications presented here can motivate new research projects involving the deployment of new instruments on the seafloor, multichannel seismic profiles across borders, and the application of innovative techniques and multi-disciplinary approaches to tackling long-standing questions in the region. The guest editors are very grateful to the authors for their excellent contributions and to colleagues who provided timely, critical, and constructive reviews of the manuscripts. We also

thank the journal editorial team for their efforts in making this Research Topic possible.

Author contributions

Editorial written by K-HK and edited by all other guest editors.

Funding

K-HK was supported by the KMA Research Development Program (KMI2022-00610). TH was supported by project 91858212, 90814011 of Natural Science Foundation China. XZ was supported by the China-ASEAN Maritime Cooperation Fund Project (No. 12120100500017001).

Conflict of interest

The authors declare that the research was conducted in the absence of any commercial or financial relationships that could be construed as a potential conflict of interest.

Publisher's note

frontiers in Earth Science

ORIGINAL RESEARCH
published: 21 October 2021
doi: 10.3389/feart.2021.753612

Crustal Anisotropy Beneath the Trans-North China Orogen and its Adjacent Areas From Receiver Functions

Xiaoming Xu[1,2]*, *Zhifeng Ding*[1,2], *Li Li*[1,2] and *Fenglin Niu*[3,4]

[1]Institute of Geophysics, China Earthquake Administration, Beijing, China, [2]Key Laboratory of Earthquake Source Physics, China Earthquake Administration, Beijing, China, [3]Department of Earth, Environmental and Planetary Sciences, Rice University, Houston, TX, United States, [4]State Key Laboratory of Petroleum Resource and Prospecting, Unconventional Gas Institute, China University of Petroleum , Beijing, China

As an important segment of the North China Craton, the Trans-North China Orogen (TNCO) has experienced strong tectonic deformation and magmatic activities since the Cenozoic and is characterized by significant seismicity. To understand the mechanism of the crustal deformation and seismic hazards, we determined the crustal thickness (*H*), *Vp*/*Vs* ratio (κ) and crustal anisotropy (the fast polarization direction φ and splitting time τ) beneath the TNCO and its adjacent areas by analyzing receiver function data recorded by a dense seismic array. The (H, κ) and (φ, τ) at a total of 309 stations were measured, respectively. The Moho depth varies from ~30 km beneath the western margin of the Bohai bay basin to the maximum value of ~48 km beneath the northern Lüliang Mountain, which shows the positive and negative correlations with the elevation and the Bouguer anomaly. The average φ is roughly parallel to the strikes of the faults, grabens and Mountains in this study area, whereas a rotating distribution is shown around the Datong-Hannuoba volcanic regions. Based on the φ measured from the Moho Ps and SKS/SKKS phases, we propose that the crustal deformation and seismic hazards beneath the TNCO could be due to the counterclockwise rotation of the Ordos block driven by the far-field effects of the India-Eurasian collision.

Keywords: North China craton, moho depth, crustal anisotropy, receiver function, ChinArray

OPEN ACCESS

Edited by:
Tianyao Hao,
Institute of Geology and Geophysics (CAS), China

Reviewed by:
Ryan Porter,
Northern Arizona University, United States
Alexis Rigo,
UMR8538 Laboratoire de géologie de l'Ecole Normale Supérieure (LG-ENS), France

***Correspondence:**
Xiaoming Xu
xuxiaoming@cea-igp.ac.cn

Specialty section:
This article was submitted to Solid Earth Geophysics, a section of the journal Frontiers in Earth Science

Received: *05 August 2021*
Accepted: *11 October 2021*
Published: *21 October 2021*

Citation:
Xu X, Ding Z, Li L and Niu F (2021) Crustal Anisotropy Beneath the Trans-North China Orogen and its Adjacent Areas From Receiver Functions. Front. Earth Sci. 9:753612. doi: 10.3389/feart.2021.753612

INTRODUCTION

The North China Craton (NCC) as the largest and oldest known Archean craton in China is located in the eastern margin of the Eurasian plate (Zhao et al., 2001). The NCC consists of the western NCC (WNCC) and the eastern NCC (ENCC), which are separated by a Paleoproterozoic orogen, the Trans-North China Orogen (TNCO) (**Figure 1**). The WNCC, mainly including the Ordos Block (OB) and its surrounding Grabens, the Hetao Graben (HTG) and the Weihe Graben (WHG), is dominated by the stable and thick lithosphere, while the ENCC underwent significant reactivation and destruction during Mesozoic and Cenozoic (Chen and Ai, 2009; Zhu et al., 2011). The TNCO, a composite unit composed of the Lüliang Mountain (LLM), the Taihang Mountain (THM) and the Fenhe Graben (FHG), was formed by the collision of the ENCC and WNCC in the Late Paleoproterozoic (~1.8 Ga), resulting in the final amalgamation of the NCC (Zhao et al., 2001). As a transition zone of the surface topography, lithospheric thickness (Chen

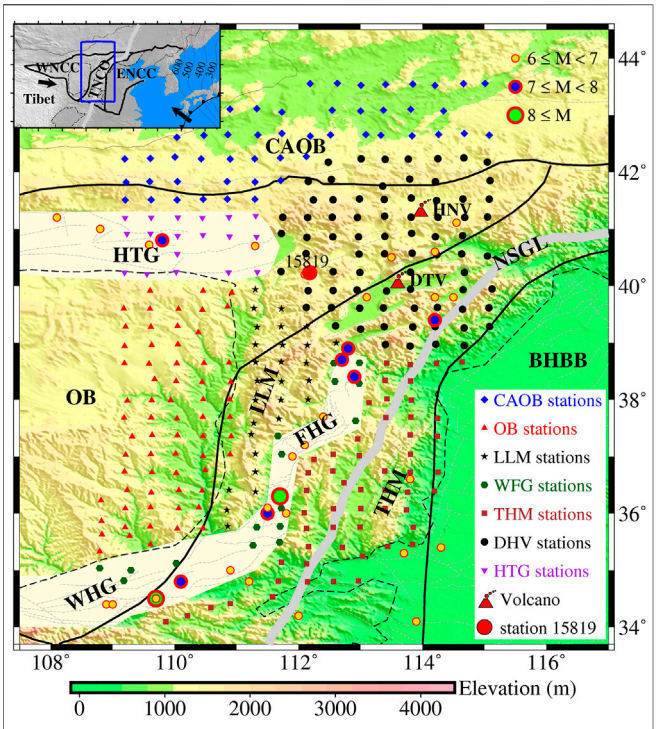

FIGURE 1 | Tectonic setting map showing the seismic stations used in this study. Stations located in different blocks are indicated with different symbols. The red solid circle represents station 15,819 as an example of the H-κ analysis and crustal anisotropy in **Figures 2**,**3**. The color circles with red solid line are the large historic earthquakes (M ≥ 6, Liu and Wang, 2012). The thick gray line denotes the North-South Gravity Line (NSGL). Lightyellow regions are Hetao, Weihe and Fenhe grabens. DTV, the Datong Volcano; HNV, the Hannuoba Volcano; CAOB, the Central Asia Orogenic Belt; OB, the Ordos Block; LLM, the Lüliang Mountain; THM, the Taihang Mountain; BHBB, the Bohai Bay Basin; HTG, the Hetao Graben; WHG, the Weihe Graben; FHG, the Fenhe Graben. Inset shows the location of the Trans-North China Orogen with the blue rectangular. The black thick arrowhead indicates the absolute plate motion (APM) direction from GSRM v2.1 model (Kreemer et al., 2014).

and Ai, 2009) and gravity anomalies (Deng et al., 2014) between the ENCC with lithospheric thinning and the WNCC remaining stable cratonic roots, the TNCO has been accompanied by complicated tectonic deformation and magmatic activity during the episodic geological evolution (Ren et al., 2002; Xu et al., 2004; Zhu et al., 2011). The relative movement of the TNCO estimated from GPS is at a rate of ~5–11 mm/year (Shen et al., 2000; Zhao et al., 2015), which is characterized by the distribution of strong earthquakes (Xu and Ma, 1992; Gao et al., 2020) (**Figure 1**). The mechanism of crustal deformation is important in understanding the tectonic evolution and seismic hazards in this study area. However, the details on crustal deformation beneath the TNCO and its adjacent areas are still being discussed and debated recently (Tian and Zhao, 2013; Zhang et al., 2016; Yang et al., 2018; Schellart et al., 2019; Zheng et al., 2019; Cai et al., 2021; Chang et al., 2021). Further studies on crustal structure and anisotropy are essential for constraining the crustal deformation mechanism.

Crustal deformation can produce anisotropy on the wavelength scale of seismic waves (Nicolas and Christensen, 1987; Mainprice and Nicolas, 1989). Therefore, measurements of crustal anisotropy can also help us understand the mechanism of crustal deformation and the process of tectonic evolution. Generally, the upper crustal anisotropy is attributed to the stress-induced alignment of cracks (Crampin and Peacock, 2008), while seismic anisotropy in the mid-to-lower crust and upper mantle is more likely to be caused by strain-induced lattice preferred orientation of minerals (Meissner et al., 2002). S waves from local earthquakes located in the upper crust have been used to estimate the upper crustal anisotropy beneath the ENCC (Gao et al., 2011). In the upper mantle, seismic anisotropy is commonly determined by the splitting of the SKS/SKKS phases (Zhao et al., 2008; Chang et al., 2017; 2021). There is a gap, obviously, between seismic anisotropy derived from local S waves and teleseismic SKS/SKKS phases to measure the mid-to-lower crustal anisotropy. Sherrington et al. (2004) pointed out that seismic anisotropy inside the mid-to-lower crust cannot be ignored when we look at the crustal deformation. The Ps phase from receiver functions, a P-to-S converted wave at the Moho, is an ideal phase to estimate seismic anisotropy within the whole crust.

We noticed that Liu and Niu (2012) developed a comprehensive technique that employed the radial (R) and transverse (T) receiver functions to compute the crustal anisotropy and Sun et al. (2012) further added a harmonic analysis to enhance the robustness of the measurements. Based on these methods, crustal anisotropy beneath the southeastern and northeastern Tibetan plateau was calculated to investigate the mechanism of the crustal deformation and thickening (Sun et al., 2012; Wang et al., 2016; Xu et al., 2018). Yang et al. (2018) and Zheng et al. (2019) also measured the splitting of the Moho Ps phases from receiver functions and observed the spatial distribution of crustal anisotropy beneath the northeastern TNCO, respectively. Results mentioned above confirmed that crustal anisotropy has been successfully estimated from the splitting of the Moho Ps phases and performed to study the crustal deformation.

To further improve the understanding of the crustal structure and deformation beneath the TNCO and its adjacent areas, we determined the Moho depth, *Vp*/*Vs* ratio and crustal anisotropy using receiver functions extracted from the teleseismic data recorded by a temporary dense array of broadband seismographs in this study. We further discussed the potential implications of the crustal structure evolution and deformation mechanism by comparing other published models (Deng et al., 2014; Shen et al., 2016; Wang et al., 2020; Chang et al., 2021; Huang et al., 2021).

DATA AND METHODS

Data

The ChinArray project plans to roll over mainland China with a transportable array consisting of more than 1,000 broadband seismographs with a station spacing of ~30–40 km in order to understand the structure of Earth's interior (ChinArray-Himalaya,

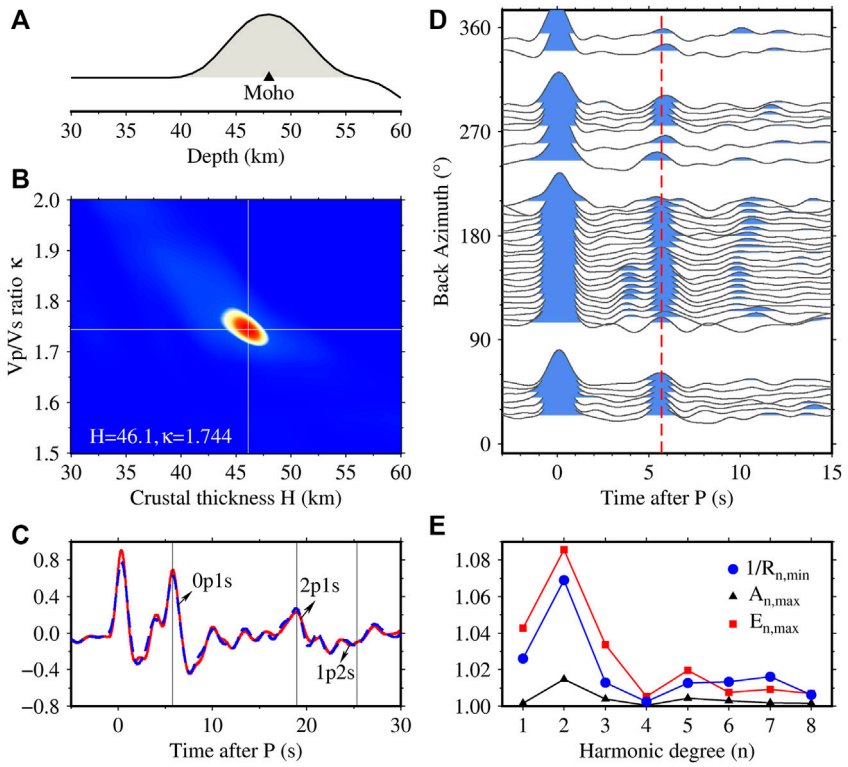

FIGURE 2 | (A) denotes the stacked receiver function after the time-to-depth conversion of station 15,819. The maximum peak marked by black triangle indicates the initial Moho depth. **(B)** is the result of *H*-κ analysis at station 15,819. The cross white lines indicate the location of the peak amplitude. **(C)** shows the time domain stacked receiver functions with the Ps slowness (red solid line) and the 2p1s slowness (blue dashed line). Note that amplitude of the phases is larger when they are stacked with the correct slowness. **(D)** plots the radial receiver functions as a function of back azimuth at the station 15,819. The red dashed lines denote the average arrival time of the Moho Ps phase. **(E)** indicates the result of harmonic analysis at station 15,819. The reciprocal of the minimum residual, the maximum value of peak amplitude and total energy are plotted as a function of the harmonic degree.

2011). The third phase deployment of the ChinArray project covers an area of 8° × 10° centered at the TNCO (**Figure 1**). Each seismograph was equipped with a Guralp CMG-3ESP or CMG-3ESPC seismometer and a Reftek 130 data logger. In this study, we used a total of 309 stations with high quality three component waveform recordings from April 2016 to January 2019 and then selected 440 earthquakes (**Supplementary Figure S1**) with a magnitude greater than 5.0 and an epicentral distance between 30° and 90° to calculate the receiver functions. As shown in **Supplementary Figure S1**, most of the teleseismic events come from inside the western Pacific subduction zone and the Java trench. However, with the other earthquakes, the overall coverages in backazimuth and distance are reasonably good.

Methods

The true orientation of the two horizontal components is important when we use the three-component recordings of the teleseismic events to generate receiver functions (Zeng, et al., 2020). Therefore we first employed the P wave particle motions of teleseismic events to estimate the true sensor orientation for each station with the method proposed by Niu and Li (2011) before rotating the two horizontal components into the radial (R) and transverse (T) directions based on the great arc raypaths connecting the events and stations.

Following the previous studies (Vinnik, 1977; Niu and Kawakatsu, 1998; Niu et al., 2007), we further projected R and T components to the principal directions (longitudinal, P, and in-plane transverse, SV) estimated from the covariance matrix in order to minimize the P wave energy in the receiver function. We then used the "water-level" deconvolution technique (Clayton and Wiggins, 1976; Ammon, 1991) to compute receiver functions in the frequency domain. The "water level" and the corner frequency of the Gaussian low pass filter were set to be 0.01 and 1.5 Hz, respectively. After careful inspection, a total of 33,772 receiver functions from the 309 stations were selected with a station average of ~109 receiver functions.

The crustal thickness and average Vp/Vs ratio were estimated at each station by the two-step analysis following Niu et al. (2007). We first computed the initial crustal thickness using the N^{th}-root stacking technique (Muirhead, 1968; Kawakatsu and Niu, 1994) with the Moho Ps phase alone. By searching for the range of 20–70 km, we defined the depth with the maximum amplitude as the initial crustal thickness. **Figure 2A** shows the depth stacking at the station 15,819 and a clear P to S conversion peak at ~48 km. Then a refined *H*-κ analysis (Zhu and Kanamori, 2000) was used to estimate the final crustal thickness, *H*, and Vp/Vs ratio, κ:

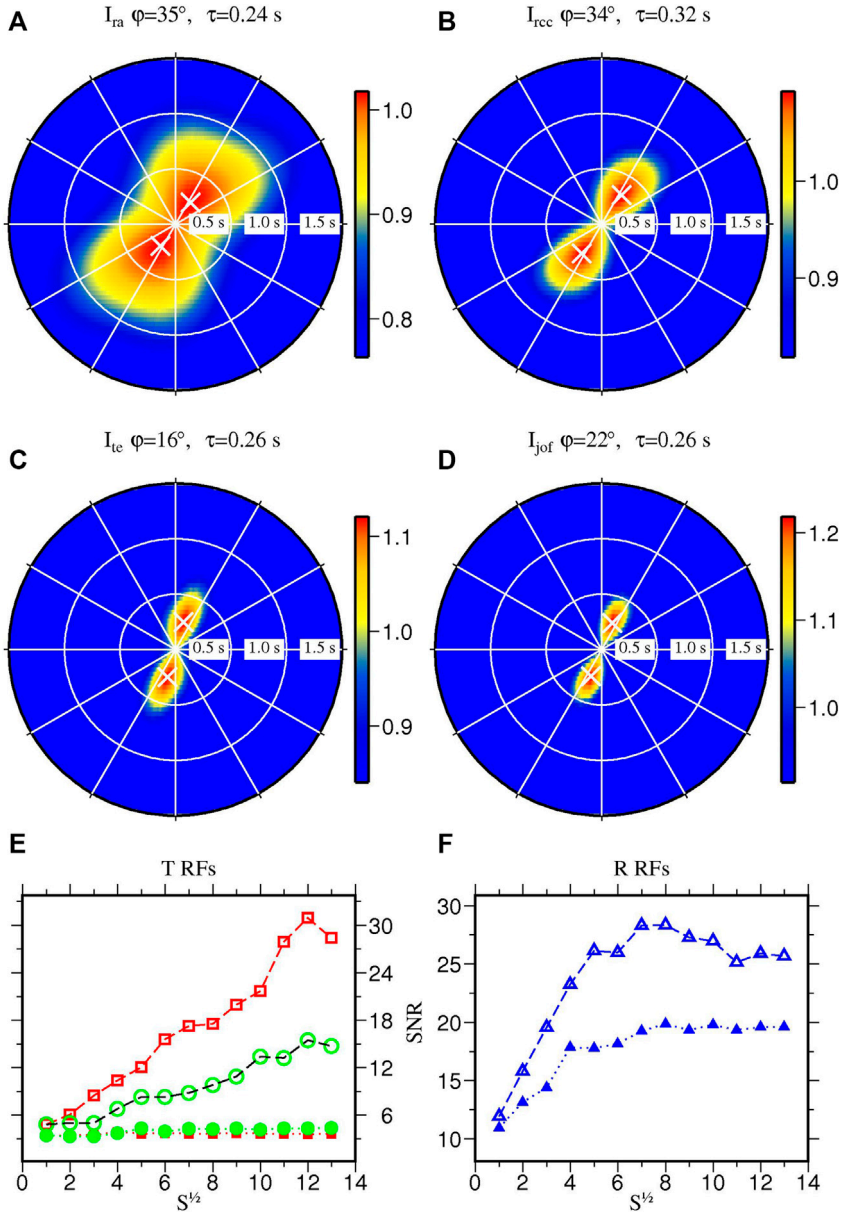

FIGURE 3 | Results of crustal anisotropy from the joint analysis with multi-component receiver function data at station 15,819. **(A–C)** show three individual methods to estimate seismic anisotropy: 1) radial energy maximization with a cosine moveout correction; 2) radial correlation coefficient maximization; 3) transverse energy minimization. (d) is the joint solution. (φ, τ) are searched in the range of 0–360° and 0–1.5 s with an increment of 1° and 0.02 s, respectively. White plus marks the measured (φ, τ) where the objective functions reach to maximum. **(E,F)** show the calculated SNRs of stacked receiver function data as a function of the square root of the subsample numbers, $S^{1/2}$. Open and filled symbols in **(E,F)** indicate SNR calculated from stacks of receiver functions before and after the removal of seismic anisotropy measured by the joint receiver function. More specifically, opened squares shown in **(E)** indicate stacks from T receiver functions without anisotropy correction but with polarity correction, while opened circles are from T receiver function with no corrections of anisotropy and polarity. Filled squares and circles represent stacks after correction of anisotropy, and with and without polarity correction, respectively.

$$s(H,\kappa) = \frac{c(\kappa)}{K}\sum_{i=1}^{K}\left(w_1 r_i(t_1) + w_2 r_i(t_2) + w_3 r_i(t_3)\right)$$

Here K denotes the total number of receiver functions at a given station and $r_i(t)$ is the amplitude of the i^{th} receiver function at the relative arrival times of the 0p1s (t_1), 2p1s (t_2) and 1p2s (t_3), following the phase notation of npms introduced by Niu et al. (2007), with respect to the direct P wave. w_1, w_2, and w_3 are the weights of the three time windows, which are assigned to 0.5, 0.25, and 0.25, respectively. c (κ) is a coherence index of the three phases, which is introduced by Niu et al. (2007) to reduce the trade off between H and κ. We searched for H within ±20 km of the initial depth derived from the depth stacking and κ in the

range of 1.5–2.0. H and κ were determined when the summed amplitude, s (H,κ), reached its maximum. The result of H-κ analysis at the station 15,819 is shown in **Figure 2B**, which gives an estimate of H = 46.1 km and κ = 1.744.

For the comprehensive analysis of crustal anisotropy (Liu and Niu, 2012), we first calculated the moveout and made corrections for each station using the estimates of the above H-κ analysis so that all the cluster receiver functions were expected to have a Moho Ps arrival time equivalent to the one with an epicentral distance of 60° and a source depth of 0 km. The R and T receiver functions were further normalized with the peak amplitude of the P wave. Then, we analyzed the R and T receiver functions as a function of back azimuth to study the systematic variations in the peak Ps arrival time of the R receiver functions and polarity changes of the T receiver functions. The normalized maximum amplitude ($A_{n,max}$), maximum energy ($E_{n,max}$), and minimum total residual ($R_{n,min}$) between each receiver function and the stacked receiver function were calculated and summed along a harmonic moveout with a degree varying from 1 to 8 by the method proposed by Sun et al. (2012). In **Figures 2D,E**, we show the R receiver functions plotted as a function of back azimuth and the result of harmonic analysis at the station 15,819. Then, we employed three individual objective functions (IFOs) and one joint objective function (JOF), and performed a statistical analysis on the robustness to estimate the crustal anisotropy beneath each station. A more detailed description on the IFOs, JOF and the statistical analysis can be found at Liu and Niu (2012). Here, the **Figure 3** shows the analysis of crustal anisotropy at station 15,819. The fast direction (φ) and the splitting time (τ) estimated from three IOFs and the JOF are shown in **Figures 3A–C** and **Figure 3D**, and show good agreement in this four measurements. The robustness of the estimated φ and τ is further evaluated by comparing the SNRs of the Ps on the R and T components before and after the correction of crustal anisotropy in **Figures 3E,F**.

RESULTS

Based on the H-κ analysis and the crustal anisotropy estimation, we obtained 309 measurements of Moho depth and Vp/Vs ratio (**Supplementary Figure S2**), and 62 robust parameters of the crustal anisotropy (**Figure 5**). All estimated results are listed in **Supplementary Table S1**, which is organized by grouping stations in the following tectonic units: the Central Asia Orogenic Belt (CAOB), the Ordos Block (OB), the Lüliang (LLM) and Taihang (THM) Mountains, the Bohai Bay Basin (BHBB), the Hetao Graben (HTG), the Weihe-Fenhe Graben (WFG) and the Datong-Hannuoba (DHV) Volcano. We also present the average crustal thickness, Vp/Vs ratio, and crustal anisotropy, together with other parameters, in **Supplementary Table S2** for the further comparison.

The estimated (H, κ) at 309 stations were interpolated into 1,419 meshed grids of 0.25° × 0.25° to show the lateral variations of Moho depth (**Figure 4A**) and Vp/Vs ratio (**Figure 4B**) beneath the study area, respectively. The Moho depth varies from ~30 to ~48 km (**Figure 4A**). Overall, the crust across the study area gradually tends to be thick from the southeast to northwest. Specifically, the thinnest crust, less than 32 km, is observed beneath the western margin of the BHBB while the thickest part (~48 km) is nearby the northern LLM. The eastern HTG appears to have the highest Vp/Vs ratio up to ~1.90, while the lowest Vp/Vs ratio, generally below 1.65, is observed between the OB and LLM. The average Vp/Vs ratio of the CAOB is relatively lower in this study area (**Supplementary Table S2**), but most of the study areas seem to be higher than the global average 1.74 (Kennet et al., 1995; Zhu, 2018).

We measured the crustal anisotropy at all the stations in the study area and listed the estimated parameters in the **Supplementary Table S1**. However, the crust with weak anisotropy or isotropy beneath the stations does not lead to the corresponding pattern of the harmonic degree (n = 2) and the SNR test (**Figure 2E** and **Figures 3E,F**). Among the 309 stations in the study area, 7 stations did not pass the SNR test. We used "–" to indicate the measurements of 42 stations without enough back azimuthal coverage for anisotropy analysis and 7 stations with the Ps phase splitting time greater than the maximum time shift (1.5 s) in the **Supplementary Table S1**. Combined with the harmonic analysis, a total of 62 reliable measurements with a harmonic order of n = 2 are finally shown in the **Figure 5** to characterize the crustal anisotropy beneath the TNCO and its adjacent areas. In addition, we take station 15,819 as an example to exhibit the crustal anisotropy beneath the western DHV (**Figure 1**), which was measured with the fast polarization direction φ = 22° and splitting time τ = 0.26 s, respectively. The average (φ, τ) of each geological block is also listed in **Supplementary Table S2**. The average φ measured from most of stations is roughly parallel to the strike of major geological blocks, for example, the strike of the CAOB, LLM, THM, HTG and WFG. The average τ at most of tectonic blocks is approximately 0.3 s and the peak average value (τ = 0.45 s) is located at the WFG. Particularly, stations located at the DHV and their surrounding regions (marked by white ellipse in **Figure 5**) are distributed in rotating fast polarization directions.

We also compared our Moho Ps fast polarization direction and splitting time at the 62 stations with those measured from the SKS/SKKS phases (blue lines, Chang et al., 2021), the GPS velocity (green arrow, Zhao et al., 2015) and the absolute plate motion (APM, thick black vectors, Kreemer et al., 2014) in the **Figure 5**. From the average results of these four datasets at each tectonic unite (**Supplementary Table S2**), we found that the datasets of the CAOB show roughly similar directions, but certain differences at other blocks, the OR, WFG, DHV, LLM and THM. Besides, the Moho Ps splitting times of the tectonic unites are much smaller than those of SKS/SKKS phase. In other words, the SKS/SKKS splitting times are mainly originated inside the mantle beneath the TNCO and its adjacent areas.

DISCUSSION

The distributions of the estimated (H, κ) and (φ, τ) show significant lateral variations, which suggests the crustal

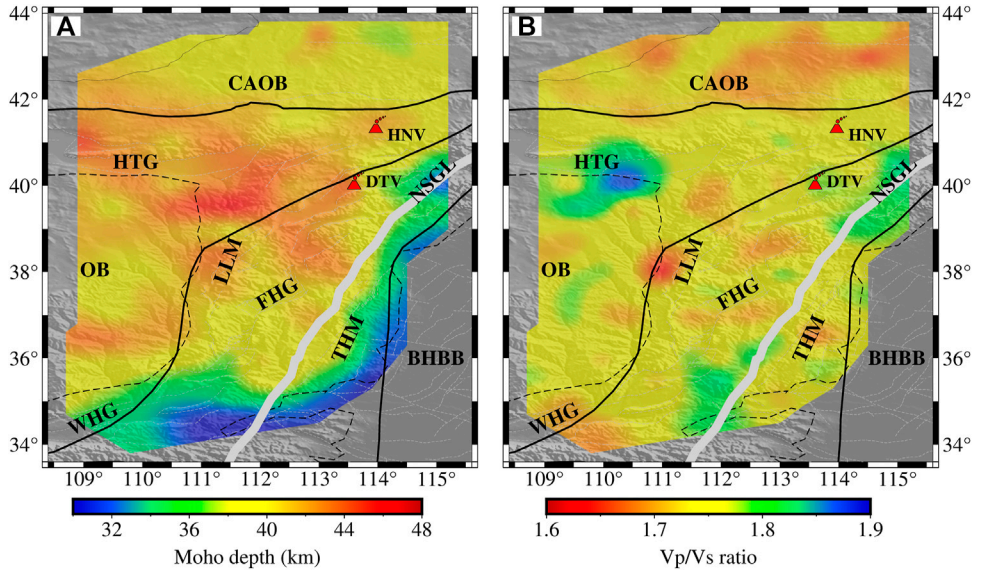

FIGURE 4 | Maps show the Moho depth **(A)** and *Vp/Vs* ratio **(B)** in this study. The abbreviations are the same as those defined in the caption of **Figure 1**.

structures beneath the TNCO and its adjacent areas are quite complicated. In fact, previous investigations revealed that the TNCO is dominated by the strong tectonic activities and intense seismicity (Xu and Ma, 1992; Liu and Wang, 2012; Li et al., 2015). At least ten earthquakes with magnitude no less than *Ms* 7.0 in Chinese history occurred beneath the TNCO. Especially, three of devastating earthquakes located in the WFG, i.e., the 1,303 Hongdong *Ms* 8.0, 1,556 Huaxian *Ms* 8.3 and 1,695 Linfen *Ms* 7.8 earthquake, caused serious damages and casualties (Wu and Jia, 1981; Rao et al., 2017). In this study, we utilized the obtained (H, κ) and (φ, τ) to understand the crustal deformation and seismic hazards beneath the TNCO and its adjacent areas.

Moho depth and *Vp/Vs* ratio are key parameters in constraining the structure and bulk average composition of the crust (Zandt and Ammon, 1995; Christensen, 1996). The crustal composition is classified as low *Vp/Vs* ratio ($\kappa \leq 1.76$), intermediate values ($1.76< \kappa \leq 1.81$) and high values ($\kappa > 1.81$) as the relative abundance of quartz (*Vp/Vs* = 1.49) and plagioclase (*Vp/Vs* = 1.87) fluctuates (Zandt and Ammon, 1995; Wang et al., 2010). An increase of plagioclase content and a decrease of quartz content usually give rise to the increase of the *Vp/Vs* ratio of a rock. Generally, felsic rocks tend to low *Vp/Vs* ratio as compared to mafic rocks. In this study, the lower *Vp/Vs* ratios observed at some local regions of the CAOB and central LLM (**Figure 4B**) imply that the crust has a more content of felsic rocks. The HTG with the highest *Vp/Vs* ratio (~1.90) represents more mafic crustal composition here. In fact, the *Vp/Vs* ratios measured at most of stations are higher than the global average in this study, which is likely to be intermediate to mafic crustal composition.

In addition, the Moho depth gradually thickens from the southeast to northwest in this study area (**Figure 4A**), which is consistent with the previous results from the receiver functions (Li et al., 2014; Cai et al., 2021), surface wave dispersion (Shen et al., 2016) and the Bouguer anomaly (Deng et al., 2014). According to the Airy isostasty and WGM2012 global model (Bonvalot et al., 2012), the larger anomalies of the negative gravity are usually located at the regions with the higher mountains and thicker crust. The Bouguer anomaly is negatively correlated with the elevation and Moho depth (**Supplementary Figure S3A–B**) in this study, which indicates that our Moho depth is reliable and robust. Here, the Airy isostatic theory was used to examine the variation of the Moho depth beneath the TNCO and its adjacent areas. Assuming the crustal density as empirical value, Wang et al. (2010) and Tugume et al. (2012) suggested that 1 km uplift of the surface topography corresponds to ~10 km predicted crustal thickening. The positive correlation between the Moho depth and elevations is shown in **Supplementary Figure S3C**, but its correlation coefficient is only 0.43. The weak correlation implies that a certain amount of mantle mafic materials compensate for the crust to keep the Airy equilibrium (Ji et al., 2009; Tugume et al., 2012). Furthermore, the *Vp/Vs* ratio increases roughly with the crustal thinning (**Supplementary Figure S3D**). Based on the widespread Cenozoic basalts and pyroclastic rocks in the TNCO and its adjacent areas (Xu et al., 2004; Qian et al., 2017), the variation and correlation of our datasets argued above support the model (Ji et al., 2009; Hu et al., 2020) that the underplating of mafic magmas from the partial melting upper mantle intruded into the deep crust to balance the crustal buoyancy. The higher *Vp/Vs* ratio demonstrates that the crustal composition was compensated by the underplated mafic intrusion when the local crust was gradually thinning during the Cenozoic tectonic extension.

We further argue that the observed crustal anisotropy, associating with other parameters (e.g., the GPS velocity, the APM direction and the φ of the SKS/SKKS phase), reflects the

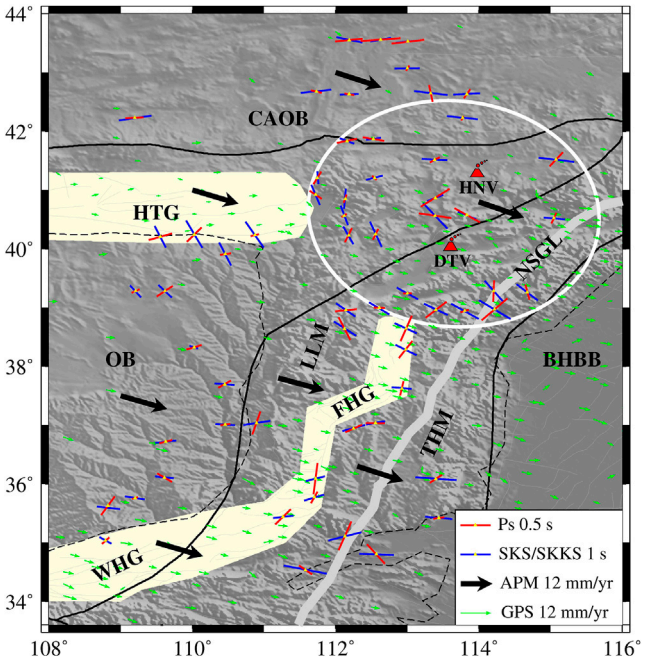

FIGURE 5 | Comparison of crustal anisotropy measured from the Moho Ps (the red bar lines) with measurements of the SKS/SKKS splitting (the blue bar lines, Chang et al., 2021), the GPS velocity (the green arrows, Zhao et al., 2015) and the absolute plate motion direction of the GSRM v2.1 model (the black arrows, Kreemer et al., 2014). White solid ellipse outlines the rotating distribution of the fast polarization directions measured from the Moho Ps. The abbreviations are the same as those defined in the caption of **Figure 1**.

complex crustal deformation beneath the TNCO and its adjacent areas. In the north of the study area, the CAOB as the largest Phanerozoic accretionary orogenic belt has grown significantly in the crust and developed a series of E-W strike slip faults since the Paleo-Asian Ocean closed (Xiao et al., 2003; Windley et al., 2007). The φ measured from Moho Ps and SKS/SKKS phases, as well as the directions of the GPS and APM, are nearly E-W beneath the CAOB (**Figure 5** and **Supplementary Table S2**), which suggests that the whole lithosphere deforms coherently along depth with a compressional direction of N-S. Around the Ordos block, the average φ of the Moho Ps phase trends NE in the southeast and rotates to E-W trending in the north (**Figure 5** and **Supplementary Table S2**). This counterclockwise rotation pattern was also observed by the φ of the SKS/SKKS phase and speculated to be derived from the corresponding asthenospheric flow caused by the northeastward growth and expansion of the Tibetan plateau (Chang et al., 2017, 2021). The ongoing collision of the Indian and Eurasian plates since ~50 Ma has driven the asthenospheric flow (Chang et al., 2021; Wang et al., 2020) and counterclockwise rotation of the Ordos block (Zhang et al., 1998), which may contribute to generating the left-lateral shear stress in the lithosphere and observed seismic anisotropy around the Ordos block. Another noteworthy feature revealed by this study is the rotating distribution of the fast Moho Ps phase directions around the DHV regions in **Figure 5**. The mode of the φ around the DHV regions is also consistent with the recently studies of SKS/SKKS splitting (Chang et al., 2021) and surface wave dispersion (Huang et al., 2021). At some active volcanic areas (e.g., the Mount Ruapehu volcano, New Zealand), the anisotropic orientation agreed with our observations and was further inferred to be due to the stress-aligned microcracks caused by the magmatic eruption (Gerst and Savage, 2004; Johnson et al., 2011). The prominent low velocity anomalies from both the traveltime and full waveform tomography have confirmed the existence of the mantle upwelling beneath the DHV regions related to the stagnancy and dehydration of the Pacific slab in the mantle transition zone (Lei, 2012; Tao et al., 2018). In addition to the anisotropies from P wave tomography (Tian and Zhao, 2013) and SKS/SKKS splitting (Chang et al., 2021), we propose that the fossil crustal anisotropy with the rotating φ around the DHV regions is resulted from the asthenosphere upwelling induced by the Pacific plate subduction.

We noticed that the historical destructive earthquakes occurred in the extensional WFG (**Figure 1**) where the observed average τ is the largest, 0.45 s, in this study area (**Supplementary Table S2**). GPS measurements, still extending with a rate of ~4 mm/year (Shen et al., 2000), and large strike-slip rate of master-faults, 5.68–7 mm/year (Xu and Ma, 1992), further indicated the strong crustal deformation inside the WFG. By analyzing the causes of crustal anisotropy and relationship between Moho depth and *Vp*/*Vs* ratio above, we speculate that the counterclockwise rotation of the Ordos block driven by the far-field effects of the India-Eurasian collision facilitated the left-lateral shear stress and extensional crustal deformation of the WFG and in turn generated the high seismic hazards.

CONCLUSION

In this study, we investigated the Moho depth, *Vp*/*Vs* ratio and crustal anisotropy beneath the TNCO and its adjacent areas using receiver function data with the *H*-κ stacking method and the joint inversion scheme. The variations of the Moho depth and *Vp*/*Vs* ratio might reveal that the underplated mafic intrusion compensated for the crustal composition and Airy equilibrium. Based on the φ of the Moho Ps and SKS/SKKS phases, we proposed that the CAOB showed a coupling deformation between the crust and mantle, under the N-S compressive stress, with the closure of the Paleo-Asian Ocean. The asthenosphere upwelling induced by the Pacific plate subduction caused the stress-aligned microcracks and the rotating distribution of the crustal anisotropic azimuths around the DHV regions. The observed average φ of the Moho Ps phase and the high seismic hazards are attributed to the counterclockwise rotation of the Ordos block driven by the far-field effects of the India-Eurasian collision.

DATA AVAILABILITY STATEMENT

The original contributions presented in the study are included in the article/**Supplementary Material**, further inquiries can be directed to the corresponding author.

AUTHOR CONTRIBUTIONS

XX estimated the receiver functions, calculated the Moho depth, *Vp*/*Vs* ratio and crustal anisotropy and wrote the manuscript. ZD provided the raw data and guided the project. LL provided many useful instruction and suggestions. FL offered the corresponding codes and proposed the main ideas of this study. All authors contributed to the article and approved the submitted version.

FUNDING

This work was supported by the National Natural Science Foundation of China (Grant Nos 41974100, U1839210) and the Special Fund of the Institute of Geophysics, China Earthquake Administration (Grant Nos DQJB16A03, DQJB17A01).

ACKNOWLEDGMENTS

The waveform data was provided by China Seismic Array Data Management Center at Institute of Geophysics, China Earthquake Administration (doi: 10.12001/ChinArray.Data). Figures in this study are plotted by the GMT (http://gmt.soest.hawaii.edu/home).

SUPPLEMENTARY MATERIAL

The Supplementary Material for this article can be found online at: https://www.frontiersin.org/articles/10.3389/feart.2021.753612/full#supplementary-material

REFERENCES

Ammon, C. J. (1991). The Isolation of Receiver Effects from Teleseismic P Waveforms. *Bull. Seism. Soc. Am.* 81 (6), 2504–2510. doi:10.1785/bssa0810062504

Bonvalot, S., Balmino, G., Briais, A., Kuhn, M., Peyrefitte, A., Vales, B. R., et al. (2012). *World Gravity Map, 1:50000000 Map*. Paris: BGI-CGMW-CNES-IRD.

Cai, Y., Wu, J., Rietbrock, A., Wang, W., Fang, L., Yi, S., et al. (2021). S Wave Velocity Structure of the Crust and Upper Mantle beneath Shanxi Rift, central North China Craton and its Tectonic Implications. *Tectonics* 40 (4), e2020TC006239. doi:10.1029/2020TC006239

Chang, L., Ding, Z., Wang, C., and Flesch, L. M. (2017). Vertical Coherence of Deformation in Lithosphere in the NE Margin of the Tibetan Plateau Using GPS and Shear-Wave Splitting Data. *Tectonophysics* 699, 93–101. doi:10.1016/j.tecto.2017.01.025

Chang, L. J., Ding, Z. F., and Wang, C. Y. (2021). Upper Mantle Anisotropy and Implications beneath the central and Western North China and the NE Margin of Tibetan Plateau. *Chin. J. Geophys. (in Chinese)* 64 (1), 114–130. doi:10.6038/cjg2021O0315

Chen, L., and Ai, Y. (2009). Discontinuity Structure of the Mantle Transition Zone beneath the North China Craton from Receiver Function Migration. *J. Geophys. Res.* 114, B06307. doi:10.1029/2008JB006221

ChinArray-Himalaya (2011). *China Seismic Array Waveform Data of Himalaya Project*. Beijing, China: Institute of Geophysics, China Earthquake Administration. doi:10.12001/ChinArray.Data.Himalaya

Christensen, N. I. (1996). Poisson's Ratio and Crustal Seismology. *J. Geophys. Res.* 101, 3139–3156. doi:10.1029/95jb03446

Clayton, R. W., and Wiggins, R. A. (1976). Source Shape Estimation and Deconvolution of Teleseismic Bodywaves. *Geophys. J. Int.* 47, 151–177. doi:10.1111/j.1365-246x.1976.tb01267.x

Crampin, S., and Peacock, S. (2008). A Review of the Current Understanding of Seismic Shear-Wave Splitting in the Earth's Crust and Common Fallacies in Interpretation. *Wave Motion* 45 (6), 675–722. doi:10.1016/j.wavemoti.2008.01.003

Deng, Y., Fan, W., Zhang, Z., and Liang, K. (2014). The Gravity and Isostatic Moho in North China Craton and Their Implications to Seismicity. *Earthq. Sci.* 27 (2), 197–207. doi:10.1007/s11589-013-0019-y

Gao, M., Grujic, D., and Cheng, Q.-M. (2020). Crustal Density Structures and Isostasy beneath the Western North China Craton, Trans-North China Orogen, and Surrounding Regions. *Geosci. Front.* 11 (2), 569–580. doi:10.1016/j.gsf.2019.07.003

Gao, Y., Wu, J., Fukao, Y., Shi, Y., and Zhu, A. (2011). Shear Wave Splitting in the Crust in north China: Stress, Faults and Tectonic Implications. *Geophys. J. Int.* 187, 642–654. doi:10.1111/j.1365-246X.2011.05200.x

Gerst, A., and Savage, M. K. (2004). Seismic Anisotropy beneath Ruapehu Volcano: a Possible Eruption Forecasting Tool. *Science* 306 (5701), 1543–1547. doi:10.1126/science.1103445

Hu, J., Jiang, N., Guo, J., Fan, W., and Liu, D. (2020). The Role of Basaltic Underplating in the Evolution of the Lower continental Crust. *Geochimica et Cosmochimica Acta* 275, 19–35. doi:10.1016/j.gca.2020.02.002

Huang, X., Ding, Z. F., and Ning, J. Y. (2021). Rayleigh Wave Phase Velocity and Azimuthal Anisotropy of central North China Craton Derived from Ambient Noise Tomography. *Chin. J. Geophys.* 64 (8), 2701. doi:10.6038/cjg2021O0442

Ji, S., Wang, Q., and Salisbury, M. H. (2009). Composition and Tectonic Evolution of the Chinese continental Crust Constrained by Poisson's Ratio. *Tectonophysics* 463 (1-4), 15–30. doi:10.1016/j.tecto.2008.09.007

Johnson, J. H., Savage, M. K., and Townend, J. (2011). Distinguishing between Stress-Induced and Structural Anisotropy at Mount Ruapehu Volcano, New Zealand. *J. Geophys. Res.* 116, B12303. doi:10.1029/2011JB008308

Kawakatsu, H., and Niu, F. (1994). Seismic Evidence for a 920-km Discontinuity in the Mantle. *Nature* 371, 301–305. doi:10.1038/371301a0

Kennett, B. L. N., Engdahl, E. R., and Buland, R. (1995). Constraints on Seismic Velocities in the Earth from Traveltimes. *Geophys. J. Int.* 122, 108–124. doi:10.1111/j.1365-246x.1995.tb03540.x

Kreemer, C., Blewitt, G., and Klein, E. C. (2014). A Geodetic Plate Motion and Global Strain Rate Model. *Geochem. Geophys. Geosyst.* 15 (10), 3849–3889. doi:10.1002/2014gc005407

Lei, J. (2012). Upper-mantle Tomography and Dynamics beneath the North China Craton. *J. Geophys. Res.* 117, a–n. doi:10.1029/2012JB009212

Li, B., Sørensen, M. B., and Atakan, K. (2015). Coulomb Stress Evolution in the Shanxi Rift System, North China, since 1303 Associated with Coseismic, post-seismic and Interseismic Deformation. *Geophys. J. Int.* 203 (3), 1642–1664. doi:10.1093/gji/ggv384

Li, Y., Gao, M., and Wu, Q. (2014). Crustal Thickness Map of the Chinese mainland from Teleseismic Receiver Functions. *Tectonophysics* 611, 51–60. doi:10.1016/j.tecto.2013.11.019

Liu, H., and Niu, F. (2012). Estimating Crustal Seismic Anisotropy with a Joint Analysis of Radial and Transverse Receiver Function Data. *Geophys. J. Int.* 188 (1), 144–164. doi:10.1111/j.1365-246X.2011.05249.x

Liu, M., and Wang, H. (2012). Roaming Earthquakes in China Highlight Midcontinental Hazards. *Eos Trans. AGU* 93 (45), 453–454. doi:10.1029/2012eo450001

Mainprice, D., and Nicolas, A. (1989). Development of Shape and Lattice Preferred Orientations: Application to the Seismic Anisotropy of the Lower Crust. *J. Struct. Geology.* 11, 175–189. doi:10.1016/0191-8141(89)90042-4

Meissner, R., Mooney, W. D., and Artemieva, I. (2002). Seismic Anisotropy and Mantle Creep in Young Orogens. *Geophys. J. Int.* 149, 1–14. doi:10.1046/j.1365-246x.2002.01628.x

Muirhead, K. J. (1968). Eliminating False Alarms when Detecting Seismic Events Automatically. *Nature* 217, 533–534. doi:10.1038/217533a0

Nicolas, A., and Christensen, N. I. (1987). Formation of Anisotropy in Upper Mantle Peridotites: A Review. *Rev. Geophys.* 25, 111–123. doi:10.1029/gd016p0111

Niu, F., Bravo, T., Pavlis, G., Vernon, F., Rendon, H., Bezada, M., et al. (2007). Receiver Function Study of the Crustal Structure of the southeastern Caribbean Plate Boundary and Venezuela. *J. Geophys. Res.* 112 (B11), B11308. doi:10.1029/2006jb004802

Niu, F., and Kawakatsu, H. (1998). Determination of the Absolute Depths of the Mantle Transition Zone Discontinuities beneath China: Effect of Stagnant Slabs on Transition Zone Discontinuities. *Earth Planet. Sp* 50 (11-12), 965–975. doi:10.1186/bf03352191

Niu, F., and Li, J. (2011). Component Azimuths of the CEArray Stations Estimated from P-Wave Particle Motion. *Earthq Sci.* 24 (1), 3–13. doi:10.1007/s11589-011-0764-8

Qian, S.-P., Ren, Z.-Y., Richard, W., Zhang, L., Zhang, Y.-H., Hong, L.-B., et al. (2017). Petrogenesis of Early Cretaceous Basaltic Lavas from the North China Craton: Implications for Cratonic Destruction. *J. Geophys. Res. Solid Earth* 122, 1900–1918. doi:10.1002/2016JB013548

Rao, G., Cheng, Y., Lin, A., and Yan, B. (2017). Relationship between Landslides and Active normal Faulting in the Epicentral Area of the AD 1556 M~8.5 Huaxian Earthquake, SE Weihe Graben (Central China). *J. Earth Sci.* 28 (3), 545–554. doi:10.1007/s12583-017-0900-z

Ren, J., Tamaki, K., Li, S., and Junxia, Z. (2002). Late Mesozoic and Cenozoic Rifting and its Dynamic Setting in Eastern China and Adjacent Areas. *Tectonophysics* 344 (3-4), 175–205. doi:10.1016/s0040-1951(01)00271-2

Schellart, W. P., Chen, Z., Strak, V., Duarte, J. C., and Rosas, F. M. (2019). Pacific Subduction Control on Asian continental Deformation Including Tibetan Extension and Eastward Extrusion Tectonics. *Nat. Commun.* 10, 4480. doi:10.1038/s41467-019-12337-9

Shen, W., Ritzwoller, M. H., Kang, D., Kim, Y., Lin, F.-C., Ning, J., et al. (2016). A Seismic Reference Model for the Crust and Uppermost Mantle beneath China from Surface Wave Dispersion. *Geophys. J. Int.* 206 (2), 954–979. doi:10.1093/gji/ggw175

Shen, Z.-K., Zhao, C., Yin, A., Li, Y., Jackson, D. D., Fang, P., et al. (2000). Contemporary Crustal Deformation in East Asia Constrained by Global Positioning System Measurements. *J. Geophys. Res.* 105 (B3), 5721–5734. doi:10.1029/1999jb900391

Sherrington, H. F., Zandt, G., and Frederiksen, A. (2004). Crustal Fabric in the Tibetan Plateau Based on Waveform Inversions for Seismic Anisotropy Parameters. *J. Geophys. Res.* 109, B02312. doi:10.1029/2002JB002345

Sun, Y., Niu, F., Liu, H., Chen, Y., and Liu, J. (2012). Crustal Structure and Deformation of the SE Tibetan Plateau Revealed by Receiver Function Data. *Earth Planet. Sci. Lett.* 349-350, 186–197. doi:10.1016/j.epsl.2012.07.007

Tao, K., Grand, S. P., and Niu, F. (2018). Seismic Structure of the Upper Mantle beneath Eastern Asia from Full Waveform Seismic Tomography. *Geochem. Geophys. Geosyst.* 19 (8), 2732–2763. doi:10.1029/2018GC007460

Tian, Y., and Zhao, D. (2013). Reactivation and Mantle Dynamics of North China Craton: Insight from P-Wave Anisotropy Tomography. *Geophys. J. Int.* 195, 1796–1810. doi:10.1093/gji/ggt333

Tugume, F., Nyblade, A., and Julià, J. (2012). Moho Depths and Poisson's Ratios of Precambrian Crust in East Africa: Evidence for Similarities in Archean and Proterozoic Crustal Structure. *Earth Planet. Sci. Lett.* 355-356, 73–81. doi:10.1016/j.epsl.2012.08.041

Vinnik, L. P. (1977). Detection of Waves Converted from P to SV in the Mantle. *Phys. Earth Planet. Interiors* 15 (1), 39–45. doi:10.1016/0031-9201(77)90008-5

Wang, C.-Y., Zhu, L., Lou, H., Huang, B.-S., Yao, Z., and Luo, X. (2010). Crustal Thicknesses and Poisson's Ratios in the Eastern Tibetan Plateau and Their Tectonic Implications. *J. Geophys. Res.* 115, B11301. doi:10.1029/2010JB007527

Wang, K., Xiong, X., Zhou, Y., and Feng, Y. (2020). Three-dimensional Thermo-Rheological Structure of the Lithosphere in the North China Craton Determined by Integrating Multiple Observations: Implications for the Formation of Rifts. *Sci. China Earth Sci.* 63, 969–984. doi:10.1007/s11430-019-9566-1

Wang, Q., Niu, F., Gao, Y., and Chen, Y. (2016). Crustal Structure and Deformation beneath the NE Margin of the Tibetan Plateau Constrained by Teleseismic Receiver Function Data. *Geophys. J. Int.* 204 (1), 167–179. doi:10.1093/gji/ggv420

Windley, B. F., Alexeiev, D., Xiao, W., Kröner, A., and Badarch, G. (2007). Tectonic Models for Accretion of the Central Asian Orogenic Belt. *J. Geol. Soc.* 164 (1), 31–47. doi:10.1144/0016-76492006-022

Wu, L., and Jia, B. Q. (1981). The M 8.0 Hongdong Earthquake. *Seismology (in Chinese)* 2, 2–19.

Xiao, W., Windley, B. F., Hao, J., and Zhai, M. (2003). Accretion Leading to Collision and the Permian Solonker Suture, Inner Mongolia, China: Termination of the central Asian Orogenic belt. *Tectonics* 22 (6), a–n. doi:10.1029/2002TC001484

Xu, X., and Ma, X. (1992). Geodynamics of the Shanxi Rift System, China. *Tectonophysics* 208, 325–340. doi:10.1016/0040-1951(92)90353-8

Xu, X., Niu, F., Ding, Z., and Chen, Q. (2018). Complicated Crustal Deformation beneath the NE Margin of the Tibetan Plateau and its Adjacent Areas Revealed by Multi-Station Receiver-Function Gathering. *Earth Planet. Sci. Lett.* 497, 204–216. doi:10.1016/j.epsl.2018.06.010

Xu, Y. G., Chung, S. L., Ma, J., and Shi, L. (2004). Contrasting Cenozoic Lithospheric Evolution and Architecture in the Western and Eastern Sino-Korean Craton: Constraints from Geochemistry of Basalts and Mantle Xenoliths. *J. Geology.* 112 (5), 593–605. doi:10.1086/422668

Yang, Y., Yao, H., Zhang, P., and Chen, L. (2018). Crustal Azimuthal Anisotropy in the Trans-North China Orogen and Adjacent Regions from Receiver Functions. *Sci. China Earth Sci.* 61 (7), 903–913. doi:10.1007/s11430-017-9209-9

Zandt, G., and Ammon, C. J. (1995). Continental Crust Composition Constrained by Measurements of Crustal Poisson's Ratio. *Nature* 374, 152–154. doi:10.1038/374152a0

Zeng, S., Zheng, Y., Niu, F., and Ai, S. (2020). Measurements of Seismometer Orientation of the First Phase CHINArray and Their Implications on Vector-Recording-Based Seismic Studies. *Bull. Seismol. Soc. Am.* 111 (1), 36–49. doi:10.1785/0120200129

Zhang, H., Huang, Q., Zhao, G., Guo, Z., and Chen, Y. J. (2016). Three-dimensional Conductivity Model of Crust and Uppermost Mantle at the Northern Trans North China Orogen: Evidence for a Mantle Source of Datong Volcanoes. *Earth Planet. Sci. Lett.* 453, 182–192. doi:10.1016/j.epsl.2016.08.025

Zhang, Y. Q., Mercier, J. L., and Vergély, P. (1998). Extension in the Graben Systems Around the Ordos (China), and its Contribution to the Extrusion Tectonics of south China with Respect to Gobi-Mongolia. *Tectonophysics* 285 (1-2), 41–75. doi:10.1016/s0040-1951(97)00170-4

Zhao, B., Huang, Y., Zhang, C., Wang, W., Tan, K., and Du, R. (2015). Crustal Deformation on the Chinese mainland during 1998-2014 Based on GPS Data. *Geodesy and Geodynamics* 6, 7–15. doi:10.1016/j.geog.2014.12.006

Zhao, G., Wilde, S. A., Cawood, P. A., and Sun, M. (2001). Archean Blocks and Their Boundaries in the North China Craton: Lithological, Geochemical, Structural and P-T Path Constraints and Tectonic Evolution. *Precambrian Res.* 107, 45–73. doi:10.1016/s0301-9268(00)00154-6

Zhao, L., Zheng, T., and Lü, G. (2008). Insight into Craton Evolution: Constraints from Shear Wave Splitting in the North China Craton. *Phys. Earth Planet. Interiors* 168, 153–162. doi:10.1016/j.pepi.2008.06.003

Zheng, T., Ding, Z., Ning, J., Liu, K. H., Gao, S. S., Chang, L., et al. (2019). Crustal Azimuthal Anisotropy beneath the central North China Craton Revealed by Receiver Functions. *Geochem. Geophys. Geosystems* 20, 2235–2251. doi:10.1029/2019gc008181

Zhu, H. (2018). High Vp/Vs Ratio in the Crust and Uppermost Mantle beneath Volcanoes in the Central and Eastern Anatolia. *Geophys. J. Int.* 214 (3), 2151–2163. doi:10.1093/gji/ggy253

Zhu, L., and Kanamori, H. (2000). Moho Depth Variation in Southern California from Teleseismic Receiver Functions. *J. Geophys. Res.* 105, 2969–2980. doi:10.1029/1999jb900322

Zhu, R., Chen, L., Wu, F., and Liu, J. (2011). Timing, Scale and Mechanism of the Destruction of the North China Craton. *Sci. China Earth Sci.* 54, 789–797. doi:10.1007/s11430-011-4203-4

Conflict of Interest: The authors declare that the research was conducted in the absence of any commercial or financial relationships that could be construed as a potential conflict of interest.

Publisher's Note: All claims expressed in this article are solely those of the authors and do not necessarily represent those of their affiliated organizations, or those of the publisher, the editors and the reviewers. Any product that may be evaluated in this article, or claim that may be made by its manufacturer, is not guaranteed or endorsed by the publisher.

frontiers in Earth Science

ORIGINAL RESEARCH
published: 03 December 2021
doi: 10.3389/feart.2021.752488

Moho Geometry of the Okinawa Trough Based on Gravity Inversion and Its Implications on the Crustal Nature and Tectonic Evolution

Liang Zhang[1,2] *and Xiwu Luan*[2,3]*

[1]Cas Key Laboratory of Marine Geology and Environment, Institute of Oceanography, Chinese Academy of Sciences, Qingdao, China, [2]Function Laboratory of Marine Mineral Resources, Qingdao National Laboratory for Marine Science and Technology, Qingdao, China, [3]Qingdao Institute of Marine Geology, China Geological Survey, Qingdao, China

The Okinawa Trough (OT) is an incipient back-arc basin, but its crustal nature is still controversial. Gravity inversion along with sediment and lithospheric mantle density modeling are used to map the regional Moho depth and crustal thickness variations of the OT and its adjacent areas. The gravity inversion result shows that the crustal thicknesses are 17–22 km at the northern OT, 11–19 km at the central OT, and 7–19 km at the southern OT. Because of the crust with a thickness larger than 17 km, the slow southward arc movement, and scarce contemporaneous volcanisms, the northern OT should be in the stage of early back-arc extension. All of the moderate crustal thickness, high heat flow, and intense volcanism at the central OT indicate that this region is probably in the transitional stage from the back-arc rifting to the oceanic spreading. A crust that is only 7 km thick, lithosphere strength as low as the mid-ocean ridge, and MORB-similar basalts at the southern OT demonstrate that the southern OT is at the early stage of seafloor spreading.

Keywords: gravity inversion, density modeling, crustal thickness, Okinawa Trough, multi-stage evolution

OPEN ACCESS

Edited by:
Tianyao Hao,
Institute of Geology and Geophysics, (CAS), China

Reviewed by:
Luis E. Lara,
Servicio Nacional de Geología y Minería de Chile (SERNAGEOMIN), Chile
Finnigan Illsley-Kemp,
Victoria University of Wellington, New Zealand

***Correspondence:**
Xiwu Luan
xluan@qnlm.ac

Specialty section:
This article was submitted to Structural Geology and Tectonics, a section of the journal Frontiers in Earth Science

Received: *03 August 2021*
Accepted: *23 September 2021*
Published: *03 December 2021*

Citation:
Zhang L and Luan X (2021) Moho Geometry of the Okinawa Trough Based on Gravity Inversion and Its Implications on the Crustal Nature and Tectonic Evolution. Front. Earth Sci. 9:752488. doi: 10.3389/feart.2021.752488

INTRODUCTION

Crust is the outermost solid shell of the Earth and the crust types vary significantly among different tectonic units, such as continental margins, oceanic basins, and island arcs. The variation of crustal thickness is a critical factor for understanding the processes of continental rifting and breakup, and determining the crust nature for the incipient back-arc basin (Sutra and Manatschal, 2012).

The Okinawa Trough (OT) is a back-arc basin developed under the area of East China Sea. Although a number of studies have been performed to examine its crustal structure (Iwasaki et al., 1990; Nakamura et al., 2003; Gungor et al., 2012; Klingelhoefer et al., 2012; Shang et al., 2017; Qi et al., 2020), it is still controversial if the nature of its crust is continental, transitional, or oceanic (Liu et al., 2016) (**Figure 1**). Iwasaki et al. (1990) and Nakahigashi et al. (2004) suggested a thinned continental crust at a rifting stage for northern OT based on OBS data. Sibuet et al. (1998) had the same suggestion for southern OT. Han et al. (2007), however, suggested that the central and southern OT are at a transitional stage based on the extremely high heat flow and intense volcanic activities. Arai et al. (2017) and some earlier researchers (Lee et al., 1980; Sibuet et al., 1987) suggested that oceanic spreading have already occurred in OT. Liu et al. (2016) and other earlier researchers (Sibuet et al., 1987; Sibuet et al., 1998) reported the founding of the linear magnetic anomalies in central OT. Also,

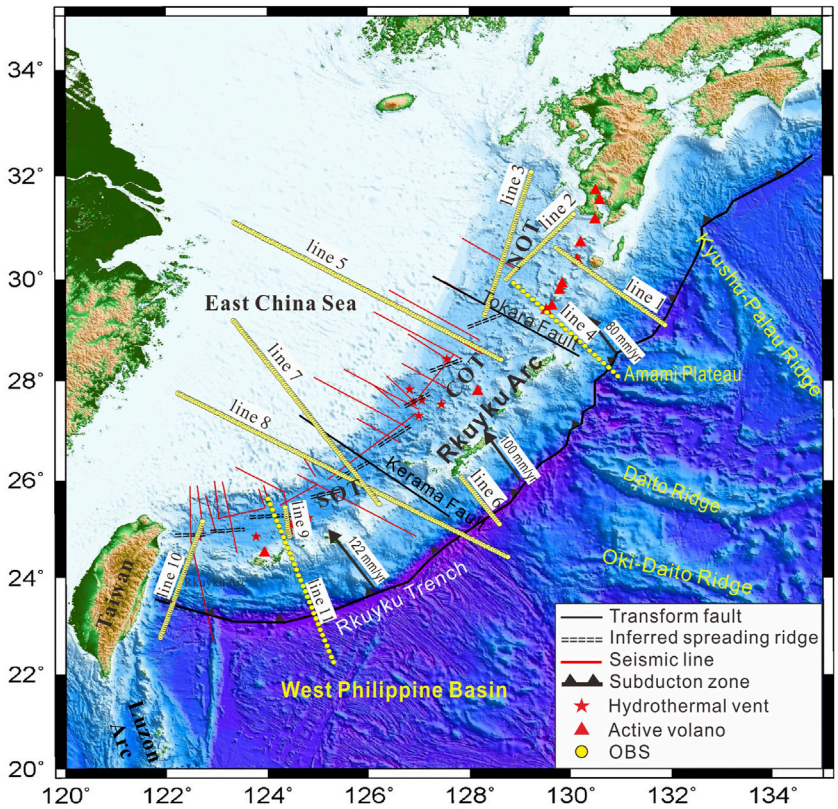

FIGURE 1 | Simplified structural map showing the tectonic setting of the Ryukyu trench-arc-basin system and its adjacent region. The base map is the ETOPO1 global relief grid. NOT: northern Okinawa Trough (OT); COT: central OT; SOT: southern OT. The boundaries of the three OT sections are the Tokara Fault and the Kerama Fault (Yan and Shi, 2014).

regarding the oceanic spreading, Kimura (1985) gave an average half spreading rate of 2 cm/year to the southern OT since early Pleistocene. The time of initial rifting of the northern and central OT is considered to be at the Middle Miocene (Gungor et al., 2012; Xu et al., 2014), while that of the southern OT is believed to be just in the Quaternary (Wu et al., 2007; Shang et al., 2017). Until now, the references have no answer to why there is so long a delay time between northern and southern OT (Shang et al., 2017).

Many researchers have mapped the Moho of the OT by gravity methods, but their results vary considerably from each other (Hao et al., 2006; Ding et al., 2017; Xuan et al., 2020). In addition, the crustal thickness predicted by gravity method is quite different from the reflection and wide-angle seismic methods in southern OT (Klingelhoefer et al., 2012; Liu et al., 2016). The reason for this difference might be that the low-density anomaly in the mantle due to magma upwelling was not considered in the previous gravity study (Zhou et al., 2001).

Recently, a new alternative gravity inversion method was provided by Bai et al. (2019b), which incorporates sediment and lithospheric mantle density corrections to map the regional Moho topography. Considering the low coverage of deep seismic refraction and broadband seismogram data (Aitken, 2010), here we adopt Bai's method to map new regional Moho topography of OT by combining it with heat flow, OBSs, and lithospheric strength data, to further examine and discuss the crustal nature of the OT and provide new insight into the ongoing processes of the back-arc basin.

GEOLOGIC SETTING

The Philippine Sea Plate is characterized by three seafloor highs, known as the Amami Plateau, the Datio Ridge, and the Oki-Daito Ridge to the north (Nishizawa et al., 2014) and relatively flat topography to the south (Taylor and Andrew, 2004). The Philippine Sea Plate is subducting beneath Ryukyu Arc along Ryukyu Trench (Sibuet et al., 1998) with a current subduction rate from ~8 to ~13 cm/year from north to south progressively (Argus et al., 2013). The earthquake data indicate that the dip of the Wadat–Benioff zone of the Philippine subduction plate is 25°–27° at the north and 55°–75° at its south.

OT extends ~1,200 km in the NE-SW direction along and at the back of Ryukyu Arc. It can be divided into northern, central, and southern OT by the Tokara Fault in the north and the Kerama Fault in the south (Fabbri et al., 2004; Gungor et al., 2012) (**Figure 1**). The depth of seafloor of the southern OT is deeper than that of the central and northern OT, suggesting more rapid

subsidence in the south. Seismic data suggest that the southern OT is characterized by well-developed symmetric deep faults, while more diffuse rifting occurred in the north (Gungor et al., 2012). It indicates that the forces along the OT are uneven (Doo et al., 2018). The OT ends at the collision zone between the Luzon Arc and the Taiwan Island since 3.5–4.0 Ma, and this collision probably induced the opening of southern OT (Letouzey and Kimura, 1986; Rateb et al., 2017).

OT has an abnormally high heat flow and intense magmatic activity (Zhang et al., 2019). The average heat flow of the OT based on the 348 available measurements from the global heat flow database of the International Heat Flow Commission is 458 mW/m^2, which is much higher than the global average value of 86 mW/m^2 (Davies, 2013). The extremely high heat flows (>1,000 mW/m^2) in the OT are almost distributed in the central axis of OT, where active volcanoes and hydrothermal vents are developed considerably (**Figure 1**) (Ishibashi et al., 2015). The geochemistry studies indicate that magmatic activity is affected obviously by fluids derived from the subducting slab dehydration (Guo et al., 2017). Active magmatism at the back-arc and non-spreading central and northern OT may be induced by subducting of the Datio Ridge and the Amami Plateau (Sibuet et al., 1998; Rateb et al., 2017).

The evolution of the OT can be divided into two (Letouzey and Kimura, 1986; Sibuet et al., 1987; Shang et al., 2017) or three stages (Kimura, 1985; Gungor et al., 2012; Liu et al., 2016). The first stage is the initial rifting, triggered by the back-arc normal faulting. The second stage is the passive extension, triggered by the strike-slip pull-apart process or transtensional NNE-trending faults. The third stage is the initial divergence indicated by the newborn oceanic crustal spreading (Liu et al., 2016).

METHODOLOGY AND DATA

The Moho defined as the boundary between crust and mantle is one of the largest density boundaries with the lithosphere (Lai et al., 2016), so gravity method can be used to image the Moho geometry.

The free air gravity anomaly (Δg_f) is given by:

$$\Delta g_f = g_m + g_b + g_s + g_t + g_o, \tag{1}$$

where g_m is the mantle residual gravity anomaly that reflects Moho undulations; g_b and g_s are the gravity anomaly induced by seawater and sediment, respectively, when taking continental crust density (2.7 g/cm^3) as the background; g_t is the anomaly that originates from mantle density perturbations because of the thermal expansion when taking the normal mantle density (3.3 g/cm^3) as the background; g_o is the gravity anomaly caused by the other sources, and this anomaly is relatively small and can be ignored (Bai et al., 2014; Kusznir et al., 2018). After the isolation of the mantle residual gravity anomaly, the Moho burial depth can be mapped based on this mantle residual gravity anomaly (g_m) in the frequency domain (Oldenburg, 1974).

Seawater density is taken as a constant of 1.03 g/cm^3, but the density variations of sediment and lithospheric mantle should be modeled in detail. The advantage of this method is that it can remove the gravity effect of density variations of sediments due to compaction and those of lithospheric mantle due to thermal expansion from the observed free air gravity anomaly by density modeling, which is essential for the gravity inversion in the back-arc basin with hot mantle upwelling (Bai et al., 2019b).

Estimating Gravity Effect of the Sediment Layer

The sediment gravity effect is unavoidable for the Moho inversion when the sediment layer is thick. The key issues for estimating gravity effect of the sediment layer are the sedimentary thickness and the density variation. The data and method for mapping sediment thickness variations will be explained in *Methodology and Data*. The relationship between sediment burial depth, porosity, and density can be used to calculate the sediment density (Sawyer, 1985; López-Coto et al., 2013; Bai et al., 2019a). The porosity variation is a function of buried depth (z) as

$$\Phi_z = \Phi_0 e^{-cz}, \tag{2}$$

where Φ_0 is the initial sediment porosity and c is an empirically determined constant with a unit of 1/depth. The parameters Φ_0 and c vary with lithology. Based on the drilling data in the Xihu Sag (**Figure 1**), $\Phi_0 = 0.55$ and $c = 0.45 \times 10^{-4}$ m^{-1} (Zhang et al., 2009). When sedimentary pore is filled by seawater, the sediment density (ρ_z) varying with depth z can be modeled *via*:

$$\rho_z = \Phi_z \rho_w + (1 - \Phi_z)\rho_g, \tag{3}$$

where ρ_w is the seawater density with a value of 1.03×10^3 kg/m^3 and ρ_g is grain density with a value of 2.65×10^3 kg/m^3 (Sawyer, 1985; López-Coto et al., 2013).

Estimating Gravity Effect of the Lithospheric Mantle

The density perturbations of the lithospheric mantle caused by thermal expansion can generate a large gravity anomaly at young oceanic basins and rifted continental margins (Chappell and Kusznir, 2008). There are different lithospheric mantle temperature modeling methods (McKenzie, 1978; Stein and Stein, 1992; Afonso et al., 2008). The gravity effect of density perturbations due to thermal expansion can be modeled based on the thermal expansion coefficient and the temperature structure (McKenzie et al., 2005). The pure shear model by McKenzie (1978) is adopted here for modeling lithospheric temperature field as the work by Chappell and Kusznir (2008).

Crustal age is an important parameter for modeling the temperature structure of lithospheric mantle (Cowie and Kusznir, 2012). The crust of the West Philippine Sea Basin is oceanic, and its age has been interpreted from marine magnetic lineation (Müller et al., 2019). The continental crust is usually much older than that of the oceanic crust, so we assigned the continental crust to have a thermal age of 300 Ma (Currie and Hyndman, 2006). Our tests show that the lithospheric mantle

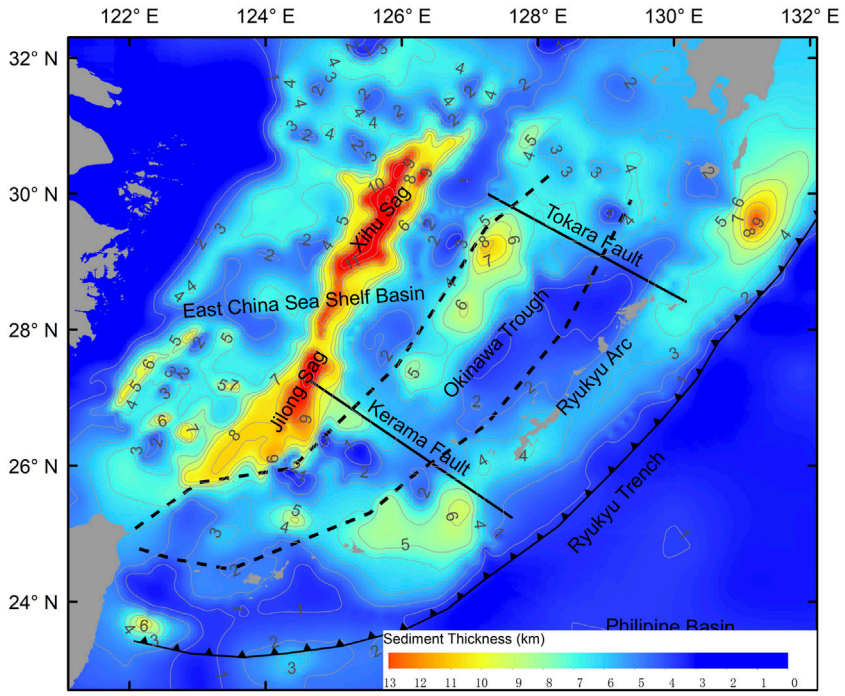

FIGURE 2 | The thickness map of the sedimentary layer in our study area. The grid is created *via* Kriging interpolation method based on the global marine sediment thickness grid (Straume et al., 2019) and recent interpretation results of seismic reflection data (Fang et al., 2020). The black dashed lines represent the boundaries of the Okinawa Trough.

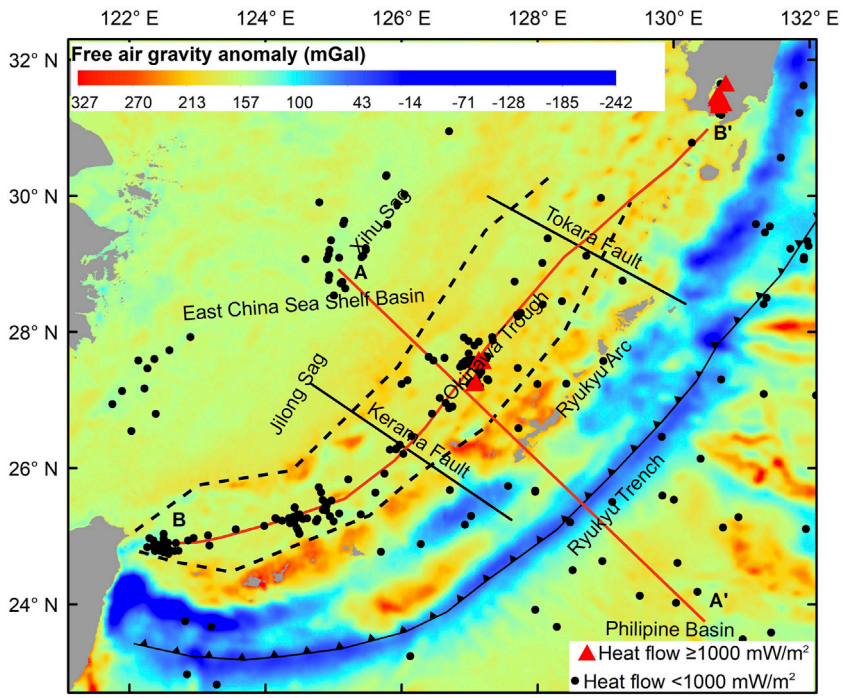

FIGURE 3 | The free-air gravity anomalies (Sandwell et al., 2014) and the heat flow stations from the database of the International Heat Flow Commission.

TABLE 1 | Information on the geophysical profiles used in this study.

Profile Index	Profile type	Data year	Length (km)	Section of the OT	Was sediment thickness interpreted?	References
Line1	OBS	1984	190	North	Yes	Iwasaki et al. (1990)
Line2	OBS	1984	295	North	Yes	Iwasaki et al. (1990)
Line3	OBS	1999	320	North	Yes	Nakahigashi et al. (2004)
Line4	OBS	1995	290	North	No	Arai et al. (2017)
Line5	GMS	1989	600	Central	No	Gao et al. (2006)
Line6	OBS	1988	120	Central	Yes	Kodaira et al. (1996)
Line7	OBS	2015	490	Central	Yes	Wu et al. (2020)
Line8	GMS	1998	725	South	No	Gao et al. (2006)
Line9	OBS	1988	195	South	Yes	Iwasaki et al. (1990)
Line10	OBS	2009	300	South	Yes	Klingelhoefer et al. (2012)
Line11	OBS	2013	400	South	No	Arai et al. (2017)

Note: OBS, ocean bottom seismic; GMS, gravity–magnetic–seismic comprehensive profile.

temperature almost does not change when the crustal age varies larger than 300 Ma. Since the crustal nature is unclear at the central and southern OT, a series of thermal ages will be assigned to examine which can yield the Moho inversion result that can best fit with the seismic interpretation.

Mapping Sediment Thickness Variations

The sediment thicknesses data used in this study are partly from the global sediment thickness model for oceans and marginal basins (Straume et al., 2019) and from recent seismic survey by CGS and reported by Fang et al. (2020). Kriging interpolation method is used to merge these two grids. **Figure 2** shows the sediment thickness data created and used in this study. The depocenters distribute in NE trending, such as the Xihu and Jilong sags. The maximum sediment thicknesses of the two sags exceed 11 km. In the OT, the maximum sediment thickness decreased from 8 km at the central OT to only 4–5 km at the northern and southern OT.

Input Data

The free-air gravity anomalies (**Figure 3**) are from the 1-min-resolution global free-air gravity model based on the altimetry data by the satellite named Geosat, ERS-1, Envisat, GryoSat-2, and Jason-1 (Sandwell et al., 2014). The bathymetric data used in gravimetric correction are from the ETOPO1, which is also a 1 arc-minute global relief model (Amante and Eakins, 2009). The Moho interpretation results of 11 geophysical (mainly OBS) profiles at the OT and the Ryukyu Arc (**Figure 1**; **Table 1**) are collected in order to estimate the gravity inversion uncertainty. The heat flow (**Figure 3**) can be used to recover the thermal structure of the Earth and the heat flow data are extracted from the global heat flow database of the International Heat Flow Commission.

GRAVITY INVERSION RESULT

According to our tests, when the ages of the southern and central OT are 1 and 10 Ma, respectively, the Moho inversion result can fit with the seismic interpretation best and the RMS between the gravity and seismic results is 2.28 km. The gravity effect of the sediment layer and lithospheric mantle are highly correlated with the sediment thickness and crustal age variations, respectively (**Figure 4**). **Figure 5** shows our final Moho inversion result and the crustal thickness map, and the later one is based on the Moho inversion, bathymetry, and sediment thickness data.

The Moho and crustal thickness are characterized by NE trending lineation, consistent with characteristic of the Ryukyu trench-arc-basin system. The Moho depths are 25–30 km in the East China Sea Shelf Basin and 15–25 km in the OT, respectively (**Figure 5A**). The southern OT holds shallowest Moho and thinnest crust in the whole OT. The crustal thickness of the northern OT is greater than that of the central OT (**Figure 5B**). One belt with highly thinned crust locates along the Xihu and Jilong sags, extending in the NE direction in the East China Sea Shelf Basin even though there is no Moho shallowing in this region.

UNCERTAINTY ANALYSIS

We evaluate the reliability of our Moho depth estimates derived from inversion of gravity data against previous seismic imaging studies, and discuss the effect of lithospheric mantle temperature on Moho inversion.

Comparison With Seismic Profiles

The Moho depths interpreted from seismic studies are considered to have a better accuracy than gravity inversion. So, seismic interpretation results are always taken as the reference for estimating gravity inversion uncertainty (Chappell and Kusznir, 2008; Bai et al., 2019b). However, note that the seismic interpretation itself also contains uncertainty. For example, at the intersection point between line 7 and line 8 (**Figure 1**), the Moho depth from line 7 is 19.0 km (Wu et al., 2020), but that from line 8 is 17.9 km (Gao et al., 2006); thus, the difference between them reaches 1.1 km. **Figure 6** shows the comparison between the Moho depths from the collected seismic interpretation and our gravity inversion. The root mean square (RMS) between the Moho depths from interpreted seismic profiles and those from our final gravity inversion at the same sampling stations is 2.28 km. However, the RMS is 4.12 km when

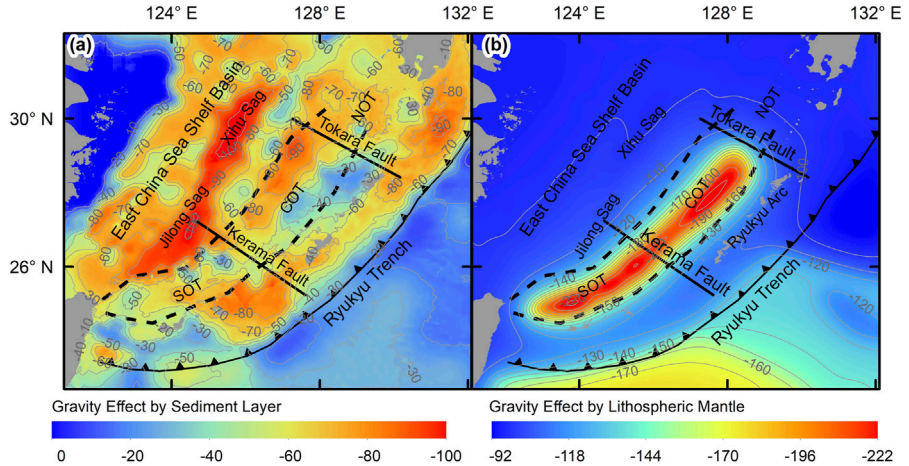

FIGURE 4 | Gravity effect induced by sediment density variations relative to normal continental crust density **(A)** and gravity effect induced by lithospheric mantle density variations relative to normal mantle density **(B)**.

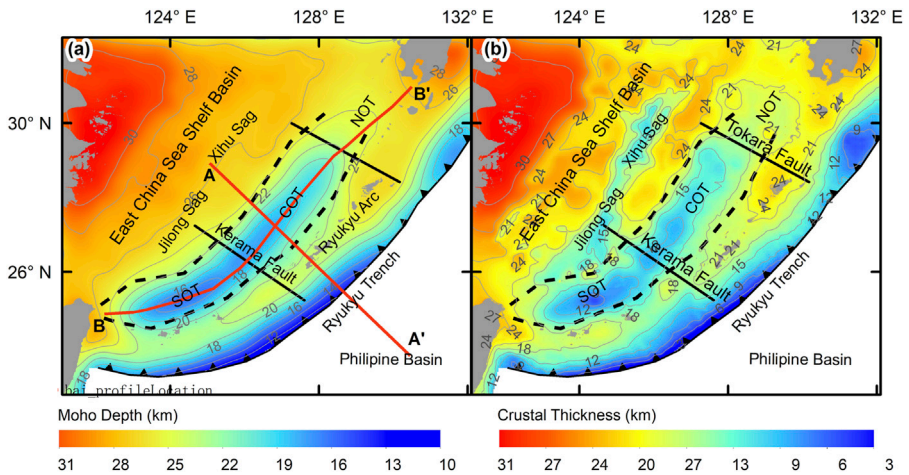

FIGURE 5 | Moho depths **(A)** determined from gravity inversion and crustal thickness **(B)**, which is obtained by subtracting the sea water depth and sediment thickness from the Moho depth. The red thick lines in the left panel represent the locations of the profiles in **Figure 7** and **Figure 8**.

ignoring gravity effect induced by both sediment and mantle, and that is 3.16 km when ignoring only the mantle gravity effect.

The Effect of Lithospheric Mantle Temperature on Moho Inversion

We set a 0–300 Ma OT crustal age span for testing. At first, each possible age pair for central and southern OT combination will be applied to temperature modeling and gravity inversion by setting age varying step as 10 Ma. When the crustal age of the central and southern OT is 10 and 0 Ma, the gravity inversion can fit with the seismic interpretation best. Then, the age step is reduced to 1 Ma; age varying range for the central OT is narrowed to 20–0 Ma, and that for the southern OT is narrowed to 10–0 Ma. Finally, when the crustal age for the central OT is 10 Ma and that for the southern OT is 1 Ma, the smallest RMS of 2.28 km is derived. Some of the results are listed in **Table 2**. Please note that, when the lithospheric mantle density perturbations due to temperature variations are ignored for gravity inversion, the RMS will be increased to 2.67 km. Therefore, the lithospheric mantle density modeling based on the age setting for the central and southern OT can improve the Moho inversion accuracy.

TECTONIC IMPLICATIONS

The large-scale Moho and crustal thickness variation trend is an important implication for the tectonic characteristics. There is no corresponding mantle upwelling beneath the Xihu and Jilong sags judging from the Moho depth (**Figure 5A** and **Figure 7**), but the

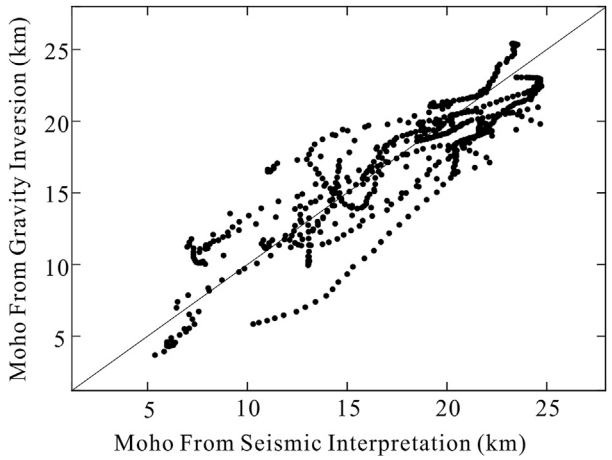

FIGURE 6 | Moho depth from gravity inversion vs. that from seismic interpretation. The root mean square (RMS) between them is 2.28 km.

TABLE 2 | The root mean square (RMS) between gravity inversion result and seismic interpretation when setting different thermal ages for the central Okinawa Trough (COT) and the southern Okinawa Trough (SOT).

Thermal age (Ma)		RMS (km)
COT	**SOT**	
300	300	3.07
40	40	2.62
20	20	2.54
10	10	2.40
1	1	2.45
1	10	2.42
10	5	2.31
10	1	2.28

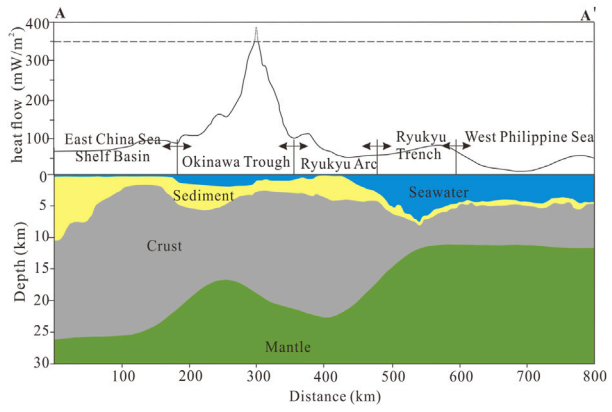

FIGURE 7 | The crustal structure and the heat flow along the profile AA′; profile location is shown in **Figure 5A**. The bathymetry is from ETOPO1, the sediment thickness is extracted from the data shown in **Figure 2**, and the Moho geometry is from our gravity inversion. The heat flow data are extracted from the global heat flow database of the International Heat Flow Commission. The dashed part of the heat flow curve represents that the heat flow here is much higher than 350 mW/m^2.

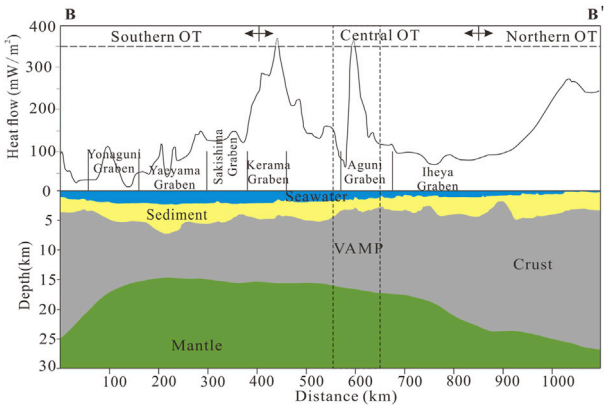

FIGURE 8 | The crustal structure and the heat flow along the profile BB′; profile location is shown in **Figure 5A**. The data sources are the same as those in **Figure 7**.

crust here has been thinned considerably (**Figure 5B** and **Figure 7**). It indicates that the attenuation of the Xihu and the Jilong sag is mainly in the upper crust. However, the mantle has upwelled under the OT and there is also obviously high heat flow at the OT. It means that the crustal thinning at the OT is not contributed by the upper crustal necking predominantly. Therefore, the crustal thinning mechanisms are different between the OT and the Xihu-Jilong sags.

The crustal thicknesses are 17–22 km at the northern OT, 11–19 km at the central OT, and 7–19 km at the southern OT (**Figure 5B**). The crustal thickness variations along the OT is quite similar to the Lau-Havre-Taupo back-arc basins (Kimura, 1985; Sibuet et al., 1987; Yan and Shi, 2014), so probably multi-evolution stages from rifting to spreading have been developed along the OT.

The Northern Okinawa Trough

The Moho depth variations at the northern OT agree with the seismic interpretation results of the OBS line 1, line 2, line 3, and line 4 (references are list in **Table 1**). Even though the velocity structures obtained from the OBSs data also indicate that the northern OT is a thinned continental crust in an arc rifting domain (Arai et al., 2017), the average crustal thickness here is larger than those of the central and southern OT. We suggest that the subduction of the seafloor highs, such as the Kyushu-Palau Ridge and the Amami Plateau, beneath the northern Ryukyu Arc had hampered the back-arc extension at the northern OT. The conversion from subduction to collision causes fore-arc rotation and also results in plate boundary curvature. In addition, GPS measurements show that the southward movement of the northeast Ryukyu Arc is much slower than that in the southwest (Nakamura et al., 2003). Contemporaneous volcanisms are concentrated on the northern Ryukyu Arc and scarcely occur in the northern OT (**Figure 1**). Therefore, the northern OT should be in the stage of early back-arc extension.

The Central Okinawa Trough

Compared with the northern OT, the crust of the central OT has been highly thinned, with the present thickness of 11–19 km and the Moho depths of 16–23 km. The seismic interpretation along

line 7 (Wu et al., 2020) and our gravity inversion result (**Figure 8**) show an obvious mantle upwelling beneath the axis of the central OT. In addition, the crust here has many similar characters with the oceanic crust, such as extremely high heat flow (**Figure 8**), hydrothermal fields, and intense volcanism (**Figure 1**) (Hao et al., 2004). Unlike only arc volcanism at the northern part of the Ryukyu trench-arc-basin system, the volcanism migrated from the arc to the back-arc region at the central OT. This is called the volcanic arc-rift migration phenomenon (VAMP) (Sibuet et al., 1987). A series of NE-trending faults occurred in the region with VAMP (Gungor et al., 2012). It indicates that the magma upwelling is correlated to the extensional faults. Active rifting structures have been observed from seismic reflection data in the Iheya Graben and the adjacent area at the central OT (Ikegami et al., 2015). However, the crust here is still not thin enough for crust break and further seafloor spreading. In addition, the volcanism here is still dispersed. Similar to the northern OT, the subduction of the Datio Ridge and the Oki-Daito Ridge beneath the central Ryukyu Arc also had hampered the spreading of the central OT. Therefore, the central OT is probably in the transitional stage from back-arc rifting to oceanic spreading, characterized by moderate crustal thinning, high heat flow, and intense magmatic activity.

The Southern Okinawa Trough

Figure 7B shows that the southern OT has the thinnest average crustal thickness among the three OT sections. However, solely based on the crust thickness, it is difficult to determine whether it is highly thinned continental crust or oceanic crust. We will further discuss this issue from the following three aspects.

1) From the thermal state. In general, the age of the oceanic crust is obviously younger than that of the continental crust. Our lithospheric mantle density modeling result indicates that the lithosphere thermal state of the southern OT is quite similar to the thermal state of the mid-ocean ridge, and so the crust here is apt to be oceanic.
2) From the plate strength. The effective elastic thickness (*Te*) of the lithosphere at the southern OT estimated from topography and gravity data is 5–7 km. The minimum effective elastic thickness occurred around the Yaeyama Graben with a thickness of 2.5–3.0 km (Fu et al., 2002), which is similar to the *Te* value of the mid-ocean ridge (Cochran, 1979).
3) From the rock type. Fresh basalts were collected by TV grab on the western end of the Yaeyama Graben, and this graben holds the thinnest crust of the whole OT (Lai et al., 2016). Furthermore, MORB-similar basalts at the southern OT is considered to be an important evidence for seafloor spreading here (Zong et al., 2016).

Therefore, we suggest that the southern OT is at the early stage of seafloor spreading, especially at the Yaeyama Graben.

Comparisons to Other Similar Tectonic Regions

The progressive variations of deformation style along the rift axis as occurred in the OT can be found in other basins, such as the East Gakkel Ridge-Laptev Sea Margin area in the Arctic Ocean (Franke et al., 2001) and the Woodlark Basin off Papua New Guinea in the western Pacific (Benes et al., 1994). The rifting to drifting transitions has generally been suggested as the result of differentiated lithospheric strength and the transfer or shear zones are always the boundaries between the rifting and drifting regions (Dunbar and Sawyer, 1996; Van Wijk and Blackman, 2005). Since the NW-SE-trending Kerama and Tokara faults, which separate the northern-central-southern OT, are thought as the result of the subduction of the high and buoyant topography in the Philippines Sea Plate (Sibuet et al., 1998; Gungor et al., 2012) and no evidence can demonstrate that pre-rifting OT has varying lithospheric strength, we suggest that the diffuse rifting in the OT is also due to the topographic high subduction.

CONCLUSION

The acoustic sedimentary basement geometry was mapped based on the published sediment thickness grid and recent seismic interpretations. The density variations in the sediment layer and the lithospheric mantle have been modeled for gravity inversion. The crustal thickness of the Ryukyu trench-arc-basin systems was estimated from the high-resolution free-air gravity anomaly.

The variations of the crustal thickness, along with the heat flow, the fault pattern, and the petrology data, indicate that the three sections of the OT are at different back-arc extension stages. The back-arc extension of the northern and central OT had been hampered by the subduction of bathymetry highs in the West Philippine Basin, but the southern section had not.

1) The northern OT holds the thickest crust among the three sections, the slow southward arc movement, and scarce contemporaneous volcanisms. These three facts indicate that the northern OT is in the stage of the early back-arc extension.
2) The central OT holds moderately thinned crustal thickness, extremely high heat flow, and intense volcanism. Therefore, the central OT is probably in the transitional stage from back-arc rifting to oceanic spreading.
3) The thinnest crust at the southern OT is only with 7 km thick. In addition, both the lithosphere thermal state and the lithospheric strength of the southern OT are quite similar to those of the mid-ocean ridge; MORB-similar basalts have been found in the southern OT. Therefore, we suggest that the southern OT is at the early stage of seafloor spreading.

DATA AVAILABILITY STATEMENT

The datasets presented in this study can be found in online repositories. The names of the repository/repositories and accession number(s) can be found in the article/ Supplementary Material.

AUTHOR CONTRIBUTIONS

LZ: Compiled the data, gravity modeling, and writing. XL: Seismic interpretation and writing—review and editing.

FUNDING

This study is supported by the China-ASEAN Maritime Cooperation Fund Project (No. 12120100500017001), the National Natural Science Foundation of China (Nos. 92055211 and 41406065), the National Program on Global Change and Air-Sea Interaction (GASI-GEOGE-02), and the Taishan Scholar Foundation of Shandong Province (ts201511061). The necessary datasets for reproducing this work can be downloaded from Zhang, Liang (2021), "data Supplementary For Moho geometry of the Okinawa Trough based on gravity inversion and its implications on the crustal nature and tectonic evolution", Mendeley Data, V1, doi: 10.17632/dt9jkphts6.1.

REFERENCES

Afonso, J. C., Fernàndez, M., Ranalli, G., Griffin, W. L., and Connolly, J. A. D. (2008). Integrated Geophysical-Petrological Modeling of the Lithosphere and Sublithospheric Upper Mantle: Methodology and Applications. *Geochem. Geophys. Geosyst.* 9, a–n. doi:10.1029/2007gc001834

Aitken, A. R. A. (2010). Moho Geometry Gravity Inversion experiment (MoGGIE): A Refined Model of the Australian Moho, and its Tectonic and Isostatic Implications. *Earth Planet. Sci. Lett.* 297, 71–83. doi:10.1016/j.epsl.2010.06.004

Amante, C., and Eakins, B. W. (2009). in *ETOPO1 1 Arc-Minute Global Relief Model: Procedures, Data Sources and AnalysisNational Geophysical Data Center-24* (United States: NOAA). doi:10.7289/V5C8276M

Arai, R., Kodaira, S., Yamada, T., Takahashi, T., Miura, S., Kaneda, Y., et al. (2017). Subduction of Thick Oceanic Plateau and High-angle normal-fault Earthquakes Intersecting the Slab. *Geophys. Res. Lett.* 44, 6109–6115. doi:10.1002/2017GL073789

Argus, D. F., Gordon, R. G., and Demets, C. (2011). Geologically Current Motion of 56 Plates Relative to the No-Net-Rotation Reference Frame. *Geochem. Geophys. Geosyst.* 12, a–n. doi:10.1029/2011GC003751

Bai, Y., Dong, D., Brune, S., Wu, S., and Wang, Z. (2019a). Crustal Stretching Style Variations in the Northern Margin of the South China Sea. *Tectonophysics* 751, 1–12. doi:10.1016/j.tecto.2018.12.012

Bai, Y., Gui, Z., Li, M., Dong, D., Wu, S., and Wang, Z. (2019b). Crustal Thickness over the NW Pacific and its Tectonic Implications. *J. Asian Earth Sci.* 185, 104050. doi:10.1016/j.jseaes.2019.104050

Bai, Y., Williams, S. E., Müller, R. D., Liu, Z., and Hosseinpour, M. (2014). Mapping Crustal Thickness Using marine Gravity Data: Methods and Uncertainties. *Geophysics* 79, G27–G36. doi:10.1190/geo2013-0270.1

Benes, V., Scott, S. D., and Binns, R. A. (1994). Tectonics of Rift Propagation into a continental Margin: Western Woodlark Basin, Papua New Guinea. *J. Geophys. Res.* 99, 4439–4455. doi:10.1029/93JB02878

Chappell, A. R., and Kusznir, N. J. (2008). Three-dimensional Gravity Inversion for Moho Depth at Rifted continental Margins Incorporating a Lithosphere thermal Gravity Anomaly Correction. *Geophys. J. Int.* 174, 1–13. doi:10.1111/j.1365-246X.2008.03803.x

Cochran, J. R. (1979). An Analysis of Isostasy in the World's Oceans: 2. Midocean ridge Crests. *J. Geophys. Res.* 84, 4713–4729. doi:10.1029/JB084iB09p04713

Cowie, L., and Kusznir, N. (2012). Gravity Inversion Mapping of Crustal Thickness and Lithosphere Thinning for the Eastern Mediterranean. *The Leading Edge* 31, 810–814. doi:10.1190/tle31070810.1

Currie, C. A., and Hyndman, R. D. (2006). The thermal Structure of Subduction Zone Back Arcs. *J. Geophys. Res.* 111, B08404. doi:10.1029/2005JB004024

Davies, J. H. (2013). Global Map of Solid Earth Surface Heat Flow. *Geochem. Geophys. Geosyst.* 14, 4608–4622. doi:10.1002/ggge.20271

Ding, W., Li, J., Wu, Z., Li, S., Lin, X., and Somerville, I. (2017). Late Mesozoic Transition from Andean-type to Western Pacific-type of the East China continental Margin-Is the East China Sea Basement an Allochthonous Terrain? *Geol. J.* 53, 1994–2002. doi:10.1002/gj.3029

Doo, W.-B., Lo, C.-L., Hsu, S.-K., Tsai, C.-H., Huang, Y.-S., Wang, H.-F., et al. (2018). New Gravity Anomaly Map of Taiwan and its Surrounding Regions with Some Tectonic Interpretations. *J. Asian Earth Sci.* 154, 93–100. doi:10.1016/j.jseaes.2017.12.010

Dunbar, J. A., and Sawyer, D. S. (1996). Three-dimensional Dynamical Model of continental Rift Propagation and Margin Plateau Formation. *J. Geophys. Res.* 101, 27845–27863. doi:10.1029/96JB01231

Fabbri, O., Monié, P., and Fournier, M. (2004). "Transtensional Deformation at the junction between the Okinawa Trough Back-Arc basin and the SW Japan Island Arc," in *Vertical and Decoupling in the Lithosphere*. Editors J. Grocott, K. J. W. Mc Caffrey, G. Taylor, and B. Tikoff (London,UK: Special Publication - Geological Society of London), 227, 297–312. doi:10.1144/GSL.SP.2004.227.01.15

Fang, P., Ding, W., Lin, X., Zhao, Z., Fang, Y., and Li, C. (2020). Neogene Subsidence Pattern in the Multi-Episodic Extension Systems: Insights from Backstripping Modelling of the Okinawa Trough. *Mar. Pet. Geology.* 111, 662–675. doi:10.1016/j.marpetgeo.2019.08.051

Franke, D., Hinz, K., and Oncken, O. (2001). The Laptev Sea Rift. *Mar. Pet. Geology.* 18, 1083–1127. doi:10.1016/S0264-8172(01)00041-1

Fu, Y., Li, A., and Qin, Y. (2002). Effective Elastic Thickness of the Oceanic and continental Marginal Lithospheres. *Mar. Geology. Quat. Geology. (in Chinese)* 22, 68–75. doi:10.16562/j.cnki.0256-1492.2002.03.011

Gao, D., Jinhai, Z., Bo, Y., and Tang, J. (2006). A Study on Lithopshere 3D Structures in the East China Sea and Adjacent Regions. *Chin. J. Geology. (in Chinese)* 41, 20–26. doi:10.1111/j.1745-4557.2006.00081.x

Gungor, A., Lee, G. H., Kim, H.-J., Han, H.-C., Kang, M.-H., Kim, J., et al. (2012). Structural Characteristics of the Northern Okinawa Trough and Adjacent Areas from Regional Seismic Reflection Data: Geologic and Tectonic Implications. *Tectonophysics* 522-523, 198–207. doi:10.1016/j.tecto.2011.11.027

Guo, K., Zeng, Z.-G., Chen, S., Zhang, Y.-X., Qi, H.-Y., and Ma, Y. (2017). The Influence of a Subduction Component on Magmatism in the Okinawa Trough: Evidence from Thorium and Related Trace Element Ratios. *J. Asian Earth Sci.* 145, 205–216. doi:10.1016/j.jseaes.2017.05.033

Han, B., Zhang, X., Pei, J., and Zhang, W. (2007). Characteristics of Crust-Mantle in East China Sea and Adjacent Regions. *Prog. Geophys. (in Chinese)* 22, 376–382. doi:10.1007/s11442-007-0020-2

Hao, T.-Y., Liu, J.-H., Guo, F., Huang, Z.-X., Xu, Y., Dai, M.-G., et al. (2004). Research on Crust Structure and Lithosphere Property beneath the Okinawa through Area. *Chin. J. Geophys.* 47, 525–532. doi:10.1002/cjg2.516

Hao, T.-Y., Xu, Y., Xu, Y., Suh, M., Liu, J.-H., Dai, M.-G., et al. (2006). Some New Understandings on the Deep Structure in Yellow Sea and East China Sea. *Chin. J. Geophys.* 49, 405–416. doi:10.1002/cjg2.849

Ikegami, F., Tsuji, T., Kumagai, H., Ishibashi, J.-i., and Takai, K. (2015). "Active Rifting Structures in Iheya Graben and Adjacent Area of the Mid-okinawa Trough Observed through Seismic Reflection Surveys," in *Subseafloor Biosphere Linked to Hydrothermal Systems: TAIGA Concept*. Editors J. i. Ishibashi, K. Okino, and M. Sunamura (Japan, Tokyo: Springer), 361–368. doi:10.1007/978-4-431-54865-2_28

Ishibashi, J.-i., Tsunogai, U., Toki, T., Ebina, N., Gamo, T., Sano, Y., et al. (2015). Chemical Composition of Hydrothermal Fluids in the central and Southern Mariana Trough Backarc basin. *Deep Sea Res. Part Topical Stud. Oceanography* 121, 126–136. doi:10.1016/j.dsr2.2015.06.003

Iwasaki, T., Hirata, N., Kanazawa, T., Melles, J., Suyehiro, K., Urabe, T., et al. (1990). Crustal and Upper Mantle Structure in the Ryukyu Island Arc Deduced from Deep Seismic Sounding. *Geophys. J. Int.* 102, 631–651. doi:10.1111/j.1365-246X.1990.tb04587.x

Kimura, M. (1985). Back-arc Rifting in the Okinawa Trough. *Mar. Pet. Geology.* 2, 222–240. doi:10.1016/0264-8172(85)90012-1

Klingelhoefer, F., Berthet, T., Lallemand, S., Schnurle, P., Lee, C.-S., Liu, C.-S., et al. (2012). P-wave Velocity Structure of the Southern Ryukyu Margin East of Taiwan: Results from the ACTS Wide-Angle Seismic experiment. *Tectonophysics* 578, 50–62. doi:10.1016/j.tecto.2011.10.010

Kodaira, S., Iwasaki, T., Urabe, T., Kanazawa, T., Egloff, F., Makris, J., et al. (1996). Crustal Structure across the Middle Ryukyu Trench Obtained from Ocean Bottom Seismographic Data. *Tectonophysics* 263, 39–60. doi:10.1016/S0040-1951(96)00025-X

Kusznir, N. J., Roberts, A. M., and Alvey, A. D. (2018). Crustal Structure of the Conjugate Equatorial Atlantic Margins, Derived by Gravity Anomaly Inversion. *Geol. Soc. Lond. Spec. Publications* 476, 83–107. doi:10.1144/SP476.5

Lai, Z., Zhao, G., Han, Z., Liu, B., Bu, X., and Leng, C. (2016). Back-arc Magma Processes in the Okinawa Trough: New Insights from Textural and Compositional Variations of Plagioclase in Basalts. *Geol. J.* 51, 346–356. doi:10.1002/gj.2767

Lee, C.-S., Shor, G. G., Bibee, L. D., Lu, R. S., and Hilde, T. W. C. (1980). Okinawa Trough: Origin of a Back-Arc basin. *Mar. Geology.* 35, 219–241. doi:10.1016/0025-3227(80)90032-8

Letouzey, J., and Kimura, M. (1986). The Okinawa Trough: Genesis of a Back-Arc basin Developing along a continental Margin. *Tectonophysics* 125, 209–230. doi:10.1016/0040-1951(86)90015-6

Liu, B., Li, S.-Z., Suo, Y.-H., Li, G.-X., Dai, L.-M., Somerville, I. D., et al. (2016). The Geological Nature and Geodynamics of the Okinawa Trough, Western Pacific. *Geol. J.* 51, 416–428. doi:10.1002/gj.2774

López-Coto, I., Mas, J. L., and Bolivar, J. P. (2013). A 40-year Retrospective European Radon Flux Inventory Including Climatological Variability. *Atmos. Environ.* 73, 22–33. doi:10.1016/j.atmosenv.2013.02.043

McKenzie, D., Jackson, J., and Priestley, K. (2005). Thermal Structure of Oceanic and continental Lithosphere. *Earth Planet. Sci. Lett.* 233, 337–349. doi:10.1016/j.epsl.2005.02.005

McKenzie, D. (1978). Some Remarks on the Development of Sedimentary Basins. *Earth Planet. Sci. Lett.* 40, 25–32. doi:10.1016/0012-821X(78)90071-7

Müller, R. D., Zahirovic, S., Williams, S. E., Cannon, J., Seton, M., Bower, D. J., et al. (2019). A Global Plate Model Including Lithospheric Deformation along Major Rifts and Orogens since the Triassic. *Tectonics* 38, 1884–1907. doi:10.1029/2018TC005462

Nakahigashi, K., Shinohara, M., Suzuki, S., Hino, R., Shiobara, H., Takenaka, H., et al. (2004). Seismic Structure of the Crust and Uppermost Mantle in the Incipient Stage of Back Arc Rifting - Northernmost Okinawa Trough. *Geophys. Res. Lett.* 31, L02614. doi:10.1029/2003GL018928

Nakamura, M., Yoshida, Y., Zhao, D., Katao, H., and Nishimura, S. (2003). Three-dimensional P- and S-Wave Velocity Structures beneath the Ryukyu Arc. *Tectonophysics* 369, 121–143. doi:10.1016/S0040-1951(03)00172-0

Nishizawa, A., Kaneda, K., Katagiri, Y., and Oikawa, M. (2014). Wide-angle Refraction Experiments in the Daito Ridges Region at the Northwestern End of the Philippine Sea Plate. *Earth Planet. Sp* 66, 25. doi:10.1186/1880-5981-66-25

Oldenburg, D. W. (1974). The Inversion and Interpretation of Gravity Anomalies. *Geophysics* 39, 526–536. doi:10.1190/1.1440444

Qi, J., Zhang, X., Wu, Z., Meng, X., Shang, L., Li, Y., et al. (2021). Characteristics of Crustal Variation and Extensional Break-Up in the Western Pacific Back-Arc Region Based on a Wide-Angle Seismic Profile. *Geosci. Front.* 12, 101082. doi:10.1016/j.gsf.2020.09.011

Rateb, A., Ching, K.-E., Kuo, C.-Y., Rau, R.-J., and Chen, C.-L. (2017). Kinematics of the Tectonic Blocks and Active Faults at the post-orogenic Stage: Northern Taiwan. *J. Asian Earth Sci.* 149, 29–40. doi:10.1016/j.jseaes.2017.07.055

Sandwell, D. T., Müller, R. D., Smith, W. H. F., Garcia, E., and Francis, R. (2014). New Global marine Gravity Model from CryoSat-2 and Jason-1 Reveals Buried Tectonic Structure. *Science* 346, 65–67. doi:10.1126/science.1258213

Sawyer, D. S. (1985). Total Tectonic Subsidence: A Parameter for Distinguishing Crust Type at the U.S. Atlantic Continental Margin. *J. Geophys. Res.* 90, 7751–7769. doi:10.1029/JB090iB09p07751

Shang, L.-N., Zhang, X.-H., Jia, Y.-G., Han, B., Yang, C.-S., Geng, W., et al. (2017). Late Cenozoic Evolution of the East China continental Margin: Insights from Seismic, Gravity, and Magnetic Analyses. *Tectonophysics* 698, 1–15. doi:10.1016/j.tecto.2017.01.003

Sibuet, J.-C., Deffontaines, B., Hsu, S.-K., Thareau, N., Le Formal, J.-P., and Liu, C.-S. (1998). Okinawa Trough Backarc basin: Early Tectonic and Magmatic Evolution. *J. Geophys. Res.* 103, 30245–30267. doi:10.1029/98JB01823

Sibuet, J.-C., Letouzey, J., Barbier, F., Charvet, J., Foucher, J.-P., Hilde, T. W. C., et al. (1987). Back Arc Extension in the Okinawa Trough. *J. Geophys. Res.* 92, 14041–14063. doi:10.1029/JB092iB13p14041

Stein, C. A., and Stein, S. (1992). A Model for the Global Variation in Oceanic Depth and Heat Flow with Lithospheric Age. *Nature* 359, 123–129. doi:10.1038/359123a0

Straume, E. O., Gaina, C., Medvedev, S., Hochmuth, K., Gohl, K., Whittaker, J. M., et al. (2019). GlobSed: Updated Total Sediment Thickness in the World's Oceans. *Geochem. Geophys. Geosyst.* 20, 1756–1772. doi:10.1029/2018GC008115

Sutra, E., and Manatschal, G. (2012). How Does the continental Crust Thin in a Hyperextended Rifted Margin? Insights from the Iberia Margin. *Geology* 40, 139–142. doi:10.1130/G32786.1

Taylor, B., and Goodliffe, A. M. (2004). The West Philippine Basin and the Initiation of Subduction, Revisited. *Geophys. Res. Lett.* 31, a–n. doi:10.1029/2004GL020136

Van Wijk, J. W., and Blackman, D. K. (2005). Dynamics of continental Rift Propagation: the End-Member Modes. *Earth Planet. Sci. Lett.* 229, 247–258. doi:10.1016/j.epsl.2004.10.039

Wu, S., Ni, X., and Guo, J. (2007). Balanced Cross Section for Restoration of Tectonic Evolution in the Southwest Okinawa Trough. *J. China Univ. Geosciences* 18, 1–10. doi:10.1016/S1002-0705(07)60013-2

Wu, Z., Zhang, X., Meng, X., Qi, J., Li, Y., Zhao, W., et al. (2020). A Profile Study of OBS Deep Geological Detect in theEast China Sea. *Chin. Sci. Bull.* 66, 2728–2744. doi:10.1360/TB-2020-0923

Xu, J., Ben-Avraham, Z., Kelty, T., and Yu, H.-S. (2014). Origin of Marginal Basins of the NW Pacific and Their Plate Tectonic Reconstructions. *Earth-Science Rev.* 130, 154–196. doi:10.1016/j.earscirev.2013.10.002

Xuan, S., Jin, S., and Chen, Y. (2020). Determination of the Isostatic and Gravity Moho in the East China Sea and its Implications. *J. Asian Earth Sci.* 187, 104098. doi:10.1016/j.jseaes.2019.104098

Yan, Q., and Shi, X. (2014). Petrologic Perspectives on Tectonic Evolution of a Nascent basin (Okinawa Trough) behind Ryukyu Arc: A Review. *Acta Oceanol. Sin.* 33, 1–12. doi:10.1007/s13131-014-0400-2

Zhang, L., Luan, X., Zeng, Z., and Liu, H. (2019). Key Parameters of the Structure and Evolution of the Okinawa Trough : Modelling Results Constrained by Heat Flow Observations. *Geol. J.* 54, 3542–3555. doi:10.1002/gj.3356

Zhang, Y., Ye, J., Kelu, S., Li, L., and Xu, J. (2009). The Burial History and Evolution of Xihu Depression. *Geotectonica et Metallogenia* 33, 215–223. doi:10.16539/j.ddgzyckx.2009.02.010

Zhou, Z. Y., Liao, Z. T., and Jin, X. C. (2001). Okinawa Trough:The Highest Stage of Continental Tension Rifting in Back-Arc Setting. *Mar. Geology. Quat. Geology. (in Chinese)* 21, 51–55. doi:10.16562/j.cnki.0256-1492.2001.01.009

Zong, T., Zhai, S., and Yu, Z. (2016). Regional Differences of Magmatism in the Okinawa Trough. *Earth Sci.* 41, 1031–1040. doi:10.3799/dqkx.2016.085

Conflict of Interest: The authors declare that the research was conducted in the absence of any commercial or financial relationships that could be construed as a potential conflict of interest.

Publisher's Note: All claims expressed in this article are solely those of the authors and do not necessarily represent those of their affiliated organizations, or those of the publisher, the editors, and the reviewers. Any product that may be evaluated in this article, or claim that may be made by its manufacturer, is not guaranteed or endorsed by the publisher.

frontiers in Earth Science

REVIEW
published: 10 January 2022
doi: 10.3389/feart.2021.808914

Research Progress on Cenozoic Volcano Genesis and Fluid Action in Northeast China

Yufeng Deng[1,2,3], *Song Huang*[1,2]*, *Xueshan Wu*[1,2,3] *and Min Li*[1,2,3]

[1]*Key Laboratory of Petroleum Resources Research, Institute of Geology and Geophysics, Chinese Academy of Sciences, Beijing, China,* [2]*Innovation Academy for Earth Science, Chinese Academy of Sciences, Beijing, China,* [3]*College of Earth and Planetary Sciences, University of Chinese Academy of Sciences, Beijing, China*

The tectonic evolution of northeast China is closely related to the subduction of the Pacific plate. The dehydration of the slab subduction process produces metasomatic agents that have important effects on the physical and chemical properties of the mantle wedge, including the decrease of seismic wave velocity and the increase of Poisson's ratio and electrical conductivity. In order to investigate the tectonic evolution and fluid action of northeast China, this paper compares the previous seismic and electromagnetic imaging results of northeast China and explores the relationship between the genesis of Cenozoic volcanoes and fluid action in northeast China through rheological analysis. The results show that the western Pacific plate subducted into the mantle transition zone beneath northeast China, and sustained dehydration occurred. The upward migration of these released water caused partial melting at the base of the upper mantle. Some of the upwelling streams pierced the weak tectonic boundary under the buoyancy effect, which finally formed the large-scale Cenozoic volcanic events in northeast China.

Keywords: volcano genesis, fluid, stagnant slab, seismic velocity, electrical conductivity

OPEN ACCESS

Edited by:
Xunhua Zhang,
Qingdao Institute of Marine Geology, China

Reviewed by:
Chuansong He,
Institute of Geophysics, China
Xin Liu,
Ocean University of China, China

***Correspondence:**
Song Huang
huangsong@mail.iggcas.ac.cn

Specialty section:
This article was submitted to Solid Earth Geophysics, a section of the journal Frontiers in Earth Science

Received: *04 November 2021*
Accepted: *21 December 2021*
Published: *10 January 2022*

Citation:
Deng Y, Huang S, Wu X and Li M (2022) Research Progress on Cenozoic Volcano Genesis and Fluid Action in Northeast China. Front. Earth Sci. 9:808914. doi: 10.3389/feart.2021.808914

INTRODUCTION

In northeast China, the northern margin of the Songliao Basin and its eastern and western flanks have developed many volcanoes, such as Changbaishan volcano, Longgang volcano, Jingpohu volcano, Abaga volcano, Halaha volcano, Wudalianchi volcano, and Nuominhe volcano. The formation mechanism of these volcanoes involves the core scientific problem of multi-layer interaction of the Earth system in Northeast Asia. Furthermore, it is the key to advancing the solution of major geoscientific issues related to the deep subduction of plates.

To investigate the volcano genesis of northeast China, many researchers have done much work and put forward some hypotheses about the formation mechanism of these volcanoes. Turcotte and Schubert (1982) suggested that the volcanoes in northeast China are hotspot volcanism formed by magma in the tail of the mantle column. (Miyashiro, 1986). proposed a "hot region" hypothesis, suggesting that the "hot region" transported beneath northeast China provided the source of volcanic activities. Tatsumi et al. (1990) explained the volcano genesis of northeast China using large-scale material injection into the crust from the Asthenosphere. Iwamori (1992) suggested that the deep primitive mantle became a molten "wet region" due to the lowering of solidus temperature by adding fluids. Buoyancy transported the partially molten mantle upward, causing crustal melting and volcanic activity near the upwelling center. Tatsumi and Eggins (1995) suggested that the thermal

upwelling of mantle peridotite separated from the stagnant slab lowered the solidus temperature of the shallow mantle and eventually triggered volcanic activity.

With more and more geophysical imaging work in northeast China, low-velocity and high-conductivity anomalies have been found in the upper mantle beneath the volcanoes in northeast China, which are located above the Pacific plate where the mantle transition has stalled. These results suggested that these volcanoes are back-arc intraplate volcanos closely linked to the subduction process of the Pacific plate (Ichiki et al., 2001; Zhao, 2004). Meanwhile, arc magmatism is usually due to corner flows in the mantle wedge and dehydration reactions during subduction. The rocks and minerals in the subduction zone contain some amount of water. During subduction, temperature and pressure changes, hydrous minerals decompose, and water is released by dehydration of the subducted crust, leading to partial melting of the subducted crust itself or the overlying mantle wedge. These processes may have led to large-scale upwelling of material from the northeast China Asthenosphere, resulting in intraplate volcanism (Zhao et al., 2011). In addition, the numerical simulation result of (Yang and Faccenda, 2020) also indicates that the Cenozoic volcanism in northeast China is the result of the interaction between the subducting Pacific slab and the hydrous mantle transition zone.

The water released during plate subduction will be metasomatic with the overlying mantle wedge minerals. The agents for mantle metasomatism will have important effects on the physical and chemical properties of the mantle wedge, including the decrease of seismic wave velocity and the increase of Poisson's ratio and conductivity (Zheng et al., 2016). To this end, this paper explores the relationship between volcano genesis and fluid action in northeast China by sorting out previous seismic and electromagnetic imaging results and extracting information on geological processes and fluid action reflected by geophysical imaging results through rheological analysis.

REGIONAL GEOLOGICAL BACKGROUND

Northeast China locates on the eastern edge of the Central Asian Orogenic Belt, surrounded by the Siberian plate in the north, the North China plate in the south, and the West Pacific plate in the east. Its internal geology is intricate and complex, forming a tectonic framework of mainly stretching and local extrusion. The general geomorphology shows a geotectonic pattern of basins and mountains arranged in an interlocking way along the northeast (Li et al., 2018).

It is generally accepted that northeast China has undergone two periods of tectonic evolution. During the Paleozoic, the tectonic evolution was mainly influenced by the Paleo-Asian Ocean between the Siberian Craton and the North China Craton; Since the Late Mesozoic, the East Asian continent has transitioned from the Paleo-Asian Ocean tectonic domain to the continental margin, and the lithosphere underwent multiple periods of extensional deformation. During this period, the Pacific plate subduction was the main factor controlling the tectonic evolution of the region. In the Early Cretaceous, the North China Craton was destroyed by the subduction of the Paleo-Pacific plate (should have already collapsed into the lower mantle). And the present stagnant Pacific slab in the mantle transition zone has contributed to the Cenozoic destruction of the East Asian continental lithosphere. (Zhou et al., 2014; Sun et al., 2015; Zhou and Li, 2017; Liu X et al., 2017; Liu Y et al., 2017). Volcanoes in northeast China are distributed linearly around the Songliao Basin. The main distribution zones are the Mishan-Dunhua Fault, the Yilan-Yitong Fault, the Heihe-Hegenshan Suture Zone, the Xiao Hinggan Mountains, and the Greater Khingan Range. Moreover, the confirmed Cenozoic volcanoes are the Changbaishan volcano, the Longgang volcano, the Jingpohu volcano, the Wudalianchi volcano, the Abaga volcano, Nuominhe volcano, among others (**Figure 1**).

SEISMIC IMAGING RESULTS

Global and regional seismic tomography results (Fukao et al., 1992; Zhao, 2004; Zhao et al., 2011; Fukao and Obayashi, 2013; Chen et al., 2017; Zhao, 2021) generally show that the northwest Pacific plate starts to subduct from the Japan Trench, and the subducted plate is as deep as the mantle transition zone and stalled above the 660-km velocity discontinuity. It can be seen in the images that there are apparent low-velocity anomalies in the upper mantle beneath northeast China. The corresponding mantle transition zone shows high-velocity anomalies (**Figures 2**, **3**). Meanwhile, for the accurate portrayal of the subduction plate morphology, regarding the westward extension distance and thickness of the Pacific slab stagnation, the P-wave imaging models of Wei et al. (2012) and Fukao and Obayashi (2013) showed that the leading edge of the stagnant slab could reach near below Abaga volcano. Li et al. (2013) and Lai et al. (2019) inferred the western boundary of the stagnant Pacific slab to be about 118°E (the stagnant slab in the mantle transition zone is about 1,200 km long and 140 km thick) by triplicated waveform modeling.

Lei and Zhao (2005) obtained the velocity structure of the upper mantle beneath Changbaishan volcano by processing the data from 19 portable stations and three permanent stations through the seismic body wave traveltime tomography method. The results showed apparent low-velocity anomalies about 10 km below Changbaishan volcano, and their extension direction corresponds well with Longgang volcano in the west and Xianjingdao volcano in the south. Moreover, these low-velocity anomalies extend to about 400 km, and high-velocity anomalies appear in the mantle transition zone. They thought that the Western Pacific subduction slab stalled in the mantle transition zone. The deep dehydration process of the plate and the convective circulation process in the big mantle wedge led to the upwelling of high-temperature asthenosphere material. And, the hot upwelling material to about 180 km was transported upwards from east to west and from north to south respectively, which became the material source of Changbaishan volcano (**Figure 4**). However, Tang et al. (2014) gained seismic images and triplicated waveform modeling results from the NECESSArray experiment. The result showed a low-velocity anomaly beneath Changbaishan

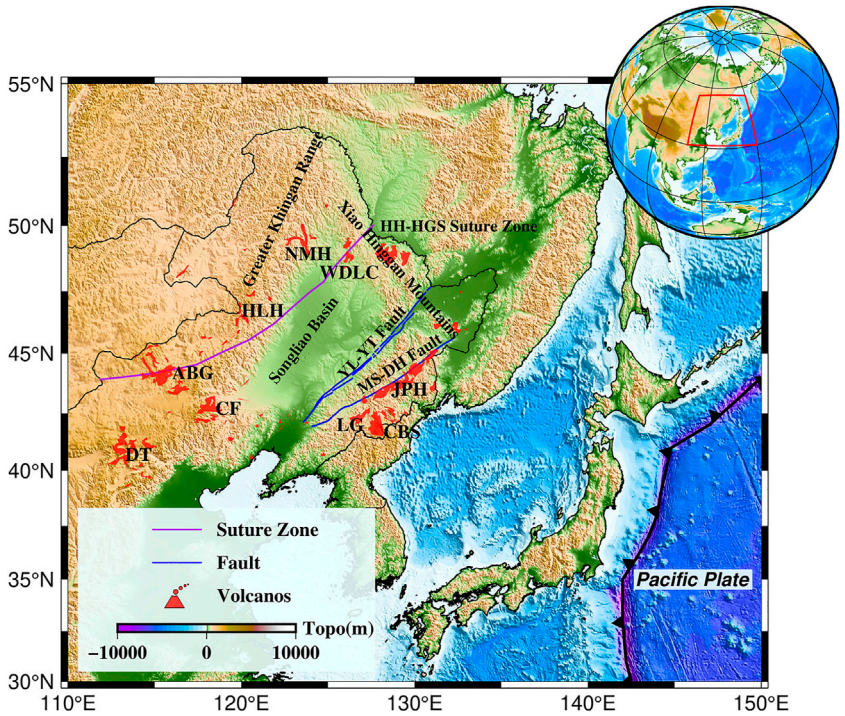

FIGURE 1 | Distribution of Cenozoic volcanoes in northeast China. Red areas represent volcanoes, CBS-Changbaishan volcano; LG-Longgang volcano; JPH-Jingpohu volcano; WDLC-Wudalianchi volcano; NMH-Nuominhe volcano; HLH -Halaha volcano; ABG - Abaga volcano; CF - Chifeng volcano; DT - Datong volcano. Blue lines indicate major fault, YL-YT Fault: Yilan-Yitong Fault; MS-DH Fault: Mishan-Dunhua Fault. Blue lines indicate major suture.

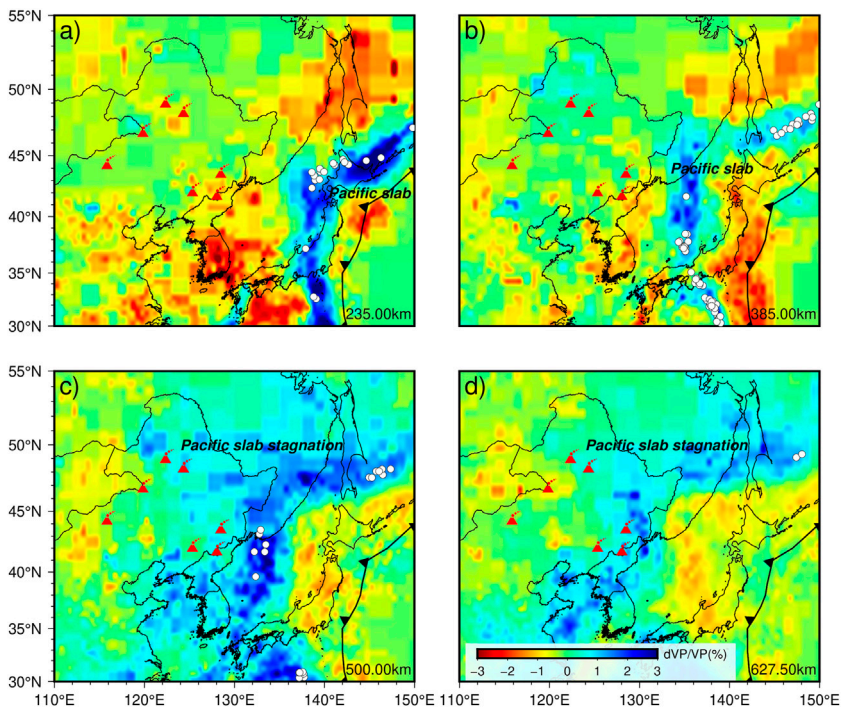

FIGURE 2 | Horizontal depth slices of P-wave velocity perturbation beneath the UU-P07 model in northeast China (Amaru, 2007). Figure **(A)**, **(B)**, **(C)**, and **(D)** respectively represents the horizontal depth slice of 235.00 km, 385.00 km, 500.00 km, and 627.00 km. Red triangles represent Cenozoic volcanoes. The white circles represent seismic events larger than magnitude 4 that occurred at this depth (±20 km) during 2019.7-2021.7.

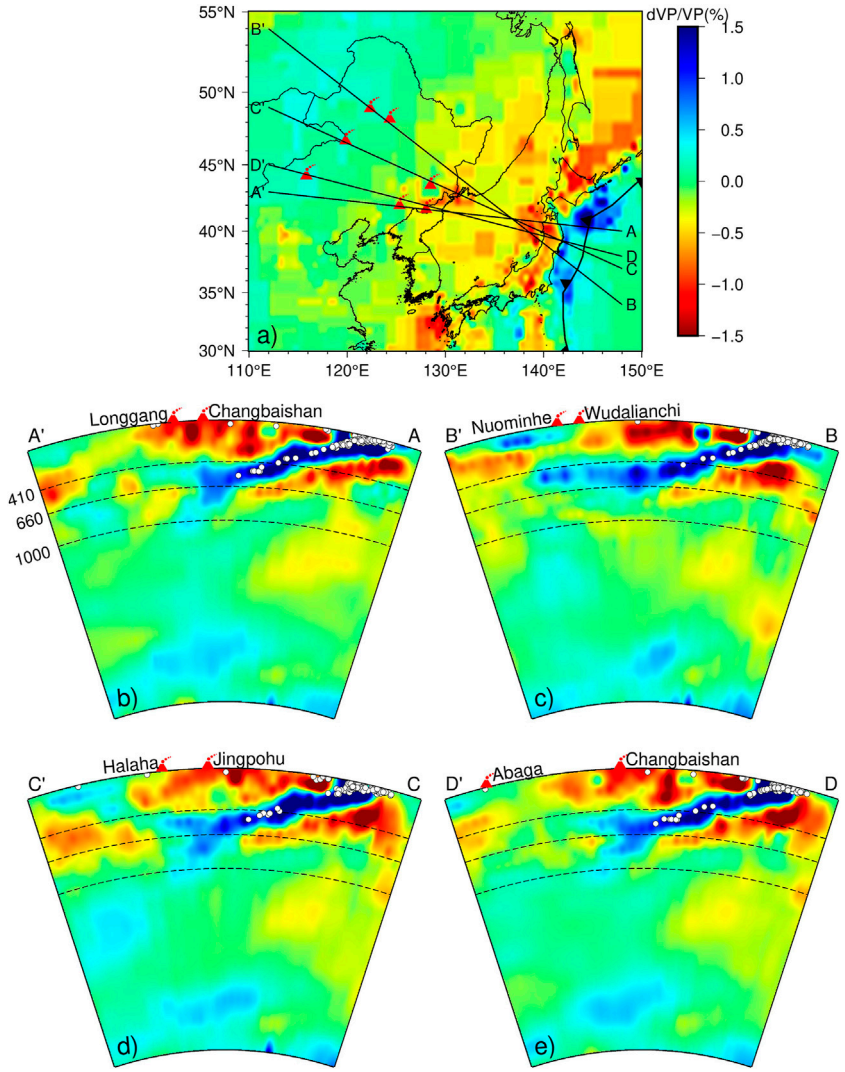

FIGURE 3 | Vertical depth profiles of P-wave velocity perturbation beneath the UU-P07 model in northeast China (Amaru, 2007). Figure **(A)** indicates the location of the four measurement lines. Figure **(B)**, **(C)**, **(D)**, and **(E)** respectively represents the vertical depth slice of measurement line AA′, measurement line BB′, measurement line CC′, and measurement line DD′. Red triangles represent Cenozoic volcanoes. The white circles represent seismic events larger than magnitude 4 that occurred in this profile (±1°) during 2019.7-2021.7.

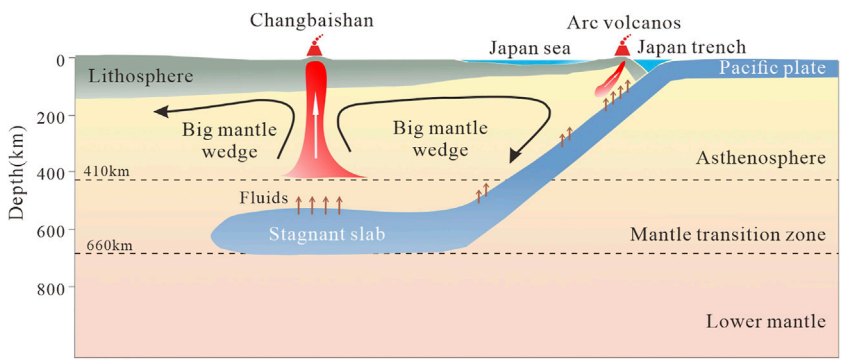

FIGURE 4 | Cartoon diagram of the model of plate dehydration in the large mantle wedge model induced volcanism in northeast China. See text for details.

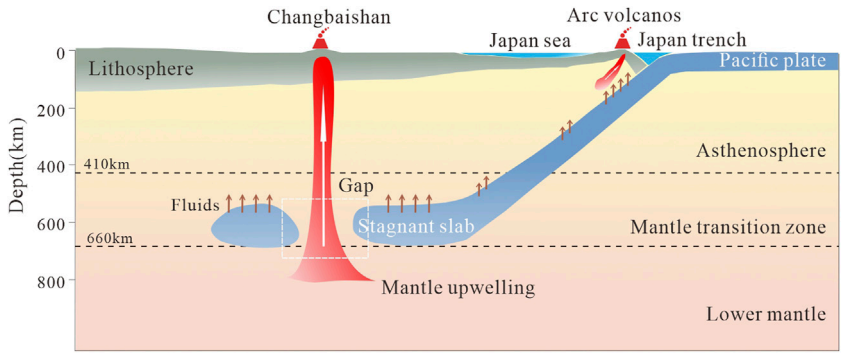

FIGURE 5 | Cartoon diagram of the model of volcanism in northeastern China induced by decompression melting from the upwelling of lower mantle material. See text for details.

volcano that continues below 660 km, with a "gap" in the stagnant Pacific slab in the transition zone. They thought that the volcanic activity of Changbaishan may be caused by the upwelling of the lower mantle material through the "gap" in the stagnant slab and decompression melting in the asthenosphere (**Figure 5**).

He and Santosh (2016) discovered the significant traces of mantle upwelling in northeast China through the receiver function and teleseismic P-wave tomography method. They speculated that these observed low-velocity anomalies might be vestiges of a mantle plume. He (2021) used the CCP (common-conversion-point) stacking technique of receiver function to delineate the structure of the upper mantle transition zone in northeast China more finely, and the study found the relics of an upwelling mantle plume beneath the Songliao basin. And combined with the finding of He et al. (2014) that the projection of the mantle plume at the surface overlies the lithosphere and crustal thinning and the location of the mafic-ultramafic regions, he speculated that the mantle plume triggered the large-scale volcanism in the Mesozoic in northeast China and may have led to the formation of the Songliao Basin. Further analysis revealed that the volcanism in northeast China showed a spatial shift from the center of the Songliao Basin to the basin margin from Mesozoic to Cenozoic. The age of volcanism products decreased from west to east in northeast China (Sun et al., 2020). These indicated that the Mesozoic mantle plume migrated and tilted toward Changbaishan in the southern Songliao Basin during the Mesozoic-Cenozoic. And finally, the mantle plume beneath the Changbaishan triggered the Cenozoic volcanism in northeast China.

The global seismic tomography results show that the Jingpohu volcano and Changbaishan volcano share similar structural features of the upper mantle and mantle transition zone. However, Duan et al. (2009) obtained the P-wave velocity structure beneath Jingpohu volcanic area by using the seismic body wave traveltime tomography method. They found that there is no obvious low-velocity anomaly in the crust, and seems to be a more apparent high-velocity anomaly extending down to the top of the mantle transition zone. Besides, the surface wave imaging results of Fu et al. (2016) and the S-wave imaging results of Fan and Chen (2019) show low-velocity anomalies from the bottom of the crust below Jingpohu volcano to the top of the asthenosphere. Still, no evident low-velocity bodies are found in the crust. These imply that partial melting may exist beneath Jingpohu volcano, but the degree of melting of the lithospheric mantle is lower than that of Changbaishan volcano (Chen et al., 2007).

Wei et al. (2019) gained the P-wave velocity structure beneath the Wudalianchi volcano and Halaha volcano utilizing a teleseismic tomography imaging method on data from two roughly parallel linear north-west oriented seismic arrays in northeast China. The results showed that a low-velocity anomaly with a width of about 80 km exists beneath the Wudalianchi volcano, which extends vertically from about 35 km to about 200 km and further southeast to the top of the mantle transition zone, and an apparent high-velocity anomaly is visible in the mantle transition zone. A low-velocity body extending into the mantle transition zone can be observed below the Halaha volcano, while a high-velocity anomaly is still visible in the mantle transition zone. Comparing global and regional seismic tomography results (Zhao, 2004; Li et al., 2013; Li et al., 2016; Lai et al., 2019), they inferred that the high-velocity anomalies in the mantle transition zone beneath Wudalianchi volcano and Halaha volcano are the Pacific subduction slab, indicating that their genesis is closely related the Pacific subduction slab. They further speculated that the formation of the Wudalianchi volcano is connected with convective circulation in the big mantle wedge above the Pacific stagnant slab. In contrast, the source of the Halacha volcano was supplied by local upwelling caused by the collapse of the stagnant slab into the lower mantle for dehydration (Schmandt et al., 2014).

Guo et al. (2016) acquired the surface wave velocity structure of the crust and upper mantle within 200 km in northeast China by seismic noise imaging. The results showed that the velocity in the Songliao Basin is relatively high in the upper mantle 50–200 km. Low-velocity anomalies extending up to 200 km can be seen beneath Changbaishan volcano and Jingpohu volcano on the eastern edge of the Songliao Basin. Low-velocity anomalies also reach about 200 km under the Halaha volcano on the western edge of the Songliao Basin. The low-velocity anomaly beneath the Abaga volcano only extends to

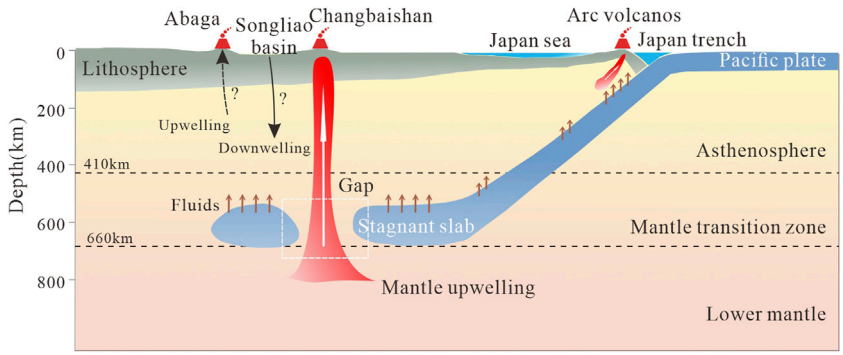

FIGURE 6 | Cartoon diagram of the model of small-scale upper mantle convection induced volcanism in northeast China. See text for details.

about 150 km. Based on the observed surface wave velocity structure and the S-wave velocity imaging results, Tang et al. (2014) proposed a small-scale upper mantle convection model to explain the genesis of intraplate volcanoes in northeast China. Among them, the upwelling from the mantle transition zone or deeper mantle below Changbaishan volcano caused local convection in the upper mantle of northeast China: the low-velocity anomaly in the upper mantle below Changbaishan volcano corresponds to the upward branch of this convective unit, and the high-velocity anomaly in the upper mantle below Songliao Basin corresponds to the downward branch of this convective unit, and the downwelling below Songliao Basin may have induced the secondary local convection in the asthenosphere below the western Greater Khingan Range, and the rising secondary local convection triggered the volcanic activities of Halaha and Abaga (**Figure 6**).

Fan et al. (2021) used ambient noise and earthquake two-plane wave tomography methods to obtain high-precision three-dimensional S-wave velocity structures of the crust and upper mantle in northeast China. The imaging results showed that the top of the upper mantle beneath Changbaishan volcano, Longgang volcano, Jingpohu volcano, Abaga volcano, Halaha volcano exhibits significant low-velocity anomalies, indicating that the upwelling asthenosphere may have reached (or approached) the Moho surface; while, the top of the upper mantle beneath Wudalianchi volcano and Nuominhe volcano exhibits relatively high-velocity anomalies, which may indicate the presence of the lithospheric mantle in the region. Combined with the results of previous petrological and geochemical studies (Foley et al., 1987), they hypothesized that the sodic basalts of a series of volcanoes, including Changbaishan volcano, are mainly from the upwelling asthenosphere mantle, while the high potassium basalts of Wudalianchi and Nuominhe volcanoes are the products of the interaction between the low degree melt of the asthenosphere and the overlying lithospheric mantle. The results of this study reveal that the significant spatial variability in intensity and scale of asthenospheric-lithospheric mantle interactions beneath northeast China due to continuous subduction of the western Pacific plate since the late Mesozoic controlled the origin of the Quaternary sodic and potassic intraplate volcanism. Zhang et al. (2021) jointly inverted new surface-wave dispersion data, surface heat flow, geoid height, and elevation data to image the fine-scale thermal and compositional structure of northeast China and inferred partial melt regions of the mantle. It was found that the location and composition of basaltic volcanism correlate well with the anomalous hot asthenosphere regions and the shallow lithosphere-asthenosphere boundary. These results suggest that intraplate volcanism's occurrence, location, and composition are controlled by the interaction of shallow asthenospheric circulation and lithospheric thickness.

Generally speaking, there are three main models for the genesis of intraplate volcanoes in northeast China under different velocity structure backgrounds: 1) the plate dehydration model in the big mantle wedge model, which suggests that there is a horizontal spreading subduction slab in the mantle transition zone with high-velocity anomaly, and the water carried by the subduction slab is released into the large mantle wedge above it, and the mantle wedge material melts under the action of water, leading to volcanic activity. 2) the decompression melting model from the upwelling of material from the lower mantle, which suggests that hot material from deep in the lower mantle is upwelling beneath the volcano through the stagnant slab vacancy created by tearing, and forming a source of volcanic activity by decompression melting. 3) the small-scale upper mantle convection model, which argues that the upwelling of hot material from the mantle transition zone or deeper mantle triggers local convection in the upper mantle, leading to volcanic activity. The latter two models are based on the presence of low-velocity anomalies at the front end of the high-velocity subduction slab, suggesting that the deep velocity structure is an essential factor constraining the volcano genesis mechanism in northeast China.

ELECTROMAGNETIC IMAGING RESULTS

Seismic wave velocities are closely related to medium elastic constants, density, and lithology. It can be used to characterize the dynamics of the Earth's interior, such as mantle convection, the evolution of subducted plates, and the origin of continents (Li

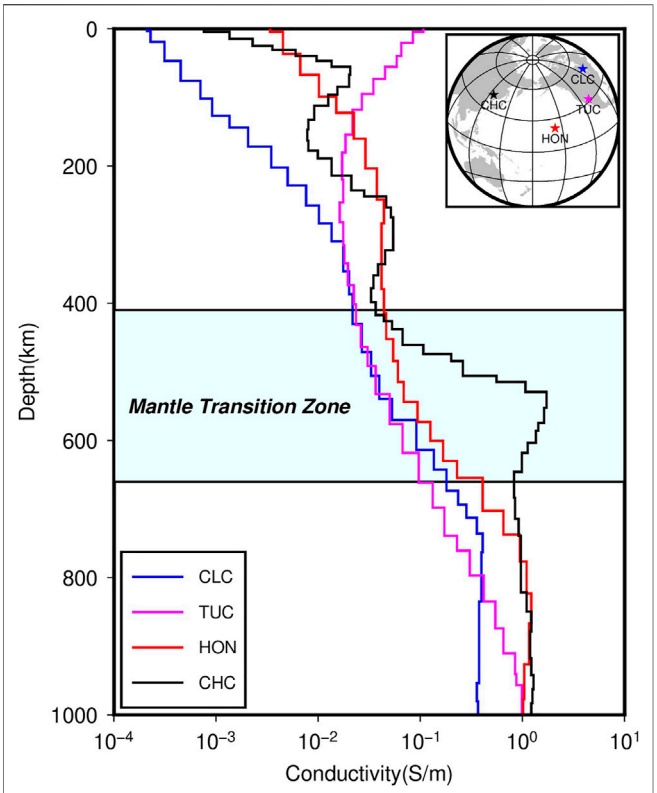

FIGURE 7 | One-dimensional electrical structure of northeast China (CHC) (Ichiki et al., 2001) compared with conductivity models of Carty Lake (CLC) in the Canadian Shield, Tucson (TUC) in the southwestern United States, and Honolulu (HON) region in the north-central Pacific Ocean (Neal et al., 2000).

and van der Hilst, 2010). However, seismic wave velocities are not sensitive to temperature, the presence of water and melt. Instead, the water content of the Earth's interior strongly influences the evolution and dynamics of the Earth, which ultimately controls the occurrence of earthquakes and volcanoes (Munch et al., 2020). Electrical conductivity is a property of rocks that varies with temperature and water content. Therefore, the electrical structure obtained from electromagnetic imaging studies can provide complementary information to seismic imaging results to more fully understand the deep structure of volcanoes.

Ichiki et al. (2001) inferred the conductivity structure of the mantle in northeast China by long-period magnetotelluric and geomagnetic depth sounding experiments. Compared with the conductivity models of Carty Lake (CLC) in the Canadian Shield, Tucson (TUC) in the southwestern United States, and Honolulu (HON) in the north-central Pacific Ocean (Neal et al., 2000) (**Figure 7**), it was found that the conductivity of the mantle transition zone beneath northeast China is nearly an order of magnitude higher than that of other tectonic environments. It is speculated that this phenomenon is likely related to the presence of water in the stagnant slab. Moreover, the global mantle conductivity models of Kelbert et al. (2009) and Semenov and Kuvshinov (2012) also showed obvious high-conductivity anomalies in the mantle transition zone beneath northeast China. Similarly, Munch et al. (2020) used a joint probabilistic density inversion of the estimated global-to-local transfer functions of the ionospheric and magnetospheric electromagnetic signals to obtain the conductivity structure of the upper mantle and mantle transition zone beneath 20 geomagnetic stations, and combined it with the mantle thermochemical structure analyzed from seismic data to gain the mantle water content, which showed that a large amount of water($C_w^{wad} \sim 0.3wt\%$) exists in the transition zone beneath the North Asian. Combined with the seismic imaging results, it can be speculated that the water carried during the subduction of the western Pacific plate beneath northeast China was released due to changes in temperature and pressure conditions, which strongly influenced the tectonic evolution of northeast China.

At present, many magnetotelluric experiments have been carried out for Cenozoic volcanoes in northeast China. The electrical structures beneath Changbaishan volcano, Jingpohu volcano, Wudalianchi volcano, and Halaha volcano have been obtained. The electromagnetic imaging results of Changbaishan volcano showed an isolated low resistance body in the range of about 10–30 km with a downward trend beneath the north and east area of Tianchi crater, which is presumed to be a crustal magma capsule formed by magma transported up from below the earth's crust (Tang et al., 2001; Qiu et al., 2014; Ruan et al., 2020). Zhu et al. (2001) conducted magnetotelluric experiments for 30 stations in the Jingpohu volcano. They found that the resistivity of the surrounding area below the volcano is high, and there is a low resistance vertical column with an irregular cross-section elongated in the northeast direction in the middle. The resistivity of this column is not uniform from top to bottom, with medium resistance at the top, high resistance at the middle, and low resistance at the bottom. It is presumed to be a former magma channel, so the resistivity is lower than the surrounding resistivity. When the volcano stopped erupting, the magma cooled, and the resistivity became higher, but it is still much lower than the resistivity on both sides. Zhan et al. (1999) processed seven magnetotelluric profiles of Wudalianchi volcano. The results showed that a rivet-like high resistance anomaly exists at a depth of several hundred meters to about 15–20 km below the surface, and the high resistance body has been connected to the upper mantle through the crust. Its resistivity gradually decreases with increasing depth, which is presumed to be a magma channel during consolidation. However, no obvious low resistance magma capsule is found in the crust. Tang et al. (2015) observed seven magnetotelluric sites at Halaha volcano. They found an alternating lateral distribution of high and low resistance in the lower and middle crust (9–30 km). The two low resistance zones are located just below two volcanic zones with the same subsurface magma pathway to the mantle.

Summarizing the results of electromagnetic studies on the individual volcano, it can be found that crustal magma capsules exist in the Changbaishan volcano. Moreover, the crustal magma

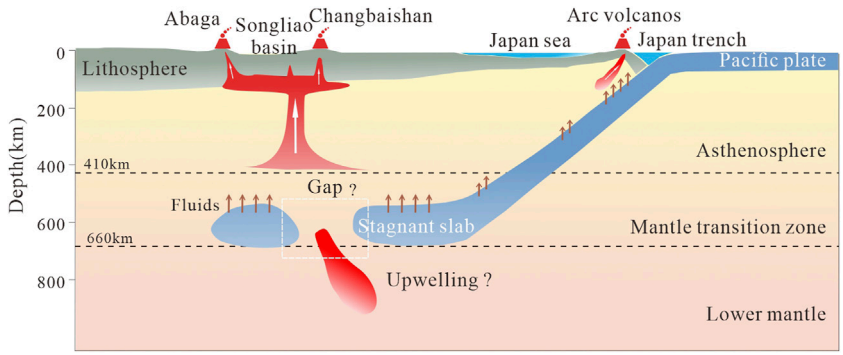

FIGURE 8 | Cartoon diagram of the model of mantle upwelling piercing the lithosphere induced volcanism in northeast China. See text for details.

capsule must directly connect with the deep mantle to ensure sufficient heat source replenishment to maintain the melt. Although no obvious crustal magma capsules are found in other volcanoes in northeast China, they all seem to have magma channels to the deep mantle. In order to explore the connection of volcanoes in northeast China at greater depths and to better understand the genesis of these volcanoes, a longer period of electromagnetic sounding is needed. Li et al. (2020) used long-period array magnetotelluric data to obtain the three-dimensional electrical structure of the upper mantle scale in northeast China. The results showed that there were several independent low-resistance anomalies in the lithospheric mantle. With the increase of depth, the scale of these low resistance anomalies became more significant. To the deep part of the upper mantle, the shape of these low resistance anomalies corresponded to the contour of the Songliao Basin. The petrophysical analysis showed that these low resistance anomalies were caused by high water content and partial melt material. We speculate that this is due to the continuous dehydration of the Pacific stagnant plate in the mantle transition zone below northeast China, which causes partial melting at the top of the mantle transition zone below Songliao Basin. The partially molten mantle hot materials were transported upward by buoyancy, melted through the asthenosphere, and bottomed out the bottom of the dry lithosphere. Finally, they pierced the weak tectonic boundary, which triggered the intraplate volcanism in northeast China (**Figure 8**). Xu et al. (2020) found that the distribution of Cenozoic high-Mg andesites in northeast China corresponds well with the leading edge of the stagnant slab in the mantle transition zone (Zhao et al., 2009), and the magnetotelluric imaging results show that there are obvious low- resistance anomalies in the mantle below the distribution area of high-Mg andesites (Li et al., 2020) by analyzing regional geophysical data. Moreover, geochemical signatures indicate that the high-Mg andesites in northeast China originated from partial melting of water-bearing mantle peridotite. Therefore, they suggest that the formation of high-Mg andesites was facilitated by the abundant recycled ancient sediments and water from the leading edge of the stagnant slab in the mantle transition zone, which provided the material source for the Cenozoic volcanism in northeast China.

DISCUSSION

During subduction, when the subducting slab reaches a certain depth, it is subjected to the high temperature and pressure of the environment. It undergoes dehydration of rocks due to phase transition, dehydration of hydrated minerals by extrusion, and water production by melting due to friction during subduction. Although most water is released from the oceanic crust at the depth of 150–200 km, in cold subduction environments such as the western Pacific slab, water can also enter the mantle transition zone or even deeper through storing in minerals such as lawsonite and dense hydrous magnesium silicates, or as nominally anhydrous minerals (Zheng et al., 2016).

The spatial resolution of seismic and electromagnetic models is a prerequisite for tectonic interpretations. The UU-P07 model, mentioned in the previous section, can resolve P-wave velocity anomalies with a horizontal variation of 0.4° in the crust and upper mantle and satisfactorily resolve the stagnant plate morphology in the upper mantle transition zone. The horizontal resolution of the big mantle wedge model proposed by Lei and Zhao (2005) is 2° × 2°, and the resolution is higher in the depth range of 10–400 km with the vertical grid node spacing is about 200 km. These indicate that the low-velocity anomalies extending to about 400 km beneath Changbaishan volcano are a reliable feature. Tang et al. (2014) confirmed the existence of the "gap" in the stagnant Pacific slab in the transition zone by examining the horizontally polarized (SH) displacement waveforms propagating through the mantle transition zone anomaly. Guo et al. (2016) performed a horizontal resolution of 2° × 2 ° detection plate test and S-wave velocity model constraint within a vertical depth of 300 km in proposing the small-scale upper mantle convection model. Similarly, Li et al. (2020) performed a resolution test, divided the electromagnetic model using a grid spacing of 30 km, and limited the model depth to 35–350 km based on the electromagnetic data period. These ensured the ability of the electromagnetic model to identify low-resistance anomalies in the mantle. In addition, most of the other seismic and electromagnetic models mentioned in the paper were also tested for the resolution to ensure the reliability of the anomaly structure.

The seismic and electromagnetic imaging results show low-velocity, high-conductivity anomalies associated with the volcanic magma system beneath the volcanoes in northeast China, and some of the low-velocity bodies extend to the top of the mantle transition zone at a depth of 410 km. There are three ways of magma production or mantle melting: 1) local mantle temperature increase (warming melting); 2) local mantle pressure decrease (depressurization melting); and 3) water released during subduction enters the overlying hot mantle peridotite by buoyancy, lowering its solidus temperature and eventually leading to partial melting of the mantle. Thus, the study of seismic wave velocities and electrical structure combined with rheological analysis suggests that the formation of volcanoes in northeast China is closely related to subduction zone structure and fluid action.

Northeast China is located in the eastern part of the Central Asian orogenic belt between the North China Craton and the Siberian plate, which consists of a succession of microcontinents including the Erguna Massif, Xing'an Massif, Songnun-Zhangguangcai Ling Massif, Jiamusi Massif, and Xingkai Massif (Zhou et al., 2018). Most of these microcontinents formed during the Rodinia supercontinent breakup. During the Paleozoic period, the mutual closure of ocean basins led to the complex collision between microcontinents. During the Mesozoic, the final closure of the Paleo-Asian Ocean transformed the tectonic system of northeast China, which was influenced by the subduction and retreat of the western Pacific Ocean plate, resulting in an overall tensional environment in northeast China, followed by collisional mountain building, extensional collapse, and post-arc extension. During this period, deep and sizeable lithospheric Fault developed in northeast China, such as the Dunhua-Mishan Fault and the Yitong-Yilan Fault (Tang et al., 2015). These suture zones and Faults provided channels for fluid upwelling in the asthenosphere, which eventually triggered volcanic activity in northeast China.

CONCLUSION

Seismic and electromagnetic imaging results show that the western Pacific subduction slab is stalled in the mantle transition zone beneath volcanoes in northeast China. There are obvious low-velocity and high-conductivity anomalies in the corresponding crust and upper mantle. Rheological analyses suggest that these anomalies are caused by the melt upwelling of deep mantle thermal materials due to the dehydration of the stagnant plate. These hot molten materials eventually punctured the weak tectonic zone of the lithosphere and triggered volcanic activity. This suggests that these volcanoes are back-arc intraplate volcanos and that their genesis is closely linked to the Pacific plate's subduction processes and fluid action.

The accuracy of the velocity and electrical structure beneath volcanoes has important implications for constraints on volcanogenic mechanisms. However, due to differences in observational data and imaging resolution, variations in the physical structure beneath northeast China obtained from different studies result in multiple models remaining for the specific controls used to explain volcano genesis. Therefore, more extensive and fine-scale geophysical imaging work is needed to accurately derive volcanogenic mechanisms in northeast China.

AUTHOR CONTRIBUTIONS

YD wrote the first draft of the manuscript. SH and YD contributed to conception and design of the study. XW and ML wrote sections of the manuscript. All authors contributed to manuscript revision, read, and approved the submitted version.

FUNDING

This work was supported by the National Natural Science Foundation of China under grant 91858214 and the National Key R&D Program of China under grant 2018YFC0604004.

ACKNOWLEDGMENTS

All Figures in this study are plotted by the GMT (http://gmt.soest.hawaii.edu/home). Seismic event catalogue downloads from the International Seismological Centre (http://www.isc.ac.uk/iscbulletin/search/catalogue/).

REFERENCES

Amaru, M. (2007). *Global Travel Time Tomography with 3-D Reference Models*. PhD Thesis: Utrecht University.

Chen, C., Zhao, D., Tian, Y., Wu, S., Hasegawa, A., Lei, J., et al. (2017). Mantle Transition Zone, Stagnant Slab and Intraplate Volcanism in Northeast Asia. *Geophys. J. Int.*, ggw491. doi:10.1093/gji/ggw491

Chen, Y., Zhang, Y., Graham, D., Su, S., and Deng, J. (2007). Geochemistry of Cenozoic Basalts and Mantle Xenoliths in Northeast China. *Lithos* 96 (1-2), 108–126. doi:10.1016/j.lithos.2006.09.015

Duan, Y., Zhao, D., Zhang, X., Xia, S., Liu, Z., Wang, F., et al. (2009). Seismic Structure and Origin of Active Intraplate Volcanoes in Northeast Asia. *Tectonophysics* 470 (3-4), 257–266. doi:10.1016/j.tecto.2009.01.004

Fan, X., Chen, Q.-F., Ai, Y., Chen, L., Jiang, M., Wu, Q., et al. (2021). Quaternary Sodic and Potassic Intraplate Volcanism in Northeast China Controlled by the Underlying Heterogeneous Lithospheric Structures. *Geology* 49 (10), 1260–1264. doi:10.1130/g48932.1

Fan, X., and Chen, Q. F. (2019). Seismic Constraints on the Magmatic System beneath the Changbaishan Volcano: Insight into its Origin and Regional Tectonics. *J. Geophys. Res. Solid Earth* 124 (2), 2003–2024. doi:10.1029/2018jb016288

Foley, S. F., Venturelli, G., Green, D. H., and Toscani, L. (1987). The Ultrapotassic Rocks: Characteristics, Classification, and Constraints for Petrogenetic Models. *Earth-Science Rev.* 24(2), 81–134. doi:10.1016/0012-8252(87)90001-8

Fu, Y. V., Gao, Y., Li, A., Li, L., Shi, Y., and Zhang, Y. (2016). Origin of Intraplate Volcanism in Northeast China from Love Wave Constraints. *J. Geophys. Res. Solid Earth* 121 (11), 8099–8112. doi:10.1002/2016jb013305

Fukao, Y., Obayashi, M., Inoue, H., and Nenbai, M. (1992). Subducting Slabs Stagnant in the Mantle Transition Zone. *J. Geophys. Res.* 97 (B4), 4809. doi:10.1029/91jb02749

Fukao, Y., and Obayashi, M. (2013). Subducted Slabs Stagnant above, Penetrating through, and Trapped below the 660 Km Discontinuity. *J. Geophys. Res. Solid Earth* 118 (11), 5920–5938. doi:10.1002/2013jb010466

Guo, Z., Chen, Y. J., Ning, J., Yang, Y., Afonso, J. C., and Tang, Y. (2016). Seismic Evidence of On-Going Sublithosphere Upper Mantle Convection for Intraplate Volcanism in Northeast China. *Earth Planet. Sci. Lett.* 433, 31–43. doi:10.1016/j.epsl.2015.09.035

He, C., Dong, S., Chen, X., Santosh, M., and Niu, S. (2014). Seismic Evidence for Plume-Induced Rifting in the Songliao Basin of Northeast China. *Tectonophysics* 627, 171–181. doi:10.1016/j.tecto.2013.07.015

He, C., and Santosh, M. (2016). Seismic Tomographic Evidence for Upwelling Mantle Plume in NE China. *Phys. Earth Planet. Interiors* 254, 37–45. doi:10.1016/j.pepi.2016.03.007

He, C. (2021). The Structure of the Upper Mantle Transition Zone beneath Northeast China Associated with Mantle Plume Migration. *Earth Space Sci.* 8 (9). doi:10.1029/2021ea001874

Ichiki, M., Uyeshima, M., Utada, H., Guoze, Z., Ji, T., and Mingzhi, M. (2001). Upper Mantle Conductivity Structure of the Back-Arc Region beneath Northeastern China. *Geophys. Res. Lett.* 28 (19), 3773–3776. doi:10.1029/2001gl012983

Iwamori, H. (1992). Degree of Melting and Source Composition of Cenozoic Basalts in Southwest Japan: Evidence for Mantle Upwelling by Flux Melting. *J. Geophys. Res.* 97 (B7), 10983. doi:10.1029/92jb00737

Kelbert, A., Schultz, A., and Egbert, G. (2009). Global Electromagnetic Induction Constraints on Transition-Zone Water Content Variations. *Nature* 460 (7258), 1003–1006. doi:10.1038/nature08257

Lai, Y., Chen, L., Wang, T., and Zhan, Z. (2019). Mantle Transition Zone Structure beneath Northeast Asia from 2-D Triplicated Waveform Modeling: Implication for a Segmented Stagnant Slab. *J. Geophys. Res. Solid Earth* 124 (2), 1871–1888. doi:10.1029/2018jb016642

Lei, J., and Zhao, D. (2005). P-wave Tomography and Origin of the Changbai Intraplate Volcano in Northeast Asia. *Tectonophysics* 397 (3-4), 281–295. doi:10.1016/j.tecto.2004.12.009

Li, C., and van der Hilst, R. D. (2010). Structure of the Upper Mantle and Transition Zone beneath Southeast Asia from Traveltime Tomography. *J. Geophys. Res.* 115. doi:10.1029/2009jb006882

Li, J., Wang, X., Wang, X., and Yuen, D. A. (2013). P and SH Velocity Structure in the Upper Mantle beneath Northeast China: Evidence for a Stagnant Slab in Hydrous Mantle Transition Zone. *Earth Planet. Sci. Lett.* 367, 71–81. doi:10.1016/j.epsl.2013.02.026

Li, S., Suo, Y., Li, X., Wang, Y., Cao, X., Wang, P., et al. (2018). Mesozoic Plate Subduction in West Pacific and Tectono-Magmatic Response in the East Asian Ocean-Continent Connection Zone. *Chin. Sci. Bull.* 63 (16), 1550–1593. doi:10.1360/n972017-01113

Li, S., Weng, A., Li, J., Shan, X., Han, J., Tang, Y., et al. (2020). Deep Origin of Cenozoic Volcanoes in Northeast China Revealed by 3-D Electrical Structure. *Sci. China Earth Sci.* 63 (4), 533–547. doi:10.1007/s11430-018-9537-2

Li, Z., Ni, S., Zhang, B., Bao, F., Zhang, S., Deng, Y., et al. (2016). Shallow Magma Chamber under the Wudalianchi Volcanic Field Unveiled by Seismic Imaging with Dense Array. *Geophys. Res. Lett.* 43 (10), 4954–4961. doi:10.1002/2016GL068895

Liu, X., Zhao, D., Li, S., and Wei, W. (2017). Age of the Subducting Pacific Slab beneath East Asia and its Geodynamic Implications. *Earth Planet. Sci. Lett.* 464, 166–174. doi:10.1016/j.epsl.2017.02.024

Liu, Y., Niu, F., Chen, M., and Yang, W. (2017). 3-D Crustal and Uppermost Mantle Structure beneath NE China Revealed by Ambient Noise Adjoint Tomography. *Earth Planet. Sci. Lett.* 461, 20–29. doi:10.1016/j.epsl.2016.12.029

Lu, C., Grand, S. P., Lai, H., and Garnero, E. J. (2019). TX2019slab: A New P and S Tomography Model Incorporating Subducting Slabs. *J. Geophys. Res. Solid Earth* 124 (11), 11549–11567. doi:10.1029/2019jb017448

Miyashiro, A. (1986). Hot Regions and the Origin of Marginal Basins in the Western Pacific. *Tectonophysics* 122(3-4), 195–216. doi:10.1016/0040-1951(86)90145-9

Munch, F. D., Grayver, A. V., Guzavina, M., Kuvshinov, A. V., and Khan, A. (2020). Joint Inversion of Daily and Long-Period Geomagnetic Transfer Functions Reveals Lateral Variations in Mantle Water Content. *Geophys. Res. Lett.* 47 (10). doi:10.1029/2020gl087222

Neal, S. L., Mackie, R. L., Larsen, J. C., and Schultz, A. (2000). Variations in the Electrical Conductivity of the Upper Mantle beneath North America and the Pacific Ocean. *J. Geophys. Res.* 105 (B4), 8229–8242. doi:10.1029/1999jb900447

Qiu, G., Fei, F., Fang, H., et al. (2014). Analysis of Magma Chamber at the Tianchi Volcano Area in Changbai Mountain. *Chin. J. Geophys.* 57 (10), 3466–3477. (in Chinese). doi:10.6038/cjg20141032

Ruan, S., Tang, J., Dong, Z., Wang, L., Deng, Y., and Han, B. (2020). Electric Structure Model of Tianchi Volcano in Changbai Mountains Based on Three-Dimensional AR-QN Magnetotelluric Inversion. *Seismology Geology.* 42 (06), 1282–1300. (in Chinese). doi:10.3969/j.issn.0253-4967.2020.06.002

Schmandt, B., Jacobsen, S. D., Becker, T. W., Liu, Z., and Dueker, K. G. (2014). Dehydration Melting at the Top of the Lower Mantle. *Science* 344 (6189), 1265–1268. doi:10.1126/science.1253358

Semenov, A., and Kuvshinov, A. (2012). Global 3-D Imaging of Mantle Conductivity Based on Inversion of observatoryC-Responses-II. Data Analysis and Results. *Geophys. J. Int.* 191 (3), no. doi:10.1111/j.1365-246X.2012.05665.x

Sun, M.-D., Xu, Y.-G., Wilde, S. A., Chen, H.-L., and Yang, S.-F. (2015). The Permian Dongfanghong Island-Arc Gabbro of the Wandashan Orogen, NE China: Implications for Paleo-Pacific Subduction. *Tectonophysics* 659, 122–136. doi:10.1016/j.tecto.2015.07.034

Sun, M., Gao, S. S., Liu, K. H., and Fu, X. (2020). Upper Mantle and Mantle Transition Zone thermal and Water Content Anomalies beneath NE Asia: Constraints from Receiver Function Imaging of the 410 and 660 Km Discontinuities. *Earth Planet. Sci. Lett.* 532, 116040. doi:10.1016/j.epsl.2019.116040

Tang, J., Deng, Q., Zhao, G., Li, W., Xuan, F., Jin, W., et al. (2001). Electric Conductivity and Magma Chamber at the Tianchi Volcano Area in Changbaishan Mountain. *Seismology Geology.* 23 (2), 191–200. (in Chinese).

Tang, J., Xu, W.-L., Wang, F., Zhao, S., and Li, Y. (2015). Geochronology, Geochemistry, and Deformation History of Late Jurassic-Early Cretaceous Intrusive Rocks in the Erguna Massif, NE China: Constraints on the Late Mesozoic Tectonic Evolution of the Mongol-Okhotsk Orogenic belt. *Tectonophysics* 658, 91–110. doi:10.1016/j.tecto.2015.07.012

Tang, Y., Obayashi, M., Niu, F., Grand, S. P., Chen, Y. J., Kawakatsu, H., et al. (2014). Changbaishan Volcanism in Northeast China Linked to Subduction-Induced Mantle Upwelling. *Nat. Geosci* 7 (6), 470–475. doi:10.1038/ngeo2166

Tatsumi, Y., and Eggins, S. (1995). *Subduction Zone Magmatism*. London: Blackwell Science, 211.

Tatsumi, Y., Maruyama, S., and Nohda, S. (1990). Mechanism of Backarc Opening in the Japan Sea - Role of Asthenospheric Injection. *Tectonophysics* 181(1-4), 299–306. doi:10.1016/0040-1951(90)90023-2

Turcotte, D., and Schubert, G. (1982). *Geodynamics*. New York: Wiley.

Wei, W., Hammond, J. O. S., Zhao, D., Xu, J., Liu, Q., and Gu, Y. (2019). Seismic Evidence for a Mantle Transition Zone Origin of the Wudalianchi and Halaha Volcanoes in Northeast China. *Geochem. Geophys. Geosyst.* 20 (1), 398–416. doi:10.1029/2018gc007663

Wei, W., Xu, J., Zhao, D., and Shi, Y. (2012). East Asia Mantle Tomography: New Insight into Plate Subduction and Intraplate Volcanism. *J. Asian Earth Sci.* 60, 88–103. doi:10.1016/j.jseaes.2012.08.001

Xu, W.-L., Chen, J.-H., Weng, A.-H., Tang, J., Wang, F., Wang, C.-G., et al. (2020). Stagnant Slab Front within the Mantle Transition Zone Controls the Formation of Cenozoic Intracontinental High-Mg Andesites in Northeast Asia. *Geology* 49 (1), 19–24. doi:10.1130/g47917.1

Yang, J., and Faccenda, M. (2020). Intraplate Volcanism Originating from Upwelling Hydrous Mantle Transition Zone. *Nature* 579 (7797), 88–91. doi:10.1038/s41586-020-2045-y

Zhan, Y., Zhao, G., Bai, D., Jin, W., Wang, X., et al. (1999). Preliminary Study of Wudalianchi Volcanic Cluster in Heilongjiang Province by MT Measurement. *Geol. Rev. (in Chinese)* 45 (S1), 400–408. doi:10.16509/j.georeview.1999.s1.049

Zhang, A., Guo, Z., Afonso, J. C., Handley, H., Dai, H., Yang, Y., et al. (2021). Lithosphere-asthenosphere Interactions beneath Northeast China and the Origin of its Intraplate Volcanism. *Geology*. doi:10.1130/g49375.1

Zhao, D. (2004). Global Tomographic Images of Mantle Plumes and Subducting Slabs: Insight into Deep Earth Dynamics. *Phys. Earth Planet. Interiors* 146 (1-2), 3–34. doi:10.1016/j.pepi.2003.07.032

Zhao, D. (2021). Seismic Imaging of Northwest Pacific and East Asia: New Insight into Volcanism, Seismogenesis and Geodynamics. *Earth-Science Rev.* 214, 103507. doi:10.1016/j.earscirev.2021.103507

Zhao, D., Tian, Y., Lei, J., Liu, L., and Zheng, S. (2009). Seismic Image and Origin of the Changbai Intraplate Volcano in East Asia: Role of Big Mantle Wedge above the Stagnant Pacific Slab. *Phys. Earth Planet. Interiors* 173 (3-4), 197–206. doi:10.1016/j.pepi.2008.11.009

Zhao, D., Yu, S., and Ohtani, E. (2011). East Asia: Seismotectonics, Magmatism and Mantle Dynamics. *J. Asian Earth Sci.* 40 (3), 689–709. doi:10.1016/j.jseaes.2010.11.013

Zheng, Y., Chen, R., Xu, Z., and Zhang, S. (2016). The Transport of Water in Subduction Zones. *Sci. China Earth Sci.* 59 (4), 651–682. doi:10.1007/s11430-015-5258-4

Zhou, J.-B., and Li, L. (2017). The Mesozoic Accretionary Complex in Northeast China: Evidence for the Accretion History of Paleo-Pacific Subduction. *J. Asian Earth Sci.* 145, 91–100. doi:10.1016/j.jseaes.2017.04.013

Zhou, J.-B., Wilde, S. A., Zhao, G.-C., and Han, J. (2018). Nature and Assembly of Microcontinental Blocks within the Paleo-Asian Ocean. *Earth-Science Rev.* 186, 76–93. doi:10.1016/j.earscirev.2017.01.012

Zhu, R., Fu, W., Meng, L., Chen, H., and Zhao, Y. (2001). Preliminary Study of Electric Structure in the Jingpohu Volcano Area of the Heilongjiang Province. *Seismology Geology. (in Chinese)* 23 (2), 186–190. CNKI:SUN:DZDZ.0.2001-02-008.

Conflict of Interest: The authors declare that the research was conducted in the absence of any commercial or financial relationships that could be construed as a potential conflict of interest.

Publisher's Note: All claims expressed in this article are solely those of the authors and do not necessarily represent those of their affiliated organizations, or those of the publisher, the editors and the reviewers. Any product that may be evaluated in this article, orclaim that may be made by its manufacturer, is not guaranteed or endorsed by the publisher.

frontiers in Earth Science

ORIGINAL RESEARCH
published: 24 January 2022
doi: 10.3389/feart.2022.812744

Estimating the Shear-Wave Velocities of Shallow Sediments in the Yellow Sea Using Ocean-Bottom-Seismometer Multicomponent Scholte-Wave Data

Yuan Wang[1,2]*, *Qingyu You*[1,2,3] *and Tianyao Hao*[1,2,3,4]*

[1]*Key Laboratory of Petroleum Resources Research, Institute of Geology and Geophysics, Chinese Academy of Sciences, Beijing, China,* [2]*Innovation Academy for Earth Science, Chinese Academy of Sciences, Beijing, China,* [3]*College of Earth and Planetary Sciences, University of Chinese Academy of Sciences, Beijing, China,* [4]*Key Laboratory of Submarine Geosciences, Ministry of Natural Resources, Beijing, China*

OPEN ACCESS

Edited by:
Nicola Alessandro Pino, National Institute of Geophysics and Volcanology (INGV), Italy

Reviewed by:
Stefania Danesi, Istituto Nazionale di Geofisica e Vulcanologia (INGV), Italy
Lili Feng, Compagnie Générale de Géophysique (Norway), Norway

***Correspondence:**
Yuan Wang
ywang@mail.iggcas.ac.cn
Tianyao Hao
tyhao@mail.iggcas.ac.cn

Specialty section:
This article was submitted to Solid Earth Geophysics, a section of the journal Frontiers in Earth Science

Received: *10 November 2021*
Accepted: *05 January 2022*
Published: *24 January 2022*

Citation:
Wang Y, You Q and Hao T (2022) Estimating the Shear-Wave Velocities of Shallow Sediments in the Yellow Sea Using Ocean-Bottom-Seismometer Multicomponent Scholte-Wave Data. Front. Earth Sci. 10:812744. doi: 10.3389/feart.2022.812744

Scholte-wave dispersion analysis is effective at imaging the relatively low shear-wave velocity of shallow marine sediments in marginal seas. The combination of a four-component ocean-bottom-seismometer (OBS) and a towed air-gun source can economically and effectively acquire the marine dispersive seismic data. Extracting higher-order dispersive Scholte wave modes is the most critical problem in the dispersion analysis method. The extremely low shear-wave velocity and severe attenuation in the top hundreds of meters of marginal sea sediment provide an uneven dispersive energy distribution for the four components of the Scholte wave data. The fundamental mode dispersive energy dominates in the vertical component and higher-order modes dominate in the horizontal component. We developed the method of the four-component OBS Scholte velocity-spectra stacking, which can effectively, rapidly, and robustly extract higher-order modes. We imaged the shear-wave velocity structure of complicated shallow marine sediment in the North Yellow Sea using an active OBS seismic profile with a large-volume air-gun array. The fourth higher-order Scholte wave mode can be imaged with the four-component velocity-spectra stacking method with a lower frequency range of 1.0–7.0 Hz. Only the second-order mode can be recognized from the dispersion energy image of the single vertical component. The joint inversion of multimode dispersion curves can provide more accuracy and deeper constraints for the inverted model; thus, the constraint depth with five modes increases by a factor of 1.9 compared with single fundamental mode inversion. The inverted profile suggests a low shear-wave velocity of 123–670 m/s and strong lateral variations within 350 m. The main regional geological structures are shown by the inverted shear-wave velocity structure.

Keywords: Scholte wave, shear-wave velocity, OBS, dispersion curves, higher-modes

INTRODUCTION

Imaging suboceanic shear-wave velocity (V_s) structures is fundamental in the geophysical investigations of marginal seas (Ewing et al., 1992; Klein et al., 2005; Kugler et al., 2007; Wang et al., 2016; Wang et al., 2020). The V_s for shallow marine sediment is treated as an important parameter in many marine engineering construction activities, such as offshore platforms, wind parks, and pipelines. Moreover, the V_s structure of shallow marine sediment provides a reliable reference model for offshore multicomponent seismic exploration (Bohlen et al., 2004; Kugler et al., 2007), ocean lithosphere shear-wave tomography (Zhao et al., 2008; Zhao et al., 2010), underwater acoustic wave attenuation (Rauch, 1980; Hughes et al., 1990; Bradshaw, 2015), and very-low-frequency geoacoustic studies (Du et al., 2020).

The dispersive characteristics of interfacial and surface waves are widely used to estimate the V_s structure of shallow marine sediment (Bohlen et al., 2004). Compared with the marine converted-body-wave survey approach, marine interfacial waves show greater promise due to the low signal-to-noise ratio of ocean-bottom body shear waves from the weak P-to-S wave conversion coefficient (Kugler et al., 2007). The dispersion curves for interfacial waves are sensitive to shear-wave velocities, which is the precondition and fundamental advantage of using interfacial waves to invert S-wave structures.

The vertical or radial component of an interfacial wave that travels on the water-sediment interface in the marine environment is known as a Scholte wave and is analogous to Rayleigh waves on land (Scholte, 1947). Its transverse component is known as a Love wave (Love, 1911), both in this case and on land. Scholte waves can be detected through a combination of a single deployed underwater seismic station and multiple air-gun shots on the sea surface, which is known as the "stationary-receiver" method (Klein et al., 2005). An ocean-bottom seismometer (OBS) (also known as an ocean-bottom hydrophone or ocean-bottom node) is generally used as the ocean-bottom seismic station as it is cheaper and technically simpler for marine fieldwork. However, acquiring marine Love-wave data is more complex because of the need for an ocean-bottom P-SH type of source (e.g., shear-wave vibrator; Socco et al., 2011).

The single vertical component of OBS active source Scholte-wave data was used to investigate the V_s structure of shallow marine sediments (Shtivelman, 2003; Shtivelman, 2004; Bohlen et al., 2004; Klein et al., 2005; Kugler et al., 2005; Kugler et al., 2007; Nguyen et al., 2009; Socco et al., 2011; Vanneste et al., 2011; Dong et al., 2012; Wang et al., 2016). Wang et al. (2020) noted that the three-component Scholte-wave dispersive analysis can extract additional higher-order modes compared with using a single vertical component. Compared with the fundamental-mode inversion, joint higher-order modes can effectively increase the inversion depth and resolution (Xia et al., 2003; Luo et al., 2007). Wang et al. (2020) demonstrated that the joint inversion of the four-mode dispersion curves can decrease the maximum inverted error by a factor of 16 compared with one fundamental mode inversion. However, the possibility of and method to image higher-order dispersive modes from the four-component (4C with three seismic components and one hydrophone component) OBS Scholte-wave data remain unknown and are worth exploring.

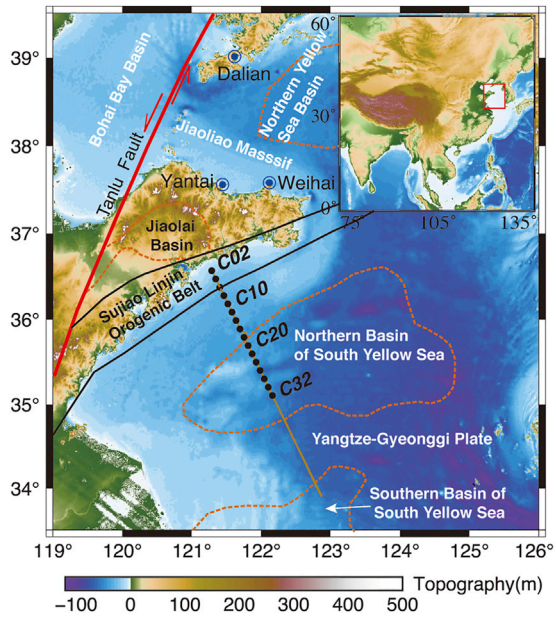

FIGURE 1 | Bathymetry/topography of OBS survey line in the Yellow Sea. The line denotes the shot profile, and the black circles denote the OBS deployment locations.

This study considers the possibility and potential of using the 4C OBS Scholte-wave data to image higher-order dispersive modes. Moreover, the feasibility of imaging the complex shallow marine sediment of marginal seas using the Scholte-wave dispersion inversion method is verified. We begin by presenting the acquisition and geometry of the OBS active-source Scholte-wave field data from the Yellow Sea and then describe the detailed 4C Scholte-wave analysis procedure from the raw OBS data to the final V_s structure. We next show the dispersion energy images obtained from the 4C Scholte-wave analysis method and finally illustrate the inverted one-dimensional (1D) and pseudo-two-dimensional (pseudo-2D) V_s structures.

SEISMIC DATA AND METHODOLOGY

Seismic Data Acquisition

As shown in **Figure 1**, a north-northwest-oriented OBS active-source survey profile with a total length of 342.2 km was acquired in the Yellow Sea of China in 2013. The geological location of the survey area is the Yangtze–Gyeonggi plate (Li et al., 2012). The survey profile crosses the continental shelf and northern basin of the South Yellow Sea and ends at the north rim of its southern basin. A CAS-Micro-4C-OBS was used as the marine seismic station, which was developed by the Institute of Geology and Geophysics of the Chinese Academy of Sciences. The CAS-Micro-

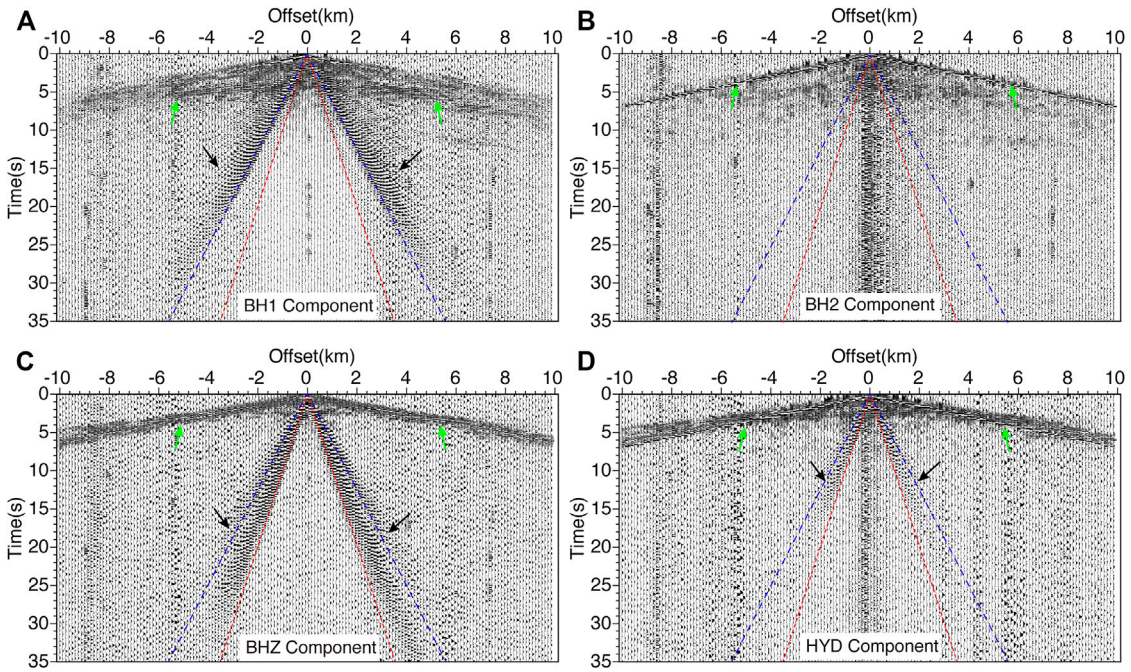

FIGURE 2 | Pre-processed common receiver gathers (CRGs) recorded at OBS station C22. Panels **(A, B)** show two horizontal seismic components with deployed random azimuths. Panels **(C, D)** show the CRGs of the vertical and hydrophone components, respectively. The red and blue dashed lines denote apparent velocities of 100 and 160 m/s, respectively. The pre-processing involved trace normalization using the mean with bandpass filtering at 0.5–6.3 Hz, and finally Wiener (least-squares) predictive error filtering. The green and black arrows denote the body and Scholte waves, respectively.

4C-OBS assemble had a 13-inch glass sphere (Vitrovex) with a maximum deployment depth of 6,000 m. It can record data for a period of 3 months with a maximum recovery period of up to 6 months. Three geophones with a frequency bandwidth of 0.1–150 Hz were installed orthogonally in the glass sphere. A low frequency (1 Hz–15 kHz) hydrophone was set up in the OBS and placed outside the glass sphere. The dynamic range of the OBS was greater than or equal to 120 dB. A 24-bit A/D converter was used with a sampling frequency freely set from 1 to 250 Hz. A 32 GB FAT32 flashcard was used to store the data. In total, 16 OBSs with an average deployment distance of ~12 km were deployed along the profile and were designated as C02–C32 with an interval of 2. However, as C02 and C04 were relatively close to the coastline where there was significant additional disturbing noise, they are excluded from this study due to low data quality; thus, only 14 OBSs were used for the Scholte-wave analysis. The air-gun shots each had a volume of 6,060 in^3, an average interval of 136 m, and were approximately 10 m below the sea surface. A differential global positioning system (DGPS) was used to control the air-gun shot timing and vessel navigation.

Combined with the shot information, the common receiver gather (CRG) was cut from the raw OBS continuous binary-format data. As an example, the 4C CRGs of the OBS from station number C22 are shown in **Figure 2**. After obtaining the traces by subtracting their means, a 0.5–6.3 Hz bandpass filter was applied. The pre-processed seismogram shows a body wave (green arrows in **Figure 2**) with a strong reflection and refraction and a visible Scholte wave (black arrows in **Figure 2**) for both the seismic components (**Figures 2A–C**) and hydrophone component (**Figure 2D**). The raw CRGs also show that the Scholte-wave energy is distributed unevenly between the seismic and hydrophone components. The Scholte-wave energy from the seismic components is stronger than that of the hydrophone component. This may be because the amplitude of the Scholte-wave decays exponentially with distance from the interface, and the geophones of the OBS instrument are directly coupled with the seafloor while the hydrophone floats in the water at 0.8 m from the seabed.

The three seismic CRGs show three primary Scholte-wave features. First, both the seismic components and hydrophone component record the Scholte wave. Second, the seismic components with different directions exhibit various energy amplitudes. A dominant Scholte wave is visible in the vertical BHZ component (**Figure 2C**), whereas a relatively weak Scholte wave is visible in the random-azimuth horizontal BH1 component (**Figure 2A**) and nearly disappears in the other horizontal BH2 component (**Figure 2B**). Third, the Scholte wave modes recorded from the different seismic components are distinct, with the BH1 component recording a higher-order mode (**Figure 2A**) and the BHZ component recording the dominant fundamental mode (**Figure 2D**).

4C Scholte-Wave Analysis Procedure

The OBS 4C Scholte-wave dispersion energy imaging (DEI) and inversion method for each OBS station involved the following four main steps.

Step 1: Preparation of 4C CRGs. Transfer the raw continuous binary OBS data to the 4C CRGs with the SEGY data format, which is followed by pre-processing the raw CRGs with trace normalization, bandpass filtering, Wiener predictive error filtering, and cutting the traces with an absolute offset of 400–5,000 m.

Step 2: 4C DEI. Calculate the velocity spectrum (VS) of each component using a phase-shift algorithm.

Step 3: 4C velocity-spectra stacking. Obtain the final stacked VS by stacking the VSs from the three seismic components with the hydrophone component.

Step 4: Extraction and inversion of the dispersion curve. Pick the multimode dispersion curves from the stacked VS and finally invert the structure for the shallow marine sediment.

Preparation of 4C CRGs

As an example, we show the 4C Scholte-wave dispersion analysis method for the OBS station C22. We begin by pre-processing the 4C CRGs following step 1, as shown in **Figure 2**. The entire CRG is split into two branches: positive and negative offsets. For each CRG branch, the minimum and maximum offset windows are chosen to cut the traces, which guarantees a high signal-to-noise ratio for use in the next step. Here, the near- and far-field effects of the CRG are the primary references used to select the offset window (from 400 to 5,000 m).

4C DEI

The pre-processed CRG branch is then transferred from the t–x domain to the f–v domain using the phase-shift algorithm (Park et al., 1998) following step 2. For one trace of the CRG data r_i (i = 1, 2, . . . ,N) in the t–x domain, its Fourier transform R_i in the frequency domain is obtained by:

$$R_i(\omega) = FFT[r_i] = A_i(\omega) \cdot P_i(\omega), \tag{1}$$

Where ω is the angular frequency, and A_i and P_i denote the amplitude and phase terms, respectively. After removing the A_i *via* normalization:

$$R_i'(\omega) = \frac{R_i(\omega)}{A_i(\omega)} = \frac{R_i(\omega)}{|R_i(\omega)|} = P_i(\omega). \tag{2}$$

We define a trial phase-velocity (c_ω) range with small increments, and the velocity spectrum (VS) in the frequency-phase-velocity domain is calculated by:

$$VS(\omega, c_\omega) = \frac{1}{N}\sum_{1}^{N} e^{j(\omega x_i / c_\omega)} R_i'(\omega);\ (i = 1, 2, \ldots, N), \tag{3}$$

Where x_i denotes the offset from the source to the receiver.

As shown in **Figure 3**, the 4C VSs are imaged using the phase-shift algorithm for the positive CRG branch of the OBS station C22. First, the 4C dispersion energy images show that both the seismic and hydrophone components can be used to image the dispersive VSs. Second, both the fundamental mode and higher-order modes are obtained simultaneously. Third, the mode energy is distributed unequally between the different components. The fundamental mode is dominant in the VS of the vertical component (**Figure 3C**) but missing in those for both horizontal components (**Figures 3A,B**). Correspondingly, the first higher-order mode is dominant in the two horizontal components. Finally, the recognizable highest dispersive Scholte-wave mode differs between the four components. Thus, the fourth higher-order mode can be distinguished from the BH1 component, the weak third higher-order mode is present in the BHZ component, and the first higher-order mode can be distinguished from the hydrophone component.

There is a significant difference between the VSs of the two horizontal components; only the first higher-order mode can be recognized from the VS of the BH2 component, whereas the VS of the BH1 component clearly shows the first four higher-order modes. **Figure 4** shows hodograms of the BH1-BH2 (**Figure 4A**) and BH2-BHZ (**Figure 4C**) components plotted using a time window of 1.7–2.2 s for a seismic trace with an offset of 1,499 m for the OBS station C22. In the BH1-BH2 hodogram, the particle vibration trajectory is characterized as a straight line along the BH1 axis, while the BH2-BHZ particle motion trajectory is a vertical straight line. These two main features of the hodograms indicate that the BH1 component corresponds almost directly to the shot-line azimuth, whereas the BH2 component is perpendicular to the shot line. For this OBS station, BH1 can be treated as the inline component, with BH2 treated as the corresponding crossline component. This explains reasonably well why there is only one relatively weak dispersive energy mode (M1 in **Figure 3B**) in the VS of BH2.

4C VS Stacking

We stack the 4C VSs together after completing the above DEI as described in step 3. The 4C stacked VSs (VS_{stack}) are obtained by

$$VS_{stack} = \frac{1}{4}(VS_{BH1} + VS_{BH2} + VS_{BHZ} + VS_{HYD}), \tag{4}$$

Where VS_{BH1}, VS_{BH2}, VS_{BHZ}, and VS_{HYD} denote the imaged VSs of the BH1, BH2, BHZ, and HYD components, respectively. Here, the precondition for the 4C VSs being directly linearly stacked is that they contain the same dispersion energy as the Scholte-wave source. As the source-to-receiver seismic wavefield propagation path can be treated as a pseudo-2D profile, only the P-SV type of Scholte waves exist along this inline profile. No P-SH-type Love waves exist as the P-wave-type acoustic waves are excited from the air-gun sources. This can also be demonstrated inversely from the concordance comparison of the 4C dispersion curves. If the VSs contain Love waves, then the dispersion curves picked from the vertical component differ from those from the horizontal component. Conversely, consistent dispersion curves from the two components suggest that only the same type of Scholte waves exist and that there are no Love waves. Therefore, we regard the two horizontal components as projections of the inline component and a direct linear stacking of their spectra without azimuthal correction.

As an example, the dispersion curves picked from the 4C VSs as shown in **Figure 5** are compared in detail. As shown in **Figure 5A**, the dispersion curves show great consistency between the different components, from the fundamental to the fourth higher-order dispersive modes. The mean of the cross-correlation coefficients between the 4C first-higher-

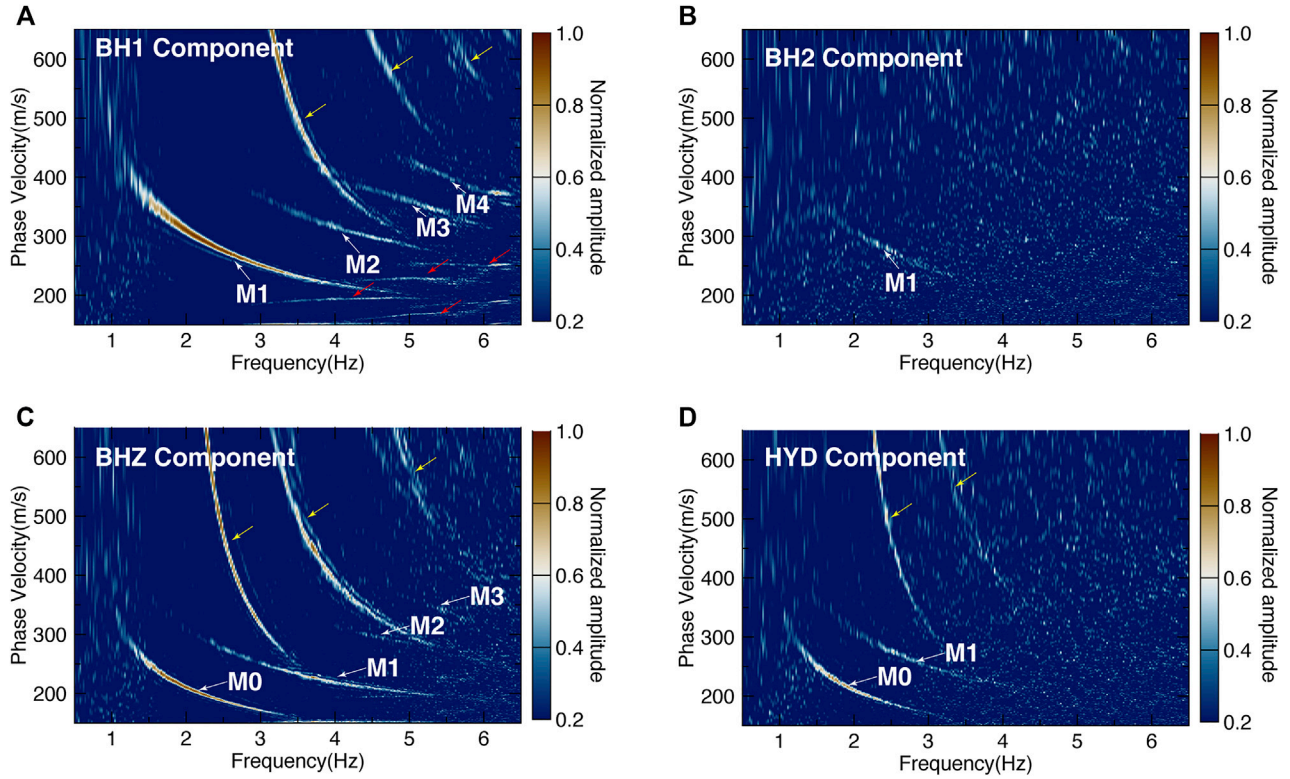

FIGURE 3 | Four-component (4C) velocity spectra (VSs) calculated from the positive branch of the 4C CRGs of OBS station C22. The M0–M4 denote the dispersive Scholte-wave mode numbers. The yellow and red arrows denote two different patterns of dispersive spectral-spatial aliasing.

order-mode dispersion curves approaches 99.88%. The correlation coefficient of the first-higher-order-mode dispersion curves produced by the BH1 and BHZ components is the highest and reaches 99.98%. The BH1 and BH2 components have the lowest correlation coefficient of 99.78%, while the other correlation coefficients between BH1 and HYD, BH2 and BHZ, BH2 and HYD, and BHZ and HYD are 99.90, 99.93, 99.80, and 99.88%, respectively. These higher correlation coefficients for the first higher-order mode between different components inversely prove that the dispersive energies come from the same wave source, which is the P-SV type of Scholte wave.

The stacked VS (SVS) is obtained from the normalized 4C VS stacking results. As shown in **Figure 5B**, the final full-mode SVS can be imaged using the proposed 4C VS stacking method, including the fundamental mode (M0 in **Figure 5B**) and the first to fourth higher-order modes. Compared with the traditional single vertical component VS, in which only the fundamental and first higher-order modes can be recognized, the fundamental to fourth higher-order modes are observed in the 4C SVS. The missed fundamental mode in the BH1 component appears in the SVS, and the missed second to fourth higher-order modes in the BHZ component are observed from the full-mode SVS.

We directly stack the 4C velocity spectra linearly using the same weights for each component. This approach has the significant advantages of being fast, stable, and effective. To verify whether the weights of the four components affect the extraction of higher-order modes for the Scholte-wave 4C VS stacking method, we chose two sets of random weights as a comparison. We denote the same weight stacking velocity spectrum as VS, which is calculated from **Eq. 4** and is shown in **Figure 6C**. Two sets of different random weights with the 4C stacking velocity spectrum are obtained by:

$$VS_0 = \frac{1}{4}\left(2.0VS_{BH1} + VS_{BH2} + 2.0VS_{BHZ} + VS_{HYD}\right),$$

$$VS_1 = \frac{1}{4}\left(0.8VS_{BH1} + 0.5VS_{BH2} + 1.2VS_{BHZ} + 0.3VS_{HYD}\right),$$

and shown in **Figures 6A,B**, respectively. All three SVSs show no visible differences and the dispersive characteristics are the same. That is, a total of five modes can be distinguished and the first two lower modes have much stronger energies with the last three higher modes being weaker.

The absolute difference between every two SVSs is calculated. Thus, the differences between the VS and VS_0, VS and VS_1, and VS_0 and VS_1 are shown in **Figures 6D–F**, respectively. The average absolute difference is 0.028 for all three SVSs, which indicates that the deviation between the VSs as calculated with the same and different weights is approximately equal to or less than 3%. The average absolute difference is 0.035 and 0.036 between the VS and VS_0 and the VS and VS_1, respectively. The absolute difference between the VSs calculated from two different weights is 0.116, which is the minimum for all three differences. This

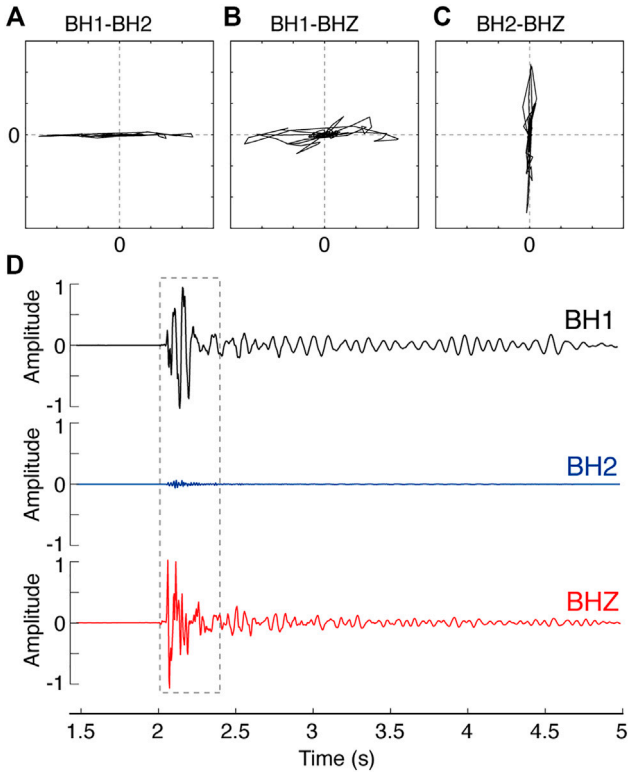

FIGURE 4 | Hodograms **(A–C)** and waveform **(D)** of the trace with an offset of 1,499 m for OBS station C22. The plotted time window of the hodogram is denoted as the gray dashed rectangle in **(D)**.

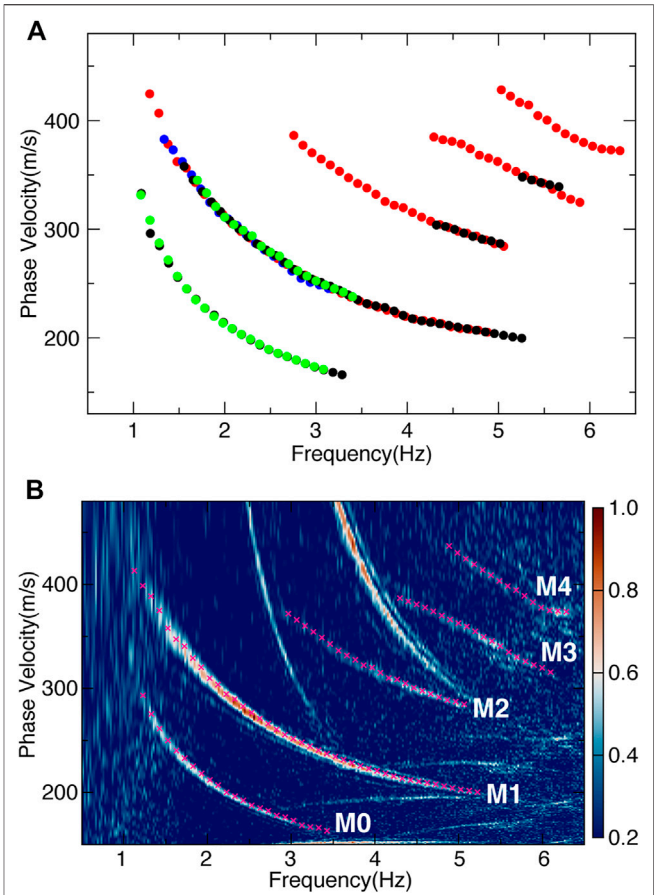

FIGURE 5 | Dispersion curves selected from the 4C VSs shown in **Figure 3 (A)** and the stacked VS **(B)**. The red, blue, black, and green dots in **(A)** denote the BH1, BH2, BHZ, and HYD components, respectively. The M0–M4 in **(B)** denote the dispersive mode numbers.

further verifies that different weights have little impact on the 4C dispersion spectrum stacking.

The 4C dispersive VS stacking method for Scholte waves can effectively image the full-mode dispersion energy. Compared with the single-vertical-component DEI method, this procedure either increases the number of recognizable higher-order modes or widens the selectable frequency range of the dispersion curves for higher-order modes. For the single-horizontal-component DEI processing, our 4C stacking method entirely avoids mistaken mode misidentification. Thus, the first higher-order mode is treated as the missed fundamental mode in the horizontal component. This also inversely demonstrates the necessity of the 4C Scholte-wave analysis and the failings of the single-component Scholte-wave imaging method.

Extraction and Inversion of Dispersion Curves

As shown in **Figure 7**, all dispersion curves were extracted manually from the 4C SVS of all 14 OBS stations. The manual selection error can be controlled within 5 m/s, which was considered in the subsequent inversion step. The numbers of extracted Scholte-wave modes differ between the OBS stations. Most stations can extract the third higher-order mode, whereas only three stations can extract the fourth higher-order mode. The highest number of extracted modes varies irregularly between the OBSs. A reasonable explanation for this phenomenon of unequal mode numbers is that it is caused by the lateral geological variations in the shallow sediment along the OBS survey line, or by differences in the degree of OBS coupling. Overall, all OBS stations can extract the available multimode dispersion curves for the subsequent inversion procedure.

The implicit relationship between the earth structure and the dispersion curves is described as (Xia et al., 2003).

$$F\left(f_i,\ c_i, v_s, v_p, \rho, h\right) = 0\ \ (i = 1, 2, \ldots, n),$$

Where n is the total number of points on the dispersion curve, $(f_i,\ c_i)$ is the frequency-phase velocity pair of the previous extracted dispersion curves, and v_s, v_p, ρ, and h are the geophysical model parameters (vector of shear-wave velocity, compressional wave velocity, density, and layer thickness, respectively).

We use the multimode-dispersion-curve joint inversion method (Xia et al., 2003; Luo et al., 2007) to image the geological structures of shallow sediment. The final convergent optimal solution was obtained using the damped iterative least-squares algorithm and was implemented in the Computer

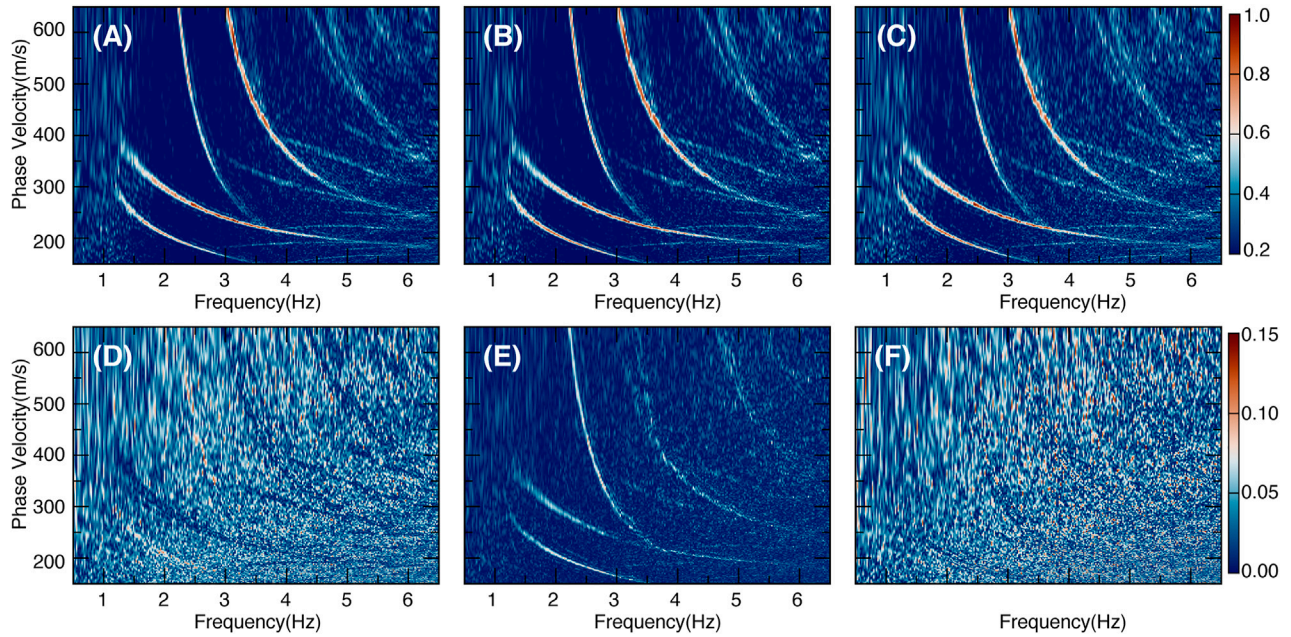

FIGURE 6 | The 4C SVS as calculated from different weights **(A, B)** and the same weight **(C)**. The absolute differences between each SVS pair **(A–C)** are shown in **(D–F)**.

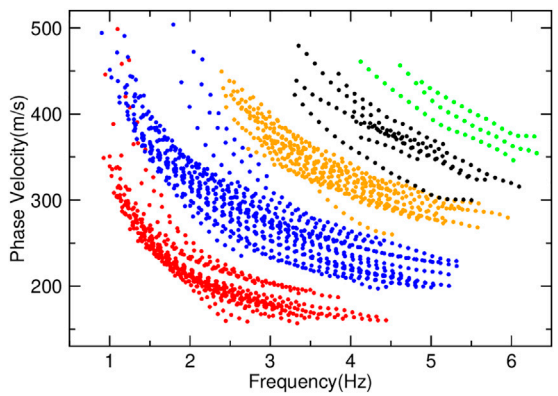

FIGURE 7 | All dispersion curves extracted from stacked VSs (SVS) of all OBS stations along the profile. The red, blue, orange, black, and green dots denote the fundamental to fourth higher-order mode, respectively.

Programs in Seismology (CPS) (Herrmann, 2013). During the iterations, only v_s is considered as a free parameter, v_p and h are fixed, and ρ is related to v_s *via* the empirical relation $\rho\ (g/cm^3) = 0.8\log(v_s) + 0.23$, with units of m/s (Herrmann, 2013). This inversion strategy has been proven reliable for the inversion of Scholte-wave dispersion curves (Wang et al., 2016; Wang et al., 2020). Wang et al. (2016) gave details on how the initialized model parameters affect the final fitting results.

The initial geophysical model is constructed as an isotropic homogenous water–sedimentary layered model with 40 total layers. For the first sea-water layer, v_s, v_p, ρ, and h are fixed during the iterations with values of zero, 1,500 m/s, 1.03 g/cm^3, and the true water depth from the sonar surveying, respectively. The water depth along the profile varies from 49.03 to 75.68 m with an average of 66.19 m. The thickness of the sedimentary layers is set as 350 m with a total of 39 layers. The top six sedimentary layers are each fixed at 5 m thick, with the remaining being 10 m thick. The bottom sedimentary layer is set as a half-space. The fixed v_p increases linearly from 1,580 m/s in the top layer to 1800 m/s in the half-space, and v_s is initialized as 200 m/s in the top layer and increases linearly to 560 m/s in the bottom layer.

To determine the deepest constraint depth during inversion, we calculate the sensitivity kernels for the five modes of the Scholte-wave dispersion curves based on the initial geophysical model. As shown in **Figure 8**, v_s is the most sensitive to the dispersion curves, v_p is the least sensitive, and ρ is in between. The statistical results show that the absolute mean sensitivities of v_s, ρ, and v_p are 3.62, 0.01, and 0.91, respectively. The mean sensitivity of v_p is only 0.38% that of v_s, and the corresponding ratio for ρ is higher at 25.05%. The sensitivity degrees for the different modes also show differences as the fundamental mode is more sensitive than the higher-order modes. The fundamental dispersive mode sensitivity of v_s is 4.16, whereas the corresponding sensitivity of the higher-order modes is approximately 3.5. However, the higher-order modes can constrain the deeper layers more than the fundamental mode. Therefore, combining the higher-order modes in the inversion allows "seeing" deeper than only using the fundamental mode.

The sensitivity kernel results illustrate this constraint in **Figure 8**. The higher-order modes have greater sensitivities to deeper layers than the fundamental mode for the same frequency.

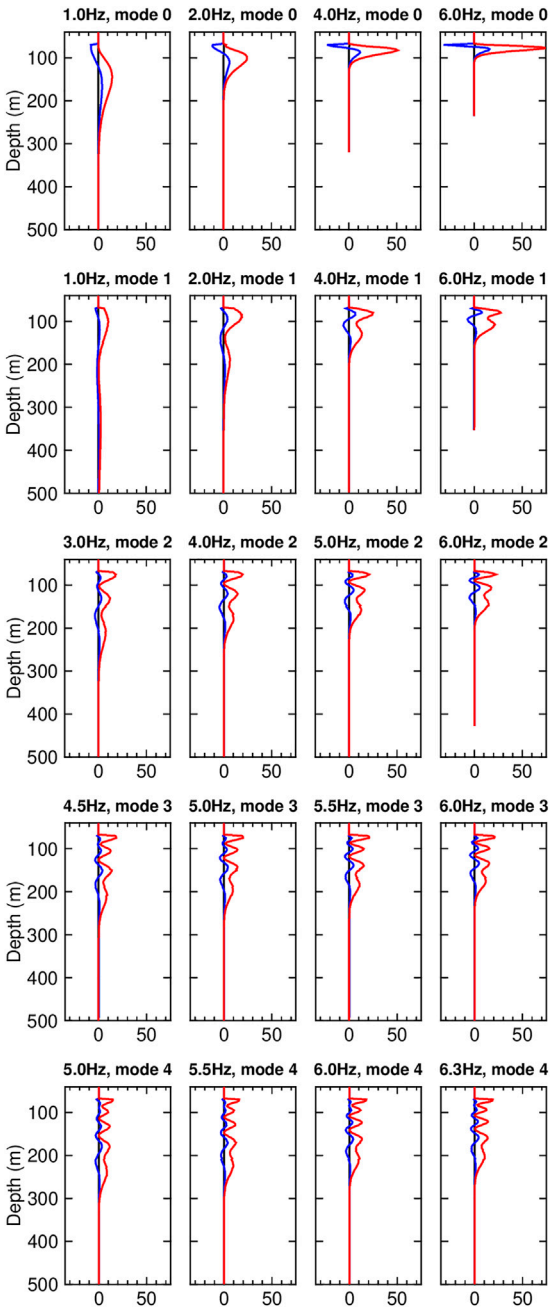

FIGURE 8 | Sensitivity kernels of the five dispersive Scholte-wave modes based on the initial marine sedimentary model. The red, blue, and black lines denote the sensitivities of v_S, ρ, and v_P, respectively. Modes 0–4 denote the Scholte-wave dispersive fundamental to the fourth higher-order modes, respectively.

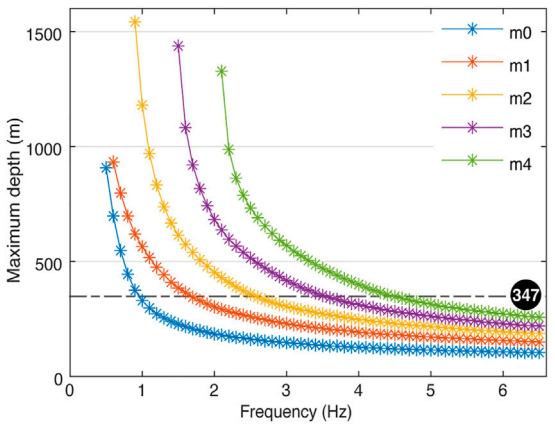

FIGURE 9 | The maximum constrained depth obtained from the given threshold of the sensitivity kernel for each mode, where m0–m4 denote the fundamental to fourth-higher-order mode.

For example, when selecting 10% of the mean sensitivity (0.362) as the threshold, the greatest depths for the fundamental to the fourth higher-order mode at 6.0 Hz are 107, 157, 195, 230, 272, and 315 m, respectively. These simple statistical results demonstrate that for the same frequency, the constraint depth of the fourth higher-order mode is 2.94 times that of the fundamental mode. Correspondingly, the higher-order Scholte-wave modes allow "seeing" deeper with an approximately linear trend compared with the fundamental mode. Finally, we choose 10% of the mean sensitivity (0.362) as the threshold to determine the deepest confidence depth for the inverted models, which is 347 m. We first obtain all maximum depth values from the sensitivity kernel of each mode for each frequency based on the threshold (**Figure 9**), and the final deepest inversion depth is the mean of these maximum depths.

We implement the five-mode joint dispersion-curve inversion to obtain the best-fit marine sedimentary model. All modes of the phase-velocity dispersion curves converge well after 20 iterations with a damping factor of 0.1 (**Figure 10**). The average signal power fit between the inverted and selected dispersion curves for all stations reaches 99.98%. The average standard fitting error for the multimode phase velocities is 4.13 m/s, where the corresponding average fitting residual is 2.46 m/s. The final best-fit v_s model is very closer to the initial model of this station, while the corresponding density model differs considerably from the initial model. To illustrate how much the Scholte-wave phase velocity changes due to the density alone, another group of predicted dispersion curves (green solid line in **Figure 10C**) were calculated based on the inverted density and the initial v_s profile. The result shows that the dispersion curves are almost the same between the initial model (blue dashed line in **Figure 10C**) and the inverted density and the initial v_s model. Furthermore, this demonstrates that the density has an ignorable influence on Scholte-wave dispersion curves inversion. In particular, the shallowest layers of the inverted model have much lower shear-wave velocities of 109.9 m/s to 137.9 m/s for the top two sedimentary layers.

RESULTS

In total, 26 dispersion-curve groups were successfully extracted from 13 OBS stations, with one station (C18) having data errors. Of the 26 dispersion-curve groups, three groups extracted a

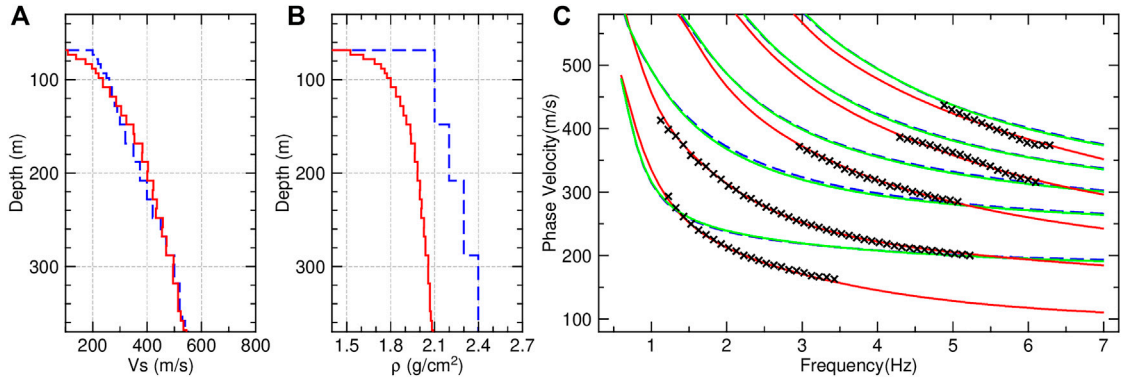

FIGURE 10 | Initial (blue dashed line) and best-fit (red solid line) geophysical models of the shear-wave velocity **(A)** and density **(B)** from the inverted multimode Scholte-wave dispersion curves **(C)**. The black crosses in **(C)** denote the picked dispersion curves, the blue dashed line, red solid line, and green solid line denotes the theoretical dispersion curves calculated based on the initial model, the best-fit model, and the best-fit density and initial v_s model, respectively.

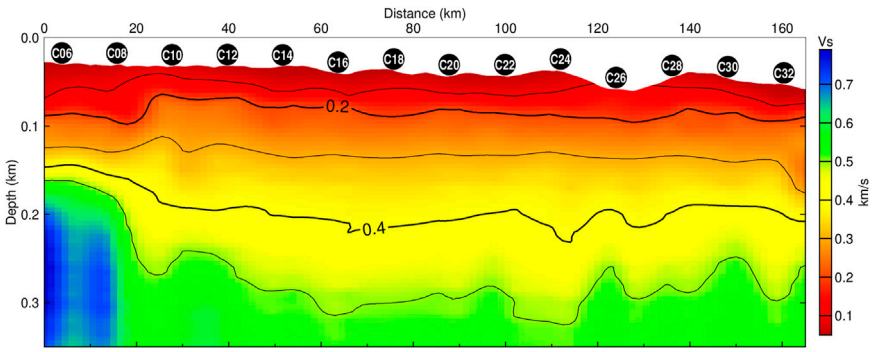

FIGURE 11 | Final 2D shear-wave velocity structure of the survey profile. C06–C32 denote the deployed OBS positions.

maximum of five modes, five groups extracted a maximum of four modes, 13 groups extracted a maximum of three modes, four groups extracted a maximum of two modes, and one group extracted a maximum of one mode. The phase velocities vary from 150 to 500 m/s for all dispersion-curve groups (**Figure 7**). The lower velocities belong to classical soft sedimentary geological conditions. Along the survey profile, the Scholte-wave phase velocities show lateral differences, which indicates strong lateral heterogeneity.

All 26 of the 1D shear-wave velocity structures were inverted from the multimode dispersion curves. As shown in **Figure 11**, the pseudo-2D shear-wave velocity profile was constructed from all the 1D velocity structures. The adjustable tension continuous curvature spline algorithm (Smith and Wessel, 1990) with a tension factor of 0.25 was adopted to interpolate the 1D V_s profiles. Relatively low shear-wave velocities of 123–257 m/s were obtained in the top 100-m-deep sedimentary layers, which increased with an average highest rate of 3.47 m/s. The bottom sedimentary layer with a depth of 280–350 m had higher S-wave velocities of 500–670 m/s, with a mid-level velocity gradient of 1.25 m/s. The middle sedimentary layer showed mid-scale shear-wave velocities that varied from 257 to 500 m/s with the lowest gradient of 0.77 m/s.

A large lateral-velocity variation appeared in the constructed 2D S-wave velocity profile. There is a strong high-velocity zone in the middle and deep areas of the northern end (left side of **Figure 11**) of the survey line, which corresponds to the geological unit of the Qianliyan uplift. The apparent velocity difference between stations C08 and C10 may be indicated as an active fault, which is part of the Qianliyan fault zone (Wu et al., 2020). This corresponds to regional deep large faults with scales that cut through multiple sedimentary layers over a long development time. The V_s profile between C10 and C22 shows the classical Quaternary sedimentary layers. At the right-hand section of the V_s profile, there is a strong "piggyback pattern" thrust nappe structure induced from the reverse active fault, which indicates this type of extrusion effect is continuous, as shown from previous reflection seismic profiles (Wu et al., 2020). Some faults are converted from a normal type in the lower part to a reverse fault in the upper part, which may indicate that the stress environment changes from tension to compression and has a typical normal inverted structure (Wu et al., 2020).

CONCLUSION

The proposed OBS multicomponent Scholte-wave dispersion analysis method can effectively image the complex, extremely low, and strong lateral velocity variation V_s structure in the shallow sediment of marginal seas. A complete, fast, and effective 2D shear-wave imaging approach using 4C OBS active-source Scholte-wave data was developed and demonstrated. The lower-frequency Scholte waves can be recorded from the three-component geophones and one-component hydrophone of the OBS. The four VSs imaged from the 4C Scholte-wave CRGs can be directly stacked linearly based on the conditions that all components record the same source of P-SV-type Scholte waves and no Love waves exist. Compared with the traditional single-vertical-component Scholte-wave DEI method, the stacking procedure can effectively image higher weak dispersive modes. Thus, the highest recognizable dispersive mode was the fourth from the SVS, whereas it was only the second higher-order mode from the single vertical component. Furthermore, the stacking procedure makes the dominant fundamental mode of the vertical component compensate perfectly for the missing fundamental mode in the horizontal components. Similarly, the dominant higher-order mode in the two horizontal components equivalently compensates for the weak energy modes in the vertical and hydrophone components. This kind of mutual benefit and disadvantage is complementarily for horizontal, vertical, and hydrophone components and illustrates the 4C Scholte-wave imaging mechanism and key points.

In total, 26 dispersion-curve groups were extracted from the negative and positive branches of 13 OBS CRGs in the North Yellow Sea. Lower phase velocities of 150–500 m/s were obtained from all dispersion-curve groups. The damped iterative least-squares algorithm effectively inverted the multimode Scholte-wave dispersion curves (>99.98% goodness-of-fit) based on the water–sedimentary layered homogenous earth model. A maximum inversion-constraint model depth of 350 m was accurately defined by the sensitivity kernel threshold (10% of maximum). The pseudo-2D shear-wave velocity profile was constructed from the 26 1D inverted models. The key geological features of the shallow sediment appeared in the shear-wave velocity profile, including the uplift, active fault, and thrust nappe structures.

DATA AVAILABILITY STATEMENT

The raw data supporting the conclusions of this article will be made available by the authors, without undue reservation.

AUTHOR CONTRIBUTIONS

YW, TH, and QY all contributed as major authors of the manuscript. YW wrote the text, processed the data, and created the figures. TH collected the marine OBS active data and performed the geological interpretation. QY developed the OBS instruments used to collect the seismic data in the study.

FUNDING

This research was funded by the National Natural Science Foundation of China (Grant Nos. 41806083 and 42176084), National Key R&D Program of China (2018YFC0308003), and Major Research Plan on West-Pacific Earth System Multispheric Interactions (project number: 91858212).

ACKNOWLEDGMENTS

The authors thank the crew members and investigators of the Chinese Geophysical Research vessel M/V Discover-2 and Xiangyanghong-2 for collecting the marine seismic data.

REFERENCES

Bohlen, T., Kugler, S., Klein, G., and Theilen, F. (2004). 1.5D Inversion of Lateral Variation of Scholte-wave Dispersion. *Geophysics* 69 (2), 330–344. doi:10.1190/1.1707052

Bradshaw, A. S., and Baxter, C. D. (2015). Measurement of Shear Wave Velocity in marine Sediments. *The J. Acoust. Soc. America* 137, 2284. doi:10.1121/1.4920337

Dong, H., Nguyen, T.-D., and Duffaut, K. (2012). Estimation of Shear-Velocity Profiles Using Shear Source Data in marine Environment. *J. Acoust. Soc. America* 131, 3278. doi:10.1121/1.4708258

Du, S., Cao, J., Zhou, S., Qi, Y., Jiang, L., Zhang, Y., et al. (2020). Observation and Inversion of Very-Low-Frequency Seismo-Acoustic fields in the South China Sea. *J. Acoust. Soc. America* 148 (6), 3992–4001. doi:10.1121/10.0002949

Ewing, J., Carter, J. A., Sutton, G. H., and Barstow, N. (1992). Shallow Water Sediment Properties Derived from High-Frequency Shear and Interface Waves. *J. Geophys. Res.* 97 (B4), 4739. doi:10.1029/92JB00180

Herrmann, R. B. (2013). Computer Programs in Seismology: An Evolving Tool for Instruction and Research. *Seismological Res. Lett.* 84 (6), 1081–1088. doi:10.1785/0220110096

Hughes, S. J., Ellis, D. D., Chapman, D. M. F., and Staal, P. R. (1990). Low-frequency Acoustic Propagation Loss in Shallow Water over Hard-rock Seabeds Covered by a Thin Layer of Elastic-Solid Sediment. *J. Acoust. Soc. America* 88 (1), 283–297. doi:10.1121/1.399951

Klein, G., Bohlen, T., Theilen, F., Kugler, S., and Forbriger, T. (2005). Acquisition and Inversion of Dispersive Seismic Waves in Shallow marine Environments. *Mar. Geophys. Res.* 26, 287–315. doi:10.1007/s11001-005-3725-6

Kugler, S., Bohlen, T., Bussat, S., and Klein, G. (2005). Variability of Scholte-Wave Dispersion in Shallow-Water marine Sediments. *Jeeg* 10 (2), 203–218. doi:10.2113/JEEG10.2.203

Kugler, S., Bohlen, T., Forbriger, T., Bussat, S., and Klein, G. (2007). Scholte-wave Tomography for Shallow-Water marine Sediments. *Geophys. J. Int.* 168, 551–570. doi:10.1111/j.1365-246X.2006.03233.x

Li, W., Lu, W., Liu, Y., and Xu, J. (2012). Superimposed versus Residual basin: the North Yellow Sea basin. *Geosci. Front.* 3 (1), 33–39. doi:10.1016/j.gsf.2011.11.001

Love, A. E. H. (1911). *Some Problems of Geodynamics*. Cambridge University Press: Cambridge University Press.

Luo, Y., Xia, J., Liu, J., Liu, Q., and Xu, S. (2007). Joint Inversion of High-Frequency Surface Waves with Fundamental and Higher Modes. *J. Appl. Geophys.* 62 (4), 375–384. doi:10.1016/j.jappgeo.2007.02.004

Nguyen, X. N., Dahm, T., and Grevemeyer, I. (2009). Inversion of Scholte Wave Dispersion and Waveform Modeling for Shallow Structure of the Ninetyeast Ridge. *J. Seismol* 13 (4), 543–559. doi:10.1007/s10950-008-9145-8

Park, C. B., Miller, R. D., and Xia, J. (1998). "Imaging Dispersion Curves of Surface Waves on Multi-channel Record," in SEG Technical Program Expanded Abstracts, 1377–1380. doi:10.1190/1.1820161

Rauch, D. (1980). Experimental and Theoretical Studies of Seismic Interface Waves in Coastal Waters. *Bottom-Interacting Ocean Acoust.* 53, 307–327. doi:10.1007/978-1-4684-9051-0_21

Scholte, J. G. (1947). The Range of Existence of Rayleigh and Stoneley Waves. *Geophys. J. Int.* 5, 120–126. doi:10.1111/j.1365-246X.1947.tb00347.x

Shtivelman, V. (2004). Estimating Seismic Velocities below the Sea-Bed Using Surface Waves. *Near Surf. Geophys.* 2 (4), 241–247. doi:10.3997/1873-0604.2004021

Shtivelman, V. (2003). Using Surface Waves for Studying the Shallow Subsurface. *Bollettino di Geofisica Teorica en Applicata* 44 (3), 223–236.

Smith, W. H. F., and Wessel, P. (1990). Gridding with Continuous Curvature Splines in Tension. *Geophysics* 55 (3), 293–305. doi:10.1190/1.1442837

Socco, V. L., Boiero, D., Maraschini, M., Vanneste, M., Madshus, C., Westerdahl, H., et al. (2011). On the Use of the Norwegian Geotechnical Institute's Prototype Seabed-Coupled Shear Wave Vibrator for Shallow Soil Characterization - II. Joint Inversion of Multimodal Love and Scholte Surface Waves. *Geophys. J. Int.* 185, 237–252. doi:10.1111/j.1365-246X.2011.04961.x

Vanneste, M., Madshus, C., Socco, V. L., Maraschini, M., Sparrevik, P. M., Westerdahl, H., et al. (2011). On the Use of the Norwegian Geotechnical Institute's Prototype Seabed-Coupled Shear Wave Vibrator for Shallow Soil Characterization - I. Acquisition and Processing of Multimodal Surface Waves. *Geophys. J. Int.* 185 (1), 221–236. doi:10.1111/j.1365-246X.2011.04960.x

Wang, Y., Li, Z., Geng, J., You, Q., Hao, T., Hu, Y., et al. (2020). Seismic Imaging of S-Wave Structures of Shallow Sediments in the East China Sea Using OBN Multicomponent Scholte-Wave Data. *Geophysics* 85 (6), EN87–EN104. doi:10.1190/geo2019-0639.1

Wang, Y., Li, Z., You, Q., Hao, T., Xing, J., Liu, L., et al. (2016). Shear-wave Velocity Structure of the Shallow Sediments in the Bohai Sea from an Ocean-Bottom-Seismometer Survey. *Geophysics* 81 (3), ID25–ID36. doi:10.1190/geo2015-0417.1

Wu, D., Zhu, X., Wang, Q., and Hou, F. (2020). Characteristics of Active Faults Related to Deep Faults in the north Western Part of the South Yellow Sea (In Chinese). *Mar. Geology. Front.* 36 (2), 12–18. doi:10.16028/j.1009-2722.2019.039

Xia, J., Miller, R. D., Park, C. B., and Tian, G. (2003). Inversion of High Frequency Surface Waves with Fundamental and Higher Modes. *J. Appl. Geophys.* 52 (1), 45–57. doi:10.1016/S0926-9851(02)00239-2

Zhao, M., Qiu, X., Xia, S., Wang, P., Xia, K., and Xu, H. (2008). Identification and Analysis of Shear Waves Recorded by Three-Component OBSs in Northeastern South China Sea. *Prog. Nat. Sci.* 18, 181–188. doi:10.1016/j.pnsc.2007.06.005

Zhao, M., Qiu, X., Xia, S., Xu, H., Wang, P., Wang, T. K., et al. (2010). Seismic Structure in the Northeastern South China Sea: S-Wave Velocity and Vp/Vs Ratios Derived from Three-Component OBS Data. *Tectonophysics* 480 (1–4), 183–197. doi:10.1016/j.tecto.2009.10.004

Conflict of Interest: The authors declare that the research was conducted in the absence of any commercial or financial relationships that could be construed as a potential conflict of interest.

frontiers in Earth Science

ORIGINAL RESEARCH
published: 31 January 2022
doi: 10.3389/feart.2021.796783

Integrated Geophysical Study of the Collision Between the North China Craton and the Yangtze Craton and Its Links With Craton Lithospheric Thinning

Lihua Liu[1,2], Tianyao Hao[1,2,3]*, Chuanchuan Lü[4], Zhiqiang Wu[5], Kwanghee Kim[6], Hanjoon Kim[7] and Ya Xu[1,2]*

[1]Key Laboratory of Petroleum Resources Research, Institute of Geology and Geophysics, Chinese Academy of Sciences, Beijing, China, [2]Institutions of Earth Science, Chinese Academy of Sciences, Beijing, China, [3]College of Earth and Planetary Sciences, University of Chinese Academy of Sciences, Beijing, China, [4]Bullard Laboratories, Department of Earth Sciences, University of Cambridge, Cambridge, United Kingdom, [5]Qingdao Institute of Marine Geology, Qingdao, China, [6]Department of Geological Sciences, Pusan National University, Busan, South Korea, [7]Korea Institute of Ocean Science and Technology, Busan, South Korea

OPEN ACCESS

Edited by:
Alexander Cruden, Monash University, Australia

Reviewed by:
Xiongwei Niu, Ministry of Natural Resources, China
Jiazheng Zhang, South China Sea Institute of Oceanology (CAS), China

***Correspondence:**
Lihua Liu
liulihua@mail.iggcas.ac.cn
Tianyao Hao
tyhao@mail.iggcas.ac.cn

Specialty section:
This article was submitted to Structural Geology and Tectonics, a section of the journal Frontiers in Earth Science

Received: *28 October 2021*
Accepted: *17 December 2021*
Published: *31 January 2022*

Citation:
Liu L, Hao T, Lü C, Wu Z, Kim K, Kim H and Xu Y (2022) Integrated Geophysical Study of the Collision Between the North China Craton and the Yangtze Craton and Its Links With Craton Lithospheric Thinning. Front. Earth Sci. 9:796783. doi: 10.3389/feart.2021.796783

Unlike stable cratons elsewhere in the world, the lithosphere is strongly thinned in the east of both the North China Craton (NCC) and the Yangtze Craton (YZC) compared with the west. We deployed four active-source onshore-offshore wide-angle seismic survey lines in the eastern NCC and YZC from 2010 to 2016 with the aim of revealing the mechanism of lithospheric thinning and the process of the collision between the NCC and YZC. We obtained high-resolution crustal P-wave velocity models for the eastern NCC and YZC based on seismic forward modeling, travel-time tomography, and finite-difference wave-field modeling. Based on our integrated geophysical study and previous work, we propose a five-stage model for the collision between the YZC and NCC, with different dominant geodynamic mechanisms in each stage. Our collision model shows that lithospheric thinning in the eastern NCC and YZC is a consequence of the NCC-YZC collision and subduction of the Pacific plate.

Keywords: North China Craton, Yangtze Craton, sulu orogenic belt, crustal structure, lithospheric thinning, wide-angle seismic survey

INTRODUCTION

North China (**Figure 1**) was formed by the convergence of the North China Craton (NCC) and the Yangtze Craton (YZC) during the Triassic (Wan, 2012). The collision between the NCC and YZC formed the world's largest ultra-high-pressure metamorphism (UHPM) tectonic unit (Zheng, 2008), the Qingling-Dabie-Sulu Orogenic Belt (QDSOB), characterized by the presence of coesite and diamond inclusions (Wang et al., 1989; Xu et al., 1992). These minerals indicate that the shallow layers of the cratonic crust were subducted to a depth >80 km (Harley and Carswell, 1995) and then exhumed to the surface after a period of UHPM. The UHPM provides a rich source of information about the deep lithosphere and therefore the QDSOB has become a natural laboratory for studying the dynamics of continent-continent collision, subduction, and exhumation (Chopin, 2003; Zheng et al., 2003; Zhang et al., 2009).

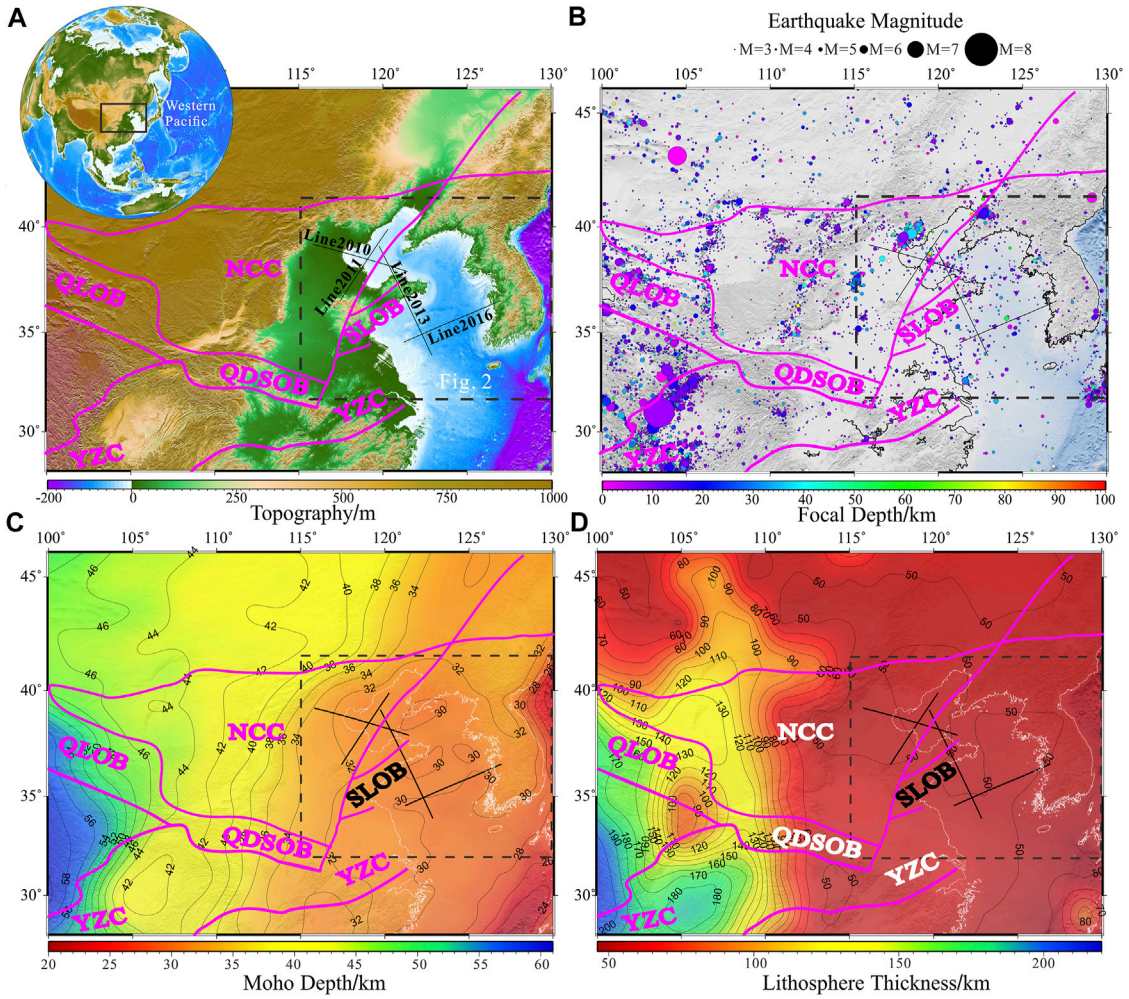

FIGURE 1 | (A) Topography of North China locating in the black box in the upper left insert map. **(B)** Seismicity with magnitude larger than 3 in North China from 1960s to 2021 (the earthquake events catalog was downloaded from IRIS: https://ds.iris.edu/ds/nodes/dmc/data/types/events/). **(C)** Moho depth of North China (after Hao et al., 2014). **(D)** Lithosphere thickness of North China (after Sun et al., 2021). The tectonic units are annotated in Figure **(A–D)**, the study area (**Figure 2**) of this paper is located in the black dashed boxes of Figure **(A–D)**. The black solid lines are active-source wide-angle seismic survey lines deployed by us from 2010 to 2016 in the study area (Liu et al., 2015; Liu et al., 2021). QLOB, qilian orogenic belt; QDSOB, qinglin-dabie-sulu orogenic belt; SLOB, sulu orogenic belt.

Figure 1 shows that both the crust and lithosphere of the NCC and YZC are thinner in eastern China than in western China, especially in the offshore domains of the Bohai Sea and the South Yellow Sea (SYS). Irrespective of how the rocks affected by UHPM were exhumed to the surface of the Sulu Orogenic Belt (SLOB), the exhumation process is clearly inseparable from the collision between the NCC and YZC and lithospheric thinning. The changes in the deep structure along the NCC, YZC, and SLOB are important in determining the mechanisms of lithospheric thinning and exhumation of the UHPM rocks, but previous studies have been limited to the onshore domains (Zhang et al., 2009; Choi et al., 2015; Li et al., 2018) and the deep structures of the offshore extensions of the NCC, YZC, and SLOB have only been inferred from the onshore results. As yet, there has been no geophysical study of the deep structures in the Bohai Sea and SYS, only shallow seismic profiles and regional-scale geophysical studies (Wan and Hao, 2009; Li et al., 2012).

We deployed four active-source onshore-offshore wide-angle seismic survey lines in the Bohai Sea and SYS from 2010 to 2016 and extended these results to the adjacent onshore regions (**Figure 1**). We obtained high-resolution crustal models in the offshore domains using seismic forward modeling, travel-time tomography, and finite-difference wave-field modeling. By integrating P-wave, gravity, and magnetic anomaly analyses, we revealed the differences in the deep structure and crustal deformation between the NCC and YZC and the offshore extension of the SLOB, in addition to the deep dynamics of lithospheric thinning and exhumation of the UHPM rocks in eastern China.

Our work provides information about the deep structures offshore and provides new geophysical data for quantitative research on lithospheric thinning in the NCC and YZC. Our results can be used to modify reference models for northern China and provide a solid foundation for understanding the

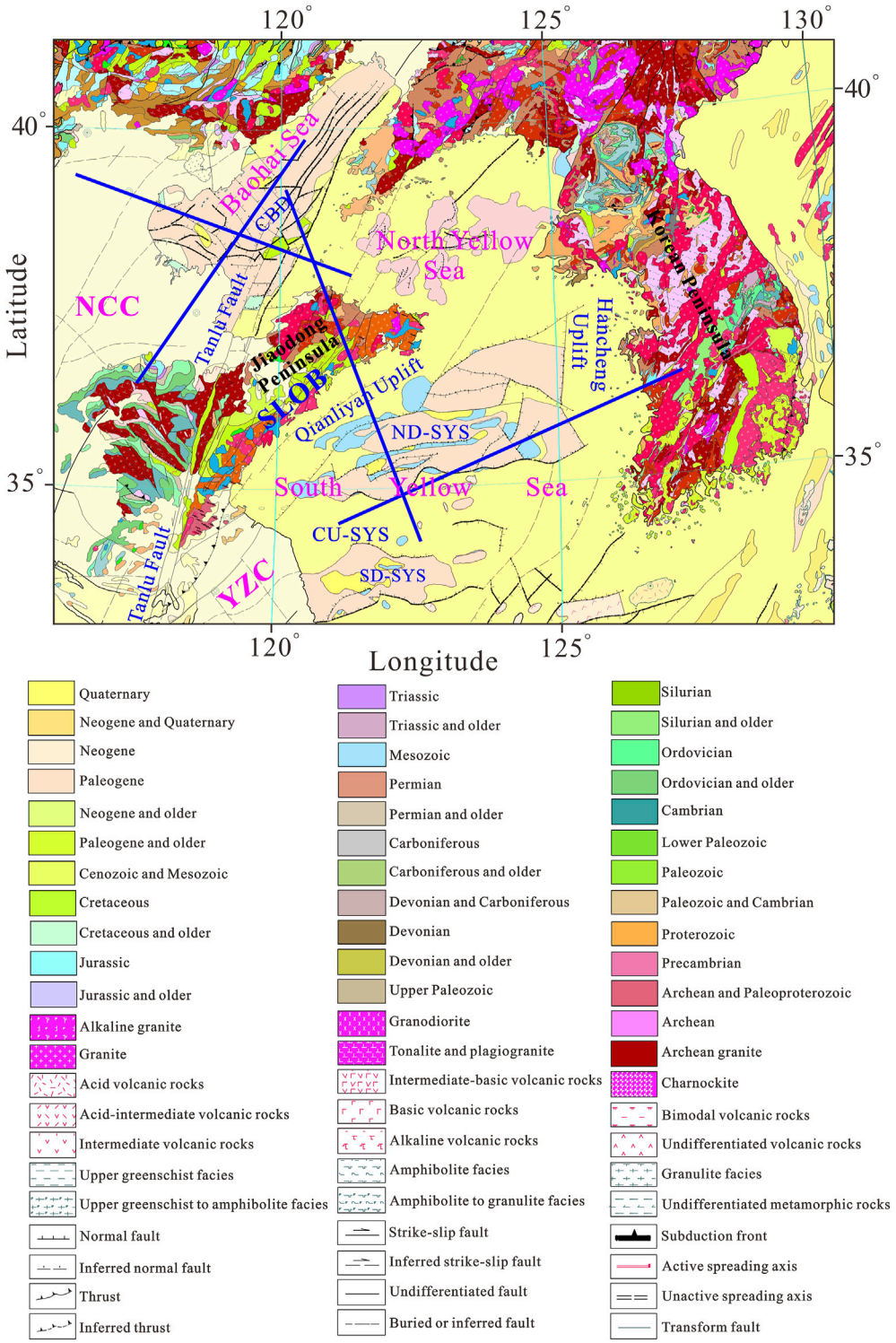

FIGURE 2 | Geological map of the study area (after Wang et al. (2017), and has the same legend as their results). The blue lines are the locations of wide-angle seismic profiles as shown in **Figure 1**. The offshore tectonic units involved include: Central Bohai Depression (CBD), Qianliyan Uplift, Northern Depression of SYS (ND-SYS), Central Uplift of SYS (CU-SYS), and Southern Depression of SYS (SD-SYS). The geological map can be accessed via: http://dcc.ngac.org.cn/geologicalData/rest/geologicalData/geologicalDataDetail/402881f75d9bbbed015d9bbbfa280000.

evolution and tectonic effects of continent-continent collision, subduction, and exhumation.

GEOLOGICAL BACKGROUNDS

The northern part of the study area is in the eastern NCC (**Figure 2**), which was formed before 1.8 Ga (Zhu et al., 2011; Zhu et al., 2012). The NCC records major tectonic processes during the early evolution of the Earth, but is different from other cratons in that it experiences frequent seismic activity (**Figure 1B**) and has undergone extensive crustal and lithospheric thinning (**Figures 1C,D**) and destruction (Wu et al., 2008; Zhu et al., 2011; Zhu et al., 2012). The NCC can be divided into three parts based on the thickness of the lithosphere (Zhu et al., 2011; Zhu et al., 2012): the stable western region (>200 km thick), the transitional central region (80–200 km thick), and the severely thinned eastern region (<80 km thick). The thickest lithosphere of 215 km is found in the Ordos Massif in the western part of the NCC and the thinnest is located in the Bohai Sea in the eastern NCC with a thickness of <60 km (Chen et al., 2009; Zhu et al., 2012). The dynamic destruction of the NCC and the large spatial extent of lithospheric thinning are well studied in craton research (Gao et al., 2004; Wu et al., 2008). Many studies have shown that there may be an important relationship between the thinning of the lithosphere in the NCC and the collision between the NCC and YZC (Gao et al., 2008; Wu et al., 2008; Liu et al., 2015).

The SLOB is located on the southern Jiaodong Peninsula and in the northern SYS (**Figure 2**) and retains a large number of structural traces generated during the collision between the NCC and YZC (Hao et al., 2010). As the eastern extension of the QDSOB, the SLOB is an important region for studying the dynamics of continent-continent collision, subduction, and re-entry (Liu et al., 2021). Based on petrological chronology research, geochemical analysis, and deep structural geophysical observations around the SLOB, early research constrained the exhumation time of the UHPM to about 120 Ma in the Cretaceous (Li et al., 2009). Various mechanisms and models have been proposed to explain the exhumation of the UHPM rocks, including buoyancy forces and extension (Platt, 1993), lower crustal delamination (Gao et al., 1998; Kern et al., 1999), the buoyancy-driven exhumation of upper crustal slices (Chemenda et al., 1995; Chemenda et al., 1996), and forced flow in a subduction channel (Gerya and Stockhert, 2002). On the basis of multi-disciplinary research, Xu et al. (2009) proposed a polyphase exhumation mode for the continental crust in which the Sulu UHPM zone is composed of several exhumed tectonic slices of the subducted continental YZC crust.

The SYS in the southern part of the study area is an important component of the YZC (**Figure 2**). Like the NCC, the YZC is divided into three parts from west to east: the upper, middle, and lower YZC. Based on magnetotelluric sounding (Xiao et al., 2014), active-source seismic sounding (Xu et al., 2014; Lü et al., 2015; Liu et al., 2021), earthquake tomography (Jiang et al., 2013; Ouyang et al., 2014; Bao et al., 2015), and receiver function analysis (Shi et al., 2013; Zheng et al., 2014), previous studies reached a consensus that the lithosphere of the YZC has undergone significant thinning from west to east (**Figure 1D**) and that the thinning reaches a maximum in the eastern YZC, with a lithospheric thickness of <80 km (An and Shi, 2006) and a crustal thickness <35 km (Zhang et al., 2009).

Because both the NCC and YZC have experienced significant lithospheric thinning in eastern China, it is natural to ask the following questions. Did the lithosphere thin gradually or suddenly in these cratons? Did the lithosphere of one craton thin first, or did they both thin at the same time? Did lithosphere thinning occur before or after the collision between the YZC and NCC? Did the crust and lithosphere of the NCC and YZC thin at the same time? Did the crust or the lithospheric mantle have a more important role in lithospheric thinning, or did they have the same level of thinning?

Radioisotope dating indicates that the UHPM rocks in the QDSOB were formed between 245 and 210 Ma (Xu et al., 2006; Zheng, 2008), which is also the time period of the collision between the YZC and NCC. The time at which the lithosphere of the NCC began to thin has not yet been determined (Wu et al., 2008), but it is thought that the upper limit is in the Mesozoic and the lower limit is in the Cenozoic (Wu et al., 2008), with the peak time of lithospheric thinning in the NCC at 130–120 Ma (Wu et al., 2008; Zhu et al., 2012). Sudden magmatic activity during the J3 period in the lower Yangtze area (Deng and Wu, 2001) indicates that the peak time of lithospheric thinning here was about 140 Ma (Late Jurassic). Based on petrological chronology, geochemical analyses, and geophysical observations of the deep structure around the QDSOB, early research (Li et al., 2005) constrained the exhumation time of the UHPM to about 120 Ma (Cretaceous). By summarizing the time relationships among the tectonic events, we see that lithospheric thinning of both the NCC and YZC occurred after their collision, close to the time at which the UHPM rocks were exhumed. This indicates that the collision of these two blocks played an important part in both lithospheric thinning and the exhumation of the UHPM rocks.

REGIONAL GRAVITY AND MAGNETIC ANOMALY ANALYSES

The overall variations of the Bouguer gravity anomalies and the reduction to pole magnetic anomalies change mildly in the Bohai Sea (**Figure 3**). Taking the NE-striking Tanlu Fault, which corresponds to the zero-value contour of the gravity and magnetic anomalies, as the boundary, the Bouguer gravity anomaly is low in the NW and high in the SE. By contrast, the reduction to pole magnetic anomaly is high in the NW and low in the SE. East of the Tanlu Fault, the gravity anomaly is mainly characterized by a large area with a small negative anomaly (−20 to 0 mGal) and a NE-striking negative anomaly trap is formed in the Central Bohai Depression (**Figure 3A**). The reduction to pole magnetic anomaly (**Figure 3B**) mainly has a low positive value (0–200 nT) and the main strike is also NE. By

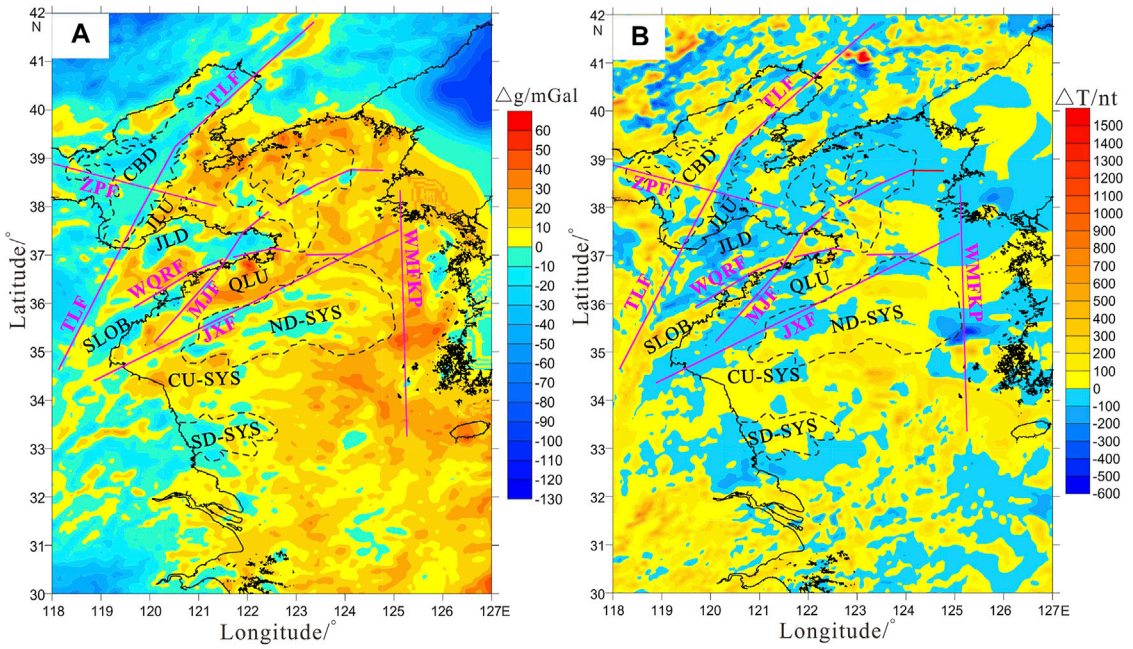

FIGURE 3 | The Bouguer gravity anomaly **(A)** and the reduction to pole magnetic anomaly **(B)** of the study area (after Hao et al., 2010). The black dashed boxes indicate the depressions in the sea area. The pink solid lines are the main great faults in the study area, including: ZPF, Zhangjiakou-Penglai Fault; TLF, Tanlu Fault; LYF, Lianyan Fault; WQRF, Wulian-Qingdao-Rongcheng Fault; MJF, Muping-Jimo Fault; JXF, Jianshan-Xiangshui Fault; WMFKP, Western Marginal Fault of Korean Peninsula. The main tectonic units include: CBD, Central Bohai Depression; JLU, Jiaoliao Uplift; JLD, Jiaolai Depression; SLOB, Sulu Orogenic Belt; QLU, Qianliyan Uplift; ND-SYS, Northern Depression of SYS; CU-SYS, Central Uplift of SYS; SD-SYS, Sourthern Depression of SYS.

contrast, the western side of the Tanlu Fault is dominated by a NE-striking small positive gravity anomaly (0–30 mGal) and a negative magnetic anomaly (−100 to 0 nT).

The gravity and magnetic anomalies of the onshore domain of the Jiaodong Peninsula are clearly different from those in the offshore domain of the Bohai Sea and the Yellow Sea (**Figure 3**). The Bouguer gravity anomalies onshore are generally low in the NE and high in the SW. A pair of negative gravity anomalies with amplitudes of −30 mGal are oriented diagonally in a northeasterly direction between the Wulian-Qingdao-Rongcheng and Muping-Jimo faults (**Figure 3A**). The reduction to pole magnetic anomaly in this region is dominated by a large range of negative anomalies and a pair of positive magnetic anomalies with an anomaly of about 200 nT is oriented diagonally in a northeasterly direction between the Wulian-Qingdao-Rongcheng and the Muping-Jimo faults (**Figure 3B**). The Wulian-Qingdao-Rongcheng and Muping-Jimo faults clearly had a role in controlling the distribution of the tectonic units and the intrusion of magmatic rocks on the Jiaodong Peninsula.

The gravity and magnetic anomalies in the SYS also show that the structural uplifts correspond to positive gravity anomalies and negative magnetic anomalies, whereas the structural depressions correspond to negative gravity anomalies and positive magnetic anomalies (**Figure 3**). In contrast with the large-scale, low-value negative Bouguer anomalies in the Bohai Sea, the gravity anomalies in the SYS are dominated by large-scale positive anomalies, with a maximum (about 60 mGal) at the Qianliyan Uplift (**Figure 3A**).

METHODOLOGY AND RESULTS

Data Acquisitions

We deployed four active-source onshore-offshore wide-angle seismic survey lines (Line 2010, Line 2011, Line 2013, and Line 2016) in the Bohai Sea and SYS from 2010 to 2016 and extended these lines onshore in the adjacent areas (**Figure 1** and **Table 1**). Line 2010 had a total length of 517 km, 160 land stations, and 52 ocean bottom seismometers (OBSs) were deployed. There were 98% of the deployed OBSs recovered, and 39 of them could provide useful seismic records. Although three kinds of air-gun arrays were designed for Line 2010, we mainly used the 1576 shots of the air gun in volume of 9300 in^3 in the modeling of this paper. Line 2011 had a total length of 450 km, 200 land stations, and 40 OBSs were deployed. All the OBSs were recovered, and only 4 of them failed to record valid signals. Two kinds of air-gun arrays were designed for Line 2011, and both had 1,118 shots, we only used the datasets of air-gun array with volume of 9000 in^3. Line 2013 was 645-km long, and extends from the central Bohai Sea through the Jiaodong Peninsula to the South Yellow Sea, 130 land stations were deployed onshore area, and 52 OBSs were deployed

TABLE 1 | Observation parameters of the wide-angle seismic survey profiles

Line #	Onshore					Offshore						
	Length/ km	No. stations	Station spacing/ km	No. shots	Shot weight/ t	Length/ km	No. deployed OBS	Useful OBS	OBS spacing/km	No. air gun	Shot spacing	Shot Volume/ in^3
Line 2010	160	120	1.2–2	2	1.8 0.8	290	52	39	6	6077	190 m 85s	9300 6000 3300
Line 2011	200	120	1.2–2	2	2.8 2.5	210	40	36	3	2236	190 m 85s	9000 6000
Line 2013	130	111	0.5–2.5	2	2.8 2.6	445	52	45	6	3577	125 m 45s	6060
Line 2016	100	13	5–20	0	0	400	31	29	13.5	4502	90 m 84s	6640

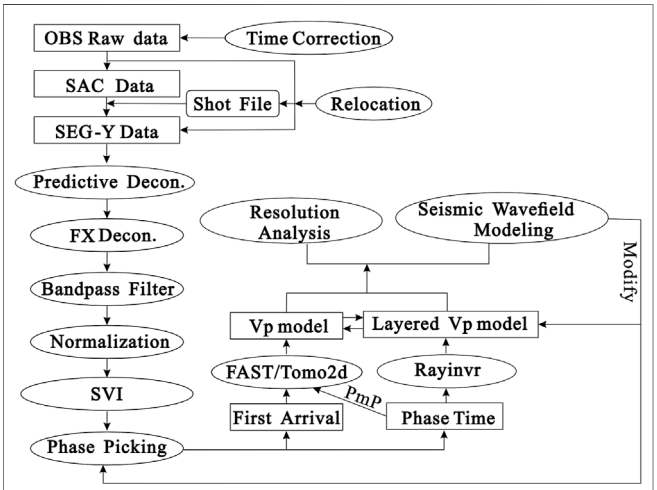

FIGURE 4 | The main flowchart of onshore-offshore wide-angle seismic data processing. The abbreviations include Decon.: Deconvolution, SVI, Super Virtual Interferometry. FAST, Tomo2d and Rayinvr are three different modeling software packages developed by Zelt and Barton (1998), Korenaga et al. (2000), and Zelt and Smith (1992), respectively.

offshore area. All the deployed OBSs were recovered, and 45 of them could provide useful traveltimes of seismic phases produced by a 6060-in^3 air-gun array. Line 2016 was 565-km long in total, 100 land stations, and 31 OBSs were deployed. All the OBSs were successfully recovered, and only one of them failed. The offshore source of Line 2016 was a 6640-in^3 air gun, and 4502 shots were fired. In summary, we deployed four dense active source wide-angle seismic survey profiles in East China, the recovery rates of OBSs were very good for all these four lines (>98%) and only a few of the recovered OBSs did not record the air-gun signals (**Table 1**).

METHODOLOGY

After pre-processing the data, including linear time drift correction, OBS relocation, denoising, and deconvolution (**Figure 4**), we picked the travel-times of the refraction and reflection seismic phases from all the useful OBSs and land stations (Liu et al., 2015; Liu et al., 2021). We found that most of the OBS stations provided useful data at offsets of up to 100 km (**Figure 5**), although a few OBS stations only provided effective observations within 60 km offsets. All the land stations had high signal-to-noise ratio land explosion records and some also had high-quality air-gun signals. The main seismic phases included in the modeling were: the direct water wave (Pw), refraction within the sediments (Ps), the reflection from the sediment basement (P1), refraction within the upper crust (Pg1), reflection from the base of the upper crust (P2), refraction within the mid-crust (Pg2), reflection from base of the mid-crust (PcP), reflection from the Moho (PmP), and refraction within the top of the upper mantle (Pn). Most of the phases in the Bohai Sea and SYS had the same distribution, but the refractions within the upper crust of the northern SYS had lower travel times and larger apparent velocities than those in the Bohai Sea from offset 0 km to about 120 km, indicating a roughly 120-km scale high-velocity anomaly in the upper crust of the northern SYS. The high-velocity anomaly was linked to the exhumation of the UHPM rocks in the SLOB (Liu et al., 2021).

The shallow structures constrained by previous studies (Cho et al., 2006; Bai et al., 2007; Wei et al., 2007; Shinn et al., 2010; Cho et al., 2013; Kim et al., 2019) were used as the shallow constraints. The average structure of the crust around the study area was used as a reference and the deep layers were set as horizontal layers, with the velocity increasing with depth, to build the initial models for these four lines. All the initial models had a depth of 50 km and six layers, including the water layer (constant velocity 1.5 km/s), the sedimentary layer (1.8–3.5 km/s), the upper crust (4.0–6.2 km/s), the mid-crust (6.3–6.6 km/s), the lower crust (6.7–7.0 km/s), and the top of the upper mantle (8.0–8.4 km/s). The initial models were continuously adjusted to gradually improve the fit of the calculated and measured travel-times (**Figure 6**) using the forward modeling software Rayinvr (Zelt and Smith, 1992), based on "trial-and-error" and "layer-stripping." The reflections were mainly used to constrain the depth of the interfaces, while the refractions were mainly used to constrain the velocity of the layers. The value of the root-mean-square travel-time (T_{rms}) and the normalized χ^2 were used as the basis for the fitting error (Zelt and Smith, 1992). T_{rms} and χ^2 were

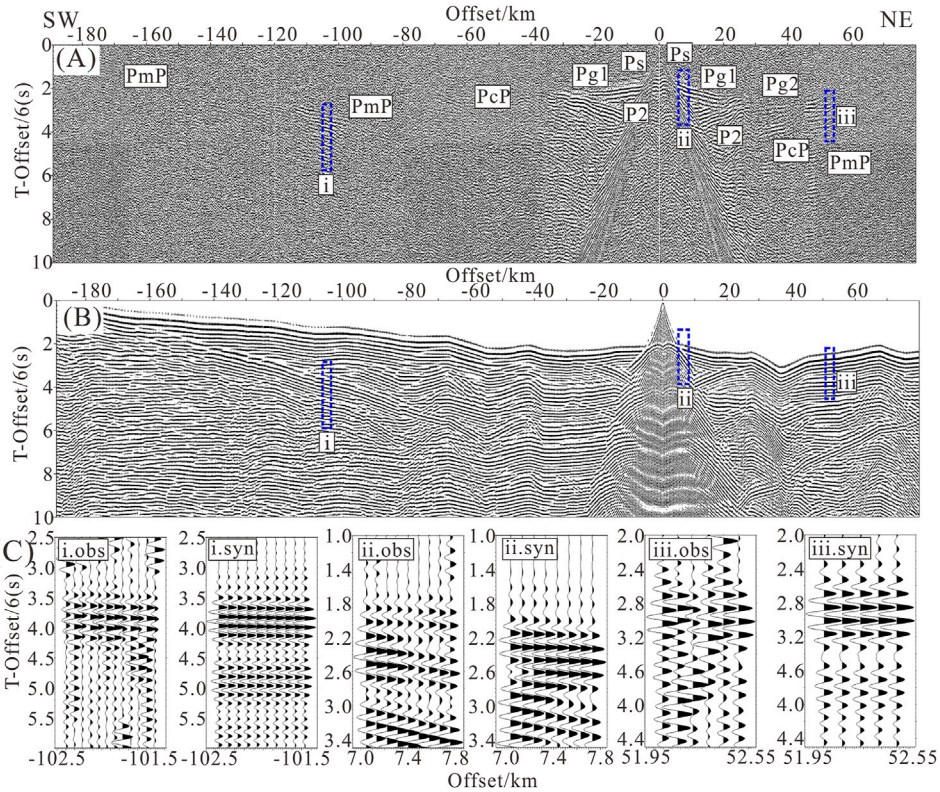

FIGURE 5 | (A) Observed seismograms after pre-processing from the hydrophone of OBS C15 located in the middle of ND-SYS on Line 2016. The blue dashed squares (i, ii, iii) that have relatively higher SNR, are displayed in Figure 5C as a close-up of the observed seismograms. **(B)** Corresponding synthetic seismograms calculated from the Vp model of Line 2016 by using the finite difference modeling code from the Seismic Unix package (Stockwell, 1999). The trace spacing was 100 m, the frequency of the source wavelet centered around 5 Hz. A free boundary condition was given to the top of the model, and the other three boundaries were set as absorbing boundary conditions. No noise was added to the synthetic seismograms. The blue dashed squares (i, ii, iii) are located at the same position as Figure 5**(A)** and are displayed in Figure 5**(C)** as a close-up of the synthetic seismograms. **(C)** The close-up image of the squares i, ii, iii in Figure 5**(A,B)**, and they are displayed with a gain and filter proportional to offset. All figures have the same reduced velocity (6 km/s).

continuously modified by adjusting the initial model until the optimum model was found—that is, the model that had a converged travel-time residual distribution, the smallest T_{rms}, and the χ^2 value closest to 1.0 (**Figure 6** and **Table 2**).

We obtained the ray coverage (**Figure 7**) of the velocity models during the forward modeling by Rayinvr package (Zelt and Smith, 1992). We can see that most of the crustal structure has good ray coverage (>200 ray hits) for these four wide-angle seismic profiles, and the common feature is that the offshore domains are better resolved than the onshore domains due to the denser stations and smaller source spacing in the offshore areas. Since the Pn phases were picked only at far offsets (>100 km) from a few stations, the ray density within the uppermost mantle is less than that within the crust. Moreover, the forward models were double checked with seismic traveltime tomography using the FAST package developed by Zelt and Barton (1998) and the Tomo2d package developed by Korenaga et al. (2000), because the forward modes usually tend to give smooth velocity structures. The smoothed forward models were taken as the initial models, and the traveltimes of first arrivals and Moho reflections used in the forward modeling were selected to inversion the Vp models by traveltime tomography methods.

Finite-difference wave-field modeling was applied to further constrain the V_p structure and the phase identification with the Seismic Unix package (Stockwell 1999). We obtained the corresponding synthetic seismograms at the locations of the stations (**Figures 5B,C**) and the land explosions. The synthetic seismograms reproduced the reflection/refraction seismic phase travel-times and apparent velocities well at different offsets, indicating that the established V_p model took most of the picked phases into account.

We estimated the resolution of the models for the four lines by applying differently sized checkerboard tests (**Figure 8**) for the inversion models and perturbation analysis and the *F*-test for the forward models (Liu et al., 2015; Liu et al., 2021). In general, the uncertainty in the velocity was between −0.3 and 0.3 km/s, the uncertainty in the depth of the Moho was <1 km, and our models were able to effectively recover checkerboard patterns larger than (30 km × 10 km) throughout the crust.

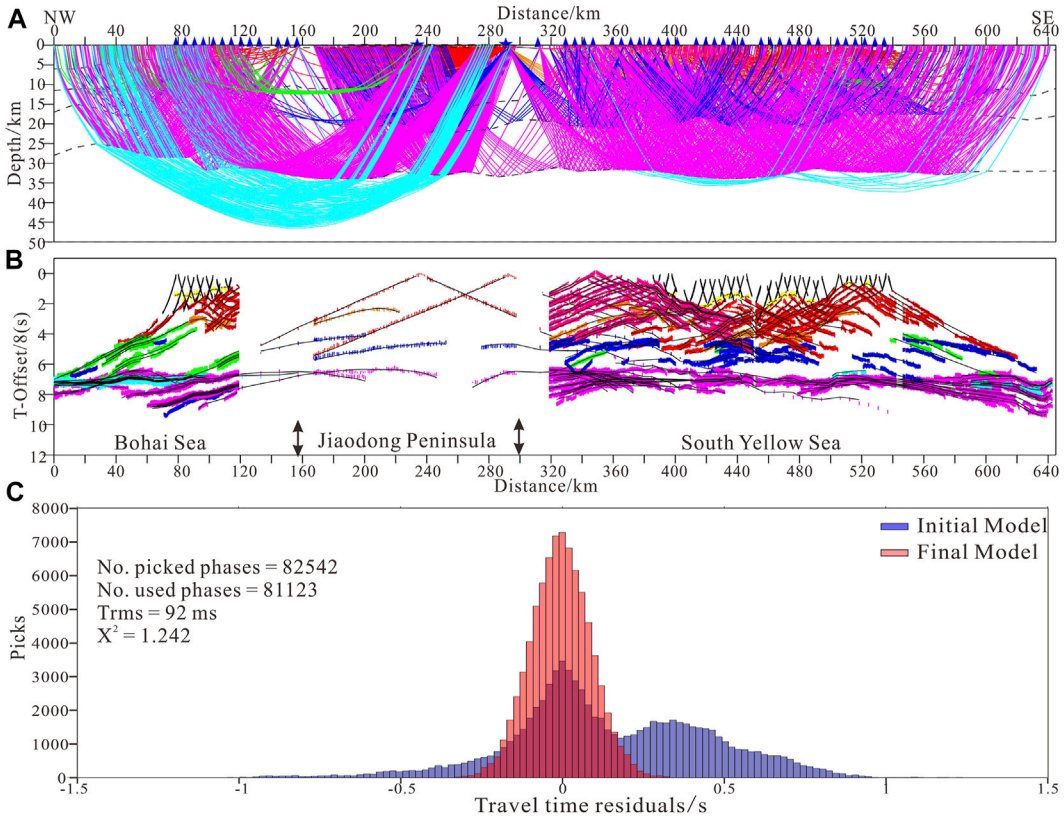

FIGURE 6 | (A) Ray paths of all phases from the sources to the receivers of Line 2013. The blue triangles on the top are useful OBSs and land stations, and only 1/50 of the air gun ray paths are displayed. **(B)** Observed traveltimes (colored short vertical lines, whose length are corresponding to picking uncertainties) and calculated traveltimes (black solid lines) for all stations of Line 2013. **(C)** Traveltime residual distribution of the initial model (blue histogram in the rear) and the finial forward model (red histogram in the front).

RESULTS

We obtained high-resolution crustal models (**Figure 9**) in the eastern NCC, eastern YZC, and across the collision belt between the two cratons in the offshore domains using forward modeling and seismic travel-time tomography. The final 2D Vp models of the four lines were divided into five layers by four interfaces: the sedimentary basement G, constained by reflections P1; the bottom of upper crust C2, constained by reflections P2; the bottom of mid-crust C3, constained by reflections PcP; and the Moho, constrained by reflections PmP. The seafloor was constrained by the echosounder and each of the models contained a water layer with a constant velocity of 1.5 km/s, although this was too shallow to distinguish in the V_p models. The resolution and uncertainty analyses showed that the top of the upper mantle was poorly resolved because there were few ray paths across this layer. We therefore do not discuss the water layer and the top upper mantle here.

The sedimentary layer lies between the seafloor and the sedimentary basement G (**Figure 9**). The velocity of the sedimentary layer increases rapidly with depth from 1.8 km/s at the top to 4.5 km/s at the base. The fluctuations in the G interface correspond well with the Cenozoic structural uplifts and depressions. The thickness of the sedimentary layer gradually decreases from the North China Plain and Bohai Sea (about 6 km) to the Jiaodong Peninsula (<1 km) and then increases to the SYS (about 3 km).

The layer between the G and C2 interfaces is the upper crust. The thickness of the upper crust is generally thicker in the SYS (average about 10 km) than in the Bohai Sea (average about 5 km). The upper crustal velocity ranges from 5.0 to 6.2 km/s in the offshore domain of both the Bohai Sea and the SYS. A roughly 120-km wide southward-dipping high-velocity zone (HVZ), controlled by the Muping-Jimo and Jiashan-Xiangshui faults, lies in the upper crust near the Qianliyan Uplift. The velocity range (6.2–6.4 km/s) of the HVZ is the closest to that of the mid-crust in the SYS (6.2–6.5 km/s), suggesting that they have a similar composition.

The layer sandwiched between interfaces C2 and C3 is the mid-crust, which shows large differences in thickness in the Bohai Sea, the Jiaodong Peninsula, and the SYS (**Figure 9**). The depth of the C3 interface increases from about 15 km in the Bohai Sea to about 21 km in the onshore domain of both the North China Plain and Jiaodong Peninsula, but does not change significantly in the SYS (about 18 km). A roughly 50-km wide southward-dipping low velocity zone (LVZ) is seen in the mid-crust

TABLE 2 | Number of picked and used phases in the forward modeling, and main uncertainties for the forward model

phase	Phase picked	Phase used	Trms/ms	χ^2
Line 2010				
Ps: Refraction within sediment	1,270	1,175	68	2.809
Pg1: Refraction within upper crust	4,264	3,963	96	1.615
Pg2: Refraction within mid-crust	2,861	2,389	102	1.197
PcP: Reflection from mid-crust bottom	1,446	1,446	100	1.044
PmP: Reflection from Moho	7,757	7,697	90	0.947
Pn: Refraction within top upper mantle	456	437	90	0.706
All phases of Line 2010	18,054	17,107	93	1.266
Line 2011				
Ps: Refraction within sediment	1,864	1,777	93	5.387
P1: Reflection from sedimentary bottom	988	954	81	0.633
Pg1: Refraction within upper crust	2,947	2,784	103	3.515
P2: Reflection from upper-crust bottom	975	874	121	1.150
Pg2: Refraction within mid-crust	1,061	921	147	2.571
PcP: Reflection from mid-crust bottom	85	76	137	2.173
PmP: Reflection from Moho	4,262	4,250	126	1.603
Pn: Refraction within top upper mantle	788	583	113	1.492
All phases of Line 2011	12,970	12,219	115	2.551
Line 2013				
Ps: Refraction within sediment	1,620	1,606	67	1.528
P1: Reflection from sedimentary bottom	836	836	72	0.786
Pg1: Refraction within upper crust	13,353	12,635	79	1.548
P2: Reflection from upper-crust bottom	3,164	2,911	85	0.913
Pg2: Refraction within mid-crust	4543	4,453	89	1.044
Pb: Head wave from high velocity zone in the upper crust of SLOB	11,050	11,044	86	1.725
PcP: Reflection from mid-crust bottom	7,327	7,244	106	1.145
PmP: Reflection from Moho	31,941	31,693	93	0.992
Pn: Refraction within top upper mantle	8,708	8,701	113	1.379
All phases of Line 2013	82,542	81,123	92	1.242
Line 2016				
Pw: Direct water wave	2,817	2,817	93	0.866
Ps: Refraction within sediment	1,786	1,755	114	1.429
P1: Reflection from sedimentary bottom	1,014	1,012	89	0.810
Pg1: Refraction within upper crust	13,836	13,447	104	1.100
P2: Reflection from upper-crust bottom	7,359	7,216	111	1.215
Pg2: Refraction within mid-crust	4,116	3,700	102	0.936
PcP: Reflection from mid-crust bottom	10,000	9,829	117	1.322
PmP: Reflection from Moho	18,702	18,687	112	1.152
Pn: Refraction within top upper mantle	1,032	1,031	174	2.389
All phases of Line 2016	60,662	59,494	111	1.173

between the Lianyan and Muping-Jimo faults (**Figure 9F**). The velocity range (6.2–6.4 km/s) of the LVZ is close to that of the lower part of the upper crust (6.2–6.3 km/s) that lies above it, suggesting that the collision of the blocks may have caused the upper crust to fold downward to the position of the mid-crust (Liu et al., 2021).

The lower crust lies between the C3 interface and the Moho. The lateral velocity of the lower crust changes very little from the Bohai Sea to the SYS, with only the velocity contours bending downward near the great faults (**Figure 9**). The velocity is about 6.6 km/s at the top of the lower crust and about 7.0 km/s at the base. The depth of the Moho in the offshore domains of the Bohai Sea and the onshore domains of the North China Plain and Jiaodong Peninsula is about 31 km and there is an uplift in the Central Bohai Depression near the Tanlu and Zhangjiakou-Penglai faults (**Figures 8D,F**, **9B**), with the shallowest part at a depth of about 25 km. The depth of the Moho in the offshore domain of the SYS (about 33 km) is deeper than that in the North China Plain and Bohai Sea.

DISCUSSION

Lithospheric Thinning of the NCC

The NCC can be divided into three parts based on the thickness of the lithosphere: the stable western NCC (>200 km); the transitional middle NCC (200–80 km); and the severely thinned eastern NCC (<80 km). The thickest lithosphere (215 km) is found under the Ordos Massif in the western NCC and the thinnest (<65 km) under the Bohai Sea in the eastern NCC (Chen et al., 2009; Zhu et al., 2012), indicating that the Bohai Sea is the core area of lithospheric thinning in the NCC.

Gao et al. (1998), Gao et al., (2004) summarized the crustal thickness, the velocity structure in the crust, and the chemical

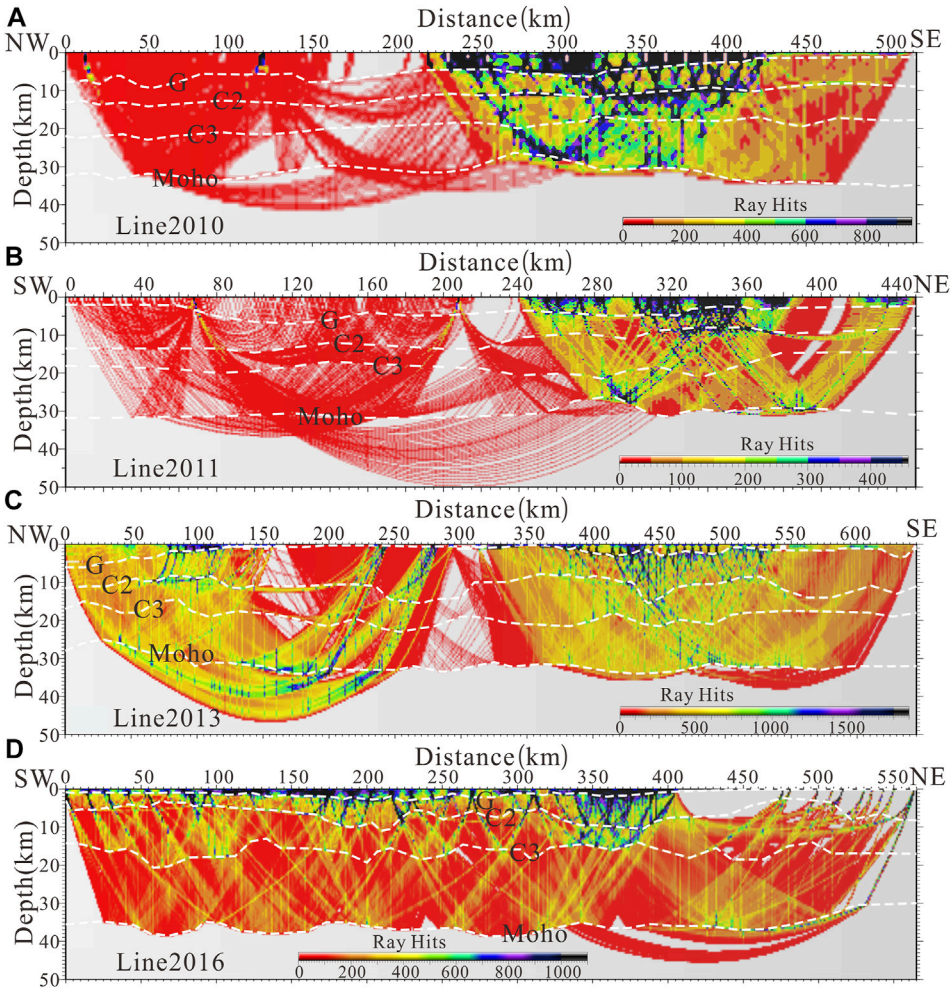

FIGURE 7 | (A) Ray hits of Line 2010 **(A)**, Line 2011 **(B)**, Line 2013 **(C),** and Line 2016 **(D)**, respectively. The regions without ray paths are shown in gray. The white dashed lines indicate the main interfaces (G, C2, C3, and Moho) in the Vp models.

composition of the different tectonic units by combining deep seismic sounding and geochemical data from different continental regions in China. Their results showed that the average crustal thickness of the NCC is 35.59 km, which is similar to the average crustal thickness (37.10 km) of the global continent. Wang et al. (2014) obtained an average thickness of the crust under the Ordos Massif of 41.3 km via a comprehensive analysis of *H-k* stacking and the teleseismic receiver function seismic sounding results. Our results from Line 2010, Line 2011, and Line 2013 all showed that the thinnest crust (25 km) in the eastern NCC lies in the Central Bohai Depression.

We took the lithospheric (215 km) and crustal (41.3 km) thickness of the Ordos Massif as the standard thicknesses in the NCC. The thickness of the lithosphere in the eastern NCC (about 65 km) has therefore been reduced by 150 km and is 69.8% thinner than the standard lithosphere in the NCC. However, the crustal thickness in the eastern NCC (25 km in the thinnest region) has been reduced by 16.3 km from the standard crustal thickness of the NCC (41.3 km), accounting for 10.9% of the total thinning of the lithosphere. By contrast, if calculated at the average Moho depth of 31 km in the Bohai Sea (where it is 24.9% thinner than the standard crust), the crustal thinning only accounts for 6.8% of the lithospheric thinning—that is, the remaining 93.2% of lithospheric thinning took place in the lithospheric mantle. This shows that thinning of the NCC was caused by the removal of the lower lithospheric mantle, with only a minor contribution from the thinning of the crust (Gao et al., 2008). This suggests that extensional thinning of the lithosphere may not be the main mechanism for lithospheric thinning in the eastern NCC because extension would cause the same degree of thinning in both the lithospheric mantle and crust.

By contrast, the results from Line 2010, Line 2011 and Line 2013 all show that the Moho is uplifted near the Tanlu and Zhangjiakou-Penglai fault beneath the Central Bohai Depression. The velocity of the lower crust and upper mantle is anomalous near these fault zones, indicating that the crust of the eastern

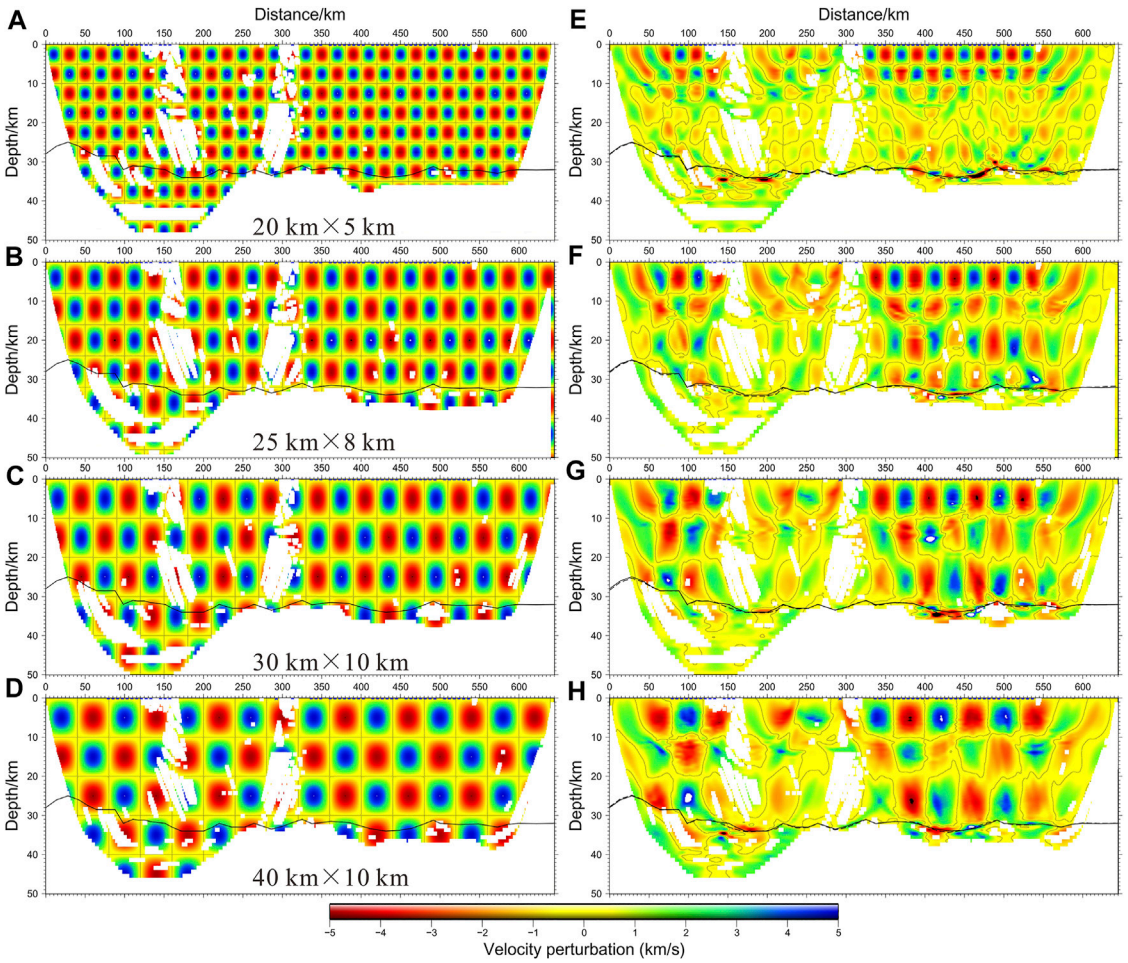

FIGURE 8 | Checkerboard tests for the tomography model of Line 2013. The input checkerboard patterns (left) and the corresponding output results (right) have the checkerboard sizes of 20 × 5 km **(A,E)**, 25 × 8 km **(B,F)**, 30 × 10 km **(C,G)**, and 40 × 10 km **(D,H)**, respectively. Regions without ray coverage are shown in white.

NCC has been subjected to intrusion and reconstruction and that the deep faults are channels for the upwelling of deep material. This upwelling is related to the intrusion of basalts along the fault zone caused by the subduction of the Pacific plate during the Jurassic and Cretaceous, indicating that lithospheric thinning in the eastern NCC is related to the remote effects of the subduction of the Pacific plate (Liu et al., 2015).

Collision Between the NCC and YZC and Mechanism of Craton Lithospheric Thinning

Based on the regional gravity (**Figure 3A**), and magnetic (**Figure 3B**) and crustal velocity structures (**Figure 9**) in the different tectonic units, we can determine the boundary between the NCC and YZC and delineate the spatial distribution of the SLOB (Liu et al., 2021). Our results imaged a roughly 120-km wide, southward-dipping HVZ in the upper crust of the southern SLOB and a roughly 50-km wide, northward-dipping LVZ in the mid-crust of the northern SLOB. Based on the location and velocity range of the HVZ, we linked the HVZ with the mid-crust of the YZC, which was decoupled from the lower crust during the collision between the NCC and YZC. The LVZ in the mid-crust of the SLOB has the same velocity range as the upper crust above, indicating that the crust of the NCC has been wedged into the detached crust of the YZC. The mid-crust of the YZC was uplifted by this wedging of the NCC and, after later denudation, remained in the position of the upper crust in the southern SLOB, forming the HVZ. By contrast, the wedged crust of the NCC in the collision belt bent downward to the position of the lower crust as a result of extrusion stress, forming the LVZ in the lower crust of the northern SLOB (Liu et al., 2021).

Based on our crustal models in the offshore domain of eastern China and other geological, geophysical, and geochemical evidences (Li, 1994; Zhai et al., 2007; Chang and Zhao, 2012), and with reference to the proposed mechanisms for the exhumation of the UHPM, we propose that the collision between the YZC and the NCC and lithosphere thinning of the cratons in eastern China took place in five main stages (**Figure 10**).

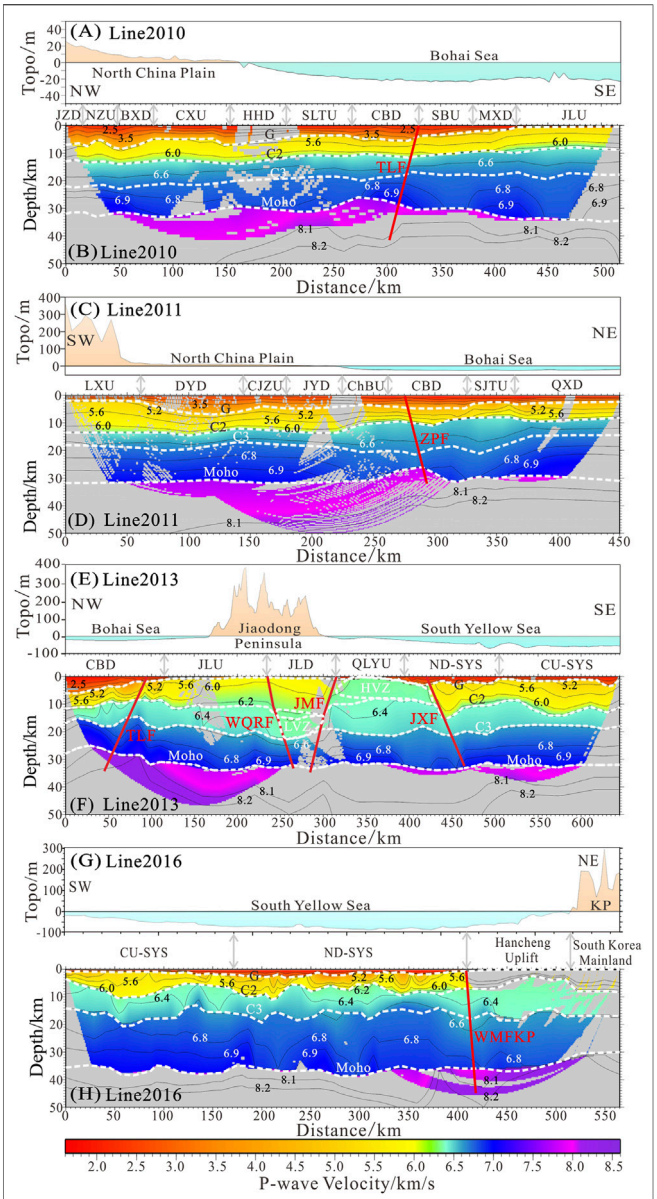

FIGURE 9 | Topography and Vp model of Line 2010 **(A,B)**, Line 2011 **(C,D)**, Line 2013 **(E,F)**, and Line 2016 **(G,H)**, respectively. Model regions without ray coverage are shown in gray. The main tectonic units, with boundaries shown in gray arrows, are annotated between the maps of topography and Vp model. The abbreviations of the names of tectonic units are listed next. JZD, Jizhong Depression; NZU, Niutuozhen Uplift; BXD, Baxian Depression; CXU, Cangxian Uplift; HHD, Huanghua Depression; SLTU, Shaleitian Uplift; CBD, Central Bohai Depression; SBU, Southern Bohai Uplift; MXD, Miaoxi Depression; JLU, Jiaoliao Uplift; LXU, Luxi Uplift; DYD, Dongying Depression; CJZU, Chenjiazhuang Uplift; JYD, Jiyang Depression; ChBU, Chenbei Uplift; SJTU, Shijiutuo Uplift; QXD, Qinxi Depression; JLD, Jiaolai Depression; QLYU, Qianliyan Uplift; ND-SYS, Northern Depression of SYS; CU-SYS, Central Uplift of SYS. The white dashed lines indicate the main interfaces (G, C2, C3, and Moho) in the Vp model, with velocity contours in black solid lines. The red lines are locations of the main great faults, which can be found in and have the same abbreviations as **Figure 3**.

(1) The subduction stage (>200 Ma) during Indosinian movement. During the Triassic, the NCC collided with the YZC and the YZC was subducted below the NCC as a result of the subduction of the oceanic plate between them (**Figure 10A**). The lithosphere of the orogenic belt began to accrete and the subducted YZC crust underwent UHPM/HPM with burial. UHPM was triggered at depths >80 km and HPM at shallower depths.

(2) The lithospheric detachment stage (200–140 Ma) during Yanshanian movement. SE China was strongly compressed during the Indosinian movement, and this compression spread to northern China, including the Yellow Sea area, and formed deep faults (Lianyan Fault, Wulian-Qingdao-Rongcheng Fault, Muping-Jimo Fault) around the orogenic belt. This resulted in decoupling of the mid-crust of the YZC along the decoupling fault (**Figure 10B**). Dehydration of the subducted oceanic plate and the western Pacific plate during the Yanshanian movement weakened the lithosphere in eastern China (**Figure 10B**). The weakened lithosphere around the SLOB broke off along the deep fault zones formed by the collision between the NCC and YZC and the subduction of the western Pacific plate. The weakened and broken lithosphere of the northern orogenic belt delaminated from the crust as a result of negative buoyancy and the decoupled mid-crust of the YZC was exhumed to the upper crust by positive buoyancy. The lithosphere of the eastern NCC was strongly thinned during this stage.

(3) The UHPM/HPM exhumation stage (140–110 Ma). The mantle flow in the collision belt domains was intensified under the combined action of the detachment and subsidence of the lithosphere and the subduction of the western Pacific plate. This, in turn, promoted large-scale lithospheric delamination and regenerated the accreted lithosphere beneath the crust (**Figure 10C**). The accreted lithosphere and mantle flow assisted the detachment of the lithosphere of the southern SLOB and YZC. The mid-crust of the YZC that had undergone UHPM/HPM was exhumed to the surface by delamination of the YZC lithosphere, resulting in a southward-dipping HVZ in the upper crust of the collision belt (**Figure 10C**). Because the accreted lithosphere is much thinner than the delaminated paleo-lithosphere, the lithospheric thickness of the NCC and YZC were both strongly thinned during this stage.

(4) The extension and rifting stage (110–40 Ma) between late Yanshanian movement and early Himalayan movement. During this stage, back-arc extension caused by the activity of the western Pacific tectonic domain began to gradually intensify and preceded the development of rifting in the SYS area. From the Late Cretaceous to early Cenozoic, the tectonic stress in the SYS and adjacent areas turned to NNW-oriented extension and the continental faulted depressions began to overlap with the Mesozoic and Paleozoic residual marine basins (Pang et al., 2017). Under both tensile stress and gravity, the upper wall of the

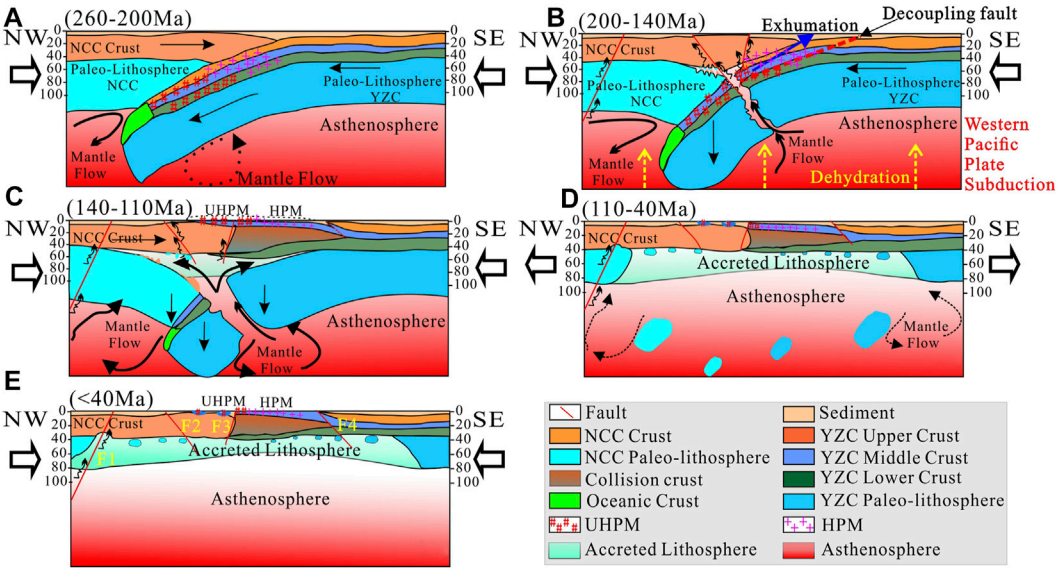

FIGURE 10 | The sketch map of the collision process between the YZC and the NCC. **(A)** 260–200 Ma, **(B)** 200–140 Ma, **(C)** 140–110 Ma, **(D)** 110–40 Ma, **(E)** < 40 Ma, respectively. The arrows outside orient the direction of the principal stress field, the arrows inside are directions of mantle flow and upwelling of the deep materials, red lines are the great faults with names in yellow texts, including F1: Tanlu Fault, F2: Lianyan fault; F3: Muping-Jimo fault; and F4, Jiashan-Xiangshui fault. In Figure 10B, the blue arrow indicates the exhumation of deep material, and the yellow dashed arrows indicate the dehydration of the subducted Pacific plate.

early thrust fault began to slide back along the fault plane and gradually changed from a reverse fault to a normal fault. The decoupling fault developed again under tensile stress as a result of the relatively fragile surrounding environment and formed a lithospheric fault (Jiashan-Xiangshui fault). As a result of tectonic subsidence, the exhumed UHPM/HPM was partly retained at the surface after long-term denudation (**Figure 10D**). The lithosphere and crust also thinned as a result of extension, but the lithospheric thinning was much less than that caused by previous lithospheric delamination.

(5) The uplifting and denudation stage (<40 Ma) of the late Himalayan. The regional sedimentary discontinuities, the widespread absence of parallel unconformities in the Oligocene-Lower Miocene and the parallel unconformities on the seismic profiles represent the overall uplift of the NCC and the YZC as a result of the westward subduction of the western Pacific plate and the collision between the Indian and Eurasian plates (Ji et al., 2018). The NCC and the YZC began to undergo strong denudation, resulting in significant thinning of the sedimentary layer in the SLOB region (**Figure 10E**).

CONCLUSION

We addressed the boundaries between the NCC, SLOB, and YZC based on the general crustal structures in our high-resolution V_p models along wide-angle seismic profiles and the regional gravity and magnetic anomalies. After calculating the degree of thinning of the crust and lithosphere in the eastern NCC, we found that there was extensive lithospheric thinning in the eastern NCC, with an overall lithospheric thinning of 69.8%. However, crustal thinning only accounted for 6.8–10.9% of the lithospheric thinning. The remaining 89.1–93.2% of lithospheric thinning occurred in the lithospheric mantle, indicating that the eastern NCC has a relatively thinned crust and a clearly thinned lithospheric upper mantle. Extension therefore only had a limited role on lithospheric thinning of the eastern NCC.

Based on our results and early research on the UHPM belt between the NCC and YZC, we suggest that the exhumation of the UHPM rocks in the SLOB is a result of the combined effect of various factors, including lithospheric delamination, buoyancy, lower crust detachment, extension, mantle flow, and the subduction of the western Pacific plate. These factors played different parts during the different stages of exhumation.

Our results show that the Moho interface was uplifted near the fault zones, including the Tanlu and Zhangjiakou-Penglai fault, which may be channels for the upwelling of deep materials. The upwelled deep materials may be related to the intrusion of basalts along the fault zone caused by the subduction of the Pacific plate during the Jurassic and Cretaceous. By contrast, the lithosphere of the eastern NCC was strongly thinned during the lithospheric delamination stage after the collision between the NCC and YZC, suggesting that lithospheric thinning in the eastern NCC was the result of the collision of the NCC with the YZC and subduction of the Pacific plate.

DATA AVAILABILITY STATEMENT

The raw data supporting the conclusion of this article will be made available by the authors, without undue reservation.

AUTHOR CONTRIBUTIONS

LL: Data acquisition, data processing, methodology, interpretation, and editing. TH: Leading of the surveys and investigations, gravity and magnetic data analyses, interpretation, and review. CL, ZW, KK, HK, and YX: Data acquisition, interpretation, and review.

FUNDING

This work was supported by the National Natural Science Foundation of China (Grant Numbers 42006070, 91858212, 42076068, and 41210005). KK was supported by The KMA Research Development Program under Grant KMI 2018-02810.

ACKNOWLEDGMENTS

The wide-angle seismic data of Line 2010, Line 2011, and Line 2013 used here was acquired by Institute of Geology and Geophysics (CAS) (http://www.igg.cas.cn/), Qingdao Institute of Marine Geology (http://www.qimg.cgs.gov.cn/), First Institute of Oceanography, SOA (http://www.fio.org.cn/), and Geophysical Prospecting Center, CEA (http://www.gec.ac.cn/). Line 2016 was acquired by Institute of Geology and Geophysics (CAS), Qingdao Institute of Marine Geology, Pusan National University (https://www.pusan.ac.kr/eng/Main.do), and Korea Institute of Ocean Science and Technology (https://www.kiost.ac.kr/eng.do). The SEG-Y format data would be available upon request to these institutions and corresponding authors of this paper. The authors expressed special thanks to all the scientists and crews involved in the field work. The open source softwares Seismic Unix, SAC, Rayinvr, and GMT were used to process the data and produce the figures in the preparation of this paper. We would like to thank Associate Editor Alexander Cruden for processing our manuscript, and thank two reviewers for their constructive comments and suggestions.

REFERENCES

An, M., and Shi, Y. (2006). Lithospheric Thickness of the Chinese Continent. *Phys. Earth Planet. Interiors* 159 (3-4), 257–266. doi:10.1016/j.pepi.2006.08.002

Bai, Z., Zhang, Z., and Wang, Y. (2007). Crustal Structure across the Dabie-Sulu Orogenic belt Revealed by Seismic Velocity Profiles. *J. Geophys. Eng.* 4, 436–442. doi:10.1088/1742-2132/4/4/009

Bao, X., Song, X., and Li, J. (2015). High-resolution Lithospheric Structure beneath Mainland China from Ambient Noise and Earthquake Surface-Wave Tomography. *Earth Planet. Sci. Lett.* 417, 132–141. doi:10.1016/j.epsl.2015.02.024

Chang, K.-H., and Zhao, X. (2012). North and South China Suturing in the East End: What Happened in Korean Peninsula? *Gondwana Res.* 22, 493–506. doi:10.1016/j.gr.2011.12.010

Chemenda, A. I., Mattauer, M., and Bokun, A. N. (1996). Continental Subduction and a Mechanism for Exhumation of High-Pressure Metamorphic Rocks: New Modelling and Field Data from Oman. *Earth Planet. Sci. Lett.* 143, 173–182. doi:10.1016/0012-821x(96)00123-9

Chemenda, A. I., Mattauer, M., Malavieille, J., and Bokun, A. N. (1995). A Mechanism for Syn-Collisional Rock Exhumation and Associated normal Faulting: Results from Physical Modelling. *Earth Planet. Sci. Lett.* 132, 225–232. doi:10.1016/0012-821x(95)00042-b

Chen, L., Cheng, C., and Wei, Z. (2009). Seismic Evidence for Significant Lateral Variations in Lithospheric Thickness beneath the central and Western North China Craton. *Earth Planet. Sci. Lett.* 286, 171–183. doi:10.1016/j.epsl.2009.06.022

Cho, H.-M., Baag, C.-E., Lee, J. M., Moon, W. M., Jung, H., Kim, K. Y., et al. (2006). Crustal Velocity Structure across the Southern Korean Peninsula from Seismic Refraction Survey. *Geophys. Res. Lett.* 33 (6), L06307. doi:10.1029/2005GL025145

Cho, H.-M., Baag, C.-E., Lee, J. M., Moon, W. M., Jung, H., and Kim, K. Y. (2013). P- and S-Wave Velocity Model along Crustal Scale Refraction and Wide-Angle Reflection Profile in the Southern Korean peninsula. *Tectonophysics* 582, 84–100. doi:10.1016/j.tecto.2012.09.025

Choi, S., Ryu, I.-C., and Götze, H. J. (2015). Depth Distribution of the Sedimentary basin and Moho Undulation in the Yellow Sea, NE Asia Interpreted by Using Satellite-Derived Gravity Field. *Geophys. J. Int.* 202, 41–53. doi:10.1093/gji/ggv108

Chopin, C. (2003). Ultrahigh-pressure Metamorphism: Tracing continental Crust into the Mantle. *Earth Planet. Sci. Lett.* 212, 1–14. doi:10.1016/S0012-821X(03)00261-9

Deng, J., and Wu, Z. (2001). Lithospheric Thinning Event in the Lower Yangtze Craton and Cu-Fe Metallogenic belt in the Middle and Lower Yangtze River Reaches. *Gelogy of Anhui* 11 (2), 86–91.

Gao, S., Rudnick, R. L., Xu, W.-L., Yuan, H.-L., Liu, Y.-S., Walker, R. J., et al. (2008). Recycling Deep Cratonic Lithosphere and Generation of Intraplate Magmatism in the North China Craton. *Earth Planet. Sci. Lett.* 270, 41–53. doi:10.1016/j.epsl.2008.03.008

Gao, S., Rudnick, R. L., Yuan, H.-L., Liu, X.-M., Liu, Y.-S., Xu, W.-L., et al. (2004). Recycling Lower continental Crust in the North China Craton. *Nature* 432, 892–897. doi:10.1038/nature03162

Gao, S., Zhang, B.-R., Jin, Z.-M., Kern, H., Ting-Chuan Luo, T., and Zhao, Z.-D. (1998). How Mafic Is the Lower continental Crust? *Earth Planet. Sci. Lett.* 161, 101–117. doi:10.1016/s0012-821x(98)00140-x

Gerya, T. V., and Stöckhert, B. (2002). Exhumation Rates of High Pressure Metamorphic Rocks in Subduction Channels: the Effect of Rheology. *Geophys. Res. Lett.* 29 (8), 102–114. doi:10.1029/2001gl014307

Hao, T., Hu, W., Xing, J., Hu, L., Xu, Y., Qin, J., et al. (2014). The Moho Depth Map (1:5000000) in the Land and Seas of China and Adjacent Areas and its Geological Implications. *Chin. J. Geophys.* 57 (12), 3869–3883. doi:10.6038/cjg20141202

Hao, T., Huang, S., Xu, Y., Li, Z., Zhang, L., Wang, J., et al. (2010). Geophysical Understanding on Deep Structure in Yellow Sea. *Chin. J. Geophys.* 53 (6), 1315–1326.

Harley, S. L., and Carswell, D. A. (1995). Ultradeep Crustal Metamorphism: A Prospective View. *J. Geophys. Res.* 100, 8367–8380. doi:10.1029/94jb02421

Ji, W., Chen, Y., Chen, K., Wei, W., Faure, M., and Lin, W. (2018). Multiple Emplacement and Exhumation History of the Late Mesozoic Dayunshan-Mufushan Batholith in Southeast China and its Tectonic Significance: 2. Magnetic Fabrics and Gravity Survey. *J. Geophys. Res. Solid Earth* 123, 711–731. doi:10.1002/2017jb014598

Jiang, G., Zhang, G., Lü, Q., Shi, D., and Xu, Y. (2013). 3-D Velocity Model beneath the Middle-Lower Yangtze River and its Implication to the Deep Geodynamics. *Tectonophysics* 606, 36–47. doi:10.1016/j.tecto.2013.03.026

Kern, H., Gao, S., Jin, Z., Popp, T., and Jin, S. (1999). Petrophysical Studies on Rocks from the Dabie Ultrahigh-Pressure (UHP) Metamorphic belt, Central China: Implications for the Composition and Delamination of the Lower Crust. *Tectonophysics* 301, 191–215. doi:10.1016/s0040-1951(98)00268-6

Kim, H.-J., Kim, C.-H., Hao, T., Liu, L., Kim, K.-H., Jun, H., et al. (2019). Crustal Structure of the Gunsan Basin in the SE Yellow Sea from Ocean Bottom Seismometer (OBS) Data and its Linkage to the South China Block. *J. Asian Earth Sci.* 180, 103881. doi:10.1016/j.jseaes.2019.103881

Korenaga, J., Holbrook, W. S., Kent, G. M., Kelemen, P. B., Detrick, R. S., Larsen, H.-C., et al. (2000). Crustal Structure of the Southeast Greenland Margin from

Joint Refraction and Reflection Seismic Tomography. *J. Geophys. Res.* 105, 21,21591–21614,614. doi:10.1029/2000JB900188

Li, H.-Y., Chen, R.-X., Zheng, Y.-F., Hu, Z., and Xu, L. (2018). Crustal Metasomatism at the Slab-Mantle Interface in a continental Subduction Channel: Geochemical Evidence from Orogenic Peridotite in the Sulu Orogen. *J. Geophys. Res. Solid Earth* 123, 2174–2198. doi:10.1002/2017jb014015

Li, S., Li, Q., Hou, Z., Yang, W., and Wang, Y. (2005). Cooling History and Exhumation Mechanism of the Ultrahigh-Pressure Metamorphic Rocks in the Dabie Mountains, central China. *Acta Petrologica Sinica* 21 (4), 1117–1124.

Li, S., Zhao, G., Dai, L., Zhou, L., Liu, X., Suo, Y., et al. (2012). Cenozoic Faulting of the Bohai Bay Basin and its Bearing on the Destruction of the Eastern North China Craton. *J. Asian Earth Sci.* 47, 80–93. doi:10.1016/j.jseaes.2011.06.011

Li, Z.-X. (1994). Collision between the North and South China Blocks: A Crustal-Detachment Model for Suturing in the Region East of the Tanlu Fault. *Geol* 22, 739–742. doi:10.1130/0091-7613(1994)022<0739:cbtnas>2.3.co;2

Li, Z., Peng, S. T., Xu, C. W., Han, Y. X., and Zhai, M. G. (2009). U-pb Ages of the Paleozoic sandstone Detrital Zircons and Their Tectonic Implications in the Tabeaksan basin, Korea. *Acta Petrologica Sinica* 25 (1), 183–192. (in chinese).

Liu, L., Hao, T., Lu, C., Wu, Z., Zheng, Y., Wang, F., et al. (2021). Crustal Deformation and Detachment in the Sulu Orogenic Belt: New Constraints from Onshore-Offshore Wide-Angle Seismic Data. *Geophys. Res. Lett.* 48, e2021GL095248. doi:10.1029/2021GL095248

Liu, L., Hao, T., Lü, C., You, Q., Pan, J., Wang, F., et al. (2015). Crustal Structure of Bohai Sea and Adjacent Area (North China) from Two Onshore-Offshore Wide-Angle Seismic Survey Lines. *J. Asian Earth Sci.* 98, 457–469. doi:10.1016/j.jseaes.2014.11.034

Lü, Q., Shi, D., Liu, Z., Zhang, Y., Dong, S., and Zhao, J. (2015). Crustal Structure and Geodynamics of the Middle and Lower Reaches of Yangtze Metallogenic belt and Neighboring Areas: Insights from Deep Seismic Reflection Profiling. *J. Asian Earth Sci.* 114, 704–716.

Ouyang, L., Li, H., Lü, Q., Yang, Y., Li, X., Jiang, G., et al. (2014). Crustal and Uppermost Mantle Velocity Structure and its Relationship with the Formation of Ore Districts in the Middle-Lower Yangtze River Region. *Earth Planet. Sci. Lett.* 408, 378–389. doi:10.1016/j.epsl.2014.10.017

Pang, Y., Zhang, X., Guo, X., Xiao, G., and Zhu, X. (2017). Mesozoic and Cenozoic Tectono-thermal Evolution Modeling in the Northern South Yellow Sea Basin. *Chin. J. Geophys.* 60 (8), 3177–3190.

Platt, J. P. (1993). Exhumation of High-Pressure Rocks: a Review of Concepts and Processes. *Terra Nova* 5, 119–133. doi:10.1111/j.1365-3121.1993.tb00237.x

Shi, D., Lü, Q., Xu, W., Yan, J., Zhao, J., Dong, S., et al. (2013). Crustal Structure beneath the Middle-Lower Yangtze Metallogenic belt in East China: Constraints from Passive Source Seismic experiment on the Mesozoic Intra-continental Mineralization. *Tectonophysics* 606, 48–59. doi:10.1016/j.tecto.2013.01.012

Shinn, Y. J., Chough, S. K., and Hwang, I. G. (2010). Structural Development and Tectonic Evolution of Gunsan Basin (Cretaceous-Tertiary) in the central Yellow Sea. *Mar. Pet. Geology.* 27, 500–514. doi:10.1016/j.marpetgeo.2009.11.001

Stockwell, J. W. (1999). The CWP/SU: Seismic Un*x Package,. *Comput. Geosciences* 25 (4), 415–419. doi:10.1016/s0098-3004(98)00145-9

Sun, P., Guo, P., and Niu, Y. (2021). Eastern China continental Lithosphere Thinning Is a Consequence of Paleo-Pacific Plate Subduction: A Review and New Perspectives. *Earth-Science Rev.* 218, 103680. doi:10.1016/j.earscirev.2021.103680

Wan, T., and Hao, T. (2009). Cenozoic Tectonoics of the Yellow Sea and its Oil-Gas Exploration. *Geoscience* 23 (3), 385–393. (in Chinese).

Wan, T. (2012). *The Tectonics of China: Data, Maps and Evolution*. Berlin, Heidelberg: Springer-Verlag. 978-3-642-11866-1,978-3-642-11868-5.

Wang, C.-Y., Sandvol, E., Zhu, L., Lou, H., Yao, Z., and Luo, X. (2014). Lateral Variation of Crustal Structure in the Ordos Block and Surrounding Regions, North China, and its Tectonic Implications. *Earth Planet. Sci. Lett.* 387, 198–211. doi:10.1016/j.epsl.2013.11.033

Wang, J., Jiang, L., Niu, B. G., Ren, J. S., He, Z. J., Jin, X. C., et al. (2017). Spatial Database of 1:5 Million International Geological Map of Asia. *Geoscientific Dara*. doi:10.23650/data.H.2017.NGA128804.T1.1.1

Wang, X., Liou, J. G., and Mao, H. K. (1989). Coesite-bearing Eclogite from the Dabie Mountains in central China. *Geol* 17, 1085–1088. doi:10.1130/0091-7613(1989)017<1085:cbeftd>2.3.co;2

Wei, W., Ye, G., Jin, S., Deng, M., and Jing, J. (2007). Three Dimensional P-Wave Velocity Structure of the Crust of North China. *Earth Sci.-J. China Univ. Geosci.* 32 (4), 441–452.

Wu, F., Xu, Y., Gao, S., and Zheng, J. (2008). Lithospheric Thinning and Destruction of the North China Craton. *Acta Petrologica Sinica* 6, 1145–1174.

Xiao, X., Wang, X., Tang, J., Zhou, C., Wang, Y., Chen, X., et al. (2014). Conductivity Structure of the Lujiang-Zongyang Ore Concentrated Area, Anhui Province: Constraints from Magnetotelluric Data. *Acta Geol. Sinica* 88 (4), 478–495. doi:10.1111/1755-6724.12379_57

Xu, S., Su, W., Liu, Y., Jiang, L., Ji, S., Okay, A. I., et al. (1992). Diamond from the Dabie Shan Metamorphic Rocks and its Implication for Tectonic Setting. *Science* 256, 80–82.

Xu, T., Zhang, Z., Tian, X., Liu, B., Bai, Z., Lv, Q., et al. (2014). Crustal Structure beneath the Middle-Lower Yangtze Metallogenic belt and its Surrounding Areas: Constraints from Active Source Seismic experiment along the Lixin to Yixing Profile in East China. *Acta Petrologica Sinica* 30 (4), 918–930.

Xu, W., Gao, S., Wang, Q., Wang, D., and Liu, Y. (2006). Mesozoic Crustal Thickening of the Eastern North China Craton: Evidence from Eclogite Xenoliths and Petrologic Implications. *Geol* 34 (9), 721–724. doi:10.1130/g22551.1

Xu, Z., Liang, F., Yang, J., Zhang, Z., and Tang, Z. (2009). Continental Deep Subduction and Exhumation Dynamics: Constraints from Holes of the Chinese Continental Scientific Drilling and the Sulu HP-UHP Metamorphic Terrane. *Acta Petrol. Sin.* 25, 1561–1574.

Zelt, C. A., and Barton, P. J. (1998). Three-dimensional Seismic Refraction Tomography: A Comparison of Two Methods Applied to Data from the Faeroe Basin. *J. Geophys. Res.* 103, 7187–7210. doi:10.1029/97jb03536

Zelt, C. A., and Smith, R. B. (1992). Seismic Traveltime Inversion for 2-D Crustal Velocity Structure. *Geophys. J. Int.* 108 (1), 16–34. doi:10.1111/j.1365-246x.1992.tb00836.x

Zhai, M., Guo, J., Li, Z., Chen, D., Peng, P., Li, F., et al. (2007). Linking the Sulu UHP belt to the Korean Peninsula: Evidence from Eclogite, Precambrian Basement, and Paleozoic Sedimentary Basins. *Gondwana Res.* 12, 388–403. doi:10.1016/j.gr.2007.02.003

Zhang, R. Y., Liou, J. G., and Ernst, W. G. (2009). The Dabie-Sulu continental Collision Zone: A Comprehensive Review. *Gondwana Res.* 16, 1–26. doi:10.1016/j.gr.2009.03.008

Zheng, T.-Y., Zhao, L., He, Y.-M., and Zhu, R.-X. (2014). Seismic Imaging of Crustal Reworking and Lithospheric Modification in Eastern China. *Geophys. J. Int.* 196 (2), 656–670. doi:10.1093/gji/ggt420

Zheng, Y.-F., Fu, B., Gong, B., and Li, L. (2003). Stable Isotope Geochemistry of Ultrahigh Pressure Metamorphic Rocks from the Dabie-Sulu Orogen in China: Implications for Geodynamics and Fluid Regime. *Earth-Science Rev.* 62, 105–161. doi:10.1016/S0012-8252(02)00133-2

Zheng, Y. (2008). A Perspective View on Ultrahigh-Pressure Metamorphism and continental Collision in the Dabie-Sulu Orogenic belt. *Sci. Bull.* 53 (20), 3081–3104. doi:10.1007/s11434-008-0388-0

Zhu, R., Chen, L., Wu, F., and Liu, J. (2011). Timing, Scale and Mechanism of the Destruction of the North China Craton. *Sci. China Earth Sci.* 54, 789–797. doi:10.1007/s11430-011-4203-4

Zhu, R., Xu, Y., Zhu, G., Zhang, H., Xia, Q., and Zheng, T. (2012). Destruction of the North China Craton. *Sci. China Earth Sci.* 55 (10), 1565–1587. doi:10.1007/s11430-012-4516-y

Conflict of Interest: The authors declare that the research was conducted in the absence of any commercial or financial relationships that could be construed as a potential conflict of interest.

Publisher's Note: All claims expressed in this article are solely those of the authors and do not necessarily represent those of their affiliated organizations, or those of the publisher, the editors, and the reviewers. Any product that may be evaluated in this article, or claim that may be made by its manufacturer, is not guaranteed or endorsed by the publisher.

frontiers in Earth Science

ORIGINAL RESEARCH
published: 07 February 2022
doi: 10.3389/feart.2022.817551

Building Precise Local Submarine Earthquake Catalogs *via* a Deep-Learning-Empowered Workflow and its Application to the Challenger Deep

Xueshan Wu[1,2,3], *Song Huang*[1,2]*, *Zhuowei Xiao*[2,3,4] *and Yuan Wang*[1,2]

[1]Key Laboratory of Petroleum Resources Research, Institute of Geology and Geophysics, Chinese Academy of Sciences, Beijing, China, [2]Innovation Academy for Earth Science, Chinese Academy of Sciences, Beijing, China, [3]College of Earth and Planetary Sciences, University of Chinese Academy of Sciences, Beijing, China, [4]Key Laboratory of Mineral Resources, Institute of Geology and Geophysics, Chinese Academy of Sciences, Beijing, China

Submarine active faults and earthquakes, which contain crucial information to seafloor tectonics and submarine geohazards, can be effectively characterized by precise submarine earthquake catalogs. However, the precise and rapid building of submarine earthquake catalogs is challenging due to the following facts: (i) intense noise in ocean seismic data; (ii) the sparse seismic network; (iii) the lack of historical near-field observations. In this paper, we built a deep-learning-based automatic workflow named ESPRH for automatically building submarine earthquake catalogs from continuous seismograms. The ESPRH workflow integrates Earthquake Transformer (EqT) and Siamese Earthquake Transformer (S-EqT) for initial earthquake detection and phase picking, PickNet for phase refinement, REAL for earthquake association and rough location, and HypoInverse, HypoDD for precise earthquake relocation. We apply ESPRH to the continuous data recorded by an array of 12 broadband Ocean Bottom Seismographs (OBS) near the Challenger Deep at the southern-most Mariana subduction zone from Dec. 2016 to Jun. 2017. In this study, we acquire a high-resolution local earthquakes catalog that provides new insights into the geometry of shallow fault zones. We report the active submarine faults by seismicity in Challenger Deep which is the deepest place on Earth. These faults are a significant reference for submarine geological hazards and evidence for serpentinization. Hence, the ESPRH is qualified to construct comprehensive local submarine earthquake catalogs automatically, rapidly, and precisely from raw OBS seismic data.

Keywords: deep learning, local earthquake catalog, submarine earthquake, Challenger Deep, seismicity

OPEN ACCESS

Edited by:
Kwang-Hee Kim,
Pusan National University, South Korea

Reviewed by:
Giltae Song,
Pusan National University, South Korea
Tae Gyu Kang,
Electronics and Telecommunications Research Institute (ETRI), South Korea

***Correspondence:**
Song Huang
huangsong@mail.iggcas.ac.cn

Specialty section:
This article was submitted to Solid Earth Geophysics, a section of the journal Frontiers in Earth Science

Received: *18 November 2021*
Accepted: *06 January 2022*
Published: *07 February 2022*

Citation:
Wu X, Huang S, Xiao Z and Wang Y (2022) Building Precise Local Submarine Earthquake Catalogs via a Deep-Learning-Empowered Workflow and its Application to the Challenger Deep. Front. Earth Sci. 10:817551. doi: 10.3389/feart.2022.817551

INTRODUCTION

Submarine seismicity and active faults are essential for the analysis and monitoring of submarine geohazards. A local earthquake catalog can reveal the detailed geometry of faults, providing critical insights into tectonics and earthquake disasters. However, seismic data is generally extensive, and it is subjective and time-consuming to extract earthquake signals by human experts manually. Many

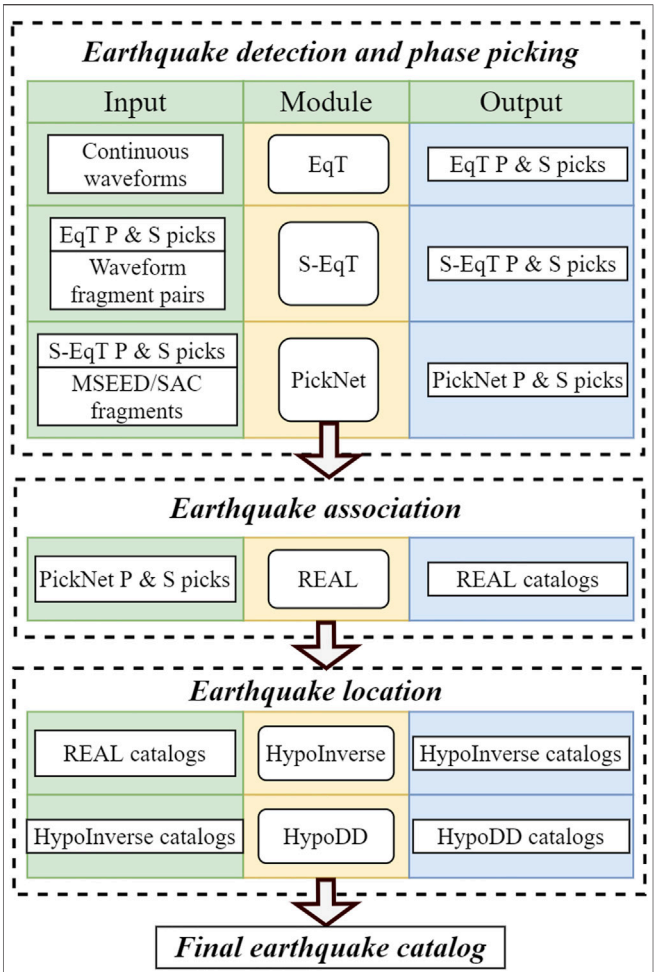

FIGURE 1 | Diagram of the ESPRH workflow.

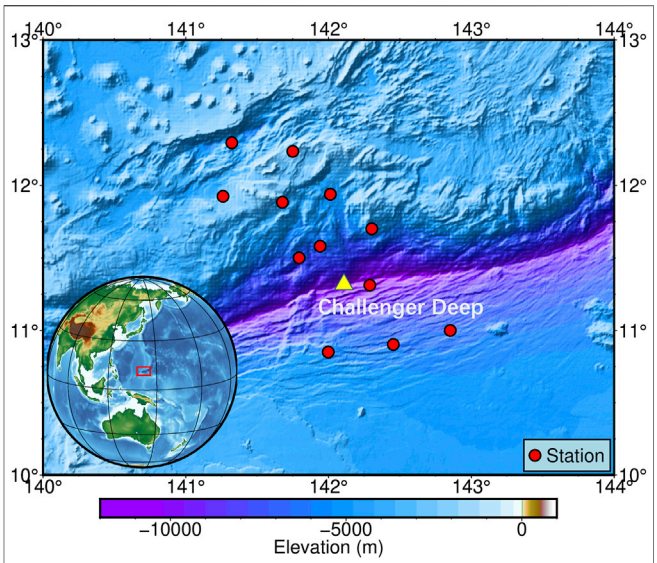

FIGURE 2 | The location of the array of 12 OBS stations. The yellow triangle is the location of the Challenger Deep. The bottom-left inset represents the location of our study area.

traditional automatic earthquake detection methods have been proposed to address this problem, such as short-term average/long-term average algorithm (STA/LTA) (Allen, 1978), autoregression with Akaike Information Criterion (AIC) (Sleeman and van Eck, 1999). However, these methods are less precise than human experts and rely on hyperparameters, limiting their performance when processing complex seismic data with different types of noise and variable signal-to-noise ratios. The template matching method (Gibbons and Ringdal, 2006; Peng and Zhao, 2009) is widely used for building earthquake catalogs by exploiting the similarity of earthquake waveforms between nearby earthquakes using previously identified earthquake templates. However, its computational cost is relatively high, and sufficient templates are generally unavailable for the OBS network due to the lack of historical observations.

Different from conventional methods that only utilize several manually designed features, machine-learning-based methods (Bishop, 2006), especially deep neural networks (Lecun et al., 2015), can automatically extract rich features from extensive seismic data. Recently, researchers have made considerable progress in earthquake detection, and phase picking via deep-learning-based methods (e.g., Perol et al., 2018; Mousavi et al., 2019b; Mousavi et al., 2020; Pardo et al., 2019; Ross et al., 2019; Wang et al., 2019; Wu et al., 2019; Zhou et al., 2019; Zhu and Beroza, 2019). The Earthquake Transformer (EqT) (Mousavi et al., 2020) model achieves the state-of-art performance of ~99% precision, ~99% recall rate, and ~0.01 s mean absolute error for picking P and S phases on the STanford EArthquake Dataset (STEAD) (Mousavi et al., 2019a), outperforming all the other popular models. Xiao et al., 2021 proposed the Siamese Earthquake Transformer (S-EqT) (Xiao et al., 2021) model to address the false-negative issue in the EqT model. However, due to the limitation of the training set distribution (e.g., 92% of seismograms in the STEAD dataset are within 110 km epicenter distance), the phase picking precision of both EqT and S-EqT would decrease on seismograms with epicenter distances larger than 110 km. Although Wang et al. (2019) propose a neural network (PickNet) (Wang et al., 2019) for regional seismic arrival picking with epicenter distances up to ~1,000 km, their method does not include earthquake detection and requires a pre-existing regional earthquake catalog.

Thus, in our study, we utilize these methods to form a practical workflow, named ESPRH, for building the submarine earthquake catalog (**Figure 1**). The workflow consists of three stages: The first stage is earthquake detection and phase picking by EqT, S-EqT, and PickNet; The second step is earthquake association and initial location by REAL; The final stage is relocating detected earthquakes by HypoInverse and HypoDD. We applied ESPRH to continuous seismic data recorded by an array of 12 broadband OBSs deployed at Challenger Deep, the deepest point in the ocean, from Dec. 2016 to Jun. 2017. Challenger Deep is located in the

TABLE 1 | Layered 1-D velocity model used in this study. The velocity corresponds to the value at the top of each layer.

Depth (km)	Vp (km/s)	Vs (km/s)
0.00	2.98	1.70
0.72	4.49	2.57
2.18	6.09	3.48
6.93	7.90	4.51
77.5	8.05	4.49
165	8.17	4.52

TABLE 2 | Earthquake number of ESPRH catalogs at different stages and restrictions (**Supplementary Material**).

Method \ Catalog	REAL	HypoInverse	HypoDD
EqT Only	469	262	173
EqT + S-EqT	3541	1270	1256
EqT + S-EqT + PickNet	3557	1285	1270

Mariana Trench, a subduction zone between the Philippine and Pacific plates. The high seismicity and unique geographical location make this data ideal for validating our workflow. As a result, we obtained a catalog containing 1,383 relocated local earthquakes, which is about two times larger than that of recent work by Zhu et al. (2019) using the same data by template matching. Our catalog reveals the detailed geometry of the faults and seismicity in Challenger Deep and shows that the ESPRH workflow is suitable for building local submarine earthquake catalogs, and it may contribute significantly to the understanding of the Earth's interior.

DATA

The data used in this study is recorded by an array of 12 OBSs (**Figure 2**) down to ocean depth greater than 8,000 m from the Southern Mariana OBS Experiment (SMOE) from Dec. 2016 to Jun. 2017. The OBS (STS-G60) equipped with a three-component sensor was developed by the Institute of Geology and Geophysics, Chinese Academy of Sciences. The OBS sensor is designed for a low-frequency response of 30 s with a sampling rate of 100 Hz. After time-correction, the data is treated differently in different processing steps: it is filtered to 1–45 Hz when feeding to the EqT and S-EqT models; it is unfiltered when providing to the PickNet model; it is filtered to 0.2–10 Hz with instrument response

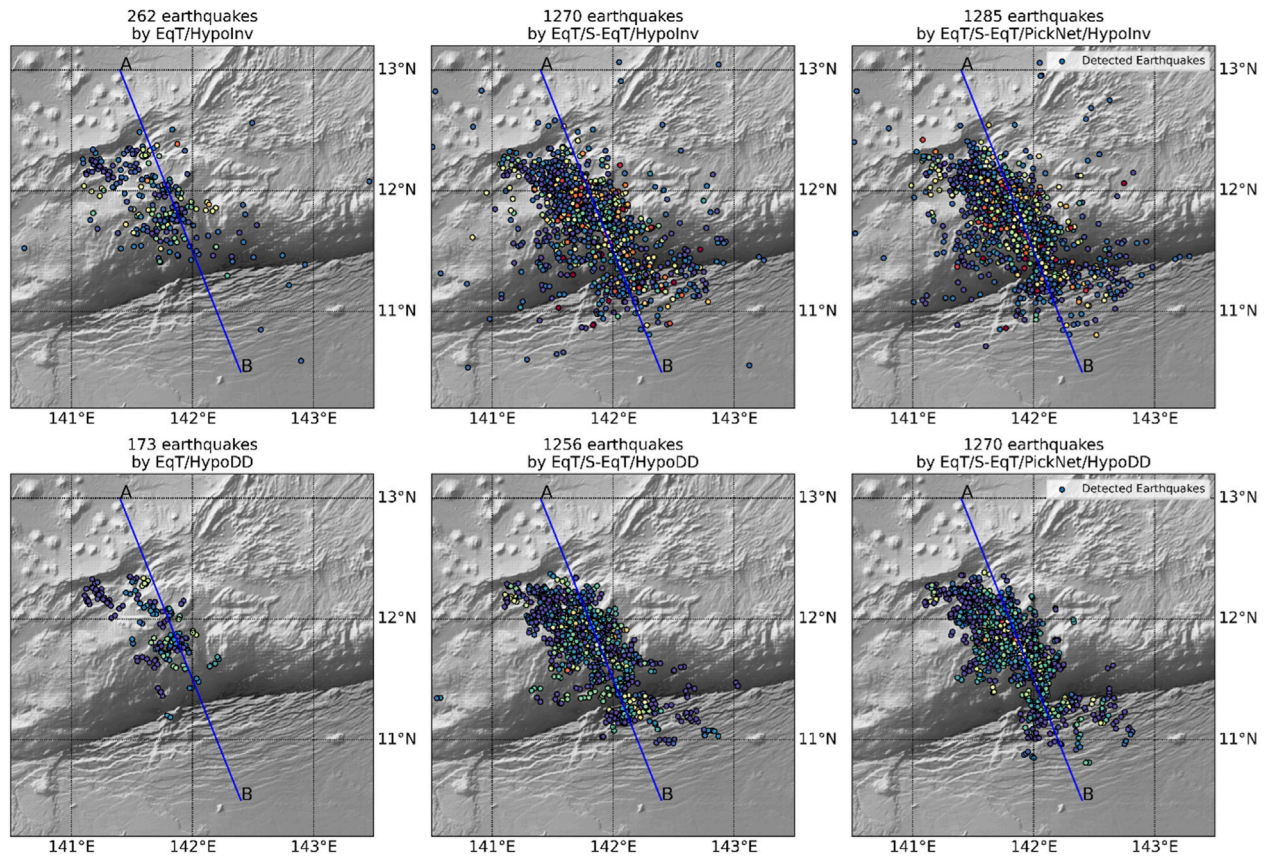

FIGURE 3 | Comparison of location results. **(A–C)** plot relocation result by of EqT only, both EqT and S-EqT, and the full process of ESPRH (EqT, S-EqT, and PickNet), respectively. In the same way, **(D–F)** plot absolute location results. Seismic events are plotted in dots, with their depth coded by color. Reference locations of sections **Panel 5** are plotted in blue lines.

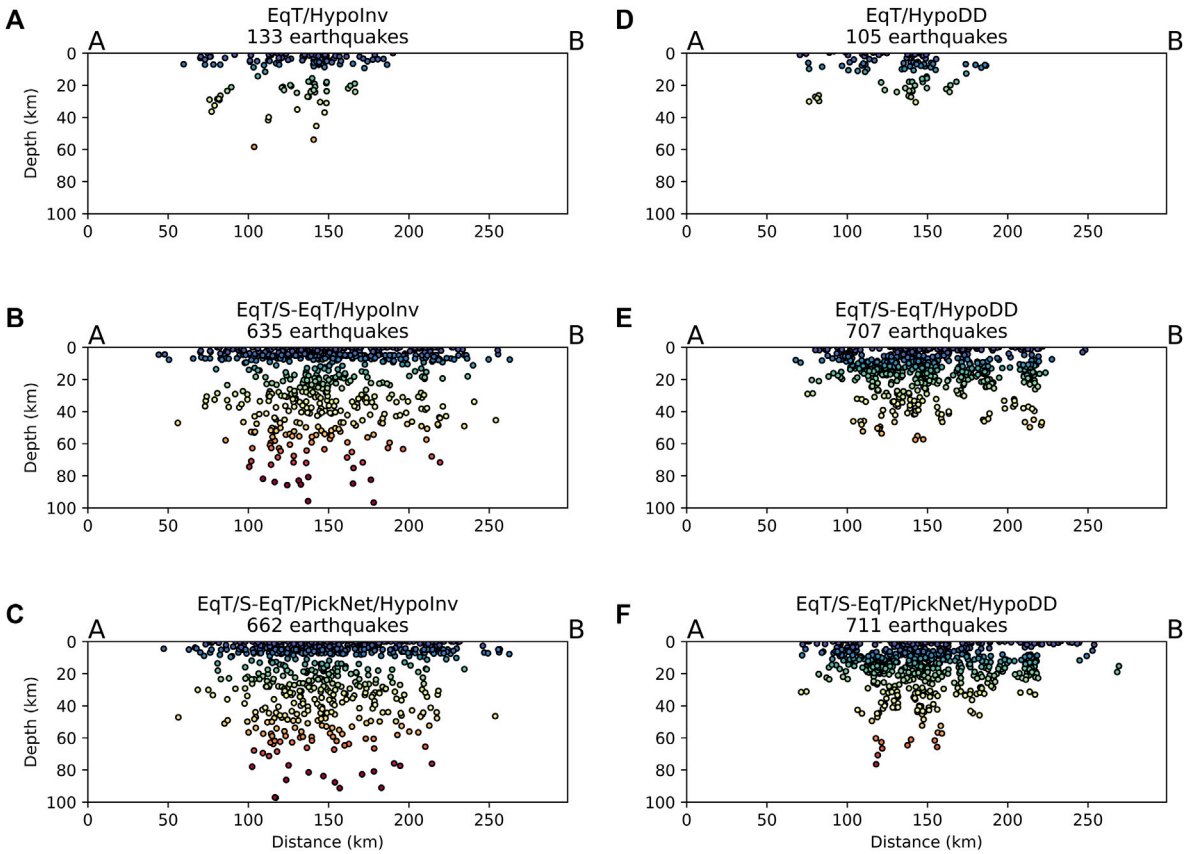

FIGURE 4 | Comparison of location results in the sections which are identified in **Panel 3**. The three pictures from top to bottom on the left, **(A–C)** correspond to **Panels 3A–C**, respectively. The three figures on the right **(D–F)** correspond to **Panels 3D–F**.

removed when calculating the amplitude for magnitude estimation.

METHODS

The ESPRH workflow is built based on serval pre-existing methods (**Figure 1**). It consists of three stages: 1) the earthquake detection and phase picking stage via EqT (Mousavi et al., 2020), S-EqT (Xiao et al., 2021), and PickNet (Wang et al., 2019) models; 2) the earthquake association stage by REAL (Zhang et al., 2019) method; 3) the earthquake location stage with HypoInverse (Klein, 2002) and HypoDD (Waldhauser and Ellsworth, 2000) methods.

In the first stage, we apply EqT for the initial earthquake detection and phase picking because it leverages the most advanced deep-learning techniques, such as transformers, residual connections, and achieves the state-of-art performance on the STEAD dataset (Mousavi et al., 2019a), which is the current largest public dataset. 92% of seismograms in STEAD are with 110 km epicenter distance. The most passive OBS experiments are within this range. Hence EqT is ideal for initial earthquake detection and phase picking. Then we feed the outputs of EqT to S-EqT to further reduce the false-negative rate of the EqT model. S-EqT is a pair-wise deep-learning model, which retrieves previously missed phase picks in low SNR seismograms based on their similarities to other confident phase picks in high-dimensional spaces. Then the outputs are feed to PickNet, which is trained for phase arrival picking using a dataset of seismograms with epicenter distances up to ~1,000 km for phase arrival time refinement. Here "refinement" means the P and S phase picks created by EqT and S-EqT are used to create input time windows for PickNet. Because the PickNet model predicts only one arrival time per time window, the refined picks by PickNet are limited within a 2-s time range from those by EqT and S-EqT to prevent it from refining one pick multiple times. The threshold for earthquake detection, P, and S phase picking in three models is 0.3, 0.1, and 0.1, respectively.

In the second stage, we utilize REAL to link these phases through grid searching. The REAL method employs grid searching, and it is rapid and reliable for these tasks. In the REAL method, the center of the searched area is at the station that recorded the initiating P phase. The coarse location of events will be at the grid point that has the maximum number of picks. If grid points with the maximum number of picks are non-unique, the grid point with the smallest residual will be chosen. We discard the events associated with less than 3 P picks or less than a total of 4 P and S picks. The magnitudes of associated earthquakes are

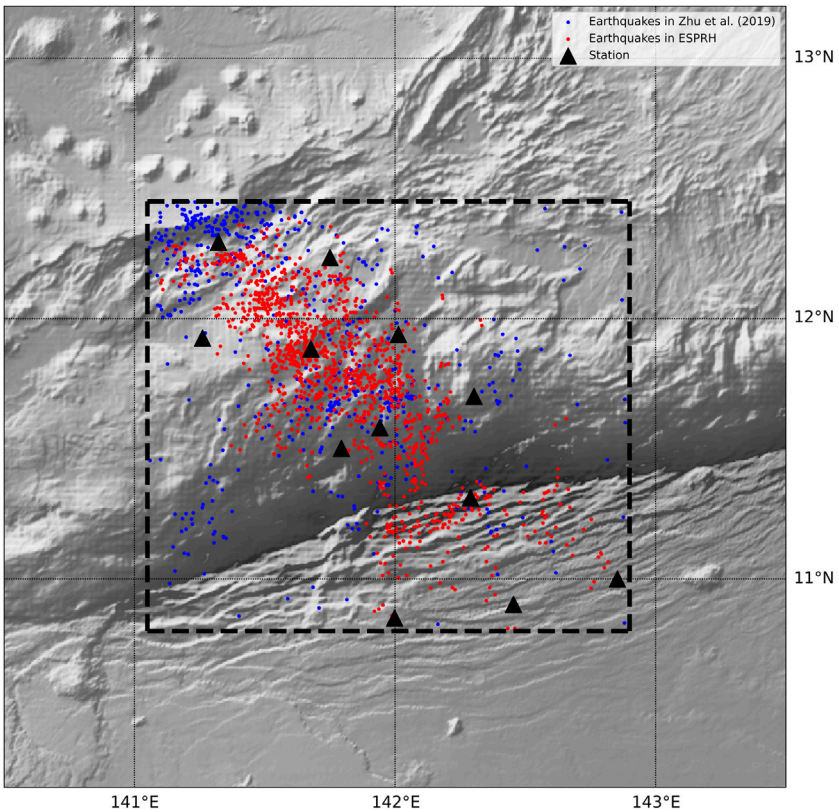

FIGURE 5 | Comparison of location result of ESPRH (blue dots) and Matched filtering (red dots) by Zhu et al. (2019) SWMR, Southwest Mariana rift.

estimated under the Richter magnitude scale (Richter, 1935) using 50-second-long slices after P and S phases.

In the third stage, we use HypoInverse to improve the grid search location results and then use HypoDD to enhance these events' relative locations further. HypoInverse is an absolute localisation method based on gradient descent. HypoDD is a double-difference hypocenter location method, which significantly improves the relative location accuracy and reveals concentrated seismic streaks. The 1D velocity model is a combination of crust 1.0 and 2-D crustal P-wave velocity models from Wan et al. (2019) and Zhu et al. (2019) (**Table 1**).

RESULTS AND DISCUSSIONS

To validate the ESPRH workflow, we apply it to OBS's continuous data of 12 stations from Dec. 2016 to Jun. 2017 and conduct ablation study to deep learning models in the first stage. As shown in **Table 2**, the combination of EqT and S-EqT detects ~7.5 times more earthquakes in the REAL catalog than using EqT only. This shows the necessity of S-EqT in the first stage. We only keep earthquakes with both horizontal location errors and depth location errors less than 20 km. Hence, the slight increment in earthquake number in HypoInverse and HypoDD catalogs after applying PickNet to refine phase indicts the arrival times are refined to higher precision.

Figure 3 show the results of HypoInverse and HypoDD corresponding to **Table 2**. The shallow earthquakes in catalogs, especially at the south side of the Challenger Deep, increased significantly after applying S-EqT, which is important for analyzing the change of seafloor topography and the coupling relationship between seafloor and seawater. **Figures 3C,F** show that the locations of these earthquakes coincide with the seafloor topography, which demonstrates the reliability of the ESPRH workflow.

As shown in profile A-B in **Figure 4**, most of the earthquakes in the catalog produced with only EqT in the first stage are shallow. Few of them reach a depth of 60 km by Hypoinverse, and all are less than 40 km by HypoDD. The combination of EqT and S-EqT detects more deep earthquakes up to 100 km by HypoInverse and 80 km by HypoDD. **Figures 4C**, **5F** show the PickNet's precise fine-tuning of the initial detection results, where subtle differences in small areas can lead to more precise positioning locations. In particular, after relocation, it is possible to see the distribution of positions that are fully consistent with the morphology of the subducting slab.

In this study, we analyze the seismicity based on the final HypoDD catalog. The relative positions of these seismic events can portray the geometric structure of the faults where the earthquakes occur. As shown in **Figure 6**, a total of 1,270 earthquakes were relocated by HypoDD during the period of OBS observation. These earthquakes are mainly distributed near the OBS array. In addition to subduction slabs, these earthquakes are distributed in the outer rise region, overriding plate and subduction interface. Divided by the trench axis, the number of earthquakes in the north is much higher than that in the southern

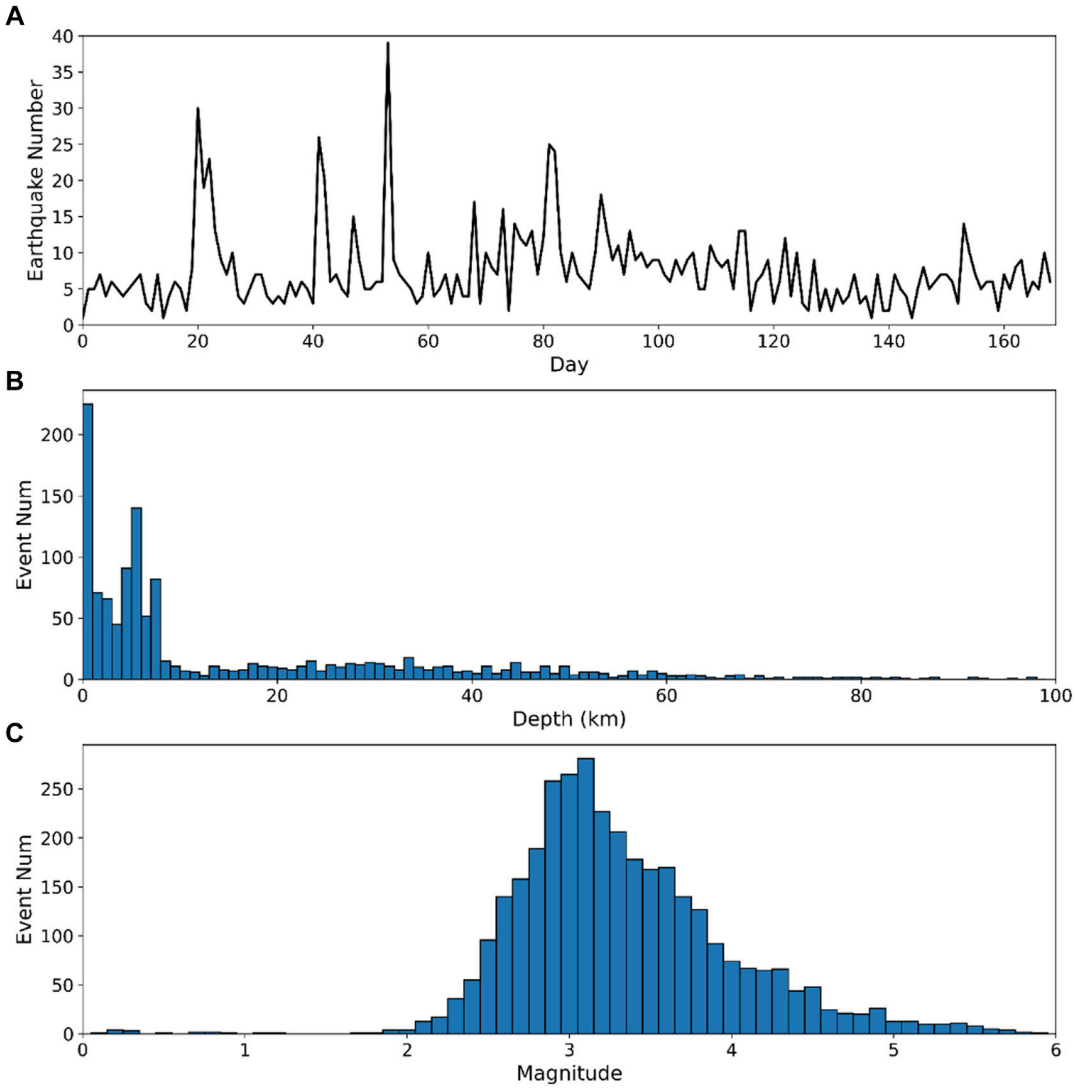

FIGURE 6 | (A) Daily occurrence times of earthquakes. (The first day of the record date is 16 December) **(B)** The depth distribution. **(C)** Magnitudes.

outer-rise region. As can be seen from the profile, the former has some very deep earthquakes distributed up to 80 km. We consider that these events outline the morphology of the subduction slab. The depth of the latter earthquakes is less than 25 km. As shown in the figure, these shallow seismic streaks can be corroborated in the topographic map. We speculate that shallow outer-rise earthquakes are normal faulting events. We also find a large number of moderately deep earthquakes above the subduction slab, which may reveal the ongoing influence of subduction activity on the overriding plate.

We further evaluate the detection performance of ESPRH by comparing it with the catalog of Zhu et al. (2019), which is based on six OBS stations of our array and a station located in Guam. A comparison with our results is shown in **Figure 5**.

Hence, we only compare the earthquake catalogs in the area near the stations (**Figure 5**). In terms of the number of detected earthquakes, we obtained 1,285 seismic events that were localized by HypoInverse with both ERH and ERZ less than 20 km, which is comparable to the number obtained by matched filtering. But 1,270 of these earthquakes can be relocated, which is almost three times the number obtained by matched filtering. In terms of the location of the earthquakes, we have a more balanced distribution, which is consistent with the local earthquake pattern. This can provide more reliable support for seismicity as well as geohazard analysis. Although the catalog of earthquakes obtained by matched filtering also contains a large number of small seismic events not found in the USGS, these are clustered in the SWMR at the south of the array, and near the trench. Although the basic structure of the subduction slab can be clearly outlined on the profiles of both catalogs. However, Zhu's catalog shows a denser aggregation pattern with gaps near the trench. Earthquakes are also relatively rare in the overriding area. Throughout the study area, the ESPRH catalog allows for a more detailed and complete analysis of

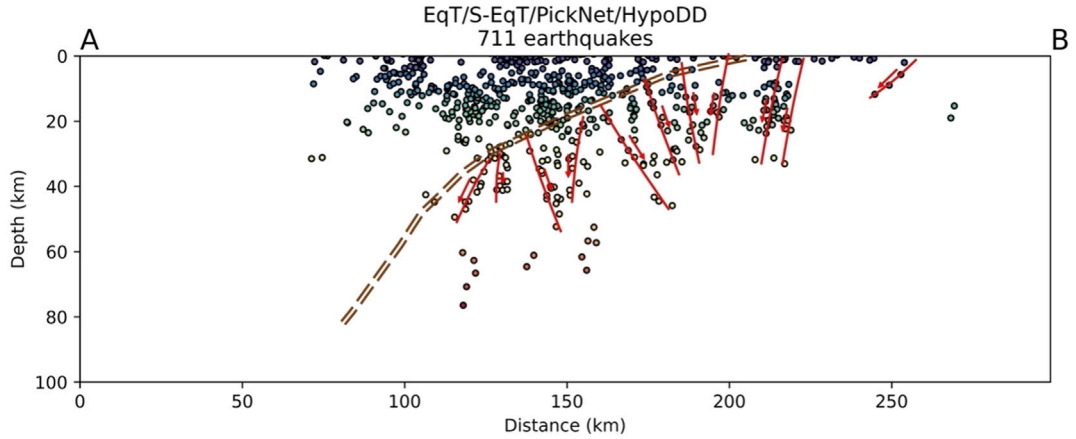

FIGURE 7 | Distribution of normal faults (red line and arrow) in the section. The slab geometry (brown dotted line) in the southern Mariana is based on SLAB2.0 model (Hayes et al., 2018).

seismicity and a more robust outline of fault geometry. In particular, the area between SWMR and Challenger Deep, above the subduction slab, can be seen as a fault produced by extrusion deformation. In overriding plates, the faults represented by the seismic strips can also be found.

This is due to the limitations of the method. The basic idea of the matching filter approach in building the catalog is to find similar earthquake events with the template. It is very difficult to detect earthquakes in blank areas in the template. Therefore, having a good template is a prerequisite for getting a complete catalog, which relies on preliminary observations. The matched filtering method can be applied well and quickly in areas with abundant seismic observations and has good performance in aftershock detection.

Most of the submarine areas lack historical near-field seismic data. It is also not possible to predict the location of earthquake occurrence when analyzing seismicity and submarine geohazards. This situation shows the advantages of ESPRH, which has the regular process: pick P&S arrivals, associate phases, and locate events.

We also analyzed the statical features of earthquakes (**Figure 6**). **Figure 6A** shows the current frequent earthquakes still occurring in the vicinity of the Challenger Deep, confirming the observation of continued subduction of the Pacific plate. The depth distribution showed that earthquakes mainly concentrate ~10 km, where submarine geological hazards occur. The distribution of magnitudes shows that most of the earthquakes are concentrated in magnitude 3, which indicates the poor quality of the seabed data.

Our localization results provide some evidence for the geological structure of the Challenger Deep. It is clear from the location of these faults, and the depth of the earthquakes, that the faults extend into the mantle (**Figure 7**). Every subducting plate inevitably undergoes a transition from horizontal to vertical motion as it passes through the outer uplift zone of each subduction trench. If plate rupture occurs, a positive fault is created, which can be observed by earthquake localization. Seismic velocity models obtained from previous surface wave imaging results show a significant low-velocity anomaly in the subducted slab that extends to a depth of about 25 km inside the mantle, indicating that the southern Marianas subducted slab carries a large amount of water into the Earth's interior (Zhu et al., 2021). Compared with central Mariana (Kato et al., 2003), the velocity reduction of the southern arc-front mantle is not as obvious, suggesting that the degree of serpentinization of the arc-front mantle is lower in the south. The difference in the degree of serpentinization of the southern and central Mariana arc-front mantle may reflect the different geological processes and development of the arc-front mantle in the two regions.

We marked the position of the faults in the subduction slab as well as the outer rise by visual retrieval. Our catalog shows that tectonic activity in the southern arc-front region is more intense due to the expansion of the Mariana Trough and the rapid retreat of the Pacific plate, and the southern-most Mariana arc-front is strongly deformed with a large number of parallel and vertical orthotropic and strike-slip faults, suggesting that the southern arc-front is experiencing strong strike and vertical tensioning along the trench. The intense tectonic activity may prevent fluid focusing and affect the degree of serpentinization in the pre-arc mantle. This provides support for the conclusions obtained by previous work with Rayleigh wave tomography.

CONCLUSION

In this study, we build a deep-learning-empowered fully automatic workflow named ESPRH that can quickly build regional earthquake catalogs with corresponding high-quality P and S wave arrival times. By applying it to an OBS array in the Challenger Deep, The ESPRH obtains a complete earthquake catalog which provides novel insights into the geometry of the faults and seismicity around the Challenger Deep and provides evidence for serpentinization of the Pacific plate in the southern Mariana Trench. Such application demonstrates that our pipeline is practical to construct comprehensive local submarine earthquake catalogs automatically, rapidly, and precisely. This study presents a comprehensive local earthquake catalog around the Challenger Deep and provides a powerful tool for future seismic studies at submarine earthquakes.

DATA AVAILABILITY STATEMENT

The earthquake catalogs that support the conclusions of this article are publicly available in the **Supplementary Material**. For the raw OBS data in this study, please contact the corresponding author.

AUTHOR CONTRIBUTIONS

XW conducted the research, plotted the figures, and wrote the manuscript. ZX helped in developing the codes of the workflow. SH and ZX contributed to the conception and design of the study. YW completed time correction. All authors contributed to manuscript revision, read, and approved the submitted version.

FUNDING

This work was supported by the National Natural Science Foundation of China under grant 91858212 and 91858214 and the National Key R&D Program of China under grant 2018YFC0604004.

ACKNOWLEDGMENTS

We gratefully acknowledge the researchers and colleagues at the R/V Shiyan 3, Tansuo-1 and Institute of Geology and Geophysics, Chinese Academy of Sciences, for their efforts of production, launch and recovery of OBS seismometers. We thank the researchers who developed and shared EqT, S-EqT, PickNet, REAL, HypoInverse and HypoDD, which are the base of this study. Plots were generated using Generic Mapping Tools (GMT) (Wessel and Smith, 1998) and Matplotlib (Hunter, 2007). The EPSRH workflow is publicly available on GitHub at https://github.com/MrXiaoXiao/ESPRH.

SUPPLEMENTARY MATERIAL

The Supplementary Material for this article can be found online at: https://www.frontiersin.org/articles/10.3389/feart.2022.817551/full#supplementary-material

REFERENCES

Allen, R. V. (1978). Automatic Earthquake Recognition and Timing from Single Traces. *Bull. Seismol. Soc. Am.* 68, 1521–1532. doi:10.1785/BSSA0680051521

Bishop, C. M. (2006). *Pattern Recognition and Machine Learning*. Delhi, India: Springer (India) Private Limited. doi:10.1007/978-3-030-57077-4_11

Gibbons, S. J., and Ringdal, F. (2006). The Detection of Low Magnitude Seismic Events Using Array-Based Waveform Correlation. *Geophys. J. Int.* 165, 149–166. doi:10.1111/j.1365-246X.2006.02865.x

Hayes, G. P., Moore, G. L., Portner, D. E., Hearne, M., Flamme, H., Furtney, M., et al. (2018). Slab2, a Comprehensive Subduction Zone Geometry Model. *Science* 362, 58–61. doi:10.1126/science.aat4723

Hunter, J. D. (2007). Matplotlib: A 2D Graphics Environment. *Comput. Sci. Eng.* 9, 90–95. doi:10.1109/MCSE.2007.55

Kato, T., Beavan, J., Matsushima, T., Kotake, Y., Camacho, J. T., and Nakao, S. (2003). Geodetic Evidence of Back-Arc Spreading in the Mariana Trough. *Geophys. Res. Lett.* 30. doi:10.1029/2002GL016757

Klein, F. W. (2002). User's Guide to HYPOINVERSE-2000, a Fortran Program to Solve for Earthquake Locations and Magnitudes. Open-File Report 2002-171. Available at: https://pubs.er.usgs.gov/publication/ofr02171. doi:10.3133/ofr02171

Lecun, Y., Bengio, Y., and Hinton, G. (2015). Deep Learning. *Nature* 521 (7553), 436.

Mousavi, S. M., Ellsworth, W. L., Zhu, W., Chuang, L. Y., and Beroza, G. C. (2020). Earthquake Transformer-An Attentive Deep-Learning Model for Simultaneous Earthquake Detection and Phase Picking. *Nat. Commun.* 11, 3952. doi:10.1038/s41467-020-17591-w

Mousavi, S. M., Sheng, Y., Zhu, W., and Beroza, G. C. (2019a). STanford EArthquake Dataset (STEAD): A Global Data Set of Seismic Signals for AI. *IEEE Access* 7, 179464–179476. doi:10.1109/ACCESS.2019.2947848

Mousavi, S. M., Zhu, W., Sheng, Y., and Beroza, G. C. (2019b). CRED: A Deep Residual Network of Convolutional and Recurrent Units for Earthquake Signal Detection. *Sci. Rep.* 9, 10267. doi:10.1038/s41598-019-45748-1

Pardo, E., Garfias, C., and Malpica, N. (2019). Seismic Phase Picking Using Convolutional Networks. *IEEE Trans. Geosci. Remote Sensing* 57, 7086–7092. doi:10.1109/TGRS.2019.2911402

Peng, Z., and Zhao, P. (2009). Migration of Early Aftershocks Following the 2004 Parkfield Earthquake. *Nat. Geosci* 2, 877–881. doi:10.1038/ngeo697

Perol, T., Gharbi, M., and Denolle, M. (2018). Convolutional Neural Network for Earthquake Detection and Location. *Sci. Adv.* 4, e1700578. doi:10.1126/sciadv.1700578

Richter, C. F. (1935). An Instrumental Earthquake Magnitude Scale. *Bull. Seismol. Soc. Am.* 25 (1), 1–32. doi:10.1126/sciadv.1700578

Ross, Z. E., Trugman, D. T., Egill, H., and Shearer, P. M. (2019). Searching for Hidden Earthquakes in Southern California. *Science* 364, 767–771. doi:10.1126/science.aaw6888

Sleeman, R., and van Eck, T. (1999). Robust Automatic P-phase Picking: an On-Line Implementation in the Analysis of Broadband Seismogram Recordings. *Phys. Earth Planet. Interiors* 113, 265–275. doi:10.1016/S0031-9201(99)00007-2

Waldhauser, F., and Ellsworth, W. L. (2000). A Double-Difference Earthquake Location Algorithm: Method and Application to the Northern Hayward Fault, California. *Bull. Seismological Soc. America* 90, 1353–1368. doi:10.1785/0120000006

Wan, K., Lin, J., Xia, S., Sun, J., Xu, M., Yang, H., et al. (2019). Deep Seismic Structure across the Southernmost Mariana Trench: Implications for Arc Rifting and Plate Hydration. *J. Geophys. Res. Solid Earth* 124, 4710–4727. doi:10.1029/2018JB017080

Wang, J., Xiao, Z., Liu, C., Zhao, D., and Yao, Z. (2019). Deep Learning for Picking Seismic Arrival Times. *J. Geophys. Res. Solid Earth* 124, 6612–6624. doi:10.1029/2019JB017536

Wessel, P., and Smith, W. H. F. (1998). New, Improved Version of Generic Mapping Tools Released. *Eos Trans. AGU* 79, 579. doi:10.1029/98EO00426

Wu, Y., Lin, Y., Zhou, Z., Bolton, D. C., Liu, J., and Johnson, P. (2019). DeepDetect: A Cascaded Region-Based Densely Connected Network for Seismic Event Detection. *IEEE Trans. Geosci. Remote Sensing* 57, 62–75. doi:10.1109/TGRS.2018.2852302

Xiao, Z., Wang, J., Liu, C., Li, J., Zhao, L., and Yao, Z. (2021). Siamese Earthquake Transformer: A Pair-Input Deep-Learning Model for Earthquake Detection and Phase Picking on a Seismic Array. *J. Geophys. Res. Solid Earth* 126, 1–15. doi:10.1029/2020JB021444

Zhang, M., Ellsworth, W. L., and Beroza, G. C. (2019). Rapid Earthquake Association and Location. *Seismol. Res. Lett.* 90, 2276–2284. doi:10.1785/0220190052

Zhou, Y., Yue, H., Kong, Q., and Zhou, S. (2019). Hybrid Event Detection and Phase-Picking Algorithm Using Convolutional and Recurrent Neural Networks. *Seismol. Res. Lett.* 90, 1079–1087. doi:10.1785/0220180319

Zhu, G., Wiens, D. A., Yang, H., Lin, J., Xu, M., and You, Q. (2021). Upper Mantle Hydration Indicated by Decreased Shear Velocity Near the Southern Mariana

Trench from Rayleigh Wave Tomography. *Geophys. Res. Lett.* 48, e2021GL093309. doi:10.1029/2021GL093309

Zhu, G., Yang, H., Lin, J., Zhou, Z., Xu, M., Sun, J., et al. (2019). Along-strike Variation in Slab Geometry at the Southern Mariana Subduction Zone Revealed by Seismicity through Ocean Bottom Seismic Experiments. *Geophys. J. Int.* 218, 2122–2135. doi:10.1093/gji/ggz272

Zhu, W., and Beroza, G. C. (2019). PhaseNet: A Deep-Neural-Network-Based Seismic Arrival Time Picking Method. *Geophys. J. Int.* 216, 261–273. doi:10.1093/gji/ggy423

Conflict of Interest: The authors declare that the research was conducted in the absence of any commercial or financial relationships that could be construed as a potential conflict of interest.

Publisher's Note: All claims expressed in this article are solely those of the authors and do not necessarily represent those of their affiliated organizations, or those of the publisher, the editors, and the reviewers. Any product that may be evaluated in this article, or claim that may be made by its manufacturer, is not guaranteed or endorsed by the publisher.

frontiers in Earth Science

ORIGINAL RESEARCH
published: 21 February 2022
doi: 10.3389/feart.2022.802052

Correlation of Seismicity With Faults in the South Korea Plateau in the East Sea (Japan Sea) and Seismic Hazard Assessment

Han-Joon Kim[1], Seonghoon Moon[1], Hyeong-Tae Jou[1], Kwang-Hee Kim[2] and Bo Yeon Yi[3]*

[1]Marine Active Fault Research, Korea Institute Off Ocean Science and Technology, Busan, South Korea, [2]Department of Geological Sciences, Pusan National University, Busan, South Korea, [3]Oil and Gas Research Center, Korea Institute of Geoscience and Mineral Resources, Daejon, South Korea

The South Korea Plateau (SKP) is a structural high at the eastern continental margin of the Korean Peninsula. Earthquakes occur frequently in the SKP although they are not larger than M_L 5.0 in magnitude. The SKP is a region of highly rifted continental crust engraved with rifts created during back-arc rifting in the NW Pacific subduction zone that led to the separation of the SW Japan Arc in the Cenozoic. The Bandal, Onnuri, and Okgye Rifts are well-defined rifts in the SKP. Multichannel seismic profiles show that the rifts in the SKP are bounded by large-offset normal faults and their subsided basement is deformed by domino-style faulting. A close spatial correlation is recognized between the epicentral locations of earthquakes with relatively large magnitude and the rift-bounding fault of the Onnuri Rift. The faults in the SKP is interpreted to be reactivated with strike-slip since the middle Miocene. The maximum expected magnitude of earthquakes (Mmax) computed statistically using the catalog including instrumentally recorded seismicity is M_L 5.42. However, Mmax estimated from the catalog including instrumentally recorded seismicity and historical records increases to M_L 6.67.

Keywords: South Korea Plateau, back-arc rifting, active faults, seismic profiles, seismic hazard assessment

OPEN ACCESS

Edited by:
Joanna Faure Walker, University College London, United Kingdom

Reviewed by:
Gianluca Vignaroli, University of Bologna, Italy
Alexis Rigo, Laboratoire de géologie de l'Ecole Normale Supérieure (LG-ENS), France

****Correspondence:***
Han-Joon Kim
hanjkim@kiost.ac.kr

Specialty section:
This article was submitted to Geohazards and Georisks, a section of the journal Frontiers in Earth Science

Received: *26 October 2021*
Accepted: *19 January 2022*
Published: *21 February 2022*

Citation:
Kim H-J, Moon S, Jou H-T, Kim K-H and Yi BY (2022) Correlation of Seismicity With Faults in the South Korea Plateau in the East Sea (Japan Sea) and Seismic Hazard Assessment. Front. Earth Sci. 10:802052. doi: 10.3389/feart.2022.802052

INTRODUCTION

The separation of the SW Japan Arc from (near) the Korean Peninsula proceeded with back-arc rifting and spreading that created the East Sea (Japan Sea), a back-arc sea behind the Japan Arc in the NW Pacific subduction zone (**Figure 1**). The South Korea Plateau (SKP) is a dominant topographic feature at the present continental margin of the middle Korean Peninsula. The SKP is further divided into the eastern and western blocks termed the ESKP and the WSKP, respectively (**Figure 2**). The SKP accommodated extensive fault-controlled crustal deformation associated with back-arc rifting in the early stage of separation of the SW Japan Arc (Kim et al., 2015); as a result, the SKP preserves the fundamental elements of rift architecture consisting of a rift basin (or a trough) rimmed by an uplifted flank.

Earthquakes occur frequently in the SKP, as recorded officially since 1 March 1982 by the Korea Meteorological Administration, although their magnitudes are less than M_L 5.0 (**Figure 2**). However, a noticeable increase in the number of events in recent years is recognized (**Figure 3**). Specifically, the average annual number of events before year 2017 is 1.1; in contrast, the average number since then

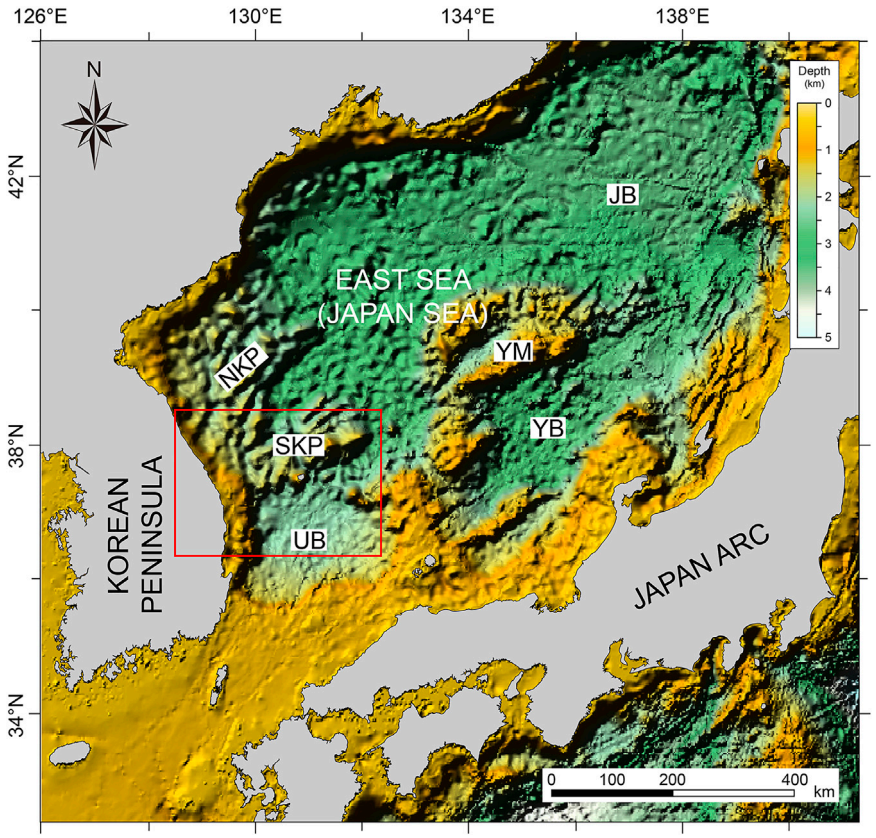

FIGURE 1 | Physiography of the continental margin of the Korean Peninsula in the East Sea (Japan Sea). JB, UB, and YB = Japan, Ulleung, and Yamato Basins, respectively. NKP, SKP, and YM (= North Korea Plateau, South Korea Plateau, and Yamato Bank, respectively) are fragmented continental crust. The red rectangle indicates the study area covering the SKP with detailed bathymetry shown in **Figure 2**.

has increased drastically to 7.8. This increase brought a need to identify active fault structures and assess the seismic hazard potential in the SKP.

The principal objectives of this study are 1) to map faults in the SKP using multichannel seismic (MCS) profiles obtained hitherto, 2) to identify active structures by correlating fault locations with ongoing seismicity, and 3) to estimate the maximum expected magnitude of earthquakes (Mmax) using the statistical method of Kijko et al. (2016). In earlier investigations to address the rifting process in the SKP, (Kim et al. 2007; Kim et al. 2015), identified faults based on a set of MCS profiles. We, in this study, utilize this set of MCS profiles to locate the faults in a more accurate manner. We, then, grouped the faults into rift-bounding faults and the faults within the rifts (i.e., intra-rift faults) to determine active seismic structures that generate the current seismicity.

Tectonic Setting of the SKP

The SKP at the eastern Korean margin is a mass of rifted continental crust segmented into two blocks of the ESKP and the WSKP separated by an about 100 km-long, narrow trough. The WSKP, connected to the Korean Peninsula, about 170 km wide E-W, is composed of several rifts and intervening topographic highs (**Figure 2**). The ESKP takes a trapezoidal shape, measuring about 120 km N-S and 70–110 km E-W. The ESKP is engraved with narrowly-spaced (<20 km), subparallel troughs alternating with ridges aligned NE-SW. These troughs and ridges constitute a system of horsts and grabens. The Bandal, Onnusi, and Okgye Rifts in the WSKP are well-recognized rift structures that are outlined by uplifted rift flanks and bounded by large-offset faults that accommodated major throw downs (**Figure 2**). The central parts of the rifts have depressed bathymetry where fault-controlled subsidence took place dominantly.

Rifting at the continental margin of the Korean Peninsula includes the following processes in Late Oligocene to Early Miocene times (Kim et al., 2015); 1) back-arc rifting and spreading behind the Japan Arc initiated in the northern margin of the Korean Peninsula, resulting in the fragmentation of the Korea Plateau (KP) from the peninsula and the opening of the Japan Basin (**Figure 4A**); 2) while back-arc spreading widened the Japan Basin, back-arc rifting occurred in the middle part of the margin of the Korean Peninsula that eventually developed into breakup and back-arc spreading behind the SW Japan Arc (**Figure 4B**). In this stage southwestward extension propagated from seafloor spreading in the Japan Basin burrowed into the WSKP to induce rifting of the Bandal Rift toward the SE direction. Kim et al. (2015)

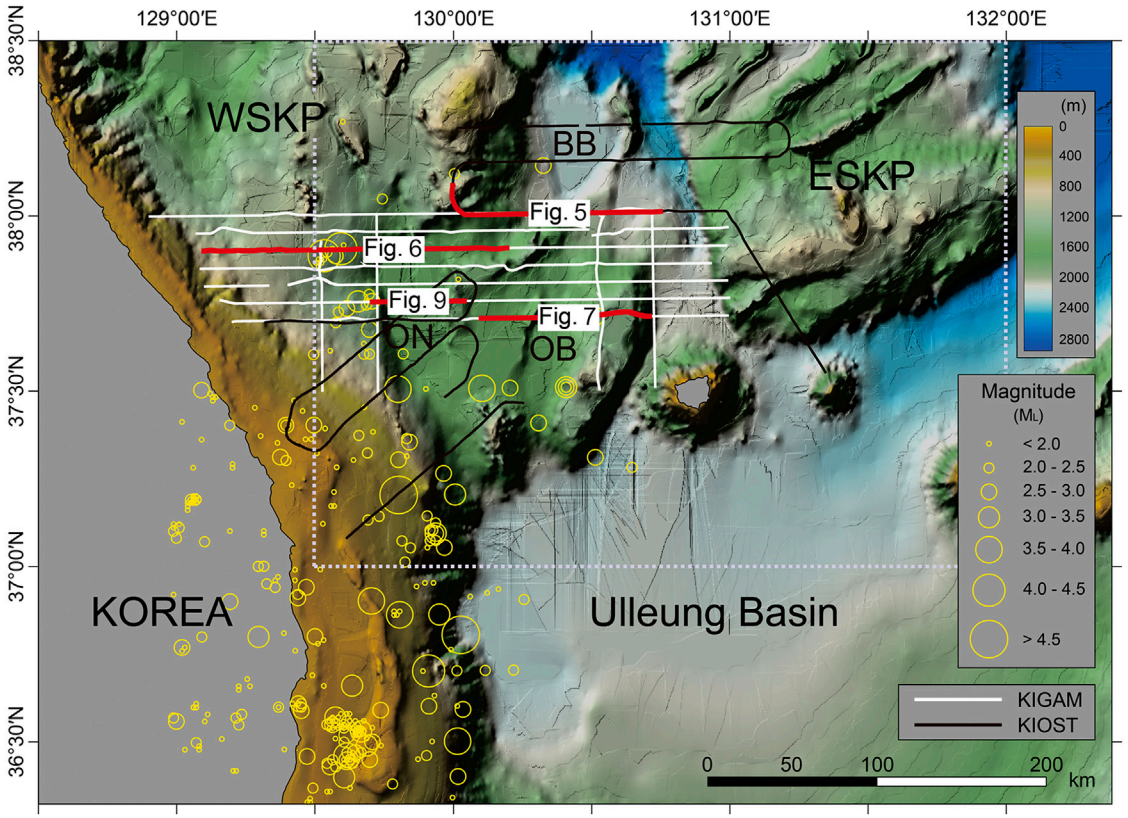

FIGURE 2 | Detailed bathymetry of the SKP overlain with the epicenters of earthquakes instrumentally recorded by the Korea Meteorological Administration (KMA) from 1982 to 2020. The black and white tracks are reflection seismic lines shot by the Korea Institute of Ocean Science and Technology (KIOST) and the Korea Institute of Geoscience and Mineral Resources (KIGAM), respectively. The locations of seismic profile sections that are referred to in the text are highlighted as thick red lines and labeled with a figure number. The dotted rectangle indicates the area for estimating the maximum expected magnitude of earthquakes (Mmax) in this study.

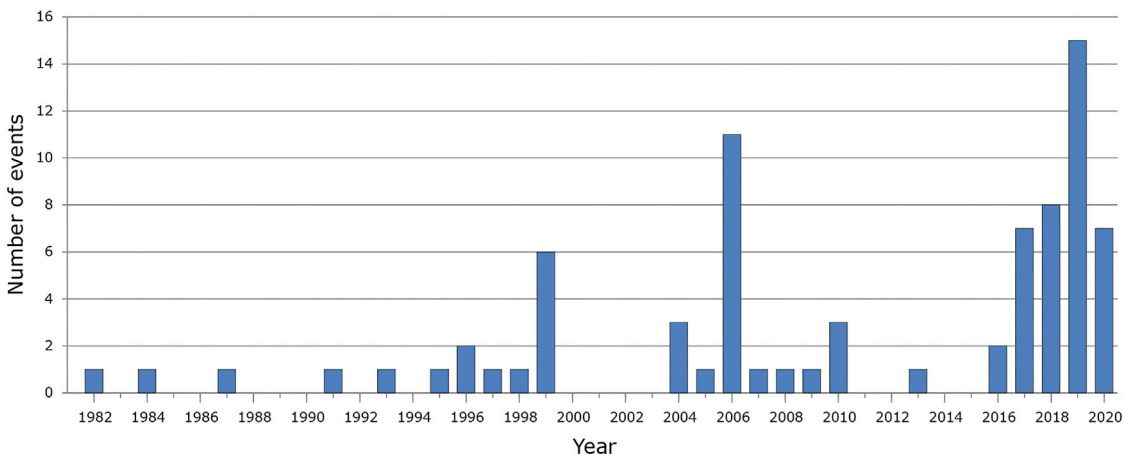

FIGURE 3 | Annual number of seismic events larger than M_L 0.8 at the SKP from 1982 to 2020. The events were recorded by the KMA.

suggested that the SKP underwent maximum extension of continental crust facilitated by depth-dependent stretching.

The Ulleung Basin is a thickly sedimented basin lying further seaward south of the continental slope of the SKP. (Kim et al., 2003; Kim et al., 2015), based on crustal structure from deep seismic sounding data, suggested that the Ulleung Basin is underlain by back-arc oceanic crust that is 2,3 km thicker than normal oceanic crust. They further suggested that 1) the thicker

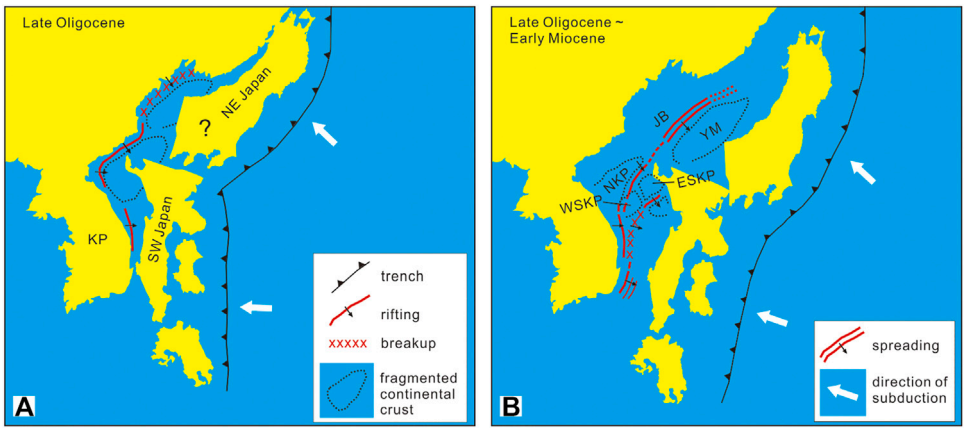

FIGURE 4 | Schematic diagrams showing the processes of back-arc rifting to breakup at the eastern Korean margin associated with the separation of the SW Japan Arc (modified from Kim et al., 2018). **(A)** Initiation of back-arc rifting and breakup at the northern Korean margin. **(B)** Back-arc rifting and breakup at the eastern Korean margin.

than normal oceanic crust underlying the Ulleung Basin was created above the hotter than normal mantle, 2) the SKP, located between the continental crust of the Korean Peninsula and the back-arc oceanic crust under the Ulleung Basin, marks the seaward limit of continental crust rifted with maximum extension, and 3) the slope base of the SKP is the site of breakup that initiated the emplacement of oceanic crust in the Ulleung Basin. In other words, the SKP represents transitional crust between the continental crust of the Korean Peninsula and the back-arc oceanic crust underlying the Ulleung Basin.

The occurrence of earthquakes shows a contrast between the SKP and the Ulleung Basin. Earthquakes occur preferentially in the SKP but rarely in the Ulleung Basin (**Figure 2**), which appears to demarcate the rifted continental crust of the SKP and the back-arc oceanic crust under the Ulleung Basin. The focal depths of the earthquakes in and around the Korean Peninsula average to ~10 km, mostly not exceeding 15 km (Sheen, 2015). However, earthquakes in the SKP occur frequently at the depth range from 15 to over 25 km (Korea Meteorological Administration (KMA) at http://www.weather.go.kr/weather/earthquakevolcano/report.jsp). Kim et al. (2015) inferred the crustal structure of the SKP that indicates the upper and lower crustal boundary at ~15 km depth. Therefore, it seems that earthquakes occur frequently at the lower crustal level. Explanations have been proposed for earthquakes in the lower continental crust such as 1) localized stress amplification in dry materials (e.g., Menegon et al., 2021), 2) faulting in the lower crust in a delamination model for rifting (Lister et al., 1986), and 3) the presence of a brittle-ductile transition in the upper part of the lower crust that sustains rigidity. However, accurate explanations for the deep crustal earthquakes are still in debate.

METHODS AND MATERIALS

The MCS profile sets used in this study include 1) approximately 800 km of 14- or 48-fold migrated seismic profiles from seismic data obtained by the Korea Institute of Ocean Science and Technology (KIOST) and 2) over 1,400 km of 40-fold stacked seismic profiles provided by the Korea Institute of Geoscience and Mineral Resources (KIGAM) (**Figure 3**). The KIOST data were obtained using a 56- or 96-channel streamer that recorded shots from a 1,380 or 690 in^3 air gun array. Processing of the KIOST data included stacking, predictive deconvolution, and 45° finite-difference time migration. The KIGAM data were obtained using an 80-channel streamer and a 924 or 1,254 in^3 air gun array. Processing of the KIGAM data included procedures from trace editing to stacking.

For computing Mmax, we used the magnitude record of the earthquakes in the SKP recorded by the KMA on the local scale (M_L). The earthquake catalog spans the period from 1982 to 2021 and covers the region from 37° to 38.5°N and from 129.5° to 132.0°E that encompasses the WSKP and the ESKP (**Figure 2**). 77 events were recorded with magnitudes ranging from M_L 0.8 to 4.7. However, the earthquakes were azimuthally not well covered by the seismic stations in the Republic of Korea, because 1) the number of seismic stations was not large before year 2000 and 2) most of the seismic stations are located in the southern Korean Peninsula west of the SKP. As a result, we were unable to compute accurate focal mechanism solutions to explain the fault activity.

RESULTS

Faults in the SKP

The faults displacing the basement in the SKP are identified on seismic profiles (**Figures 5**–**7**). We categorize the faults into the rift-bounding and intra-rift faults that occur along the boundaries of rifts and within the rifts, respectively (**Figure 8**). The faults bounding the grabens in the ESKP are considered as rift-bounding faults. Faults identified between the Korean Peninsula and the Onnuri Rift are not categorized as either rift-bounding or intra-rift faults because they occur outside the rifts.

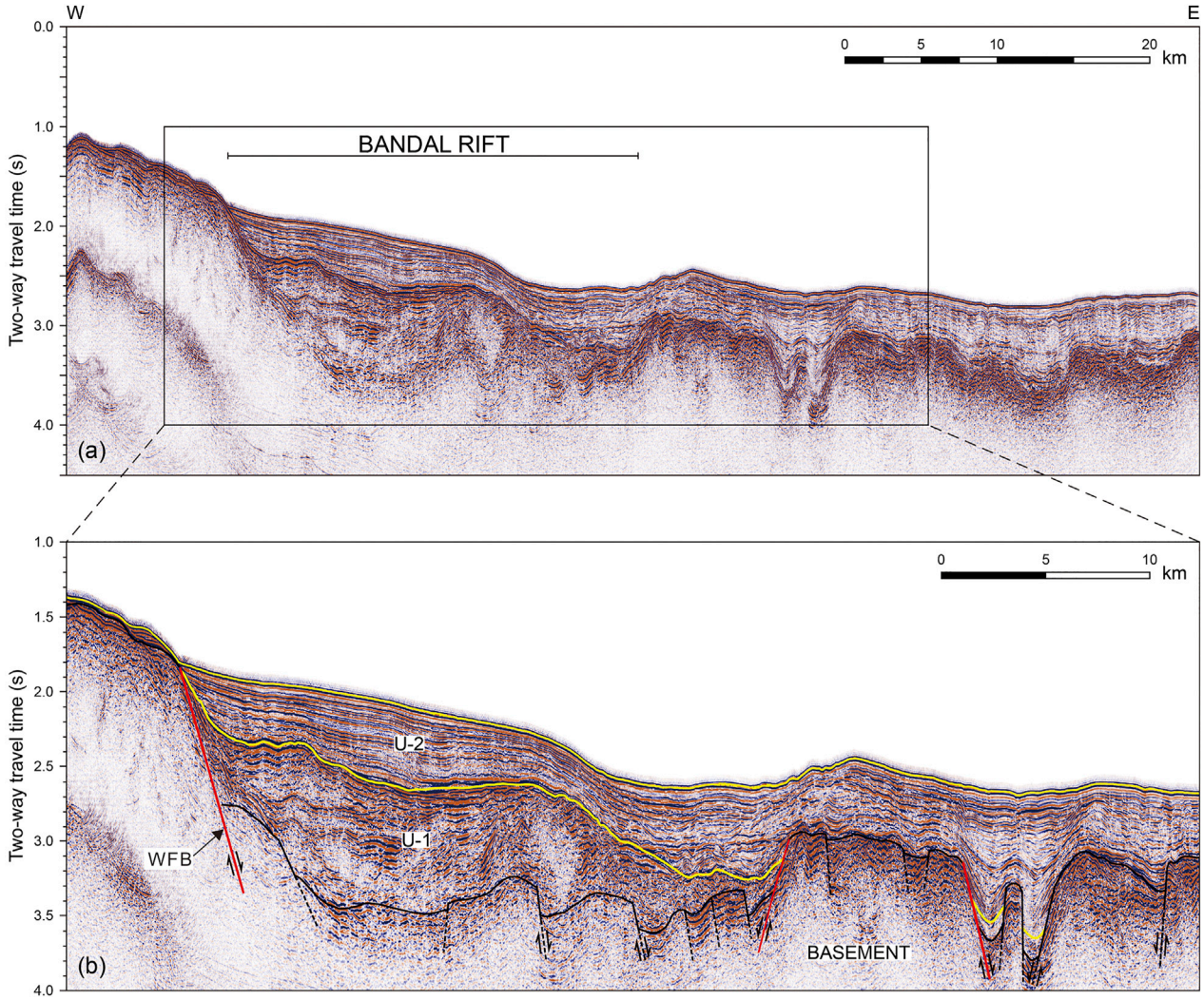

FIGURE 5 | (A) Seismic profile showing the structure of the Bandal Rift (see **Figure 2** for location) and **(B)** its interpretive line drawings. The rift-bounding fault is depicted in red. WFB = western bounding fault of the Bandan Rift. U-1 and U-2 = syn-rift and post-rift sedimentary units, respectively.

Rift-Bounding Faults

For individual rifts in the WSKP, the rift-bounding faults consists of one (or more) fault(s) and occur along the cliff of an uplifted flank that is arcuate outward (**Figures 5**–**8**). Although the spacing of MCS lines seems too large to unequivocally constrain the fault trace and geometry, the faults bounding the rifts are well recognized and traced on MCS profiles in conjunction with bathymetric data. The rift-bounding faults created first-order subsidence of the basement with a major throw down expected by extensional rifting (**Figures 5**–**7**).

Overall, the rifts in the WSKP show an asymmetric profile with the hanging wall tilted down toward the major rift-bounding fault zone on one side that accommodated a large throw down. The Okgye Rift is typical of a half-graben bounded by a large-offset fault on one side (**Figure 7**). The Bandal and Onnuri Rifts are bounded by a large-offset fault zone on one side and a subsidiary fault zone on the opposing side with much smaller offset (**Figures 5**, **6**). Specifically, the bounding fault of the Onnuri Rift on the eastern side (fault "EFO" in **Figure 6**) is well recognized that induced a large vertical displacement. In contrast, the western bounding fault of the Onnuri Rift is difficult to identify because 1) a large-offset fault antithetic to the EFO is not readily recognized in the western border fault zone and 2) the western flank of the Onnuri Rift is broad and highly deformed by faults (**Figure 6**), causing local depressions of the basement rocks. However, we interpret fault WFO (**Figure 6**) as the western bounding fault of the Onnuri Rift because it is antithetic to fault EFO and bounds the intra-rift zone deformed by domino-style faulting which will be explained later in "2) Intra-rift faults". Continental rifting includes formation of a half-graben tilted down toward a large-offset fault zone (e.g., Rosendahl et al., 1986). In a more advanced stage, a half-graben develops into a full-graben with an antithetic fault zone on the opposing side. Therefore, it appears that the

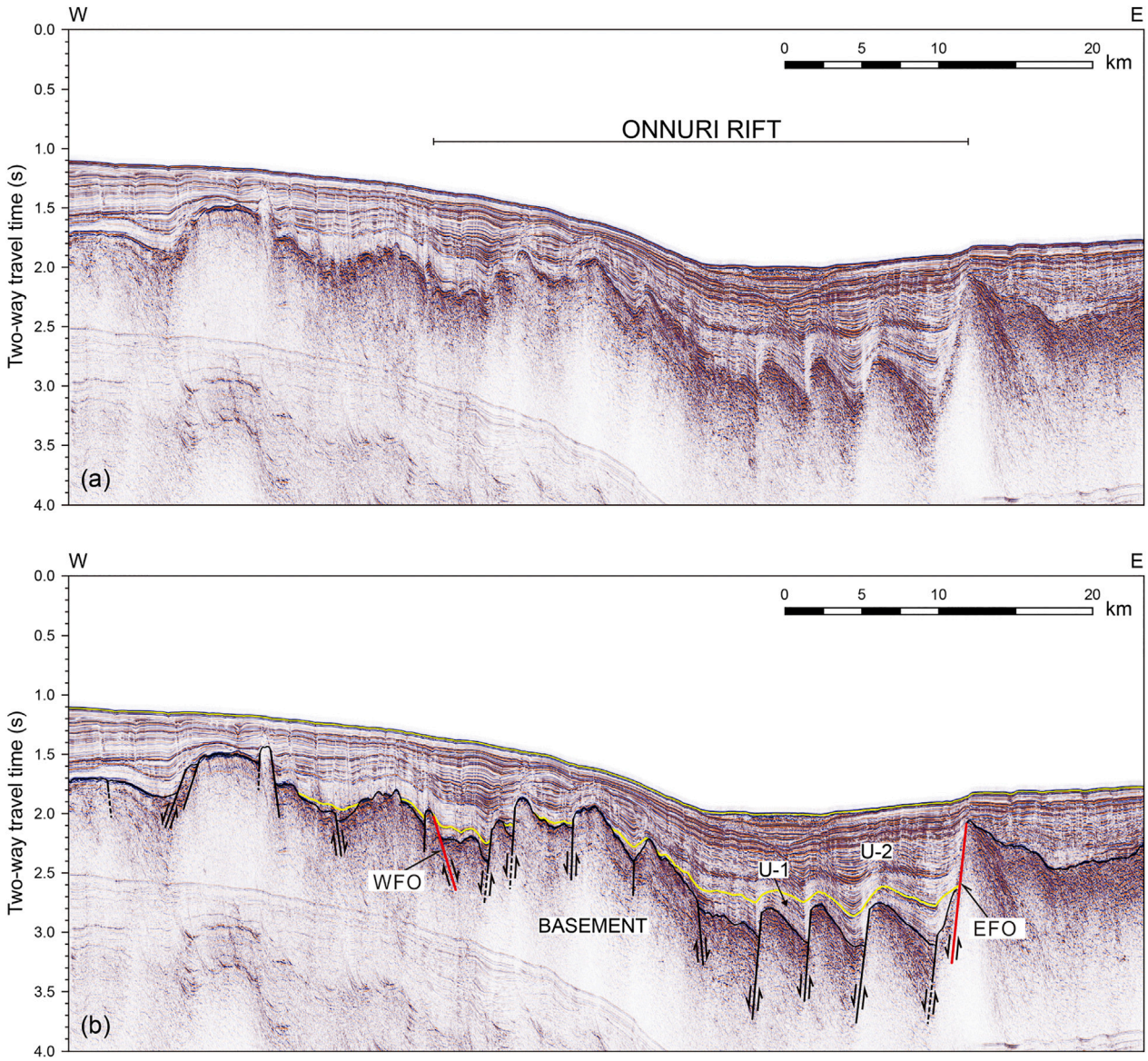

FIGURE 6 | (A) Seismic profile showing the structure of the Onnuri Rift (see **Figure 2** for location) and **(B)** its interpretive line drawings. Note that the basement of the Onnuri Rift is deformed by domino-style normal faulting between the eastern and antithetic western bounding faults, EFO and WFO, respectively (see the text). The rift-bounding fault is depicted in red. U-1 and U-2 = syn-rift and post-rift sedimentary units, respectively.

Bandal and Onnuri Rifts underwent a more advanced stage of rifting.

The orientation of the rift-bounding faults is perpendicular to the direction of extension induced by initial rifting. If we assume that extension occurred seaward, rifting occurred to the SE direction in the Bandal Rift, eastward in the Onnuri Rift, and dominantly eastward in the Okgye Rift. The uplifted flank occurring along the SE boundary of the Bandal Rift is well recognized on the bathymetry map (**Figure 8**), extending southwestward to the N-S trending eastern boundary fault of the Onnuri Rift; it also cuts the N-S trending intra-rift faults in the Okgye Rift. In other words, the uplifted flank of the Bandal Rift overprinted the NS-trending structures of the Okgye Rifts, suggesting that rifting in the Bandal Rift persisted after the initiation of rifting in the Okgye Rift.

Intra-Rift Faults

The central part of the rifts bounded by rift-bounding faults shows depressed bathymetry where prominent subsidence and deposition of thick sediments took place. The depression is clearly recognized in the Bandal and Onnuri Rifts, whereas it is less clear in the Okgye Rift. The subsided acoustic basement in the rifts is dissected by numerous intra-rift faults. In the Onnuri and Okgye Rifts, the intra-rift faults created basement highs alternating with lows (**Figures 6**, **7**). Here, back-tilting of the surface of a fault block between two consecutive faults is recognized, being representative

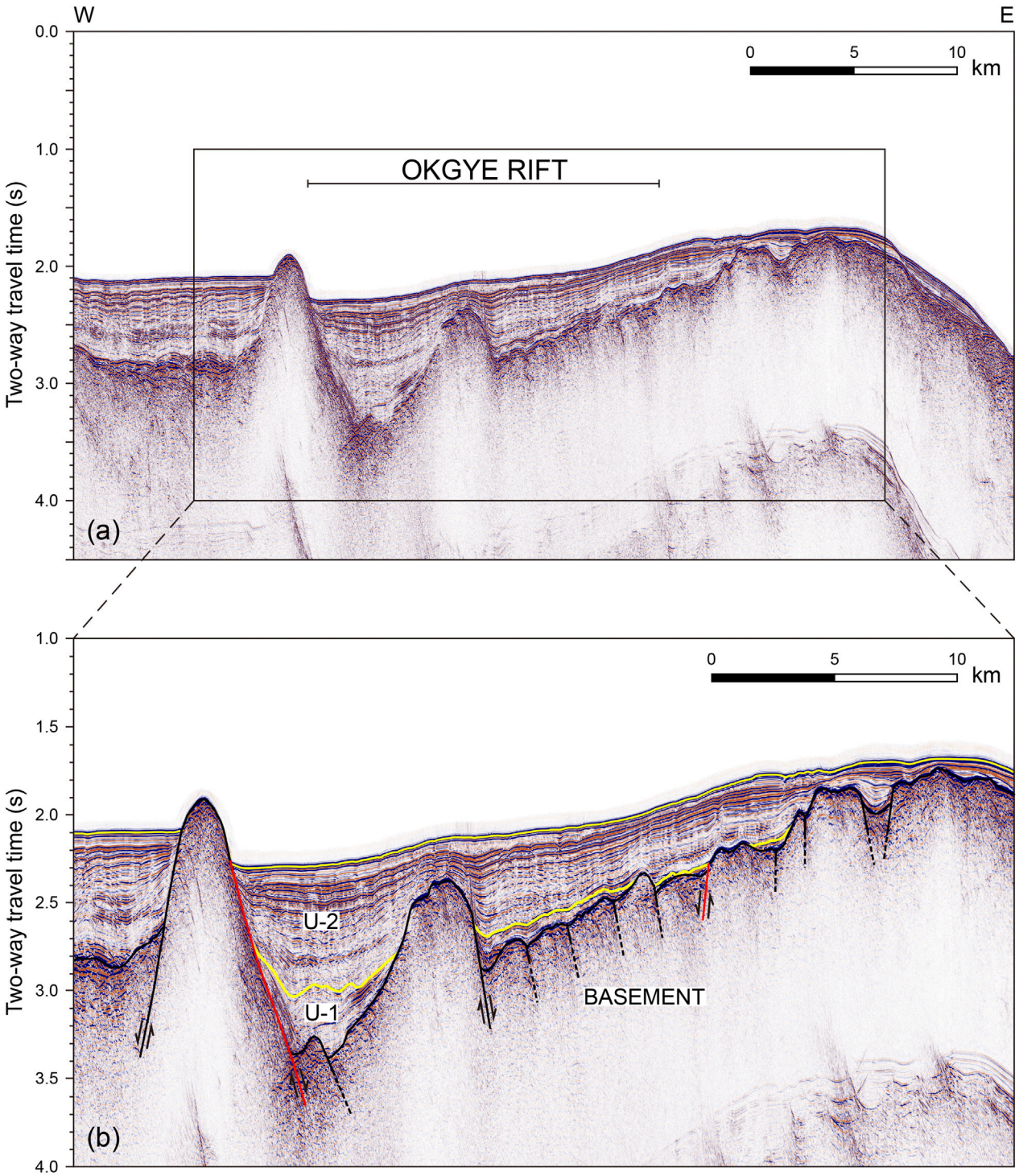

FIGURE 7 | (A) Seismic profile showing the structure of the Okgye Rift (see **Figure 2** for location) and **(B)** its interpretive line drawings. The rift-bounding fault is depicted in red. U-1 and U-2 = syn-rift and post-rift sedimentary units, respectively.

of domino-style normal faults (Kim et al., 2015). The domino faults are well traced in the Onnuri Rift; the domino faults tend to be evenly spaced and subparallel to the rift-bounding fault. The central part of the Onnuri Rift that is wider than other parts between two rift-bounding faults (**Figure 8**) is interpreted to have experienced a higher degree of extension.

In the Bandal Rift, domino-fault structure showing back-tilting of the surface of a fault block is not so explicitly

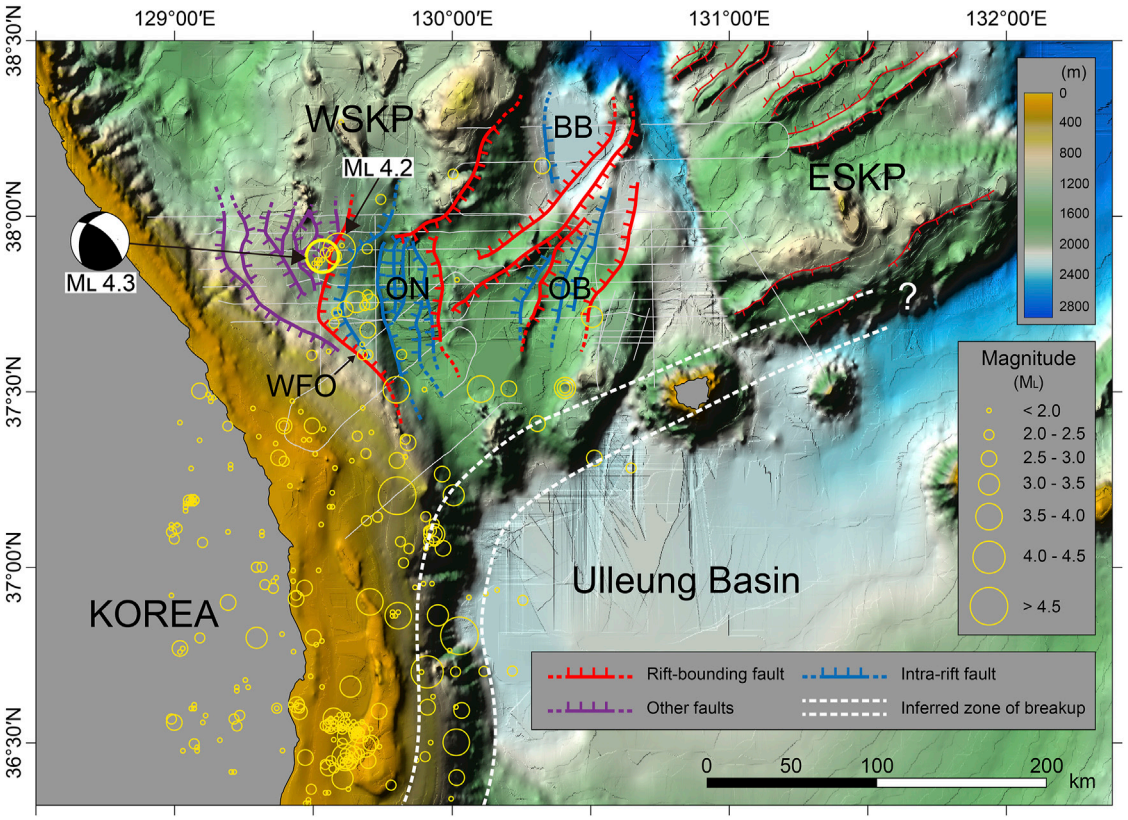

FIGURE 8 | Geologic structural map of the South Korea Plateau overlain with the epicenters of earthquakes. WFO, Western bounding fault of the Onnuri Rift.

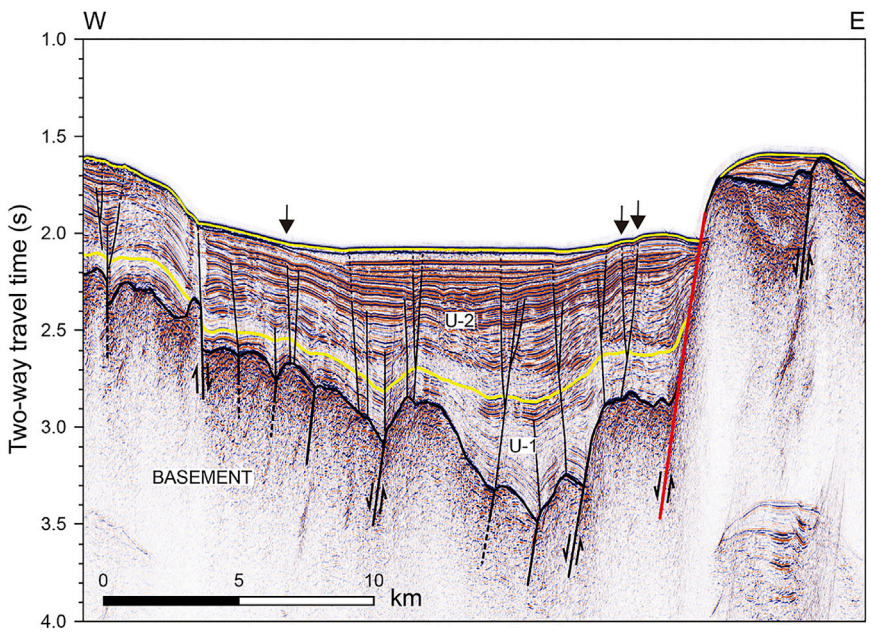

FIGURE 9 | Seismic profile showing sedimentary structure above the acoustic basement in the Onnuri Rift (see **Figure 2** for location). The arrows indicate faults that enable the recognition of increasing vertical separations of the sedimentary layers with depth in post-rift unit U-2.

TABLE 1 | Maximum magnitude of earthquakes (Mmax) expected at the SKP and their return period (RP) computed by the HA3 software (Kijko et al., 2016).

Procedures	[1)]Mmax (M_L)/RP (yr.) (B-value)	[2)]Mmax (M_L)/RP (yr.) (B-value)
Maximum likelihood	4.86 ± 0.25/370 (0.63 ± 0.10)	6.59 ± 0.40/1920 (0.66 ± 0.07)
Gibowicz-Kijko	6.07 ± 1.40/1,680 (0.67 ± 0.09)	6.52 ± 0.24/124 (0.74 ± 0.06)
Gibowicz-Kijko-Bayes	5.63 ± 0.95/2,250 (0.66 ± 0.09)	6.61 ± 0.39/1860 (0.66 ± 0.07)
Kijko-Sellevoll	5.49 ± 0.81/600 (0.65 ± 0.09)	6.92 ± 0.67/1,370 (0.66 ± 0.07)
Kijko-Sellevoll-Bayes	5.26 ± 0.59/670 (0.65 ± 0.09)	6.54 ± 0.33/4,150 (0.65 ± 0.07)
Tate-Pisarenko	Failed	Failed
Tate-Pisarenko-Bayes	Failed	6.71 ± 0.47/2,120 (0.66 ± 0.07)
Non-parametric (Gaussian)	5.18 ± 0.52/440 (0.65 ± 0.09)	6.82 ± 0.58/1,210 (0.66 ± 0.07)
Average	5.42 ± 0.75/1,002 (0.65 ± 0.09)	6.67 ± 0.44/1980 (0.67 ± 0.07)

[1)]The catalog includes instrumentally recorded events.
[2)]The catalog includes instrumentally recorded events and historical events.

recognized as in the Onnuri Rift. However, intra-rift faults toward the western major bounding fault in the Bandal Rift ("WFB" in **Figure 5**) appears to be sub-parallel and dipping in the similar direction, suggesting a certain component of domino faulting. We note that we traced a limited number of the intra-rift faults that appear to be traced continuously over consecutive profiles, although the basement is deformed by abundant faults.

Faults in Sediments

The rifts in the WSKP are filled with well-stratified sedimentary sequences that consist of underlying syn-rift (U-1) and overlying post-rift (U-2) units (**Figures 5–7**). Kim et al. (2015) inferred the age of U-1 to be Late Oligocene to Early Miocene, which is consistent with paleontological age dating of sediments by Tsoy et al. (2017) and the subsidence curves at the southern part of the eastern Korean margin derived by Ingle. (1992). The U-1 unit takes an overall wedge form across the rifts, placing the thick end on a major large-offset rift bounding fault. The wedge form implies tilting of the hanging wall during deposition. The thickening of U-1 is also recognized toward the individual hanging wall of domino faults. In addition, the syn-rift unit is uplifted alternatingly above the tilted basement highs. These features indicate that domino-style faulting persisted during the deposition of U-1.

Overall, the overlying post-rift unit, U-2, consists of parallel reflections, which suggests insignificant tectonic activities during its deposition. Numerous faults are identified within the sediments that extend to the uppermost sequences or to the seafloor (**Figure 9**). These faults occur not only across the subsided hanging wall blocks but also in the uplifted footwall blocks, implying diffuse deformation in the SKP by the current stress field. In many places, the faults developed into branching splays spreading upward (**Figure 9**), representative of a flower structure created by strike-slip faulting. The flower structures are recognized noticeably in the U-2 unit.

Although faults in the post-rift unit, U-2, are noticeable, vertical displacement of sedimentary sequences caused by faulting is small or not readily recognized. As the main reason, strike-slip faulting did not cause large vertical displacement of post-rift sediments that were deposited horizontally. As another reason, small vertical displacement is not resolved on seismic profiles obtained using an air-gun source. Nevertheless, an increase in vertical displacement with depth caused by faulting in the U-2 unit is recognized along some faults (**Figure 9**), which indicates faulting took place coevally with the deposition of the sequences. If faulting had occurred as a single event after deposition, the sequences cut by the faults would have equal vertical displacement. We, therefore, interpret that strike-slip faulting has been a dominant mode of deformation in the SKP since the middle Miocene.

DISCUSSION

Analysis of Seismic Hazards in the SKP

Correlation of Faults With Seismicity

All the recorded earthquakes have occurred in the WSKP (**Figure 8**); in contrast, earthquakes in the ESKP have not been recorded. In the WSKP, earthquakes have small-to-medium magnitude not exceeding. Only two earthquakes (M_L 4.3 and 4.2) occurred with magnitude larger than M_L 4.0 in the WSKP north of 37°30′N where rifts are identified on seismic profiles. The majority of earthquakes in the SKP occurs on or close to the WFO in the western part of the Onnuri Rift (**Figure 8**), suggesting a spatial correlation between the epicentral locations and rift structures. In contrast, the abundant rift-bounding and intra-rift faults elsewhere in the SKP generate much less earthquakes, although seismic profiles show intra-rift faults extend upward to the seafloor. In particular, the WFO appears to be a prominent active structure with more concentrated seismicity than others; seismicity here includes all of the two relatively large earthquakes with magnitude greater than M_L 4.0. The WFO appears to extend southeastward toward the inferred zone of breakup along the base of the continental slope at the eastern continental margin the Korean Peninsula (**Figure 8**), marking the site of the majority of seismic events at the entire Korean margin in magnitude as well as in number.

Extension at the eastern Korean margin during back-arc rifting and spreading ceased in the middle Miocene (around 14–15 Ma), then, the margin became subjected to compression in the NNW-SSE (or N-S) direction (e.g., Lee et al., 2011). The compressional stress changed its direction again to ENE-WSW

TABLE 2 | Historical earthquake record from A.D. 2 to 1904 (Kyung, 2012).

Date (year. month. day)	Intensity (I)	[1)]Magnitude (M_L)
1,511. 03. 21	IV	3.98
1,521.10. 12	IV	3.98
1,522. 01. 19	IV	3.98
1,526. 04. 01	IV	3.98
1,546. 12.16	III	3.41
1,558. 12. 09	IV	3.98
1,681. 06.21	VIII	6.28
1,681. 06. 27	VIII	6.28
1,681. 12. 20	VI	5.12

[1)]*Equation for conversion from intensity (I) to magnitude (ML) is ML, 1.7 + 0.57 I (Kim and Kyung, 2015).*

since the Pliocene. The ENE-WSW compression has persisted to the present, as indicated by focal mechanism solutions of earthquakes in and around the Korean Peninsula (Rhie and Kim, 2010). These directions of compressive stress since the middle Miocene are different from the direction of extension during back-arc rifting. The WFO and its adjacent faults that are inferred to be active structures are orientated dominantly N-S or NW-SE (**Figure 8**), which is oblique to the directions of compression since the middle Miocene. We. therefore, interpret that the active structures in the SKP have been reactivated with a strike (or oblique) slip component.

The largest earthquake ever recorded in the SKP is the M_L 4.3 event that occurred recently on April 19, 2019. The focal mechanism solution of this event is available from the International Seismological Center (ISC) and the National Research Institute for Earth Science and Disaster Resilience (NIED). The focal mechanism solution indicates with reverse slip with a strike-slip component with strike = 194° (or 316°), dip = 34° (or 70°), and rake = 142° (or 62°) (**Figure 8**). Our interpretation appears to be in agreement with the focal mechanism solution.

Assessment of Seismic Hazards in the SKP

The potential maximum magnitude of earthquakes (Mmax) expected on a fault can be estimated using the length of the fault (e.g., Anderson et al., 1996). However, it is difficult to define the coseismic segments of faults in the SKP based on seismic profiles because the faults, rift-bounding and intra-rift, do not consist of straight portions; instead, they have arcuate or curvilinear traces. Non-straight faults cause a scatter in the relationship between the maximum throw and the surface rupture length (Iezzi et al., 2018, 2020), making it difficult to estimate Mmax using the fault length. In addition, large earthquakes with aftershocks have not occurred that enable us to trace the length of coseismic source structures.

In this study, Mmax in the SKP and their return period (RP) were estimated statistically using the software, HA3 (Kijko et al., 2016), suited for a specific area based on the catalog of instrumentally recorded events and historical records. The seismicity catalog for HA3 includes 56 events recorded since 1 March 1982 that are larger than M_L 2.0, a threshold magnitude for computation. Six statistical procedures were performed successfully by HA3 (**Table 1**). Mmax ranges from M_L 4.86 to M_L 6.07, averaging to M_L 5.42 with the return period of 1,000 years, suggesting that the potential seismic hazard is not high in the SKP.

The b-value in the Korean Peninsula computed from the instrumental earthquake catalog is 1.11 (Noh et al., 2000), which is higher than the b-value at the entire continental margin of the Korean Peninsula ranging from 0.85 to 0.88 (Hong et al., 2020). The b-value in the SKP from the instrumental catalog ranges from 0.63 to 0.67, averaging to 0.62 (**Table 1**), which is noticeably lower than the b-values in the Korean Peninsula and its entire continental margin. The low-to-intermediate b-values may suggest the dominance of relatively large earthquakes over smaller earthquakes (e.g., Wu et al., 2018).

Although the magnitude of instrumentally recorded earthquakes is not large, the historical record from A.D. 2 to 1904 compiled by the Korea Meteorological Administration (2012) indicates occurrences of 10 earthquakes with relatively large intensities felt in the coastal area north of 37°N (**Table 2**) that were interpreted to have occurred in the coastal and offshore region encompassing the SKP. The intensities of those earthquakes are mostly larger than or equal to IV. Two of them had remarkably large intensity of VIII. The intensity of the historical events can be converted to the M_L magnitude using the relation proposed by Kim and Kyung (2015) (**Table 2**). Conversion suggests the M_L magnitude of the two historical events in 1,681 is as large as 6.28. Including historical earthquakes in the catalog resulted in average Mmax of M_L 6.67 with the return period of 1980 years (**Table 1**). Therefore, we find that 1) the long-term Mmax value is significantly larger than that estimated from the current seismicity and 2) the hazard potential of the long-term Mmax is not high, considering its return period of about 2000 years. The historical record includes four events larger than M_L 4.0 for about 500 years since 1,511, whereas instrumental record includes three events larger than M_L 4.0 for less than 40 years since 1982. Therefore, we note that the historical record may be subjected to incompleteness, considering offshore earthquakes were difficult to be felt on land unless their magnitudes were large enough.

As mentioned previously, the basement blocks in the rifts in the SKP are tilted toward the rift-bounding faults and deformed by abundant domino-style normal faulting. Tilting of the hanging wall during rifting is frequently caused by slip on the listric normal fault (e.g., McClay, 1990). Back-tilting of domino-fault blocks is facilitated by slip on the lower flatter portion of a listric normal faults below (e.g., McCann and Saintot, 2003). Therefore, the rift bounding faults in the SKP are interpreted to have been created as listric normal faults. Wu et al. (2018) suggested that the thrust faulting regions have lower b-values than normal faulting regions. The lower, flatter portions of listric fault planes are easily reactivated as thrusts, whereas reactivation of the higher steeper portions as reverse faults is mechanically more difficult (Jain et al., 2013). Therefore, the low b-values in the SKP may indicate the dominance of thrust faulting on the lower flatter portions of the rift-bounding faults and intra-rift faults.

CONCLUSION

The South Korea Plateau (SKP) preserves fault-controlled rift structures associated with back-arc rifting in the

Cenozoic. We identified faults in the SKP and correlated them with ongoing seismicity. The results of our study are as follows:

1 The deformation of the SKP during back-arc rifting is explained by normal faulting along the rift boundaries and domino-style extensional faulting within the rifts.
2 The deformation of the post-rift sequences suggests the reactivation of the faults as strike-slip faults under the current compressive stress.
3 All the recorded earthquakes have occurred in the western block of the SKP. The western bounding fault zone of the Onnuri Rift is a prominent active structure with concentrated seismicity with relatively large magnitude.
4 The maximum possible magnitude of earthquakes (Mmax) in the SKP, estimated statistically from the instrumental seismicity catalog is M_L 5.42 on average with the return period of 1,000 years. Mmax estimated from the catalog including both instrumentally recorded and historical earthquakes increases to M_L 6.67 with the return period of 2000 years.
5 The average b-value of .65 in the SKP is lower than that in the Korean Peninsula, which may suggest the dominance of thrust faulting on the listric rift-bounding faults.

DATA AVAILABILITY STATEMENT

The raw data supporting the conclusion of this article will be made available by the authors, without undue reservation.

AUTHOR CONTRIBUTIONS

H-JK: conception, design, and writing of the work. SM: interpretation of seismic data. H-TJ, K-HK and BY: acquisition and processing of seismic and earthquake data.

FUNDING

This work was funded by the Korea Institute of Ocean Science and Technology (Grant PE99941), the Korea Meteorological Administration (Grant KMI 2018-02810-4), and the Ministry of Oceans, and Fisheries of Korea (Grant PG55261).

ACKNOWLEDGMENTS

H-JK thanks Dr. A. Kijko for providing the HA3 software. He appreciates Dr. J. Faure Walker and reviewers for constructive comments.

REFERENCES

Anderson, J. G., Wesnousky, S. G., and Stirling, M. W. (1996). Earthquake Size as a Function of Fault Slip Rate. *Bull. Seismol. Soc. Am.* 86, 638–690.

Hong, T.-K., Park, S., Lee, J., and Kim, W. (2020). Spatiotemporal Seismicity Evolution and Seismic hazard Potentials in the Western East Sea (Sea of Japan). *Pure Appl. Geophys.* 177, 3761–3774. doi:10.1007/s00024-020-02479-z

Iezzi, F., Mildon, Z., Walker, J. F., Roberts, G., Goodall, H., Wilkinson, M., et al. (2018). Coseismic Throw Variation across Along-Strike Bends on Active Normal Faults: Implications for Displacement Versus Length Scaling of Earthquake Ruptures. *J. Geophys. Res. Solid Earth* 123, 9817–9841. doi:10.1029/2018JB016732

Iezzi, F., Roberts, G., and Faure Walker, J. (2020). Throw-rate Variations within Linkage Zones during the Growth of normal Faults: Case Studies from the Western Volcanic Zone, Iceland. *J. Struct. Geology.* 133, 103976. doi:10.1016/j.jsg.2020.103976

Ingle, J. C., Jr. (1992). "Subsidence Pattern of the Japan Sea: Stratigraphic Evidence from ODP Sites and Onshore Sections," in *Pro. ODP Sci. Res.* Editors K. Tamaki, K. Suyehiro, J. Allan, and M. McWilliams, 127/128, 1197–1218.

Jain, A., Verma, A. K., Vishal, V., and Singh, T. N. (2013). Numerical Simulation of Fault Reactivation Phenomenon. *Arab J. Geosci.* 6, 3293–3302. doi:10.1007/s12517-012-0612-8

Kijko, A., Smit, A., and Sellevoll, M. A. (2016). Estimation of Earthquake Hazard Parameters from Incomplete Data Files. Part III. Incorporation of Uncertainty of Earthquake-Occurrence Model. *Bull. Seismological Soc. America* 106, 1210–1222. doi:10.1785/0120150252

Kim, H.-h., and Kyung, J. B. (2015). Analysis on the Relationship between Intensity and Magnitude for Historical Earthquakes in the Korean Peninsula. *J. Korean Earth Sci. Soc.* 36, 643–648. doi:10.5467/jkess.2015.36.7.643

Kim, H.-J., Jou, H.-T., Cho, H.-M., Bijwaard, H., Sato, T., Hong, J.-K., et al. (2003). Crustal Structure of the continental Margin of Korea in the East Sea (Japan Sea) from Deep Seismic Sounding Data: Evidence for Rifting Affected by the Hotter Than normal Mantle. *Tectonophysics* 364, 25–42. doi:10.1016/s0040-1951(03)00048-9

Kim, H.-J., Jou, H.-T., and Lee, G. H. (2018). Neotectonics of the Eastern Korean Margin Inferred from Back-Arc Rifting Structure. *Ocean Sci. J.* 53, 601–609. doi:10.1007/s12601-018-0036-9

Kim, H.-J., Lee, G. H., Choi, D.-L., Jou, H.-T., Li, Z., Zheng, Y., et al. (2015). Back-arc Rifting in the Korea Plateau in the East Sea (Japan Sea) and the Separation of the Southwestern Japan Arc from the Korean Margin. *Tectonophysics* 638, 147–157. doi:10.1016/j.tecto.2014.11.003

Kim, H.-J., Lee, G. H., Jou, H.-T., Cho, H.-M., Yoo, H.-S., Park, G.-T., et al. (2007). Evolution of the Eastern Margin of Korea: Constraints on the Opening of the East Sea (Japan Sea). *Tectonophysics* 436, 37–55. doi:10.1016/j.tecto.2007.02.014

Korea Meteorological Administration (2012). *Historical Earthquake Records in Korea*. Seoul: Korea Meteorological Administration, 279pp.

Lee, G. H., Yoon, Y., Nam, B. H., Lim, H., Kim, Y.-S., Kim, H. J., et al. (2011). Structural Evolution of the Southwestern Margin of the Ulleung Basin, East Sea (Japan Sea) and Tectonic Implications. *Tectonophysics* 502, 293–307. doi:10.1016/j.tecto.2011.01.015

Lister, G. S., Etheridge, M. A., and Symonds, P. A. (1986). Detachment Faulting and the Evolution of Passive continental Margins. *Geol* 14, 246–250. doi:10.1130/0091-7613(1986)14<246:dfateo>2.0.co;2

McCann, T., and Saintot, A. (2003). Tracing Tectonic Deformation Using the Sedimentary Record: an Overview. *Geol. Soc. Lond. Spec. Publications* 208, 1–28. doi:10.1144/gsl.sp.2003.208.01.01

McClay, K. R. (1990). Extensional Fault Systems in Sedimentary Basins: a Review of Analogue Model Studies. *Mar. Pet. Geology.* 7, 206–233. doi:10.1016/0264-8172(90)90001-w

Menegon, L., Campbell, L., Mancktelow, N., Camacho, A., Wex, S., Papa, S., et al. (2021). The Earthquake Cycle in the Dry Lower continental Crust: Insights from Two Deeply Exhumed Terranes (Musgrave Ranges, Australia and Lofoten, Norway). *Phil. Trans. R. Soc. A.* 379, 20190416. doi:10.1098/rsta.2019.04110.1098/rsta.2019.0416

Noh, M. H., Lee, S. K., and Choi, K. R. (2000). Minimum Magnitude of Earthquake Catalog of Korea Meteorological Agency for the Estimation of Seismicity Parameters. *J. Korean Geophys. Soc.* 3, 261–268.

Rhie, J., and Kim, S. (2010). Regional Moment Tensor Determination in the Southern Korean Peninsula. *Geosci. J.* 14, 329–333. doi:10.1007/s12303-010-0038-9

Rosendahl, B. R., Reynolds, D. J., Lorber, P. M., Burgess, C. F., McGill, J., Scott, D., et al. (1986). "Structural Expressions of Rifting: Lessons from Lake Tanganyika, Africa,".*Geol. Soc. Spec. Publ. Sedimentation in the African Rifts*. Editor L. E. Frostick (Boston, Blackwell Scientific Publications), 25, 29–43. doi:10.1144/gsl.sp.1986.025.01.04

Sheen, D.-H. (2015). Comparison of Local Magnitude Scales in South Korea. *Journal of the geological society of Korea* 51, 415–424. doi:10.14770/jgsk.2015.51.4.415

Tsoy, I. B., Gorovaya, M. T., Vasilenko, L. N., Vashchenkova, N. G., and Vagina, N. K. (2017). Age and Conditions of Formation of Sedimentary Cover of the Ulleung Plateau of the Sea of Japan According to Micropaleontological Data. *Stratigr. Geol. Correl.* 25, 99–121. doi:10.1134/s0869593817010063

Wu, Y.-M., Chen, S. K., Huang, T.-C., Huang, H.-H., Chao, W.-A., and Koulakov, I. (2018). Relationship Between Earthquake B -Values and Crustal Stresses in a Young Orogenic Belt. *Geophys. Res. Lett.* 45, 1832–1837. doi:10.1002/2017GL076694

Conflict of Interest: The authors declare that the research was conducted in the absence of any commercial or financial relationships that could be construed as a potential conflict of interest.

frontiers in Earth Science

ORIGINAL RESEARCH
published: 25 February 2022
doi: 10.3389/feart.2022.839712

Two Distinct Back-Arc Closure Phases of the East Sea: Stratigraphic Evidence From the SW Ulleung Basin Margin

*Jae-Hyuk Lee[1], Jae-Ho Lee[1], Seok-Hoon Yoon[2], Hyun-Suk Lee[3], Hoon-Young Song[4] and Gi-Bom Kim[1]**

[1]Department of Geological Sciences, Pusan National University, Busan, South Korea, [2]Department of Earth and Marine Sciences, Jeju National University, Jeju, South Korea, [3]Petroleum & Marine Research Division, Korea Institute of Geoscience and Mineral Resources, Dajeon, South Korea, [4]Domestic Exploration Department, Korea National Oil Corporation, Ulsan, South Korea

OPEN ACCESS

Edited by:
Han-Joon Kim,
Korea Institute of Ocean Science and Technology, South Korea

Reviewed by:
Serge Lallemand,
UMR5243 Géosciences Montpellier, France
Laurent Jolivet,
Sorbonne Universités, France

***Correspondence:**
Gi-Bom Kim
kimgb@pusan.ac.kr

Specialty section:
This article was submitted to Structural Geology and Tectonics, a section of the journal Frontiers in Earth Science

Received: *20 December 2021*
Accepted: *24 January 2022*
Published: *25 February 2022*

Citation:
Lee J-H, Lee J-H, Yoon S-H, Lee H-S, Song H-Y and Kim G-B (2022) Two Distinct Back-Arc Closure Phases of the East Sea: Stratigraphic Evidence From the SW Ulleung Basin Margin. Front. Earth Sci. 10:839712. doi: 10.3389/feart.2022.839712

This study focuses on revisiting the tectostratigraphic framework of the Ulleung Basin and conceptualizing neotectonics around the western East Sea margin. Based on the analysis of 2D and 3D multi-channel seismic reflection data and offshore drill wells, we divided the entire sedimentary successions of the Ulleung Basin into four tectostratigraphic sequences, named TS1 (c. 23–16 Ma), TS2 (c. 16–9 Ma), TS3 (c. 9–4 Ma), and TS4 (c. 4 Ma–present), in ascending order. The results show that each sequence has been deformed once or multiple times in different periods by juxtaposing two major compressional structures named the Dolgorae Thrust-Fold Belt and the Gorae Anticline. Interpretation of the stratal deformation and termination patterns of the syn- and post-deformational sequences of each structures suggests that the thrusting and folding of the Dolgorae Thrust-Fold Belt was active from c. 16 Ma to c. 9 Ma under the NNW–SSE compressional stress regime (Stage-2), whereas the Gorae Anticline was active from 4 Ma to the present under the ENE–WSW compressional stress regime (Stage-4). Between these two compressional events, there was an intervening period of regional slow subsidence driven by thermal contraction of the back-arc lithosphere and isostatic sedimentary loading (Stage-3). Based on the stratigraphic and structural reconstruction, we propose a 4-stage tectonic model: Stage-1) back-arc opening stage associated with the southward drift of the Japanese islands (c. 23–16 Ma), Stage-2) tectonic-inversion stage in association with the reorganization of the Pacific and Philippine Sea plates and clockwise rotation of SW Japan (c. 16–9 Ma), Stage-3) post-inversion stage with regional thermal and isostatic subsidence (c. 9–4 Ma), and Stage-4) neotectonic stage in which embryonic subduction is nucleating on the East Sea margins under the E–W compressional stress regime (c. 4 Ma–present).

Keywords: neotectonics, post-Miocene tectonic deformations, tectostratigraphy, seismic stratigraphy, Ulleung Basin, Dolgorae Thrust-Fold Belt, Gorae Anticline

1 INTRODUCTION

The East Sea (Japan Sea) is a semi-enclosed marginal sea formed by the Cenozoic back-arc extension behind the Japanese Island Arc (Tamaki, 1988). Dextral pull-apart style extension with associated rotation of the southwestern Japanese Island Arc resulted in the characteristic parallelogramic geomorphological evolution of the East Sea (Lallemand and Jolivet, 1986; Jolivet, et al., 1991). Around 15 Ma, the young Philippine Sea Plate moving along the Ryukyu Trench reached south of present-day Kyushu in Japan by replacing the southern end of the pre-existing Pacific Plate (Hall, 2002). This plate reorganization caused cessation of back-arc extension (Jolivet and Tamaki, 1992; Lee et al., 2011), leaving behind a regional compressional structure on the southwestern margin of the East Sea (Lee et al., 1999; Kim et al., 2008). At present, the entire East Sea and surrounding regions are under the influence of the E–W compressional stress that started around 4 Ma (Taira, 2001). This stress regime appears to convert the strike-slip margins of the sea into compressional zones, which potentially evolve into incipient subduction zones (Tamaki and Honza, 1985; No et al., 2014; Gi-Bom Kim et al., 2018).

The Ulleung Basin, located in the southwest of the East Sea, was one of the three back-arc opening centers in the East Sea along with the Japan, and Yamato basins (Yoon and Chough, 1995). On the southern margin of the basin, over 10 km thick sedimentary successions preserve superimposed stratigraphic records of subsidence/uplift and structural deformations in association with the back-arc opening and subsequent tectonic inversions throughout the Miocene and post-Miocene periods. In particular, the two major compressional structures of this region, the Dolgorae Thrust-Fold Belt (DTFB) and the Gorae Anticline, might be markers for the two important compressional tectonic events initiated in the Middle Miocene and Pliocene, respectively (Yoon et al., 2003; Kim et al., 2008). However, the structures have not yet been properly investigated in terms of their activation periods and relations with changing background tectonics. Such a rough tectostratigraphic conception of this region hinders a proper understanding of the neotectonic nature of the East Sea and the Korean Peninsula.

In this study, we propose a new 4-stage tectostratigraphic model of the Ulleung Basin to better understand the tectonic evolution of the East Sea and obtain a proper conceptualization of the neotectonics around the Korean Peninsula. For this purpose, we precisely analyzed the stratigraphic characteristics of the DTFB and the Gorae Anticline, based on the entire large amounts of 2D and 3D multi-channel seismic reflection data of the southwestern marginal region of the East Sea provided by the Korea National Oil Corporation (KNOC). To control the age of newly defined sequence boundaries, we used foraminiferal biostratigraphy constructed based on six deep drill cores recovered in this region (Yi et al., 2020).

2 REGIONAL SETTING

The East Sea is a semi-enclosed marginal sea or back-arc basin located in northeastern Asia (**Figure 1**) (Chough et al., 2000). The sea comprises three sedimentary basins, namely the Japan, Yamato, and Ulleung basins, that are demarcated by three topographic highs, namely the Korea Plateau, the Yamato Rise, and the Oki Bank (**Figure 1A**). It is broadly accepted that the back-arc extension of the East Sea was initiated at the Early Oligocene (c. 32 Ma) (Tamaki, 1986; Ingle, 1992). Lallemand and Jolivet (1986) proposed that two dextral shear zones along the eastern and western margins of the sea guided the pull-apart style back-arc opening.

The pull-apart back-arc opening continued until the Middle Miocene (c. 15 Ma) when the Philippine Sea Plate started to induce clockwise pivotal rotation of the southwestern Japan (Jolivet and Tamaki, 1992; Hall, 2002). The rotation resulted in regional compressional deformation over the southwestern margin of the East Sea, which created Tsushima Island and Dolgorae-San'in Thrust-Fold Belts (Chough and Barg, 1987; Yamamoto, 1993; Fabbri et al., 1996; Kim et al., 2008). The reconstruction of the subsidence history from the ODP Leg 127/128 suggests that the clockwise rotation of the southwestern Japanese islands ceased in the late Middle Miocene (c. 12 Ma). Thereafter, the entire East Sea subsided slowly by the thermal contraction of the back-arc lithosphere until the onset of the post-Miocene neotectonic phase of the sea (Ingle, 1992; Jolivet and Tamaki, 1992; Taira, 2001).

Previous studies have summarized the neotectonics of the East Sea as an incipient subduction system, where the back-arc crust of the East Sea (the eastern margin of the Amur Plate) thrusts down below the northeastern Japanese islands (the Okhotsk Plate or the western end of the North American Plate) Nakamura, 1983; Tamaki and Honza, 1985; Lallemand and Jolivet, 1986; Jolivet and Tamaki, 1992; No et al., 2014). Lines of evidence, including the M 6.9–7.7 five earthquakes from 1940 to 1983, east-dipping and linear aftershock distribution, and p-wave velocity structures, strongly support rupture of the lithosphere and incipient subduction along the eastern margin of the East Sea (Tamaki and Honza, 1985; Sato et al., 1986). The uplifting terraces on western Honshu are also circumstantial evidence of subduction initiation (Okada and Ikeda, 2012).

In contrast to the eastern margin of the East Sea, where a new subduction zone is initiating, the western counterpart has long been regarded as a tectonically inactive intraplate setting, despite evidence of active compressional tectonics, such as coastal terraces (Choi et al., 2008), frequent earthquakes (Choi et al., 2012), and Quaternary faults along the onland and offshore regions of the eastern Korean Peninsula (Han-Joon Kim et al., 2016; Cheon et al., 2020). Such a perception began to change since the Magnitude 5.8 and 5.4 earthquakes in 2016 and 2017 respectively (YoungHee Kim et al., 2016; Kwang-Hee Kim et al., 2018). Gi-Bom Kim et al. (2018) suggested the possibility of creating an incipient subduction zone with associated crustal buckling along the western margin of the East Sea.

The Ulleung Basin, located in the southwestern corner of the East Sea, is a deep marine basin (over 2,000 m)

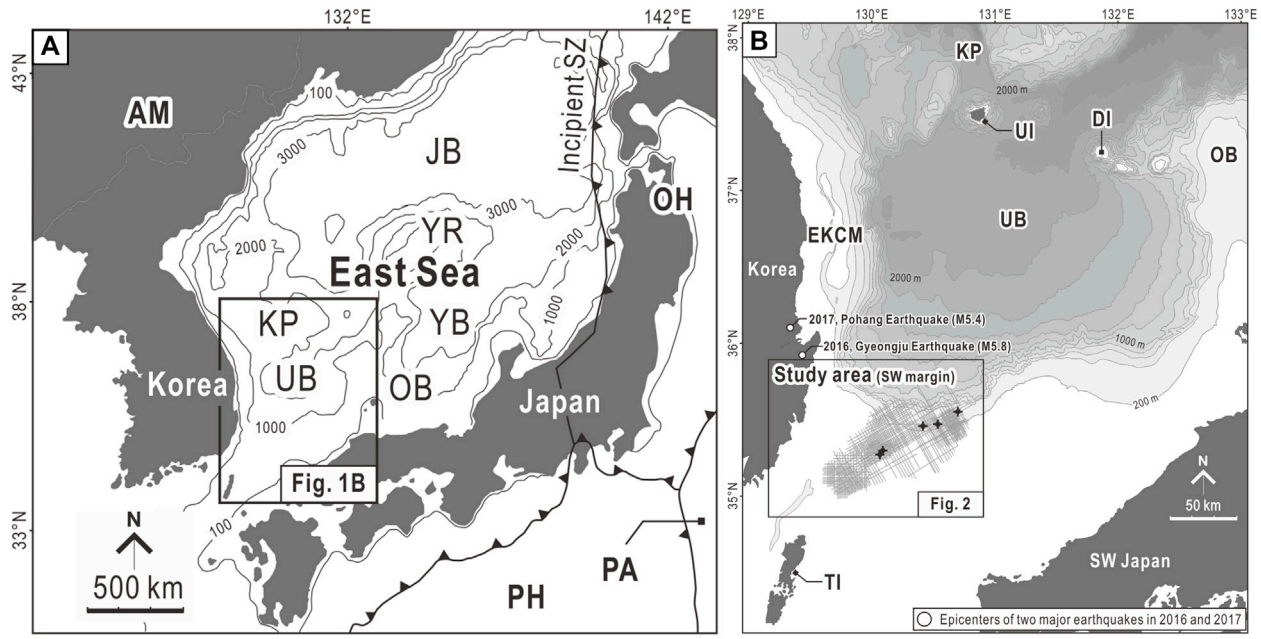

FIGURE 1 | (A) Map showing the physiography and plate locations around the East Sea. **(B)** Bathymetric map of the Ulleung Basin showing the location of the study area. AM, Amur Plate; PH, Philippine Sea Plate; PA, Pacific Plate; OH, Okhotsk Plate; JB, Japan Basin; YB, Yamato Basin; UB, Ulleung Basin; YR, Yamato Rise; OB, Oki Bank; KP, Korea Plateau.

(**Figure 1B**), filled with sedimentary sequences with a total thickness of ~10 km in the southern part and ~5 km in the northern part. The tectonic evolution of the Ulleung Basin was divided into two stages. The first stage was initiated in the Early Miocene when the rhombic-shaped Ulleung Basin was constructed via a pull-apart-style back-arc extension that associated two dextral strike-slip principal deformation zones on the western and eastern boundaries (Yoon and Chough, 1995). Kim and Yoon (2017) proposed a simple-shear-style lithospheric extension model that explains juxtaposed asymmetric features in syn-extensional volcanism, fault pattern, sediment thickness, and crustal structure. The back-arc extension of the Ulleung Basin ceased in the Middle Miocene (c. 15 Ma), when the background stress regime was inverted from NNW–SSE extension to NNW–SSE compression in association with the rotation of the southwestern Japanese islands (Kim et al., 2008; Lee et al., 2011; Yoon et al., 2014). The tectonic inversion induced regional compressional deformation of the southwestern margin of the Ulleung Basin and constructed the Tsushima and Goto islands and Dolgorae-San'in Thrust-Fold belts (Yamamoto, 1993; Fabbri et al., 1996; Kim et al., 2008).

Hitherto, this two-stage tectonic scenario is most widely referred to as the evolutionary framework of the Ulleung Basin (Bahk et al., 2017; Cukur et al., 2018; Park et al., 2019; Horozal et al., 2021; Park et al., 2021). However, the scenario omits the final tectonic phase of the East Sea, marked by the nucleation of a new embryonic subduction system under E–W compressional stress since the Early Pliocene.

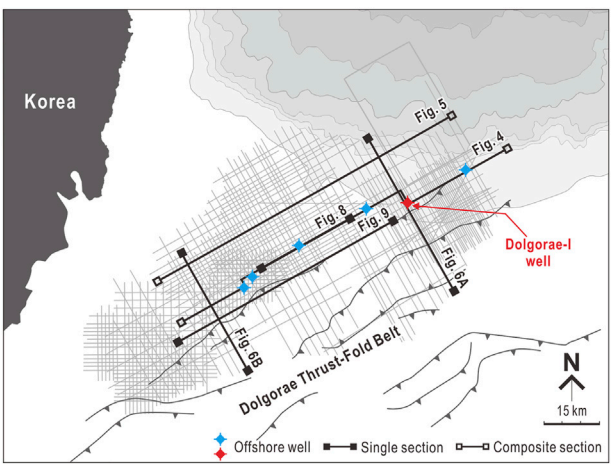

FIGURE 2 | Map showing seismic tracklines and well locations in the study area.

3 DATA AND METHODS

To reconstruct the tectostratigraphic evolution of the southwestern margin of the Ulleung Basin, we analyzed the stratal termination

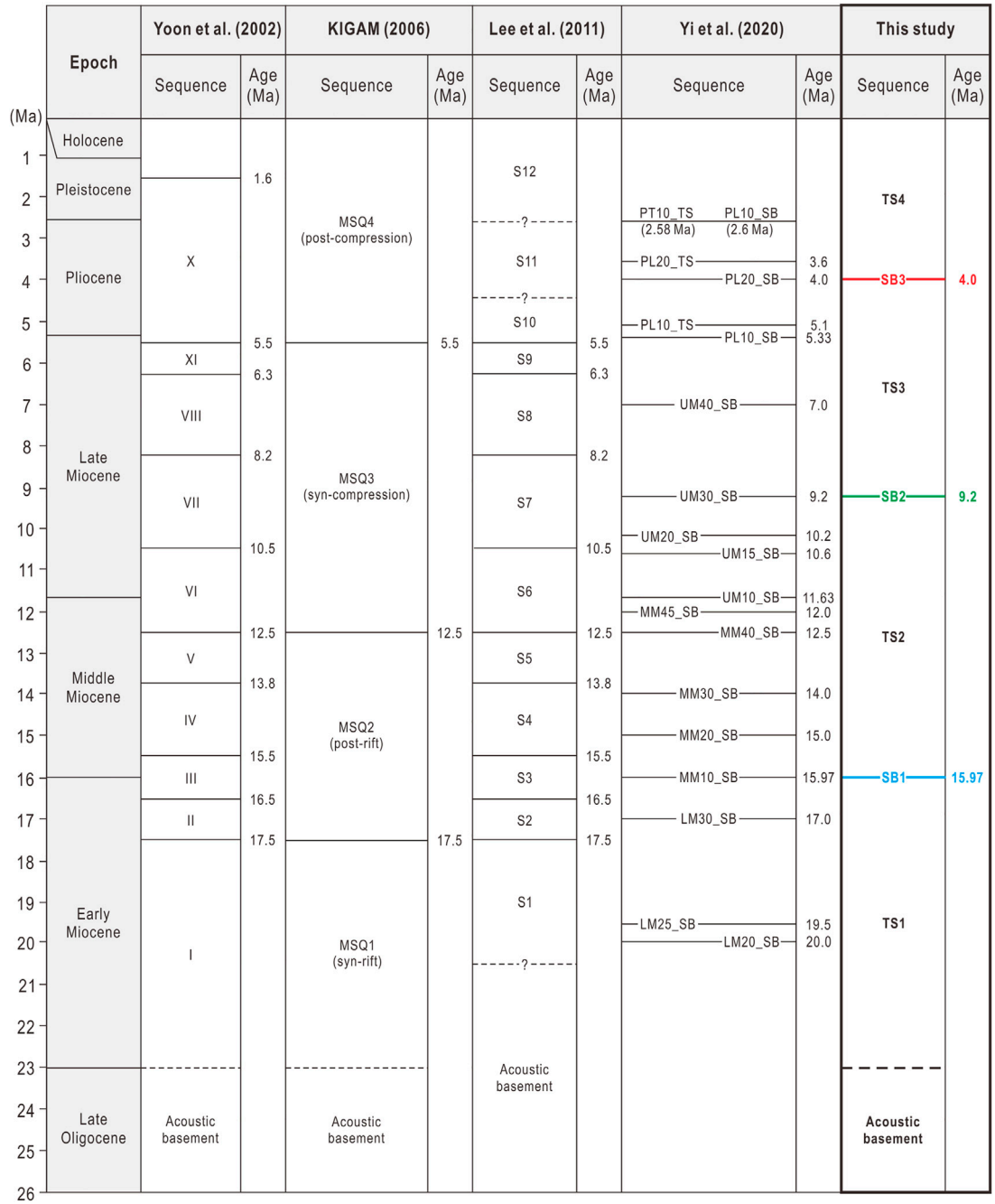

FIGURE 3 | Comparison of stratigraphic frameworks of the Ulleung Basin.

pattern, seismic facies, and deformation structures of the Neogene sedimentary succession based on 2D (a total of 6,448 line-km) and 3D multi-channel seismic reflection dataset acquired by the KNOC in 1983, 1988, 1989, 1992, 2005, and 2006 (**Figure 2**). The migrated seismic reflection data were fully digitized into SEG-Y format and uploaded to the PETREL™ (Schlumberger, Ltd., France) software for defining stratigraphic boundaries, correlating absolute ages, tracing the 3-dimensional geometry of the deformation structures, and creating time-structural and isochronal maps.

4 TECTOSTRATIGRAPHY OF THE SOUTHWESTERN ULLEUNG BASIN

For the last 40 years, considerable efforts have been made to understand the structural evolution and depositional history of the southwestern Ulleung Basin. Yet, the stratigraphic framework of this region is not in consensus (**Figure 3**). Yi et al. (2020) recently proposed an integrated chronostratigraphic framework of this region based on microfossil analysis of recovered sediment

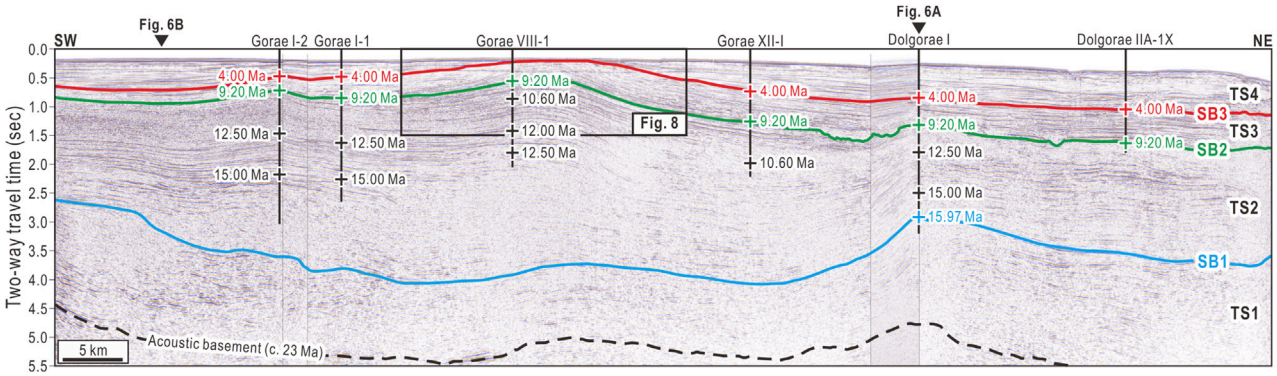

FIGURE 4 | NE–SW composite seismic reflection profile showing four tectostratigraphic sequences and ages of three sequence boundaries. For the locations of the seismic profile, see **Figure 2**. TS: Tectostratigraphic Sequence, SB: Sequence Boundary.

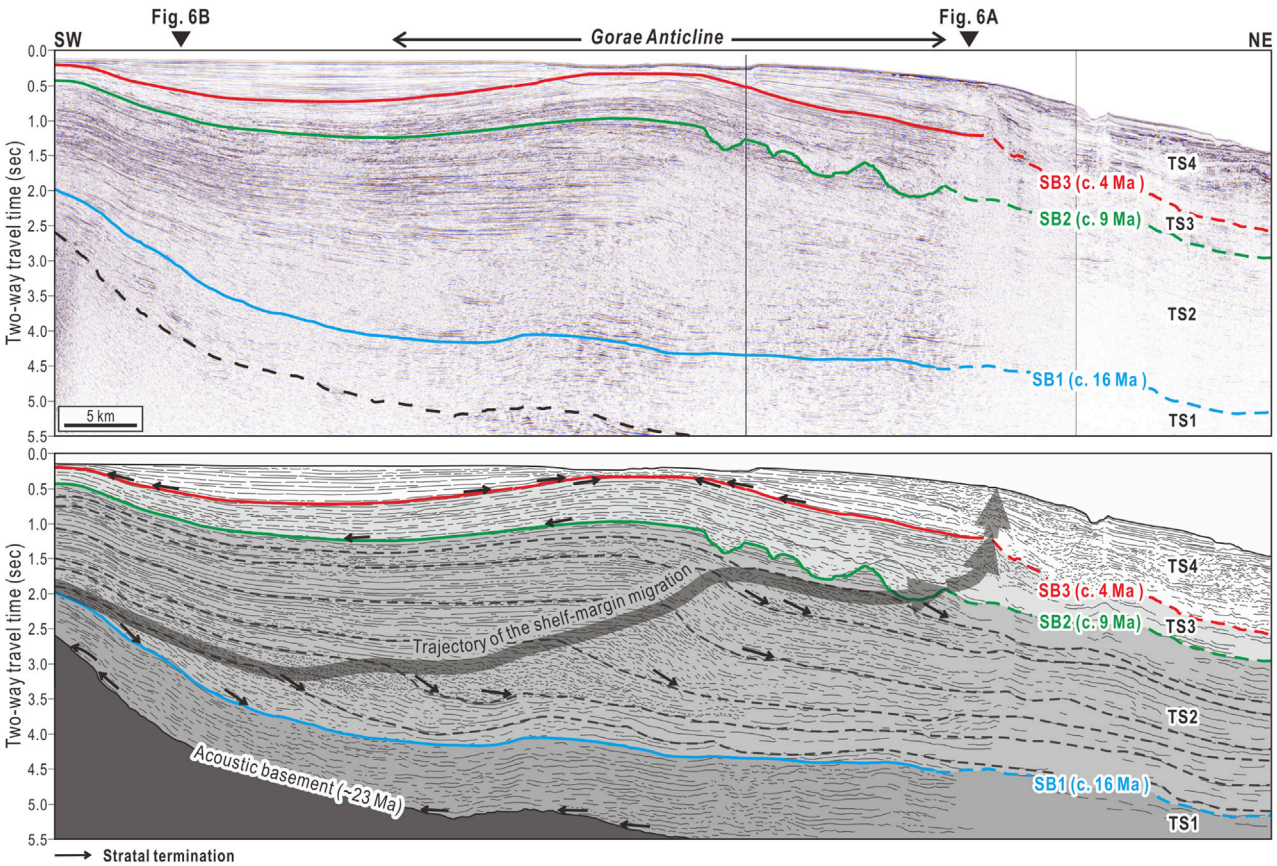

FIGURE 5 | NE–SW composite seismic reflection profile showing stratal configurations and external forms of the four tectostratigraphic sequences. For the locations of the seismic profile, see **Figure 2**. TS: Tectostratigraphic Sequence, SB: Sequence Boundary.

cores and correlation of drill wells with 2D and 3D multi-channel seismic reflection data (**Figure 3**). The new stratigraphic model divides the entire sedimentary succession of the southwestern Ulleung Basin into 20 chronostratigraphic units. We followed this framework.

In this study, we regrouped the 20 units into four tectostratigraphic sequences based on changes in deposition trends and characteristics of regional deformation, which are entitled TS1, TS2, TS3, and TS4, respectively (**Figure 4**). The respective boundaries of these sequences are named SB1, SB2, and

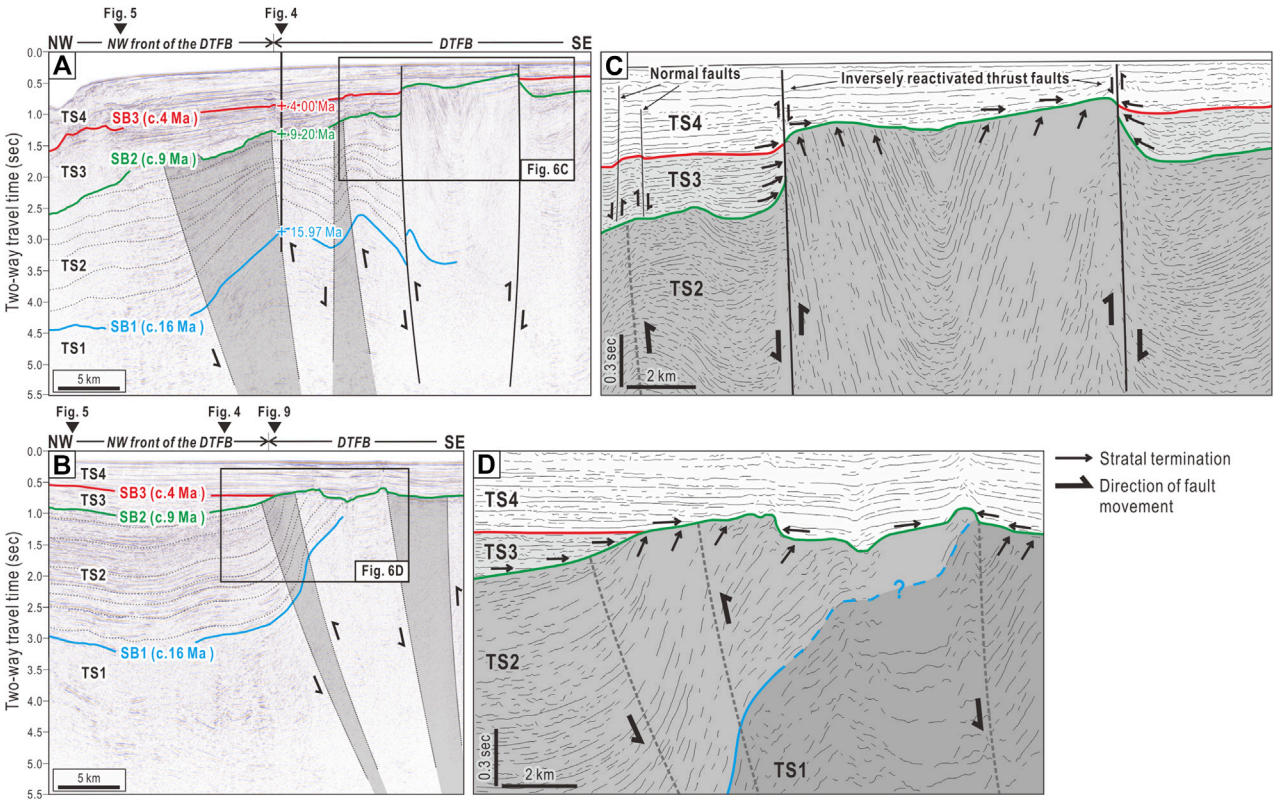

FIGURE 6 | Selected NW–SE seismic reflection profiles showing the Dolgorae Thrust-Fold Belt (DTFB). For the locations of the seismic profiles, see **Figure 2**. TS: Tectostratigraphic Sequence, SB: Sequence Boundary.

SB3, which are coeval with the boundaries, MM10_SB (c. 16 Ma), UM30_SB (c. 9 Ma), and PL20_SB (c. 4 Ma), proposed by Yi et al. (2020) (**Figure 3**). The terminology used to describe the external forms and reflection configurations of the tectostratigraphic sequences of this study follows Mitchum et al. (1977).

4.1 TS1 (c. 23? –16 Ma)

TS1 is the lowermost tectostratigraphic sequence of the Ulleung Basin, which as a whole exhibits a wedge-shaped fill-type external form (Mitchum et al., 1977) (**Figure 5**). The sequence gradually thickens toward the center of the basin with thickness ranging from 0.5 to 2.0 s TWT (two-way traveltime). On the southwestern slope of the Ulleung Basin, TS1 comprises discontinuous high-amplitude reflectors with lenticular or mounded depositional structures (**Figure 5**). These stratal characteristics are interpreted as accumulated submarine lobe or deep-sea fan deposits transported by high-concentration sediment gravity-flows, such as submarine debris flows (Weimer, 1990).

Toward the center of the basin, the proximal debris flow facies changes into distal dilute sediment gravity-flow facies, such as turbidite, marked by continuous, and subparallel reflectors with low reflection amplitudes (**Figure 5**) (Weimer, 1990). The strata in the lower part of TS1 show onlap termination against the slope of the acoustic basement (**Figure 5**). The lateral facies transition and lap-out character suggest that the TS1 comprises submarine mass-transport succession deposited in deep-sea-slope and basin-floor environments during the syn-rift phase of the Ulleung Basin evolution.

The acoustic basement under TS1 has a topography gradually gentle toward the center of the Ulleung Basin, below which the reflection character is faintly stratified or chaotic (**Figure 5**). Such seismic reflection facies are interpreted as rifted continental crust comprising the Jurassic–Cretaceous extrusive/intrusive/accretionary complex (Chough and Sohn. 2010), and syn-rift volcanic/sedimentary complexes (Yoon et al., 2003). SB1, the upper boundary of TS1, is correlated with MM10_SB (c. 16 Ma) (**Figure 3**).

4.2 TS2 (c. 16–9 Ma)

TS2 is the thickest tectostratigraphic sequence of the Ulleung Basin, complicated by syn-depositional thrust faults and folds (**Figure 6**). The thrusts and folds generally have ENE–WSW strikes and as a whole comprise a regional belt of thrust faults and folds, named DTFB, in the southern part of the study area (**Figure 7**). The stratal characteristics and external form of the TS2 within the domain of the DTFB are substantially different from those found in the northwestern frontal area of the DTFB (**Figure 7A**).

Within the DTFB, the original external form and stratal configurations of TS2 are destroyed by densely populated and imbricated thrust faults and folds (**Figures 6A,B**). Reflectors in this region show high-angle inclinations and truncational

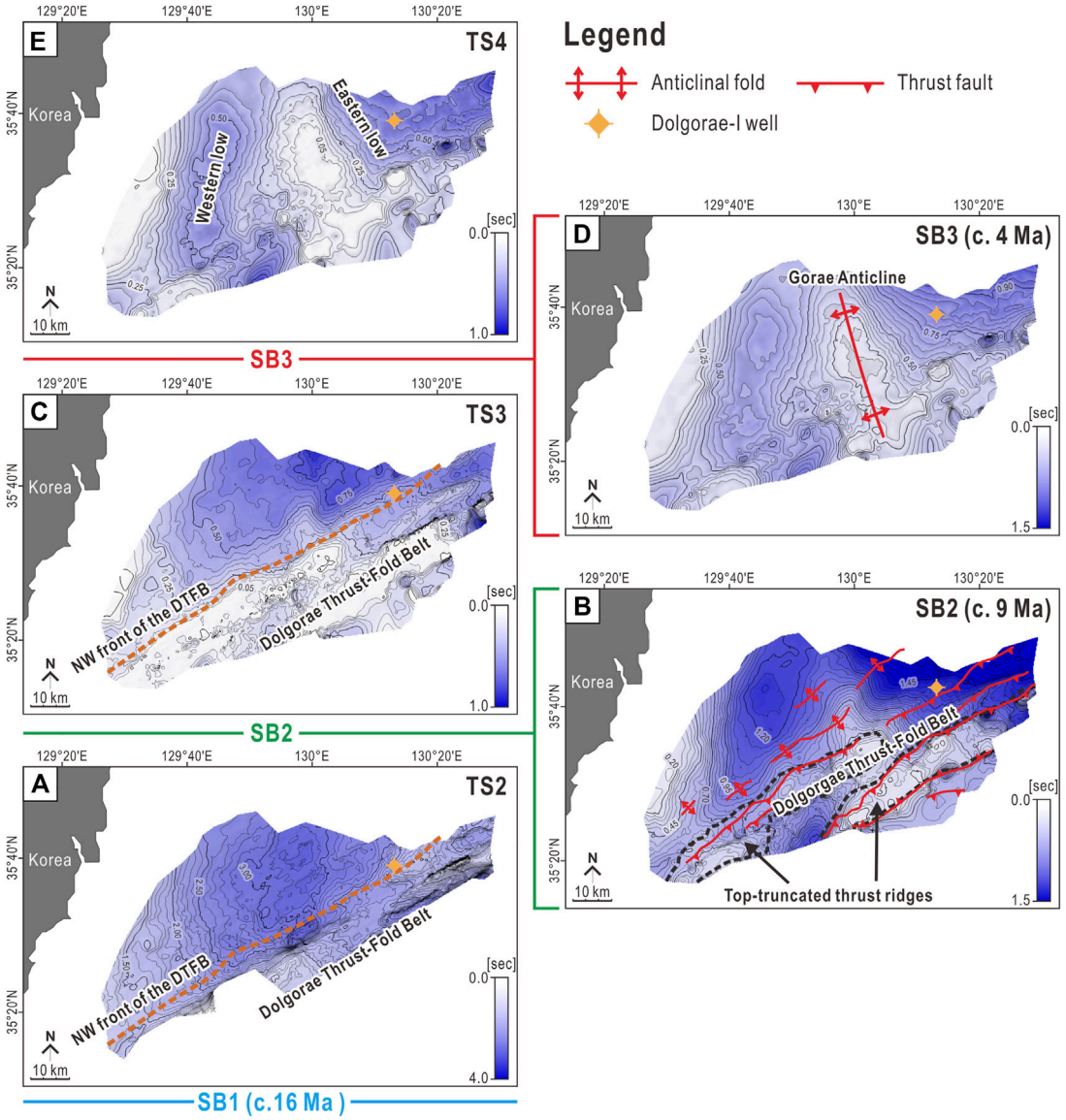

FIGURE 7 | (A), **(C)**, and **(E)** Isochronal maps showing spatial thickness variations of the TS2, TS3, and TS4. **(B)** and **(D)** Time-structural maps showing the topography of the SB2 and SB3. The thickness of the TS1 is not mappable due to poor definition of the acoustic basement and the SB1 in the study area. TS: Tectostratigraphic Sequence, SB: Sequence Boundary.

terminations against the upper boundary of the sequence (SB2) (**Figures 6C,D**). Such an erosional feature indicates shallow-marine wave planation of sedimentary substratum that emerged above sea level by compressional tectonic uplift (Kim et al., 2013). The top-truncational surfaces are situated on top of the two thrust ridges elongated more than 70 km toward the ENE in the study area (**Figure 7B**). Such a regional array of thrust ridges that accommodated a large amount of vertical tectonic uplift is identical to those found in the orogens and accretionary wedges (Miall, 1995).

On the northwestern front of the DTFB, TS2 comprises minorly deformed, continuous, and high-amplitude reflectors with divergent stratal configuration, indicating growth strata (**Figures 6A,B**). In this area, the sequence has a maximum thickness of approximately 3.5 s TWT and exhibits a slope-front-fill external form (Mitchum et al., 1977) (**Figure 6B**). Toward the basin center, the strata show a sigmoid-oblique progradational configuration (Mitchum et al., 1977), clearly divided into topset, foreset, and bottomset (**Figure 5**). Such a stratal character is interpreted as a prograding sedimentary wedge developed in a shelf-margin environment (Porębski and Steel, 2003). The aggradation/progradation ratio (A/P ratio) of the prograding wedge progressively increases throughout TS2, but abruptly decreases near the top of the sequence (**Figure 5**). Such a variation in the A/P ratio suggests accelerated relative sea level rise and accommodation creation during the early to middle

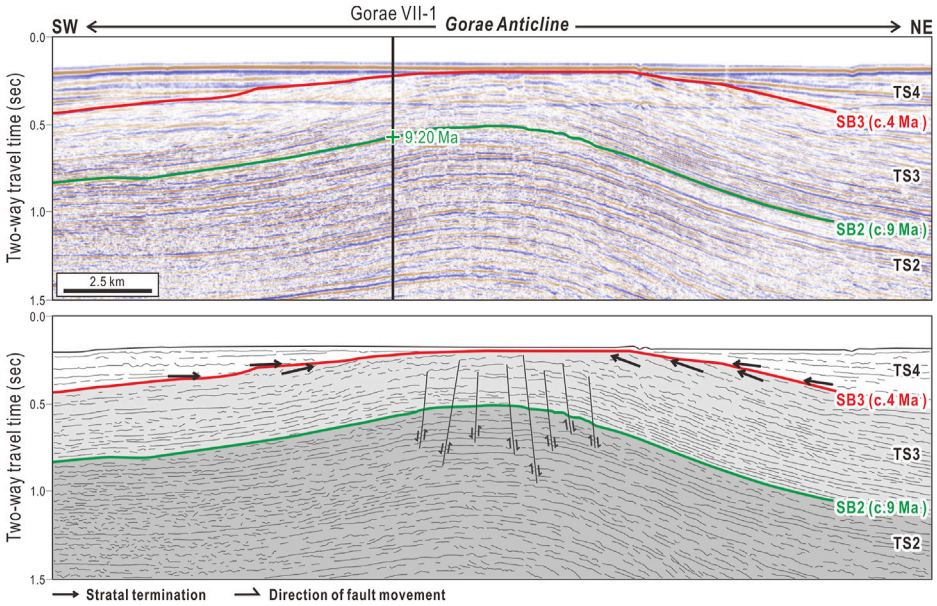

FIGURE 8 | Magnified NE–SW seismic reflection profile showing the details of the Gorae Anticline. For the position of the seismic profile, see **Figure 4**. TS: Tectostratigraphic Sequence, SB: Sequence Boundary.

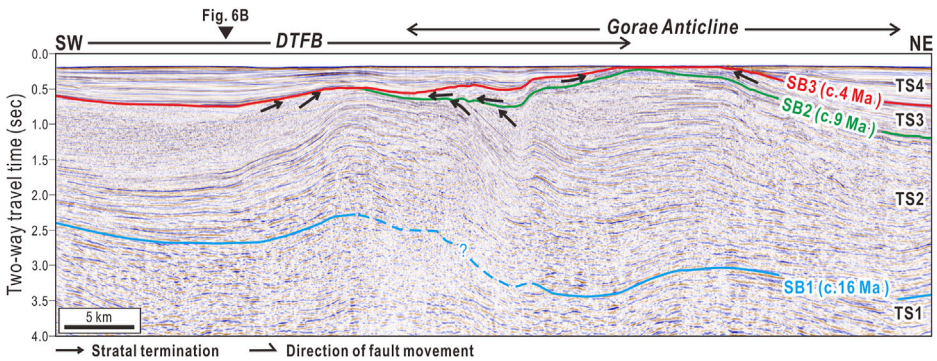

FIGURE 9 | Selected NE–SW seismic reflection profile showing the superposed feature of the DTFB and the Gorae Anticline. Two syn-deformational sequences (TS2 and TS4) of each structures are separated by intervening TS3 deposited during the Late Miocene. For the locations of the seismic profile, see **Figure 2**. TS: Tectostratigraphic Sequence. SB: Sequence Boundary.

depositional stages of the TS2, followed by abrupt deceleration of both in the terminal stage. SB2, the upper boundary of TS2, marks the end of the progradational deposition of TS2. The boundary is correlated with the UM30_SB (c. 9 Ma) of the existing chronostratigraphic framework (**Figure 3**).

4.3 TS3 (c. 9–4 Ma)

TS3 is the Late Miocene tectostratigraphic sequence of the Ulleung Basin, showing variable fill-type external forms. Within the domain of the DTFB, the TS3 fills topographic lows between ENE–WSW elongated thrust ridges with a maximum thickness of approximately 0.4 s TWT (**Figure 7C**). In this region, the strata composing the interior of the TS3 do not show any divergent configurations, but they show parallel alignment with high-angle onlap termination against fault scarps and fold limbs of the DTFB (**Figures 6C,D**). This stratal character suggests that TS3 was deposited not during but after the structural deformation of the DTFB.

On the northwestern front of the DTFB, TS3 has a wedge-shaped external form (Mitchum et al., 1977) that gradually thickens toward the northeast (**Figures 4**, **5**). In contrast to the underlying TS2, the TS3 in this region comprises strata not progradational but parallel, which terminates at a low angle against the lower boundary, SB2 (**Figure 5**). Ubiquitous channels are found near the base of TS3. The channels are generally 1–4 km wide and scour the marginal topset of the uppermost TS2 with a maximum erosional depth of 500 m

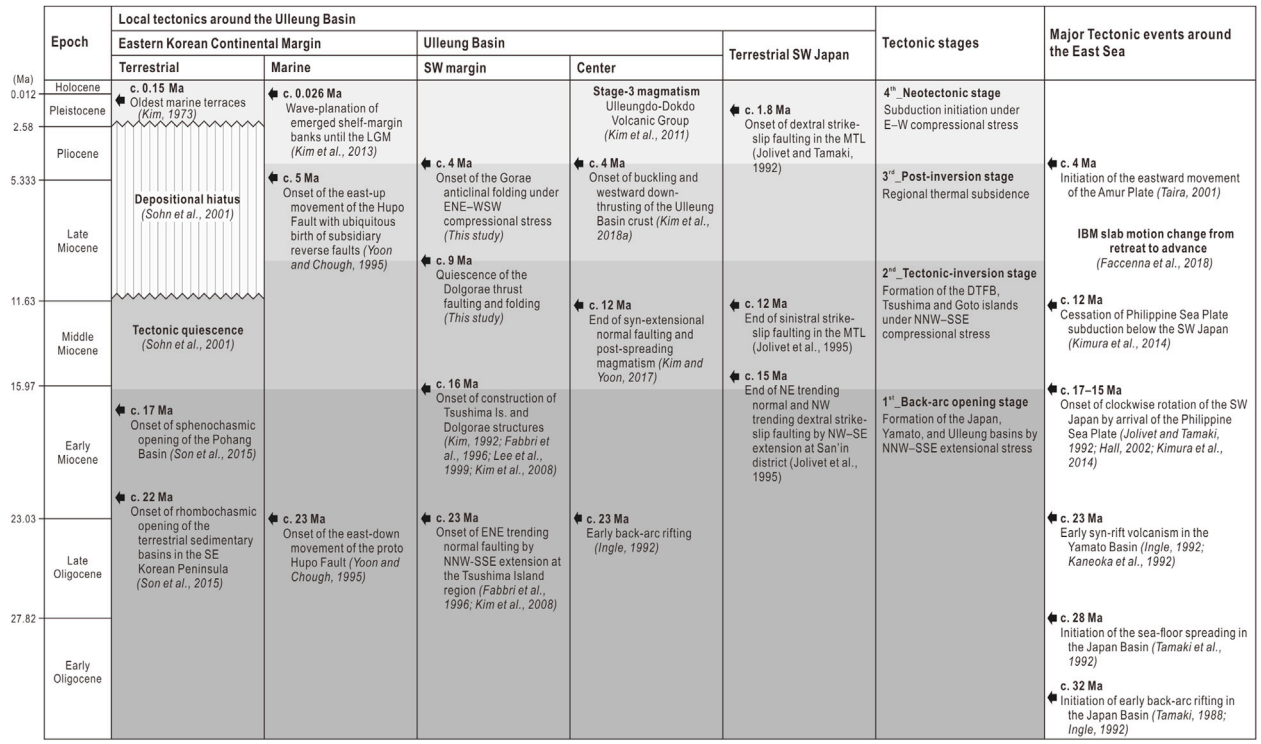

FIGURE 10 | Stratigraphic chart showing major tectonic events in the Ulleung Basin and surrounding regions. MTL: Median Tectonic Line, IBM: Izu-Bonin-Mariana.

(**Figure 5**). Such an erosional structure is interpreted as a shelf-margin channel formed by underloaded subaqueous sediment gravity-flows generated under condition of decreased sediment supply associated with relative sea level rise (Catuneanu, 2006; Arnott, 2010).

The upper boundary of the TS3 (SB3), correlated with the PL20_SB (c. 4 Ma) (**Figure 3**), has a conformable relationship with the overlying TS4 in almost all locations of the study area (**Figures 4**, **5**), except for the top of the NNW–SSE elongated anticlinal fold, named Gorae Anticline (**Figure 7D**).

4.4 TS4 (c. 4 Ma–present)

TS4 is the uppermost tectostratigraphic sequence of the Ulleung Basin that divergently fills two topographic lows to the west and east of the Gorae Anticline (**Figures 8**, **9**). TS4 is in a lenticular-fill external form on the west of the Gorae Anticline with a maximum thickness of approximately 0.5 s TWT, whereas in a wedge form on the east of the anticline, the thickness gradually increases toward the center of the Ulleung Basin (**Figure 7E**). Some of thrust faults in the DTFB extend upward and separate the strata of the TS3 and TS4 with inversed sense compared with that of the underlying TS2 (**Figure 6C**). This feature indicates that the thrust faults in the DTFB were normally reactivated during the deposition of the TS4 and possibly the TS3. The TS4 showing pronounced divergent-fill stratal configuration is interpreted as growth strata, suggesting that TS4 is the syn-deformational sedimentary sequence of the Gorae Anticline.

5 DISCUSSION

5.1 Stratigraphic Implications of the DTFB

We investigated the geometry and duration of the DTFB and Gorae Anticline based on the deformation and termination patterns of sedimentary strata in the syn- and post-deformational sequences of each structures. One of our key findings is that the DTFB and Gorae Anticline were formed during different periods under different tectonic settings.

The DTFB, comprising thrust faults and fault-propagation folds dipping southeastward, deforms TS1 and TS2 on the southwestern margin of the Ulleung Basin (**Figure 6**). The duration of structural deformation in the DTFB is difficult to constrain based only on seismic reflection analysis because densely populated thrust faults and folds disrupt the original sedimentary strata of the pre-and syn-deformational sequences. However, paleomagnetic and structural evidence found in the Korean Peninsula and the Tsushima-Goto islands region suggests that the DTFB started to develop at approximately 15 Ma (Kim, 1992; Fabbri et al., 1996; Lee et al., 1999; Kim et al., 2008). For the tectonic control of this regional compressional deformation, a hypothesis of pivotal rotation of SW Japan by the northeastward migration of the young Philippine Sea Plate during the early Middle Miocene was proposed (Kim, 1992; Lee et al., 1999). The pivotal rotation resulted in a dramatic change in tectonic stress from NNW–SSE extensional to NNW–SSE compressional. We entitle this

period of tectonic regime change as the "tectonic-inversion stage" (**Figure 10**).

Fabbri et al. (1996) suggested that the compressional deformation of the southwestern Ulleung Basin continued until approximately 10 Ma based on fault fracture analysis on the outcrop and radiometric ages of extrusive alkaline basalts that overlie the syn-deformational sedimentary units. This age constraint corresponds well with our results showing that the thrust faults of the DTFB cutting the TS1 and TS2 do not further deform the overlying TS3 deposited since c. 9 Ma (**Figures 6**, **9**). The parallel strata with high-angle onlap termination against fault scarps and fold limbs of the DTFB indicate that TS3 is a post-compressional sedimentary sequence that fills the topography of SB2.

The flattened top of the thrust ridges situated along the center of the DTFB is interpreted to have formed by wave planation of the emerged thrust blocks (Kim et al., 2013). These time-transgressive erosional surfaces are correlated with SB2 (c. 9 Ma) in the northwestern frontal area of the DTFB (**Figures 6A,B**). This suggests that the wave planation of the emerged thrust blocks ceased at approximately 9 Ma.

5.2 Gorae Anticline: A Product of Compressional Neotectonics on Eastern Eurasia

The Gorae Anticline is a typical symmetrical fold with a near-vertical axial plane oriented ~ N22W (**Figure 9C**). The fold deforms the entire sedimentary succession below SB3 (c. 4 Ma). This indicates that anticlinal deformation initiated at approximately 4 Ma. The TS4 around the Gorae Anticline has a typical growth stratal configuration, which implies that the deformation is in progress during the Quaternary period.

The tectonic control underlying the Gorae Anticline remains unsettled. However, given the age and fold-axis orientation, the anticlinal fold is inferred to have a genetic relationship with the major thrust and crustal buckles in the Ulleung Basin, which may imply embryonic subduction initiated in the Early Pliocene (Gi-Bom Kim et al., 2018). Gi-Bom Kim et al. (2018) proposed that the regional E–W compressional far-field stress predominated over eastern Eurasia since the Early Pliocene induced crustal shortening and embryonic subductions along the western and eastern margins of the East Sea. We envisage that the Gorae Anticline, located on the southwestern margin of the Ulleung Basin, is also a product of the compressional neotectonics governing eastern Eurasia since the Early Pliocene.

5.3 Post-Inversion Tectonic Quiescence

Tectonic stresses gradually deform the topography of the sedimentary basins over time. The progressive increase in sedimentary accommodation by tectonic deformation results in a characteristic style of stratal configuration, the so-called growth strata. If the tectonic event is over, subsequent sediment deposition proceeds in a way that sediments simply fill the topography, leaving behind parallel onlap-fill stratal configurations. Thus, people utilize the seismic facies

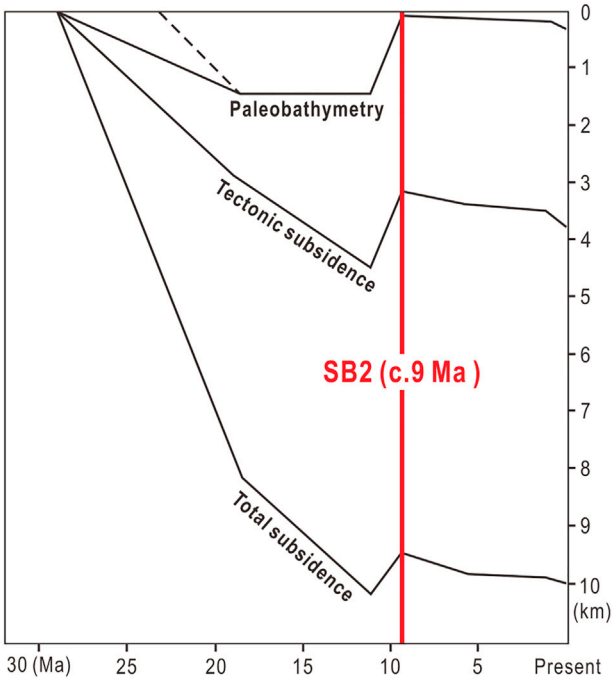

FIGURE 11 | Subsidence curves recovered from paleobatymetric data of the Dolgorae-I exploratory well (modified after Chough and Barg, 1987 and Ingle, 1992). Total subsidence is the sum of the thermotectonic subsidence, isostatic sedimentary loading, and sediment compaction. Note: the red line marks the inflection point of subsidence rate from negative to positive. The abrupt change in subsidence rate implies that the uplifting of the DTFB was ceased at c. 9 Ma.

boundary between the growth and onlap-fill stratal configurations as a marker of the cessation of a certain tectonic event (Shaw et al., 2005).

The TS3 overlying the growth strata of TS2 shows apparent parallel onlap-fill stratal patterns (**Figure 6**). Reverse faults and fault-tip folds of the DTFB are no longer found in this sequence. Such lines of evidence indicate that TS3 was deposited after the cessation of the preceding compressional tectonics. The TS3 as a whole gradually thickens toward the center of the Ulleung Basin without any progradational sedimentary feature (**Figures 4**, **5**). This infers a slow and consistent sagging of the entire southwestern Ulleung Basin region, most likely due to the combined influence of sedimentary loading and thermal contraction of the back-arc lithosphere. We entitle this quiescent tectonic stage from 9 to 4 Ma to the "post-inversion stage" (**Figure 10**). In this period, the motion of the Izu-Bonin-Mariana (IBM) slab was changed from retreat to advance (Faccenna et al., 2018). We infer that this post-inversion tectonic quiescence is genetically related with the cessation of the Philippine Sea Plate subduction below the SW Japan (Kimura et al., 2014).

The subsidence rates during this post-inversion stage of the East Sea, calculated from the ODP and DSDP cores on the East Sea margins, range from 50 to 100 m/Myr, which is significantly lower than the subsidence rate during the period of the Miocene

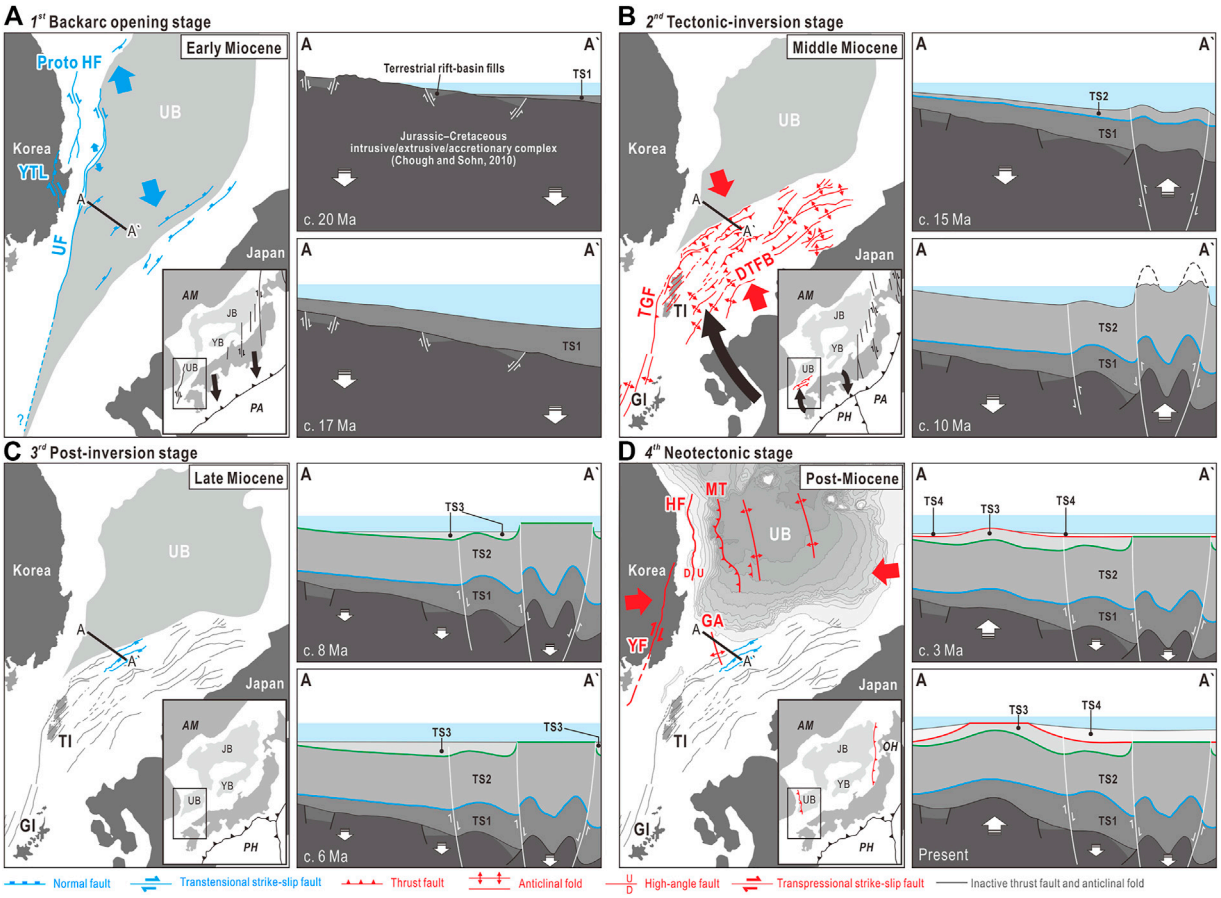

FIGURE 12 | Four-stage tectonic model of the Ulleung Basin showing details of structural characteristics in association with changes in relative locations of the surrounding tectonic plates. **(A)** Back-arc opening stage (c. 23–16 Ma). **(B)** Tectonic-inversion stage (c. 16–9 Ma). **(C)** Post-inversion stage (c. 9–4 Ma). **(D)** Neotectonic stage (c. 4 Ma–present). AM: Amur Plate, PA: Pacific Plate, PH: Philippine Sea Plate, OH: Okhotsk Plate, UB: Ulleung Basin, YB: Yamato Basin, JB: Japan Basin, TI: Tsushima Island, GI: Goto Island, YTL: Yeonil Tectonic Line, UF: Ulleung Fault. TGF: Tsushima-Goto Fault, DTFB: Dolgorae Thrust-Fold Belt, YF: Yangsan Fault, HF: Hupo Fault, MT: Major Thrust, GA: Gorae Anticline.

back-arc extension (>900 m/Myr) (Ingle, 1992). The paleobathymetric data of the Dolgorae-1 well shows that the uplift of the DTFB was terminated at approximately 9 Ma, which was followed by slow subsidence (~100 m/Myr in total subsidence rate) continued until the present (**Figure 11**) (Chough and Barg, 1987; Ingle, 1992).

5.4 A New 4-Stage Tectonic Model of the Ulleung Basin

Previous seismic reflection studies of the southwestern Ulleung Basin have interpreted the Gorae anticlinal folding as a continuous deformation feature of the DTFB (Lee et al., 2011; Yoon et al., 2014). Based on this structural interpretation, the tectonic evolution of the Ulleung Basin was divided into two phases: the back-arc opening phase (c. 23–16 Ma) and the back-arc closure phase (after c. 16 Ma). In this study, we report that the DTFB and the Gorae Anticline are temporally and tectonically separable events with an intervening phase of tectonic quiescence lasting for more than 5 Myr. Based on this new structural interpretation, we propose a new 4-stage tectonic model of the Ulleung Basin (**Figure 12**).

5.4.1 Stage I: Back-Arc Opening Stage (c. 23–16 Ma)

The first-stage tectonic evolution of the Ulleung Basin is marked by a pull-apart-style back-arc opening during the Early Miocene (Lallemand and Jolivet, 1986). At this stage, continental rifting was guided by NNW-oriented strike-slip faults, such as the Ulleung Fault, the proto Hupo Fault, and the Yeonil Tectonic Line, together comprising the western principal deformation zone (**Figure 12A**) (Yoon and Chough, 1995; Yoon et al., 1997; Son et al., 2015). In the southwestern margin of the Ulleung Basin, early continental rifting began to form graben or half-graben basins on the Jurassic or Cretaceous basement (Chough and Sohn, 2010). Around 20 Ma, it appears that the entire Ulleung Basin region was converted to a marine environment (Kim et al., 2013). The study area might have been located on the southwestern lower slope of this early marine basin, where sediment gravity-flows pile up a thick syn-extensional sedimentary sequence of the TS1 (**Figure 12A**).

Given the Early Miocene marine sandstones and siltstones exposed on Tsushima and Goto islands (Fabbri et al., 1996), we infer that the early Ulleung Basin covered a much wider area toward the SW compared with the present realm of the basin.

5.4.2 Stage II: Tectonic-Inversion Stage (c. 16–9 Ma)

At approximately 16 Ma, the young Philippine Sea Plate migrating northeastward along the Ryukyu Trench began to replace the pre-existing Pacific Plate (Hall, 2002). The onset of a young subduction zone began to rotate the southwestern Japanese islands clockwise (Jolivet and Tamaki, 1992), which consequently induced crustal shortening in the southwestern Ulleung Basin margin. This stage of stress regime change from extension to compression is called the tectonic-inversion stage.

In this tectonic-inversion stage, a regional NNE-to ENE-trending curvilinear array of contractile structures, such as the DTFB and the Tsushima and Goto islands, were formed (**Figure 12B**). The TS2 deposited during the tectonic inversion was gradually compressed and uplifted to form ENE-elongated submarine thrust ridges. When the thrust ridges reached sea level, wave action began to cut and bevel the emerged summits of the ridges, and leaving behind broad wave planation surfaces (**Figure 12B**). Our stratigraphic correlation indicates that the compressional uplifting and wave planation of the TS2 continued until approximately 9 Ma.

Sediments originating from variable terrestrial sources and slope-failure events during the tectonic inversion were transported toward the northwestern frontal area of the DTFB, which constructed a gigantic progradational sedimentary structure (**Figure 5**).

5.4.3 Stage III: Post-Inversion Stage (c. 9–4 Ma)

At approximately 10 Ma, the Philippine Sea Plate appears to have arrived at the present-day position (Hall, 2002). Given the parallel onlap-fill stratal configurations of the TS3 lacking deformation by reverse fault, the inversion tectonics of the DTFB has not been active since this time. Paleobathymetric investigation of the sediment drill core recovered from the Dolgorae-I exploratory well (see **Figures 2**, **7** for the well location) show that the period of tectonic uplift ceased at approximately 9 Ma (**Figure 12C**). The significantly decreased subsidence rates thereafter (~100 m/Myr) may suggest that a new tectonic stage of slow thermal subsidence began at this time (Chough and Barg, 1987; Ingle, 1992).

As the regional compressional stress perished at approximately 9 Ma, the DTFB and Tsushima-Goto islands began to subside slowly by isostatic loading and thermal contraction of the back-arc lithosphere. Some of the thrust faults in the DTFB began to reactivate normally (**Figure 12C**). Moreover, the wave planation process on the thrust ridges ceased as the southwestern Ulleung Basin region began to subside again. Sediments supplied during this post-inversion stage formed TS3 by simply filling the deformation topography.

5.4.4 Stage IV: Neotectonic Stage (c. 4 Ma–Present)

Geodetic investigations suggested that the Amur Plate initiated its present eastward movement relative to the Pacific Plate at approximately 4 Ma (Taira, 2001). This new relative plate motion since 4 Ma induced a regional E–W compressional stress over the northeastern Asia, which began to tectonically deform the East Sea and adjacent regions in a style entirely different from those during the preceding tectonic stages (**Figure 12D**).

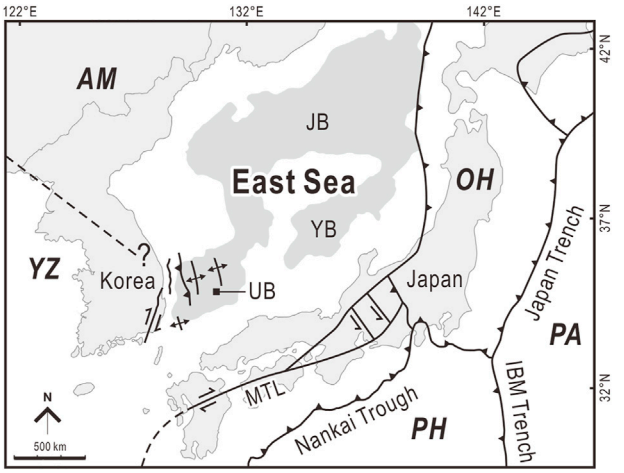

FIGURE 13 | Regional map showing parallelly aligned neotectonic structures over the East Sea. AM: Amur Plate, OH: Okhotsk Plate, PA: Pacific Plate, PH: Philippine Sea Plate, YZ: Yangtze Plate, MTL: Median Tectonic Line, IBM: Izu-Bonin-Mariana, UB: Ulleung Basin, YB: Yamato Basin, JB: Japan Basin.

Such an E–W compression made the extended back-arc crust of the Ulleung Basin buckled and thrusted down below the eastern Korean continental margin (Gi-Bom Kim et al., 2018). Along with this compressional deformation of the Ulleung Basin center, the southwestern margin began to develop the Gorae anticlinal fold. Given the identical ages (c. 4 Ma) and fold-axis orientations (~N22W), we infer that the Gorae Anticline and the crustal buckles have a common tectonic origin.

In the eastern Korean continental margin, the proto Hupo Fault with east-down normal fault-plane geometry was reactivated in the present east-up sense (Yoon and Chough, 1995). This fault reactivation formed a wedge-shaped post-Miocene sedimentary basin, named the Hupo Basin on the offshore Korean margin (**Figure 12D**). The NNE–SSW trending terrestrial Yangsan Fault on the southeastern Korean Peninsula was reactivated into a dextral strike-slip fault under this Quaternary E–W compressional stress regime (Han-Joon Kim et al., 2016).

On the eastern margin of the East Sea, there have been at least five abnormally large-magnitude seismic events over M6.9 since 1940 (Tamaki and Honza, 1985). To understand the tectonic origin of such earthquakes in this marginal region, a large amount of geological and geophysical efforts has been made (Nakamura, 1983; Tamaki and Honza, 1985; Lallemand and Jolivet, 1986; Sato et al., 1986; Tamaki, 1986; Tamaki, 1988; Jolivet et al., 1991; Ingle, 1992; Jolivet and Tamaki, 1992; Jolivet et al., 1995; Taira, 2001; No et al., 2014). Based on the monitoring of large-magnitude earthquakes and their aftershock distributions, people visualize crustal-scale rupture along the boundary between NE Japan and

the East Sea, and which may imply a modern subduction initiation (Sato et al., 1986; No et al., 2014). Based on geodetic and structural investigations, the northeastern Japanese islands are broadly accepted as a plate independent from the Amur Plate, and named the Okhotsk Plate (**Figure 13**) (Nakamura, 1983; Taira, 2001).

In contrast to the Japanese side, the Korean side of the East Sea has long been regarded as tectonic dormancy. This is largely due to the absence of large-magnitude earthquakes during the last decades in the Korean Peninsula and partly to the poor understanding of the Quaternary structures around the eastern Korean margin. However, such an old stereotype is slowly changing since two earthquakes with magnitudes of 5.8 and 5.4 occurred in 2016 and 2017, respectively, on the southeastern margin of the Korean Peninsula (YoungHee Kim et al., 2016; Kwang-Hee Kim et al., 2018). More recently, Gi-Bom Kim et al. (2018) reported crustal buckling and westward underthrusting of the Ulleung Basin, which may indicate the early stage of incipient subduction (**Figure 13**). The incipient subduction is very subtle and unclear as to whether it is still active. However, one thing is obvious that the eastern margin of the Korean Peninsula is not tectonically dormant, given lines of evidence, such as the Holocene marine terraces (Choi et al., 2008) and frequent moderate-magnitude seismic activities (Choi et al., 2012). We believe that our new tectostratigraphic concept will aid in understanding the nature of the Korean and East Sea neotectonics.

6 CONCLUSION

In this study, we investigated tectostratigraphic evolution of the southwestern Ulleung Basin margin based on the 2D and 3D multi-channel seismic reflection data set and offshore drilled wells. This research has drawn following conclusions:

1) Sedimentary successions on the southwestern margin of the Ulleung Basin are divided into four tectostratigraphic sequences (TS1, TS2, TS3, and TS4).
2) The DTFB was active from approximately 16 Ma to 9 Ma under NNW–SSE compressional stress regime.
3) The Gorae Anticline has been active from approximately 4 Ma to the present.
4) Tectonic quiescent stage existed between the formations of the DTFB and the Gorae Anticline.
4) The tectonic evolution of the Ulleung Basin is summarized into four stages: Stage-1) back-arc opening stage (c. 23–16 Ma), Stage-2) tectonic-inversion stage (c. 16–9 Ma), Stage-3) post-inversion stage (c. 9–4 Ma), and Stage-4) neotectonic stage (c. 4 Ma–present).

The post-Miocene neotectonic stage of the Ulleung Basin is first conceptualized in our study. This tectonic regime contains variable geological features juxtaposed along the western margin of the East Sea (i.e., the major thrust, crustal buckles, Hupo Fault, marine terraces, and Gorae Anticline). To understand their genetic relationship, more surgical investigations based on geodetic, and geophysical methods are required.

DATA AVAILABILITY STATEMENT

The seismic reflection and well data used for this study are important properties of the KNOC and are not open access. However, the data may become accessible to people who have been permitted by KNOC.

AUTHOR CONTRIBUTIONS

J-HL: formal analysis, investigation, and writing—original draft, J-HL: formal analysis, S-HY: validation, H-SL: validation and project administration, H-YS: data curation, G-BK: conceptualization, writing—original draft, writing—review and editing, and supervision.

FUNDING

This research was supported by the Korea Institute of Geoscience and Mineral Resources (No. GP2020-006), Korea Meteorological Administration Research Development Program (KMI 2018-02810), National Research Foundation of Korea (NRF-2018R1A1A1A0507746513), Basic Research Program of Pusan National University (202014360001 and 202015720001), and Ministry of the Interior and Safety as Human Resource Development Project in Earthquake Disaster Management.

ACKNOWLEDGMENTS

We appreciate editor, H-JK, and two reviewers, SL and LJ, for their kind comments. We also thank the KNOC for permission to use data set.

REFERENCES

Arnott, R. W. C. (2010). "Deep-Marine Sediments and Sedimentary Systems," in *Facies Models 4*. Editors N. P. James and R. W. Dalrymple (Canada: Geological Association of Canada Press), 295–322.

Bahk, J.-J., Kang, N. K., Yi, B.-Y., Lee, S.-H., Jeong, S.-W., Urgeles, R., et al. (2017). Sedimentary Characteristics and Processes of Submarine Mass-Transport Deposits in the Ulleung Basin and Their Relations to Seismic and Sediment Physical Properties. *Mar. Geology.* 393, 124–140. doi:10.1016/j.margeo.2017.05.010

Catuneanu, O. (2006). *Principles of Sequence Stratigraphy*. Amsterdam: Elsevier Press.

Cheon, Y., Choi, J.-H., Kim, N., Lee, H., Choi, I., Bae, H., et al. (2020). Late Quaternary Transpressional Earthquakes on a Long-Lived Intraplate Fault: A Case Study of the Southern Yangsan Fault, SE Korea. *Quat. Int.* 553, 132–143. doi:10.1016/j.quaint.2020.07.025

Choi, S.-J., Merritts, D. J., and Ota, Y. (2008). Elevations and Ages of Marine Terraces and Late Quaternary Rock Uplift in Southeastern Korea. *J. Geophys. Res.* 113 (B10), 1–15. doi:10.1029/2007JB005260

Choi, H., Hong, T.-K., He, X., and Baag, C.-E. (2012). Seismic Evidence for Reverse Activation of a Paleo-Rifting System in the East Sea (Sea of Japan). *Tectonophysics* 572-573 (17), 123–133. doi:10.1016/j.tecto.2011.12.023

Chough, S. K., and Barg, E. (1987). Tectonic History of Ulleung Basin Margin, East Sea (Sea of Japan). *Geology* 15 (1), 45–48. doi:10.1130/0091-7613(1987)15<45:thoubm>2.0.co;2

Chough, S. K., and Sohn, Y. K. (2010). Tectonic and Sedimentary Evolution of a Cretaceous Continental Arc–Backarc System in the Korean Peninsula: New View. *Earth-Science Rev.* 101 (3–4), 225–249. doi:10.1016/j.earscirev.2010.05.004

Chough, S. K., Lee, H. J., and Yoon, S. H. (2000). *Marine Geology of Korean Seas*. Amsterdam: Elsevier Press.

Cukur, D., Um, I.-K., Bahk, J.-J., Chun, J.-H., Horozal, S., Kim, S.-R., et al. (2018). Seismic Stratigraphy and Structural Characteristics of the Northeastern Continental Margin of Korea in the East Sea (Sea of Japan). *Mar. Pet. Geology.* 98, 706–717. doi:10.1016/j.marpetgeo.2018.09.013

Fabbri, O., Charvet, J., and Fournier, M. (1996). Alternate Senses of Displacement along the Tsushima Fault System during the Neogene Based on Fracture Analyses Near the Western Margin of the Japan Sea. *Tectonophysics* 257 (2–4), 275–295. doi:10.1016/0040-1951(95)00151-4

Faccenna, C., Holt, A. F., Becker, T. W., Lallemand, S., and Royden, L. H. (2018). Dynamics of the Ryukyu/Izu-Bonin-Marianas Double Subduction System. *Tectonophysics* 746, 229–238. doi:10.1016/j.tecto.2017.08.011

Hall, R. (2002). Cenozoic Geological and Plate Tectonic Evolution of SE Asia and the SW Pacific: Computer-Based Reconstructions, Model and Animations. *J. Asian Earth Sci.* 20 (4), 353–431. doi:10.1016/S1367-9120(01)00069-4

Horozal, S., Chae, S., Seo, J. M., Lee, S. M., Han, H. S., Cukur, D., et al. (2021). Quaternary Evolution of the Southeastern Korean Continental Shelf, East Sea: Paleo-Incised Valley and Channel Systems. *Mar. Pet. Geology.* 128, 105011. doi:10.1016/j.marpetgeo.2021.105011

Ingle, J. C. J. (1992). Subsidence of the Japan Sea: Stratigraphic Evidence from ODP Sites and Onshore Sections. *Proc. ODP. Sci. Results* 127/128 (2), 1197–1218. doi:10.2973/odp.proc.sr.127128-2.132.1992

Jolivet, L., and Tamaki, K. (1992). Neogene Kinematics in the Japan Sea Region and Volcanic Activity of the Northeast Japan Arc. *Proc. ODP. Sci. Results* 127/128 (2), 1311–1331. doi:10.2973/odp.proc.sr.127128-2.239.1992

Jolivet, L., Huchon, P., Brun, J. P., Le Pichon, X., Chamot-Rooke, N., and Thomas, J. C. (1991). Arc Deformation and Marginal basin Opening: Japan Sea as a Case Study. *J. Geophys. Res.* 96 (B3), 4367–4384. doi:10.1029/90JB02455

Jolivet, L., Shibuya, H., and Fournier, M. (1995). "Paleomagnetic Rotations and the Japan Sea Opening," in *Active Margins and Marginal Basins of the Western Pacific, Geophys. Monogr. Ser. 88*. Editors B. Taylor and J. Natland (Washington D. C.: AGU Press), 355–369. doi:10.1029/GM088p0355

Kaneoka, I., Notsu, K., Takigami, Y., Fujioka, K., and Sakai, H. (1990). Constraints on the Evolution of the Japan Sea Based on ^{40}Ar-^{39}Ar Ages and Sr Isotopic Ratios for Volcanic Rocks of the Yamato Seamount Chain in the Japan Sea. *Earth Planet. Sci. Lett.* 97 (1–2), 211–225. doi:10.1016/0012-821X(90)90109-B

Kaneoka, I., Takigami, Y., Takaoka, N., Yamashita, S., and Tamaki, K. (1992). 40Ar-39Ar Analysis of Volcanic Rocks Recovered from the Japan Sea Floor: Constraints on the Age of Formation of the Japan Sea. *Proc. ODP. Sci. Results* 127/128 (2), 819–836. doi:10.2973/odp.proc.sr.127128-2.200.1992

KIGAM (Korea Institute of Geoscience and Mineral Resources) (2006). Research on Stratigraphy and Tectonics of Southeastern Korean Offshore Using Seismic Exploration Technology OAA2004005-2006 (3), 332.

Kim, G. B., and Yoon, S.-H. (2017). An Insight into Asymmetric Back-Arc Extension: Tecto-Magmatic Evidences from the Ulleung Basin, the East Sea (Sea of Japan). *Tectonophysics* 717, 182–192. doi:10.1016/j.tecto.2017.07.016

Kim, H. G., Song, C. W., Kim, J. S., Son, M., and Kim, I. S. (2008). Tertiary Geological Structures and Deformation History of the Southern Tsushima Island, Japan. *J. Geo. Soc. Korea* 44 (2), 175–198.

Kim, G. B., Yoon, S. H., Chough, S. K., Kwon, Y. K., and Ryu, B. J. (2011). Seismic Reflection Study of Acoustic Basement in the South Korea Plateau, the Ulleung Interplain Gap, and the Northern Ulleung Basin: Volcano-Tectonic Implications for Tertiary Back-Arc Evolution in the Southern East Sea. *Tectonophysics* 504 (1–4), 43–56. doi:10.1016/j.tecto.2011.02.004

Kim, G. B., Yoon, S. H., Sohn, Y. K., and Kwon, Y. K. (2013). Wave-Planation Surfaces in the Mid-Western East Sea (Sea of Japan): Indicators of Subsidence History and Paleogeographic Evolution of Back-Arc Basin. *Mar. Geology.* 344, 65–81. doi:10.1016/j.margeo.2013.07.008

Kim, H.-J., Moon, S., Jou, H.-T., Lee, G. H., Yoo, D. G., Lee, S. H., et al. (2016). The Offshore Yangsan Fault Activity in the Quaternary, SE Korea: Analysis of High-Resolution Seismic Profiles. *Tectonophysics* 693, 85–95. doi:10.1016/j.tecto.2016.10.034

Kim, Y., Rhie, J., Kang, T.-S., Kim, K.-H., Kim, M., and Lee, S.-J. (2016). The 12 September 2016 Gyeongju Earthquakes: 1. Observation and Remaining Questions. *Geosci. J.* 20 (6), 747–752. doi:10.1007/s12303-016-0033-x

Kim, G.-B., Yoon, S.-H., Kim, S.-S., and So, B.-D. (2018). Transition from Buckling to Subduction on Strike-Slip Continental Margins: Evidence from the East Sea (Japan Sea). *Geology* 46 (7), 603–606. doi:10.1130/G40305.1

Kim, K.-H., Ree, J.-H., Kim, Y., Kim, S., Kang, S. Y., and Seo, W. (2018). Assessing whether the 2017 Mw 5.4 Pohang Earthquake in South Korea Was an Induced Event. *Science* 360 (6392), 1007–1009. doi:10.1126/science.aat6081

Kim, S. W. (1973). A Study on the Terraces along the Southeastern Coast (Bang-Eojin–Pohang) of the Korean Peninsula. *J. Geo. Soc. Korea* 9 (2), 89–121. doi:10.3348/jkrs.1973.9.1.16

Kim, I. S. (1992). Origin and Tectonic Evolution of the East Sea (Sea of Japan) and the Yangsan Fault System: A New Synthetic Interpretation. *J. Geo. Soc. Korea* 28 (1), 84–109.

Kimura, G., Hashimoto, Y., Kitamura, Y., Yamaguchi, A., and Koge, H. (2014). Middle Miocene Swift Migration of the TTT Triple Junction and Rapid Crustal Growth in Southwest Japan: A Review. *Tectonics* 33 (7), 1219–1238. doi:10.1002/2014TC003531

Lallemand, S., and Jolivet, L. (1986). Japan Sea: A Pull-Apart Basin? *Earth Planet. Sci. Lett.* 76 (3–4), 375–389. doi:10.1016/0012-821X(86)90088-9

Lee, Y. S., Ishikawa, N., and Kim, W. K. (1999). Paleomagnetism of Tertiary Rocks on the Korean Peninsula: Tectonic Implications for the Opening of the East Sea (Sea of Japan). *Tectonophysics* 304 (1–2), 131–149. doi:10.1016/S0040-1951(98)00270-4

Lee, G. H., Yoon, Y., Nam, B. H., Lim, H., Kim, Y.-S., Kim, H. J., et al. (2011). Structural Evolution of the Southwestern Margin of the Ulleung Basin, East Sea (Japan Sea) and Tectonic Implications. *Tectonophysics* 502 (3), 293–307. doi:10.1016/j.tecto.2011.01.015

Miall, A. D. (1995). "Collision-Related Foreland Basins," in *Tectonics of Sedimentary Basins*. Editors C. J. Busby and R. V. Ingersoll (Massachusetts: Blackwell Science Press), 393–424.

Mitchum, R. M., Vail, P. R., and Sangree, J. B. (1977). "Seismic Stratigraphy and Global Changes of Sea Level, Part 6: Stratigraphic Interpretation of Seismic Reflection Patterns in Depositional Sequences[1]," in *Seismic Stratigraphy – Applications to Hydrocarbon Exploration*. Editor C. E. Payton (Tulsa: AAPG Press), 117–133. doi:10.1306/M26490

Nakamura, K. (1983). Possible Nascent Trench along the Eastern Japan Sea as the Convergent Boundary between Eurasian and North American Plates. *Bull. Earthq. Res. Inst. Univ. Tokyo* 58, 711–722.

No, T., Sato, T., Kodaira, S., Ishiyama, T., Sato, H., Takahashi, N., et al. (2014). The Source Fault of the 1983 Nihonkai-Chubu Earthquake Revealed by Seismic Imaging. *Earth Planet. Sci. Lett. Sci. Lett.* 400 (15), 14–25. doi:10.1016/j.epsl.2014.05.026

Okada, S., and Ikeda, Y. (2012). Quantifying Crustal Extension and Shortening in the Back-Arc Region of Northeast Japan. *J. Geophys. Res.* 117 (B1), 1404. doi:10.1029/2011JB008355

Park, Y., Yoo, D., Kang, N., and Yi, B. (2019). Origin and Evolution of Stacked Cut-And-Fill Structures on the Southwestern Margin of the Ulleung Basin, East Sea (Japan Sea). *J. Sediment. Res.* 89 (7), 679–700. doi:10.2110/jsr.2019.36

Park, Y., Yoo, D., Kang, N., Yi, B., and Kim, B. (2021). Tectonic Control on Mass-Transport Deposit and Canyon-Fed Fan System in the Ulleung Basin, East Sea (Sea of Japan). *Basin Res.* 33 (2), 991–1016. doi:10.1111/bre.12501

Porębski, S. J., and Steel, R. J. (2003). Shelf-Margin Deltas: Their Stratigraphic Significance and Relation to Deepwater Sands. *Earth-Sci. Rev.* 62 (3–4), 283–326. doi:10.1016/S0012-8252(02)00161-7

Sato, T., Kosuga, M., and Tanaka, K. (1986). Aftershock Distribution of the 1983 Nihonkai-Chubu (Japan Sea) Earthquake Determined from Relocated Hypocenters. *J. Phys. Earth.* 34 (3), 203–223. doi:10.4294/jpe1952.34.203

Shaw, J. H., Connors, C., and Suppe, J. (2005). *Seismic Interpretation of Contractional Fault-Related Folds: An AAPG Seismic Atlas.* Tulsa, Oklahoma: American Association of Petroleum Geologists, 53. doi:10.1306/St531003

Sohn, Y. K., Rhee, C. W., and Shon, H. (2001). Revised Stratigraphy and Reinterpretation of the Miocene Pohang Basinfill, SE Korea: Sequence Development in Response to Tectonism and Eustasy in a Back-Arc Basin Margin. *Sediment. Geol.* 143 (3–4), 265–285. doi:10.1016/S0037-0738(01)00100-2

Son, M., Song, C. W., Kim, M.-C., Cheon, Y., Cho, H., and Sohn, Y. K. (2015). Miocene Tectonic Evolution of the Basins and Fault Systems, SE Korea: Dextral, Simple Shear during the East Sea (Sea of Japan) Opening. *J. Geol. Soc.* 172 (5), 664–680. doi:10.1144/jgs2014-079

Taira, A. (2001). Tectonic Evolution of the Japanese Island Arc System. *Annu. Rev. Earth Planet. Sci.* 29 (1), 109–134. doi:10.1146/annurev.earth.29.1.109

Tamaki, K., and Honza, E. (1985). Incipient Subduction and Deduction along the Eastern Margin of the Japan Sea. *Tectonophysics* 119 (1–4), 381–406. doi:10.1016/0040-1951(85)90047-2

Tamaki, K., Suyehiro, K., Allan, J., Ingle, J. C. J., and Pisciotto, K. A. (1992). Tectonic Synthesis and Implications of Japan Sea ODP Drilling. *Proc. ODP. Sci. Results* 127/128 (2), 1333–1348. doi:10.2973/odp.proc.sr.127128-2.240.1992

Tamaki, K. (1986). Age Estimation of the Japan Sea on the Basis of Stratigraphy, Basement Depth, and Heat Flow Data. *J. Geomagn. Geoelec* 38 (5), 427–446. doi:10.5636/jgg.38.427

Tamaki, K. (1988). Geological Structure of the Japan Sea and its Tectonic Implications. *Bull. Geol. Surv. Jpn.* 39 (5), 269–365.

Weimer, P. (1990). Sequence Stratigraphy, Facies Geometries, and Depositional History of the Mississippi Fan, Gulf of Mexico (1). *Bulletin* 74 (4), 425–453. doi:10.1306/0C9B2321-1710-11D7-8645000102C1865D

Yamamoto, H. (1993). Submarine Geology and Post-Opening Tectonic Movements in the Southern Region of the Sea of Japan. *Mar. Geol.* 112 (1–4), 133–150. doi:10.1016/0025-3227(93)90165-R

Yi, S., Yun, H., Park, B., Koo, W. M., Yoo, S., and Kang, S. (2020). Biostratigraphy of the Ulleung Basin, East Sea (Japan Sea). *Mar. Pet. Geology.* 122, 104697. doi:10.1016/j.marpetgeo.2020.104697

Yoon, S. H., and Chough, S. K. (1995). Regional Strike Slip in the Eastern Continental Margin of Korea and its Tectonic Implications for the Evolution of Ulleung Basin, East Sea (Sea of Japan). *Geol. Soc. America Bull.* 107 (1), 83–97. doi:10.1130/0016-7606(1995)107<0083:rssite>2.3.co;2

Yoon, S. H., Park, S. J., and Chough, S. K. (1997). Western Boundary Fault Systems of Ulleung Back-Arc Basin: Further Evidence of Pull-Apart Opening. *Geosci. J.* 1 (2), 75–88. doi:10.1007/BF02910479

Yoon, S. H., Park, S. J., and Chough, S. K. (2002). Evolution of Sedimentary Basin in the Southwestern Ulleung Basin Margin: Sequence Stratigraphy and Geologic Structures. *Geosci. J.* 6 (2), 149–159. doi:10.1007/BF03028286

Yoon, S. H., Chough, S. K., and Park, S. J. (2003). Sequence Model and its Application to a Miocene Shelf–Slope System in the Tectonically Active Ulleung Basin Margin, East Sea (Sea of Japan). *Mar. Pet. Geology.* 20 (10), 1089–1103. doi:10.1016/j.marpetgeo.2003.08.001

Yoon, S. H., Sohn, Y. K., and Chough, S. K. (2014). Tectonic, Sedimentary, and Volcanic Evolution of a Back-Arc Basin in the East Sea (Sea of Japan). *Mar. Geology.* 352, 70–88. doi:10.1016/j.margeo.2014.03.004

Conflict of Interest: Author H-YS is employed by the KNOC.

The remaining authors declare that the research was conducted in the absence of any commercial or financial relationships that could be construed as a potential conflict of interest.

Publisher's Note: All claims expressed in this article are solely those of the authors and do not necessarily represent those of their affiliated organizations, or those of the publisher, the editors and the reviewers. Any product that may be evaluated in this article, or claim that may be made by its manufacturer, is not guaranteed or endorsed by the publisher.

frontiers in Earth Science

ORIGINAL RESEARCH
published: 02 March 2022
doi: 10.3389/feart.2021.763050

New Insights into the Distribution and Evolution of WNW-Directed Faults in the Liaodong Bay Subbasin of the Bohai Bay Basin, Eastern China

Wei Li[1,2], *Meifang Meng*[1,2], *Tongjie Zhang*[3]*, *Xingpeng Chen*[1,2], *Yiming Liu*[1,2], *Di Wang*[1,2], *Haifeng Yang*[3] *and Chengmin Niu*[3]

[1]School of Geosciences, China University of Petroleum (East China), Qingdao, China, [2]Shandong Provincial Key Laboratory of Deep Oil and Gas, Qingdao, China, [3]Tianjin branch of CNOOC, Tianjin, China

OPEN ACCESS

Edited by:
Xunhua Zhang,
Qingdao Institute of Marine Geology (QIMG), China

Reviewed by:
Wang Jun,
Chengdu University of Technology, China
Chengchuan Gu,
Anhui University of Science and Technology, China

***Correspondence:**
Tongjie Zhang
zhangtj13@cnooc.com.cn

Specialty section:
This article was submitted to Structural Geology and Tectonics, a section of the journal Frontiers in Earth Science

Received: *23 August 2021*
Accepted: *17 December 2021*
Published: *02 March 2022*

Citation:
Li W, Meng M, Zhang T, Chen X, Liu Y, Wang D, Yang H and Niu C (2022) New Insights into the Distribution and Evolution of WNW-Directed Faults in the Liaodong Bay Subbasin of the Bohai Bay Basin, Eastern China. Front. Earth Sci. 9:763050. doi: 10.3389/feart.2021.763050

WNW-directed faults are widespread in eastern China, but debates regarding their distributions and evolutionary processes remain unsettled. Based on the latest 3-D seismic data, a series of WNW-directed faults south of the Liaodong Bay subbasin was identified, for which the evolution and formation mechanisms were discussed. The results show that four WNW-directed faults are characterized by poor continuity and nearly parallel orientations. Vertically, they exhibit listric geometries and cut through Paleozoic and Mesozoic formations. Since the late Triassic, these faults began as reverse faults under nearly S-N horizontal compression. In the Jurassic, those faults maintained their reverse-faulting activities with dramatically decreased intensities. In the Early Cretaceous, the WNW-directed faults were changed into normal faults under regional extension and were influenced by the sinistral strike-slip movement along the Tan-Lu fault zone. In the Late Cretaceous, the WNW-directed normal faults probably stopped moving due to a regional compressional event. During the Paleogene, the WNW-directed faults were reactivated with decreased intensities and were cut by NNE-directed faults. Here, we emphasize that the evolution of the WNW-directed faults could shed light on the regional tectonics. The WNW-trending faults that developed in the Liaodong Bay subbasin are closely related to the faults in the Yanshan orogenic belt. Therefore, investigating the characteristics and origin of WNW-induced faults will provide evidence for the tectonic evolution of the North China Block. In addition, the development of WNW-directed faults in the southern Liaodong Bay subbasin was conducive to the formation of buried Mesozoic and Paleozoic hills and hydrocarbon accumulations. In addition, we suggest that the compressional segment of the conjugated strike-slip transition zone that was formed by the interaction of the WNW- and NNE-directed strike-slip faults was conducive to hydrocarbon accumulations.

Keywords: WNW-directed faults, development characteristics, evolution process, formation mechanism, Liaodong Bay subbasin

INTRODUCTION

The North China block (NCB) is bounded by the Qinling-Dabie orogenic belt (QDOB) to the south and Yinshan–Yanshan orogenic belt to the north (Menzies and Xu, 1998; Zhao, 2001; Ren et al., 2002; Hu et al., 2006; Yang et al., 2008; Zhu et al., 2011; Wang et al., 2018b) (**Figure 1A**). Numerous faults with various orientations have developed since the Mesozoic in this area due to plate subduction, mantle upwelling, and lithospheric thinning. Previous studies have focused mainly on the NE-, NNE-, and nearly E-W-directed faults (Jia et al., 2021), while the WNW-directed faults have not been deeply studied. In particular, the distribution ranges and the formation mechanisms of the WNW-directed faults are still frequently debated (Li, et al., 2009; Suo, et al., 2013; Guo et al., 2015; Zhang, et al., 2017).

The Liaodong Bay subbasin is located in the northeastern Bohai Bay Basin (BBB), offshore China (**Figure 1B**) (Qi et al., 2008; Li L et al., 2012) and covers an area of more than 20,000 km^2. The Liaodong Bay subbasin includes six ENE-oriented subunits and from west to east are the Liaoxinan uplift, Liaoxi sag, Liaoxi uplift, Liaozhong sag, and Liaodong uplift (**Figure 1B**) (Hsiao et al., 2004; Xu et al., 2015; Hu et al., 2018; Li et al., 2018; Liu L et al., 2019). The formation and evolution of this subbasin is mainly controlled by diverse faults, which have caused the most important tectonic deformations in this subbasin. Various fault types have developed in the LDB, which include extensional, strike-slip, and transtensional faults (Hu et al., 2018; Hu P et al., 2019; Hu Z W et al., 2019; Liu Y M et al., 2019). According to their orientations, the faults in the Liaodong Bay subbasin can be divided into three groups: NNE-directed, NE-directed, and NEE- or nearly E-W-directed, among

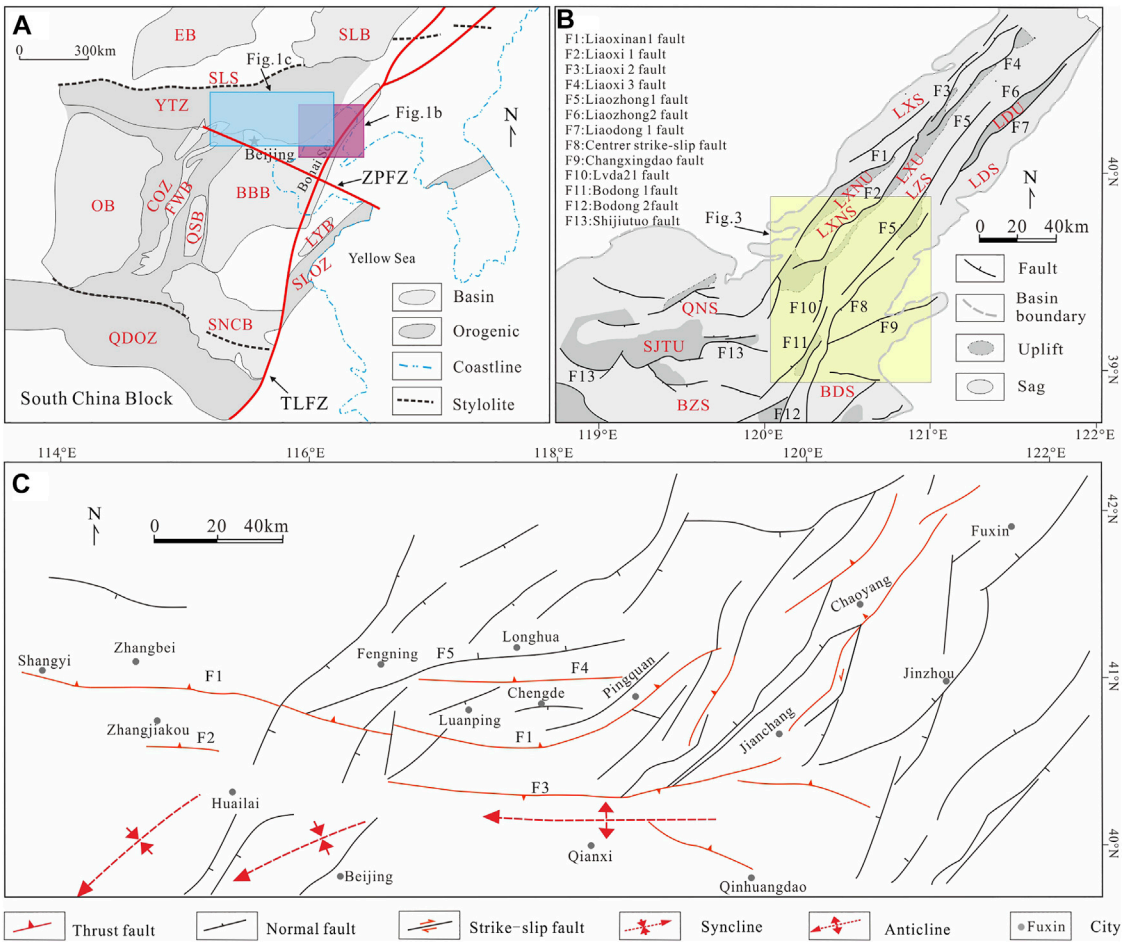

FIGURE 1 | (A) Simplified tectonic map showing the North China block (NCB) and adjacent geologic elements. (Modified from Zheng Yadong et al., 2000 and Zheng Jianping et al., 2018). The purple box is the location of **(B)**. The blue box is the location of **(C)**. Abbreviations are as follows: EB, Erlian Basin; SLB; Songliao Basin; OB, Ordos Basin: LYB, Laiyang Basin; QSB, Qinshui Basin; BBB, Bohai Bay Basin; FWB, Fenwei Basin; SNCB, southern North China Basin. YOB, Yanshan Orogenic Belt; COZ, Central Orogenic Zone; QDOZ, Qinling, Dabie Orogenic Zone; SLOZ, Sulu Orogenic Zone; SLS, Suolun Stylolite; TLFZ, Tanlu Fault Zone; ZPFZ, Zhangjiakou, Penglai Fault Zone. (b) Map of the tectonic framework of Liaodong Bay Depression. The yellow box is the location of **Figure 3**. Abbreviations are as follows: LXS, Liaoxi Sag; LXNS, Liaoxinan Sag; LZS, Liaozhong Sag; LDS, Liaodong Sag; QNS, Qinnan Sag; BZS, Bozhong Sag; BDS, Bodong Sag; LXNU, Liaoxinan Uplift; LXU, Liaoxi Uplift; LDU, Liaodong Uplift; SJTU, Shijiutuo Uplift. **(C)** Map of the tectonic framework of the northern margin of the North China Craton Modified from (Deng et al., 2007; Liu et al., 2015) Abbreviations are as follows: F1, Shangyi; Pingquan fault; F2, Zhangjiakou fault; F3, Qianxi fault; F4, Chengde fault.

which there are seven main NNE-directed faults, and the secondary fault directions are diverse (Cheng et al., 2015; Nan et al., 2015; Xu et al., 2015; Wu et al., 2016; Li et al., 2018).

The Yanshan orogenic belt (YOB) is located west of the Liaodong Bay subbasin. The western and central parts are characterized by nearly E-W- and WNW-directed compressional structures (Davis et al., 1998; Davis et al., 2001; Zhang et al., 2001; Ge et al., 2014; Wang et al., 2018a; Wang et al., 2018b), e.g., the Fengning-Longhua fault and Shangyi-Pingquan fault (Liu et al., 2004; Liu et al., 2018), and the Shangyi-Chongli-Chicheng fault (Zhang et al., 2006), which developed across Chengde, Luanping and Zhangjiakou Cities, Hebei Province, and Northern China.

In summary, although the research on the YOB (Davis et al., 2001; Zhang et al., 2001; Zhang et al., 2006; Cope et al., 2007; Zhang et al., 2011; Li et al., 2019; Li et al., 2021a) and Liaodong Bay subbasin (Cheng et al., 2015; Xu et al., 2015; Liu et al., 2016; Hu et al., 2018; Li et al., 2018; Li et al., 2021b) has achieved much progress and scientific understanding in previous studies, there are few results that are related to the origin of the WNW-directed faults. Regionally, the Liaodong Bay subbasin is located east of the YOB and is related to the E-W-directed tectonic system of the YOB in the extensional direction; thus, there may be an evolutionary and genetic relationship between them. It is suggested that the large-scale WNW-directed Zhangjiakou-Penglai Fault Zone (ZPFZ) developed north of the NCB and passes through the YOB, BBB, and Tan-Lu Fault Zone (TLFZ) (Wang et al., 2005; Suo et al., 2013; Guo et al., 2015; Peng et al., 2018). However, the ZPFZ traverses the middle of the BBB (Fu et al., 2004; Suo et al., 2013; Guo et al., 2015; Peng et al., 2018), and there have been no previous, relevant discussions regarding the WNW-directed fault system in the Liaodong Bay subbasin.

In this study, the fault system and stratigraphic features were explained in detail based on the latest 3-D seismic data. More importantly, WNW-directed fault systems were first recognized in the southern Liaodong Bay subbasin. The spatial geometries and temporal evolution processes were systematically investigated, and the genetic mechanisms were discussed. This study provides new evidence for the existence of the WNW-directed fault in the northern NCB and is conducive to clarifying the tectonic evolution and transition mechanism of the Liaodong Bay subbasin and even the entire eastern part of the NCB and will provide a reference for hydrocarbon exploration in the Liaodong Bay subbasin.

GEOLOGICAL SETTING

The Liaodong Bay subbasin is located in the northeastern Bohai Sea, which is a part of the BBB, and is situated in eastern offshore China (**Figure 1A**) and consists of a Mesozoic-Cenozoic superimposed basin that developed on a Paleozoic platform (Chang, 1991; He and Wang, 2003; Qi, 2004; Qi and Yang, 2010; Zuo et al., 2011). The numerous faults in different regions of the Bohai Sea differ greatly in their orientations: (1) in the Bozhong subbasin, the faults mainly strike NE, NEE, and WNW (Sun et al., 2008); (2) in the Bodong subbasin, the faults mainly strike NNE, NE, and NEE (Wu et al., 2013); (3) in the Bonan subbasin, the faults mainly strike WNW, EW, and NNE (Zhang et al., 2017; Liu et al., 2020); and (4) in the Liaodong Bay subbasin, the faults mainly strike NNE and NE (Cheng et al., 2015; Li et al., 2015; Nan et al., 2015; Xu et al., 2015; Li et al., 2018; Hu et al., 2018) (**Figure 1B**). These faults with different directions controlled the formation and evolution of the Bohai Sea in the Mesozoic and Cenozoic and caused differences in basin architectures, hydrocarbon migration, and accumulation in different regions (Qi, 2004; Qi and Yang, 2010; Zuo et al., 2011; Li S et al., 2012).

The TLFZ traverses the eastern part of the Bohai Sea (**Figure 1A**) and now acts as a right-lateral strike-slip zone. It consists of several NNE-directed, steeper erect basement faults. The TLFZ controls the structural deformation and basin evolution of its interior and nearby areas and causes obvious transformations in these areas. The TLFZ exhibits obvious segmentation along the distribution direction in the Bohai Sea and can be divided into the Liaodong Bay segment, Bodong segment, and Bonan segment. From north to south, the TLFZ gradually widens, and the number of faults gradually increases (Deng, 2001; Hu et al., 2003; Wang et al., 2006; Gong et al., 2007; Wan et al., 2009).

The YOB is located north of the NCB and to the northwest of the Bohai Sea. It can extend westward to Baotou, Inner Mongolia, with a total length of over 1100 km (Xu and Liu, 2017). The YOB is characterized by folds and reverse faults, and the distribution directions of the structures are mainly E-W (in the west) and NE-NNE (in the east), with a gradual transition between them (**Figure 1C**) (Davis et al., 2001; Liu et al., 2004; Yang et al., 2006; Cope and Graham, 2007; Hu et al., 2010; Liu et al., 2015; Liu et al., 2018).

Since the Late Paleozoic, the NCB, where the Bohai Sea and YOB are located, has experienced plate subduction and continental collision in different directions (Menzies and Xu, 1998; Zhai and Liu, 2003; Zhu et al., 2011; Liu et al., 2013; Liu J et al., 2017; Liu et al., 2018). At the same time, it has been under the joint control of the Tethys tectonic domain, Paleo-Asian tectonic domain, and Paleo-Pacific tectonic domain (Chen, 1998; Dong et al., 2015; Wang et al., 2018a; Liu et al., 2021). The transformations and interactions of the three tectonic domains led to spatial and temporal differences at different stages between the regional dynamic background and local tectonic stress fields. In turn, these factors caused complex structural characteristics, evolution (Meng, 2003; Lin S Z et al., 2013; Meng et al., 2014; Dong et al., 2015; Liu S et al., 2017; Liu et al., 2018), and metamorphic core complexes (Liu et al., 2005; Lin et al., 2008; Davis and Darby, 2010; Wang et al., 2011; Ji et al., 2015; Zhu et al., 2015; Liu J et al., 2017).

Regarding the stratigraphic units, the LDB developed on the Archean and Paleoproterozoic metamorphic crystalline basement, which is consistent with the NCB. The overlying strata consist of Meso- to Neo-Proterozoic shallow sea carbonate and clastic sediments, Cambrian and Ordovician (Є + O) shallow sea carbonate and clastic sediments, Carboniferous and Permian (C + P) marine to continental transitional sediments, and Mesozoic and Cenozoic continental clastic

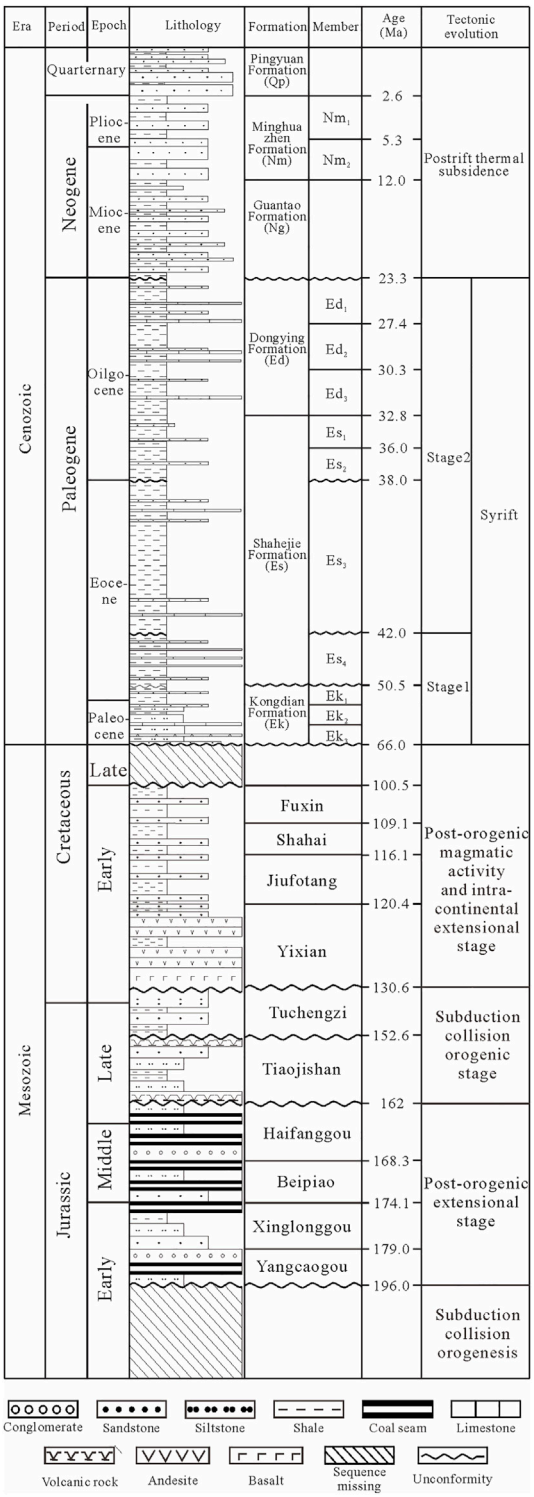

FIGURE. 2 | The Mesozoic and Cenozoic stratigraphic column of the Bohai Sea area (modified from Hsiao et al., 2004; Hu et al., 2018; Huang, 2019; Xi et al., 2019).

sequences. Among these, the Mesozoic and Cenozoic deposits are mainly controlled by fault activity and can be subdivided into two mega-sequences. The Mesozoic mega-sequence can be divided

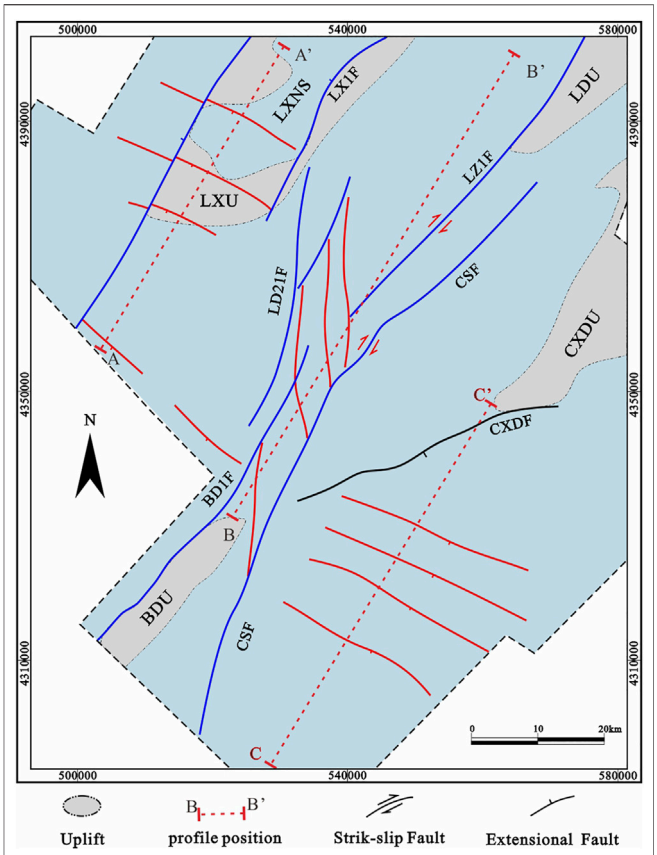

FIGURE 3 | Map of the tectonic framework of the south of Liaodong Bay sub-basin. The position is shown in the yellow box in **Figure 1B**, the dotted line is the section position in **Figure 4**. The NE-directed faults are indicated by blue lines. The WNW-directed faults are indicated by red lines. The NEE-directed fault is indicated by black lines. Abbreviations are as follows: LXNS, Liaoxinan Sag; LZS, Liaozhong Sag; LDS, Liaodong Sag; LXNU, Liaoxinan Uplift; LXU, Liaoxi Uplift; LDU, Liaodong Uplift; BDU, Bodong Uplift; LX1F, Liaoxi 1 Fault; LD21F, Lvda 21 Fault; LZ1F, Liaozhong 1 Fault; CSF, Central Strike, slip Fault; CXDF, Changxingdao Fault; BD1F, Bodong 1 Fault.

into two sequences: the Jurassic (J) and Lower Cretaceous (K1) (Huang, 2019; Tong et al., 2019; Xi et al., 2019). The Triassic and Upper Cretaceous sequences are missing (Tong et al., 2019; Xi et al., 2019) (**Figure 2**). The Cenozoic is relatively complete in the Bohai Sea and includes Paleogene synrift and Neogene-Quaternary postrift mega-sequences (Hsiao et al., 2004; Cheng et al., 2015; Nan et al., 2015; Hu et al., 2018). The sediments that were deposited during the syn-rift stage are primary lacustrine formations, which include the Kongdian (Ek), Shahejie (Es), and Dongying (Ed) Formations, and the postrift stage is characterized by the deposition of the Guantao (Ng), Minghuazhen (Nm), and Pingyuan (Qp) Formations (**Figure 2**) (Hsiao et al., 2004; Hu et al., 2018).

DATA AND METHODS

This study is based on 3-D seismic reflection data that were provided by the Tianjin Oil Company Ltd., CNOOC (China

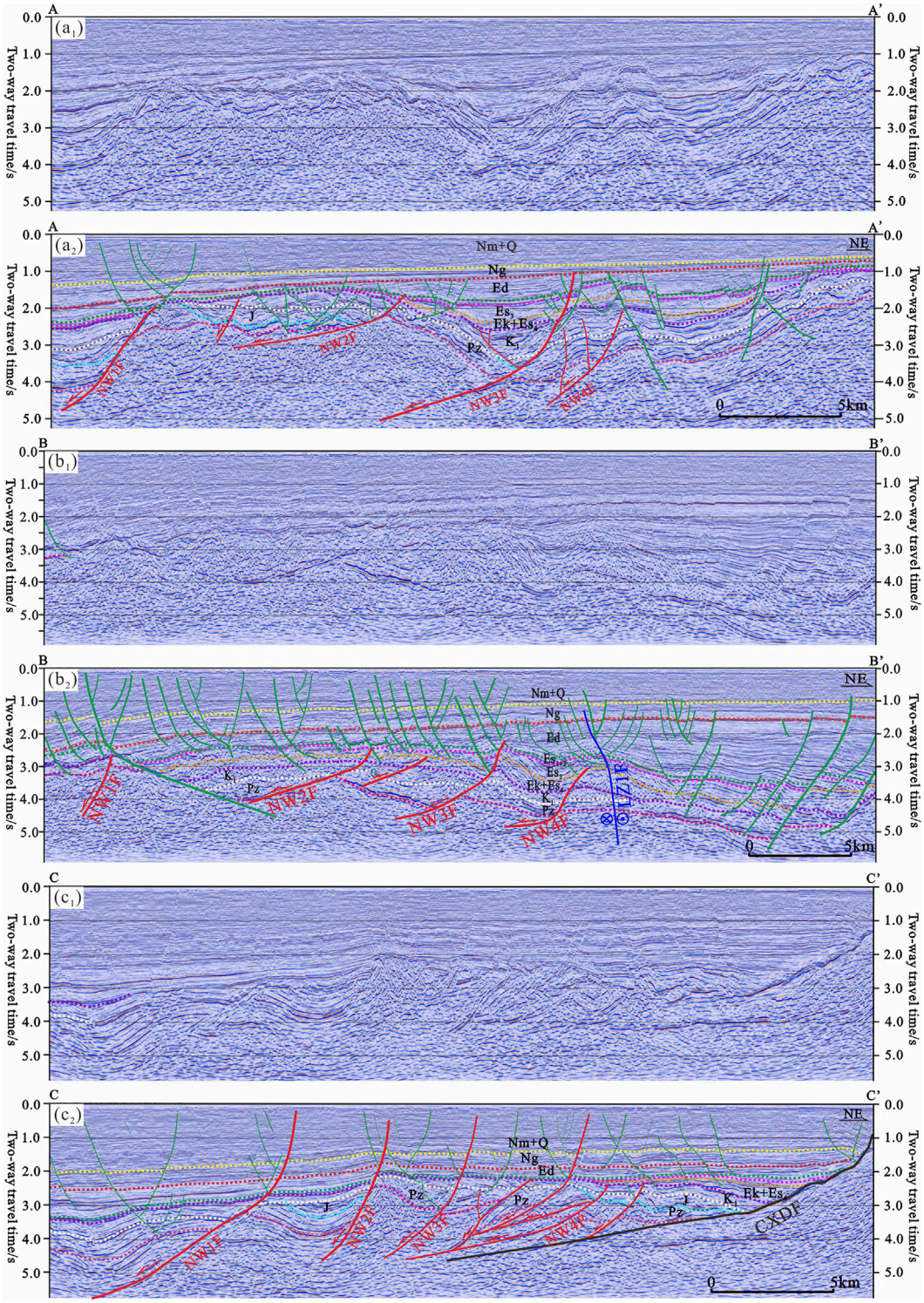

FIGURE 4 | (a_1) Uninterpreted and **(a_2)** interpreted versions of SW-NE-direction seismic profile of A-A'. **(b_1)** Uninterpreted and **(b_2)** interpreted versions of the SW-NE-direction seismic profile of B-B'. **(c_1)** Uninterpreted and **(c_2)** interpreted versions of the SW-NE-direction seismic profile of C-C'. See Panel 4 for its location of the faults and profile. The section position was shown by a dotted line in **Figure 3**.

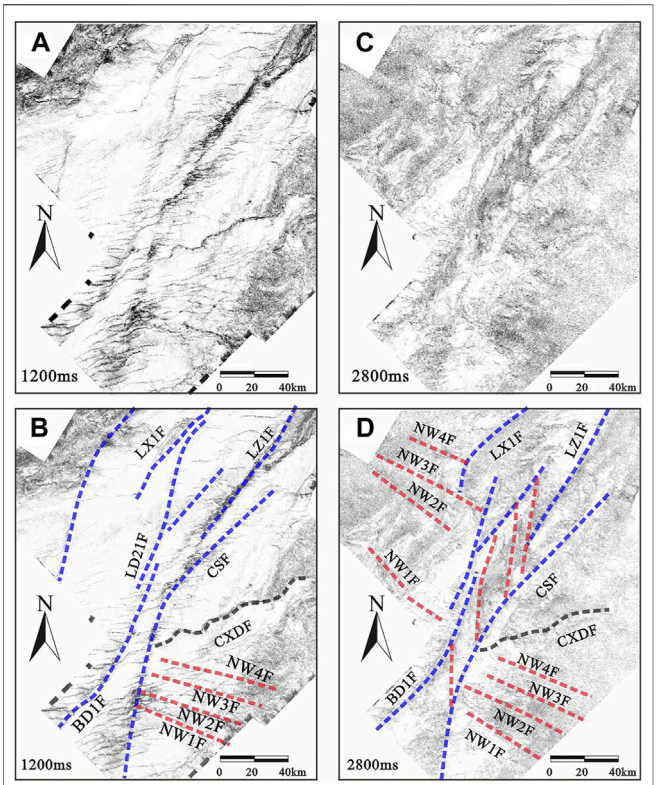

FIGURE 5 | (A) Uninterpreted **(A, C)** and interpreted **(B, D)** coherent slices of the southern part of Liaodong Bay Depression, with their locations given in **Figure 3**. Major faults are the same as those in **Figure 3**.

National Offshore Oil Corporation). The 3-D seismic data include an intact seismic cube that was merged by the Tianjin Oil Company Ltd., CNOOC from several seismic cubes. The seismic cube covers an area of approximately 18,000 km^2 with a line spacing of 12.5 m, and it images down to 6.0 s TWT. The 3-D seismic data were also processed by the companies introduced above by using calibrations with several deep wells.

A three-dimensional seismic interpretation was employed to identify and describe the geometry of the WNW-directed faults, and well logging and lithological data were also used to improve the correlations among the seismic reflectors and well data. This was followed by an interpretation of the main, regionally continuous seismic reflections and reflection terminations. The fault activity rate parameters and balanced cross-sections were used to determine the evolution of the WNW-directed faults.

RESULTS

Geometric Characteristics of the WNW-Directed Faults in the Southern Liaodong Bay Subbasin

Detailed seismic data interpretations provide the basis for fault identification in petroliferous basins. Based on the detailed interpretation of the latest seismic data mentioned above, four WNW-directed faults were identified south of the LBD (**Figure 3**).

In this section, these WNW-directed faults mainly developed in the pre-Paleogene and deep Paleogene, with some extending to the Neogene. These WNW-directed faults are mostly characterized by low-angle listric normal faults, with great cutting depths and multiple cutting layers. In some segments, the WNW-directed faults and other secondary faults comprise multiple Y-shaped or negative flower-shaped structures (**Figure 4**), so we infer that these WNW-directed faults are probably transtensional faults. In addition, some of the WNW-directed faults are terminated by NE- or ENE-directed faults, which indicates that the WNW-directed faults formed earlier than the NE- or NEE-directed faults.

In the plane view, the seismic coherency time slices reveal that (1) the WNW-directed faults are discontinuous and are cut by the NNE-directed Lvda-21 Fault (LD21F) and Central Strike-slip Fault (CSF). (2) The WNW-directed faults are mainly distributed on both sides of the NNE-directed strike-slip faults. However, between the LD21F and CSF, those faults become N-S-directed. (3) The WNW-directed faults are relatively apparent at depth, with a parallel orientation. In the shallow layers, the WNW-directed faults were barely detected on both sides of the CSF and LD21F (**Figure 5**).

Stratigraphic Units Controlled by WNW-Directed Faults

The seismic reflection analysis shows that the strata controlled by the WNW-directed faults in the local area mainly include the Є + O, C + P, J, K1, and Ek to the fourth member of Es (Ek-Es4) and the third member of Es to Ed (Es3-Ed). The Є + O and C + P are characterized by continuous parallel high-amplitude seismic reflections, which gradually thin toward the WNW-directed faults (**Figure 4**). The Jurassic is characterized by mid-continuous high-amplitude seismic reflections, which gradually overlap and thin toward the WNW-striking faults (**Figure 4**). The Lower Cretaceous is characterized by basinward prograding discontinuous, low-amplitude chaotic seismic reflections that are thick and generally wedge-like, which gradually overlap and thin toward the WNW-striking faults (**Figure 4**). The Ek-Es4 sequence consists of chaotic, low-amplitude, discontinuous seismic reflections that are locally developed in the deep depression areas (**Figures 4A,B**). Es3-Ed is widely deposited in the LDB but in local areas, it is controlled by WNW-directed faults (**Figure 4A**).

In addition, the Jurassic-Paleozoic and Lower Cretaceous units exhibit two opposite wedges and when combined with the characteristics of the seismic reflections, suggest that WNW-directed faults may have undergone structural inversion.

Regional Geophysical Evidence for the Existence of WNW-Directed Faults in the Southern Liaodong Bay Subbasin

Apart from the properties indicated by the 3-D seismic reflection data, the Bouguer gravity anomalies, aeromagnetic anomalies,

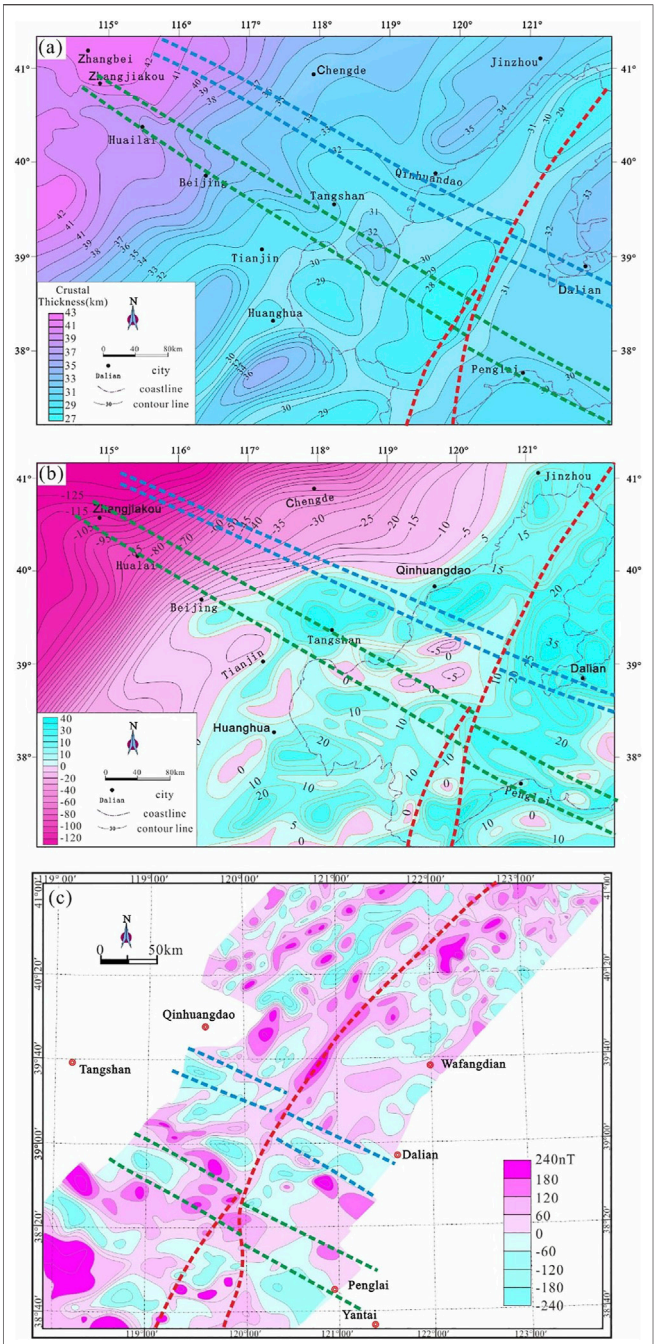

FIGURE 6 | Crustal thickness isopach map **(A)**, Bouguer gravity anomaly isopach map **(B),** and aeromagnetic anomaly isopach map **(C)** in the Bohai area and adjacent area. The red, green, and blue dotted lines, respectively, represent the TLFZ, the ZPFZ, and the QLFZ (Qi et al., 2010).

and crustal thicknesses also effectively reveal the existence of WNW-directed faults. (1) On the crustal thickness isopach map, along Chengde to Qinhuangdao, the contour trend changes from NE to NW. To the east of Qinhuangdao, two NE-trending Moho high values are separated (**Figure 6A**), and the separation belt extends southeast to Dalian. (2) On the Bouguer gravity anomaly map, the contour trend changes from NE to NW near Qinhuangdao. To the south of Qinhuangdao and Dalian, although the anomaly contours are complex, a NW-trending separation belt still exists (**Figure 6B**). (3) On the aeromagnetic anomaly map, NNE-NE-trending beading, such as positive anomaly zones, indicates the existence of the TLFZ (**Figure 6C**). On both sides of the NNE-NE-directed positive anomaly zone and south of Qinhuangdao and Dalian, the anomaly contours are clearly WNW-NW oriented.

Based on the above analysis, the presence of WNW-directed faults in the southern Liaodong Bay subbasin can be inferred. In previous studies, the Liaodong Bay subbasin and Bodong-Bozhong subbasin were thought to be separated by the WNW-directed Dalian-Qinhuangdao (Gong et al., 2007) or Qinhuangdao-Lvshun fault zone (Zhan et al., 2013), which contributed to confirming the existence of the WNW-directed faults in the southern Liadong Bay subbasin.

DISCUSSION

Kinematics of the WNW-Directed Faults in the South Part of the Liaodong Bay Subbasin

Previous studies have suggested that the NNE- and NE-directed faults were the main basin-controlling faults in the Liaodong Bay subbasin, and their formation mechanism has been discussed in detail (Hsiao et al., 2004; Xu et al., 2015; Hu et al., 2018; Li et al., 2018). In contrast, the WNW-directed faults in the Liaodong Bay subbasin are rarely mentioned, which contain significant information regarding the regional tectonics. Therefore, an integrated investigation of the kinematics of the WNW-directed faults is overdue. By combining the dip-slip faulting rates, balanced cross-sections, and newly published geological evidence, the evolution of these faults and their coupling relationships to the surrounding plates were discussed.

Thrusting Stage During the Late Triassic and Jurassic

The WNW-directed faults were initiated during the Late Triassic of the Mesozoic era, and the negative fault activity rate suggests that these faults are reverse faults (**Figures 7**, **8H**). Since the Middle Triassic, the Yangtze Plate has experienced the subduction of the southern Tethys Plate, which gradually strengthened in the Late Triassic (Lv et al., 2003; Hacker et al., 2009). This subduction event led to northward drifting of the Yangtze Plate, which ended up colliding with the NCB (Li et al., 2007; Li et al., 2013). After this collision, the Yangtze Plate continued to move northward with the NCB. Previously, the NCB collided and was spliced with the Siberian Plate during the Late Paleozoic, and the Mongolia-Okhotsk Ocean closed (Kravchinsky et al., 2002), so the northern margin of the NCB became a fixed boundary in the Late Triassic. From that time, the NCB experienced SSW- or SN-directed horizontal extrusion (Davis et al., 2001; Liu et al., 2012; Kim and Ree, 2013), which caused an overall uplift of the NCB that was accompanied by erosion of the Lower-Middle Triassic strata. Apatite fission track

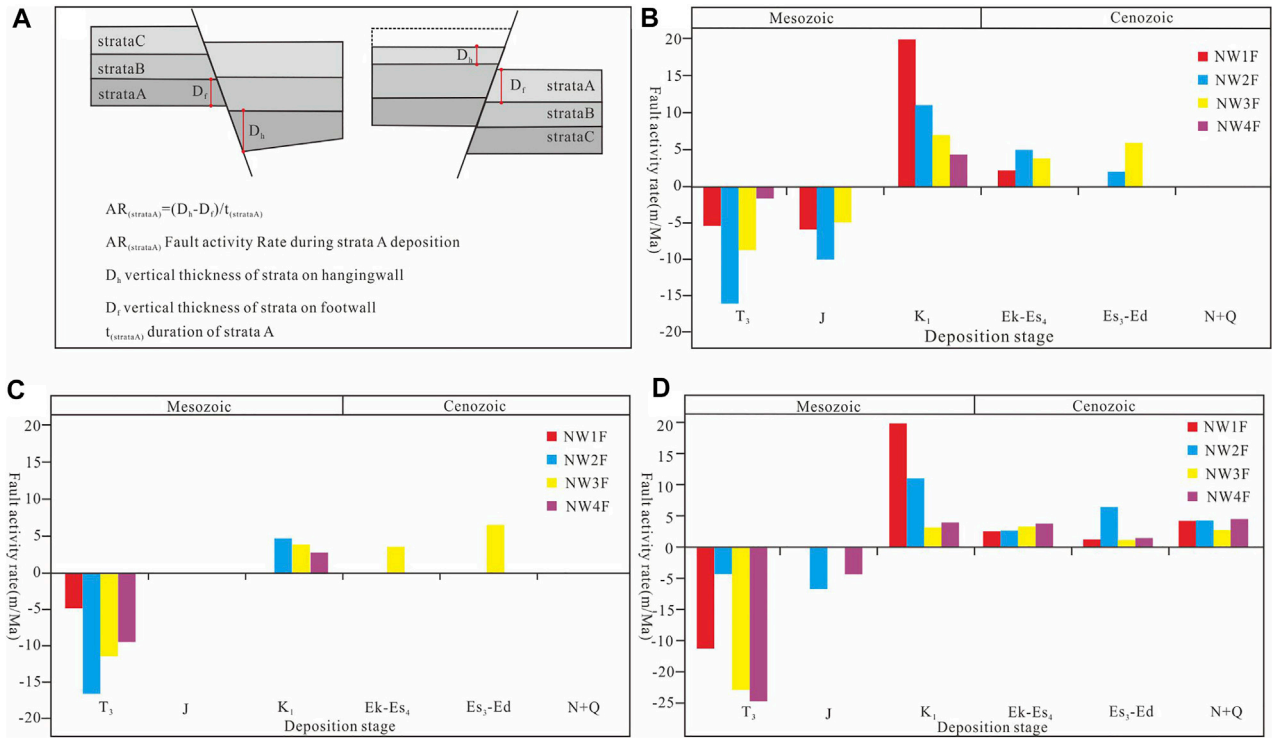

FIGURE 7 | (A) Map showing how the faulting activity rate is measured. Fault activity rates of the WNW-striking faults in different areas (the western **(B)**, central **(C),** and eastern **(D)** part of Liaodong Bay subbasin) during different periods are shown **(B–D)**.

analysis of the samples from the Huanghua depression reveals uplift and cooling in the Late Triassic (239–200 Ma) and Jurassic (160–140 Ma) (Wu et al., 2020). The zircon shrimp dating of the inner-basin debris also shows 2 orogenic events in that period (Zhu et al., 2020). All the above results indicate a compressional stress field. Meanwhile, a series of compressional structures developed in the NCB, which included the embryonic form of WNW-directed faults that exhibited thrust faulting signatures.

During the Jurassic (196–136 Ma), the tectonic setting of eastern China transformed from the Tethys domain to the marginal Pacific domain; subsequently, Paleo-Pacific tectonics dominated the evolution of eastern China (Zhao et al., 2004; Zhang et al., 2007; Wang et al., 2018a). At that time, North China experienced a complicated convergent process between the Eurasian and Paleo-Pacific Plates, along with variations in the convergence directions, rates, and subduction angles of the slab. This dynamic background caused a weakened SSW or N-S horizontal contraction. New geochronological data reveal that the strata that were previously considered to be Late Jurassic should belong to the Early Cretaceous, which indicates that the Jurassic strata in the study area were deposited earlier than ~136 Ma (Zhang et al., 2019). As a result, the NCB experienced intracontinental deformation, and the WNW-directed faults in the Liaodong Bay subbasin retained their reverse faulting characteristics (**Figures 7**, **8G**, **9B**). Consequently, the region evolved into a fold-thrust belt-induced flexural basin system and a high-standing block (horst)-rift-basin system (Liu S et al., 2017), which is consistent with the contemporaneous development of thrust nappe structures and molasse formation (Dong et al., 2013).

Extension Stage During the Early Cretaceous

The tectonic contraction in the Jurassic extended into the earliest Early Cretaceous (Meng, 2003; Liu J et al., 2017) and from approximately 136 Ma, the regime changed to extension (Cheng et al., 2018). Lithospheric thinning occurred underneath the NCB (Yang, 2003; Zhai et al., 2007; Zhu et al., 2011; Wu et al., 2014) and led to the formation of widespread and intensive extensional structures (**Figure 9C**). Meanwhile, some metamorphic core complexes and extensional domes developed in Yanshan and southern Liaoning Provinces, such as the Fangshan magma dome (Shan et al., 2006; Yan et al., 2006), Yunmengshan core complex (Zhu et al., 2015), Kalaqin extensional dome (Lin et al., 2014), Waziyu core complex (Zhang et al., 2012), and Linglong extensional dome (Lin W et al., 2013). The isotopic ages of these structures are constrained to between 135 and 129 Ma. Analysis of volcanic rocks and debris in the BBB also shows that there were 2 ages of volcanic rocks (e.g., 125–120 Ma and 110–100 Ma)., which indicated that regional extension occurred in the Early Cretaceous. In addition, the NNE-directed TLFZ experienced large-scale sinistral shear at the beginning of the Early Cretaceous (Zhu et al., 2005), which could have been derived from NNE- or SN-directed extension. Under the joint control of the deep dynamic

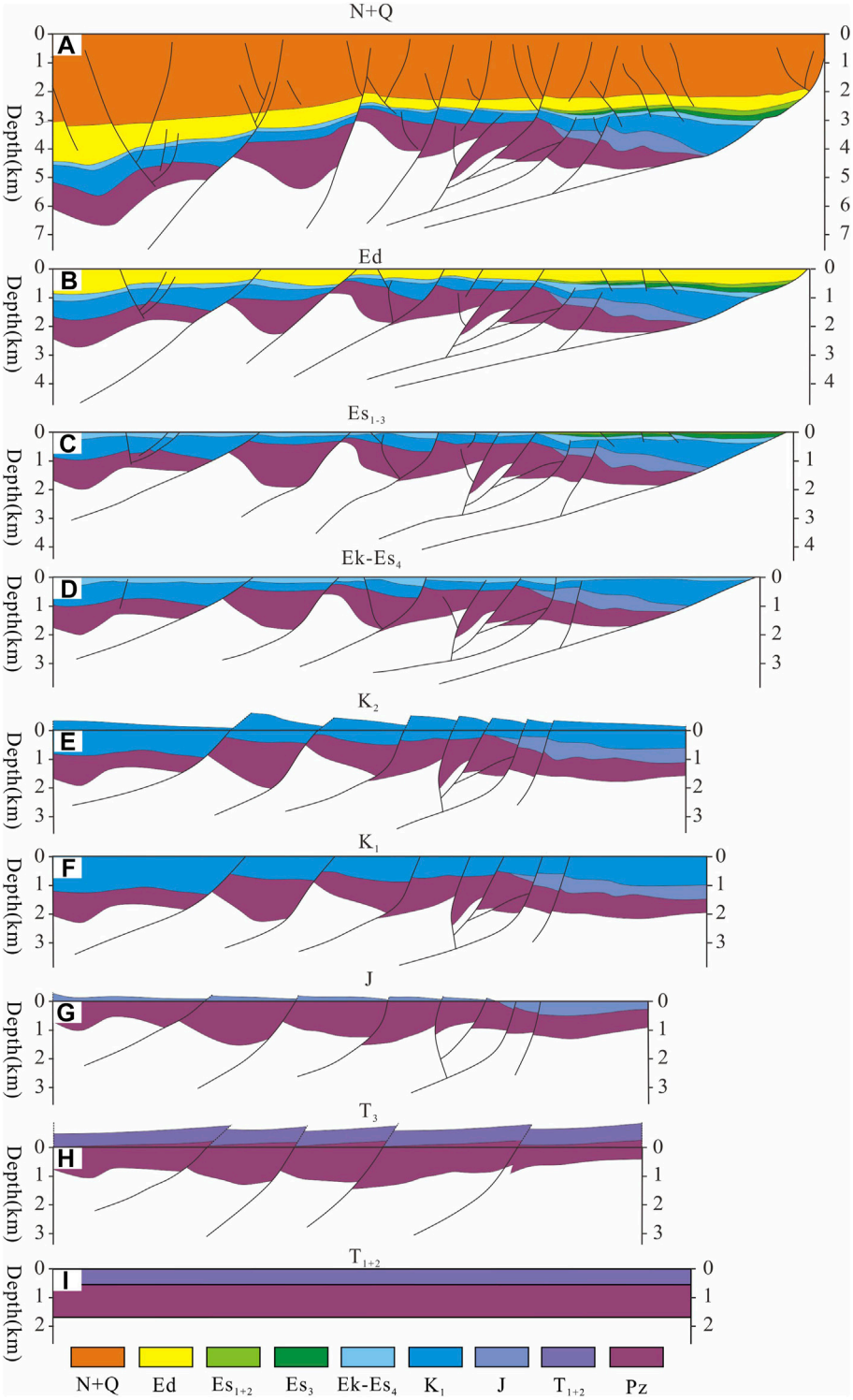

FIGURE 8 | The balanced cross-section restoration of line C-C'. **(A)** Seismic line C-C′ converted to depth. **(B)** Entire converted section restored to the Ed sequence. **(C)** Entire converted section restored to the Es_{1-3} sequence. **(D)** Entire converted section restored to the Ek-Es_4 sequence. **(E)** Entire converted section restored to the erosion of the K_2 sequence. **(F)** Entire converted section restored to the K_1 sequence. **(G)** Entire converted section restored to the J sequence. **(H)** Entire converted section restored to T_3 compression. **(I)** Entire converted section restored to T_{1+2}. See **Figure 3** for its location.

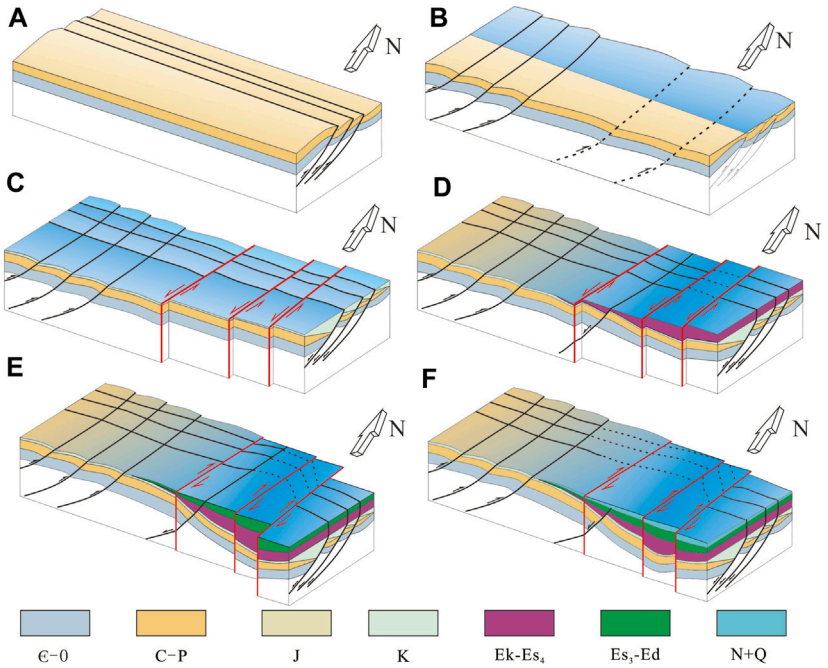

FIGURE 9 | The evolution pattern WNW-directed fault in the study area at different evolutionary stages. **(A)** The Late Triassic, **(B)** the Jurassic, **(C)** the Early Cretaceous, **(D)** the Paleocene and the Early Eocene, **(E)** the Middle Eocene-Oligocene, **(F)** the Neogene, and Quaternary.

background and shallow NNE-directed extension derived from the left-lateral movement of the TLFZ, the early WNW-directed faults were transformed into normal faults, with large amounts of displacement (**Figures 7**, **8F**, **9C**).

Thrusting Stage During the Late Cretaceous

During the Late Cretaceous (93.9–65 Ma), a new lithospheric mantle formed under the NCB (Wu et al., 2014). The gravitational influence of the newly formed lithosphere caused contraction of the shallow crust and thus superimposed the compression on the early extensional fault basin (Ying et al., 2006). At the same time, the Izanagi Plate in the Western Pacific Ocean was completely subducted under the Eurasian Plate in the Late Cretaceous (85 Ma), and the WNW-ward subduction of the Kula Plate (Zhang et al., 2008) caused the transformation of the regional stress field in the NCB into nearly NW-SE compression (Li S Z et al., 2005; Li W et al., 2005). Thus, the Early Cretaceous extensional fault basins were inverted under the regional contraction regime. A certain number of reverse faults and folds developed, such as the Chengbei-20 Fault in the Jiyang depression and Cangxian uplift in the Huanghua depression (Zhou et al., 2003; Li and Gao, 2010; Li et al., 2021a). In the study area, the WNW-directed faults ceased their normal faulting motions, and some local segments were transformed into thrust faults (**Figure 8E**). From a regional tectonics standpoint, this interpretation is also evidenced by a regional tectonic inversion event that occurred between 90 and 65 Ma in the Hailaer, Songliao, and Sanjiang Basins in Northeast China (Liu S et al., 2017; Liu et al., 2020). Meanwhile, this event is synchronous with the extensive fold development and striking angular unconformity within most of East Asia (Liu et al., 2020), which demonstrates an extensive compressional deformation history during the Late Cretaceous.

Reactivation and Extension Stage During the Cenozoic

During the Paleogene (66–23 Ma), deep mantle upwelling caused extension in the shallow crust, and the WNW-directed faults were reactivated locally.

During the depositional period of the Ek-Es4 sequence (e.g., Paleocene to Early Eocene), the motion along the TLFZ still consisted of sinistral shear (Hu et al., 2003). Some pre-existing WNW-directed faults were reactivated and controlled the lacustrine deposition (**Figures 7**, **8D**, **9D**), which indicates the inheritance of the Early Cretaceous tectonics (Hou and Hari, 2014). In addition, the main WNW-directed faults in the middle part of the BBB have similar characteristics, such as the Jiyang subbasin (Cheng et al., 2018; Liu et al., 2020), Chengbei subbasin (Liu L et al., 2019), and Huanghekou and Laizhouwan subbasins (Zhang et al., 2017), which reflect the prevalence of WNW-directed fault inheritance and reactivation during the Paleocene to early Eocene.

Since the Middle Eocene (the depositional period of the Es3-Ed sequence), the subduction direction of the Pacific Plate changed to WNW-directed, and the motion of the TLFZ then transformed into dextral shear (Zhu et al., 2021), which was derived from NW-directed extension and NE-directed compression. Since the direction of the derived compression was vertical to the WNW-directed faults, the activity of the WNW-directed faults weakened and gradually stopped

(**Figures 7**, **8B**,**C**, **9E**). Instead, NNE-directed faults began to activate and became the main basin-controlling faults in the Liaodong Bay subbasin (Hu et al., 2003). Consequently, the NNE- and NE-directed faults cut across the WNW-directed faults and reconstructed the previous tectonic patterns (**Figure 9E**). Additionally, due to the right-lateral strike-slips of the NNE-directed faults, the strikes of the WNW-directed faults between the Lvda21 and Central Strike-slip faults changed in the N-S direction (**Figures 3** and **5**). Similar to the study area, in the Zhanhua subbasin and Chengbei subbasin in the southeastern BBB, the strikes of the Mesozoic basin-controlling WNW-directed faults also changed to the N-S direction due to the close distance to the TLFZ (Li et al., 2006; Cheng et al., 2015).

During the depositional period of the Neogene-Quaternary sequence (e.g., Miocene-Holocene), the Bohai Sea area entered a postrift thermal subsidence stage, and the subsidence center migrated to the Bozhong sag (**Figure 9F**). Since the depositional period of the upper Minghuazhen subsequence, regional N-S extension (Li L et al., 2012) caused the WNW-directed faults to reactivate (Suo et al., 2013), and the motion was extensional with a sinistral shear sense.

Implications for the Distribution of the WNW-Directed Fault System in the Northern Part of the NCB

When compared with the NNE- and NE-directed faults, WNW-directed faults are not obvious in eastern China and are generally distributed in a dispersed manner (Suo et al., 2013). Previous studies have suggested that a large-scale WNW-directed fault zone developed in the northern NCB, namely, the Zhangjiakou-Penglai Fault Zone (Gao et al., 2001; Xu et al., 2012; Suo et al., 2013) or Zhangjiakou-Bohai Fault Zone (Lai et al., 2004), which is composed of many NW-, WNW-, and nearly E-W-directed faults. These faults in the ZPFZ have mutual cutting relationships with the nearly N-S- and NNE-directed faults. The ZPFZ can be divided into an onshore part in the west and offshore part in the east. The onshore part includes the Zhangjiakou-HuaiLai section and Beijing-Tianjin section, and both of them are located south of the Shangyi-Chicheng-Chongli fault, which is the western section of the southern boundary fault of the YOB (Zhang et al., 2011) (**Figure 1**). The offshore part includes the Bohai section located in the Bohai Sea and Penglai-Weihai section located in the north part of the Shandong Peninsula, and the Bohai section is mainly composed of the Weibei fault, Sha'nan fault, Huanghekou fault, and Laibei fault, all of which are located in the middle of the Bohai Sea area (Gao et al., 2001).

The Liaodong Bay subbasin is in the northern Bohai Sea, while few studies have been conducted on the WNW-directed faults. Based on the regional geophysical data and the offset of the NNE- and NE-directed TLFZ, it is suggested that a WNW-directed fault zone may have developed between the Liaodong Bay subbasin and Bodong-Bozhong subbasin, which is called the Qinhuangdao-Lvshun fault zone (Qi et al., 2004; Li and Hou, 2019). Based on the analysis in this study, we speculate that the WNW-directed faults in the south part of the Liaodong Bay subbasin should extend westward to the YOB and connect inland with the Shangyi-Pingquan fault.

However, the fault properties of the YOB are significantly different from the extensional deformations in the offshore basins. The nearly E-W- and WNW-directed faults in the YOB are generally considered to be reverse faults (Davis et al., 2001; Zhang et al., 2001; Zhang et al., 2011; Cope et al., 2007), while the Liaodong Bay subbasin is typically considered to be a strike-slip and extensional basin (e.g., Wenxian). The differences in the tectonic properties led to a lack of attention to the WNW-directed faults in the study area. In this study, we find that although the WNW-directed faults in the Liaodong Bay subbasin were mainly extensional and strike-slip in the Cenozoic, they had been reversed faults during the Late Triassic and Jurassic (**Figures 7**, **8G**,H), which are consistent with the nearly E-W- and WNW-directed faults in the YOB. The nearly E-W- and WNW-directed reverse faults in the YOB mainly acted during the Mesozoic (Davis et al., 2001; Zhang et al., 2001; Cope et al., 2007; Zhang et al., 2011) and being affected by continuous uplift during the Cenozoic, these faults ceased being active. Based on the above analysis, we speculate that the formation mechanism and evolution of the WNW-directed faults in the Liaodong Bay subbasin are similar to those in the YOB. In addition to the ZPFZ, another nearly WNW-directed fault zone should be present in the northern NCB along Jining-Shangyi-Pingquan and Qinhuangdao-Lvshun.

Implications for Hydrocarbon Exploration in the Southern Liaodong Bay Subbasin

Previous exploration efforts have confirmed the potential for oil and gas accumulations in the southern Liaodong Bay subbasin (Jia et al., 2018). The oil-source correlation analysis shows that these oils were derived from the source rocks of the Es1 and Ed3 strata. Hydrocarbon migration and accumulation primarily occurred during the depositional period of the Ed and N + Q sequences (Xu et al., 2011; Wang et al., 2014; Teng et al., 2016). As one of the hydrocarbon-rich depressions in the Bohai Sea, the Liaodong Bay subbasin has witnessed discoveries of several large and medium oil and gas fields, such as LD27, LD21, and LD16. After decades of exploration, the level of oil and gas exploration of the Paleogene reservoir in the Bohai Sea has been relatively high, and the pre-Paleogene reservoir is now the focus and hotspot of exploration in the BBB (Tong et al., 2012; Zhao et al., 2015; Xu et al., 2019). To date, hydrocarbon accumulations in the volcanic rocks of the Mesozoic and carbonates in the Paleozoic have been found in the Liaodong Bay subbasin, north of the BBB. However, until now, only 10 buried hill reservoirs have been discovered in the Bohai Sea (Deng, 2015), and the degree of exploration is significantly lower than that of the Cenozoic.

In this study, the WNW-directed faults that formed in the Mesozoic were discovered south of the Liaodong Bay subbasin. In addition, the residual strata of the Mesozoic and Paleozoic were revealed based on their seismic reflection characteristics. Thus, we speculate that the southern Liaodong Bay subbasin has a stratigraphic basis for the formation of buried hills. Moreover,

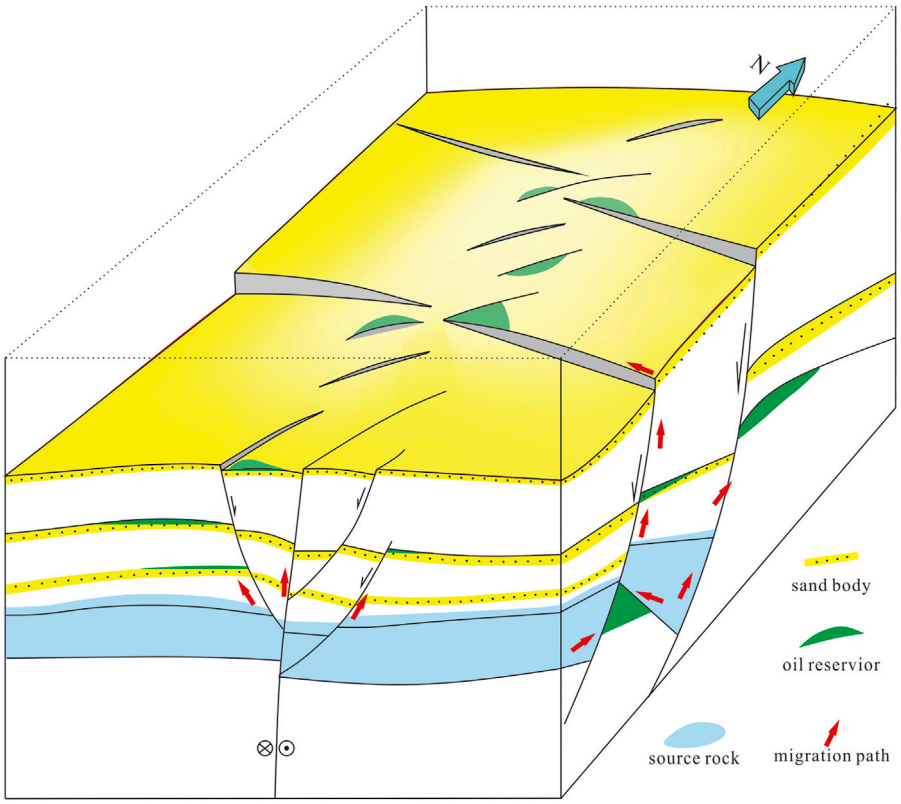

FIGURE10 | Diagram showing the hydrocarbon accumulation under the control of newly identified WNW-directed faults in the southern Liaodong Bay Depression.

the multistage reverse movements along the WNW-directed faults caused the formation of multiple angular unconformities during the uplift and erosion stages, which significantly improved the physical reservoir properties (Tian and Jiang, 2008). These tectonic activities simultaneously resulted in the formation of effective traps (**Figures 4** and **10**). In terms of hydrocarbon migration, the unconformities provide long-term continuous migration pathways (Zhao et al., 2015). Oil and gas can migrate from the hydrocarbon generation centers to the highpoints of the buried hills through extensional faults and these key unconformities. In addition, the late, active NNE-directed strike-slip faults can effectively seal the oil and gas accumulations. Based on the aforementioned analysis, buried Mesozoic and Paleozoic hills can be the subsequent exploration domain in the future (**Figure 10**).

Another issue worthy of attention is the distribution of oil and gas in the study area. At present, it is believed that oil and gas accumulations are abundant along the TLFZ, which has been confirmed by the exploration results (Gong et al., 2007; Zhu et al., 2019). However, drilling failures occurred during the exploration of structural traps along the TLFZ. Previous research has revealed the superior genetic potential of the source rocks in the southern part of the LBD (Huang et al., 2013). The key factor for hydrocarbon accumulations is whether there are effective traps and sealing faults. The NNE-directed strike-slip faults in the southern part of the LBD did not have a simple linear distribution but were slightly bending (**Figures 3** and **5**). The Late Paleogene to Neogene was a key period for oil accumulation. When the NNE-directed strike-slip faults mainly exhibited dextral shear, the WNW-directed faults exhibited sinistral shear (Suo et al., 2013; Peng et al., 2018). These two sets of strike-slip faults with conjugate strikes and opposite patterns simultaneously formed a conjugate strike-slip transition zone (**Figure 10**). Both the bending and the conjugation of the main strike-slip faults could result in local extension and compression, between which compression was conducive to the formation of fault gouges, so the permeabilities were lower, which contributed to the preservation of oil and gas (Wang et al., 2016). Previous studies have suggested that compressional strike-slip transfer zones or strike-slip derived structures are favorable locations for hydrocarbon accumulations and could therefore easily form large- and medium-sized oil and gas reservoirs (Xu, 2016). Therefore, in future exploration efforts, not only fine-scale seismic interpretations but also local stress field analyses are required, especially in the locations of extensional and compressional zones, which should be specified.

CONCLUSION

1) Four WNW-directed faults developed south of the Liaodong Bay subbasin and are mainly distributed on both sides of

NNE-directed strike-slip faults, with poor continuity and parallel orientations and controlled the deposition of the Jurassic and Lower Cretaceous strata of the Mesozoic and Ek-Es4 of the Cenozoic. Between the two NNE-directed strike-slip faults, the faults controlling the Mesozoic and Ek-Es4 are nearly N-S-directed instead of WNW-directed.

2) The WNW-directed faults in the south part of the Liaodong Bay subbasin initially were reverse faults beginning in the Late Triassic. During the Jurassic, these reverse WNW-directed faults became less active. The WNW-directed faults transformed into normal faults in the Early Cretaceous with intensive activity. During the Cenozoic, the WNW-directed faults were reactivated as normal faults during the depositional period of the Ek-Es4 sequence and then gradually became inactive.
3) The formation mechanism and evolution of the WNW-directed faults in the Liaodong Bay subbasin are similar to those in the YOB. In addition to the ZPFZ, another nearly E-W- and WNW-directed fault zone should be developed in the northern part of the NCB along Jining-Shangyi-Pingquan and Qinhuangdao-Lvshun.
4) The development of WNW-directed faults in the southern Liaodong Bay subbasin is conducive to the formation of buried Mesozoic and Paleozoic hills and hydrocarbon accumulations. In addition, we suggest that the compressional segment of the conjugated strike-slip transition zone that formed by the interaction of the WNW- and NNE-directed strike-slip faults is conducive to hydrocarbon accumulations.

DATA AVAILABILITY STATEMENT

The raw data supporting the conclusions of this article will be made available by the authors, without undue reservation.

AUTHOR CONTRIBUTIONS

W.L.: Conceptualization, methodology, writing-original draft; M.M. and T.Z.: Methodology, software, writing-reviewing and editing; X.C., Y.L., and D.W.: Revising the manuscript critically for important intellectual content; C.N. and H.Y.: Acquisition of data; supervision.

FUNDING

This study was funded by grants from the Ministry of Science and Technology of China (2016ZX05006-007 and 2016ZX05024-002). We thank the TianJin Oil Company, Ltd., CNOOC, and individuals who contributed the seismic data for this work.

REFERENCES

Chen, A. (1998). Geometric and Kinematic Evolution of Basement-Cored Structures: Intraplate Orogenesis within the Yanshan Orogen, Northern China. *Tectonophysics* 292 (1-2), 17–42. doi:10.1016/s0040-1951(98)00062-6

Cheng, Y., Wu, Z., Lu, S., Li, X., Lin, C., Huang, Z., et al. (2018). Mesozoic to Cenozoic Tectonic Transition Process in Zhanhua Sag, Bohai Bay Basin, East China. *Tectonophysics* 730, 11–28. doi:10.1016/j.tecto.2018.02.010

Cheng, Y., Wu, Z., Yan, S., Xu, C., Li, W., Zhang, J., et al. (2015). Cenozoic Tectonic Evolution of Liaodong Dome, Northeast Liaodong Bay, Bohai, Offshore China, Constraints from Seismic Stratigraphy, Vitrinite Reflectance and Apatite Fission Track Data. *Tectonophysics* 659, 152–165. doi:10.1016/j.tecto.2015.07.039

Cheng-yong Chang, C. Y. (1991). Geological Characteristics and Distribution Patterns of Hydrocarbon Deposits in the Bohai Bay Basin, east China. *Mar. Pet. Geology.* 8 (1), 98–106. doi:10.1016/0264-8172(91)90048-6

Cope, T. D., and Graham, S. A. (2007). Upper Crustal Response to Mesozoic Tectonism in Western Liaoning, North China, and Implications for Lithospheric Delamination. *Geol. Soc. Lond. Spec. Publications* 280 (1), 201–222. doi:10.1144/SP280.10

Cope, T. D., Shultz, M. R., and Graham, S. A. (2007). Detrital Record of Mesozoic Shortening in the Yanshan belt, NE China: Testing Structural Interpretations with basin Analysis. *Basin Res.* 19 (2), 253–272. doi:10.1111/j.1365-2117.2007.00321.x

Davis, G. A., Cong, W., Yadong, Z., Jinjiang, Z., Changhou, Z., and Gehrels, G. E. (1998). The Enigmatic Yinshan Fold-And-Thrust belt of Northern China: New Views on its Intraplate Contractional Styles. *Geol* 26 (1), 43–46. doi:10.1130/0091-7613(1998)026<0043:teyfat>2.3.co;2

Davis, G. A., and Darby, B. J. (2010). Early Cretaceous Overprinting of the Mesozoic Daqing Shan Fold-And-Thrust belt by the Hohhot Metamorphic Core Complex, Inner Mongolia, China. *Geosci. Front.* 1 (1), 1–20. doi:10.1016/j.gsf.2010.08.001

Davis, G. A., Yadong, Z., Cong, W., Darby, B. J., Changhou, Z., and Gehrels, G. (2001). Mesozoic Tectonic Evolution of the Yanshan Fold and Thrust belt, with Emphasis on Hebei and Liaoning Provinces, Northern China. *Paleozoic Mesozoic Tectonic Evol. Cent. East. Asia: Continental Assembly Intracontinental Deformation.* doi:10.1130/0-8137-1194-0.171

Deng, Y. H. (2001). Control of the NeotectonismAalong Tancheng-Lujiang Fracture Zone on Hydrocarbon Accumulationin the Eastern Bohai Sea. *China Offshore Oil and Gas* 05, 301–305. (in Chinese). 0.2001-05-000.

Deng, Y. H. (2015). Formation Mechanism and Exploration Practice of Large-Medium Buried-hill Oil fields in Bohai Sea. *Acta Petrolei Sinica* 36 (3), 253–261. (in Chinese). doi:10.7623/syxb201503001

Dong, S., Gao, R., Yin, A., Guo, T., Zhang, Y., Hu, J., et al. (2013). What Drove Continued Continent-Continent Convergence after Ocean Closure? Insights from High-Resolution Seismic-Reflection Profiling across the Daba Shan in central China. *Geology* 41, 671–674. doi:10.1130/g34161.1

Dong, S., Zhang, Y., Li, H., Shi, W., Xue, H., Li, J., et al. (2018). The Yanshan Orogeny and Late Mesozoic Multi-Plate Convergence in East Asia-Commemorating 90th Years of the "Yanshan Orogeny". *Sci. China Earth Sci.* 61, 1888–1909. doi:10.1007/s11430-017-9297-y

Dong, S., Zhang, Y., Zhang, F., Cui, J., Chen, X., Zhang, S., et al. (2015). Late Jurassic-Early Cretaceous continental Convergence and Intracontinental Orogenesis in East Asia: A Synthesis of the Yanshan Revolution. *J. Asian Earth Sci.* 114, 750–770. doi:10.1016/j.jseaes.2015.08.011

Feng, C. J., Zhang, P., and Meng, J. (2017). *In Situ* stress Measurement at Deep Boreholes along the Tanlu Fault Zone and its Seismological and Geological Significance. *Prog. Geophys.* 32, 946–967. (in Chinese).

Fu, Z., Liu, J., and Liu, G. (2004). On the Long-Term Seismic hazard Analysis in the Zhangjiakou-Penglai Seismotectonic Zone, China. *Tectonophysics* 390 (1-4), 75–83. doi:10.1016/j.tecto.2004.03.021

Gao, Z. W., Xu, J., Song, C. Q., et al. (2001). The Segmental Character of Zhangjiakou-Penglai Fault. *North China Earthquake Sci.* 19 (1), 35–42. (in Chinese).

Ge, X. H., Liu, J. L., Ren, S. M., et al. (2014). The Formation and Evolution of the Mesozoic-Cenozoic continental Tectonics in Eastern China. *Geology. China* 41 (1), 19–38. (in Chinese).

Gong, Z. S., Cai, D. S., and Zhang, G. C. (2007). Dominating Action of Tanlu Fault on Hydrocarbon Accumulation in Eastern Bohai Sea Area [J]. *Acta Petrolei Sinica* 28 (4), 1. (in Chinese). doi:10.1016/S1872-5813(07)60034-6

Guo, L., Li, S., Suo, Y., Ji, Y., Dai, L., Yu, S., et al. (2015). Experimental Study and Active Tectonics on the Zhangjiakou-Penglai Fault Zone across North China. *J. Asian Earth Sci.* 114 (DEC.15PT.1), 18–27. doi:10.1016/j.jseaes.2015.03.045

Hacker, B. R., Wallis, S. R., McWilliams, M. O., and Gans, P. B. (2009). 40Ar/39Ar Constraints on the Tectonic History and Architecture of the Ultrahigh-Pressure Sulu Orogen. *J. Metamorphic Geoloy* 27 (9), 827–844. doi:10.1111/j.1525-1314.2009.00840.x

He, L. J., and Wang, J. Y. (2003). Cenozoic thermal History of the Bohai Bay Basin: Constraints from Heat Flow and Coupled basin–mountain Modeling. *Phys. Chem. Earth, Parts A/B/C* 28 (9-11), 421–429. doi:10.1016/s1474-7065(03)00062-7

Hou, G., and Hari, K. R. (2014). Mesozoic-Cenozoic Extension of the Bohai Sea: Contribution to the Destruction of North China Craton. *Front. Earth Sci.* 8 (2), 202–215. doi:10.1007/s11707-014-0413-3

Hou, G., Wang, Y., and Hari, K. R. (2010). The Late Triassic and Late Jurassic Stress fields and Tectonic Transmission of North China Craton. *J. Geodynamics* 50 (3-4), 318–324. doi:10.1016/j.jog.2009.11.007

Hsiao, L.-Y., Graham, S. A., and Tilander, N. (2004). Seismic Reflection Imaging of a Major Strike-Slip Fault Zone in a Rift System: Paleogene Structure and Evolution of the Tan-Lu Fault System, Liaodong Bay, Bohai, Offshore China. *Bulletin* 88 (1), 71–97. doi:10.1306/09090302019

Hu, J., Zhao, Y., Liu, X., and Xu, G. (2010). Early Mesozoic Deformations of the Eastern Yanshan Thrust belt, Northern China. *Int. J. Earth Sci. (Geol Rundsch)* 99 (4), 785–800. doi:10.1007/s00531-009-0417-5

Hu, P., Yang, F., Tian, L., Wu, K., and Wang, W. (2019). Stress Field Modelling of the Late Oligocene Tectonic Inversion in the Liaodong Bay Subbasin, Bohai Bay Basin (Northern China): Implications for Geodynamics and Petroleum Accumulation. *J. Geodynamics* 126, 32–45. doi:10.1016/J.JOG.2019.01.003

Hu, P., Yang, F., Wang, W., Xu, C., Zhang, R., Hu, Y., et al. (2018). Thermal Anomaly Profiles Inferred from Fluid Inclusions Near Extensional and Strike-Slip Faults of the Liaodong Bay Subbasin, Bohai Bay Basin, China: Implications for Fluid Flow and the Petroleum System. *Mar. Pet. Geology.* 93, 520–538. doi:10.1016/J.MARPETGEO.2018.03.035

Hu, S., Raza, A., Min, K., Kohn, B. P., Reiners, P. W., Ketcham, R. A., et al. (2006). Late Mesozoic and Cenozoic Thermotectonic Evolution along a Transect from the north China Craton through the Qinling Orogen into the Yangtze Craton, central China. *Tectonics* 25, a–n. doi:10.1029/2006TC001985

Hu, W. S., Lv, B. Q., Guan, D. Y., et al. (2003). Characteristics of Tanlu Fault Zone and Development of Mesozoic and Cenozoic Basins along it. *Mar. Geology. Quat. Geology.* 23 (4), 51–58.

Hu, Z. W., Xu, C. G., Wang, D. Y., et al. (2019). Superimposed Characteristics and Genetic Mechanism of Strike-Slip Faults in the Bohai Sea, China. *Pet. Exploration Dev.* 46 (02), 63–77. doi:10.1016/s1876-3804(19)60007-8

Huang, D. Y. (2019). Jurassic Integrative Stratigraphy and Timescale of China. *Sci. China Earth Sci.* 62 (01), 227–259. doi:10.1007/s11430-017-9268-7

Huang, X. B., Xu, C. G., and Zhou, X. H. (2013). Hydrocarbon Distribution Characteristics and Accumulation Period of Second Member of Dongying Formation in the South of Liaozhong Sag. *Pet. Geology. Engneering* 27 (4), 16–19. (in Chinese). doi:10.3969/j.issn.1673-8217.2013.04.005

Ji, M., Liu, J., Hu, L., Shen, L., and Guan, H. (2015). Evolving Magma Sources during continental Lithospheric Extension: Insights from the Liaonan Metamorphic Core Complex, Eastern North China Craton. *Tectonophysics* 647-648, 48–62. doi:10.1016/j.tecto.2015.01.023

Jia, N., Liu, C. Y., Zhang, G. C., and Lei, H. (2015). Cenozoic Multiple Faulting and Tecnotic Evolution in the Liaodong Bay Depression. *Chin. J. Geology. (Scientia Geologica Sinica)* 50 (2), 377–390. (in Chinese). doi:10.3969/j.issn.0563-5020.2015.02.003

Jia, N., Liu, C., and Zhou, L. (2018). Characteristics of Fault Structure and its Control on Hydrocarbons in the Liaodong Bay Depression[J]. *J. Northwest University(Natural Sci. Edition)* 48 (06), 839–849.

Jia, N., Huang, L., Liu, C., Li, D., and Xu, C. (2021). Differential Faulting in a Narrow Rift basin Influenced by Synchronous Strike-Slip Motion: The Liaodong Bay sub-basin, Offshore Bohai Bay Basin, China. *Mar. Pet. Geology.* 124, 104853. doi:10.1016/j.marpetgeo.2020.104853

Kim, H. S., and Ree, J.-H. (2013). Permo-Triassic Changes in Bulk Crustal Shortening Direction during Deformation and Metamorphism of the Taebaeksan Basin, South Korea Using Foliation Intersection/inflection Axes: Implications for Tectonic Movement at the Eastern Margin of Eurasia during the Songrim (Indosinian) Orogeny. *Tectonophysics* 587, 133–145. doi:10.1016/j.tecto.2012.08.033

Kravchinsky, V. A., Cogne, J.-P., Harbert, W. P., and Kuzmin, M. I. (2002). Evolution of the Mongol-Okhotsk Ocean as Constrained by New Palaeomagnetic Data from the Mongol-Okhotsk Suture Zone, Siberia. *Geophys. J. Int.* 148 (1), 34–57. doi:10.1046/j.1365-246x.2002.01557.x

Kusky, T. M., and Li, J. (2003). Paleoproterozoic Tectonic Evolution of the North China Craton. *J. Asian Earth Sci.* 22 (4), 383–397. doi:10.1016/s1367-9120(03)00071-3

Kusky, T. M., Windley, B. F., and Zhai, M.-G. (2007). Tectonic Evolution of the North China Block: From Orogen to Craton to Orogen. *Geol. Soc. Lond. Spec. Publications* 280 (1), 1–34. doi:10.1144/SP280.1

Lai, X.-L., Zhang, X.-K., Cheng, S.-X., and Fang, S.-M. (2004). Study on Crust-Mantle Transitional Zone in West Margin of Zhangjiakou-Bohai Fault Belt. *Chin. J. Geophys.* 47 (5), 900–907. doi:10.1002/cjg2.567

Li, J., and Hou, G. (2019). Stress Development in Heterogeneous Lithosphere: Insights into Earthquake Initiation in the Tan-Lu Fault Zone. *Tectonophysics* 750, 329–343. doi:10.1016/j.tecto.2018.11.018

Li, J., Zhang, Y., Dong, S., and Shi, W. (2013). Structural and Geochronological Constraints on the Mesozoic Tectonic Evolution of the North Dabashan Zone, South Qinling, central China. *J. Asian Earth Sci.* 64 (Mar.5), 99–114. doi:10.1016/j.jseaes.2012.12.001

Li, L., Zhong, D. L., and Yang, C. C. (2012). Extension Order and its Deep Geological Background: Evidence from Western Shandong Rise and Jiyang Depression in the Late Mesozoic-Cenozoic. *Earth Sci. Front.* 19 (5), 255–273. (in Chinese).

Li, L., and Zhong, D. (2018). Tectonic Uplift Recorded by Detrital Zircon Fission Track Age in Jiyang Depression, Bohai Bay Basin. *Acta Petrologica Sinica* 34, 483–494. (in Chinese).

Li, S. Z., Wang, J. D., and Liu, J. Z. (2005). Mesozoic Structure and its Tectonic Setting in the Western Shandong Block. *Acta Geologica Sinica* 79 (4), 487–497. (in Chinese). doi:10.3321/j.issn:0001-5717.2005.04.006

Li, S., Kusky, T. M., Wang, L., Zhang, G., Lai, S., Liu, X., et al. (2007). Collision Leading to Multiple-Stage Large-Scale Extrusion in the Qinling Orogen: Insights from the Mianlue Suture. *Gondwana Res.* 12 (1-2), 121–143. doi:10.1016/j.gr.2006.11.011

Li, S., Zhao, G., Dai, L., Zhou, L., Liu, X., Suo, Y., et al. (2012). Cenozoic Faulting of the Bohai Bay Basin and its Bearing on the Destruction of the Eastern North China Craton. *J. Asian Earth Sci.* 47, 80–93. doi:10.1016/j.jseaes.2011.06.011

Li, W., and Gao, R. S. (2010). Development Characteristics of Positive Inversion Tectonics and its Controlling to Hydrocarbon Accumulation in Jiyang Depression. *China Pet. Exploration* 15 (5), 17–22. (in Chinese). doi:10.3969/j.issn.1672-7703.2010.05.004

Li, W., Guo, T. T., and Wu, Z. P. (2019). Application of Balanced Cross-Section Method in Extension, Strike-Slip Superposition and Ratio Analysis: A Case Study of Liaodong Bay Depression, Bohai Bay Basin. *Geol. Rev.* 65 (06), 1501–1514.

Li, W., Meng, M. F., and Chen, X. P. (2021b). Quantitative Characterization of Extension and Compression Derived from Bending Strike-Slip Faults and Their Petroleum Geological Significance of the Eastern Bohai Sea. *J. China Univ. Petroleum(Edition Nat. Science)* 45 (05), 23–32.

Li, W., Ping, M. M., and Zhou, D. H. (2018). Estimation of the Cenozoic Strike-Slip Displacement for Major Faults in the Liaodong Bay Depression and its Geological Significance. *Geotectonica et Metallogenia* 42 (03), 445–454.

Li, W., Ren, J., and Liu, Y. (2015). Development and Formation Mechanism of Cenozoic Tectonics in the East Area of Liaodong Bay Depression. *Geol. Sci. Tech. Inf.* 34 (006), 63–69. (in Chinese). 0.2015-06-008.

Li, W., Wu, Z. P., and Liu, H. (2009). Mesozoic and Cenozoic basin Evolution and Coal-Derived Gas Accumulation of Upper Paleozoic in the Area of Bohai Bay Basin. *Pet. Geology. Recovery Efficiency* 16 (1), 13–16. (in Chinese). doi:10.3969/j.issn.1009-9603.2009.01.004

Li, W., Wu, Z. P., and Zhang, M. H. (2006). Development Characteristic of Mesozoic and Cenozoic Faults and its Control over Deposition in Chengdao Area. *J. China Univ. Pet. (Edition Nat. Science)* 30 (1), 1–6+11. (in Chinese). doi:10.3321/j.issn:1000-5870.2006.01.001

Li, W., Wu, Z. P., and Zhou, Y. Q. (2005). Reconstruction of the Thickness of the Mesozoic Strata and Mesozoic Proto-type Basin in the Jiyang Depression. *Geol. Rev.* 51 (05), 507–516. (in Chinese). doi:10.3321/j.issn:0371-5736.2005.05.004

Li, W., Jia, H., Wu, Z., Niu, C., and Chen, X. (2021a). Controls of Strike-Slip Faults on Geomorphology and Sediment Dispersal in the Paleogene Bohai Bay Area-From a Source to Sink Perspective. *Mar. Pet. Geology.* 126, 104946. doi:10.1016/j.marpetgeo.2021.104946

Lin, S. Z., Zhu, G., and Yan, L. J. (2013). Discussion on Uplifting Mechanism of the Linglong Batholith in Eastern Shandong. *Geol. Rev.* 59 (5), 832–844. (in Chinese). doi:10.3969/j.issn.0371-5736.2013.05.004

Lin, S., Zhao, T., Song, L., Zhu, G., and Liu, B. (2014). Structural Characteristics and Formation Mechanism of the Kalaqin Metamorphic Core Complex in the Yanshan Area, China. *Chin. Sci. Bull.* 59, 3174–3189. (in Chinese). doi:10.1360/n972014-00100

Lin, W., Charles, N., Chen, Y., Chen, K., Faure, M., Wu, L., et al. (2013). Late Mesozoic Compressional to Extensional Tectonics in the Yiwulüshan Massif, NE China and Their Bearing on the Yinshan-Yanshan Orogenic belt. *Gondwana Res.* 23 (1), 78–94. doi:10.1016/j.gr.2012.02.012

Lin, W., Faure, M., Monié, P., Schärer, U., and Panis, D. (2008). Mesozoic Extensional Tectonics in Eastern Asia: The South Liaodong Peninsula Metamorphic Core Complex (NE China). *J. Geology.* 116 (2), 134–154. doi:10.1086/527456

Liu, J., Davis, G. A., Lin, Z., and Wu, F. (2005). The Liaonan Metamorphic Core Complex, Southeastern Liaoning Province, North China: A Likely Contributor to Cretaceous Rotation of Eastern Liaoning, Korea and Contiguous Areas. *Tectonophysics* 407 (1-2), 65–80. doi:10.1016/j.tecto.2005.07.001

Liu, J., Gan, H., Jiang, H., and Zhang, J. (2017). Rheology of the Middle Crust under Tectonic Extension: Insights from the Jinzhou Detachment Fault Zone of the Liaonan Metamorphic Core Complex, Eastern North China Craton. *J. Asian Earth Sci.* 139 (May 15), 61–70. doi:10.1016/j.jseaes.2016.12.024

Liu, J., Zhao, Y., Liu, A., and Ye, H. (2015). Late Jurassic to Early Cretaceous Sedimentary-Tectonic Development in the Chengde Basin, Yanshan Fold-Thrust belt, North China Craton. *J. Asian Earth Sci.* 114 (DEC.15PT.4), 611–622. doi:10.1016/J.JSEAES.2014.08.019

Liu, J., Zhao, Y., Liu, X., Wang, Y., and Liu, X. (2012). Rapid Exhumation of Basement Rocks along the Northern Margin of the North China Craton in the Early Jurassic: Evidence from the Xiabancheng Basin, Yanshan Tectonic Belt. *Basin Res.* 24 (5), 544–558. doi:10.1111/j.1365-2117.2011.00538.x

Liu, L., Chen, H., Wang, J., Zhong, Y., Du, X., Gan, X., et al. (2019). Geomorphological Evolution and Sediment Dispersal Processes in Strike-Slip and Extensional Composite Basins: A Case Study in the Liaodong Bay Depression, Bohai Bay Basin, China. *Mar. Pet. Geology.* 110, 73–90. doi:10.1016/J.MARPETGEO.2019.07.023

Liu, L., Zhong, Y., Chen, H., Xu, C., and Wu, K. (2016). Seismically Induced Soft-Sediment Deformation Structures in the Palaeogene Deposits of the Liaodong Bay Depression in the Bohai Bay basin and Their Spatial Stratigraphic Distribution. *Sediment. Geology.* 342, 78–90. doi:10.1016/J.sedgeo.2016.06.014

Liu, S., Gurnis, M., Ma, P., and Zhang, B. (2017). Reconstruction of Northeast Asian Deformation Integrated with Western Pacific Plate Subduction since 200 Ma. *Earth-Science Rev.* 175, 114–142. doi:10.1016/j.earscirev.2017.10.012

Liu, S., Li, Z., and Zhang, J. F. (2004). Mesozoic basin Evolution and Tectonic Mechanism in Yanshan, China. *Sci. China Ser. D* 47, 24–31. doi:10.1360/04zd0022

Liu, S., Lin, C., Liu, X., and Zhuang, Q. (2018). Syn-tectonic Sedimentation and its Linkage to Fold-Thrusting in the Region of Zhangjiakou, North Hebei, China. *Sci. China Earth Sci.* 61, 681–710. doi:10.1007/s11430-017-9175-3

Liu, S., Su, S., and Zhang, G. (2013). Early Mesozoic basin Development in North China: Indications of Cratonic Deformation. *J. Asian Earth Sci.* 62, 221–236. doi:10.1016/j.jseaes.2012.09.011

Liu, Y. M., Liu, L. J., and Wu, Z. P. (2020). New Insight into East Asian Tectonism since the Late Mesozoic Inferred from Erratic Inversions of NW-Trending Faulting within the Bohai Bay Basin. *Gondwana Res.* doi:10.1016/j.gr.2020.01.022

Liu, Y. M., Wu, Z. P., and Liu, L. F. (2019). Cenozoic Fault System and Tectonic Framework of Chengbei Sag and its Adjacent Areas, Bohai Bay Basin[J]. *Geotectonica et Metallogenia* 43 (6), 1133–1143.

Liu, Y. M., Wu, Z. P., and Liu, L. J. (2021). Cenozoic Structure and Tectonics of the Northern Beibu Gulf basin, Northern South China Sea. *Tectonophysics* 812, 228912. doi:10.1016/j.gr.2020.01.022

Lv, H. B., Zhang, Y. X., and Xia, B. (2003). Syn-sedimentary Compression Structures in the Middle Triassic Flysch of the Nanpan Jiang Basin,SW China. *Geol. Rev.* 49 (5), 449–456. (in Chinese). doi:10.1016/S0955-2219(02)00073-0

Meng, Q. R. (2003). What Drove Late Mesozoic Extension of the Northern China-Mongolia Tract. *Tectonophysics* 369 (3-4), 155–174. doi:10.1016/s0040-1951(03)00195-1

Meng, Q.-R., Wei, H.-H., Wu, G.-L., and Duan, L. (2014). Early Mesozoic Tectonic Settings of the Northern North China Craton. *Tectonophysics* 611, 155–166. doi:10.1016/j.tecto.2013.11.015

Menzies, M. A., and Xu, Y. (1998). Geodynamics of the North China Craton. *Mantle Dyn. Plate Interactions East Asia* 27, 155–165. doi:10.1029/gd027p0155

Peng, J. S., Wei, A. J., and Sun, Z. (2018). Sinistral Strike Slip of the Zhangjiakou-Penglai Fault and its Control on Hydrocarbon Accumulation in the Northeast of Shaleitian Bulge, Bohai Bay Basin, East China. *Pet. Exploration Dev.* 45 (02), 27–38. doi:10.1016/s1876-3804(18)30025-9

Qi, J. F., Yang, Q., and Lu, K. Z. (2004). Geologic Map of Sub-outcrop and its Implied Information of Tectogenesis in Bohai Bay basin Province. *Earth Sci. Front.* 11, 299–307. (in Chinese). doi:10.1007/BF02873097

Qi, J. F., Zhou, X. H., and Wang, Q. S. (2010). Structural Model and Cenozoic Kinematics of Tan-Lu Deep Fracture Zone in Bohai Sea Area[J]. *Geology. China* 37 (5), 1231–1242.

Qi, J. F. (2004). Two Tectonic Systems in the Cenozoic Bohai Bay basin and Their Genetic Interpretation. *Chin. Geology.* 31 (1), 15–22. (in Chinese).

Qi, J., and Yang, Q. (2010). Cenozoic Structural Deformation and Dynamic Processes of the Bohai Bay basin Province, China. *Mar. Pet. Geology.* 27 (4), 757–771. doi:10.1016/j.marpetgeo.2009.08.012

Qi, J., Zhou, X., Deng, R., and Zhang, K. (2008). Structural Characteristics of the Tan-Lu Fault Zone in Cenozoic Basins Offshore the Bohai Sea. *Sci. China Ser. D-earth Sci.* 51, 20–31. doi:10.1007/s11430-008-6013-x

Ratschbacher, L., Hacker, B. R., and Calvert, A. (2003). Tectonics of the Qinling (Central China): Tectonostratigraphy, Geochronology, and Deformation History. *Tectonophysics* 366 (1), 1–53. doi:10.1016/s0040-1951(03)00053-2

Ren, J., Tamaki, K., Li, S., and Junxia, Z. (2002). Late Mesozoic and Cenozoic Rifting and its Dynamic Setting in Eastern China and Adjacent Areas. *Tectonophysics* 344, 175–205. doi:10.1016/s0040-1951(01)00271-2

Santosh, M., Zhao, D., and Kusky, T. (2010). Mantle Dynamics of the Paleoproterozoic North China Craton: A Perspective Based on Seismic Tomography. *J. Geodynamics* 49 (1), 39–53. doi:10.1016/j.jog.2009.09.043

Shan, Y., Gong, F., Lin, G., Wang, Y., Yan, D.-P., Zhou, M.-F., et al. (2006). Discussion on Mesozoic Extensional Structures of the Fangshan Tectonic Dome and Their Subsequent Reworking during Collisional Accretion of the North China BlockJournal, Vol. 163, 2006, 127-142. *J. Geol. Soc.* 163 (6), 1051–1055. doi:10.1144/0016-76492006-026

Sun, Y. H., Qi, J. F., and Lv, Y. F. (2008). Characteristics of Fault Structure and its Control to Hydrocarbon in Bozhong Depression. *Acta Petrolei Sinica* 29 (05), 669–675. (in Chinese). doi:10.3321/j.issn:0253-2697.2008.05.007

Suo, Y. H., Li, S. Z., and Liu, X. (2013). Structural Characteristics of NWW-Directed Active Fault Zones in East China: A Case Study of the Zhangjiakou-Penglai Fault Zone. *Acta Petrologica Sinica* 29 (03), 953–966. (in Chinese). CNKI:SUN:YSXB. 10.2013-03-018.

Teng, C., Hao, F., Zou, H., Zhou, X., and Xu, C. (2016). Tan-Lu Fault System and its Significance in Oil Accumulation in the central Liaodong Bay Subbasin, Bohai Bay Basin, China. *Bulletin* 100 (02), 289–314. doi:10.1306/10221515011

Tian, F. H., and Jiang, Z. X. (2008). Promotion of Strata Uplift and Erosion to Hydrocarbon Accumulation. *J. Southwest Pet. Univ. (Science Tech. Edition)* 30 (5), 37–40+13. (in Chinese). doi:10.3863/j.issn.1000-2634.2008.05.008

Tong, H. M., Zhao, B. Y., and Cao, Z. (2013). Structural Analysis of Faulting System Origin in the Nanpu Sag, Bohai Bay BasinCNKI:SUN:DZXE. *Acta Geologica Sinica* 87 (11), 1647–1661. (in Chinese). 0.2013-11-002.

Tong, J., Chu, D., Liang, L., Shu, W., Song, H., Song, T., et al. (2019). Triassic Integrative Stratigraphy and Timescale of China. *Sci. China Earth Sci.* 62 (1), 189–222. doi:10.1007/s11430-018-9278-0

Tong, K., Zhao, C., Lü, Z., Zhang, Y., Zheng, H., Xu, S., et al. (2012). Reservoir Evaluation and Fracture Chracterization of the Metamorphic Buried hill Reservoir in Bohai Bay Basin. *Pet. Exploration Dev.* 39, 62–69. doi:10.1016/S1876-3804(12)60015-9

Wan, G. M., Tang, L. J., and Zhou, X. H. (2009). Tectonic Characteristics of the Tanlu Fault Zone in Bodong Area of Bohai Sea. *ACTA PETROLEI SINICA* 30 (03), 342–346. (in Chinese). doi:10.3321/j.issn:0253-2697.2009.03.004

Wang, G., Mitchell, T. M., Meredith, P. G., Nara, Y., and Wu, Z. (2016). Influence of Gouge Thickness and Grain Size on Permeability of Macrofractured basalt. *J. Geophys. Res. Solid Earth* 121 (12), 8472–8487. doi:10.1002/2016jb013363

Wang, Q., Zou, H., Hao, F., Zhu, Y., Zhou, X., Wang, Y., et al. (2014). Modeling Hydrocarbon Generation from the Paleogene Source Rocks in Liaodong Bay, Bohai Sea: A Study on Gas Potential of Oil-Prone Source Rocks. *Org. Geochem.* 76, 204–219. doi:10.1016/j.orggeochem.2014.08.007

Wang, R. B., Gu, G. H., and Xu, J. (2005). Discussion on Characteristics of Crustal Deformation along the Zhangjiakoubohai Seismotectonic Zone. *Earthquake Res. China* 19 (03), 327–337. (in Chinese). doi:10.1007/BF02873097

Wang, T., Zheng, Y., Zhang, J., Zeng, L., Donskaya, T., Guo, L., et al. (2011). Pattern and Kinematic Polarity of Late Mesozoic Extension in continental NE Asia: Perspectives from Metamorphic Core Complexes. *Tectonics* 30 (6), a–n. doi:10.1029/2011TC002896

Wang, Y., Sun, L., Zhou, L., and Xie, Y. (2018a). Discussion on the Relationship between the Yanshanian Movement and Cratonic Destruction in North China. *Sci. China Earth Sci.* 61 (5), 499–514. doi:10.1007/s11430-017-9177-2

Wang, Y., Zhou, L., Liu, S., Li, J., and Yang, T. (2018b). Post-cratonization Deformation Processes and Tectonic Evolution of the North China Craton. *Earth-Science Rev.* 177, 320–365. doi:10.1016/j.earscirev.2017.11.017

Wang, Z.-c., Deng, Q.-d., Du, X.-s., Chao, H.-t., Wu, Z.-q., Xiao, L.-x., et al. (2006). Active Fault Survey on the Tanlu Fault Zone in Laizhou Bay. *Acta Seimol. Sin.* 19 (5), 530–541. doi:10.1007/s11589-006-0506-5

Wu, F., Xu, Y., Zhu, R., and Zhang, G. (2014). Thinning and Destruction of the Cratonic Lithosphere: A Global Perspective. *Sci. China Earth Sci.* 57 (12), 2878–2890. doi:10.1007/s11430-014-4995-0

Wu, Z. P., Hou, X. B., and Li, W. (2007). Discussion on Mesozoic Basin Patterns and Evolution in the Eastern North China Block. *Geotectonica et Metallogenia* 31 (04), 385–399. (in Chinese). doi:10.3969/j.issn.1001-1552.2007.04.001

Wu, Z. P., Zhang, F. P., and Li, W. (2020). Apatite Fission Track Evidence of Mesozoic Tectonic Evolution in the Huanghua Depression. *J. China Univ. Mining Tech.* 49 (01), 123–136. (in Chinese).

Wu, Z. P., Zhang, J., and Ren, J. (2016). Development Characteristic of Strike-Slip Duplex in the Eastern Part of Liaodong Bay Depression and its Petroleum Geological Significance. *Acta Geologica Sinica* 90 (05), 848–856. (in Chinese). doi:10.3969/j.issn.0001-5717.2016.05.002

Wu, Z., Cheng, Y., Yan, S., Su, W., Wang, X., Xu, C., et al. (2013). Development Characteristics of the Fault System and its Control on basin Structure, Bodong Sag, East China. *Pet. Sci.* 10 (04), 450–457. doi:10.1007/s12182-013-0295-0

Xi, D., Wan, X., Li, G., and Li, G. (2019). Cretaceous Integrative Stratigraphy and Timescale of China. *Sci. China Earth Sci.* 62 (1), 256–286. doi:10.1007/s11430-017-9262-y

Xu, C. G., Ren, J. Y., and Wu, Z. P. (2015). Cenozoic Fault System and Tectonic Evolution of the Eastern Liaodong Bay Depression. *Geol. J. China Universities* 21 (2), 215–222. (in Chinese). doi:10.16108/j.issn1006-7493.2014170

Xu, C. G. (2016). Strike-Slip Transfer Zone and its Control on Formation of Medium and Large-Sized Oilfields in Bohai Sea Area. *Editorial Committee Earth Science-Journal China Univ. Geosciences* 41 (09), 1548–1560. doi:10.3799/dqkx.2016.508

Xu, C., Yu, H., Wang, J., and Liu, X. (2019). Formation Conditions and Accumulation Characteristics of Bozhong 19-6 Large Condensate Gas Field in Offshore Bohai Bay Basin. *Pet. Exploration Dev.* 46, 27–40. (in Chinese). doi:10.11698/PED.2019.01.0310.1016/s1876-3804(19)30003-5

Xu, G., Zhao, Y., and Gao, R. (2006). Mesozoic Basin Deformation of Yanshan Folded Fault Belt — Records of the Intraplate Deformation Process : A Case Study of Xiabancheng , Chengde — Shangbancheng and Beitai Basins. *Acta Geoscientia Sinica* 27 (1), 1. doi:10.1007/s11442-006-0415-5

Xu, G., Ma, R., Gong, D., Zhou, D., Li, J., Guo, Y., et al. (2011). Features of the Fault System and its Relationship with Migration and Accumulation of Hydrocarbon in Liaodong Bay. *Pet. Sci.* 8 (03), 251–263. doi:10.1007/s12182-011-0142-0

Xu, H., and Liu, Y. Q. (2017). Jurassic–Cretaceous Transition Terrestrial Red Beds in Northern North China and Their Regional Paleogeography, Paleoecology, and Tectonic Evolution. *Acta Geoscientia Sinica* 38 (z1), 25–28. (in Chinese). doi:10.3975/cagsb.2017.s1.08

Xu, J., Zhou, B. G., and Ji, F. J. (2012). Features of Seismogenic Structures of Great Earthquakes in the Bohai Bay Basin Area,North China. *Seismology Geology.* 34 (004), 618–636. (in Chinese). doi:10.3969/j.issn.0253-4967.2012.04.008

Yan, D.-P., Zhou, M.-F., Song, H.-L., Wang, G.-H., and Sun, M. (2006). Mesozoic Extensional Structures of the Fangshan Tectonic Dome and Their Subsequent Reworking during Collisional Accretion of the North China Block. *J. Geol. Soc.* 163 (1), 127–142. doi:10.1144/0016-764904-154

Yang, J.-H., Wu, F.-Y., Wilde, S. A., Belousova, E., and Griffin, W. L. (2008). Mesozoic Decratonization of the North China Block. *Geol* 36 (6), 467–470. doi:10.1130/G24518A.1

Yang, J., Wu, F., Shao, J., Wilde, S., Xie, L., and Liu, X. (2006). Constraints on the Timing of Uplift of the Yanshan Fold and Thrust Belt, North China. *Earth Planet. Sci. Lett.* 246 (3-4), 336–352. doi:10.1016/j.epsl.2006.04.029

Yang, W. C. (2003). Flat Mantle Reflectors in Eastern China: Possible Evidence of Lithospheric Thinning. *Tectonophysics* 369 (3), 219–230. doi:10.1016/S0040-1951(03)00215-4

Ying, J., Zhang, H., Kita, N., Morishita, Y., and Shimoda, G. (2006). Nature and Evolution of Late Cretaceous Lithospheric Mantle beneath the Eastern North China Craton: Constraints from Petrology and Geochemistry of Peridotitic Xenoliths from Jünan, Shandong Province, China. *Earth Planet. Sci. Lett.* 244 (3-4), 622–638. doi:10.1016/j.epsl.2006.02.023

Zhai, M. G., and Liu, W. J. (2003). Palaeoproterozoic Tectonic History of the North China Craton: a Review. *Precambrian Res.* 122 (1-4), 183–199. doi:10.1016/s0301-9268(02)00211-5

Zhai, M., Fan, Q., Zhang, H., Sui, J., and Shao, J. a. (2007). Lower Crustal Processes Leading to Mesozoic Lithospheric Thinning beneath Eastern North China: Underplating, Replacement and Delamination. *Lithos* 96 (1-2), 36–54. doi:10.1016/j.lithos.2006.09.016

Zhan, R., Zhu, G., and Yang, G. L. (2013). The Genesis of the Faults and the Geodynamic Environment during Neogene for Offshore of the Bohai Sea. *Earth Sci. Front.* 20 (4), 151–165. (in Chinese).

Zhang, B., Zhu, G., Chen, Y., Piao, X., Ju, L., and Wang, H. (2012). Deformation Characteristics and Genesis of the Waziyu Metamorphic Core Complex in Western Liaoning of China. *Sci. China Earth Sci.* 55 (011), 1764–1781. doi:10.1007/s11430-012-4495-z

Zhang, C. H., Song, H. L., and Wang, G. H. (2001). Mesozoic Dextral Strike-Slip Structural System in Middle Segment of Intraplate Yanshan Orogenic belt, Northern China. *J. China Univ. Geosciences* 26 (05), 464–472. (in Chinese). doi:10.3321/j.issn:1000-2383.2001.05.004

Zhang, C. H., Zhang, Y., and Li, H. L. (2006). Late Mesozoic Thrust Tectonics Framework in the Western Part of the Yanshan Orogenic belt and the Western Hills of Beijing:characteristics and Significance. *Earth Sci. Front.* 02, 165–183. (in Chinese). doi:10.3321/j.issn:1005-2321.2006.02.015

Zhang, C., Li, C., Deng, H., Liu, Y., Liu, L., Wei, B., et al. (2011). Mesozoic Contraction Deformation in the Yanshan and Northern Taihang Mountains and its Implications to the Destruction of the North China Craton. *Sci. China Earth Sci.* 54 (6), 798–822. doi:10.1007/s11430-011-4180-7

Zhang, J., Li, W., and Wu, Z. P. (2017). Structural Characteristics of Tan-Lu Fault Zone in South Area of Bohai Sea and its Control on Basin Structure[J]. *Earth Sci.* 42 (9), 1549–1564.

Zhang, Q., Wang, Y. L., and Jin, W. J. (2008). Eastern China Plateau during the Late Mesozoic: Evidence, Problems and Implication. *Geol. Bull. China* 27 (9), 1404–1430.

Zhang, X. Q., Wu, Z. P., and Zhou, X. H. (2017). Cenozoic Tectonic Characteristics and Evolution of the Southern Bohai Sea. *Geotectonica et Metallogenia* 41 (1), 50–60. doi:10.16539/j.ddgzyckx.2017.01.004

Zhang, Y. Q., Dong, S. W., and Zhao, Y. (2007). Jurassic Tectonics of North China: a Synthetic View. *Acta Geologica Sinica* 81 (11), 1462–1480. (in Chinese). doi:10.3321/j.issn:0001-5717.2007.11.002

Zhao, G. (2001). Palaeoproterozoic Assembly of the North China Craton. *Geol. Mag.* 138 (1), 87–91. doi:10.1017/S0016756801005040

Zhao, X., Jin, F., Wang, Q., and Bai, G. (2015). Buried-hill Play, Jizhong Subbasin, Bohai Bay basin: A Review and Future Propespectivity. *Bulletin* 99 (01), 1–26. doi:10.1306/07171413176

Zhao, Y., Xu, G., and Zhang, S. H. (2004). Yanshanian Movement and Conversion of Tectonic Regimes in East Asia. *Earth Sci. Front.* 11 (3), 319–328. (in Chinese) doi:10.3321/j.issn:1005-2321.2004.03.030

Zhou, L. H., Li, S. Z., and Liu, J. Z. (2003). The Yanshanian Structural Style and basin Prototypes of the Mesozoic Bohai Bay Basin. *Prog. Geophys.* 18 (4), 692–699. (in Chinese). doi:10.3969/j.issn.1004-2903.2003.04.019

Zhu, G., Liu, G. S., and Niu, M. L. (2003). Transcurrent Movement and Genesis of the Tan-Lu Fault Zone. *Geol. Bull. China* 22, 200–207. doi:10.1016/S0955-2219(02)00073-0

Zhu, G., Chen, Y., Jiang, D., and Lin, S. (2015). Rapid Change from Compression to Extension in the North China Craton during the Early Cretaceous: Evidence from the Yunmengshan Metamorphic Core Complex. *Tectonophysics* 656, 91–110. doi:10.3969/10.1016/j.tecto.2015.06.009

Zhu, G., Liu, G. S., Niu, M. L., Xie, C. L., Wang, Y. S., and Xiang, B. (2009). Syn-collisional Transform Faulting of the Tan-Lu Fault Zone, East China. *Int. J. Earth Sci. (Geol Rundsch)* 98 (1), 135–155. doi:10.1007/s00531-007-0225-8

Zhu, G., Wang, Y., Liu, G., Niu, M., Xie, C., and Li, C. (2005). 40Ar/39Ar Dating of Strike-Slip Motion on the Tan-Lu Fault Zone, East China. *J. Struct. Geology.* 27 (8), 1379–1398. doi:10.1016/j.jsg.2005.04.007

Zhu, J. C., Feng, Y. L., and Meng, Q. R. (2020). Late Mesozoic Tectonostratigraphic Division and Correlation of Bohai Bay basin: Implications for the Yanshanian Orogeny. *Yanshanian Orogeny* 50 (01), 28–49.

Zhu, R., Chen, L., Wu, F., and Liu, J. (2011). Timing, Scale and Mechanism of the Destruction of the North China Craton. *Sci. China Earth Sci.* 54 (006), 789–797. doi:10.1007/s11430-011-4203-4

Zhu, Y., Liu, S., Zhang, B., Gurnis, M., and Ma, P. (2021). Reconstruction of the Cenozoic Deformation of the Bohai Bay Basin, North China. *Basin Res.* 33 (1), 364–381. doi:10.1111/bre.12470

Zuo, Y., Qiu, N., Zhang, Y., Li, C., Li, J., Guo, Y., et al. (2011). Geothermal Regime and Hydrocarbon Kitchen Evolution of the Offshore Bohai Bay Basin, North China. *Bulletin* 95 (5), 749–769. doi:10.1306/09271010079

Conflict of Interest: Author ZT, NC and YH are employed by CNOOC.

The remaining authors declare that the research was conducted in the absence of any commercial or financial relationships that could be construed as a potential conflict of interest.

frontiers | Frontiers in Earth Science

ORIGINAL RESEARCH
published: 06 April 2022
doi: 10.3389/feart.2022.843173

Submarine Landslides in the West Continental Slope of the South China Sea and Their Tsunamigenic Potential

Xiaoyi Pan[1], Linlin Li[1,2], Hồng Phương Nguyễn[3,4,5]*, Dawei Wang[2,6] and Adam D. Switzer[7,8]*

[1]Guangdong Provincial Key Laboratory of Geodynamics and Geohazards, School of Earth Sciences and Engineering, Sun Yet-Sen University, Guangzhou, China, [2]Southern Marine Science and Engineering Guangdong Laboratory (Zhuhai), Zhuhai, China, [3]Institute of Geophysics, Vietnam Academy of Science and Technology, Hanoi, Vietnam, [4]Graduate University of Science and Technology, Vietnam Academy of Science and Technology, Hanoi, Vietnam, [5]IRD, Sorbonne Universités, UPMC Univ Paris 06, Unité Mixte Internationale de Modélisation Mathématique, Hanoi, Vietnam, [6]Institute of Deep-Sea Science and Engineering, Chinese Academy of Sciences, Sanya, China, [7]Asian School of the Environment, Nanyang Technological University, Singapore, Singapore, [8]Earth Observatory of Singapore, Nanyang Technological University, Singapore, Singapore

The 109 meridian fault is located in the west of the South China Sea (SCS) connecting to the offshore Red River Shear Zone. Seismic data from the central Vietnamese shelf indicates that many submarine landslides were developed along the steep continental slope in this offshore region. Here, we analyze the potential for such landslides to trigger damaging tsunamis based on the local geological background and sedimentary environment. We assess their tsunamigenic potential along the coast of Southern Central Vietnam (SCV). We point out that the evolutionary processes of the 109° meridian fault: striking-subsidence of the adjacent basin, combined with the high sediment input from numerous montane rivers of the hinterland generate conditions that likely favor the development of submarine landslides along the well-defined and steep continental slope near SCV. To estimate the impact of tsunami waves on the SCV coastline, we conducted a pilot study using two numerical models: NHWAVE and FUNWAVE-TVD to model 4 representative landslides with volumes ranging between 1.3 and 14 km^3 and water depth of 300–1000 m. The submarine landslides were treated as rigid slump and deformable slide corresponding to two different sedimentary environments. Our results show that the tsunami waves generated by rigid slump can reach up to 20 m height in the landslide source area and ~5 m when arriving at the closest coastline. Tsunami waves could arrive at the central Vietnam coast within 30 min in eight scenarios. Our initial results also suggest that seafloor topography, i.e., waveguide effects of ocean ridges, shelf resonance and the potential bay resonance cause significant variability in potential run-up. We note that ocean ridges located in the deep basin of the SCS focus the tsunami energy propagating towards the northwest coast of Luzon Island, Philippines where tsunami wave heights of ~2.3 m wave height are modeled. These findings underscore the importance of tsunami hazard assessments that account for both earthquake generated and earthquake triggered tsunamis. Our work also highlights a continued need to examine tsunami sources in the region as mitigation and preparedness for the socio-economically important and heavily populated coastlines of the SCS is reliant on a detailed understanding of the hazard.

Keywords: submarine landslide, tsunami, South China Sea, strike-slip fault, trigger mechanism

OPEN ACCESS

Edited by:
Han-Joon Kim,
Korea Institute of Ocean Science and Technology (KIOST), South Korea

Reviewed by:
David Iacopini,
University of Naples Federico II, Italy
Chong Xu,
Ministry of Emergency Management, China
Gang Wang,
Hohai University, China

****Correspondence:***
Linlin Li
lilinlin3@mail.sysu.edu.cn
Hồng Phương Nguyễn
phuong.dongdat@gmail.com

Specialty section:
This article was submitted to Geohazards and Georisks, a section of the journal Frontiers in Earth Science

Received: *25 December 2021*
Accepted: *16 February 2022*
Published: *06 April 2022*

Citation:
Pan X, Li L, Nguyễn HP, Wang D and Switzer AD (2022) Submarine Landslides in the West Continental Slope of the South China Sea and Their Tsunamigenic Potential. Front. Earth Sci. 10:843173. doi: 10.3389/feart.2022.843173

1 INTRODUCTION

Submarine landslides, in addition to submarine earthquakes, are one of the principal causes of large tsunamis (Løvholt et al., 2020). Since the 1998 Papua New Guinea event which caused more than 2000 fatalities, people have become increasingly aware of the hazard posed by tsunamis with landslide causes (Tappin and Grilli, 2021). The need for increased awareness was further raised by two recent events in Indonesia in 2018: the 2018 Palu tsunami (Liu et al., 2020; Nakata et al., 2020; Gatter et al., 2021; Schambach et al., 2021) and the 2018 Anak Krakatau event (Hunt et al., 2018; Grilli et al., 2019; Ye et al., 2020; Grilli et al., 2021) both involving landslide mechanisms.

Submarine landslides have been identified at various geological environments worldwide, i.e., passive, convergent and strike-slip margins as well as volcanic regions (Hampton et al., 1996; Gee et al., 1999; McAdoo et al., 2000; Urgeles and Camerlenghi, 2013; Wang W. et al., 2018; Gatter et al., 2021; Tappin and Grilli, 2021). As one of the largest marginal seas in the world, the South China Sea (SCS) contains a variety of continental margins, some of which that provide favorable environments for the development of submarine landslides with various scale (Moscardelli and Wood, 2016). The SCS has wide and passive continental margins in the south and north, a subduction belt in the east, strike-slip margin in the west and numerous isolated carbonate platforms inside the sea basin.

Over the last 15 years several submarine explorations have identified a large number of submarine landslides with various volumes in the SCS [e.g., Gee et al. (2007), Wu et al. (2011), Wang et al. (2014), Li W. et al. (2015), Sun et al. (2017), Sun et al. (2018a), Sun et al. (2018b)]. Some of these landslides are among the largest slides in the world with volumes exceeding 1,000 km^3, such as the Brunei Slide has estimated volume of 1,200 km^3 (Gee et al., 2007) and the Baiyun complex has ~1,035 km^3 (Sun et al., 2008; Sun et al., 2017; Sun et al., 2018a; Wang J. et al., 2018). Besides the giant slides observed in the open continental slopes, the majority of submarine landslides in the SCS are relatively small, typically on the order of a few km^3, especially those developed in the submarine canyons (He et al., 2014; Chen et al., 2016; Zhou et al., 2019), steep continental slope in the west (Fyhn et al., 2009a; Fyhn et al., 2009b; Hong Nguyen et al., 2012) and carbonate islands (Wang W. et al., 2018; Huang et al., 2020). Previous studies generally focus on interpreting the characteristics of submarine landslides themselves (e.g., morphology, geometric features, evolution processes etc.) through high-resolution bathymetric and 2D/3D seismic data (Gee et al., 2007; Sun et al., 2008; Fyhn et al., 2009a; Huang et al., 2020). Whether those landslides are tsunamigenic and to what extent they can cause hazard are still poorly understood, particularly for submarine landslides with relatively small scales. A few studies investigated the tsunamigenic potential of the two giant landslides in the SCS: the Brunei slide (Tan et al., 2017) and the Baiyun complex (Li et al., 2019; Ren et al., 2019; Sun and Leslie, 2020). These studies highlight the potential catastrophic tsunami effect on the densely populated coastal regions (e.g., the southern China) in the SCS (Li et al., 2019). Compared with landslides with giant sizes, landslides with volumes on the order of a few km^3 generally generate shorter wavelengths and its wave amplitudes decay faster, and therefore affecting relatively limited coastal areas (Janin et al., 2019). Nonetheless, when such tsunami events occur in densely populated region, small-scale landslides can also trigger non negligible tsunami disasters. Examples include the 1998 PNG tsunami (Tappin et al., 2008), the 1979 Nice airport tsunami (Assier-Rzadkieaicz et al., 2000). Therefore, quantitative assessments of tsunamigenic potential of small-scale landslides are needed.

In this study, we investigate the potential tsunami hazard posed by submarine landslides in the western continental slope of the SCS. The available seismic data reveals that numerous landslides exist along the 109° meridian fault area (Pham Nang Vu, 2009). Evidences can also be observed in other seismic profiles in Gwang and Watkins (1998), Fyhn et al. (2009b), Tan et al. (2014), Vu et al. (2017). The 109° meridian fault located in the western SCS belongs to a giant strike-slip fault system: Red River-Ailao fault system which runs through the west part of the South China Sea. The geological evolution of this fault system shaped the rapidly changing topography in east Sunda shelf (Fyhn et al., 2009a; Fyhn et al., 2009b) and formed an abrupt shelf break with the slope more than 10° in the offshore region near Central Vietnam. The well-developed submarine landslides are located over a steep slope (10°) starting at ~200 m water depth, ~40 km away from city Nha Trang in central Vietnam. Similar landslides today may become potential tsunami sources threatening the nearby region, especially the central Vietnamese coast (**Figure 1**).

Historical documents and field surveys suggest that Vietnamese coast has been frequently attacked by coastal flooding events (Hong Nguyen et al., 2012). Among all the historical records, five of them located near the meridian fault region (**Figure 1**) are thought to be tsunami events (Nguyen et al., 2007). As part of the Red River-Ailao fault system, the 109° meridian fault is still seismically active. During 1919–2005, 18 earthquakes were recorded along the 109° meridian fault, with the maximum magnitude of Mw 6.1 that located in 109.0°E, 10.1°N, happened in 1923 (Hong Phuong, 2001; Hong Nguyen et al., 2012). Seismic activity is one of the potential triggers for mass failures on the slope (e.g., Tappin et al., 2008). The frequency of a tsunami either triggered by underwater earthquake or submarine landslide is commonly at a scale of decades, hundreds of years or even longer (Talling, 2014), therefore, the tsunami hazard is often ignored or overlooked (Giuliani et al., 2019). If a submarine landslide that is either earthquake independent or a combination failure of the meridian fault and a triggered landslide was to occur it would likely cause a tsunami that would affect the Vietnamese coast. To date this has not been quantitatively addressed.

Here, we conduct a pilot series of numerical experiments to investigate the tsunamigenic potential of submarine landslides near central Vietnam. We first briefly summarize the tectonic evolution of western SCS and analyze the potential factors affecting the slope instability. Then based on the constraints from geological information and seismic data, we specify the geometric parameters of four representative landslides. We then presents the modeling procedure which includes a non-hydrostatic 3D model NHWAVE (Tehranirad et al., 2012) for tsunami generation and the fully non-linear dispersive

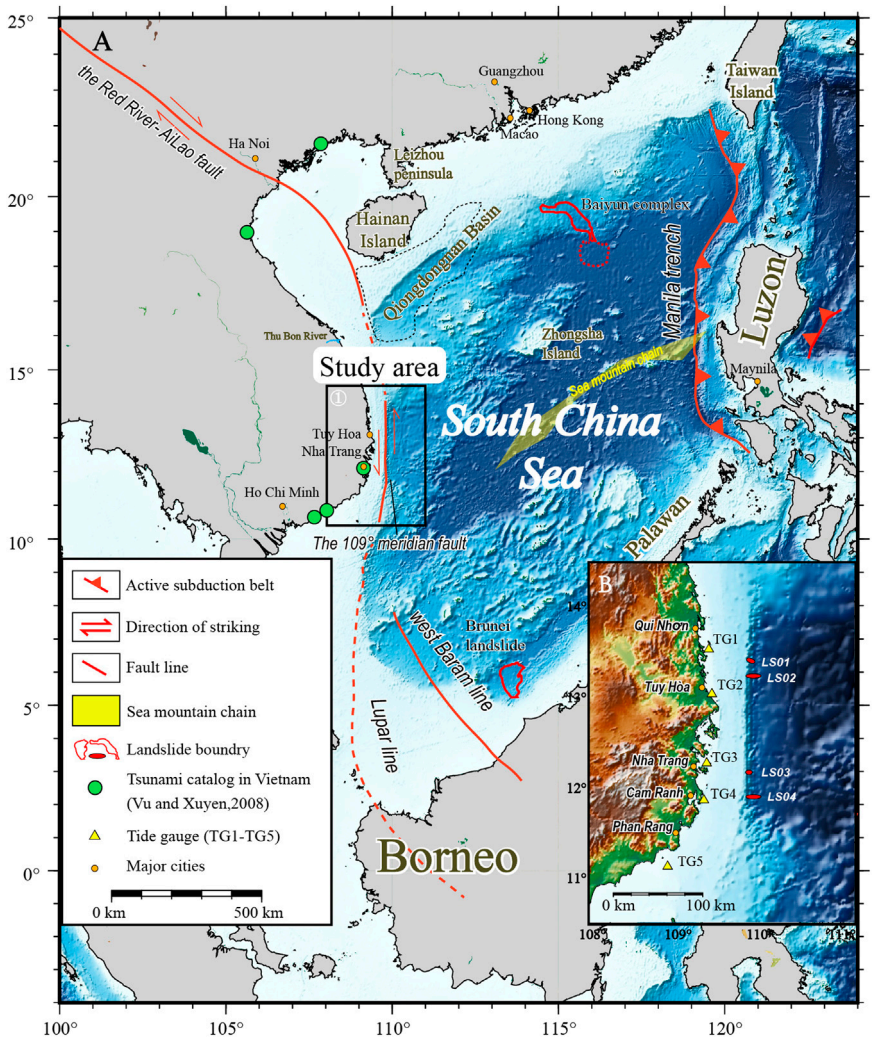

FIGURE 1 | The tectonic setting of the study area **(A)**. South China Sea (SCS), containing the major tectonic structure, geographic location and major cities. The black rectangle indicates the study area where the 109° meridian fault is located. The inset figure **(B)** shows the spatial distributions of the selected landslides (red ellipse), synthetic gauges (yellow triangles) and major coastal cities in SCV.

FUNWAVE-TVD model (Shi et al., 2012) for tsunami wave propagation in a larger domain. We conclude by describing the potential characteristics of tsunamis generated by the modeled landslides with reference to the implications for tsunami hazard locally in Vietnam and in the broader SCS region.

2 GEOLOGICAL BACKGROUND

2.1 Geological History of the Western SCS

The geologic structures of the western SCS are mainly related to the large-scale strike-slip systems: The Red River-Ailao fault in the north (Briais et al., 1993) connects the 109°meridian fault offshore of central Vietnam, and extends to the Lupar line in the south (**Figure 1**). The Red-River Ailao fault originates from the Ailao Mountain, and stops southwest of Hainan Island, likely connecting to the northern tip of the 109° meridian fault (Fyhn et al., 2009a) which developed along the continental shelf - slope transition zone in eastern Vietnam (Morley, 2002; Clift et al., 2008). The 109° meridian is located on the shelf break, and has a total length ~800 km (Sun et al., 2006), covering a latitude range between 17°N and 10°N. Three successive deformation phases for the Red-River Ailao fault and the 109° meridian fault have been inferred and include left-lateral movement from ~30 to 16 Ma, a transitional phase between 16 and 5.5 Ma when slip velocity decreased and eventually ceased, and right-lateral movement with low rates after 5.5 Ma (Tapponnier et al., 2001; Clift and Sun, 2006; Zhu et al., 2009). The 109° meridian fault has the Zhongjiannan Basin/Phu Khanh Basin located offshore to the east. It was likely formed by intensive spreading during the Middle-Late Eocene (Hongfang and Ling, 2006). From the Late Oligocene to Early Miocene (~28–13.8 Ma B.P), the basin experienced a right-lateral transition and extension rifting

stage (Lei et al., 2015). The late Neogene (~10.4 Ma B.P) uplift occurred in the south and central Vietnam, which suggested the seaward tilting of the region onshore and offshore of central Vietnam (Fyhn et al., 2009a; Wang et al., 2013). During the same period, onshore fission track studies reveal the onset of major uplift evidenced offshore by an acceleration in the rate of late Neogene cooling (9–15°C/Ma) (Carter et al., 2000). The uplift and related increase in offshore sediment supply influenced the Zhongjiannan Basin/Phu Khanh Basin, resulting in the high slope gradient continental slope along the western SCS (Hongfang and Ling, 2006; An et al., 2013; Wang et al., 2013).

The elevation difference of the steep continental slope approaches 1,500 m at many places. Although the slope has been subsequently adjusted and modified by sediment deposition, most of the slope gradient still maintains above 10°. Moreover, the east coast of Vietnam is located in a tropical monsoon zone and has numerous montane rivers that drain the 10,350 km^2 range that extends most of the way down the Vietnam and reaches highest of 2,819 m (Souvignet et al., 2014; Tan et al., 2014). Holocene sedimentation rates on the offshore shelf of the Thu Bon River mouth are very high, ranging between 10.1 and 124.5 cm/ka (Schimanski and Stattegger, 2005). The high sedimentation rates on the continental shelf off the coast of Vietnam form fundamental conditions for developing submarine landslides. For example, in the central Vietnam offshore, during the late Miocene (~5.5 Ma), a large-scale submarine landslide with an area of approximately 18,000 km^2 and a maximum thickness of 930 m formed in the deep-water region of the Qiongdongnan basin (Wang et al., 2016). The identification of several large-scale submarine landslides in the geological record implies that strike-slip activity on the Red-River Ailao fault and the 109° meridian fault along with consistent and high sediment supply have an influence on the stability of the continental slope.

2.2 Affecting Factors of Slope Instability

2.2.1 Oversteepening

Oversteepening is regarded as a crucial precondition prior to many slope failures. According to the mechanics and slope readjustment model of Ross et al. (1994), if the applied shear stress exceeds the shear strength of marine slope sediments, a submarine landslide will occur. The steep, sediment laden slopes of the study area is the final product of tectonic activity which offset part of depositional profile, leading to erosion and oversteepening that eventually promoted the slope instability (Fyhn et al., 2009b). In addition to tectonic factors, high sediment-deposition rates contribute to the oversteepening process. In the process of slope evolution of the central Vietnam continental slope, the excessive steepness of the basement caused by tectonic activity and the large amount of sediment brought by the central rivers would likely result in significant excess in sediment supply to the continental slope. With these contributions, a large number of submarine landslides were developed on the continental slope of eastern Vietnam (**Figure 2**).

2.2.2 Seismic Activity

Earthquakes are identified as the most common triggers of submarine landslides in many regions (Locat and Lee, 2002; Urgeles and Camerlenghi, 2013; Huhn et al., 2019). Previous studies suggest that earthquake recurrences are remarkably correlated to the failure possibilities of submarine landslide (Urgeles and Camerlenghi, 2013). Along the 109° meridian fault, historical documents report 18 earthquakes during 1919–2005 with the maximum magnitude up to M = 6.1 (Hong Nguyen et al., 2012). Statistically, there are 71 earthquakes ranging from M = 3.0 to M = 6.1 since 1715, including volcanogenic and tectonic events (Nguyễn Hồng Phương, 2017). The former can be regarded as a direct trigger of submarine landslides, and the latter can promote the slope instability by deducing the shear strength of sediment (Posamentier and Martinsen, 2011; Huhn et al., 2019). The earthquake swarms are largely distributed near the south of the Tuy Hòa shear zone (~12°N) (Vu et al., 2008). Hong Phuong (2001) use the peak ground acceleration (a_{max}) to evaluate quantitatively the geodynamic regime of the central Vietnam coast, and find that there are two anomaly zones of a_{max}. One of them is completely superimposed on the seismically active fault segment of the 109° meridian fault system, suggesting that there is a high possibility of slope mass failure triggered by earthquakes along this fault.

2.2.3 Relative Sea Level Change and High Sedimentation Rate

Since the late Pleistocene (~20 ka), the regional sea level offshore Vietnam has changed dramatically, especially during 9–13 ka B.P, rising from −80 m to −20 m (Schimanski and Stattegger, 2005). According to Pham Pham Nang Vu (2009), the studied submarine landslides probably occurred during 10–12 ka B.P between the transition time of the last glacial and the last interglacial when the sea level steadily rose. Some previous studies suggested that landslides occur more frequently during periods of sea level rise and lowstand (Day and Maslin, 2005; Lebreiro et al., 2009; Locat et al., 2009; Georgiopoulou et al., 2010; Smith et al., 2013), although Urgeles and Camerlenghi (2013) pointed out that no strong global correlation of landslide frequency with sea level changes. The possible mechanisms about how the climate-driven sea level change affect the landslide frequency thus still remains controversial (Tappin, 2010; Smith et al., 2013; Urgeles and Camerlenghi, 2013). Factors associated with hydrate dissociation, increased overpressure in sediments and seismic activity are proposed as probable causes of landslide during periods of sea level rise (Smith et al., 2013). In a much shorter time-scale, the sea level fluctuations caused by storm waves affect the slope stability via altering the stress regime at the seafloor, but the direct impact of changing sea level on slope is minor (Weaver and Kuijpers, 1983; Lee et al., 1996). To summarize, the change of sea level in the offshore east Vietnam coast serves more like a precondition than a direct trigger.

Rapid sedimentation is another common cause of submarine landslide through increasing the pore pressure and decreasing the effectives stress in the sediment (Harbitz et al., 2006).

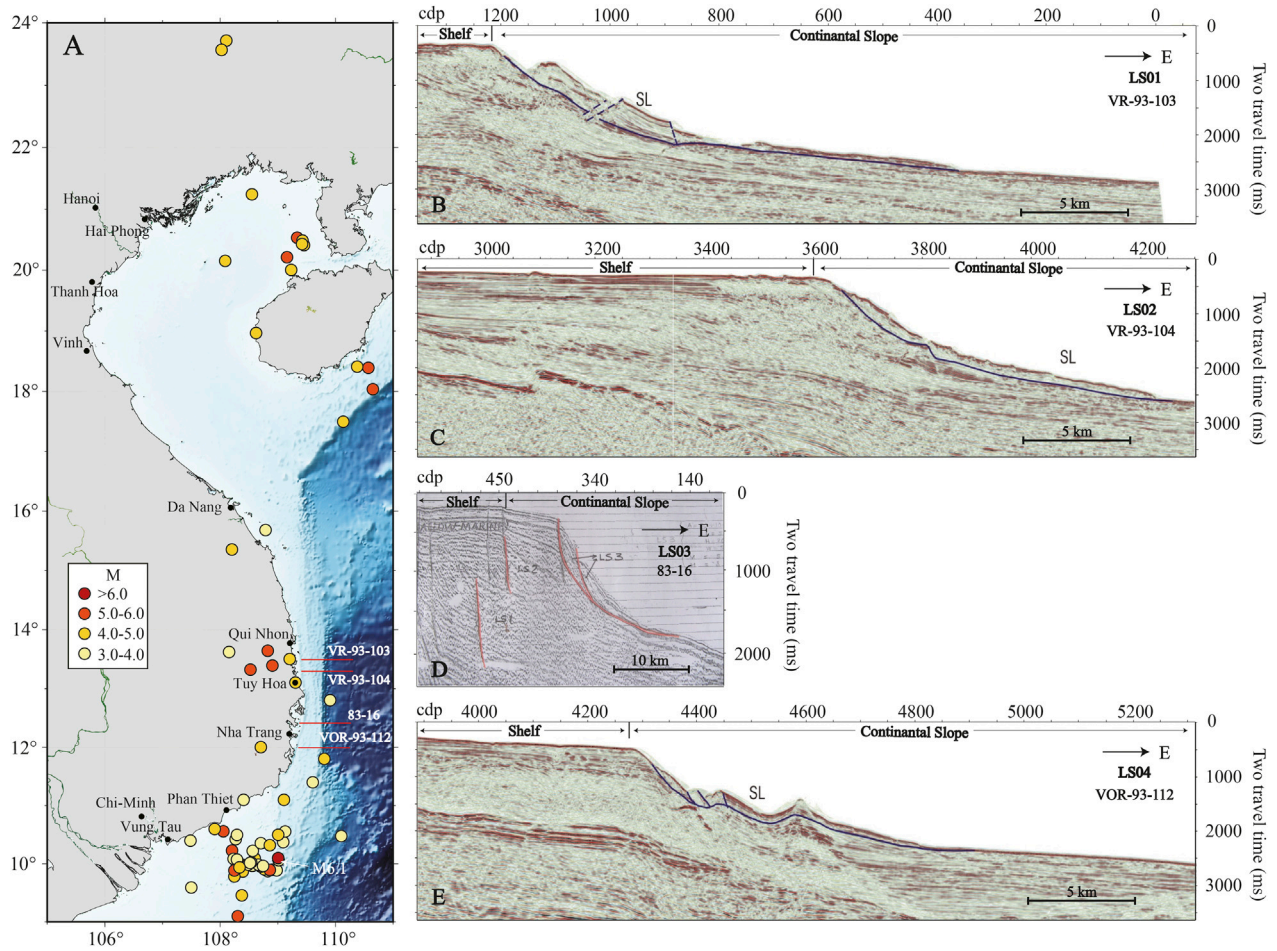

FIGURE 2 | (A) Earthquake catalog and profiles of western SCS. **Dots**: earthquakes [data from NCEDC, https://ncedc.org/cgi-bin/catalog-search2.pl, Nguyễn Hồng Phương (2017), Phuong and Truyen (2015)]. **Yellow dots**: cities of Vietnam. **Blue lines**: seismic profiles. **(B–E)**: seismic profiles of LS01-LS04 (Pham Nang Vu, 2009).

Overpressure is more likely to be found in locations with rapid sedimentation. Schimanski and Stattegger (2005) analyze sediment core from Vietnam shelf and date the sediment samples with the AMS-^{14}C technique. Some data of the cores, locate in the narrow central shelf, showing high-sediment rates, with a MAR (mass accumulation rates) of 60–120 g/cm^2 ky. These values exceed MAR of other shelves in the SCS at least by a factor of 2–4 (Schimanski and Stattegger, 2005), occurring in early Holocene times, which greatly increase the instability of the slope.

2.2.4 Volcanic Activities

The volcanic activities in the 109° meridian fault were noted to have started in the late Miocene (Fyhn et al., 2009a). Volcanic activity can influence the instability of slopes in two ways. Firstly, volcanic activity beneath East Vietnam leads to an uplift of the coastal topography which was accompanied by activation of rivers (Carter et al., 2000; Clift et al., 2004; Tan et al., 2014; Maselli et al., 2020). The increased elevation strengthens the downcutting of river. With the abundant rainfall brought by the southwest monsoon, the river transport capacity is significantly enhanced, resulting boosted sedimentation rates and increased sediment thickness on East Vietnam shelf. All these factors form the precondition of slope instability. Secondly, the volcanic activities lead to the magmatic intrusions in central Vietnam coast (Clift et al., 2004; Fyhn et al., 2009a). During the process of magma cooling which produced by, the release of hydrothermal fluid and overpressure gas can rise to surface through fractures or passages in the slope, becoming one of the triggers of submarine mass failure (Fyhn et al., 2009a). A series of normal, high angle faults forming graben-like structure in the basement (Tan et al., 2014), which means that the high-angle faults of the geologic structure may become the main passages of gas transport to the shallower layer. The rising gas pass by the finer layer and then accumulates, forming local overpressure, which reduces the effective stress and the shear strength, leading to slope mass failure.

3 NUMERICAL MODELING OF SUBMARINE LANDSLIDES

To estimate the tsunamigenic potential of the submarine landslides on the steep continental slope near Vietnam, we conducted a pilot study using four representative landslides

TABLE 1 | Key parameters of submarine landslides.

	Landslide 1 (LS01)	Landslide 2 (LS02)	Landslide 3 (LS03)	Landslide 4 (LS04)
Latitude (◦)	13.4167	13.25	12.166667	11.9176
Longitude (◦)	109.8	109.8	109.8	109.8
Length (km)	10	20	5	20
Width (km)	5	5	5	5
Depth (m)	250–2,500	300–1,000	300–2,000	300–1,500
Volume (km^3)	3.5	14.0	1.3	10.5
Thickness (m)	200	400	150	300
Mean local slope angle (◦)	20–30	30	30	25
Azimuth of motion (◦ East)	–20	0	0	0
Terminal velocity (m/s)	54.2525	57.9	60.6676	65.1278

TABLE 2 | Locations of synthetic gauges.

Locations	Lon (°)	Lat (°)
TG1	109.3500	13.5444
TG2	109.3840	13.0523
TG3	109.3254	12.2880
TG4	109.2941	11.8806
TG5	109.0500	11.5001

based on the constraint of the limited information from 2D seismic data (**Figure 2**). From north to south, four submarine landslides are parameterized with different geometry, thickness, and kinematics. The submarine landslides are estimated as 5–20 km long, and 5–10 km in width with the maximum thicknesses in the range of 150–400 m. These landslides are generally distributed in water depth of 250–2,500 m between latitudes of 11.9176° and 13.4167° (see the key parameters in **Table 1**). Due to the limited spatial coverage of seismic data, we simplify the shape of these landslides as ellipse. Each submarine landslide has an elliptical footprint on the slope, centered as its estimated initial location. The thickness distributions of these landslides are assumed to be quasi-Gaussian. Additionally, five virtual gauges are specified near the coastline of major cities to better visualize the tsunami propagation process. The exact locations of these gauges are listed in **Table 2**.

We used the combination of NHWAVE-FUNWAVE models for tsunami generation and propagation. The landslide materials are treated as rigid slump and deformable slide, corresponding to rigid block and mud flow, respectively. NHWAVE can predict the instantaneous surface elevation and 3D flow field, and provides a numerical solution to the 3D Euler equations for incompressible flow in a terrain and surface-following σcoordinates (Ma et al., 2012). It has been validated for highly dispersive landslide tsunami generation by comparing simulated surface elevations with laboratory experimental data (Enet and Grilli, 2007; Shi et al., 2012). The dynamic landslide failure process and the resultant initial tsunami wave were modeled using fully dispersive non-hydrostatic wave model NHWAVE (Ma et al., 2012). Thus, by treating landslide as a rigid slump, we expect to provide a conservative (i.e., the worst-case scenario) estimate of tsunami generation and coastal impact.

For rigid slump, as in Enet and Grilli (2007), the landslide geometry is idealized as having a "Quasi-Gaussian" shape of elevation $\zeta(x, y)$, and the steepness is controlled by the ε (here $\varepsilon = 0.717$). The elliptical footprint of downslope length b, width w, and maximum thickness T are defined as

$$\zeta(x, y) = \frac{T}{1-\varepsilon}\max\{0, \operatorname{sech}(k_b\xi)\operatorname{sech}(k_w\chi) - \varepsilon\}$$

where (ξ, χ) are the local downslope and spanwise horizontal coordinates, $k_b = 2C/b$, $k_w = 2C/w$, with $C = \operatorname{acosh}(1/\varepsilon)$. Based on these parameters, the landslide volume is given by $V_s = bwT\frac{I_2}{C^2}(\frac{I_1-\varepsilon}{1-\varepsilon})$ with

$$I_{1;2} = \int_0^C f(\mu)d\mu; g(\mu)d\mu$$

And

$$f(\mu) = \operatorname{sech}\mu \operatorname{a\,tan}(\sinh g(\mu)), g(\mu) = \operatorname{acosh}\left(\frac{sech\mu}{\varepsilon}\right)$$

For the specified ε, we find $C = 0.8616$, $I_1 = 0.4804$, $I_2 = 0.5672$ and $V_s = 0.3508bwT$.

The kinematic motion of rigid slump is prescribed based on a set of semiempirical formulas given in Enet and Grilli (2007), Grilli et al. (2002). E.g. the terminal speed was calculated according to Grilli et al. (2002), $U_t = \sqrt{gb\frac{\pi(\gamma-1)}{2C_d}\sin\theta}$, where θ is slope angle, b is the length of landslide, γ is the specific gravity of the slide material, $C_d = 1$ is the added mass coefficients. For the deformable slide, we specify the kinematic viscosity to be 0.1 and the Manning coefficient for the viscous slide is 0.1. The Cartesian computational grids were used in tsunami simulations with ~500 m resolution-based grid from GBECO (General Bathymetric Chart of Oceans), which covers the whole SCS.

In this study, the tsunami waves in the first 30 min after failure were simulated by NHWAVE and serve as initial condition of FUNWAVE-TVD for propagation modeling in larger domain. The surfaces wave height and horizontal velocity of the tsunami wave are then interpolated into the whole SCS gridded data for FUNWAVE-TVD (Tehranirad et al., 2011; Shi et al., 2012; Kirby et al., 2016). FUNWAVE-TVD is developed based on the fully nonlinear Boussinesq equations and is used a "total variation diminishing" scheme to better model wave breaking dissipation

and dispersion (Chiocci et al., 2008; Shi et al., 2012). The combination of NHWAVE-FUNWAVE modeling approach has been validated for the Tohoku 2011 tsunami (Tappin et al., 2014) and applied in many events (Li L. et al., 2015; Grilli et al., 2017; Grilli et al., 2019; Li et al., 2019; Schambachand Lauren, 2020; Schambach et al., 2021).

According to the seismic profiles (Pham Nang Vu, 2009), we identified four representative submarine landslides (**Figure 2**). Due to a lack of accurately mapped bathymetric data, the initial slide is modeled as a sediment mound of quasi-Gaussian cross-sections, with maximum thickness T, and an elliptical footprint of down slope length b and width w. **Table 1** gives the geometric parameters and initial location estimated for each modeled landslide base on the seismic profiles.

4 RESULTS

4.1 Tsunami Wave Generations

Figure 3 shows the tsunami surface elevation generated by both deformable and rigid material of LS01-LS04 at t = 10 min after the release of each slide. The spatial distributions of tsunami surface elevation are similar in shape but differ significantly in magnitudes (**Figure 3**). The initial waves generated by rigid slumps of all scenarios are much higher than that generated by their deformable counterparts (**Figure 3**). With all the other key parameters (initial water depth and slope gradient) being similar, slides with larger volumes (e.g., LS02 and LS04) generate larger initial tsunami wave heights than those with smaller volumes (LS01 and LS03). **Figure 4** shows the extracted surface elevations at t = 10 min along four transects which generally follow the central axis of each slide. The heights of initial surface elevation generated by rigid slump are 1.5–3 times larger than that generated by deformable slide (**Figure 4**). LS02 that has the largest volume among all the slides triggers the highest tsunami waves ~15 m while the initial wave generated by the smallest slide (LS03) is ~ 5 m (**Table 1**; **Figure 4**). The initial waves generated by rigid slump and deformable slide consist similar waveform pattern but with different level of irregularity (**Figure 4**). Taking LS02 as an example (**Figure 4B**), after being released, in the sliding direction, the wavefront is a large crest followed by a large trough and a series of wave train with some of them even larger than the leading wave, while in the opposite direction of the slide motion, large leading depression wave followed by a crest with similar amplitude propagates backward toward the coast (**Figure 4**).

Figure 5 show the snapshots of surface elevations generated by LS02 and LS04 at 15 and 25 min. The spatial distributions of surface elevation generated by all slides demonstrate as radical circles/ripples, with longer wave lengths in the deep sea and shorter landward wave lengths in the continental shelf (**Figure 5**). When the tsunami waves propagate toward the coastlines over continental shelf, the velocity of the landward wave trains slows down due to the shoaling effect and forms a shell-shape wave pattern (**Figure 5**). For all cases, the propagation directions of leading waves are similar which largely direct towards the east.

4.2 Tsunami Propagation

4.2.1 Characteristics of Tsunami Propagation

Figure 6 shows the snapshots of tsunami surface elevations generated by the rigid slumps of LS02 and LS04. Surface elevations generated by the deformable slides of LS02 and LS04 are shown in **Supplementary Figure S2**. In all the scenarios, tsunami waves are largely featured with a leading crest followed by a wave trough (**Figure 6**). Only a narrow portion of tsunami waves propagating opposite to the slide direction are led by a depression wave followed by a positive crest wave (**Figure 6**, also refer to **Figure 5**). The orientations of wave fronts are determined by the seafloor bathymetry and significantly affected by the presence of seafloor relief, including Xisha, Zhongsha, Nansha islands and the seamount chains. The tsunami waves slow down when they encounter the deep-sea islands/seamounts and bend around the islands before meeting behind them due to the strong wave reflection and diffraction effect (**Figures 6B,E**). The wave amplitudes increase when tsunami waves approach the continental slope and then propagate into the continental shelf due to the shoaling effect.

We investigate the wave evolution characteristics by extracting wave profiles at t = 5, 15, 25, 35, 40, 45, 50, 55, 60 min time snapshots along transects EE′ and FF′ for rigid slump LS02 and LS04 (**Figures 7A,B**). In both scenarios, the tsunami waves evolve with similar pattern. The initial tsunami wave crests and troughs could reach ~30 m/−40 m for LS02 and ~15 m/−30 m for LS04 in the source region right above the slumps, then the waves split into two groups and depart in two opposite directions. The one propagating toward the coast experiences shortened wavelength, first increased and then decreased wave amplitude due to the combined effect of shoaling and bottom dissipation. The waves propagating towards the deep sea experiences the opposite effect with stretched wavelength and decreased wave amplitude. We observe that the wave amplitude declines significantly in both propagation directions. For LS02 (**Figure 7A**), the amplitude of landward wave crest drops from ~30 m in the source region to ~3 m near the coastline (**Figure 7A**). From longitude 109.8°E toward east where water depths of both profiles are over 1,000 m, the amplitude of seaward wave trough decreases from −40 m to −1.5 m in the deep sea at 60 min. Similarly, in the case of LS04, the amplitude of wave crest drops from 15 to 1.0 m in the landward direction with the wave trough decaying from −40 m to −0.7 m in the seaward direction (**Figure 7B**).

4.2.2 Nearshore Impacts in Central Vietnam

The central Vietnamese coast has extremely complex bathymetry and morphology featured with many chains of islands and many half-enclosed bays. When tsunami waves propagate towards such an irregular coastline, interference including wave reflection, diffraction, refraction and resonance are expected. **Figure 8** shows the snapshots of tsunami surface elevation generated by rigid slumps of LS01-LS04. Due to the difference of geographical

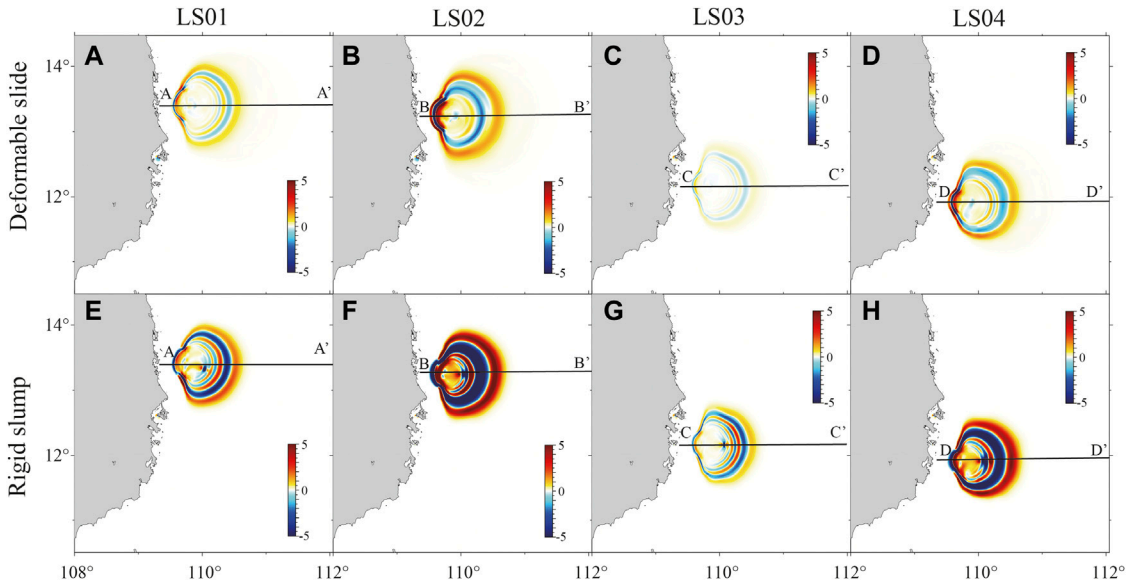

FIGURE 3 | Spatial distributions of the tsunami surface elevation at t = **10** min **(A–D)**: deformable slide of LS01-LS04; **(E–H)**: rigid slump of LS01-LS04.

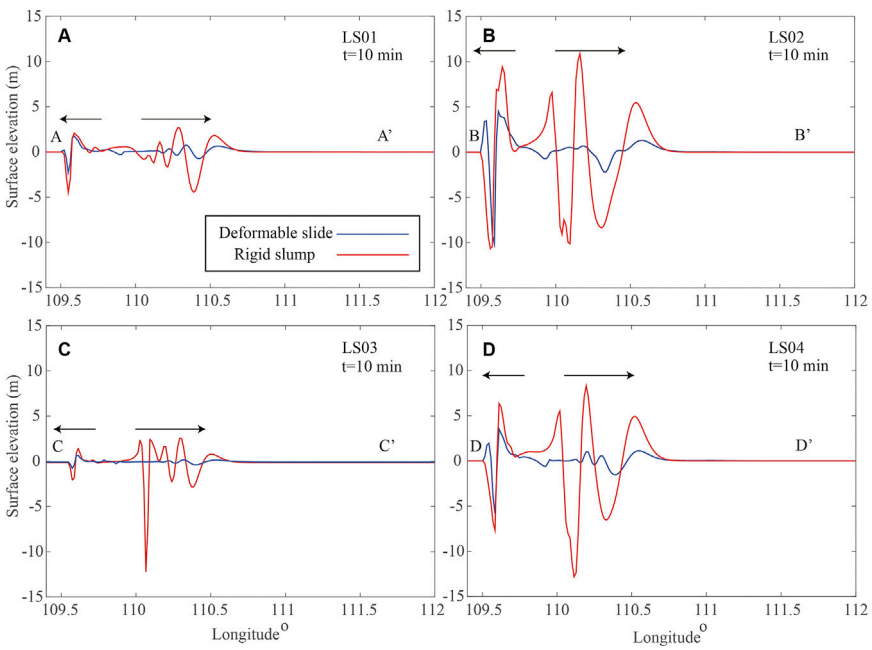

FIGURE 4 | The profiles of tsunami surface elevation generated by **(A)** LS01, **(B)** LS02, **(C)** LS03, **(D)** LS04 along transects **AA′–DD′** at t = 10 min. See locations of **AA′–DD′** in **Figure 3**.

locations, LS01 and LS02 generate tsunami waves propagating dominantly towards southwest during the shoaling stage, while the main tsunami direction generated by LS03 and LS04 is toward northwest. Consequently, tsunami waves generated by LS01 and LS02 reach cities in the north, e.g., Qui Nhon, Tuy Hoa earlier than cities in the south, e.g., Nha Trang and Cam Ranh, while tsunami waves generated by LS03 and LS04 arrive southern cities first. Significant wave refraction occurs at the coastal island chains along the complex coastline, focusing wave energy and amplify wave height behind the lee side of the islands, i.e., Hon Lon, Hon Tre and Cu lao Xuanh (**Figure 8**). For coastlines with half-enclosed bays, particular attention should be given to tsunami amplifications due to resonance effects (Rabinovich, 2010; Bellotti et al., 2012). When the tsunami period matches the natural

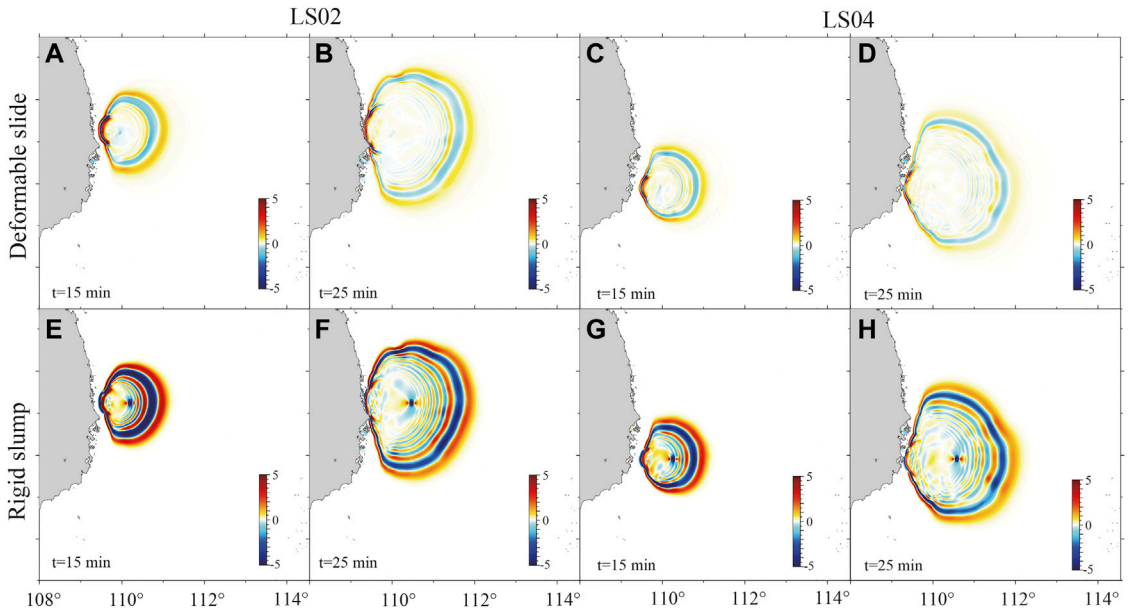

FIGURE 5 | Snapshots of tsunami surface elevation simulated by NWAVE at t = 15, 25 min after initiation. **(A–D)**: Deformable slide; **(E–H)** Rigid slump; **(A,B,E,F)**: LS02; **(C,D,G,H)**: LS04.

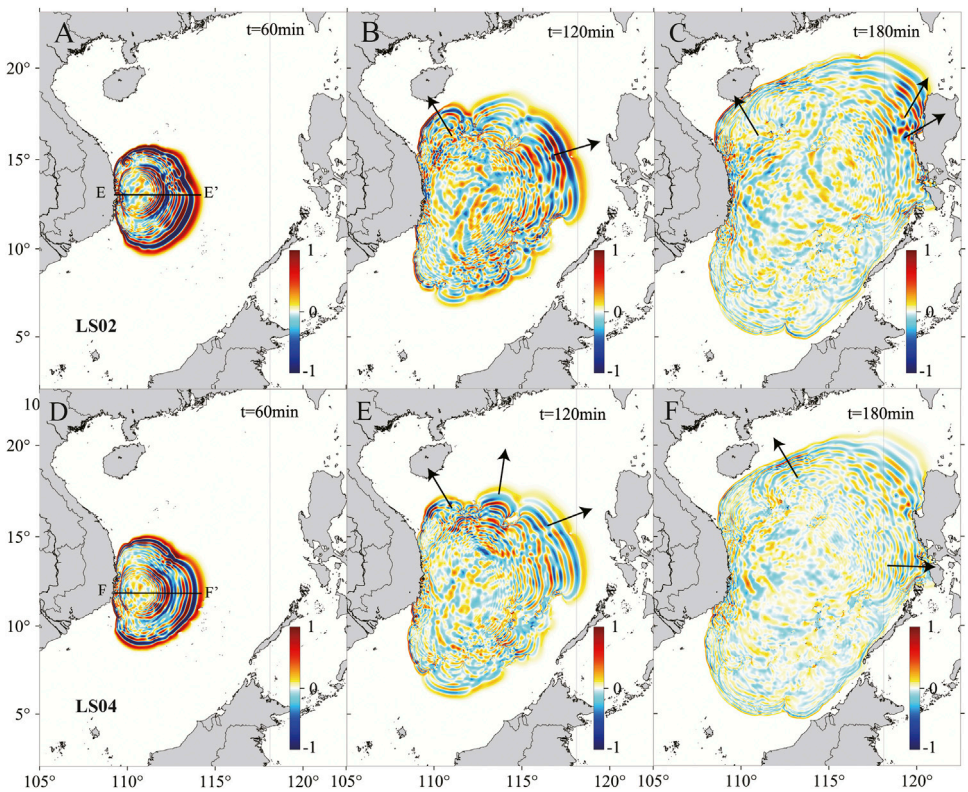

FIGURE 6 | Snapshots of surface elevations simulated by FUNWAVE-TVD at time = 60, 120, 180 min for **(A–C)** LS02 and **(D–F)** LS04. **Black arrows**: the dominant direction of tsunami wave propagation.

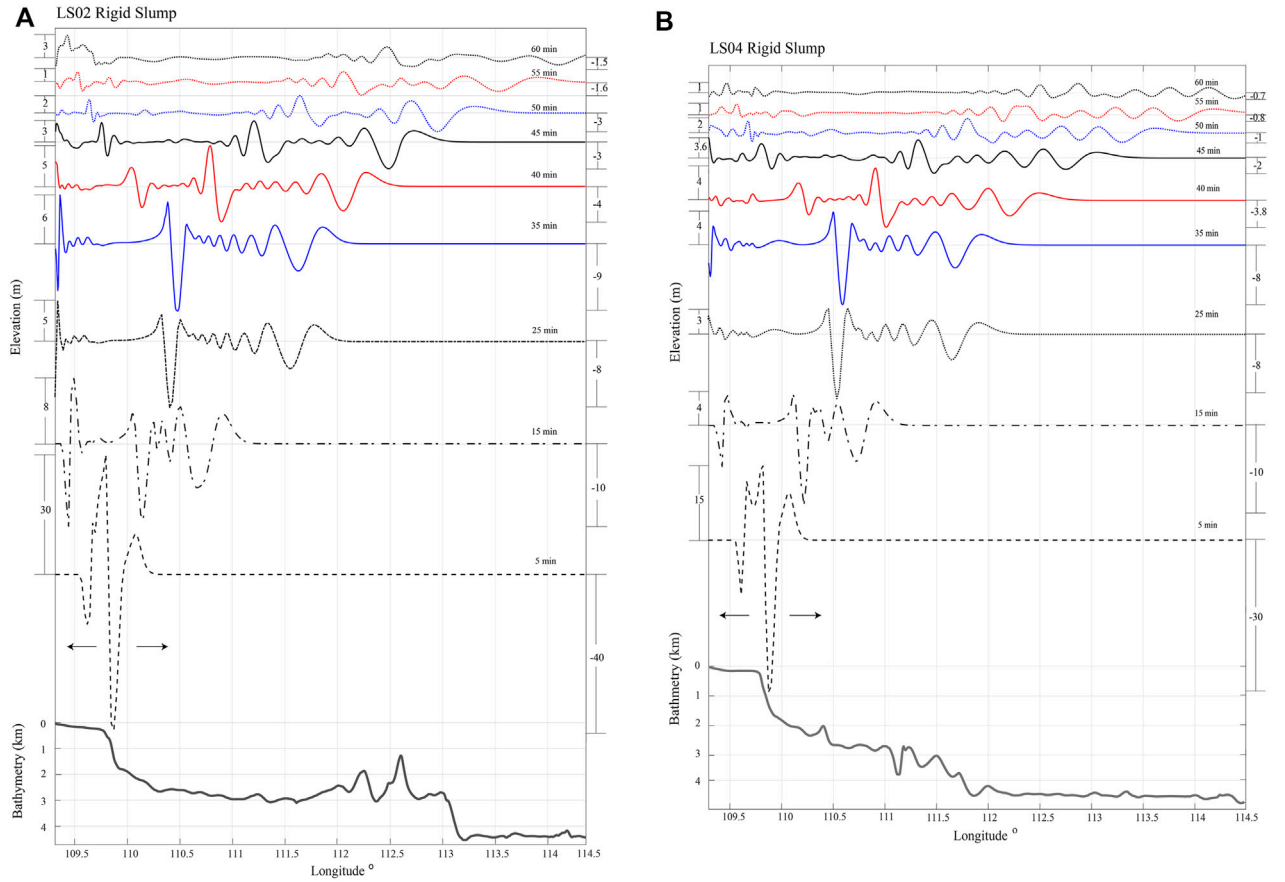

FIGURE 7 | Profiles of tsunami surface elevation generated by rigid slumps of **(A)**: LS02 (CC′) and **(B)**: LS04 (DD′) at t = 5, 15, 25, 35, 40, 45, 50,55,60 min. **Black arrows**: the propagation direction of tsunami wave.

oscillation modes of these bays, tsunami wave heights can be enhanced, resulting exacerbated coastal damage (Lepelletier, 1981). The tsunami hazard related to resonance effect in this region deserves more detailed future study. To predict the onshore tsunami wave heights, numerical simulations based on high-resolution bathymetric data and topographic data is required.

4.2.3 Maximum Surface Elevation

The maximum wave height distributions of all the eight scenarios are shown in **Figure 10**. We also overlay the tsunami travel time contours in every 30 min on the maps. The studied landslides, especially the deformable slides (**Figures 10A–D**), generate very localized tsunami impact with most of the wave energy concentrating in the central Vietnam. With other factors (initial water depth, slide material etc.) being similar, the total volume of slide is the key factor determining the tsunami generation capacity. We can see relative smaller slides (LS01 and LS03) produce much smaller spatial distributions and wave amplitudes. Similarly, besides the geological location, the only difference between LS02 and LS04 is that the LS04 is thinner. As a result, LS04 produces relatively compact and smaller wave heights. (**Figure 10**).

A combination of directivity from the slide orientation and the influence of bathymetry determine the final distribution of maximum wave height. In the near-source region, the shapes of the maximum surface distribution interestingly resemble "volcanic-like" (**Figures 10E–H**) or "flank collapsed volcanic-like" shape from a 3D view (**Figures 10A–D**). The crater of these "wave volcanos" are the source areas right above the continental slope. The collapsed flanks are formed due to the continental slope reflection which will be explained in detail in the discussion section. In the relatively far-field, seafloor topography determines the propagation direction of tsunami energy. One notable phenomenon, the ocean ridge in the middle of the SCS basin guides tsunami wave energy towards the west coast of Philippines (**Figures 10F,H**), resulting relatively high tsunami waves in the coastline of western Luzon.

Using LS02 as an example, **Figure 10** illustrates a more quantitative comparison between the maximum surface elevation generated by deformable slide and rigid slump. While the maximum wave heights reach 4–4.6 m in both scenarios along the coastlines near the source region, the majority of remaining coastlines (i.e., southern coast of China) only experience minor or moderate tsunami wave heights (tens of

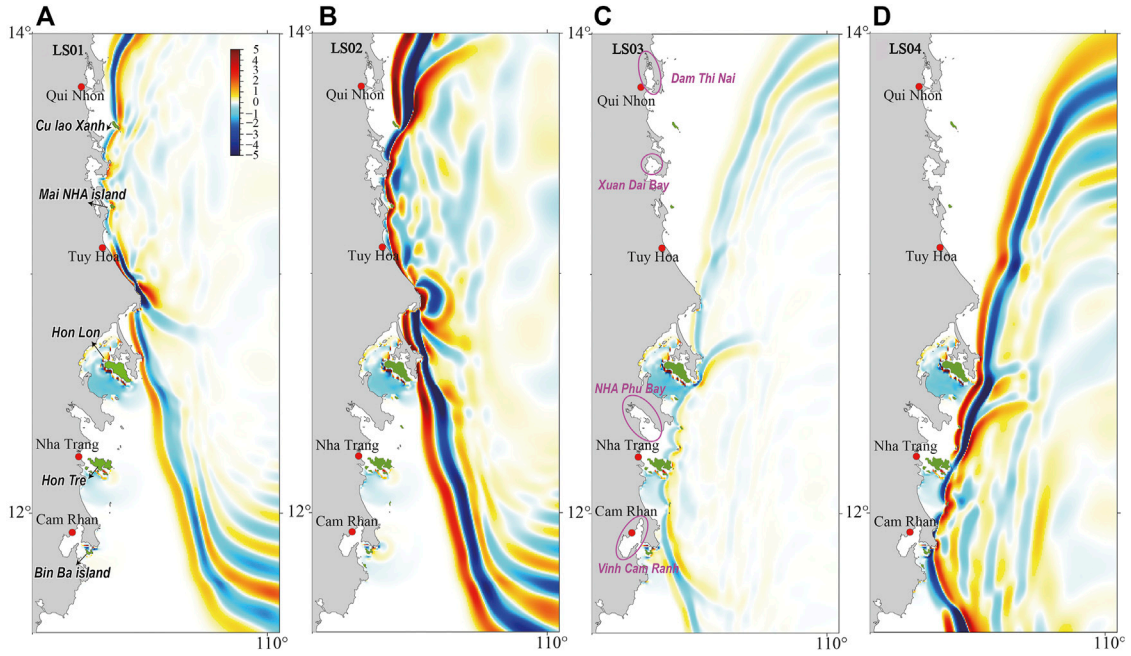

FIGURE 8 | Nearshore propagation of tsunami waves generated by rigid slump of **(A)** LS01; **(B)** LS02; **(C)** LS03; **(D)** LS04. **Red dots**: major cities in central Vietnam coast. **Green polygons** indicate the locations of nearshore islands mentioned in the context. Bays mentioned in 5.2 are marked by **purple circles**.

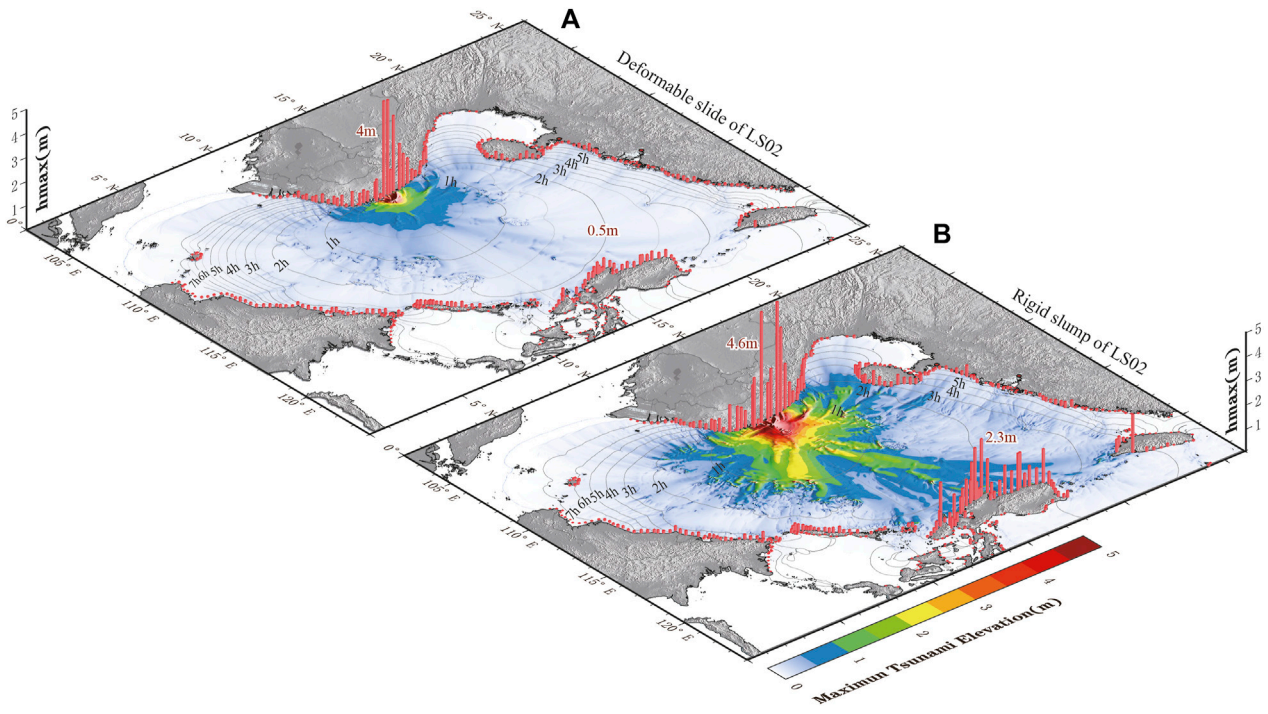

FIGURE 9 | The distribution of maximum wave height generated by **(A)** deformable slide and **(B)** rigid slump of LS02. The maximum wave amplitudes are also shown in red bars at synthetic wave gauges along the 20 m isobath.

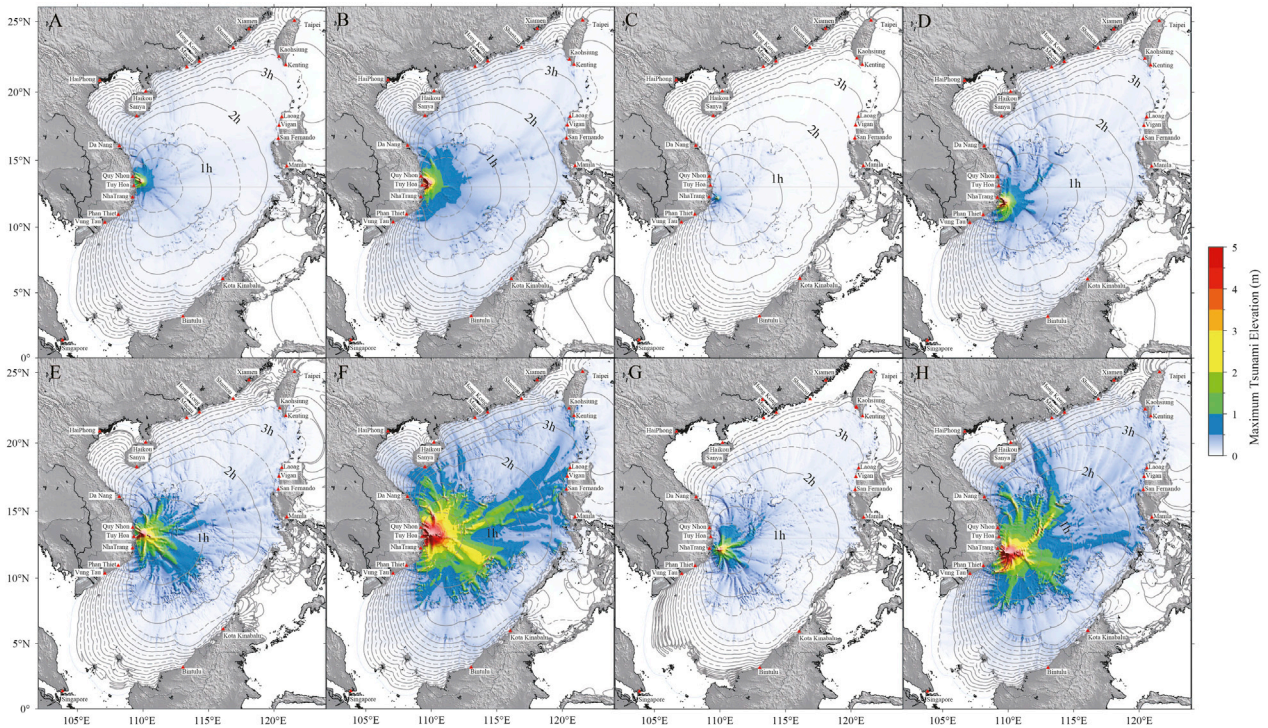

FIGURE 10 | The distributions of maximum surface elevation and tsunami arrival time generated by **(A–D)** deformable slides of LS01-LS04 and **(E–H)** rigid slumps of LS01-04.

cm). The waveguide effect of ocean ridge is more evident in the rigid slump scenario which includes 2.3 m high tsunami waves across the SCS in west Luzon (**Figure 9B**). We also observe one coastal location in southeast Taiwan has exceptionally high wave amplitude (~1.6 m) compared with its nearby gauges (tens of cm). When closely examining the animation of tsunami propagation in this specific region (**Supplementary Video S1**), we show that such typically higher amplitude is at least partially related to the unique double-arc structure in the Luzon strait (Yang et al., 1996). The role of mid-ocean ridges in guiding tsunami propagation has been clearly demonstrated in previous tsunami events, e.g., the 1833 event in South Sumatra (Okal and Synolakis, 2008), the 2004 Indian Ocean Tsunami (Titov et al., 2005), the 2006 Kuril tsunami (Kowalik et al., 2008) and the 2011 Tohoku tsunami (Song et al., 2012). Special attention should be given to coastal regions which are located in the terminus of such waveguide structures.

4.2.4 Tsunami Wave Arrival Time

In all simulated scenarios the first tsunami waves arrive at central Vietnam coast within 30 min. Major cities including Quy Nhơn, Tuy Hòa, Nha Trang, Cam Ranh and Phan Rang would experience the first tsunami wave between 30–60 min (**Figure 10**). Depending on the landslide locations, the tsunami arrival time is ~1–1.5 h for nearby archipelagos inside the SCS, like Xisha and Zhongsha. The west Luzon coast is affected by tsunami waves (~2.5 h) in the relatively far-field where the tsunami directivity effect and relatively deep bathymetry between the studied landslide cause a relatively higher projected tsunami. Elsewhere in the SCS the arrival time is commonly between 2.5–3 h for southeast Hainan, ~3.5 h for southwest Taiwan Island and north Borneo Island, ~5–6 h for the southern coast of mainland China and more than 10 h for east coast of Malay Peninsula and Singapore (**Figure 10**).

5 DISCUSSION

5.1 Is the Tsunami Hazard Enhanced by the Steep Continental Slope?

The modeling suggests the potential for one particularly interesting phenomenon; that the tsunami waves pile up in front of the sharply bathymetry change at the continental slope near central Vietnam. This leads to a stripe-like wave hump parallel to the edge of continental shelf (see the maximum surface elevation in **Supplementary Figure S1**). To illustrate the locations of the wave hump, we extract the profiles of maximum wave height and their corresponding bathymetry along seven transects perpendicular to the orientation of the edge of continental shelf (**Figure 11**). From north to south, the peak locations of the wave humps are 110 ± 0.1° which correspond to water depth ~1,500–2,000 m (**Figure 11**). We hypothesize that the linear wave hump feature is likely largely caused by the combined effects of wave refraction and shoaling effect on the continental slope. Due to the steepness of this specific continental slope, a large difference between the propagation speed at the top (~200 m depth) and bottom edge

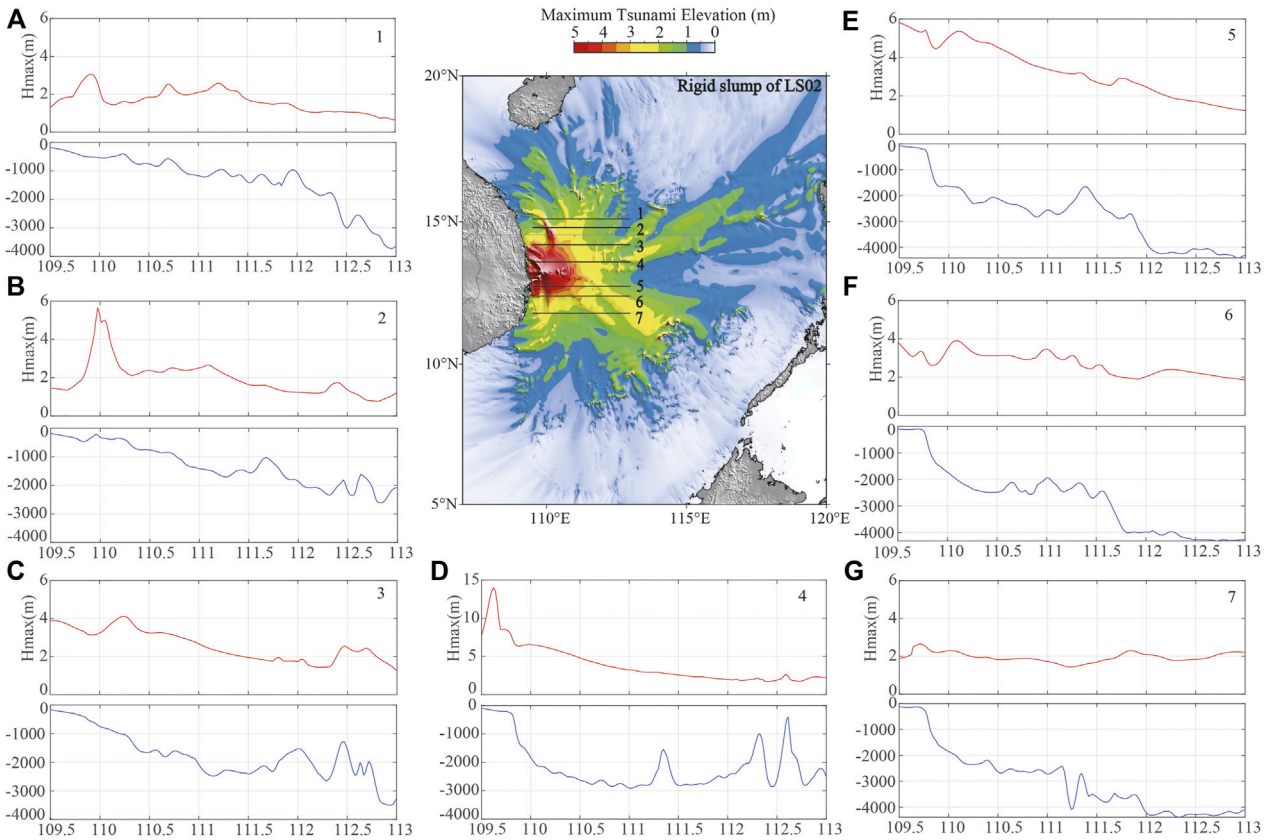

FIGURE 11 | The profiles of maximum surface elevation and their corresponding bathymetry along seven transects marked in the subplot in the middle.

(2000 m depth) leads to rapid shortening of the wavelength and dramatic localized increase in wave height. At the same time, the orientations of tsunami wavefront is adjusted by strong wave refraction so that the wave trace roughly follows the orientations of bathymetry with the largest gradient difference in the deeper water.

5.2 Spectral Analysis

Figure 12 show time series of tsunami wave amplitude generated by LS02 (**Figure 12**) at five selected gauges and their wavelet analysis (**Figure 12**, see **Table 2**). We first compare the tsunami waveforms generated by deformable and rigid slides, which show dramatic difference in wave height and wave period at all stations. In general, we find that the surface elevation generated by rigid slump (~2–3 m) is ~2–3 times larger than that generated by deformable slide (~1 m). In most scenarios, gauges closer to the source region experience larger tsunami waves (**Figure 12**). One interesting wave feature at TG04 is that a noticeably larger wave train occurs between 1–1.5 h after the first group of energetic tsunami waves. A similar feature is also shown in the wavelet plots where larger wave energy appears again 1.0–1.5 h after the first energetic wave patch. Such delayed energetic waves are commonly associated with edge waves which travel alongshore with much slower speed than normal tsunami wave (Ursell, 1952).

The subplots of wavelet analyses reveal the frequency-time content of the tsunami waveforms recorded by five synthetic gauges (**Figure 12**). The wavelet plots clearly show strong tsunami energy at the period band of 5–10 min in all the waveforms generated by both deformable and rigid slides. We attribute these energy patches to the tsunami periods associated with the landslide sources themselves. The energetic patches last much longer in tsunami signals generated by rigid slump (~5 h) than deformable slide (~2 h), indicating the tsunami energy decays much faster in scenarios of deformable slide than those of rigid slump.

The wavelet plot generated by LS02 shows distinct patches of tsunami energy at the period band of 8–15 min which we attribute to the landslide source of this tsunami (**Figure 12**). The expected tsunami period of LS02 can be roughly estimated using formulae $T = \frac{2L}{\sqrt{gd}}$, where T is tsunami period, L is source dimension, g is gravitational acceleration (9.81 m s^{-1}) and d is water depth at the source location (Rabinovich, 2010; Heidarzadeh and Satake, 2014). We calculate the tsunami period with source dimensions of 20 km for LS02 and a water depth in the range of 300–1000 m (**Table 2**), and the resulting period are 6.7–12.3 min for LS02. There theoretical values are close to those shown in the spectral analysis.

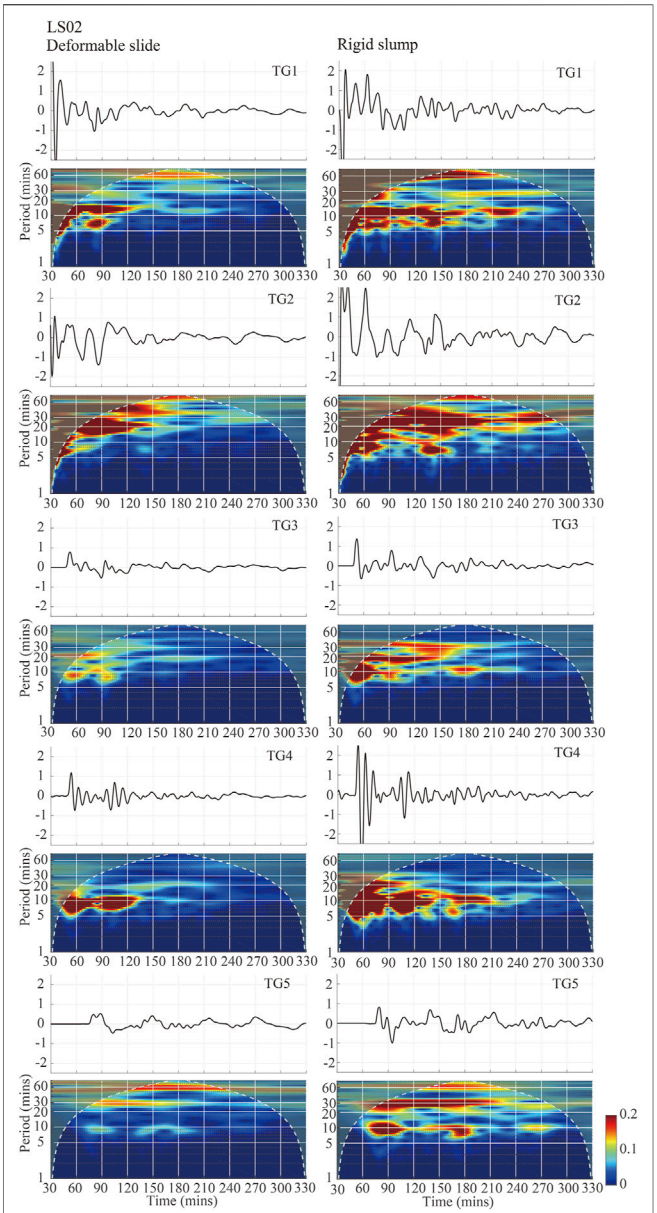

FIGURE 12 | Wavelet analysis of the tsunami waves generated by LS02 at TG1-TG5 for both deformable slide and rigid slump. Note: We use the CWT (continuous wavelet transforms) to analyze the periods of tsunami waves. The cone of influence indicates where edge effects occur in the CWT. Gray regions outside the dashed white line delineate regions where edge effects are significant.

We also observe larger bandwidths centered in 20 min, 30 min and 60–80 min in most of the wavelet plots, especially at locations of TG1, TG2, and TG5. The waves with longer periods are very persistent in TG1 and TG5 lasting ~240–330 min. Such long wave periods and long-lived waves are often related to shelf resonance which is caused by the wave reflection between the coastline and the edge of continental shelf [e.g., Yamazaki et al. (2011), Melgar et al. (2018), Wang et al. (2021)]. Stronger resonance is expected in this particular shelf due to the sharp continental slope.

Harbor resonance is another factor which could significantly amplify tsunami wave amplitude and induce strong current (Rabinovich, 2010). To better understand whether the tsunami wave could generate resonance in the harbor, we choose four bays (namely Dam Thi Nai, Xuan Dai Bay, NHA Phu Bay and Vinh Cam Ranh from north to south) in the latitude range of 11.5°–14°N (see the locations of these harbors in **Figure 8**) to roughly calculate their eigen periods following the formula proposed by Rabinovich (2010) as $T_n = \frac{4L}{(2n+1)\sqrt{gh}}$, for mode $n = 0,1,2,\ldots$ where L is length of the harbor; h is the average water depth in the harbor, g is gravitational acceleration, 9.81 m/s^2; n stands for the number of nodal lines which equals the mode number. When $n = 0$, we obtain the fundamental period (Rabinovich, 2010) which is the lowest mode, known as the *Helmholtz mode* which is of particular importance for any given harbor. The formula given above provide an approximately estimated calculation for the period of the Helmholtz and other harbor modes. The normalized periods of various modes have a specific ratio with a simple geometry of the harbor, which into a relationship of 2/(2n+1) on the basis of the period for closed-basin with constant water depth, $T_n = \frac{2L}{\sqrt{gh}}$ (Rabinovich, 2010). For rough calculations, we use the most basic pattern here, and the others can refer to (Wilson, 1972) depending on the harbor geometry and water depth.

The lengths of the bays are 9.7, 6.5, 16.7 and 4.22 km (**Figure 8**). By extracting the bathymetry profiles, we obtain that the average water depths of the entrance are 2.5 m, 4.4 m, 37 m, and 1 m. We take $n = 0, 1, 2$ for a rough calculation and the results show that the longest natural period of harbor is 130.6 min and the shortest is 11.7 min with the common range of 18–30 min (**Supplementary Table S1**). Except waveforms recorded at TG1 and TG4 in the scenarios of deformable slide, waveforms recorded by other tide gauges contain wave periods of 18–30 min, indicating that there is the possibility that harbor resonance could be induced. Although the tsunami affected regions are limited in many of the presented scenarios, exacerbated tsunami hazard may occur in certain bays or harbors when the natural resonance periods match the tsunami periods or fundamental period of shelf resonance (Kulikov et al., 1994; Pattiaratchi and Wijeratne, 2009). It would be very interesting to further investigate the role of bay and shelf resonance in tsunami amplification along this specific coast based on more sophisticated approach (Yamazaki et al., 2011; Wang et al., 2021), e.g., using finite element numerical models (Bellotti et al., 2012).

We should note that the scenarios we presented in this study only represent limited number of typical cases in this region. Due to the limited spatial coverage of seismic data, we reconstructed these landslides with simplified shapes. In reality, the geometric parameters of landslides could be much more diverse. To reconstruct the initial spatial distribution of landslides more accurately, more detailed geophysical and geotechnical data, including 2D/3D seismic data, multi-beam bathymetric data and sediment cores should be collected in future. Another limitation of this study is that we treat the landslide material as rigid block and viscous mudflow. The tsunamigenic capacity highly depends on the landslide dynamics (sliding, slump, debris flow and turbidity flow etc.) (Zengaffinen et al., 2020) (Harbitz et al., 2014). Future studies

should consider different landslide material as well as rheological behaviors, etc. (Lovholt et al., 2015; Løvholt et al., 2017; Schambach et al., 2018; Kim et al., 2019), e.g., granular flow or multi-phase flow (Shi et al., 2019; Si et al., 2018; Zhang et al., 2021a; Zhang et al., 2021b).

6 CONCLUSION

In this study, we summarize the potential for tsunamigenic landslide failures in the west continental slope of SCS along the 109° fault line. By reviewing previous studies about the geological evolution of the western SCS, we conclude that slope physiography is the final product of series of tectonic activities, seismic deformation, relative sea level changes, relatively high sediment rates and localized volcanism that directly or indirectly promote the slope instability through changing the shear stress of sediment on the slope.

Using a coupled approach: NHWAVE and FUNWAVE-TVD, we simulate the tsunami generation and propagation process of four representative landslides. By examining the hydrodynamic characteristics of the tsunami waves, we summarize our key findings below:

1) The tsunami hazard level depends heavily on the landslide materials and their volumes. Among the studied landslides with volumes ranging between 1.3–14 km^3, the rigid slumps with larger volumes produce larger tsunami impact, e.g., initial surface elevation generated by LS02 reaches 30 m in the offshore region right above the source area and the nearshore tsunami wave heights could reach ~5 m in certain coastline. The LS02 with rigid material is also the only scenario which could cause considerable tsunami impact in the relatively far-field. For all the other scenarios, the tsunami energy decays very fast, especially for those with deformable material, resulting very localized tsunami impacts. Large tsunami wave energy only concentrates in the coastline of central Vietnam and the immediately offshore region near the source. The maximum wave heights generated by these landslides differ significantly, ranging between 5 and 30 m. We roughly calculate the areas of ocean surface with wave height larger than 1 m and find the coverages are 192.3–10614.8 km^2 for deformable slides and 7,367.3 km^2–107327.0 km^2 for rigid slumps. The strong disturbance caused by tsunami waves pose grave threat for ocean engineering in the deep sea.

2) Besides being directly influenced by landslide geometries and their kinematic features, the spatial distribution of tsunami impact is also strongly affected by the seafloor bathymetry along the path of tsunami wave propagation. We observe very interesting hydrodynamic phenomenon associated with the seamount chain, steep continental slope and the double-arc structure in Luzon strait. These seafloor structures either serve as waveguide which facilitate the focused tsunami energy in relatively far-field, or cause strong refraction along the continental slope, forming the stripe-like wave hump parallel to the 109°meridian fault.

3) The wavelet analysis of five virtual gauges in the coastal region disclose that the periods of the landslide tsunami are ~5–10 min. We notice that there are tsunami waves with longer periods centered at 20 min, 30 min and 60–80 min in some locations. Such persistent energy patches are commonly associated with shelf resonance. These periods are found to be within the range of the natural resonance periods of some coastal bays (8–96 min). The potential coincidence suggest amplified tsunami waves with much longer oscillation duration may occur in this region.

4) We should note that the tsunami waves in all simulated scenarios reach the coast of central Vietnam within 30 min after the landslide failure. Loss and damage could be particularly serious for such local tsunamis due to the concentrated tsunami energy and limited evacuation time, as illustrated by the 1998 Papua New Guinea event.

DATA AVAILABILITY STATEMENT

The original contributions presented in the study are included in the article/**Supplementary Material**, further inquiries can be directed to the corresponding authors.

AUTHOR CONTRIBUTIONS

XP, LL, and HN designed the study. XP conducted the study and wrote the manuscript with contributions from all other co-authors. All authors contributed to the discussion and interpretation of the results.

FUNDING

This work was supported by Guangdong Province Introduced Innovative R&D Team of Geological Processes and Natural Disasters around the South China Sea (2016ZT06N331), Innovation Group Project of Southern Marine Science and Engineering Guangdong Laboratory (Zhuhai) (No. 311021002), National Natural Science Foundation (No. 41976197) and Key Research and Development Program of Hainan Province (No. ZDYF2020209). Research by ADS is partially supported by the Singapore Ministry of Education Academic Research Fund MOE2019-T3-1-004 and MOE2018-T2-1-030, the National Research Foundation Singapore, the Singapore Ministry of Education under the Research Centers of Excellence initiative, and by the Nanyang Technological University. ADS and LL are also supported by the National Research Foundation, Singapore, and National Environment Agency, Singapore under the National Sea Level Programme Funding Initiative (Award No. USS-IF-2020-2). This work is granted by the Program for supporting scientific research activities for 1st rank senior researcher by Vietnam Academy of Science and Technology under grant number NCVCC12.03/22-22.

SUPPLEMENTARY MATERIAL

The Supplementary Material for this article can be found online at: https://www.frontiersin.org/articles/10.3389/feart.2022.843173/full#supplementary-material

REFERENCES

An, H., Li, S., Suo, Y., Liu, X., Dai, L., Yu, S., et al. (2013). Basin-controlling Faults and Formation Mechanism of the Cenozoic basin Groups in the Western South China Sea. *Mar. Geology Quat. Geology* 32, 95–111. doi:10.3724/sp.j.1140.2012.06095

Assier-Rzadkieaicz, S., Heinrich, P., Sabatier, P. C., Savoye, B., and Bourillet, J. F. (2000). Numerical Modelling of a Landslide-Generated Tsunami: the 1979 Nice Event. *Pure Appl. Geophys.* 157, 1707–1727. doi:10.1007/pl00001057

Bellotti, G., Briganti, R., and Beltrami, G. M. (2012). The Combined Role of bay and Shelf Modes in Tsunami Amplification along the Coast. *J. Geophys. Res. Ocean.* 117, C08027. doi:10.1029/2012jc008061

Briais, A., Patriat, P., and Tapponnier, P. (1993). Updated Interpretation of Magnetic Anomalies and Seafloor Spreading Stages in the South China Sea: Implications for the Tertiary Tectonics of Southeast Asia. *J. Geophys. Res.* 98, 6299–6328. doi:10.1029/92jb02280

Carter, A., Roques, D., and Bristow, C. S. (2000). Denudation History of Onshore central Vietnam: Constraints on the Cenozoic Evolution of the Western Margin of the South China Sea. *Tectonophysics* 322, 265–277. doi:10.1016/s0040-1951(00)00091-3

Chen, D., Wang, X., Völker, D., Wu, S., Wang, L., Li, W., et al. (2016). Three Dimensional Seismic Studies of Deep-Water hazard-related Features on the Northern Slope of South China Sea. *Mar. Pet. Geology* 77, 1125–1139. doi:10.1016/j.marpetgeo.2016.08.012

Chiocci, F. L., Romagnoli, C., Tommasi, P., and Bosman, A. (2008). The Stromboli 2002 Tsunamigenic Submarine Slide: Characteristics and Possible Failure Mechanisms. *J. Geophys. Res. Solid Earth* 113, B10102. doi:10.1029/2007jb005172

Clift, P. D., Layne, G. D., and Blusztajn, J. (2004). Marine Sedimentary Evidence for Monsoon Strengthening, Tibetan Uplift and Drainage Evolution in East Asia. *Geophys. Monogr. Ser.* 149, 255–282. doi:10.1029/149GM14

Clift, P. D., and Sun, Z. (2006). The Sedimentary and Tectonic Evolution of the Yinggehai–Song Hong basin and the Southern Hainan Margin, South China Sea: Implications for Tibetan Uplift and Monsoon Intensification. *J. Geophys. Res. Solid Earth.* 111, B06405. doi:10.1029/2005JB004048

Clift, P., Lee, G. H., Anh Duc, N., Barckhausen, U., Van Long, H., and Zhen, S. (2008). Seismic Reflection Evidence for a Dangerous Grounds Miniplate: No Extrusion Origin for the South China Sea. *Tectonics* 27, TC3008. doi:10.1029/2007tc002216

Day, S., and Maslin, M. (2005). Linking Large Impacts, Gas Hydrates, and Carbon Isotope Excursions through Widespread Sediment Liquefaction and continental Slope Failure: The Example of the K-T Boundary Event. *Large Meteorol. Impacts* 384, 239–258. doi:10.1130/0-8137-2384-1.239

Enet, F., and Grilli, S. T. (2007). Experimental Study of Tsunami Generation by Three-Dimensional Rigid Underwater Landslides. *J. Waterway, Port, Coastal, Ocean Eng.* 133, 442–454. doi:10.1061/(asce)0733-950x(2007)133:6(442)

Fyhn, M. B. W., Boldreel, L. O., and Nielsen, L. H. (2009a). Geological Development of the Central and South Vietnamese Margin: Implications for the Establishment of the South China Sea, Indochinese Escape Tectonics and Cenozoic Volcanism. *Tectonophysics* 478, 184–214. doi:10.1016/j.tecto.2009.08.002

Fyhn, M. B. W., Nielsen, L. H., Boldreel, L. O., Thang, L. D., Bojesen-Koefoed, J., Petersen, H. I., et al. (2009b). Geological Evolution, Regional Perspectives and Hydrocarbon Potential of the Northwest Phu Khanh Basin, Offshore Central Vietnam. *Mar. Pet. Geology* 26, 1–24. doi:10.1016/j.marpetgeo.2007.07.014

Gatter, R., Clare, M., Kuhlmann, J., and Huhn, K. (2021). Characterisation of Weak Layers, Physical Controls on Their Global Distribution and Their Role in Submarine Landslide Formation. *Earth-Science Rev.* 233, 103845. doi:10.1016/j.earscirev.2021.103845

Gee, M. J. R., Masson, D. G., Watts, A. B., and Allen, P. A. (1999). The Saharan Debris Flow: an Insight into the Mechanics of Long Runout Submarine Debris Flows. *Sedimentology* 46, 317–335. doi:10.1046/j.1365-3091.1999.00215.x

Gee, M. J. R., Uy, H. S., Warren, J., Morley, C. K., and Lambiase, J. J. (2007). The Brunei Slide: A Giant Submarine Landslide on the North West Borneo Margin Revealed by 3D Seismic Data. *Mar. Geology* 246, 9–23. doi:10.1016/j.margeo.2007.07.009

Georgiopoulou, A., Masson, D. G., Wynn, R. B., and Krastel, S. (2010). Sahara Slide: Age, Initiation, and Processes of a Giant Submarine Slide. *Geochem. Geophys. Geosys.* 11, 7014. doi:10.1029/2010GC003066

Giuliani, S., Bellucci, L. G., and Nhon, D. H. (2019). The Coast of Vietnam: Present Status and Future Challenges for Sustainable Development. *World Seas: Environ. Eval. Volume Indian Ocean Pac.*, 415–435. doi:10.1016/B978-0-08-100853-9.00027-0

Grilli, S. T., Tappin, D. R., Carey, S., Watt, S. F. L., Ward, S. N., Grilli, A. R., et al. (2019). Modelling of the Tsunami from the December 22, 2018 Lateral Collapse of Anak Krakatau Volcano in the Sunda Straits, Indonesialateral Collapse of Anak Krakatau Volcano in the Sunda Straits, Indonesia. *Sci. Rep.* 9, 11946. doi:10.1038/s41598-019-48327-6

Grilli, S. T., Shelby, M., Kimmoun, O., Dupont, G., Nicolsky, D., Ma, G., et al. (2017). Modeling Coastal Tsunami hazard from Submarine Mass Failures: Effect of Slide Rheology, Experimental Validation, and Case Studies off the US East Coast. *Nat. Hazards* 86, 353–391. doi:10.1007/s11069-016-2692-3

Grilli, S. T., Vogelmann, S., and Watts, P. (2002). Development of a 3D Numerical Wave Tank for Modeling Tsunami Generation by Underwater Landslides. *Eng. Anal. Boundary Elem.* 26, 301–313. doi:10.1016/S0955-7997(01)00113-8

Grilli, S. T., Zhang, C., Kirby, J. T., Grilli, A. R., Tappin, D. R., Watt, S. F. L., et al. (2021). Modeling of the Dec. 22nd 2018 Anak Krakatau Volcano Lateral Collapse and Tsunami Based on Recent Field Surveys: Comparison with Observed Tsunami Impact. *Mar. Geology* 440, 106566. doi:10.1016/j.margeo.2021.106566

Gwang, H., and Watkins, J. S. (1998). Seismic Sequence Stratigraphy and Hydrocarbon Potential of the Phu Khanh Basin, Offshore central Vietnam, South China Sea. *Bulletin* 82 (1998), 1711–1735. doi:10.1306/1d9bcb83-172d-11d7-8645000102c1865d

Hampton, M. A., Lee, H. J., and Locat, J. (1996). Submarine Landslides. *Rev. Geophys.* 34, 33–59. doi:10.1029/95RG03287

Harbitz, C. B., Løvholt, F., and Bungum, H. (2014). Submarine Landslide Tsunamis: How Extreme and How Likely? *Nat. Hazards* 72, 1341–1374. doi:10.1007/s11069-013-0681-3

Harbitz, C. B., Løvholt, F., Pedersen, G., and Masson, D. G. (2006). Mechanisms of Tsunami Generation by Submarine Landslides: a Short Review. *Nor. J. Geol. Geol. Foren* 86.

He, Y., Zhong, G., Wang, L., and Kuang, Z. (2014). Characteristics and Occurrence of Submarine canyon-associated Landslides in the Middle of the Northern continental Slope, South China Sea. *Mar. Pet. Geology* 57, 546–560. doi:10.1016/j.marpetgeo.2014.07.003

Heidarzadeh, M., and Satake, K. (2014). Possible Sources of the Tsunami Observed in the Northwestern Indian Ocean Following the 2013 September 24 Mw 7.7 Pakistan Inland Earthquake. *Geophys. J. Int.* 199, 752–766. doi:10.1093/gji/ggu297

Hong Nguyen, P., Cong Bui, Q., and Dinh Nguyen, X. (2012). Investigation of Earthquake Tsunami Sources, Capable of Affecting Vietnamese Coast. *Nat. Hazards* 64, 311–327. doi:10.1007/S11069-012-0240-3

Hong Phuong, N. (2001). Probabilistic Seismic hazard Assessment along the Southeastern Coast of Vietnam. *Nat. Hazards* 24, 53–74. doi:10.1023/a:1011149523444

Hongfang, G., and Ling, C. (2006). An Analysis of Structural Framework and Formation Mechanism of Zhongjiannan basin in the West of South China Sea. *Oil Gas Geol.* 27, 512–516.

Huang, X., Betzler, C., Wu, S., Bernhardt, A., Eagles, G., Han, X., et al. (2020). First Documentation of Seismic Stratigraphy and Depositional Signatures of Zhongsha Atoll (Macclesfield Bank), South China Sea. *Mar. Pet. Geology* 117, 104349. doi:10.1016/j.marpetgeo.2020.104349

Huhn, K., Arroyo, M., Cattaneo, A., Clare, M. A., Gràcia, E., Harbitz, C. B., et al. (2019). Modern Submarine Landslide Complexes. *Submar. Landslides Subaqueous Mass Transp. Depos. Outcrops Seism. Profiles*, 181–200. doi:10.1002/9781119500513.ch12

Hunt, J. E., Tappin, D. R., Watt, S. F. L., Susilohadi, S., Novellino, A., Ebmeier, S. K., et al. (2018). Submarine Landslide Megablocks Show Half of Anak Krakatau Island Failed on December 22nd, 2018. *Nat. Commun.* 12, 2827–2915. doi:10.1038/s41467-021-22610-5

Janin, A., Rodriguez, M., Sakellariou, D., Lykousis, V., and Gorini, C. (2019). Tsunamigenic Potential of a Holocene Submarine Landslide along the North Anatolian Fault (Northern Aegean Sea, off Thasos Island): Insights from

Numerical Modelling. *Nat. Hazards Earth Syst. Sci.* 19, 121–136. doi:10.5194/nhess-19-121-2019

Kim, J., Løvholt, F., Issler, D., and Forsberg, C. F. (2019). Landslide Material Control on Tsunami Genesis-The Storegga Slide and Tsunami (8,100 Years BP). *J. Geophys. Res. Oceans* 124, 3607–3627. doi:10.1029/2018JC014893

Kirby, J. T., Shi, F., Nicolsky, D., and Misra, S. (2016). The 27 April 1975 Kitimat, British Columbia, Submarine Landslide Tsunami: a Comparison of Modeling Approaches. *Landslides* 13, 1421–1434. doi:10.1007/s10346-016-0682-x

Kowalik, Z., Horrillo, J., Knight, W., and Logan, T. (2008). Impact at Crescent City by Distant Scattering. *Kuril Islands Tsunami Novemberj. Geophys. Res. Ocean* 113, 1020. doi:10.1029/2007JC004402

Kulikov, E. A., Rabinovich, A. B., Thomson, R. E., and Bornhold, B. D. (1996). The Landslide Tsunami of November 3, 1994, Skagway Harbor, Alaska. *J. Geophys. Res. Ocean.* 101, 6609–6615. doi:10.1029/95JC03562

Lebreiro, S. M., Voelker, A. H. L., Vizcaino, A., Abrantes, F. G., Alt-Epping, U., Jung, S., et al. (2009). Sediment Instability on the Portuguese continental Margin under Abrupt Glacial Climate Changes (Last 60kyr). *Quat. Sci. Rev.* 28, 3211–3223. doi:10.1016/j.quascirev.2009.08.007

Lee, H. J., Chough, S. K., and Yoon, S. H. (1996). Slope-stability Change from Late Pleistocene to Holocene in the Ulleung Basin, East Sea (Japan Sea). *Sediment. Geology* 104, 39–51. doi:10.1016/0037-0738(95)00119-0

Lei, C., Ren, J. Y., and Zhang, J. (2015). Tectonic Province Divisions in the South China Sea: Implications for Basin Geodynamics. *Earth Sci.* 40, 744–762.

Lepelletier, T. G.. (1981). Tsunamis–Harbor Oscillations Induced by Nonlinear Transient Long Waves. Dissertation/PhD thesis. California Institute of Technology. doi:10.7907/05TE-BH74

Li, L., Shi, F., Ma, G., and Qiu, Q. (2019). Tsunamigenic Potential of the Baiyun Slide Complex in the South China Sea. *J. Geophys. Res. Solid Earth* 124, 7680–7698. doi:10.1029/2019jb018062

Li, L., Switzer, A. D., Wang, Y., Weiss, R., Qiu, Q., Chan, C.-H., et al. (2015). What Caused the Mysterious Eighteenth Century Tsunami that Struck the Southwest Taiwan Coast? *Geophys. Res. Lett.* 42, 8498–8506. doi:10.1002/2015gl065567

Li, W., Alves, T. M., Wu, S., Völker, D., Zhao, F., Mi, L., et al. (2015). Recurrent Slope Failure and Submarine Channel Incision as Key Factors Controlling Reservoir Potential in the South China Sea (Qiongdongnan Basin, South Hainan Island). *Mar. Pet. Geology* 64, 17–30. doi:10.1016/j.marpetgeo.2015.02.043

Liu, P. L.-F., Higuera, P., Husrin, S., Prasetya, G. S., Prihantono, J., Diastomo, H., et al. (2020). Coastal Landslides in Palu Bay during 2018 Sulawesi Earthquake and Tsunami. *Landslides* 17, 2085–2098. doi:10.1007/s10346-020-01417-3

Locat, J., and Lee, H. J. (2002). Submarine Landslides: Advances and Challenges. *Can. Geotech. J.* 39, 193–212. doi:10.1139/t01-089

Locat, J., Lee, H., ten Brink, U. S., Geist, E., Sansoucy, M., and Sansoucy, M. (2009). Geomorphology, Stability and Mobility of the Currituck Slide. *Mar. Geology* 264, 28–40. doi:10.1016/j.margeo.2008.12.005

Løvholt, F., Bondevik, S., Laberg, J. S., Kim, J., and Boylan, N. (2017). Some Giant Submarine Landslides Do Not Produce Large Tsunamis. *Geophys. Res. Lett.* 44, 8463–8472. doi:10.1002/2017GL074062

Løvholt, F., Glimsdal, S., and Harbitz, C. B. (2020). On the Landslide Tsunami Uncertainty and hazard. *Landslides* 17, 2301–2315. doi:10.1007/s10346-020-01429-z

Løvholt, F., Pedersen, G., Harbitz, C. B., Glimsdal, S., and Kim, J. (2015). On the Characteristics of Landslide Tsunamis. *Phil. Trans. R. Soc. A.* 373, 20140376. doi:10.1098/rsta.2014.0376

Ma, G., Shi, F., and Kirby, J. T. (2012). Shock-capturing Non-hydrostatic Model for Fully Dispersive Surface Wave Processes. *Ocean Model.* 43-44, 22–35. doi:10.1016/j.ocemod.2011.12.002

Maselli, V., Iacopini, D., Ebinger, C. J., Tewari, S., de Haas, H., Wade, B. S., et al. (2020). Large-scale Mass Wasting in the Western Indian Ocean Constrains Onset of East African Rifting. *Nat. Commun.* 11, 3456. doi:10.1038/s41467-020-17267-5

McAdoo, B. G., Pratson, L. F., and Orange, D. L. (2000). Submarine Landslide Geomorphology, US continental Slope. *Mar. Geology* 169, 103–136. doi:10.1016/s0025-3227(00)00050-5

Melgar, D., Ruiz-Angulo, A., Garcia, E. S., Manea, M., Manea, V. C., Xu, X., et al. (2018). Deep Embrittlement and Complete Rupture of the Lithosphere during the Mw 8.2 Tehuantepec Earthquake. *Nat. Geosci.* 11, 955–960. doi:10.1038/s41561-018-0229-y

Morley, C. K. (2002). A Tectonic Model for the Tertiary Evolution of Strike-Slip Faults and Rift Basins in SE Asia. *Tectonophysics* 347, 189–215. doi:10.1016/s0040-1951(02)00061-6

Moscardelli, L., and Wood, L. (2016). Morphometry of Mass-Transport Deposits as a Predictive Tool. *Geol. Soc. America Bull.* 128, B31221.1–80. doi:10.1130/B31221.1

Nakata, K., Katsumata, A., and Muhari, A. (2020). Submarine Landslide Source Models Consistent with Multiple Tsunami Records of the 2018 Palu Tsunami, Sulawesi, Indonesia. *Earth, Planets Sp.* 72, 1–16. doi:10.1186/s40623-020-01169-3

Nguyễn Hồng Phương, V. V. P. (2017). *Possibility of Near-Field Tsunami Generation in the Southern Central Coast of Vietnam*. Vietnam, Hanoi: IOC UNESCO Meeting on South China Sea.

Nguyen, V. L., Duong, Q. H., Bui, T. X., and Nguyen, B. D. (2007). Characteristics and Properties of Earthquake in South China Sea and Surrounding Areas. *Rep. Submitt. IMHEN*, 41.

Pham Nang Vu (2009). Submarine Landslides in the Coastal Zone of Vietnam. In (Scientific Report of the National Scientific Research Project Code DTDL 2007g/45, Institute of Geophysics, Hanoi, 2010 (In Vietnamese)).

Okal, E. A., and Synolakis, C. E. (2008). Far-field Tsunami hazard from Mega-Thrust Earthquakes in the Indian Ocean. *Geophys. J. Int.* 172, 995–1015. doi:10.1111/j.1365-246X.2007.03674.x

Pattiaratchi, C. B., and Sarath Wijeratne, E. M. (2009). Tide Gauge Observations of 2004-2007 Indian Ocean Tsunamis from Sri Lanka and Western Australia. *Pure Appl. Geophys.* 166, 233–258. doi:10.1007/s00024-008-0434-5

Phuong, N. H., and Truyen, P. T. (2015). Probabilistic Seismic hazard Assessment for the South Central Vietnam. *Tcckhvtd* 36, 451–461. doi:10.15625/0866-7187/36/4/6433

Posamentier, H. W., and Martinsen, O. J. (2011). The Character and Genesis of Submarine Mass-Transport Deposits: Insights from Outcrop and 3D Seismic Data. *Mass-Transport Deposits in Deepwater Settings* 96, 7–38. doi:10.2110/sepmsp.096.007

Rabinovich, A. B. (2010). "Seiches and Harbor Oscillations," in *Handbook of Coastal and Ocean Engineering* (World Scientific).

Ren, Z., Zhao, X., and Liu, H. (2019). Numerical Study of the Landslide Tsunami in the South China Sea Using Herschel-Bulkley Rheological Theory. *Phys. Fluids* 31, 56601. doi:10.1063/1.5087245

Ross, W. C., Halliwell, B. A., May, J. A., Watts, D. E., and Syvitski, J. P. M. (1994). Slope Readjustment: a New Model for the Development of Submarine Fans and Aprons. *Geol* 22, 511–514. doi:10.1130/0091-7613(1994)022<0511:sranmf>2.3.co;2

Schambach, L., Grilli, S. T., Kirby, J. T., and Shi, F. (2018). Landslide Tsunami Hazard along the Upper US East Coast: Effects of Slide Deformation, Bottom Friction, and Frequency Dispersion. *Pure Appl. Geophys.* 176, 3059–3098. doi:10.1007/s00024-018-1978-7

Schambach, L., Grilli, S. T., and Tappin, D. R. (2021). New High-Resolution Modeling of the 2018 Palu Tsunami, Based on Supershear Earthquake Mechanisms and Mapped Coastal Landslides, Supports a Dual Source. *Front. Earth Sci.* 8, 627. doi:10.3389/feart.2020.598839

Schambach, and Lauren (2020). Investigation of Landslide-Induced Tsunami Generation and Propagation through Numerical Modeling. Dissertation/PhD thesis. University of Rhode Island.

Schimanski, A., and Stattegger, K. (2005). Deglacial and Holocene Evolution of the Vietnam Shelf: Stratigraphy, Sediments and Sea-Level Change. *Mar. Geology* 214, 365–387. doi:10.1016/j.margeo.2004.11.001

Shi, F., Kirby, J. T., Harris, J. C., Geiman, J. D., and Grilli, S. T. (2012). A High-Order Adaptive Time-Stepping TVD Solver for Boussinesq Modeling of Breaking Waves and Coastal Inundation. *Ocean Model.* 43-44, 36–51. doi:10.1016/j.ocemod.2011.12.004

Shi, H., Si, P., Dong, P., and Yu, X. (2019). A Two-phase SPH Model for Massive Sediment Motion in Free Surface Flows. *Adv. Water Resour.* 129, 80–98. doi:10.1016/j.advwatres.2019.05.006

Si, P., Shi, H., and Yu, X. (2018). A General Numerical Model for Surface Waves Generated by Granular Material Intruding into a Water Body. *Coastal Eng.* 142, 42–51. doi:10.1016/j.coastaleng.2018.09.001

Smith, D. E., Harrison, S., and Jordan, J. T. (2013). Sea Level Rise and Submarine Mass Failures on Open Continental Margins. *Quat. Sci. Rev.* 82, 93–103. doi:10.1016/j.quascirev.2013.10.012

Song, Y. T., Fukumori, I., Shum, C. K., and Yi, Y. (2012). Merging Tsunamis of the 2011 Tohoku-Oki Earthquake Detected over the Open Ocean. *Geophys. Res. Lett.* 39, L05606. doi:10.1029/2011gl050767

Souvignet, M., Laux, P., Freer, J., Cloke, H., Thinh, D. Q., Thuc, T., et al. (2014). Recent Climatic Trends and Linkages to River Discharge in Central Vietnam. *Hydrol. Process.* 28, 1587–1601. doi:10.1002/hyp.9693

Sun, L. T., Sun, Z., Zhan, W. H., Sun, Z. X., Zhao, M. H., Xia, S. H., et al. (2006). Western Fault Zone of South China Sea and its Physical Simulation Evidences. *Acta Oceanol. Sin.* 3, 58–67.

Sun, Q., Alves, T. M., Lu, X., Chen, C., and Xie, X. (2018a). True Volumes of Slope Failure Estimated from a Quaternary Mass-Transport Deposit in the Northern South China Sea. *Geophys. Res. Lett.* 45, 2642–2651. doi:10.1002/2017gl076484

Sun, Q., Cartwright, J., Xie, X., Lu, X., Yuan, S., and Chen, C. (2018b). Reconstruction of Repeated Quaternary Slope Failures in the Northern South China Sea. *Mar. Geology* 401, 17–35. doi:10.1016/j.margeo.2018.04.009

Sun, Q., Alves, T., Xie, X., He, J., Li, W., and Ni, X. (2017). Free Gas Accumulations in Basal Shear Zones of Mass-Transport Deposits (Pearl River Mouth Basin, South China Sea): An Important Geohazard on continental Slope Basins. *Mar. Pet. Geology* 81, 17–32. doi:10.1016/j.marpetgeo.2016.12.029

Sun, Q., and Leslie, S. (2020). Tsunamigenic Potential of an Incipient Submarine Slope Failure in the Northern South China Sea. *Mar. Pet. Geology* 112, 104111. doi:10.1016/j.marpetgeo.2019.104111

Sun, Y. B., Wu, S. G., Wang, Z. J., Li, Q. P., Wang, X. J., Dong, D. D., et al. (2008). The Geometry and Deformation Characteristics of Baiyun Submarine Landslide. *Mar. Geol. Quat. Geol.* 28, 69–77. doi:10.3726/SP.J.1140.2008.06069

Talling, P. J. (2014). On the Triggers, Resulting Flow Types and Frequencies of Subaqueous Sediment Density Flows in Different Settings. *Mar. Geology* 352, 155–182. doi:10.1016/j.margeo.2014.02.006

Tan, M. T., Dung, L. V., Bach, N., Nghi, T., LongVan, H. V., and Huong, P. T. (2014). Pliocene-Quaternary Evolution of the continental Shelf of central Vietnam Based on High Resolution Seismic Data. *J. Asian Earth Sci.* 79, 529–539. doi:10.1016/j.jseaes.2013.08.001

Tan, W. K., Teh, S. Y., and Koh, H. L. (2017). Tsunami Run-Up and Inundation along the Coast of Sabah and Sarawak, Malaysia Due to a Potential Brunei Submarine Mass Failure. *Environ. Sci. Pollut. Res.* 24, 15976–15994. doi:10.1007/s11356-017-8698-x

Tappin, D. R., Grilli, S. T., Harris, J. C., Geller, R. J., Masterlark, T., Kirby, J. T., et al. (2014). Did a Submarine Landslide Contribute to the 2011 Tohoku Tsunami? *Mar. Geology* 357, 344–361. doi:10.1016/j.margeo.2014.09.043

Tappin, D. R., and Grilli, S. T. (2021). The Continuing Underestimated Tsunami Hazard from Submarine Landslides. *Understanding and Reducing Landslide Disaster Risk* 2020, 343–350. doi:10.1007/978-3-030-60196-6_24

Tappin, D. R. (2010). Submarine Mass Failures as Tsunami Sources: Their Climate Control. *Phil. Trans. R. Soc. A.* 368, 2417–2434. doi:10.1098/rsta.2010.0079

Tappin, D. R., Watts, P., and Grilli, S. T. (2008). The Papua New Guinea Tsunami of 17 July 1998: Anatomy of a Catastrophic Event. *Nat. Hazards Earth Syst. Sci.* 8, 243–266. doi:10.5194/nhess-8-243-2008

Tapponnier, P., Zhiqin, X., Roger, F., Meyer, B., Arnaud, N., Wittlinger, G., et al. (2001). Oblique Stepwise Rise and Growth of the Tibet Plateau. *Science* 294, 1671–1677. doi:10.1126/science.105978

Tehranirad, B., Kirby, J. T., Ma, G., and Shi, F. (2012). Tsunami Benchmark Results for Non-hydrostatic Wave Model NHWAVE Version 1.1. *Res. Rep. CACR.* 12, 3.

Tehranirad, B., Shi, F., Kirby, J. T., Harris, J. C., and Grilli, S. (2011). Tsunami Benchmark Results for Fully Nonlinear Boussinesq Wave Model FUNWAVE-TVD, Version 1.0. *Cent. Appl. Coast. Res. Univ. Delaware, Tech. Rep.. CACR-11-02.*

Titov, V., Rabinovich, A. B., Mofjeld, H. O., Thomson, R. E., and Gonza´lez, F. I. (2005). The Global Reach of the 26 December 2004 Sumatra Tsunami. *Science* 309, 2045–2048. doi:10.1126/science.1114576

Urgeles, R., and Camerlenghi, A. (2013). Submarine Landslides of the Mediterranean Sea: Trigger Mechanisms, Dynamics, and Frequency-Magnitude Distribution. *J. Geophys. Res. Earth Surf.* 118, 2600–2618. doi:10.1002/2013jf002720

Ursell, F. (1952). Edge Waves on a Sloping beach. *Proc. R. Soc. Lond. Ser. A. Math. Phys. Sci.* 214, 79–97. doi:10.1098/rspa.1952.0152

Vu, A. T., Wessel Fyhn, M. B., Nguyen, T. T., Hoang, D. N., Pham, L. T., Van, H. N., et al. (2017). Cenozoic Tectonic and Stratigraphic Development of the Central Vietnamese continental Margin. *Mar. Pet. Geology* 86, 386–401. doi:10.1016/j.marpetgeo.2017.06.001

Vu, P. N., Vu, P. N. H., and Binh, N. X. (2008). Young Volcanic Eruption (Pliocene-Quaternary) Activities on the Southern continental Shelf of Vietnam (According to Geophysical Data). *Vietnam J. Earth Sci.* 30, 289–301.

Wang, D., Wu, S., Li, C., and Yao, G. (2016). Submarine Slide Evidence for Late Miocene Strike-Slip Reversal of the Red River Fault. *Sci. China Earth Sci.* 59, 2231–2239. doi:10.1007/s11430-015-5534-9

Wang, D., Wu, S., Qin, Z., Spence, G., and Lü, F. (2013). Seismic Characteristics of the Huaguang Mass Transport Deposits in the Qiongdongnan Basin, South China Sea: Implications for Regional Tectonic Activity. *Mar. Geology* 346, 165–182. doi:10.1016/j.margeo.2013.09.003

Wang, J., Pang, X., Liu, B., Zheng, J., and Wang, H. (2018). The Baiyun and Liwan Sags: Two Supradetachment Basins on the Passive continental Margin of the Northern South China Sea. *Mar. Pet. Geology* 95, 206–218. doi:10.1016/j.marpetgeo.2018.05.001

Wang, W., Wang, D., Wu, S., Völker, D., Zeng, H., Cai, G., et al. (2018). Submarine Landslides on the north continental Slope of the South China Sea. *J. Ocean Univ. China* 17, 83–100. doi:10.1007/s11802-018-3491-0

Wang, L., Wu, S.-G., Li, Q.-P., Wang, D.-W., and Fu, S.-Y. (2014). Architecture and Development of a Multi-Stage Baiyun Submarine Slide Complex in the Pearl River Canyon, Northern South China Sea. *Geo-Mar. Lett.* 34, 327–343. doi:10.1007/s00367-014-0372-4

Wang, X., Wang, Y., Tao, F., and Liu, A. (2021). New Paradigm of Data-Driven Smart Customisation through Digital Twin. *J. Manufacturing Syst.* 58, 270–280. doi:10.1016/j.jmsy.2020.07.023

Weaver, P. P. E., and Kuijpers, A. (1983). Climatic Control of Turbidite Deposition on the Madeira Abyssal plain. *Nature* 306, 360–363. doi:10.1038/306360a0

Wilson, B. W. (1972). "Seiches," in *Advances in Hydroscience* (Elsevier), Vol. 8, 1–94. doi:10.1016/B978-0-12-021808-0.50006-1

Wu, S.-G., Qin, Z.-L., Wang, D.-W., Peng, X.-C., Wang, Z.-J., Yao, G.-S., et al. (2011). Analysis on Seismic Characteristics and Triggering Mechanisms of Mass Transport Deposits on the Northern Slope of the South China Sea. *Chin. J. Geophys.* 54, 1056–1068. doi:10.1002/cjg2.1684

Yamazaki, Y., Cheung, K. F., and Kowalik, Z. (2011). Depth-integrated, Non-hydrostatic Model with Grid Nesting for Tsunami Generation, Propagation, and Run-Up. *Int. J. Numer. Meth. Fluids* 67, 2081–2107. doi:10.1002/fld.2485

Yang, T. F., Lee, T., Chen, C.-H., Cheng, S.-N., Knittel, U., Punongbayan, R. S., et al. (1996). A Double Island Arc between Taiwan and Luzon: Consequence of ridge Subduction. *Tectonophysics* 258, 85–101. doi:10.1016/0040-1951(95)00180-8

Ye, L., Kanamori, H., Rivera, L., Lay, T., Zhou, Y., Sianipar, D., et al. (2020). The 22 December 2018 Tsunami from Flank Collapse of Anak Krakatau Volcano during Eruption. *Sci. Adv.* 6, eaaz1377. doi:10.1126/sciadv.aaz1377

Zengaffinen, T., Løvholt, F., Pedersen, G. K., and Harbitz, C. B. (2020). Effects of Rotational Submarine Slump Dynamics on Tsunami Genesis: New Insight from Idealized Models and the 1929 Grand Banks Event. *Geol. Soc. Lond. Spec. Publications* 500, 41–61. doi:10.1144/SP500-2019-201

Zhang, C., Kirby, J. T., Shi, F., Ma, G., and Grilli, S. T. (2021a). A Two-Layer Non-hydrostatic Landslide Model for Tsunami Generation on Irregular Bathymetry. 1. Theoretical Basis. *Ocean Model.* 159, 101749. doi:10.1016/j.ocemod.2020.101749

Zhang, C., Kirby, J. T., Shi, F., Ma, G., and Grilli, S. T. (2021b). A Two-Layer Non-hydrostatic Landslide Model for Tsunami Generation on Irregular Bathymetry. 2. Numerical Discretization and Model Validation. *Ocean Model.* 160, 101769. doi:10.1016/j.ocemod.2021.101769

Zhou, Q., Li, X., Zhou, H., Liu, L., Xu, Y., Gao, S., et al. (2019). Characteristics and Genetic Analysis of Submarine Landslides in the Northern Slope of the South China Sea. *Mar. Geophys. Res.* 40, 303–314. doi:10.1007/s11001-018-9369-0

Zhu, M., Graham, S., and McHargue, T. (2009). The red river Fault Zone in the Yinggehai Basin, South China Sea. *Tectonophysics* 476, 397–417. doi:10.1016/j.tecto.2009.06.015

Author Disclaimer: Any opinions, findings and conclusions or recommendations expressed in this material are those of the author(s) and do not reflect the views of the National Research Foundation, Singapore, and National Environment Agency, Singapore.

Conflict of Interest: The authors declare that the research was conducted in the absence of any commercial or financial relationships that could be construed as a potential conflict of interest.

Publisher's Note: All claims expressed in this article are solely those of the authors and do not necessarily represent those of their affiliated organizations, or those of the publisher, the editors and the reviewers. Any product that may be evaluated in this article, or claim that may be made by its manufacturer, is not guaranteed or endorsed by the publisher.

frontiers | Frontiers in Earth Science

ORIGINAL RESEARCH
published: 26 April 2022
doi: 10.3389/feart.2022.832744

Geodynamic Characteristics in the Southwest Margin of South China Sea

Yongjian Yao[1,2], *Jian Zhang*[3]*, *Miao Dong*[4], *Rongwei Zhu*[1,2], *Zhiying Xu*[1,2], *Xiaodong Yang*[5] *and Hailing Liu*[5]

[1]Guangzhou Marine Geological Survey, Guangzhou, China, [2]Southern Marine Science and Engineering Guangdong Laboratory (Guangzhou), Guangzhou, China, [3]University of Chinese Academy of Sciences, Beijing, China, [4]Institute of Geology and Geophysics, Chinese Academy of Sciences, Beijing, China, [5]South China Sea Institute of Oceanology, Chinese Academy of Sciences, Guangzhou, China

OPEN ACCESS

Edited by:
Xunhua Zhang,
Qingdao Institute of Marine Geology (QIMG), China

Reviewed by:
Jiangxin Chen,
Qingdao Institute of Marine Geology (QIMG), China
Minghui Zhao,
South China Sea Institute of Oceanology (CAS), China
Xingwei Guo,
Qingdao Institute of Marine Geology (QIMG), China

***Correspondence:**
Jian Zhang
zhangjian@ucas.ac.cn

Specialty section:
This article was submitted to Structural Geology and Tectonics, a section of the journal Frontiers in Earth Science

Received: 13 December 2021
Accepted: 07 February 2022
Published: 26 April 2022

Citation:
Yao Y, Zhang J, Dong M, Zhu R, Xu Z, Yang X and Liu H (2022) Geodynamic Characteristics in the Southwest Margin of South China Sea. Front. Earth Sci. 10:832744. doi: 10.3389/feart.2022.832744

The strike-slip fault system in the southwestern margin of South China Sea (SCS) lies on the transition zone between the continental shelf and slope of SCS, which is an important ocean–continent boundary. By using submarine heat flow data, a seismic shear wave tomography model, and gravity potential field data, this paper investigates the distribution of submarine heat flow in the southwestern margin of SCS, the thermal–rheological structure of the crust and mantle, the temperature–viscosity characteristics of the upper mantle V_s low-velocity layer, the tangential stress field of the rheological boundary layer at the lithosphere base, and the convective velocity structure of the mantle asthenosphere. Our new results show that the deep geothermal activity in the southwestern margin of SCS is intense, and the high heat flow area of the mantle with Q_m/Q_s >70% is distributed along an NNE-trending strip. Moreover, both the east and west sides of the strike–slip fault zone correspond to two low-value areas with a viscosity coefficient of 10^{21}–10^{22} Pa·s at Moho depth, and beneath the Nansha Block are strong and cold blocks with a viscosity coefficient of 10^{24}–10^{25} Pa·s. The northward and eastward shear stress components τ_N and τ_E of the rheological boundary layer at the base of the lithosphere mantle decrease with depth. At 65-km depth, both τ_N and τ_E are greater than 5.5×10^8 N/m^2. At 100-km depth, both τ_N and τ_E are less than 1×10^8 N/m^2. The calculation results based on the seismic shear wave model of the upper mantle and the gravimetric geoid model indicate that the depth of 120–250 km is the low-velocity layer, and the average temperature of the mantle at 180-km depth can be up to 1,300°C. Moreover, the average effective viscosity coefficient is close to 10^{18} Pa·s, which satisfies the temperature and viscosity conditions for partial melting or convective migration of mantle material. The mantle convection calculation results show that the average flow rate is 8.5 cm/a at 200-km depth and 2.2 cm/a at 400-km depth.

Keywords: south of the western margin of the South China Sea, submarine heat flow, three-dimensional V_s model, crust–mantle thermal–rheological structure, rheological boundary of lithospheric mantle, asthenosphere of upper mantle

INTRODUCTION

The southwestern margin of South China Sea (SMSCS) lies on the transition zone from continental shelf to continental slope (Ding and Li, 2016; Dong et al., 2020), with direct geodynamic effect from the extrusion of Indosinia Block. It is the key region of plate convergence within the great circular subduction system of Southeast Asia (Lu et al., 2016) and also marks the tectonic termination where the oceanic crust of South China Sea (SCS) advances from east to west during "plate-edge rifting" (Wang et al., 2019). The southwestern margin of SCS is undergoing structural interactions between the strike–slip faulting and tectonic extrusion; thus, it has the most complicated tectonic elements but the lowest degree of geodynamic study in the periphery of SCS (Tapponnier et al., 1986; Yao et al., 1994; Liu, 1999; Ren and Li, 2000; Li et al., 2006; Li et al., 2012; Xu et al., 2016). Over the last decades or so, there are two major geodynamic questions that remain to be answered. The first is as follows: during the southward propagation of the strike–slip fault zone in the SMSCS, is there any continuity or connection between the Zhongjian Fault, Wanan Fault, Lupar Fault, and Tinja Fault? The second is also as follows: during the tectonic extrusion of the Indosinian Peninsula, the circular subduction of Southeast Asia, and the rifting-expansion of SCS, how do the tectonic forces interact with each other during different periods and at various directions?

These two major questions have been subjected to intensive study in association with the geodynamic history of SCS (Yao et al., 2004; Liu et al., 2015; Sun et al., 2006; Fyhn et al., 2009). It is necessary to "observe the SCS by stepping out of the SCS" and "observe the SCS by going deep into the SCS". Substantial data and results have been obtained after many years of marine scientific research in SCS (Li et al., 2010; Xu et al., 2016; Xu et al., 2016; Dong et al., 2018). Since the 1980s, especially Guangzhou Marine Geological Survey has carried out a series of comprehensive geological and geophysical surveys on "oil and gas resources" and obtained significant gravity, magnetic, seismic, and heat flow data. In recent years, the Program for Marine Basic Geological Survey has enriched the geological understanding of the southwestern margin of SCS. With measured submarine heat flow data at the southwestern end of the Southwest Basin in the SCS (Xu et al., 2005; Li et al., 2010; Xu et al., 2016; Dong et al., 2018) and based on seismic and gravity data, this paper analyzes the thermal structure of the crust in the southwestern margin of the SCS, the rheological characteristics of the base of the lithospheric mantle, and the geodynamic background of the deep convective mantle, providing a reference for studying of the region and having important significance for understanding of the dynamic model of seafloor spreading of the SCS and

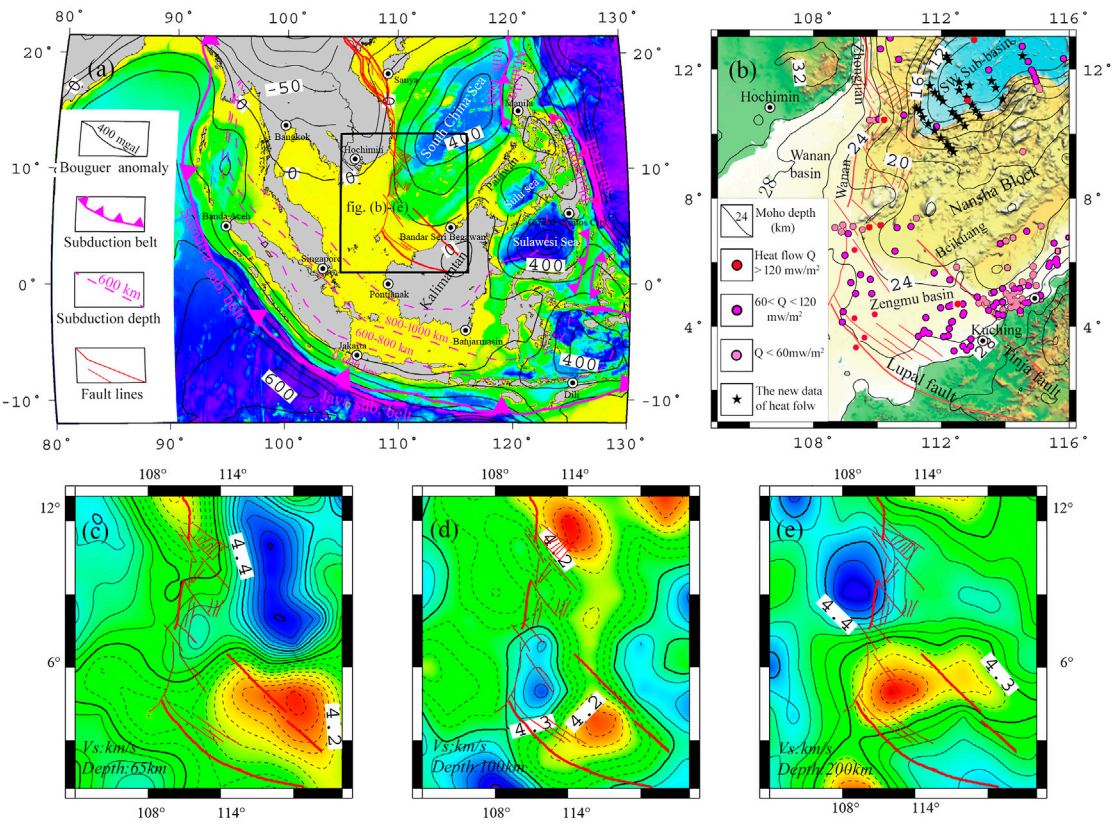

FIGURE 1 | Regional map of the southwestern margin of South China Sea (SCS). **(A)** Tectonic map of the southwestern margin of SCS. **(B)** Map of the geothermal geology in the study area. **(C–E)** V_S map at depths of 65, 100, and 200 km (Chen et al., 2021).

reconstruction of the Asian tectonic framework in the geodynamic process and deep material circulation, tectonic deformation and dynamic mechanism.

GEODYNAMIC BACKGROUND

The study area is located at the center of the curved convergent system in Southeast Asia (**Figure 1A**). Seismological studies (Huang and Zhao, 2006; Zhao and Ohtani, 2009) indicate that the oceanic slabs on both the east and west sides of the annular subduction belt in Southeast Asia present opposite subduction directions (Fukao et al., 1992), which form a convergent system of subduction fronts with different depths and origins in three directions, *i.e.*, east, west, and south. The convergence of multi-directional subduction slabs affects the circulation of deep mantle material, thermal-viscosity structure, and rheological property.

Geology Setting

The southwestern margin of SCS (**Figure 1B**) represents the extensional area of the Southwest Basin in the SCS. It is bound by the Indosinian Peninsula in the northwest and by Kalimantan Island in the southeast, respectively. The fault zone in the western margin of SCS runs southward through the study area from the east side of the Indosinian Peninsula and then bends toward southeast into Kalimantan Island. It marks the western boundary of SCS and is primarily deformed by strike–slip faulting (Fyhn et al., 2009; Lin et al., 2009; Gao, 2011; Xu et al., 2016). Overall, the strike–slip fault zone is composed of a series of faults that trend roughly NNW–SSE. Its north termination starts from the Yinggehai Sea with connection to the Red River Fault and Yinggehai Fault. Towards the south, the fault zone comprises the Zhongjian Fault, Wanan Fault, Lupal Fault, and Tinja Fault. Moreover, the south termination runs deep into Borneo Island. In the study area, Zhongjiannan Basin, Wanan Basin, Nanweixi Basin, and Zengmu Basin are developed along this strike–slip fault zone (Zhan et al., 1995; An et al., 2012; Yao et al., 2013). Geomorphologically, the strike–slip fault zone is situated at the transition from the continental shelf to the slope in the west SCS; as such, the topographic and geomorphic features on both sides of the fault zone appear to be quite different. In the west side, the water depth at the outer shelf edge is 200–250 m, and the shelf itself is narrow, with a topographic slope of 10–22°. The landform from Da Nang to the south of Ho Chi Minh City in Vietnam is relatively broad and flat, with a topographic slope of 4.7°. In the east side, the continental slope has a water depth ranging between 200 and 4,000 m. The topography is complicated with distinct variations. From north to south, there are Xisha Trough, Xisha Islands, Zhongsha Islands, West Basin Ridge, West Basin Canyon, Southwest Basin Ridge, *etc.*, with a topographic slope of 6.7–17.6°.

Since the Cenozoic period, the strike-slip fault zone in the western margin of SCS has evolved into three distinct segments in the upper crust from north to south, i.e., the Ailaoshan-Honghe fault zone, the Yinggehai-Zhongjian fault zone, and the Wanna-Lupal fault zone. Spatially, these strike-slip fault zones show different sense of movements, such as left-lateral slip and right-lateral slip. Despite of this, these faults are geodynamically governed by the southeastward intrusion of the Indo-China block induced by the collision between the Indian plate and the Eurasian plate, as well as the seafloor spreading of SCS (Liu et al., 2015).

Characteristics of Gravity Field

In the regional gravity Bouguer anomaly map (**Figure 1A**), it can be seen that the east, south, and west sides of the study area are dominated by high Bouguer anomaly with a value of up to 600 mgal, while the north side is characterized by low continental Bouguer gravity anomaly, with a value of ≤50 mgal. The strike–slip fault zone is marked by the boundary between the low gravity of the Indosinian Peninsula and the high gravity of SCS. For this gravity anomaly transition zone, the fault strike, dip, and slip can be estimated through a calculation of the change rate of the gravity gradient. Taken together, the gravity inversion results show (**Figure 1B**) that the overall Moho depth in the study area ranges between 8 and 32 km (Zhang et al., 2017). Specifically, the Indosinian Peninsula in the northwest and Kalimantan Island in the southeast belong to the continental crust whose Moho surface is deep, *i.e.*, maximum of 32 km. In contrast, the Southwest Basin of SCS is part of the oceanic crust whose Moho is shallow, with a minimum value of 10 km. The rest of the area represents the geomorphic transition area. Its Moho depth appears to become deeper along the axis of the Southwest Basin at 16–28 km, forming a "mirror reflection" with the submarine topography.

Characteristics of Submarine Heat Flow

The submarine heat flow contains information such as the thermal state of the oceanic crust and the mantle as well as the thermal structure of the lithosphere, which lays the foundation for the dynamic analysis of marine geological structures. Many research progresses have been made in studying the submarine heat flow and its characteristics in SCS (Qian, 1992; Yao et al., 1994; Nissen et al., 1995; Shi et al., 2003; Xu et al., 2005; Li et al., 2010). With the advancement of basic marine geological survey and exploration of deep-water oil and gas and natural gas hydrate resources, the total number of submarine heat flow data in the SCS has exceeded 1,250. The submarine heat flow measurement sites in SCS are mainly located on the southern and northern continental margins of the SCS, and the data obtained from temperature measurement in oil drilling sites on the continental shelf are more than that taken from the submarine probes. According to a statistical analysis (Zhang and Wang, 2000), about 42.6% of heat flow data came from the southern margin of the SCS, with an average value of 80.8 mW/m^2. The southern SCS can be divided into the east and west heat flow regions by the Beikuang-Tinja Fault, which correspond to the low-heat-flow region of Nansha Islands and the high-heat-flow region of Zengmu Basin, respectively. Due to the irregular distribution of heat flow measurement sites, especially the scarcity of heat flow data along the strike–slip fault zone, the reef area on Nansha Islands and Nansha Trough, an in-depth analysis of geothermal

field and thermal state on the western margin of the SCS has been largely inhibited.

From 2015 to 2018, during the oceanic expedition of "Marine, 4th" HY4201508 of Guangzhou Marine Geological Survey, an additional 30 new submarine heat flow datasets were obtained in the southwest sub-basin of the SCS (Xu et al., 2016; Dong et al., 2018). The geographic range of the measurement sites of these data is between 112°22′43″–114°31′47″ E and 9°26′29″–12°24′01″ N (**Figure 1B**). The variation range of the thermal conductivity of sediments at the 30 measurement sites is at 0.77–1.07 W/(m·K), with an average of 0.86 W/(m·K). Based on the content of uranium, thorium, and potassium from 13 survey sites, the range of heat production rate is calculated to be 0.78–1.41 μW/m^3, with an average value of 1.12 μW/m^3. Thus, the distribution of the submarine heat flow at each survey site is estimated to be 75.9–126.1 mW/m^2, with an average value of 94.1 mW/m^2. The combined newly acquired and previously existing submarine heat flow data is able to well reflect the temporal and spatial distribution of the current geothermal field and deep thermal state in this study area.

Deep S Wave Velocity Characteristics

A recent study proposed the new generation of high-resolution 3D shear wave velocity model for SCS (Chen et al., 2021). The model presents 3D shear wave velocities across the SCS and its adjacent areas at the depth ranging between 15 and 250 km by joint inversion of ambient noise and surface wave dispersion. It has a high resolution of the crust–mantle structure and can provide accurate seismic wave depth anomalies. Therefore, the latest marine shear wave model is suitable for a deep dynamic analysis of the SCS.

Figures 1C,D,E are the 3D shear wave velocity model slices at 65-, 100-, and 200-km depth, respectively. At 65-km depth (**Figure 1C**), the tectonic characteristics of the SCS Basin gradually diminishes, while the characteristics of the strike–slip fault zone in the western margin of the SCS increasingly becomes obvious. Moreover, a low-velocity region consistent with the strike–slip fault is observed. The Zengmu Basin in the southwestern margin of the SCS shows a low V_s anomaly of ≤4.2 km/S, indicative of the upwelling of asthenospheric material, whereas the Nansha Block presents a high V_s anomaly of ≥4.4 km/S, suggesting the presence of cold strong blocks. At 100-km depth (**Figure 1D**), the N–S-trending low-velocity anomaly zone from the Zhongjiannan Basin to the Zengmu Basin is very obvious, implicating the existence of a low-velocity weak region in the upper mantle. The NW–NS–NE clockwise rotation gradually becomes distinct, which coincides with the clockwise rotation during the sinistral movement of the Indosinian Peninsula relative to the South China Block since Mesozoic. At 200-km depth (**Figure 1E**), the characteristics of the strike–slip fault appears to be gone, reflecting the material migration in the mantle asthenosphere and the deep dynamic process, whereas the Zengmu Basin still shows a low V_s anomaly, indicating that the upwelling channel of the deep asthenosphere material in the Zengmu Basin has the characteristics of continuity, which supports the continuous partial melting of the asthenosphere;

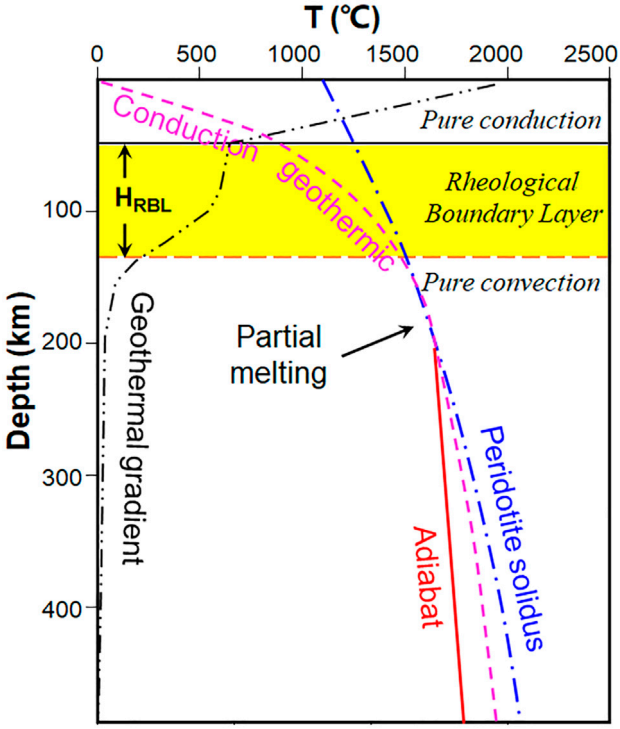

FIGURE 2 | Diagram of the crust–mantle thermal structure model.

however, a significant high-velocity anomaly of ≥4.4 km/S is observed beneath the Wanan Basin, indicating that the lithosphere base is cold and thick and might have to be squeezed into a rigid block during the strike–slip faulting. It reflects the dynamic evolution of the East Asian continental margin due to the subduction of the Pacific Plate as well as the great shear extrusion of the Tibet Plateau.

DEEP THERMAL-DYNAMIC STRUCTURE MODEL AND CALCULATION METHOD

Crust–Mantle Thermal Structure Model

Global seismological observations and studies showed that there is a low-velocity seismic layer caused by partial melting of the mantle material at 60-km depth beneath the sea or at 120- to 250-km depth beneath the continent, and the partially molten mantle material in the layer has formed a slow-flowing asthenosphere in a semi-viscous state. The mantle convection studies indicated (Doin et al., 1997; Dixon et al., 2004; Paulson et al., 2010) that there is a rheological boundary layer (RBL) with a certain thickness between the solid lithosphere (crust and solid mantle) and the fluid mantle. Above the RBL is the solid lithosphere dominated by heat conduction, beneath the RBL is the upper mantle asthenosphere dominated by thermal convection, and between the lithospheric mantle and the asthenospheric mantle is a RBL where heat conduction and heat convection coexist. **Figure 2** shows the theoretical

TABLE 1 | Thermophysical property parameters (Zhang et al., 2005; Meng and Zhang, 2014).

Position	Thermal conductivity [W/(m·K)]	Density (kg/m^3)	Specific heat capacity [J/(kg·K)]	Heat production rate (μW/m^3)
Marine layer	0.54	1,031	4,200	-
Layer N	0.86	2,400	900	1.12
Layer C1	3.0	2,550	900	1.3
Layer C2	2.3	2,700	800	0.4
Layer C3	3.3	2,900	1,200	0.1
Layer LM	2.5	3,280	1,000	0.024

geothermal line (conduction geothermic), the melting temperature line of mantle material (peridotite solidus), and the adiabatic compression temperature line (adiabat) of mantle material calculated based on the one-dimensional Fourier heat conduction equation. The three lines meet at a depth of 120–250 km, which is the partial melting zone of the mantle material. The location of the seismic low-velocity layer in the southwestern margin of the SCS roughly corresponds to the partial melting depth zone of mantle material (**Figure 2**). Based on this, it can be inferred that there is material convection or migration activity at this depth range. Considering that the temperature and pressure state of the upper mantle material is close to the adiabatic compression process, the mantle convection may actually involve thicker layers, and the lower boundary can extend to 440 km.

Calculation Method

(1) Calculation method for crust and upper mantle temperature

The method of solving the steady-state heat conduction equation is mainly used for the calculation of crust temperature. The steady-state heat conduction equation can be expressed as:

$$\nabla \cdot (K\nabla T) = -A \tag{1}$$

In **Eq. 1**, the distribution of temperature T depends on the heat production rate A and thermal conductivity K, and its parameter range is shown in **Table 1**.

In real calculation, the steady-state conduction temperature field is obtained, while factors such as the unsteady-state lateral heat transfer caused by the submarine shallow structure are not taken into account.

The upper mantle lacks thermal constraints, and the rheological state does not meet the conditions of steady-state heat conduction, so the steady-state heat conduction equation cannot be used to calculate the mantle temperature. The upper mantle temperature can be calculated by using the relation between shear wave V_s inelastic component and temperature T and pressure P. In the depth range of 50–250 km, the lithological inelasticity is mainly affected by temperature, which is the main factor for controlling the seismic wave velocity (Sobolev et al., 1996; Goes et al., 2000; An and Shi, 2007). Under high temperature conditions, by means of inelastic correction of the quality factor Q, the calculation formula of temperature-dependent V_s wave velocity after inelastic correction can be obtained as follows:

$$\begin{cases} Vs(P,T,\omega) = Vs(P,T)\left[1 - \dfrac{Q^{-1}(\omega,T)}{2\tan(\pi a/2)}\right] \\ Q(\omega,T) = A\omega^a e^{\left(a\frac{E+PV}{RT}\right)} \end{cases} \tag{2}$$

In **Eq. 2**, A and a are inelastic constants, ω is inelastic effect frequency, E is activation energy, V is activation volume, and R is gas constant.

In real calculation, it is considered that, within the depth range of 50–250 km, the change of wave velocity caused by mineral composition is small, but the change of wave velocity caused by temperature is relatively large. If the shear wave velocity structure at each depth of the upper mantle is known, the difference value of ΔV_s between the wave velocity and the observed wave velocity can be calculated through iterative inversion under given initial conditions, and the initial temperature model can be continuously corrected to decrease ΔV_s (less than 0.1%) to obtain the 3D temperature field distribution of the mantle.

With the V_S wave velocity model and the calculated temperature, the viscous structure of the crust–mantle material can be calculated by the following formula:

$$\begin{cases} \eta = \eta_0 \exp\left[\dfrac{E}{R}\left(\dfrac{1}{T} - \dfrac{1}{T-\Delta T}\right)\right] \\ \Delta T = -\dfrac{\lambda}{\alpha}\cdot\dfrac{\Delta Vs}{Vs} \qquad \lambda:\ [0\Pi 1] \end{cases} \tag{3}$$

In **Eq. 3**, η is viscosity coefficient, E is activation energy, λ is adjustment coefficient, α is coefficient of thermal expansion, R is gas constant, and T is Kelvin temperature.

(2) Calculation method for shear stress field of the rheological layer of the crust and mantle

Deformation is the result of diffusion and transfer of viscous materials. This diffusion is carried out by means of pressure melting (pressure solution). Under the action of bearing deviatoric stress or tectonic stress, the rocks in the deformation region transfer the material from the high-intergranular-pressure-and-stress region to the low-pressure-and-stress region, resulting in creep. Both dislocation creep and diffusion creep can realize the "plastic" flow of solid matter. The dislocation (or power law) creep stress index $n \approx 2.5$–3.5, and the diffusion creep $n = 1$. Laboratory studies support the dislocation creep at the shallow upper mantle (Turcotte, 2014). According to the

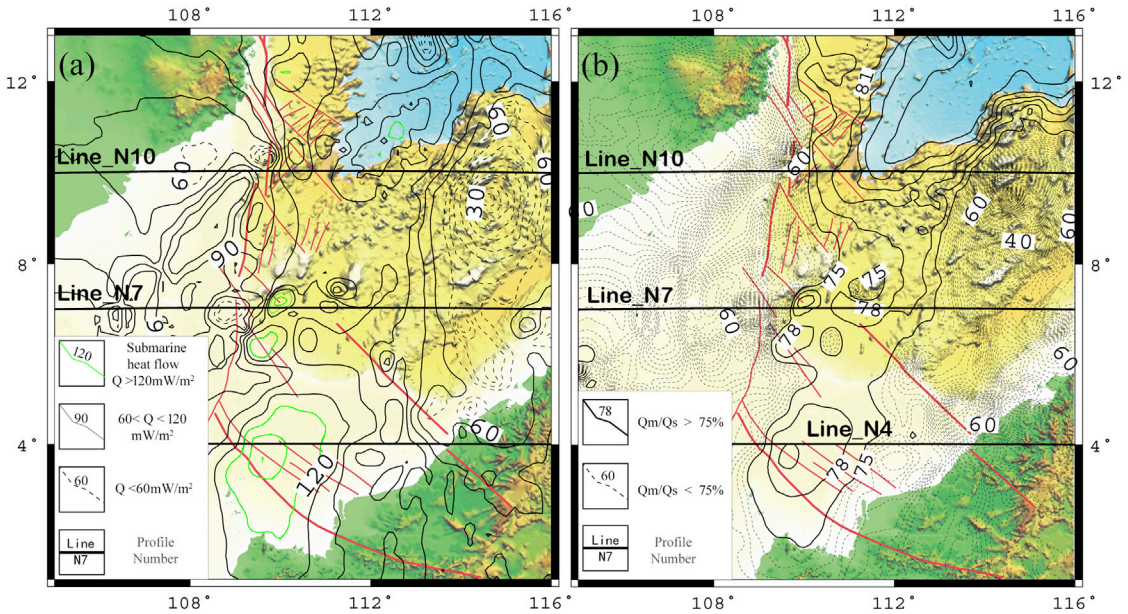

FIGURE 3 | Contour maps of the submarine heat flow and the Q_m/Q_s heat flow structure in the southwestern margin of South China Sea. **(A)** Submarine heat flow Q_s: mW/m^2. **(B)** Q_m/Q_s: %.

spherical harmonic function coefficients Cnm and Snm provided by the satellite gravity and the spherical function Pnm, the shear stress field τ at different depths of the lithosphere can be calculated (Runcorn, 1964; Runcorn, 967) with the following formula:

$$\begin{cases} U(r,\phi,\lambda) = \dfrac{GM_e}{r}\left[1 + \sum\limits_{n=2}^{\infty}\sum\limits_{m=0}^{n}\left(\dfrac{R_e}{r}\right)^n X_{nm}\right] \\ X_{nm} = P_{nm}(\sin\theta)\cdot(C_{nm}\cos m\theta + S_{nm}m\theta) \\ \tau_E = \sum\limits_{n=2}^{\infty}\sum\limits_{m=0}^{n}\left[\dfrac{M_e}{4\pi r^2}\left(\dfrac{R_e}{r}\right)^{n+1}\dfrac{2n+1}{n+1}\dfrac{dX_{nm}}{d\theta}\right] \\ \tau_N = \sum\limits_{n=2}^{\infty}\sum\limits_{m=0}^{n}\left[\dfrac{M_e}{4\pi r^2}\left(\dfrac{R_e}{r}\right).^{n+1}\dfrac{2n+1}{n+1}\dfrac{dX_{nm}}{d\varphi}\right] \end{cases} \quad (4)$$

In **Eq. 4**, U is the gravitational disturbance potential calculated based on Molodensky theory, σ_N and σ_E are north and east shear stress components generated by the rheological layer on the lithosphere base.

In actual calculation, the relation between the spherical harmonic order n at any point and the mass buried depth D_n at the corresponding equivalent point is taken as (Bowin, 1983) $D_n = R / (n - 1)$, where R is 6,371 m.

(3) Calculation method for the flow field of asthenospheric mantle material

Supposedly the temperature variation only affects the density of asthenospheric material, and then this density change may lead to convective activity. The thermal convection equation that describes this density change is as follows:

$$\begin{cases} \dfrac{\partial V}{\partial t} + V\cdot\nabla = \dfrac{\eta}{\rho}\nabla^2 V - \dfrac{1}{\rho}\nabla P - g\gamma T \\ \nabla\cdot\rho V = 0 \\ \dfrac{\partial T}{\partial t} + V\cdot\nabla T = \kappa\nabla^2 T + \dfrac{A}{\rho c} \end{cases} \quad (5)$$

In **Eq. 5**, V is convective velocity, P is pressure, g is gravity, η is viscosity coefficient, ρ is density, κ is thermal diffusion coefficient, A is heat production rate, c is constant pressure specific heat, T is temperature, and α is coefficient of thermal expansion.

In real calculation, the asthenosphere will be considered as a kind of high-viscosity fluid movement on a geological time scale. Viscosity is an important factor for controlling the viscous flow of the mantle. With the depth-dependent viscosity and seismic shear wave velocity V_s obtained by simulating the geoid height anomaly, the flow field of the asthenospheric mantle can be solved.

CRUSTAL THERMAL–RHEOLOGICAL STRUCTURE AND UPPER MANTLE DYNAMICS

Crustal Temperature and Viscosity

The submarine heat flow distribution (**Figure 3A**) drawn by Kriging interpolation using the new heat flow data (indicated with black five-pointed stars) and the existing heat flow data

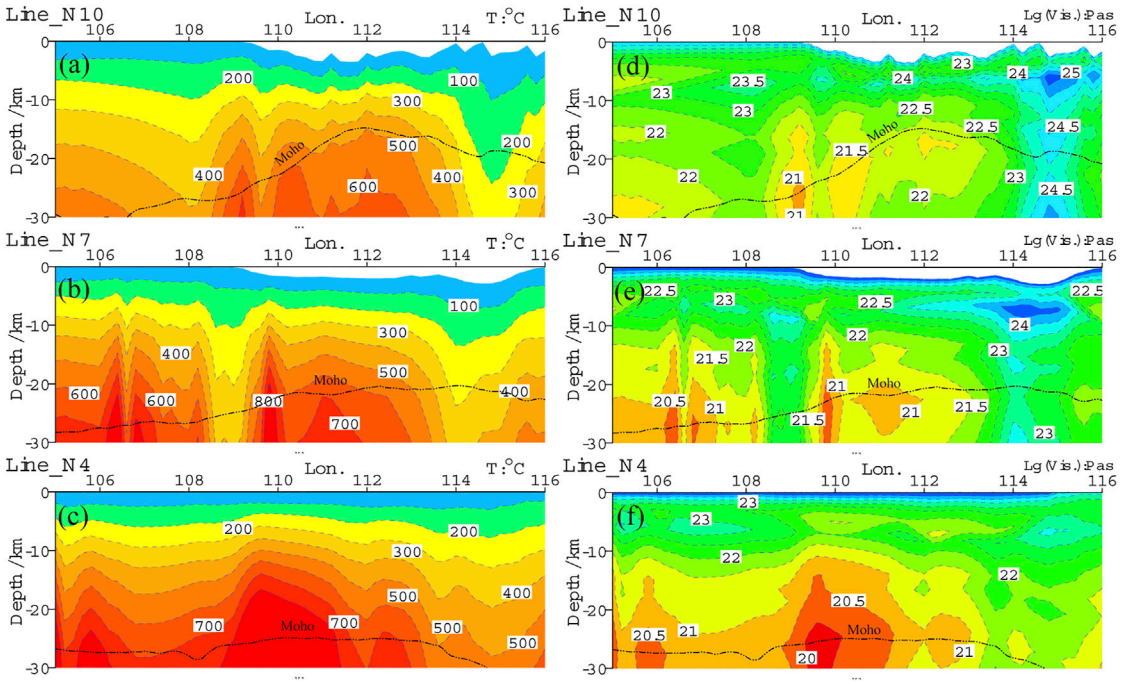

FIGURE 4 | Temperature and viscosity coefficient profiles in the southwestern margin of South China Sea. **(A–C)** Temperature profiles at Line_N10, Line_N7, and Line_N4. **(D–F)** Viscosity coefficient profiles at Line_N10, Line_N7, and Line_N4. The position of the profiles is shown in **Figure 3**, and the earth surface is the starting point of depth.

(indicated with red and blue circles) show that the submarine heat flow Q_s in the study area shows an obvious NNE-trending strip-shaped distribution pattern. Along the axis of the Southwest Basin, the SSW-trending and strip-shaped high-value heat flow anomaly is observed. At the north and south terminations of the high heat flow strip, there are high heat flow areas in the Southwest Basin and the Zengmu Basin, respectively. On the east side of the high heat flow, a low heat flow anomaly is seen on the Nansha Block, while on its west side a high-value heat flow anomaly area is observed in the Wanan Basin.

The submarine heat flow Q_s is equal to the sum of the crustal heat flow Q_c and the mantle heat flow Q_m, and the ratio of the crust and mantle components Q_m/Q_s of the submarine heat flow is an important parameter for studying the heat flow distribution of the crust and the mantle. With the submarine heat flow data Q_s (**Figure 3A**), the Moho depth obtained by gravity inversion, and the heat production rate (**Table 1**), the calculated Q_m/Q_s results (**Figure 3B**) indicate that the NNE-trending strip-shaped distribution pattern of Q_m/Q_s is very clear, and the area with Q_m/Q_s >70% shows a distinct strip shape, which extends to the southwest region along the axis of the Southwest Basin. The Q_m/Q_s on both the east and west sides of the strip is less than 60%, and the Q_m/Q_s in the local area is less than 40%. This crust–mantle heat flow ratio indicates that the heat from the mantle is much higher than that of the crust from the Southwest Basin to the Zengmu Basin, and it is a "hot mantle" zone. On both sides of this strip, especially in the Nansha Block, the mantle heat is relatively low, and it is a "cold mantle" zone.

After de-peaking to the submarine heat flow data in the study area (**Figure 3A**) (Q_s >140 mW/m^2, 140 mW/m^2 is taken; Q_s <40 mW/m^2, and 40 mW/m^2 is taken, in order to eliminate the non-conductive heat effect caused by hydrothermal activity), the steady-state heat conduction equation is solved with the crust–mantle structure of gravity inversion and thermophysical parameters (**Table 1**) (Zhang et al., 2005), and the temperature results of the profiles at N10°, N7°, and N4° (the location of the profiles is shown in **Figure 3**) are shown in **Figures 4A–C**. The results of the profile viscosity calculated from the temperature distribution and the V_s wave velocity distribution are shown in **Figures 4D–F**.

The starting point for the depth of each profile (**Figure 4**) is the sea level, of which on the profile at N10° (**Figure 4A**), E108°, and E115°, there are two low-temperature zones at depth, with Moho temperatures of 390 and 180°C, respectively. However, high-temperature zones appear on the east and west sides of the strike–slip fault zone (at E110°), and the Moho temperature is higher than 600°C. Beneath the corresponding strike–slip fault zone, the Moho temperature is lower than 500°C. On the profile at N7° (**Figure 4B**), a clear low-temperature zone appears at E109°, which corresponds to the intersection area of the strike–slip zones in the southeastern margin of Wanan Basin, and in the western margin, the Moho temperature is lower than 350°C. To the east of E114°, there is also a low-temperature zone, with the Moho temperature being lower than 300°C. The low-temperature zone on the east side corresponds to the Nansha Block and Nansha Trough, which is caused by the abnormal cooling of the

mantle (Zhang et al., 2017). On the profile at N4° (**Figure 4C**), the temperature distribution has changed significantly. This profile corresponds to the Lupal Fault Zone and the Tinja Fault Zone in which the strike–slip fault zone in the western margin bends to the southeast. The deep geothermal activity caused by tectonic activity is intense, and the Moho temperature is significantly higher than that of the N10° profile and N7° profile on the north side, of which the Moho temperature in the Zengmu Basin at E110° is as high as 900°C.

With the temperature profiles (**Figures 4A–C**) and based on the 3D shear wave velocity structure (Chen et al., 2021), the calculated viscosity coefficient profiles are shown in **Figures 4D–F**, of which on the profile at N10° (**Figure 4D**), at Moho depth on the east and west sides beneath the strike–slip fault zone in the western margin, these are characterized by two low-viscosity-coefficient regions, with a viscosity coefficient at 10^{21}–10^{22} Pa·s. Beneath the Nansha Block is a high-viscosity-coefficient region that is vertically extended, with a viscosity coefficient at 10^{24}–10^{25}Pa·s. On the profile at N7° (**Figure 4E**), on both the east and west sides of the strike–slip fault zone are two separate low-viscosity-coefficient regions, but their separation distance is larger than that of the north side, and the viscosity coefficient on the east side is much lower, which can be as low as 10^{20} Pa·s at 110°C. However, the vertically extended high-viscosity-coefficient region beneath the Nansha Block shrinks upward, forming a "hard core" with a viscosity coefficient of greater than 10^{24} Pa·s at a depth of 5–10 km. On the profile at N4° (**Figure 4F**), due to the increase in temperature, the viscosity coefficient near the Moho surface is low, and a "weak rheological zone" with a viscosity coefficient of less than 10^{20} Pa·s is formed near the Moho surface, and partial melting may exist.

Upper Mantle Dynamics

Thermal–rheological analysis of gravity and seismic data is an important method for deep dynamic study. The comprehensive analyses of the gravity field EGM2008 model, the satellite gravity data, and the seismic shear wave model (Chen et al., 2021) indicated that, at 40-km depth or beneath the Moho in the southwestern margin of SCS, the influence of the tectonics of the SCS Basin is gradually decreasing, and the characteristics of the strike–slip structure in the western margin is becoming progressively clear; at 70-km depth or below, a low-velocity uplift consistent with the strike–slip structure trend is observed; at 100-km depth or below, the characteristics of the strike–slip structure in the western margin of the SCS are gradually weakening, and the NW–NS–NE clockwise rotation effect steadily becomes prominent, which coincides with the clockwise rotation during the sinistral movement of the Indosinian Peninsula relative to the South China Block after the Mesozoic; at 200-km depth or below, the clockwise rotation effect is gradually weakening, and the NE-trending structure becomes more obvious.

According to the crust–mantle thermal structure model given in **Figure 2**, there is a RBL in a specific thickness interval at the lithosphere base. The rheological boundary layer can transfer the tangential stress generated by the mantle flow to the lithosphere to form a lithospheric stress and to deform the lithosphere. If it is assumed that there is a Newtonian viscous laminar flow beneath the rheological boundary layer and an elastic lithosphere above the rheological boundary layer, then an equilibrium equation at $r = r'$ on the upper boundary of the mantle flow is constructed by the gravitational disturbance potential generated by Navier–Stokes equation and uneven density. Suppose the radial component of the velocity at $r = r'$ is zero. In this case, equilibrium equation can be solved with this equilibrium equation and the spherical harmonic function of the gravitational potential to obtain the north and east shear stress components at different depths in the rheological boundary layer τ_N, τ_E (Runcorn, 1964; Runcorn, 1967; Bowin, 1983; Wu and Liu, 1992; Fu et al., 1994). The depth at the lithosphere base fluctuates, and the thickness of the rheological layer is uneven. The stress distribution at a depth of 65 and 100 km in the study area (**Figure 5**) is calculated with **Eq. 4**.

The southwestern margin of the SCS has experienced intense shear deformation and tectonic extrusion caused by the subduction of the Pacific Plate in the Mesozoic as well as the creeping, rifting, and drifting of the South China continent towards the southeast along with mantle convection, which left traces in the upper mantle. Therefore, an analysis can be carried out with the northward shear stress component τ_N and the eastward shear stress component τ_E at the depth of 65 and 100 km in the rheological boundary layer calculated from the gravity potential data (**Figure 5**). The northward shear stress component τ_N at 65-km depth in the rheological boundary layer is -5.78–6.32×10^8 N/m^2 (**Figure 5A**). In the middle section of the strike–slip fault zone, τ_N is a "positive" value, whereas in the southern part of the strike–slip fault zone, the Zengmu Basin between the Lupal Fault Zone and Tinja Fault Zone is an NW-trending strip zone where τ_N is characterized by alternation of "positive" and "negative" values. The eastward shear stress component τ_E at 65-km depth in the rheological boundary layer of this area is at -11.09–8.66×10^8 N/m^2 (**Figure 5B**). Overall, τ_E is distributed alternately in a long S–N-trending strip from west to east. The eastward shear stress component τ_E is a "positive" value zone on the west side of the strike–slip fault zone and a "negative" value zone on the east side. The northward shear stress component τ_N at 100-km depth in the rheological boundary layer of the study area is at -1–1×10^8 N/m^2 (**Figure 5C**). The Zengmu Basin between the Lupal Fault Zone and the Tinja Fault Zone in the southern section of the strike–slip fault is a "negative" low-value shear stress zone, and this "negative" value area forms a long-axis NW–SE-trending ellipse. The "negative" stress zone in Zengmu Basin extends toward the northwest. After crossing the middle section of the strike–slip fault zone in the western margin, it forms a "negative" value zone in the long axis near the N–S-trending ellipse on the north side of Wanan Basin. This "negative" value zone and the "positive" value zone in the long axis near the NS-trending ellipse in Zhongjiannan Basin are distributed in parallel to each other in the west and east of the middle section of the strike–slip fault zone, forming a southward shear zone on the west side and a northward shear zone on the east side. The eastward shear stress component τ_E at 100 km depth in the rheological boundary layer of this area is at -1~1×10^8 N/m^2 (**Figure 5D**). At this depth, the southern section of the

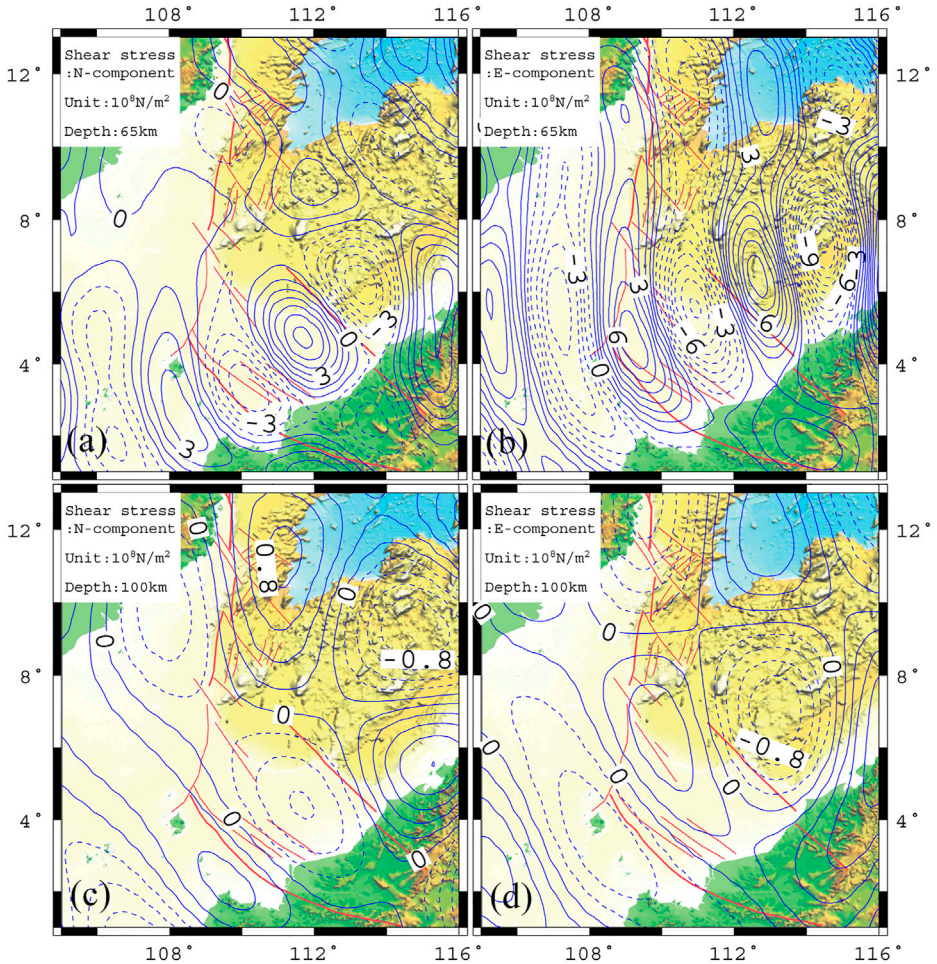

FIGURE 5 | Stress field at the rheological boundary of the upper mantle in the southwestern margin of South China Sea. **(A)** Northward shear stress τ_N at 65-km depth. **(B)** Eastward shear stress τ_E at 65-km depth. **(C)** Northward shear stress τ_N at 100-km depth. **(D)** Eastward shear stress τ_E at 100-km depth. τ_N—positive in the north and negative in the south; τ_E—positive in the east and negative in the west.

strike–slip fault zone in the western margin and Zengmu Basin between the Lupal Fault Zone and Tinja Fault Zone are all in a NW-SE-trending "positive" shear stress zone. This "positive" value zone extends towards the northwest and directly reaches beneath the eastern continent of Vietnam, forming an obvious eastward shear strip. On the south side of the Lupal Fault Zone, there is an NW–SE-trending "negative" shear stress zone. The Nansha Block is also an obvious "negative" shear stress zone.

With the 3D shear wave velocity model (Chen et al., 2021) (**Figure 6A**) and **Eq. 2**, the temperature distribution of the upper mantle at a depth of 50–250 km can be calculated (**Figure 6B**). It can be found that the seismic shear wave velocity corresponding to the strike–slip structure is in a low-velocity zone of less than 4.3 km/s (**Figure 6A**). This low-velocity zone is slightly bended from the NNW direction to the S–N direction from shallow to deep area, forming a low-velocity uplift beneath the Wanan Fault and the Wanan Basin, which is a high-temperature area of the mantle (**Figure 6B**). Overall, the seismic shear wave velocity reflects the tectonic characteristics formed during the mantle material migration and deep dynamic process, and the seismic shear wave velocity of 4.1–4.3 km/s varies from NNW to SSE considerably. The shear velocity reaches a maximum value beneath Borneo Island, indicating that shear stress is concentrated at a great depth.

Theoretically, *S* wave velocity is determined by shear modulus and density, and it is related to temperature, pressure, mineral composition and structure, fluid, and other parameters (Nolet and Zielhuis, 1994; Sobolev et al., 1996). Due to the lack of measured data on the lithologic structure of the upper mantle in the western margin of SCS, it is assumed that the proportion of lithologic components in the upper mantle is, respectively, as follows: olivine—68%, orthopyroxene—18%, clinopyroxene—11%, and garnet—3% (Goes et al., 2000; An and Shi, 2007). According to the lithologic components, the temperature distribution of the upper mantle in the strike–slip fault zone can be inverted from the V_s wave velocity by means of **Eq. 2** (**Figure 6B**). According to the results in **Figure 6B** and **Eq.**

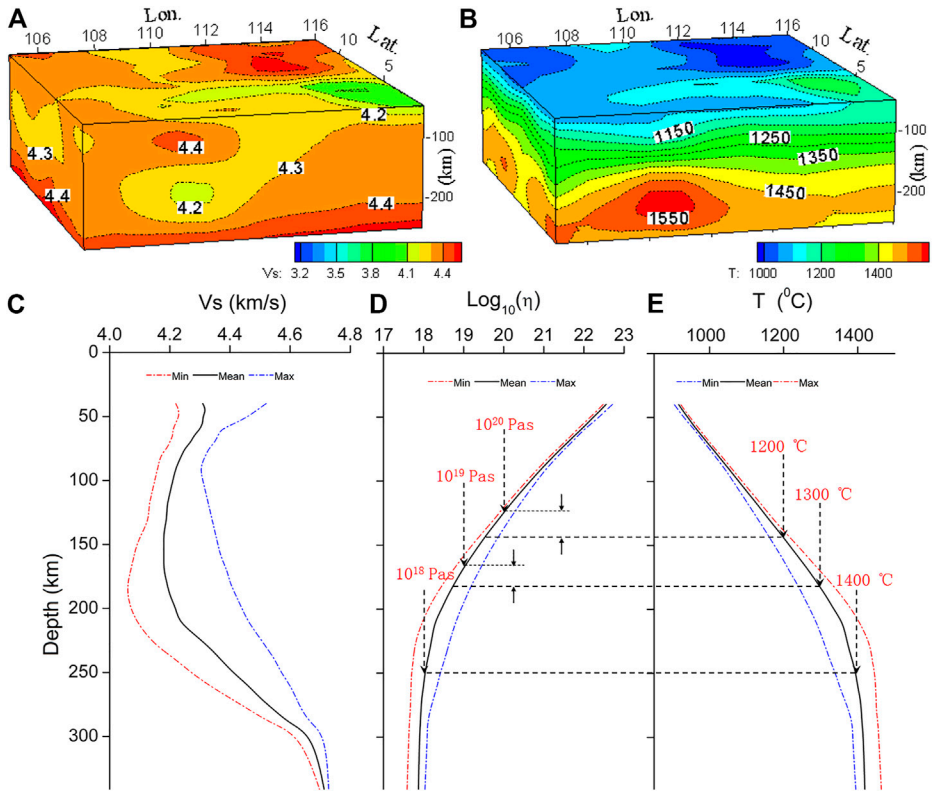

FIGURE 6 | Diagram of the S-wave velocity characteristics and dynamic analysis of the mantle in the southwestern margin of SCS. **(A)** S-wave velocity 3D model (km/s). **(B)** Temperature chart (50–250 km) calculated by wave velocity model (°C). **(C)** Average S-wave velocity structure varying with depth. **(D)** Logarithm of the effective viscosity coefficient of the mantle with variations at depth. **(E)** Mantle temperature varying with depth.

3, the viscosity distribution corresponding to temperature can be calculated.

The new-generation 3D shear wave velocity model proposed by Chen *et al.* (2021) is only available for up to 250-km depth. Considering that its deep wave structure is similar to that proposed by Mei and An (2010), we integrated the V_s data at a depth of 250–400 km from the model of Mei and An (2010) into the model of Chen *et al.* (2021). The model is expanded to marine shear wave model available for a deep dynamic analysis of the southwestern margin of the SCS. The average velocity, effective viscosity coefficient, and temperature curve of the upper mantle that varied with depth are calculated (**Figure 6C–E**). **Figure 4C** shows the variation in the V_s shear wave velocity with depth obtained by averaging statistics layer by layer. It can be seen that, at a depth range of 50–200 km, the shear wave velocity V_S gradually decreases with depth, and the average velocity decreases from 4.36 to 4.17 km/s. In the depth from 200 to 300 km, the V_s value gradually increases, and the average velocity gradually rises from 4.17 to >4.6 km/s. **Figures 6D,E** show the variation of the logarithm of effective viscosity coefficient η of the mantle with depth and the variation of the mantle temperature T with depth obtained by averaging the mantle temperature and viscosity layer by layer. By comparing **Figures 6D, E**, it can be found that η is "mirroring" and symmetrical with T in the depth range of 50–300 km. Near the depth of 150 km, the average temperature of the mantle reaches 1,200°C, and the average effective viscosity coefficient is 10^{19}–10^{20} Pa·s; at 180-km depth, the average temperature of the mantle is 1,300°C, and the average effective viscosity coefficient is at 10^{18}–10^{19} Pa·s; at 250-km depth, the average temperature of the mantle is 1,400°C, and the average effective viscosity coefficient is slightly less than 10^{18} Pa·s. Below the depth of 180 km, the temperature and viscosity can meet the temperature and viscosity conditions required for partial melting or convective migration of the mantle material (Milne G A, et al., 2001; Mitrovica J X, et al., 2004).

The convective activity in the upper mantle asthenosphere is an important element in the creation of lithospheric tectonic dynamics, magmatic activity, and material circulation. The asthenosphere is closely related to the seismic low-velocity zone, and the asthenospheric mantle convection controlled by the viscosity structure may cause the geoid to have positive and negative anomalies. Therefore, the geoid anomaly is an essential constraint for calculating the convective viscosity structure of the mantle. By constraining the velocity–density–temperature conversion factor with the geoid (WGM 2012) R-squared, the viscosity change of the upper mantle can be calculated. Note that this viscosity rheology is different from the above-mentioned lithospheric thermal rheology. Viscosity is the key parameter for controlling the mantle convection. Under the condition that the viscosity structure of the mantle is

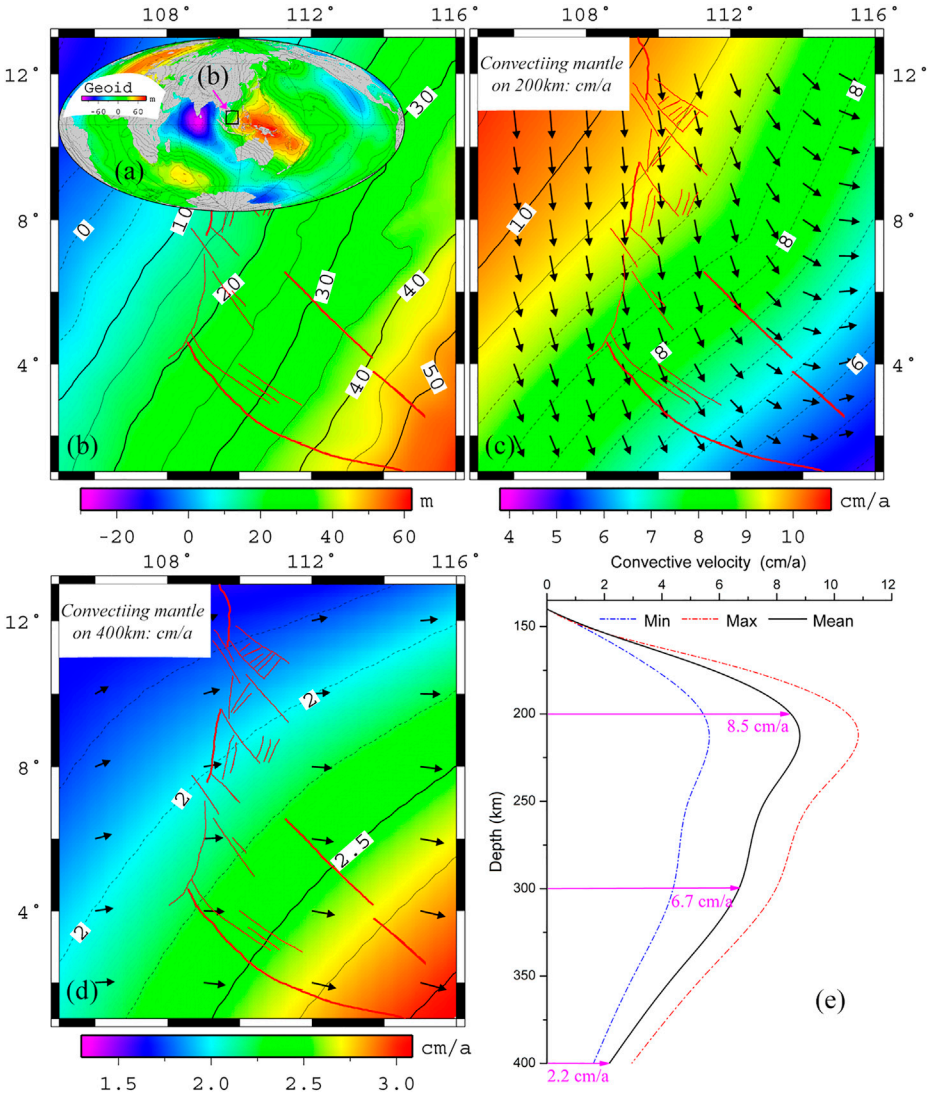

FIGURE 7 | Analysis of convection in the upper mantle asthenosphere of the southwestern margin of South China Sea (SCS). **(A)** Global geoid anomaly (m). **(B)** Geoid anomaly (m) in the southwestern margin of SCS. **(C)** Convective velocity of the mantle at 200-km depth (cm/a). **(D)** Convective velocity of the mantle at 400-km depth (cm/a). **(E)** Variation of convective velocity of the asthenospheric mantle with depth (cm/a).

determined, the stress conditions that drive the mantle convection can be set up to calculate the convective velocity field of the mantle asthenosphere. The stress that drives the mantle convection can originate from density differences. Temperature change may affect the density of convective material, and density change may lead to convective activity. The heat convection equation describing this density change includes the following: the kinematic equation of a viscous fluid, the continuity equation under the assumption of incompressibility, and the heat transfer equation including the convection term, *i.e.*, **Eq. 5**.

Based on the temperature model and thermal viscosity structure obtained from the seismic V_s analysis, the gravimetric geoid anomaly model (WGM 2012) was used to calculate the convection of the mantle asthenosphere (**Figure 7**). The global geoid anomaly map (**Figure 7A**) shows that the southwestern margin of the SCS is located between the negative anomaly zone of the Indian Ocean geoid and the positive anomaly zone of the Pacific geoid. The geoid height anomaly in the study area is at −15.56–58.86 m (**Figure 7B**). Overall, it is a geoid anomaly cascade that is low in NW and high in SE. The geoid height in the northwest corner is negative, while the geoid height in the southeast corner is positive. **Figures 7C,D** show the convective velocity field at 200–400-km depth in the mantle asthenosphere in the southwestern margin of the SCS as calculated by **Eq. 5** under the constraints of the geoid model and seismic shear wave model. By comparing the convective velocity field of the

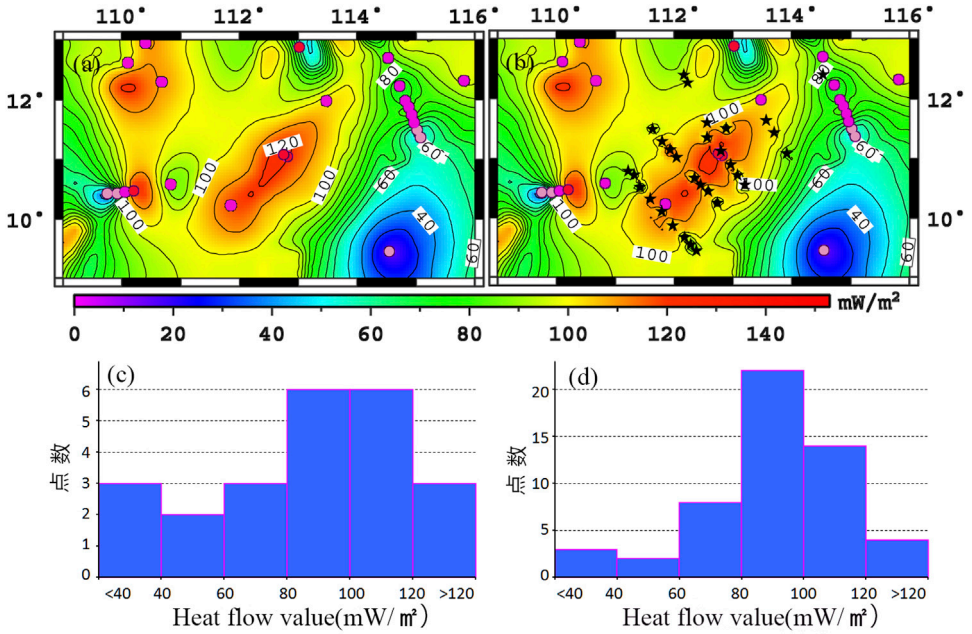

FIGURE 8 | Comparison and analysis of new and old submarine heat flow data. **(A)** Submarine heat flow map with previous data. **(B)** Submarine heat flow map with the added new data. **(C)** Diagram of statistical distribution using the old data. **(D)** Diagram of statistical distribution using the added new data.

mantle at the depth of 200–400 km, it can be found that the flow direction of the mantle asthenosphere varies greatly from shallow to deep area. At 200-km depth, the material flows toward the nearly south–north direction in the eastern continent of Vietnam. The flow changes to the east–south direction in the middle part and changes to nearly east–west direction beneath Borneo Island. The flow velocity is at 4.85–10.63 cm/a, which gradually decreases from northwest to southeast. At 200-km depth, the overall flow direction changes to east–west direction. The flow velocity is at 1.58–3.09 cm/a. There are two velocity zones, *i.e.*, northwest and southeast. The northwest is a low-velocity zone, while the southeast is a high-velocity zone. The flow velocity at 400-km depth is not only greatly smaller than that at 200-km depth but also the distributions of high- and low-velocity zones are completely opposite. **Figure 7E** shows the variation of convective velocity of asthenosphere with depth. It can be seen that the material flow velocity gradually increases from 150 km below, and at 200-km depth, the flow velocity reaches a maximum value, which can reach an average of 8.5 cm/a. At 200-km depth or below, the material flow velocity gradually decreases. At 300-km depth, the average flow velocity decreases to 6.7 cm/a. At 400-km depth, the average flow velocity decreases to 2.2 cm/a.

DISCUSSION AND CONCLUSION

New and Old Heat Flow Data

In the area where 30 sites of new heat flow data were present (**Figure 1B** and **Figure 3**), there are also 23 sites of previous heat flow data (Yao et al., 1994; Nissen et al., 1995). **Figure 8** shows the comparison of overall 53 heat flow data.

Figures 8A,C are diagrams of distribution and statistics of heat flow from 23 old data, while **Figures 8B,D** are diagrams of distribution and statistics of heat flow from the added 30 new data. The average heat flow value of 23 old data is 86.86 mW/m^2, with a large difference between high and low heat flow values and a high dispersion (**Figure 8C**). After the inclusion of 30 new data, the average heat flow value in the study area is 91 mW/m^2, and the distribution interval is relatively reasonable (**Figure 8D**). However, after a comparison between the results in **Figures 8A,B**, it seems that the addition of new data does not change the overall distribution pattern of submarine heat flow. Instead it only changes the detailed distribution of the heat flow in local areas. Therefore, in addition to making full use of the dynamic information obtained from the 30 new data, taking advantage of previous submarine heat flow data still lays an important foundation for geothermal analysis in the whole region.

Mantle Viscosity and Rheological Boundary Layer

The effective viscosity coefficient of the mantle depends on temperature, pressure, grain size, water content, *etc.* The higher the temperature, the lower the viscosity coefficient, and the higher the pressure, the higher the viscosity coefficient. In the uppermost mantle, the effective viscosity coefficient is mainly related to temperature, and the viscosity coefficient decreases with depth as temperature increases. However, in the deep mantle (below the asthenosphere and the lower mantle), due to the adiabatic (isothermal) compression effect, the pressure that increased with depth will make the viscosity coefficient

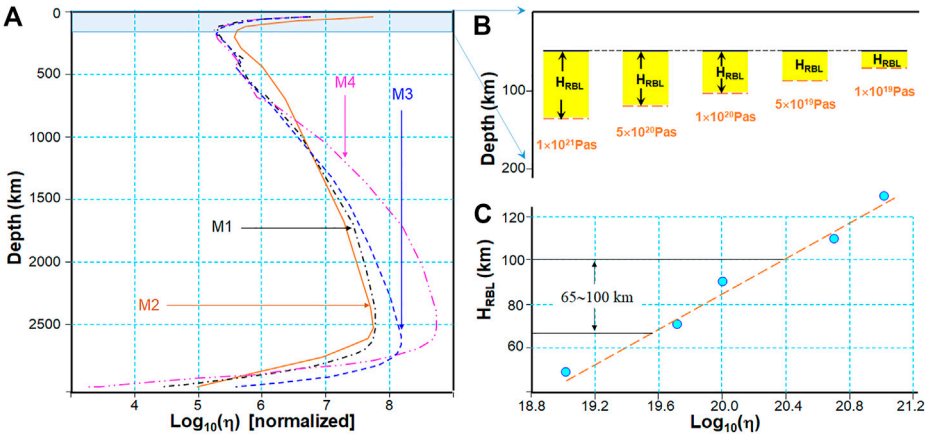

FIGURE 9 | Analysis of mantle viscosity and rheological boundary. **(A)** Normalized mantle viscosity model (Steinberger and Arthur 2006). **(B)**, **(C)** Changes of rheological boundary layer with mantle viscosity (He, 2014).

increase with depth, which is greater than the effect that the temperature increase will have to make the viscosity coefficient decrease. Therefore, the viscosity tends to increase with depth, while the viscosity coefficient will not decrease gradually until the base of the mantle. **Figure 9A** shows the variation of the normalized mantle viscosity coefficient with depth calculated from different mineral physical constraint models (Steinberger and Arthur, 2006), from which it can be found that the viscosity of the mantle has a strong depth dependence, and the viscosity structure of the upper and lower mantles is very different.

The viscosity coefficient of the upper mantle based on the post-glacial rebound and gravity equilibrium is 4–10 × 10^{20} Pa·s (Mitrovica and Forte, 2004). The GPS space geodetic study has obtained the asthenosphere viscosity coefficient of 5–10 × 10^{20} Pa·s (Milne et al., 2001), and the viscosity coefficient of the asthenosphere obtained from GRACE satellite gravity data and relative sea level data is 5.3 × 10^{20} Pa·s (Paulson et al., 2010). The viscosity coefficient of the asthenosphere in the lower part of the oceanic lithosphere is about 7 × 10^{18} Pa·s (Doin et al., 1997), and the viscosity coefficient of the asthenosphere below the active tectonic region of the continental lithosphere is about 10^{18}–10^{19} Pa·s (Dixon et al., 2004). The effective viscosity coefficient of the low-velocity layer in the upper mantle in the southwestern margin of the SCS is at 10^{18}–10^{20} Pa·s (**Figure 6D**), which is consistent with the results of previous studies.

The effective viscosity coefficient of the mantle is not only the key parameter controlling the mantle convection but also the key factor controlling the thickness and the bottom boundary of the upper rheological boundary layer. According to the change characteristics of the geothermal gradient curve (**Figure 2**), the upper mantle can be divided into three layers: the upper is a pure conduction layer, the middle is a rheological boundary layer with a thickness of H_{RBL}, in which heat conduction and heat convection coexist, and the geothermal gradient drops to below 4–5°C/km; the lower is a pure convection layer, in which the geothermal gradient is very small, and the adiabatic temperature gradient is 0.5°C/km. Due to the coexistence of conduction and convection, there is no obvious interface between the solid lithosphere and the fluid mantle in the RBL, and the bottom boundary is mainly affected by the effective viscosity coefficient of the mantle (He, 2014). The higher the effective viscosity coefficient of the mantle, the thicker the rheological boundary layer H_{RBL}, and the lower the effective viscosity coefficient of mantle, the thinner the rheological boundary layer H_{RBL}. Based on this, it is inferred that if the $\log_{10}(\eta)$ of the asthenosphere in the southwestern margin of the SCS decreases from 20 to 18, the bottom of the rheological boundary layer (**Figure 9B**) or the thickness (**Figure 9C**) can be uplifted from 100 km or thinned to 65 km.

CONCLUSION

The southwestern margin of the SCS is located on the transition zone between the continental shelf and the slope. The strike–slip fault zone that runs through this zone has formed an important Cenozoic ocean–continent tectonic boundary. The strike–slip fault zone constrains the overall tectonic framework of the western margin of the South China Sea, and it is a key structural zone for understanding the geological evolution and continental margin dynamics of the SCS. The main study conclusions of this paper are as follows:

1. The newly acquired 30 submarine heat flow data have facilitated the study of geothermal field and thermal state in the western margin of the SCS. After the merging of new and old geothermal data, there is a series of submarine high-heat-flow areas along the strike–slip fault zone, of which the southern section of Zhongjiannan Basin, the southwestern margin of the Southwest Basin in the SCS, Wanan Basin, and Zengmu Basin are all at high-value areas with a heat flow of >90 mw/m^2, whereas Nansha Island and Reef Area as well as Nansha Trough are at the low-value areas of submarine heat flow. The proportion of the crust and mantle components of the submarine heat flow in this

area shows a clear NNE-trending strip-shaped distribution pattern. The southwest sea area along the axis of the Southwest Basin and the Zengmu Basin are of high-value areas of Q_m/Q_s >70%, in which the heat from the mantle is much higher than that of the crust, so it is a "hot mantle" strip, whereas Nansha Block has low mantle heat and is a "cold mantle" area with a low Q_m/Q_s value.

2. The Moho temperature calculated with the submarine heat flow data in this area is between 200 and 950°C. The Moho temperature in the Nansha sea area is the lowest, while the Moho temperature in the southern part of the Zengmu Basin is the highest, reaching >900°C. The Moho temperature in the Wanan Basin is also higher, which can reach over 800°C in some areas. The highest Moho temperature in the Zhongjiannan Basin is around 600°C. The strike–slip fault zone in the western margin of the SCS bends to the southeast into the Lupal Fault Zone and Tinja Fault Zone, beneath which the Moho temperature is obviously high, indicating that the deep geothermal activity caused by tectonic activity is intense. In the thermal–rheological structure of the lithosphere, there are two low-viscosity-coefficient regions at Moho depth on both the east and west sides of the strike–slip fault zone, with a viscosity coefficient at 10^{21}–10^{22} Pa·s. Beneath the Nansha Block is a high-viscosity-coefficient region that is vertically extended, with a viscosity coefficient at 10^{24}–10^{25} Pa·s. Beneath the Zengmu Basin is a "weak rheological zone" with a viscosity coefficient of less than 10^{20} Pa·s near the Moho, and partial melting magmatism may exist.

3. The new-generation high-resolution 3D shear wave velocity model for SCS can clearly reflect the tectonic characteristics at various depths. In the southwestern margin of SCS, if the V_s velocity structure is above the Moho, it mainly reflects the changes in ocean–continent tectonics; if the V_s velocity structure is beneath the Moho surface, it mainly shows the characteristics of the strike–slip fault structure in the western margin of the SCS. A low-velocity uplift from the mantle corresponding to the strike–slip structure appears to be beneath the study area. Below the depth of 100 km, the characteristics of the strike–slip structure are gradually weakening; below the depth of 200 km, the seismic shear wave velocity reflects the characteristics of material migration in the mantle asthenosphere and deep dynamic process. After entering the mantle, there is a low-velocity layer below the depth of 180 km. According to the conversion calculation of velocity–density–temperature constrained by a gravimetric geoid model, the average temperature of the mantle at 250-km depth can reach 1,400°C, and the average effective viscosity coefficient is close to 10^{18} Pa·s, which meets the temperature and viscosity conditions for partial melting or convective migration of mantle material.

4. The calculation results of the north and east shear stress components τ_N and τ_E in the rheological boundary layer show that the closer upward to the Moho surface, the greater the absolute value of τ_N and τ_E, and the closer the seismic shear low-velocity layer is, the smaller the absolute τ_N and τ_E. At 65-km depth, τ_N is at -5.78–6.32×10^8 N/m^2, and τ_E is at -11.09–8.66×10^8 N/m^2. At 100-km depth, both τ_N and τ_E are at -1–1×10^8 N/m^2. The thickness and the bottom depth of the rheological boundary layer are mainly controlled by the effective viscosity coefficient of the lower convective mantle layer.

5. The partial melting depth zone of the upper mantle material in the southwestern margin of the SCS roughly corresponds to the location of a low-velocity layer of the seismic shear wave beneath the lithosphere. Based on this, it can be inferred that the depth zone where the low-velocity layer and the partial melting of the mantle overlap is the convective layer where the material of the upper mantle migrates. The convective velocity of the mantle varies greatly from 200 to 400 km at depth. At 200-km depth, the average convective velocity is 8.5 cm/a, gradually decreasing from northwest to southeast; at 400-km depth, the average flow velocity is 2.2 cm/a. The flow velocity at 400-km depth is not only smaller than that at 200 km depth but also the distributions of high- and low-flow velocity areas are also opposite.

DATA AVAILABILITY STATEMENT

The raw data supporting the conclusion of this article will be made available by the authors without undue reservation.

AUTHOR CONTRIBUTIONS

All authors listed have made a substantial, direct, and intellectual contribution to the work and approved it for publication.

FUNDING

This study was supported by NSFC-Guangdong Joint Fund (grant no. U20A20100), Key Special Project for Introduced Talents Team of Southern Marine Science and Engineering Guangdong Laboratory (Guangzhou) (grant no. GML2019ZD0201), the National Natural Science Foundation of China (Grant No.42106079), National Natural Science Foundation Youth Fund (grant no. 42106079), Guangdong Natural Science Fund Research Team (grant no. 2107A030312002), Basic Marine survey project (Grant No. DD20221712, DD20221719) and National Marine and Land Mineral Resources Map Compilation and Update Project (grant no. DD20190368).

ACKNOWLEDGMENTS

We are grateful to Zhiwei Li and Meijian An for their extremely helpful discussions and suggestions which have helped to significantly improve the manuscript. Two reviewers and scientific editors are thanked for their very careful reviews and constructive suggestions, which greatly enhanced the scientific and technical level of the paper.

REFERENCES

An, H., Li, S., Suo, Y., Liu, X., Dai, L., Shan, Y., et al. (2012). Basin-controlling Faults and Formation Mechanism of the Cenozoic Basin Groups in the Western Margin of South China Sea. *Mar. Geology. Quat. Geology.* 31 (6), 95–111.

An, M., and Shi, Y. (2007). Three-dimensional Temperature Field of the Crust and Upper Mantle in Chinese Mainland. *Sci. China (D)* 37 (6), 736

Bowin, C. (1983). Depth of Principal Mass Anomalies Contributing to the Earth's Geoid Undulations and Gravity Anomlies. *Mar. Geodesy* 7, 61–101. doi:10.1080/15210608309379476

Chen, H., Li, Z., and Luo, Z. (2021). Crust and Upper Mantle Structure of the South China Sea and Adjacent Areas from the Joint Inversion of Ambient Noise and Earthquake Surface Wave Dispersions. *Geochem. Geophys. Geosystems* 22, e2020GC009356. doi:10.1029/2020gc009356

Ding, W., and Li, J. (2016). Conjugate Margin Pattern of the Southwest sub-basin, south china Sea: Insights from Deformation Structures in the Continent-Ocean Transition Zone. *Geol. J.* 51, 524

Dixon, J. E., Dixon, T. H., and Bell, D. R. (2004). Lateral Variation in Upper Mantle Viscosity: Role of Water. *Earth Planet. Sci. Lett.* 222 (2), 451–467. doi:10.1016/j.epsl.2004.03.022

Doin, M. P., Fleitout, L., and Christensen, U. (1997). Mantle Convection and Stability of Depleted and Undepleted Continental Lithosphere. *J. Geophys. Res. Solid Earth* 102 (B2), 2771–2787. doi:10.1029/96jb03271

Dong, M., Wu, S., Zhang, J., Xing, X., Gao, J., and Song, T. (2020). Lithospheric Structure of the Southwest South China Sea: Implications for Rifting and Extension. *Int. Geology. Rev.* 62 (7-8), 924–937. doi:10.1080/00206814.2018.1539926

Dong, M., Zhang, J., Xu, X., and Wu, S.-G. (2018). The Differences between the Measured Heat Flow and BSR Heat Flow in the Shenhu Gas Hydrate Drilling Area, Northern South China Sea. *Energy Exploration & Exploitation* 37, 756–769. doi:10.1177/0144598718793907

Fu, R., Huang, J., and Liu, W. (1994). Correlation Equation between Regional Gravity Isostatic Anomalies and Small Scale Convection in the Upper Mantle. *Chin. J. Geophys.* 37, 638

Fukao, Y., Obayashi, M., Inoue, H., and Nenbai, M. (1992). Subducting Slabs Stagnant in the Mantle Transition Zone. *J. Geophys. Res.* 97, 4809–4822. doi:10.1029/91JB02749

Fyhn, M., Boldreel, L. O., and Nielsen, L. H. (2009). Geological Development of the Central and South Vietnamese Margin:Implications for the Establishment of the South China Sea, Indochinese Escape Tectonics and Cenozoic Volcanism. *Tectonophysics* 478 (3), 184–214. doi:10.1016/j.tecto.2009.08.002

Gao, H. (2011). A Tentative Discussion on Strike-Slipping Character and Formation Mechanism of Western-Edge Fault Belt in South China Sea. *Geology. China* 10 (03), 537

Goes, S., Govers, R., and Vacher, P. (2000). Shallow Mantle Temperatures under Europe from P and S Wave Tomography. *J. Geophys. Res.* 105 (B5), 11153–11169. doi:10.1029/1999jb900300

He, L. (2014). The Rheological Boundary Layer and its Implications for the Difference between the Thermal and Seismic Lithospheric Bases of the North China Craton. *Chin. J. Geophys.* 57 (1), 53

Huang, J., and Zhao, D. (2006). High-resolution Mantle Tomography of China and Surrounding Regions. *J. Geophys. Res.* 111, B9. doi:10.1029/2005JB004066

Li, J., Ding, W., Wu, Z., Zhang, J., and Dong, C. (2012). The Propagation of Seafloor Spreading in the Southwestern Subbasin, South China Sea. *Chin. Sci. Bull.* 57 (24), 3182–3191. doi:10.1007/s11434-012-5329-2

Li, Y., Luo, X., and Xing, X. (2010). Seafloor *In-Situ* Heat Flow Measurements in the Deep-Water Area of the Northern Slop, South China Sea. *Chin. J. Geophys.* 53 (9), 2161–2170. doi:10.1002/cjg2.1547

Lin, C., Tang, Y., and Tan, Y. (2009). Geodynamic Mechanism of Dextral Strike-Slip of Western-Edge Faults of the South China Sea. *Acta Oceanologica Sinica (Chinese Version)* 29 (01), 159

Lin, M., and Zhang, J. (2014). Thermal Simulation on Magma Activity Mechanism of Residual Ridge in the Southwest Basin of the South China Sea. *Sci. China (D)* 44 (6), 239

Liu, B., Xia, B., Li, X., Zhang, M., Niu, B., Zhong, L., et al. (2006). Southeastern Extension of the Red River Fault Zone (RRFZ) and its Tectonic Evolution Significance. *Sci. China (D)* 36 (10), 914

Liu, H. (1999). On an Extension-contraction-type Dextral Strike-Slip Duplex System in Western Nansha Waters of South China Sea and its Dynamic Process. *Mar. Geology. Quat. Geology.* 19 (3), 11

Liu, H., Yao, Y., Shen, B., Cai, Z., Zhang, Z., Xu, H., et al. (2015). On Linkage of the Western Boundary Faults of the South China Sea. *Earth Scienc* 40 (4), 615–632

Lu, L., Stephenson, R., and Clift, P. D. (2016). The canada basin Compared to the Southwest south china Sea: Two Marginal Ocean Basins with Hyper-Extended Continent-Ocean Transitions. *Tectonophysics* 691, 171

Mei, F., and An, M. (2010). Lithospheric Structure of the Chinese Mainland Determined from Joint Inversion of Regional and Teleseismic Rayleigh-Wave Group Velocities. *J. Geophys. Res.* 115, B06317. doi:10.1029/2008JB005787

Milne, G. A., Davis, J. L., and Mitrovica, J. X. (2001). Space-geodetic Constraints on Glacial Isostatic Adjustment in Fennoscandia. *Science* 291 (5512), 2381–2385. doi:10.1126/science.1057022

Mitrovica, J. X., and Forte, A. M. (2004). A New Inference of Mantle Viscosity Based upon Joint Inversion of Convection and Glacial Isostatic Adjustment Data. *Earth Planet. Sci. Lett.* 225 (1), 177–189. doi:10.1016/j.epsl.2004.06.005

Nissen, S. S., Hayes, D. E., and Bochu, Y. (1995). Gravity, Heat Flow, and Seismic Constraints on the Process of Crustal Extension: Northern Margin of the South China Sea. *J. Geophys. Research:Solid Earth* 100 (B11), 22447–22483. doi:10.1029/95jb01868

Nolet, G., and Zielhuis, A. (1994). Low S Velocities under the Tornquist-Teisseyre Zone: Evidence for Water Injection into the Transition Zone by Subduction. *J. Geophys. Res.* 99, 15813–15820. doi:10.1029/94jb00083

Paulson, A., Zhong, S., and Wahr, J. (2010). Inference of Mantle Viscosity from GRACE and Relative Sea Level Data. *Geophys. J. Int.* 171 (2), 497

Qian, Y. (1992). Survey and the Results of Geothermal Flow in the Northern Part of South China Sea. *Mar. Geology. Quat. Geology.* 2 (4), 102

Ren, J., and Li, S. (2000). Expansion Process and Dynamic Background of the Western Pacific Marginal Basin. *Earth Sci. Front.* 7 (3), 203

Runcorn, S. K. (1967). Flow in the Mantle Inferred from Low Degree Harmonics of the Geopotential. *J. Geophys. Res.* 72, 375

Runcorn, S. K. (1964). Satellite Gravity Measurements and a Laminar Viscous Flow Model of the Earth's Mantle. *J. Geophys. Res.* 69, 4389–4394. doi:10.1029/jz069i020p04389

Shi, X., Qiu, X., and Xia, K. (2003). Characteristics of Surface Heat Flow in the South China Sea. *J. Asian Earth Sci.* 22 (3), 265–277. doi:10.1016/s1367-9120(03)00059-2

Sobolev, S. V., Zeyen, H., and Stoll, G. (1996). Upper Mantle Temperatures from Teleseismic Tomography of French Massif Central Including Effects of Composition, Mineral Reactions, Anharmonicity, Anelasticity and Partial Melt. *Earth Planet. Sci. Lett.* 139, 147–163. doi:10.1016/0012-821x(95)00238-8

Steinberger, B., and Arthur, R. C. (2006). Models of Large-Scale Viscous Flow in the Earth's Mantle with Constraints from Mineral Physics and Surface Observations. *Geophys. J. Int.* 167 (4), 1461–1481. doi:10.1111/j.1365-246x.2006.03131.x

Sun, Z., Zhong, Zg., Zhou, D., Xia, B., Qiu, X., Zeng, Z., et al. (2006). Study on Developmental Mechanism of South China Sea: Evidence from Similar Simulations. *Sci. China (D)* 36 (09), 797

Tapponnier, P., Peltzer, G., and Armijo, R. (1986). On the Mechanics of the Collision between India and Asia. *Geol. Soc. Lond. Spec. Publications* 19 (1), 113–157. doi:10.1144/gsl.sp.1986.019.01.07

Turcotte, D. (2014). *Geodynamics*. Cambridge: Cambridge University Press.

Wang, P., Huang, C., Lin, J., Zhimin, J., Sun, Z., and Zhao, M. (2019). The south china Sea Is Not a mini-atlantic: Plate-Edge Rifting vs Intra-plate Rifting. *Natl. Sci. Rev.* 6 (05), 54–65. doi:10.1093/nsr/nwz135

Wu, J., and Liu, Y. (1992). A Study on the Relation between Satellite Gravity Anomalies, Mantle Convection Stress and Modern Plates Movement. *Acta Geophysica Sinica* 35 (5), 604

Xing, X., Lu, J., and Luo, X. (2005). The Marine Heat Flow Survey and the Result Discussion in the Northern Part of South China Sea. *Prog. Geophys.* 20 (2), 562

Xing, X., Yao, Y., and Deng, P. (2018). The Characteristics and Analysis of Heat Flow in the Southwest Sub-basin of South China Sea. *Chin. J. Geophys.* 61 (7), 2915

Xu, Z., Wang, Q., Li, Z., Li, H., Cai, Z., Liang, F., et al. (2016). Indo-Asian Collision: Tectonic Transition from Compression to Strike Slip. *Acta Geologica Sinica* 90 (01), 1

Yao, B., Wan, L., and Wu, N. (2004). Cenozoic Plate Tectonic Activities in the Great South China Sea Area. *Geology. China* 31 (2), 113–122.

Yao, B., Zeng, W., and Hayes, D. E. (1994). *The Geological Memoir of South China Sea Surveyed Jointly by China and USA*. Wuhan: China University of Geosciences Press, 140

Yao, Y., Yang, C., Li, X., Ren, J., Jiang, T., Dianjun, X., et al. (2013). The Seismic Reflection Characteristics and Tectonic Significance of the Tectonic Revolutionary Surface of Mid-Miocene (T3 seismic interface) in the Southern South China Sea8 Zhang Jian, Dong Miao, Wu Shiguo, et al. 2017. Lithosphere Thermal-rheological Structure and Geodynamic Evolution Model of the Nansha Trough Basin, South China Sea. *Chin. J. GeophysicsEarth Sci. Front.* 5624 (43), 127427

Zhan, W., Liu, Y., and Zhong, Ji. (1995). The Preliminary Analysis of Neotectonic Movement and Dynamic Evolution in the Southern DIWA Region of South China Sea. *Geotectonica Et Metallogenia* 19 (2), 95

Zhang, J., Song, H., and Li, J. (2005). Thermal Modeling of the Tectonic Evolution of the Southwest Sub-basin in the South China Sea. *Chin. J. Geophys.* 48 (6), 1357

Zhang, J., and Wang, Jg. (2000). The Deep Thermal Characteristic of Continental Margin of the Northern South China Sea. *Chin. Sci. Bull.* 145 (10), 1095–1100. doi:10.1007/bf02898994

Zhao, D., and Ohtani, E. (2009). Deep Slab Subduction and Dehydration and Their Geodynamic Consequences: Evidence from Seismology and Mineral Physics. *Gondwana Res.* 16, 401–413. doi:10.1016/j.gr.2009.01.005

Conflict of Interest: The authors declare that the research was conducted in the absence of any commercial or financial relationships that could be construed as a potential conflict of interest.

The reviewer MZ declared a shared affiliation, with no collaboration, with one of the authors, HL, to the handling editor at the time of the review.

Publisher's Note: All claims expressed in this article are solely those of the authors and do not necessarily represent those of their affiliated organizations or those of the publisher, the editors, and the reviewers. Any product that may be evaluated in this article or claim that may be made by its manufacturer is not guaranteed or endorsed by the publisher.

frontiers | Frontiers in Earth Science

ORIGINAL RESEARCH
published: 27 May 2022
doi: 10.3389/feart.2022.836168

Occurrence of Local Tsunamis Along the Eastern Coast of the Korean Peninsula Based on Numerical Modeling of Historical Earthquakes

*Taemin Ha[1], Jae-Seon Yoon[2], Jai Bok Kyung[3], Seok-Hoon Yoon[4], Dong-Woo Lee[1] and Kwang-Hee Kim[5]**

[1]Department of Civil Engineering, Kangwon National University, Samcheok, South Korea, [2]Rural Research Institute, Korea Rural Community Corporation, Ansan, South Korea, [3]Department of Earth Science Education, Korea National University of Education, Cheongju, South Korea, [4]Department of Earth and Marine Sciences, Jeju National University, Jeju, South Korea, [5]Department of Geological Sciences, Pusan National University, Busan, South Korea

Korean historical literature records a major offshore earthquake with an associated tsunami in the East Sea of Korea in 1681. The event also generated strong ground motion and landslides over the Korean Peninsula. This study examined the occurrence and characteristics of the reported tsunami along the eastern coast of the peninsula using numerical modeling of tsunami propagation from submarine faults identified in a recently compiled marine fault map. Results from some scenarios indicated runup heights in good agreement with descriptions in historical records. We also examined the time required for tsunamis to travel from the causative faults to vulnerable areas along the eastern coast under various scenarios. Our results successfully hindcast the occurrence and effects of local tsunamis in the historical literature and have important implications for assessing tsunami hazard and risk for coastal areas of the Korean Peninsula.

Keywords: historic tsunami, numerical model, fault parameter, local tsunami, runup height

OPEN ACCESS

Edited by:
Gang Rao,
Southwest Petroleum University, China

Reviewed by:
Kenji Satake,
The University of Tokyo, Japan
Jörn Behrens,
Universität Hamburg, Germany

****Correspondence:***
Kwang-Hee Kim
kwanghee@pusan.ac.kr

Specialty section:
This article was submitted to Geohazards and Georisks, a section of the journal Frontiers in Earth Science

Received: *16 December 2021*
Accepted: *09 May 2022*
Published: *27 May 2022*

Citation:
Ha T, Yoon J-S, Kyung JB, Yoon S-H, Lee D-W and Kim K-H (2022) Occurrence of Local Tsunamis Along the Eastern Coast of the Korean Peninsula Based on Numerical Modeling of Historical Earthquakes. Front. Earth Sci. 10:836168. doi: 10.3389/feart.2022.836168

1 INTRODUCTION

The duration of an earthquake spans only a few seconds or minutes, but the direct or indirect human, material, economic, and social damage caused by earthquakes can be significant. However, when accompanied by a tsunami, the scope and magnitude of damage may increase dramatically, posing a considerable threat to human lives and infrastructure. Large earthquakes occur mostly at plate boundaries and cause significant casualties and infrastructural/property damage. However, large destructive earthquakes also occur inside plates, as observed during the 1976 Tangshan, China, earthquake (e.g., Butler et al., 1979) and the 1811–1812 New Madrid earthquakes in the central United States (e.g., Johnston and Schweig, 1996).

Historical earthquakes and tsunamis in Korea are well documented in various historical records. For example, two major earthquakes and tsunamis, which occurred in 1643 and 1681 in the East Sea of Korea, are recorded in the Annals of the Joseon Dynasty (Kyung et al., 2010). Earthquakes in the instrumental observation period since 1905 in Korea have occurred sporadically over a wide area both on land and offshore (KMA, 2022). Recent earthquakes with a local magnitude (M_L) of 5.8 in Gyeongju and M_L 5.4 in Pohang caused substantial damage in the epicentral areas (Kim et al., 2016; Ministry of Public Safety and Security, 2017; Kim et al., 2018a, b; Ministry of the Interior and Safety, 2018). In addition, although not damaging, large earthquakes with a magnitude of >5 have occurred

frequently in the eastern offshore area of the Korean Peninsula, including two M_S (surface wave magnitude) 6.0 earthquakes in 1963, an M_L 5.2 earthquake in 1999, an M_L 5.2 earthquake in 2004, and most recently an M_L 5.0 earthquake in 2016 (ISC, 2022; KMA, 2022). Consequently, an understanding of earthquakes, faults and tsunamis is considered paramount in better understanding the nature of coastal hazards in Korea (Chiu and Kim, 2004; Lee and Yang, 2006; Kyung et al., 2010).

Frequent large earthquakes are presumed to occur by the reactivation of submarine faults that formed during the opening of the East Sea during the late Oligocene to early Miocene. It is also suspected that faults potentially hosting large earthquakes exist in regions where the transition from oceanic to continental crust occurs (Kim, 1982). Although it is necessary to monitor offshore earthquakes in the East Sea and characterize them to understand their hazards and risks, this monitoring is challenging compared with continental earthquakes.

This study examined the records of earthquakes and tsunamis in the East Sea of Korea that are recorded in historical literature. These historical earthquakes are presumed to have been centered in the eastern offshore of the Korean Peninsula and generated local tsunamis without widespread triggering. We identified 15 potential faults after carefully reviewing historical records of earthquakes, as well as modern marine seismic information and generated 15 scenarios (corresponding to the 15 identified faults) for numerical tsunami modeling. We then compare the results with tsunami records in the historical literature and discuss the potential for and risks of local tsunami occurrences in the East Sea.

2 DATA AND METHODOLOGY

Historical earthquake reports, including for more than 470 events with a modified Mercalli intensity (MMI) of greater than or equal to V, are available for the period between AD 2 and AD 1904 (e.g., Lee and Yang, 2006; Kyung et al., 2010). Reports of a series of earthquakes in June 1681 are particularly interesting, as the series shows a typical foreshock–mainshock–aftershock sequence. The historical records also mention a small-scale tsunami. Felt and damage reports were made throughout the Korean Peninsula. To gain an appreciation for the type of information available concerning the 1681 earthquake and tsunami, consider the following descriptions contained in the Diaries of the Royal Secretariat:

> Residences were shaken, and windows were rattled. People ran in fear, and trees were also shaken. ... Three aftershocks occurred in 1 day. ... Stone fences collapsed, and roof tiles were displaced. Some rocks were split by the force. ... The coastal line changed as if the tide had gone out. It was an extraordinary event.

The historical events are usually reported in historical literature but their descriptions are only anecdotal and qualitative in nature, although are sufficiently clear to be interpreted in terms of the occurrence and behavior of a tsunami:

> There were earthquakes reported in several areas of Gangwon province followed by thunderous sound, and a strange collapse of the rocky cliff in Doota Mountain was witnessed. Broken boulders up to 30 m were observed in the sea, and the coast shaped as a receding tide, but where water was full on a regular day was around 100 steps or 5–60 steps exposed at several beaches located in the Samcheok area.

When a large tsunami approaches the coast, a strong backwash is commonly observed on the coast because of the conservation of mass. It is thought that the historical literature quoted above described the strong backwash of a tsunami. Therefore, in this study, the local tsunami event that occurred in 1681 was selected for study, as the event recorded the maximum intensity reported in historical documents and contained the most detailed description of a tsunami-like phenomenon in the Diaries of the Royal Secretariat. The occurrence of this event was validated (see **Section 3.2**). **Figure 1** shows the approximate location of the 1681 earthquake epicenter (red star) and areas of felt reports (red dots), as reported by the Diaries of the Royal Secretariat.

2.1 Fault Scenarios

For studies of earthquakes and tsunamis, the timing, location, and size of the event are essential data. In the recent compilation of Kyung et al. (2010), epicenters, magnitudes, and intensities were estimated on the basis of descriptions and felt areas in the historical literature. Those authors estimated the magnitude of the largest event in the sequence as a local magnitude 6.7 with MMI = VIII–IX, with the epicenter located offshore between Yangyang and Samcheok (37.9°N, 120.1°E).

We reviewed the available marine geological fault databases and selected significant faults to assess the potential for tsunamis in the East Sea. During the review, we considered instrumental records of seismicity available from the Korea Meteorological Administration (KMA, 2022), the International Seismological Centre (ISC, 2022), and published papers (e.g., Park and Mori, 2005; Kim et al., 2016; Han et al., 2019; Park et al., 2020); the high-resolution bathymetry map published by the Korea Hydrographic and Oceanographic Agency (KIGAM, 2016); an inventory of submarine landslides compiled by Yoon et al. (2015); and faults identified from marine seismic data (Schulter and Chun, 1974; KIGAM, 2010). We also reviewed sedimentological and stratigraphic studies to help estimate recent fault activity (Yoon, 1994; Yoo et al., 2019).

Locations of faults and corresponding fault parameters generating the maximum initial surface displacement were identified from the integrated database of the recently revised geological structural map of the area around the East Sea continental margin (KIGAM, 2016). Then, tsunami scenarios were improved by changing the fault parameters (**Figure 2**), including introduced earthquake magnitude and fault

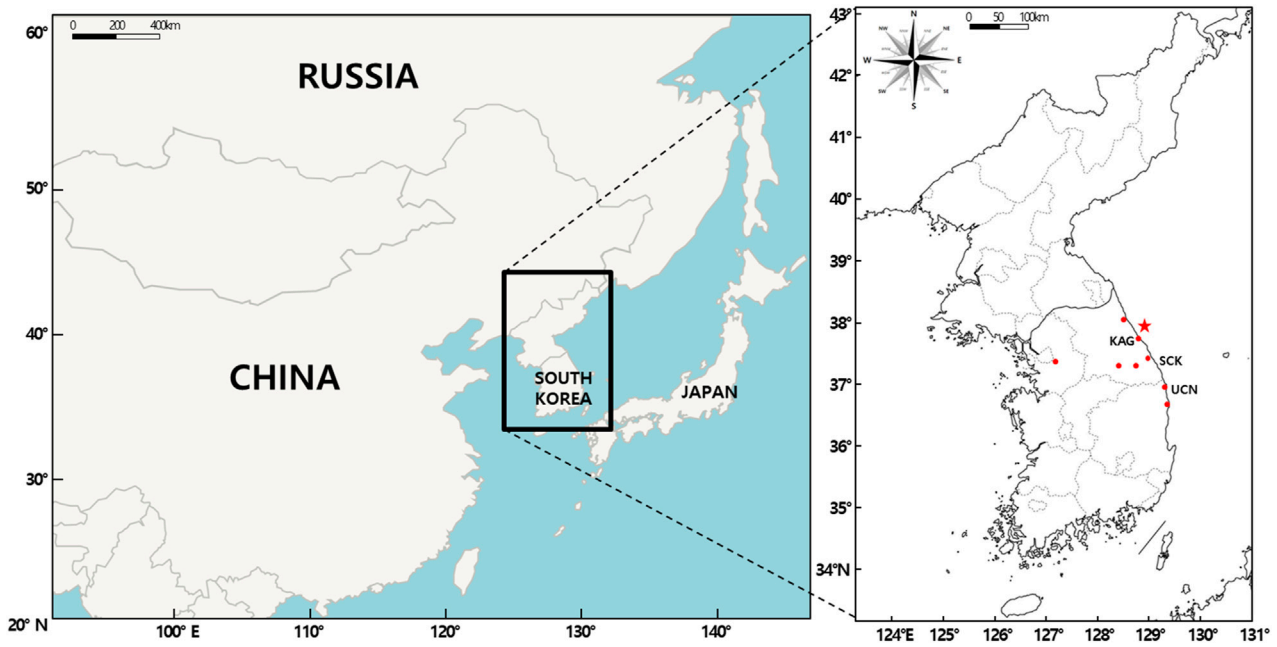

FIGURE 1 | Location maps showing the Korean Peninsula and the location of the epicenter (red star) of the mainshock of the 1681 earthquake in the East Sea, which caused a tsunami on the eastern coast of the peninsula.

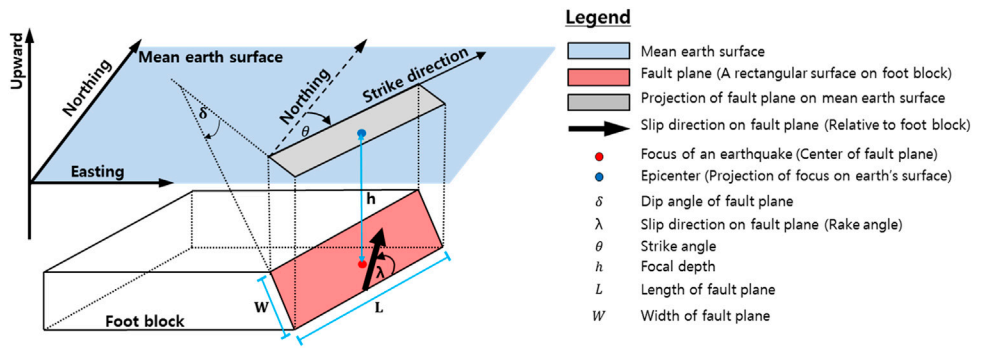

FIGURE 2 | Sketch of a fault plane and definitions of fault parameters used in this study (from Wang, 2009).

displacement. In addition, tsunami impact was examined *via* the formation of the initial sea surface displacement according to the fault-parameter scenario and numerical modeling of tsunamis.

Our review of recently compiled marine fault databases and related studies identified 15 faults potentially responsible for major earthquakes or discontinuities in marine seismic data in the eastern offshore of the Korean Peninsula (**Figure 3**). For those faults, we assigned fault parameters for tsunami scenarios. Each fault scenario consisted of earthquake magnitude and vertical displacements, estimated on the basis of empirical equations (**Figure 2** and **Table 1**; Matsuda, 1975; Bonilla et al., 1984; Wells and Coppersmith, 1994; Anderson, 1996; Vakov, 1996). Although there are large uncertainties, we assumed a fault dip of 90°.

2.2 Calculation of the Initial Sea Surface Displacement Based on Fault-Parameter Scenarios

In this study, the COMCOT v1.7 (Wang, 2009) was used for tsunami modeling and the Okada model (Okada, 1985) included in the COMCOT v1.7 was applied to generate the initial sea surface displacement. The Okada model has been utilized in tsunami-related research fields for calculating the initial sea surface displacement of tsunamis generated by submarine earthquakes. This model can be applied to a variety of fields, as it is fully validated in quantitative and qualitative aspects (Son et al., 2011; Wang and Liu, 2011; Lynett P. J. et al., 2012; Wijetunge, 2012; Chai et al., 2014; Ha and Cho, 2015; Kim K.

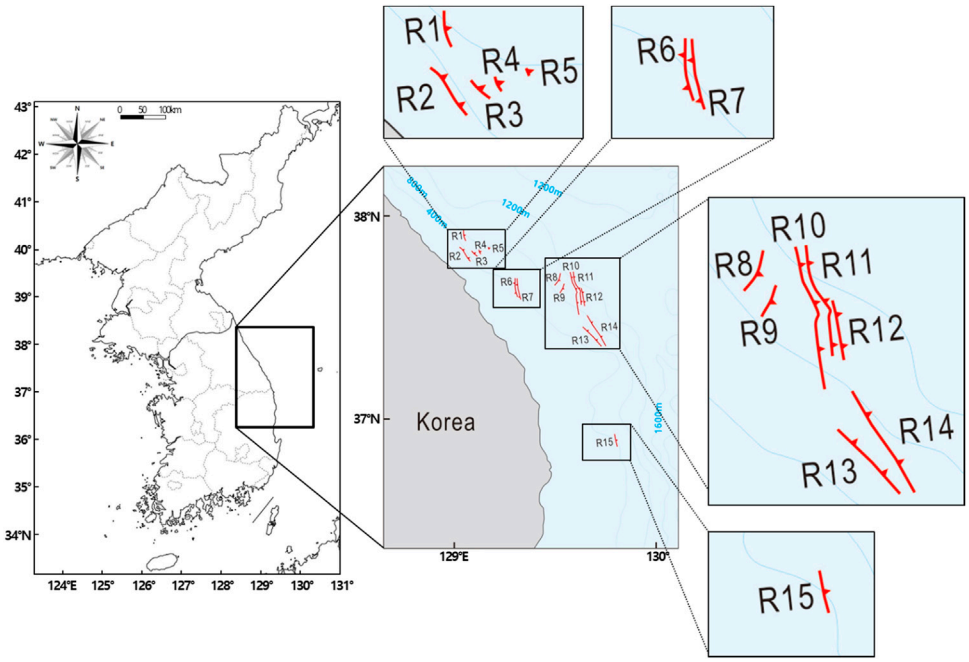

FIGURE 3 | Major East Sea fault zones identified from the fault/seismic databases described in **Section 2.1** Scenarios R1–R15 refer to tsunamis generated by earthquakes caused by rupture on each of the 15 different fault zones.

H. et al., 2018; Lee E. et al., 2019). In this study, the initial sea surface displacement were generated according to each fault-parameter scenario mentioned above in **Section 2.1**. As the sizes of the initial sea surface displacement calculated for scenarios R03 to R05 and R08 to R09 were very small and the maximum wave heights less than 0.1 m, those five scenarios were excluded from the analysis of tsunami impact. Scenario R01 showed a maximum wave height of >0.1 m, but the location of the generated tsunami was similar to the location of occurrence of scenario R02, resulting in the additional exclusion of scenario R01 from the analysis. As a result, the tsunamis of nine scenarios were generated, for which the initial sea surface displacement are illustrated in **Figure 4**.

The initial sea surface displacement manifested differently according to variation in fault parameters. The major propagation directions of the tsunami were varied according to the fault plane strike angle. The tsunami source area was presumed to be proportional to fault length and width. In general, the maximum runup height of tsunamis is the most critical variable in tsunami hazard assessments on the coast. Of the fault parameters, the maximum wave height calculated through tsunami modeling is quantitatively most closely related to the maximum displacement of the initial sea surface displacement. The maximum displacement of the initial tsunami wave in this study was calculated according to the extent of fault plane displacement and the upper fault plane depth, for which an initial tsunami wave with less than 0.5 m maximum displacement was generated in most scenarios. However, a large tsunami with a maximum displacement of >0.5 m was generated in a few scenarios, such as R10, R11, and R14, considered as presenting high tsunami potentials and related risks. In particular, large tsunamis that exceeded a maximum displacement of 1.5 m were generated in some scenarios. The maximum value was adopted for the dip angle of the fault plane so that the maximum displacement would be generated. When the absolute size of the tsunami calculated according to the maximum value decreased, the initial sea surface displacement of the tsunami was recalculated by appropriately combining the middle and lowest values so that the maximum value was yielded. Quantitative verification was difficult for the generated initial sea surface displacement because no previous data were observed for comparison. Therefore, the initial tsunami wave deformation according to variation in fault parameters was analyzed qualitatively. It was determined that the initial sea surface displacement changed fairly consistently with respect to fault parameter modifications, despite the seafloor topography and water depth of the fault zones being unique for all examined regions.

2.3 Configuration of Numerical Modeling and the High-Resolution Grid System of the East Sea

A high-resolution digital bathymetric model of the East Sea for numerical modeling of tsunami propagation was generated using numerical topographic data obtained from the KMA (**Figure 5**) so that the digital bathymetric model can be linked with the existing KMA database (Park et al., 2020). Thus, the maximum wave heights of tsunamis calculated using the scenarios can be added to the national disaster prevention plan for tsunami hazard

TABLE 1 | Fault parameter scenarios corresponding to the major East Sea fault zones. The definitions of these parameters are referred to **Figure 2**.

Fault name	Seismic sections	Longitude (°E)	Latitude (°N)	H (km)	θ (°)	λ (°)	L (km)	W (km) CombA	W (km) CombB	D (km) CombA	D (km) CombB	δ (°)			
												Top	Middle	Bottom	Mean
R1	02GH-08, 09	129.046 129.057	37.931 37.878	1.3	355.0	90.0	5.71	2.8	2.85	0.285	0.216	74.6 (165–826 m)	55.6 (826–1487 m)	40.1 (1487–2148 m)	56.8
R2	00AD-8, 9	129.025 129.080	37.847 37.769	0.5	330.0	90.0	9.30	2.9	4.65	0.530	0.400	58.6 (57–622 m)	42.8 (622–1187 m)	30.7 (1186–1752 m)	44.0
R3	00AD-8, 02GH-07A	129.085 129.114	37.829 37.802	0.8	320.0	90.0	4.10	3.6	2.05	0.205	0.150	44.6 (74–652 m)	26.0 (652–1230 m)	18.9 (1230–1808 m)	29.8
R4	00AD-8, 02GH-07A	129.121 129.131	37.834 37.812	0.9	343.0	90.0	2.50	1.6	1.25	0.130	0.090	83.8 (73–602 m)	57.3 (602–1131 m)	37.5 (1131–1660 m)	59.5
R5	00AD-8, 02GH-07A	129.168 129.172	37.846 37.835	1.3	345.0	90.0	1.28	1.7	0.64	0.080	0.048	76.3 (200–623 m)	49.7 (623–1046 m)	28.5 (1046–1469 m)	51.5
R6	00AD-5, 11, 02GH-03, 04	129.301 129.313	37.694 37.601	0.6	358.0	90.0	9.78	2.5	4.89	0.575	0.432	80.9 (56–926 m)	63.5 (926–1796 m)	47.8 (1796–2666 m)	64.1
R7	00AD-5, 02GH-03, 04	129.311 129.329	37.693 37.589	0.8	356.0	90.0	11.11	2.3	5.56	0.715	0.528	77.5 (32–827 m)	56.7 (827–1622 m)	46.6 (1622–2417 m)	60.3
R8	02GH-03, 04, 14	129.526 129.497	37.719 37.659	1.4	33.0	90.0	6.95	2.5	3.48	0.355	0.272	74.9 (39–559 m)	39.8 (559–1079 m)	22.2 (1079–1599 m)	45.6
R9	02GH-03, 14	129.545 129.523	37.667 37.620	1.3	31.0	90.0	5.38	2.4	2.69	0.265	0.202	66.4 (31–587 m)	34.5 (587–1143 m)	23.1 (1143–1699 m)	41.3
R10	00AD-02, 03, 04, 02GH-01, 02, 03, 04	129.573 129.617	37.724 37.513	1.3	355.0	90.0	22.57	2.6	11.28	3.025	1.856	57.9 (94–683 m)	34.2 (683–1272 m)	20.8 (1272–1861 m)	37.6
R11	00AD-03, 04, 02GH-01, 02, 03, 04	129.589 129.629	37.727 37.563	1.5	353.0	90.0	17.67	1.9	8.83	1.730	1.146	58.2 (51–499 m)	43.7 (499–947 m)	29.4 (947–1395 m)	43.8
R12	00AD-03, 02GH-01, 02	129.629 129.645	37.635 37.557	1.4	356.0	90.0	9.42	1.6	4.71	0.540	0.410	64.0 (94–542 m)	43.2 (542–990 m)	31.8 (990–1438 m)	46.3
R13	01GH-11, 12, 13	129.636 129.729	37.454 37.359	0.9	323.0	90.0	13.90	0.7	6.95	1.045	0.740	71.0 (134–400 m)	36.7 (400–666 m)	21.8 (666–932 m)	43.2
R14	01GH-11, 12, 13, 14	129.658 129.740	37.511 37.361	1.1	335.0	90.0	18.45	1.2	9.23	1.880	1.230	54.1 (64–335 m)	31.9 (335–606 m)	22.7 (606–877 m)	36.2
R15	05GH-36, 38, 01GH-02	129.794 129.808	36.927 36.864	0.9	354.0	90.0	11.28	0.8	5.64	0.740	0.546	88.1 (61–278 m)	86.1 (278–495 m)	79.3 (495–712 m)	84.5

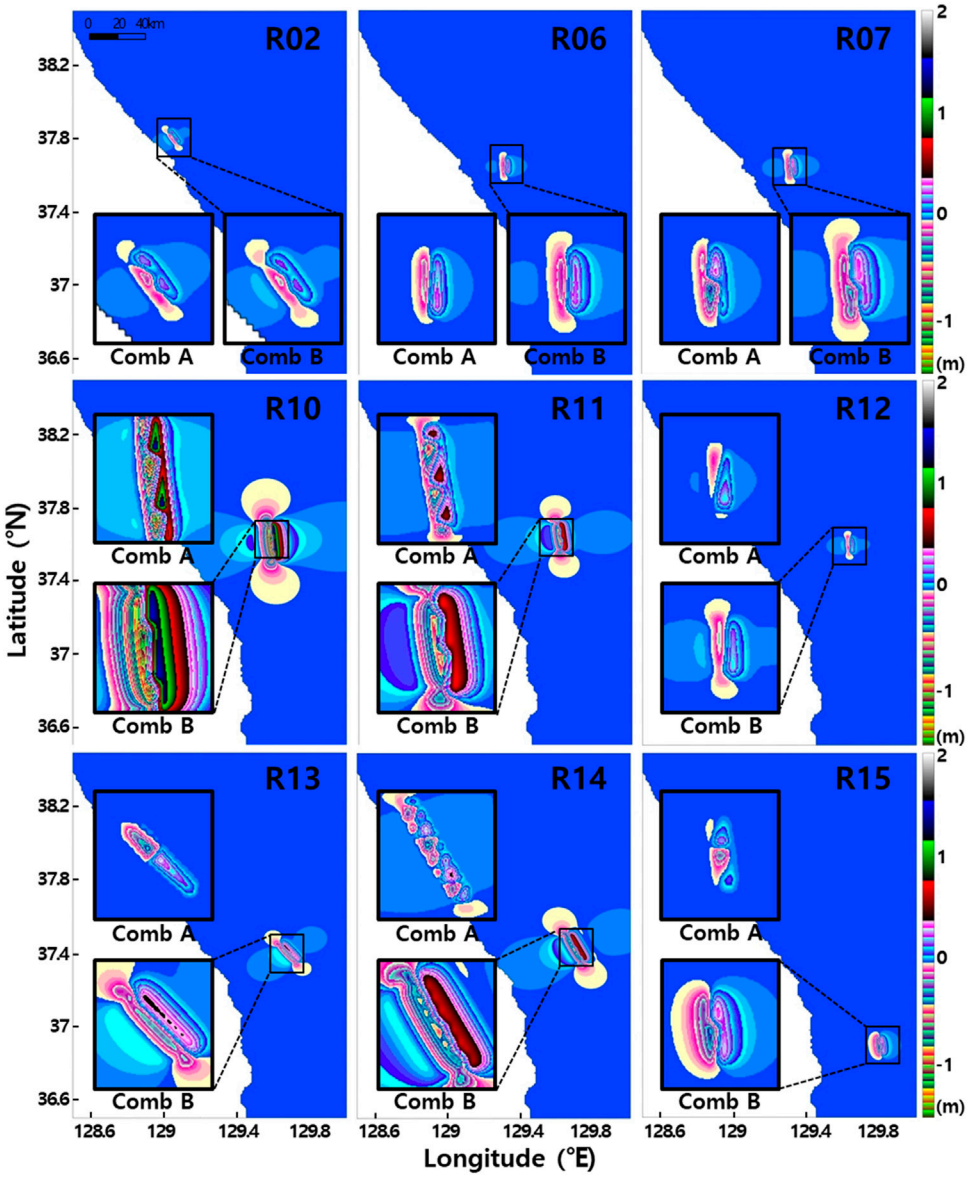

FIGURE 4 | The initial sea surface displacement according to variations in fault parameters (see **Section 2.2** for details). "Comb" is "combination" (see **Section 3.1** for details). "R" refers to scenario (fault zone) number.

in conjunction with the existing tsunami database (Lee et al., 2019b; Park et al., 2020). This wave-height information could also be used to forecast a possible future tsunami if used together with existing data. This study aimed to assess the potential of occurrence of local tsunamis in the East Sea. As existing observational data were not based on accurate recordings from on-land areas, the impact of possible local tsunamis was estimated by calculating the tsunami runup height at the coast using Green's law rather than computing landward inundation in the model directly. Therefore, numerical modeling of tsunami inundation for land areas was not performed in the present study. However, the tsunami wave height increases owing to the shoaling effect caused by the decrease of water depth at the coast. In such a case, the maximum wave height on the coast can be affected with an increase in the nonlinearity of waves. Therefore, a tsunami inundation model (COMCOT v1.7), which employs a nonlinear shallow-water equation, was applied to calculate the maximum tsunami elevation in the numerical domain near the coast to consider the above-mentioned phenomena.

For deep-marine areas, a tsunami propagation model that employs a linear shallow-water equation was used to simulate tsunami propagation since the nonlinearity of a tsunami wave can be neglected in deep water. In general, the wavelength of a tsunami is usually very long and a tsunami wave can be modeled using the shallow water wave theory even in deep

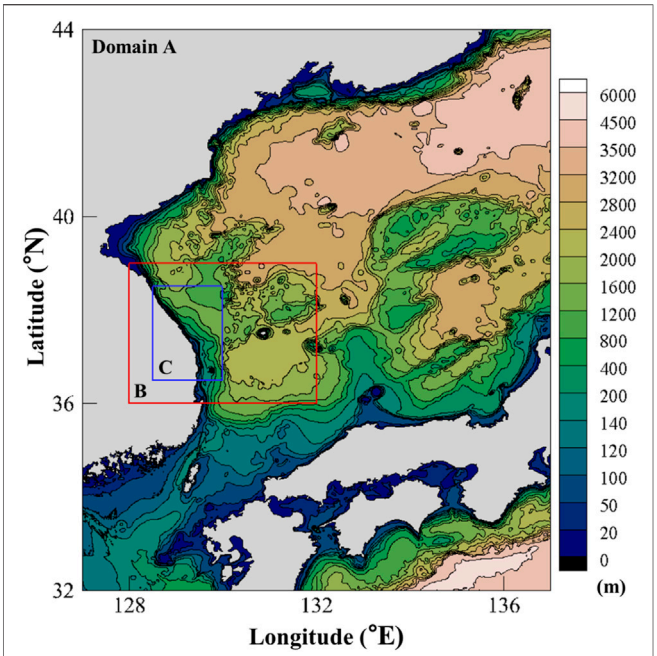

FIGURE 5 | High-resolution grid system of the East Sea and bathymetric data used for numerical modeling.

water. A grid system for tsunami modeling was built by establishing a total of three numerical domains (grid size: $\Delta x = \Delta y = 0.01° - 0.00111°$) within the geographic coordinate system and dividing them into three stages from A to C using the grid-nesting technique. We introduced three different bathymetric data sources to generate gridded data systems: the gridded data ($\Delta x = \Delta y = 0.01°$) held by the KMA for tsunami modeling, the 2021 15 arc-second gridded bathymetric data of GEBCO Compilation Group (2021), and bathymetric data produced by KHOA specifically for the operation of marine numerical models with ~150 m horizontal intervals (Yoo et al., 2019). After careful manipulation to match the datum level, the three bathymetric data sources were implemented to establish the high-resolution grid system for tsunami modeling using the Generic Mapping Tools (GMT; Wessel et al., 1998) program. A description of the grid system is presented in **Table 2**.

3 ESTIMATION OF TSUNAMI WAVE HEIGHT AND VERIFICATION OF HISTORICAL TSUNAMI RECORDS ON THE EASTERN COAST OF THE KOREAN PENINSULA

3.1 Estimation of Tsunami Maximum Wave Height Using Local Tsunami Scenarios

Numerical modeling of tsunami propagation was performed to calculate the maximum wave height of tsunamis based on local tsunami scenarios generated for the eastern coast of the Korean Peninsula. First, we generated 15 virtual local tsunamis following the scenarios described in **Section 2.1** and simulated tsunami propagation along the eastern coast of the Korean Peninsula. The 6 scenarios described in **Section 2.2** were then excluded after thorough investigation of the numerical results since the generated tsunamis barely affected the eastern coast of the Korean Peninsula. The numerical results varied depending on different combinations (**Table 3**) of the empirical equations adopted in the modeling. Of the various combinations, the two combinations with the highest potential of realistic occurrence considering various scenarios of historical tsunami events and the maximum tsunami wave height were selected by assessing the computed tsunami wave heights. These two combinations are as follows:

▷ Combination A: the mean value of calculated displacement from the empirical equations proposed by Matsuda (1975) and Wells & Coppersmith (1994) + the added displacement calculated from the value of the maximum slip angle.
▷ Combination B: the mean displacement calculated from the five different empirical equations + the added displacement calculated from the upward adjustment following the relationship between fault width and length [W (km) = 0.5 L (km)] + the added displacement calculated from the value of the mean slip angle.

Figures 6, **7** present the numerical results of the highest surface elevation of the tsunamis generated according to each scenario constructed with the two combinations above and their propagation in the East Sea. These two figures display the maximum wave heights of proposed local tsunamis, whereas **Figures 8**, **9** show the spatial distribution of the lowest surface elevation of the tsunamis. Overall, the maximum wave heights of the tsunamis were distributed over larger areas for the scenarios using Combination B in comparison with those using Combination A. In most scenarios, the tsunami source area were parallel to the eastern coast of the Korean Peninsula, and the maximum and minimum values were developed perpendicular to the coast. The wave heights of the tsunamis gradually increased as the tsunamis propagated toward the coast mostly because of the shoaling effect, and the maximum wave heights were observed near the coast for the scenarios using both combinations. The absolute value of the highest surface elevation was more than two times higher than that of the lowest surface elevation.

Figure 10 shows the maximum wave heights of the tsunamis generated on the eastern coast of the Korean Peninsula. As some scenarios generated relatively low wave heights less than 0.1 m and were similar in the location of occurrence compared with other fault parameter scenarios as described above in **Section 2.2**,

TABLE 2 | Description of the East Sea high-resolution grid system used in the present study.

Domain	Grid system	Grid size (°)	Time step (s)
A	1,001 × 1,201	0.01000	3.00000
B	1,201 × 1,901	0.00333	1.00000
C	1,351 × 1,801	0.00111	0.33333

TABLE 3 | Estimation of the maximum displacement of the fault plane (m) calculated according to various combinations of empirical equations (R: reverse type only, All: reverse type + strike-slip type + normal type).

Fault name	Magnitude (Mean)	Matsuda (1975)	Slemmons (1988, R)	Bonilla et al. (1984, All)	Wells and Coppersmith (1994, R)	Wells and Coppersmith (1994, All)	Maximum displacement (mean)
R1	6.10	0.46	0.29	0.06	0.11	0.16	0.216
R2	6.35	0.65	0.46	0.13	0.41	0.35	0.400
R3	5.93	0.36	0.22	0.03	0.05	0.09	0.150
R4	5.67	0.25	0.14	0.01	0.01	0.04	0.090
R5	5.32	0.16	0.07	0.00	0.00	0.01	0.048
R6	6.38	0.67	0.48	0.15	0.48	0.38	0.432
R7	6.45	0.74	0.55	0.19	0.69	0.47	0.528
R8	6.20	0.52	0.35	0.08	0.19	0.22	0.272
R9	6.07	0.44	0.28	0.05	0.09	0.15	0.202
R10	6.82	1.24	1.05	0.68	4.81	1.50	1.856
R11	6.69	1.03	0.83	0.44	2.43	1.00	1.146
R12	6.36	0.65	0.47	0.14	0.43	0.36	0.410
R13	6.56	0.86	0.66	0.28	1.23	0.67	0.740
R14	6.71	1.06	0.86	0.47	2.70	1.06	1.230
R15	6.46	0.75	0.56	0.20	0.73	0.49	0.546

6 of the 15 scenarios were excluded from the comparison of maximum wave heights of the tsunamis. A higher maximum wave height was observed for Combination B relative to Combination A, noting that the maximum fault displacement was used in Combination A, whereas the mean value was used in Combination B. It was thought that despite using the mean fault displacement in Combination B, the tsunami energy was higher than for the maximum fault displacement owing to the greater size of the fault zone used for this combination and therefore resulted in higher wave heights of tsunamis on the coast. Maximum wave heights of <0.1 m were calculated for fault parameter scenarios with relatively small fault zone sizes, indicating that the impacts of these tsunamis on the coast were insubstantial for these scenarios. In contrast, the maximum wave heights increased as the size of the fault zone increased, and the most significant impact across the studied coastal area was observed for the R10 scenario, in which the size of the fault zone was the largest of the 15 scenarios.

3.2 Comparison and Verification of Tsunami Records in the Diaries of the Royal Secretariat

Slopes of the major beaches located on the studied part of the eastern coast of the Korean Peninsula, such as Gangneung and Samcheok beaches, are quite shallow less than 0.05. The natural beach widths of those areas are approximately 100–200 m, whereas their highest points are located 5–10 m above mean sea level. The Diaries of the Royal Secretariat described the tsunami as "shaped as a receding tide, but where water was full on a regular day was around 100 steps or 5–60 steps exposed." Here, 100 steps converted to the SI unit system measures about 150 m, which is similar to natural beach widths along the studied coastline. The phenomenon described in the historical text is considered to be similar to a tsunami rundown, in which coastal waters recede and then amplify the wave height of a tsunami that approached nearshore before the tsunami runup. The runup phenomenon following the rundown exhibits similar wave heights to those of numerical results, with runup heights of 5–10 m along the beach slope. Numerical modeling for the tsunami scenarios suggests that a maximum runup height occurrence of 5–10 m in the location described in the Diaries of the Royal Secretariat is plausible (**Figures 10**, **11**). Furthermore, the damage caused by a local tsunami as described in historical tsunami records is also plausible considering the maximum runup heights as possible. Although the verification is qualitative in nature, the numerical modeling results based on tsunami scenarios in combination with tsunami records in the Diaries of the Royal Secretariat indicate that there is a risk of local tsunamis on the eastern coastline of the Korean Peninsula.

4 POTENTIAL FOR LOCAL TSUNAMI GENERATION IN THE EAST SEA

4.1 Tsunami Propagation in the East Sea and Arrival Time to the Coastline From the Source

The initial sea surface displacement were modeled according to each tsunami scenario, following which tsunami propagation through the East Sea was modeled to calculate the propagation distance and arrival time of the tsunami (**Figure 12**).

As seen in **Figure 12**, tsunamis are generated at a distance of 10–50 km from the eastern coast of the Korean Peninsula and reach the East Sea coast between 5 and 20 min after initiation. The current tsunami forecasting system in South Korea is capable of handling local tsunamis around the Korean Peninsula based on the tsunami elevation database established by KMA. Although local tsunamis are routinely computed in the database, their impact on the eastern coast has not been thoroughly studied. In contrast, tsunami-related forecasts in Japan are executed within 3 minutes after an earthquake and include various local

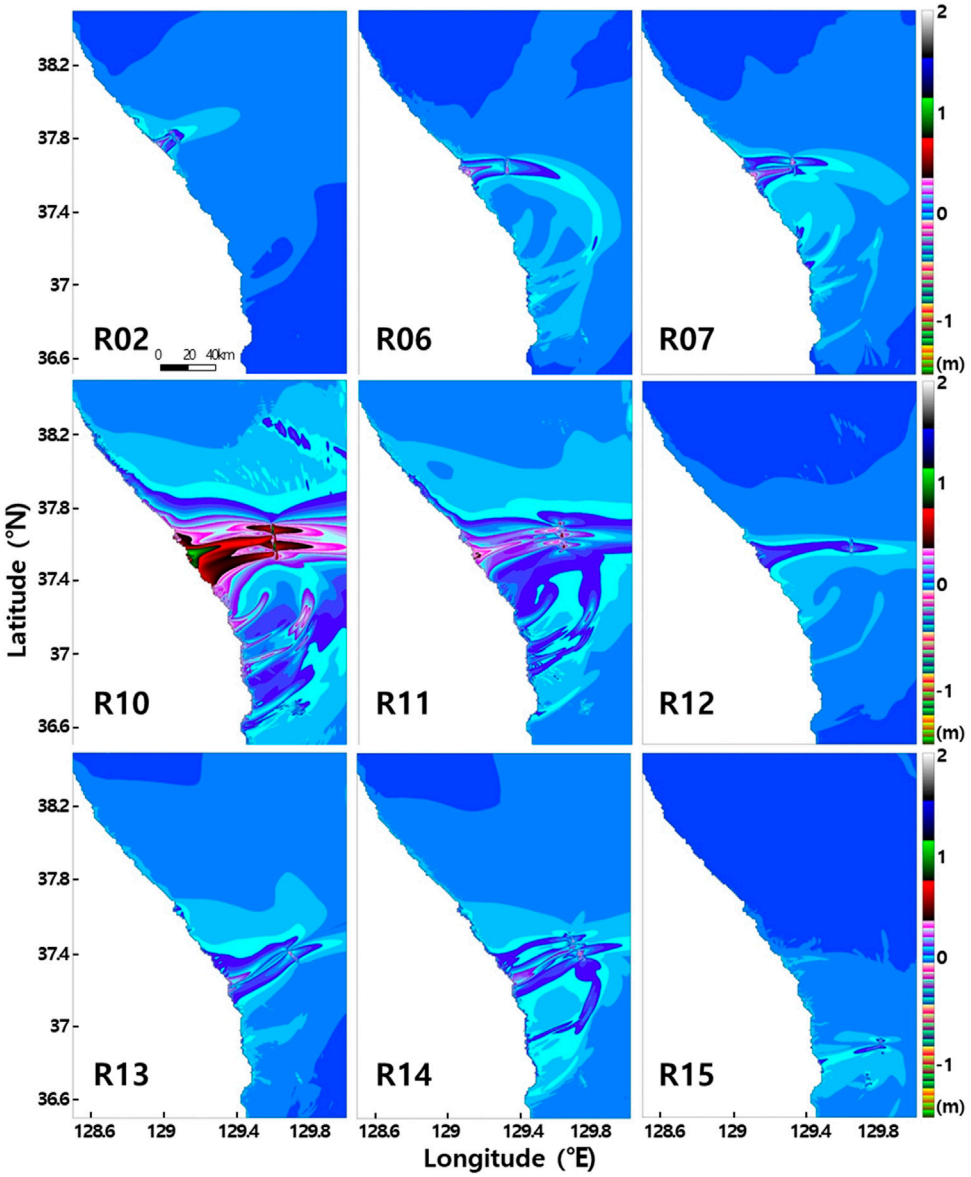

FIGURE 6 | Maximum wave height of tsunamis in the East Sea, estimated from numerical modeling for different scenarios (fault zones; Combination A).

tsunami scenarios. A rapid warning system for forecasting local tsunamis has not been established in South Korea's national tsunami disaster prevention measures, meaning that potentially hazardous tsunamis (with wave heights above a certain level, for example, higher than 1.0 m near the Samcheok area) may occur without warning. In addition, tsunamis could reach the beaches of Gyeongpo, Mangsang, Maengbang, and Samcheok, which are popular summer tourist attractions, and Uljin Nuclear Power Station. However, the fault-parameter-based scenarios adopted in this study are not directly applicable to the national earthquake and tsunami forecasting system and the national disaster prevention plan because they estimate the worst-cases of tsunami threat of local tsunamis in the East Sea. Nevertheless, considering that tsunamis can lead to large-scale disasters once generated, the potential risks must be considered in advance when building the national disaster prevention system with respect to the hazard presented by tsunamis. A detailed analysis of this issue is discussed below in **Section 4.3**

4.2 Quantitative Evaluation of Local Tsunami Hazard in the East Sea

As described above, the maximum runup heights of tsunamis that can be generated on the eastern coast were calculated, and these are presented in **Figure 10**. In general, even if a grid nesting technique is used to construct a precise grid during tsunami numerical modeling, the accuracy of tsunami reproduction is low

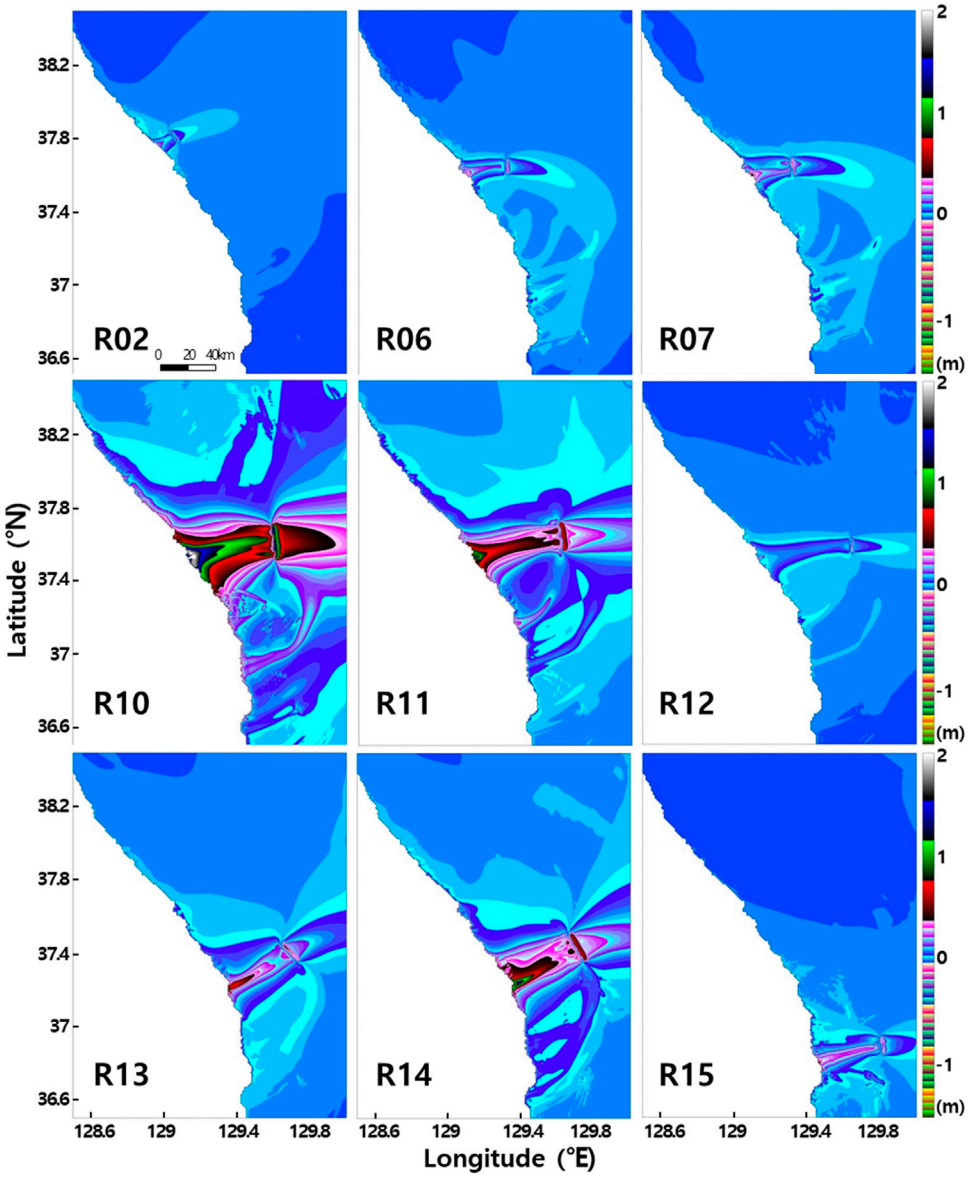

FIGURE 7 | Maximum wave height of tsunamis in the East Sea, estimated from numerical modeling for different scenarios (fault zones; Combination B).

in areas with shallow water depths and complicated bathymetry near the coast owing to the constant size of the computational grid. Calculation methods such as composing finer calculation grids near the coast are available to overcome this issue. However, such methods are time consuming and impractical to calculate for the entire peninsula. Alternatively, the Japan Meteorological Agency (JMA) applies Green's law to estimate tsunami wave heights in coastal waters with minor errors for the purpose of tsunami forecasting and warning. It has been shown that Green's law is valid only outside the source region (Fine et al., 2013; Sandanbata et al., 2018) and that tsunami runups calculated for tsunami sources outside of the source region, such as that of the 2011 Great East Japan Earthquake tsunami (which was located very close to the coastline of Japan) are very different from those calculated using Green's law. In this study, potential local tsunamis originate offshore from the eastern coast of the Korean Peninsula, meaning that Green's law can be suitably applied to estimate the probable maximum runup of tsunamis. The JMA has applied Green's law to obtain the wave height at 1 m water depth and whose value is taken as the tsunami wave height at the coast (Mulia et al., 2020). This study estimated maximum tsunami runup heights along the studied eastern Korea coastline by following the method adopted by the JMA. The risk of tsunami for the studied coastline was analyzed using the values obtained.

Figure 11 presents the maximum tsunami runup heights calculated by applying Green's law to the numerical modeling results for the studied tsunami scenarios. "Combination A″ in **Figure 11** is based on a combination of the mean value from the

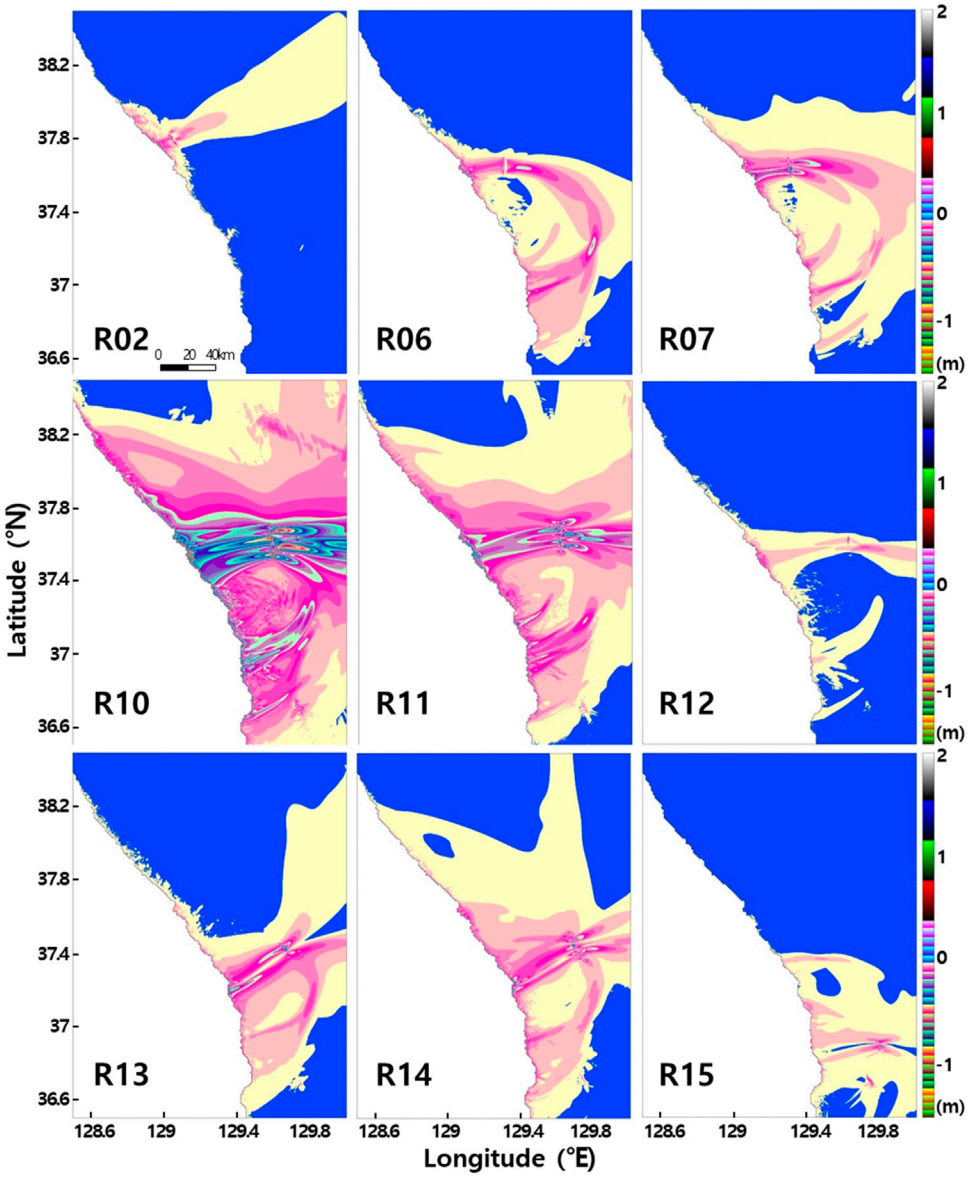

FIGURE 8 | Lowest elevation of tsunamis in the East Sea, estimated from numerical modeling for different scenarios (fault zones; Combination A).

empirical equations of Matsuda (1975) and Wells & Coppersmith (1994) and the slip angle value of the top fault zone (see **Table 1**). Results show that maximum runup heights exceeding 0.5 m in areas of 1 m water depth are widely observed. In particular, high runup heights of >2.0 m are estimated to occur across a wide area along the studied coastline for scenario R10. This wide area includes beaches, where approximately one million tourists visit on an average day during summer. Therefore, an early warning system and a plan for immediate evacuation of residents and tourists to safe locations are essential. In contrast, port infrastructure located on the eastern coast may be fairly safe with respect to the estimated tsunami wave heights, as they have ~3.0 m freeboards, but vessels inside the harbors may be damaged. Lynett P. et al. (2012) found that local tsunamis with the highest tsunami wave height less than 0.5 m can generate extreme currents in harbors, causing economic loss, and tsunami-induced currents near the coast should be carefully considered in addition to tsunami wave heights when evaluating tsunami hazards.

"Combination B″ in **Figure 11** is based on a combination of the mean slip angle value (see **Table 1**) of the tsunami-instigating fault zone and the amplified initial sea surface displacement due to an upward adjustment of fault zones along with the mean displacement value from five empirical equations (see **Table 3**). In contrast to the results from Combination A, maximum runup heights were estimated to exceed 1.5 m at a 1 m water depth for some areas. In particular, for scenarios R7, R10, and R11, runup heights were predicted to exceed 4.0 m, potentially inundating large areas and threatening human lives, property, and infrastructure along the eastern coast. Therefore, additional research into forecasting

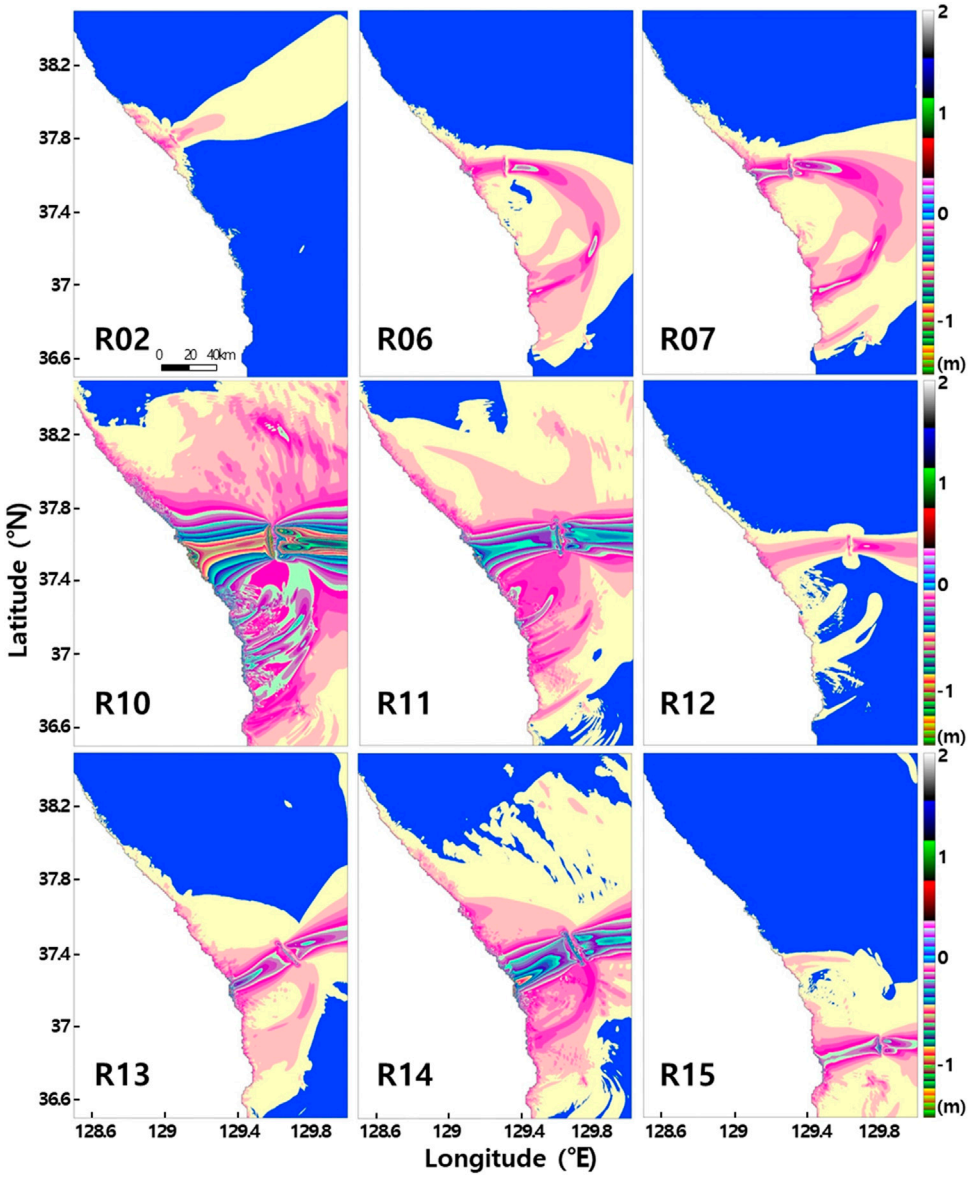

FIGURE 9 | Lowest elevation of tsunamis in the East Sea, estimated from numerical modeling for different scenarios (fault zones; Combination B).

tsunamis and the propagation of tsunami energy for risk assessment of coastal areas is necessary, possibly implementing recently proposed methodologies, such as new the paradigm for mass, momentum, and energy of nearshore tsunamis developed by Kim and Son (2018, 2019).

4.3 Scenario-Based Assessment of the Potential Threat and Damage Caused by Local Tsunamis in the East Sea

The 2011 Great East Japan Earthquake tsunami was an extremely large tsunami with an estimated recurrence interval of ≥1000 years, and it caused damage estimated at 300 billion U.S. dollars (Daniell et al., 2011). The Japanese government had developed its tsunami response system without considering such extremely large tsunamis in the possible range, meaning that unexpected levels and types of damage occurred, such as the inundation and meltdown of the Fukushima Nuclear Power Plant. South Korea and China were also affected by radiation derived from the nuclear accident. Japan has since entirely revised its national tsunami response system. Given the example of Japan, the threat posed by tsunamis to the eastern coastline of Korea must be properly quantified and a response system established with respect to the full range of estimated tsunami sizes.

After numerical modeling of tsunami propagation in the East Sea according to each fault parameter scenario (**Section 4.1**), an index of tsunami intensity proposed by Boschetti and Ioualalen

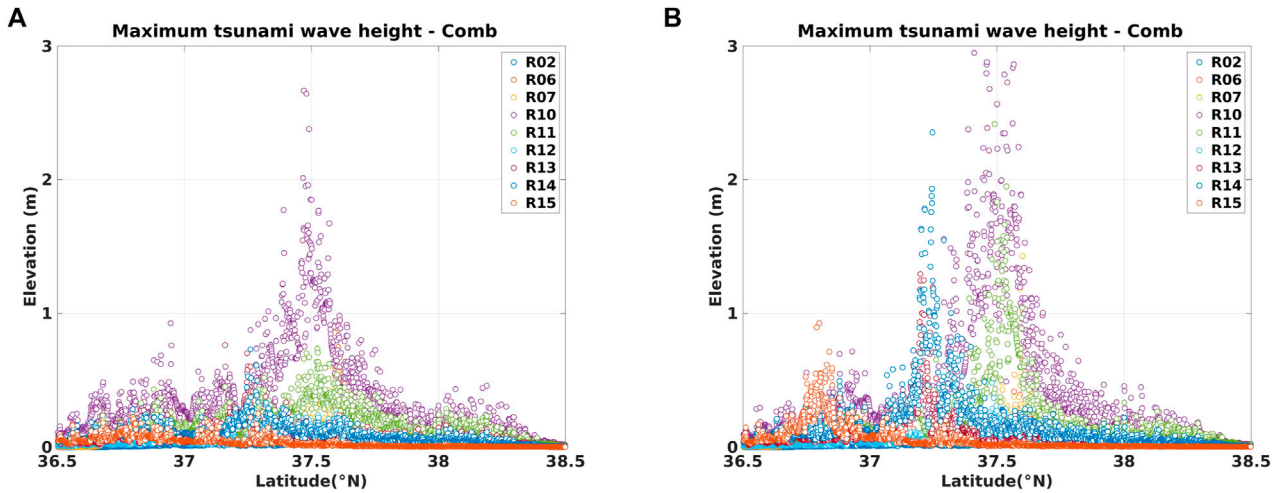

FIGURE 10 | Maximum tsunami wave height along the eastern coast of the Korean Peninsula, estimated from modeling for 11 scenarios ("R") and 2 combinations [**(A)**: Combination A; **(B)**: Combination B] of fault parameters.

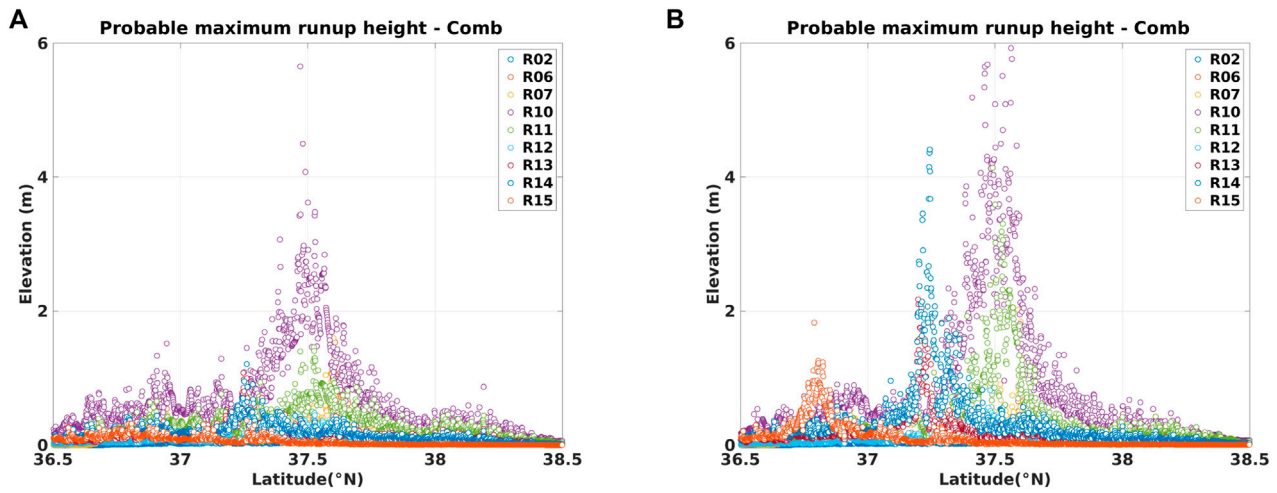

FIGURE 11 | Probable maximum runup height along the eastern coast of the Korean Peninsula estimated from modeling using Green's law for 11 scenarios ("R") and 2 combinations [**(A)**: Combination A; **(B)**: Combination B] of fault parameters.

(2021) was used to assess tsunami hazard along the eastern coast considering tsunami currents as well as tsunami wave heights. Lynett et al. (2014) first proposed the index to connect current speed of a tsunami with damage state and the index was divided into the six damage states, which were 0: no damage/impacts, 1: small buoys moved; 2: 1–2 docks/small boats damaged and/or large buoys moved; 3: moderate dock/boat damage (<25% of docks/vessels damaged) and/or midsized vessels off moorings; 4: major dock/boat damage (<50% of docks/vessels damaged) and/or large vessels off moorings; 5: extreme/complete damage (>50% of docks/vessels damaged). Boschetti and Ioualalen (2021) extended the Lynett et al.'s and integrated several approaches (Shuto, 1993; Graszk et al., 1999; Papadopoulos and Imamura, 2001; Misea, 2012; Charvet et al., 2014) connecting the tsunami magnitude to damages on structures and persons. They finally proposed the new intensity scale based on the maximum tsunami wave height and current speed [see **Section 4**, **Figure 4** and Table 5 in Boschetti and Ioualalen (2021)].

This type of assessment, which has large uncertainties and only broad constraints on data, usually demands a probabilistic approach (Geist and Parsons, 2006; Grezio et al., 2017; Satake et al., 2022). The present study, however, was originally motivated by historical evidence for possible tsunami events initiated in the East Sea and affecting the eastern coast of the Korean Peninsula. The possible tsunami events recorded in the Diaries of the Royal Secretariat contained anecdotal evidence that was interpreted in terms of the expected behavior of a tsunami, so the evidence was

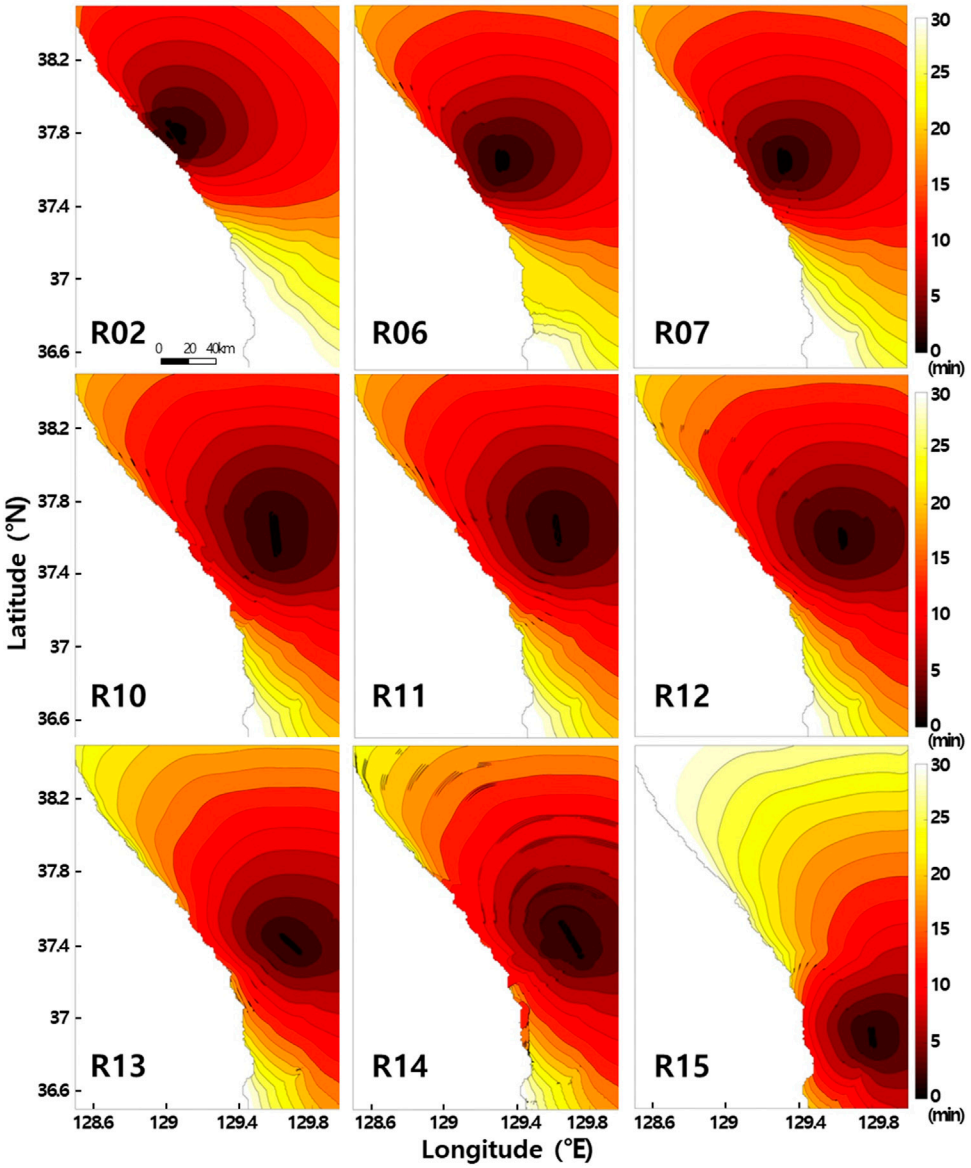

FIGURE 12 | Modeled propagation extent (distance) and arrival time to the eastern Korean coast of tsunamis generated in the East Sea for various scenarios.

validated qualitatively rather than involving detailed hindcasting. Therefore, an index of tsunami intensity, rather than probabilistic tsunami hazard analysis, was employed to evaluate tsunami threat along the Korean coast of the East Sea. **Figure 13** presents the estimated latitudinal distribution of the index of tsunami intensity calculated using combinations A and B. The fault-parameter scenario generating the most damage on the studied coast was R10 in both combinations, and the highest level of tsunami intensity observed along the coast was 6. In comparison with tsunami wave height, tsunami-induced currents produced smaller effects on tsunami intensity for both combinations, but they resulted in the higher values of tsunami intensity estimated for Combination B compared with Combination A. As a result, a highest level of tsunami intensity of 6 was reached for scenarios R07, R10, and R11 in Combination B, whereas only R10 reached this value in Combination A.

An estimated runup height of >11.0 m could occur in a scenario R10, which could generate considerable damage at the coast. The fault-parameter scenarios examined in this study were generated based on past observational data, including seismic survey records, and it is concerned that excessive variables can be introduced for fault parameter scenarios. Few raised doubts on the realistic response and relevant research for the coastal waters of the Korean Peninsula, which had no risk of tsunami occurrence in the last hundreds of years. However, it is important to note that the Japanese government did not consider the 2011 Great East Japan

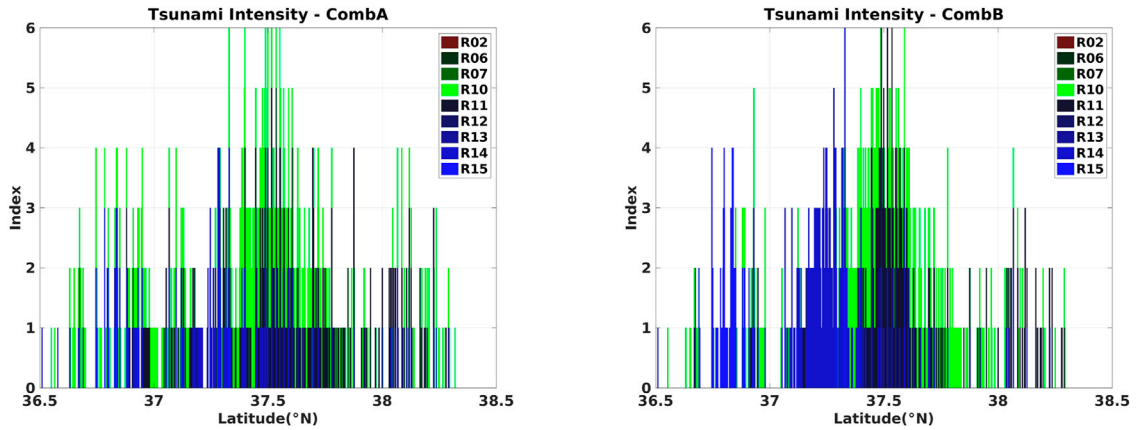

FIGURE 13 | Estimated index of tsunami intensity for the eastern coast of the Korean Peninsula for 11 scenarios ("R") and 2 combinations [**(A)**: Combination A; **(B)**: Combination B] of fault parameters.

Earthquake tsunami as a possible scenario in their economic and political decision-making process, despite Japanese scientists being aware of the possibility of such large tsunami-causing earthquakes (Synolakis and Kanoglu, 2015). Furthermore, coastal events that can be regarded as local tsunamis in the East Sea have been recorded in the historical literature for various parts of the eastern coast of Korea. Underestimating the threat posed by tsunamis is a risk in terms of potential loss of human life and infrastructural and economic damage. The present study examined local tsunamis with the aim of better understanding their occurrence and impact as a basis for informing the development of a prediction and warning system and the establishment of mitigation measures. It should be noted that this study did not consider a fault parameter scenario in which simultaneous tsunamis were generated by simultaneously activated multiple fault zones, as was the case for the 2011 Great East Japan Earthquake tsunami. Such a large-magnitude-tsunami scenario for the eastern coast of Korea was considered to be immoderate although we estimated the most extreme conditions of local tsunamis based on past observational data, including seismic survey records.

5 CONCLUDING REMARKS

In this study, we assessed the possibility of a submarine earthquake occurring in the East Sea by examining historical records and investigating fault zones, and modeled the propagation of a potential local tsunami along the East Sea coast of the Korean Peninsula. Tsunami numerical modeling with different scenarios of fault parameters reproduced the features inferred from presumed tsunamis recorded in the historical documents, including the maximum runup height, which was consistent with the range interpreted from historical records. The historical records and numerical modeling results from this study suggest that local tsunamis have occurred on the eastern seaboard of Korea in the past and are therefore likely to do so in the future. Our results should help inform tsunami forecasting, preparedness, and mitigation on the eastern coast of Korea, including the development of warning systems and the inclusion of tsunami hazards in the national disaster prevention system.

DATA AVAILABILITY STATEMENT

The original contributions presented in the study are included in the article/supplementary material, further inquiries can be directed to the corresponding author.

AUTHOR CONTRIBUTIONS

TH applied the methodology and drafted the manuscript; TH and K-HK critically revised the paper and supervised the study; JK, S-HY, D-WL, and J-SY provided suggestions on the results. All authors contributed to the article and approved the submitted version.

FUNDING

This work was funded by the Korea Meteorological Administration Research and Development Program under Grant KMI2022-00610 and the Basic Science Research Program through the National Research Foundation of Korea (NRF) funded by the Ministry of Science and ICT (NRF-2020R1A2C2011751).

REFERENCES

Anderson, J. R. (1996). ACT: A Simple Theory of Complex Cognition. *Am. Psychol.* 51 (4), 355–365. doi:10.1037/0003-066x.51.4.355

Bonilla, M. G., Villalobos, H. A., and Wallace, R. E. (1984). Exploratory Trench across the Pleasant Valley Fault, Nevada. *Prof. Pap. U.S. Geol. Surv.* 1274, 1–34.

Boschetti, L., and Ioualalen, M. (2021). Integrated Tsunami Intensity Scale Based on Maxima of Tsunami Amplitude and Induced Current. *Nat. Hazards* 105 (1), 815–839. doi:10.1007/s11069-020-04338-5

Butler, R., Stewart, G. S., and Kanamori, H. (1979). The July 27, 1976 Tangshan, China Earthquake-A Complex Sequence of Intraplate Events. *Bull. Seismol. Soc. Am.* 69 (1), 207–220. doi:10.1785/bssa0690010207

Chai, M. F., Lau, T. L., and Majid, T. A. (2014). RETRACTED: Potential Impacts of the Brunei Slide Tsunami over East Malaysia and Brunei Darussalam. *Ocean. Eng.* 81, 69–76. doi:10.1016/j.oceaneng.2014.02.028

Charvet, I., Suppasri, A., and Imamura, F. (2014). Empirical Fragility Analysis of Building Damage Caused by the 2011 Great East Japan Tsunami in Ishinomaki City Using Ordinal Regression, and Influence of Key Geographical Features. *Stoch. Environ. Res. Risk Assess.* 28, 1853–1867. doi:10.1007/s00477-014-0850-2

Chiu, J.-M., and Kim, S. G. (2004). Estimation of Regional Seismic Hazard in the Korean Peninsula Using Historical Earthquake Data between A.D. 2 and 1995. *Bull. Seismol. Soc. Am.* 94, 269–284. doi:10.1785/0120010256

Daniell, J. E., Khazai, B., Wenzel, F., and Vervaeck, A. (2011). The CATDAT Damaging Earthquakes Database. *Nat. Hazards Earth Syst. Sci.* 11 (8), 2235–2251. doi:10.5194/nhess-11-2235-2011

Fine, I. V., Kulikov, E. A., and Cherniawsky, J. Y. (2013). Japan's 2011 Tsunami: Characteristics of Wave Propagation from Observations and Numerical Modelling. *Pure Appl. Geophys.* 170, 1295–1307. doi:10.1007/s00024-012-0555-8

GEBCO Compilation Group (2021). *GEBCO 2021 Grid*. Berlin: GEBCO. doi:10.5285/a29c5465-b138-234d-e053-6c86abc040b9

Geist, E. L., and Parsons, T. (2006). Probabilistic Analysis of Tsunami Hazards*. *Nat. Hazards* 37 (3), 277–314. doi:10.1007/s11069-005-4646-z

Graszk, E., Roy, J. L., Garry, G., Guyot, P., and Hubert, T. (1999). *Plans de prévention des risques naturels (PPR): Risques d'inondation—Guide méthodologique*. Paris, Aubervilliers: La documentation Française.

Grezio, A., Babeyko, A., Baptista, M. A., Behrens, J., Costa, A., Davies, G., Geist, E. L., Glimsdal, S., González, F. I., Griffin, J., Harbitz, C. B., LeVeque, R. J., Lorito, S., Løvholt, F., Omira, R., Mueller, C., Paris, R., Parsons, T., Polet, J., Power, W., Selva, J., Sørensen, M. B., and Thio, H. K. (2017). Probabilistic Tsunami Hazard Analysis: Multiple Sources and Global Applications. *Rev. Geophys.* 55 (4), 1158–1198. doi:10.1002/2017rg000579

Ha, T., and Cho, Y.-S. (2015). Tsunami Propagation over Varying Water Depths. *Ocean. Eng.* 101, 67–77. doi:10.1016/j.oceaneng.2015.04.006

Han, M., Kim, H.-J., Kang, S. Y., Kim, K.-H., Yoon, S. H., and Kyung, J. B. (2019). Detection of Microearthquakes and Identification of Their Causative Structures in the Eastern Offshore Region of South Korea. *Tectonophysics* 750, 36–44.

Johnston, A. C., and Schweig, E. S. (1996). The Enigma of the New Madrid Earthquakes of 1811–1812. *Annu. Rev. Earth Planet. Sci.* 24, 339–384. doi:10.1146/annurev.earth.24.1.339

KIGAM (2016). *Marine Geological and Geophysical Mapping of the Korean Seas*. Daejeon, South Korea: Ministry of Science, ICT and Future Planning.

KIGAM (2010). *Study on the Coastal Geohazard Factors Analysis*. Daejeon, South Korea: Ministry of Land, Infrastructure, and Transport.

Kim, C. S. (1982). Submarine Geology of Continental Margin of the East Sea, Korea. *Min. Geol.* 15, 65–88.

Kim, D.-H., and Son, S. (2019). Role of Shelf Geometry and Wave Breaking in Single N-type Tsunami Runup under Geophysical-Scale. *Ocean. Model.* 138, 13–22. doi:10.1016/j.ocemod.2019.05.001

Kim, D. H., and Son, S. (2018). Lagrangian-like Volume Tracking Paradigm for Mass, Momentum and Energy of Nearshore Tsunamis and Damping Mechanism. *Sci. Rep.* 8 (1), 1–11. doi:10.1038/s41598-018-32439-6

Kim, K.-H., Kang, T.-S., Rhie, J., Kim, Y., Park, Y., Kang, S. Y., et al. (2016). The 12 September 2016 Gyeongju Earthquakes: 2. Temporary Seismic Network for Monitoring Aftershocks. *Geosci. J.* 20, 753–757. doi:10.1007/s12303-016-0034-9

Kim, K.-H., Ree, J.-H., Kim, Y., Kim, S., Kang, S. Y., and Seo, W. (2018b). Assessing whether the 2017 M W 5.4 Pohang Earthquake in South Korea Was an Induced Event. *Science* 360, 1007–1009. doi:10.1126/science.aat6081

Kim, K. H., Kim, J., Han, M., Kang, S. Y., Son, M., Kang, T. S., et al. (2018a). Deep Fault Plane Revealed by High-Precision Locations of Early Aftershocks Following the 12 September 2016 ML 5.8 Gyeongju, Korea, Earthquake. *Bull. Seismol. Soc. Am.* 108, 517–523. doi:10.1785/0120170104

Kim, K. H., Yoon, S. H., Kyung, J. B., Seo, M. C., Kim, J. K., and Ha, T. (2018c). *Seismicity in the West Sea and the Evaluation of Localized Tsunami Potential in the East Sea*. Seoul: Korea Meteorological Administration.

Kyung, J. B., Jung, M. K., Baek, J. J., Im, Y. J., and Lee, K. (2010). *Historic Earthquake Catalog in the Korea Peninsula*. Seoul: Korea Meteorological Administration, 475.

Lee, E., Jung, T., Kim, J.-C., and Shin, S. (2019a). A Study of the Optimal Deployment of Tsunami Observation Instruments in Korea. *J. Ocean. Eng. Technol.* 33 (6), 607–614. doi:10.26748/ksoe.2019.100

Lee, K., and Yang, W. S. (2006). Historical Seismicity of Korea. *Bull. Seismol. Soc. Am.* 96, 846–855. doi:10.1785/0120050050

Lee, W.-D., Kim, J.-O., and Hur, D.-S. (2019b). Effects of Waveform Distribution of Tsunami-like Solitary Wave on Run-Up on Impermeable Slope. *J. Ocean. Eng. Technol.* 33 (1), 76–84. doi:10.26748/ksoe.2018.059

Lynett, P. J., Borrero, J. C., Weiss, R., Son, S., Greer, D., and Renteria, W. (2012a). Observations and Modeling of Tsunami-Induced Currents in Ports and Harbors. *Earth Planet. Sci. Lett.* 327-328, 68–74. doi:10.16/j.epsl.2012.02.002

Lynett, P. J., Borrero, J., Son, S., Wilson, R., and Miller, K. (2014). Assessment of the Tsunami-Induced Current Hazard. *Geophys. Res. Lett.* 41 (6), 2048–2055. doi:10.1002/2013gl058680

Lynett, P., Weiss, R., Renteria, W., De La Torre Morales, G., Son, S., Arcos, M. E. M., et al. (2012b). Coastal Impacts of the March 11th Tohoku, Japan Tsunami in the Galapagos Islands. *Pure Appl. Geophys.* 170, 1189–1206. doi:10.1007/s00024-012-0568-3

Matsuda, T. (1975). Magnitude and Recurrence Interval of Earthquakes from a Fault. *Jssj* 28, 269–283. doi:10.4294/zisin1948.28.3_269

Ministry of Public Safety and Security (2017). *Earthquake Whitepaper*. Seoul, Korea: Ministry of Interior and Safety.

Ministry of the Interior and Safety (2018). *Pohang Earthquake Whitepaper*. Seoul, Korea: Ministry of Interior and Safety.

Miseà, j. (2012). "Plan de prévention des risques naturels d'inondation: Bassin versant de l'Etang de Thau, Commune de Villeveyrac," in *Direction Départementale des Territoires et de la Mer—Service Eau et Risques* (Paris, Aubervilliers: Préfecture de l'Hérault).

Mulia, I. E., Ishibe, T., Satake, K., Gusman, A. R., and Murotani, S. (2020). Regional Probabilistic Tsunami Hazard Assessment Associated with Active Faults along the Eastern Margin of the Sea of Japan. *Earth Planets Space* 72 (1), 1–15. doi:10.1186/s40623-020-01256-5

Okada, Y. (1985). Surface Deformation Due to Shear and Tensile Faults in a Half-Space. *Bull. Seismol. Soc. Am.* 75 (4), 1135–1154. doi:10.1785/bssa0750041135

Papadopoulos, G. A., and Imamura, F. (2001). "A Proposal for a New Tsunami Intensity Scale," in Int. Tsunami Symp. 2001 Proc, 7–9 Aug. 2001 (Seattle, Washington: IOC/UNESCO), 569–577.

Park, S.-C., and Mori, J. (2005). Source Parameters of the May 29, 2004 South Korea Earthquake (ML 5.2). *Earth, Planets Space* 57, 471–475.

Park, S.-C., You, S., Choi, M., and Lee, H.-W. (2020). Application of Tsunami Scenario Database and Numerical Simulation to Tsunami Warning and Notification Process. *Korea Soc. Coast. Disaster Prev.* 7 (1), 11–20. doi:10.20481/kscdp.2020.7.1.11

Sandanbata, O., Watada, S., Satake, K., Fukao, Y., Sugioka, H., Ito, A., et al. (2018). Ray Tracing for Dispersive Tsunamis and Source Amplitude Estimation Based on Green's Law: Application to the 2015 Volcanic Tsunami Earthquake Near Torishima, South of Japan. *Pure Appl. Geophys.* 175, 1371–1385. doi:10.1007/s00024-017-1746-0

Satake, K., Ishibe, T., Murotani, S., Mulia, I. E., and Gusman, A. R. (2022). Effects of Uncertainty in Fault Parameters on Deterministic Tsunami Hazard Assessment: Examples for Active Faults along the Eastern Margin of the Sea of Japan. *Earth Planets Space* 74 (1), 1–20. doi:10.1186/s40623-022-01594-6

Schluter, H. V., and Chun, W. C. (1974). Seismic Survey of the East Coast of Korea. *U. N. ECAFE/CCOP Tech. Bull.* 8, 1–16.

Shuto, N. (1993). "Tsunami Intensity and Disasters," in *Tsunamis in the World*. Editor S. Tinti (Dordrech: Kluwer Academic Publishers), 197–216. doi:10.1007/978-94-017-3620-6_15

Slemmons, D. B. (1988). "Crustal Extension: Continental Extensional Tectonics," in *Published for the Geological Society by Blackweil Scientific*. Editors M. P. Coward, J. F. Dewey, and P. L. Hancock (Palo Alto, CA: Geological Society Special Publication). doi:10.1126/science.239.4844.1185.a

Son, S., Lynett, P. J., and Kim, D.-H. (2011). Nested and Multi-Physics Modeling of Tsunami Evolution from Generation to Inundation. *Ocean. Model.* 38 (1-2), 96–113. doi:10.1016/j.ocemod.2011.02.007

Synolakis, C., and Kânoğlu, U. (2015). The Fukushima Accident Was Preventable. *Phil. Trans. R. Soc. A* 373, 20140379. doi:10.1098/rsta.2014.0379

Vakov, A. V. (1996). Relationships between Earthquake Magnitude, Source Geometry and Slip Mechanism. *Tectonophysics* 261 (1-3), 97–113. doi:10.1016/0040-1951(96)82672-2

Wang, X., and Liu, P. L.-F. (2011). An Explicit Finite Difference Model for Simulating Weakly Nonlinear and Weakly Dispersive Waves over Slowly Varying Water Depth. *Coast. Eng.* 58, 173–183. doi:10.1016/j.coastaleng.2010.09.008

Wang, X. (2009). *User Manual for COMCOT Version 1.7*. New Zealand: Institute of Geological & Nuclear Science.

Wells, D. L., and Coppersmith, K. J. (1994). New Empirical Relationships Among Magnitude, Rupture Length, Rupture Width, Rupture Area, and Surface Displacement. *Bull. Seismol. Soc. Am.* 84 (4), 974–1002.

Wessel, P., Smith, W. H. F., Scharroo, R., Luis, J., and Wobbe, F. (1998). Generic Mapping Tools: Improved Version Released. *EOS Trans. Amer. Geophys. U.* 94 (45), 409–410.

Wijetunge, J. J. (2012). Nearshore Tsunami Amplitudes off Sri Lanka Due to Probable Worst-Case Seismic Scenarios in the Indian Ocean. *Coast. Eng.* 64, 47–56. doi:10.1016/j.coastaleng.2012.02.005

Yoo, S. C., Mun, J. Y., Park, W., Seo, G. H., Gwon, S. J., and Heo, R. (2019). Development of Bathymetric Data for Ocean Numerical Model Using Sea-Floor Topography Data: BADA ver.1. *J. Korean Soc. Coast Ocean. Eng.* 31 (3), 146–157. doi:10.9765/kscoe.2019.31.3.146

Yoon, S.-H., Kim, G. B., Joe, Y. J., Koh, C. S., and Kwon, Y. K. (2015). Origin and Evolution of Geologic Basement in the Korean Continental Margin of East Sea, Based on the Analysis of Seismic Reflection Profiles. *jgsk* 51 (1), 37–52. doi:10.14770/jgsk.2015.51.1.37

Yoon, S. H. (1994). The Eastern Continental Margin of Korea: Seismic Stratigraphy, Geologic Structure and Tectonic Evolution. Seoul: Seoul National University. Ph.D. thesis.

Conflict of Interest: JSY is employed by the Korea Rural Community Corporation.

The remaining authors declare that the research was conducted in the absence of any commercial or financial relationships that could be construed as a potential conflict of interest.

Advantages of publishing in Frontiers

OPEN ACCESS
Articles are free to read for greatest visibility and readership

FAST PUBLICATION
Around 90 days from submission to decision

HIGH QUALITY PEER-REVIEW
Rigorous, collaborative, and constructive peer-review

TRANSPARENT PEER-REVIEW
Editors and reviewers acknowledged by name on published articles

Frontiers
Avenue du Tribunal-Fédéral 34
1005 Lausanne | Switzerland

Visit us: www.frontiersin.org
Contact us: frontiersin.org/about/contact

REPRODUCIBILITY OF RESEARCH
Support open data and methods to enhance research reproducibility

DIGITAL PUBLISHING
Articles designed for optimal readership across devices

FOLLOW US
@frontiersin

IMPACT METRICS
Advanced article metrics track visibility across digital media

EXTENSIVE PROMOTION
Marketing and promotion of impactful research

LOOP RESEARCH NETWORK
Our network increases your article's readership